
THE UNIVERSITY
*of* EDINBURGH

# Investigating the protein targets of the neuroprotective E3 ligase, CHIP

**Catarina Dias**


THE UNIVERSITY
*of* EDINBURGH

Doctor of Philosophy

The University of Edinburgh

2019

# Declaration

I hereby declare that I am the author of this thesis. The work herein is entirely my own unless otherwise clearly indicated and acknowledged. I can confirm that this thesis has been submitted for the degree of Doctor of Philosophy and no part of this work has been submitted for any other degree or professional qualification.

Catarina Dias

October 2019

*In memory of a fighter of dementia, Aurora Dias Madaleno*

# Acknowledgements

It is only when you step outside of your comfort zone that you truly discover yourself and conquer great things. This PhD experience has certainly been proof of this. To overcome this challenge in a “controlled” manner (i.e. while keeping sane!), I relied on my support system.

First of all, I would like to express my deepest gratitude to my supervisor, Kathryn L. Ball. For believing in me since that very first PhD interview that I attended at the University of Edinburgh, where she stood quietly within the panel, but recruited me once the right opportunity arose. I thank you, Kathryn, for teaching me your way of perceiving science differently, for all your guidance and trust, and for giving me the creative freedom that is essential when discovering the unknown. Beyond being my advocate in the world of science, I appreciate all the advice you gave me outside of science.

Secondly, I would like to thank my second supervisor, Tilo Kunath, for everything that he taught me, for his motivation and contagious happiness. I also owe a big thank you to Jesper Nylandsted, who hosted me so wonderfully in his lab and opened doors of opportunities for me. Ted Hupp was also very supportive during my PhD and his intellectual insight was like a breath of fresh air at key stages. Similarly, I cannot stress enough how thankful I am of everyone from Kathryn’s, Ted’s and Tilo’s groups who were present during my time, for the friendships and support. In particular, Ashita, Erisa, Maria, Ainhoa, Jack, Jia, Fiona, Aiman, Stephen, Nicola, Yixi and Karamjit, who actively contributed to my project in one form or another.

I want to thank our collaborators, Dr Jakub Faktor, Dr Bořivoj Vojtesek, Dr Jimi Wills, Dr Alex von Kriegsheim, Dr Irena Dapic and Dr Laura Bindila, and past students in the lab (Vikram, Mariana and Jia), from whom I gratefully “inherited” plasmids, antibodies and recombinant proteins. With regards to my funding body, Alzheimer’s Research UK, I am thankful for believing in our project and for all the opportunities that I had to represent this charity as vice-president of the Alzheimer’s Research UK Edinburgh Fundraising Group.

Undoubtedly, the main people who made sure I kept my balance and remained positive throughout this journey were my parents, my brother, close friends and

husband-to-be. I thank my parents not only for believing in the power of an international education and experience, but for giving me the foundations to study abroad. Thank you for teaching me that we are responsible for everything the we do, the good and the bad, and for reminding me that beyond chasing opportunities, we have to be open to embrace them once they arrive.

Henrique, thank you for always being there for me and for knowing what I need before I realise it. You showed me the value of leaving my comfort zone, helped me manage the anxiety along the way and took me on countless “escapes”. Above all, thank you for relocating twice during my PhD, for us. These 3.5 years have definitely been the most fulfilling, both personally and professionally, with lots of milestones achieved.

But with me every day was this view. It reminded me that when it gets dark eventually rays of light shine through, and if you focus on the light you see/achieve great things. Thank you, Kathryn, for allocating me the lab bench with the best view over the city and castle of Edinburgh!

# Abstract

Identifying early defects in protein homeostasis (“proteostasis”) in neurodegeneration could shed light into disease-promoting events and provide promising therapeutic targets for disease modification. A key player in the regulation of proteostasis is the dual function chaperone and E3 ligase C-terminus of Hsc-70 interacting protein (CHIP). Its role in neurodegenerative diseases, including dementia with Lewy bodies, and the severe progeria and proteotoxic phenotype seen in CHIP KO mice support its neuroprotective effects, but the underpinning molecular mechanisms remain largely unknown and understudied. This project aimed to identify the protein targets of CHIP in a neuronal cell model of disease.

I knocked out CHIP expression using CRISPR/Cas9 technology from induced-pluripotent stem cells (iPSC) derived from a synucleinopathy patient with dementia and differentiated them into cortical neurons. A label-free quantitative mass spectrometry to analyse CHIP-dependent changes was conducted and the proteome defined. This comparative proteomic analysis revealed that of all the proteins identified and significantly changed between CHIP KO and WT lines, only 35 proteins could be (directly or indirectly) regulated by CHIP. This supports the emerging hypothesis that CHIP can be chaperone-independent docking-dependent E3 ligase, having tight specificity for substrates, in this model of synucleinopathy with mild proteotoxic stress.

Annexin and other calcium-binding proteins, in particular Annexin A2 and its interacting protein S100-A11, were the most over-represented proteins in the CHIP KO cortical neurons. From this comprehensive target discovery investigation, I have validated Annexin A2 increases in CHIP KO cells and have detected an endogenous Annexin A2:CHIP interaction, both *in vitro* and *in situ*, in different CHIP cell models. Moreover, CHIP-dependent ubiquitination of Annexin A2 was also identified, both *in vitro* and *in situ*. Single-chain antibodies against CHIP have been engineered to modulate its activity. By collapsing the higher molecular weight structures of CHIP, CHIP-dependent ubiquitination of Annexin A2, but not other substrates, is enhanced.

Annexins are a conserved family of calcium-regulated phospholipid-binding proteins that are required for membrane repair and maintenance of membrane homeostasis. Given these functions, several types of membrane damage assays were conducted

and suggested that CHIP KO cells are more sensitive to damage, despite retaining the ability to repair. This impairment in membrane resilience was also seen in CHIP KO cells expressing a E3 ligase-dead CHIP mutant, but the phenotype was partly rescued in the cell lines expressing a chaperone-dead CHIP mutant or wild-type CHIP. Compromised Annexin A2:S100A11 interactions (important for the repair complex) and a different lipidomic profile between CHIP WT and KO cells could contribute to this phenotype.

Although there are reports of annexins being overexpressed in some neurodegenerative diseases, there have been no follow-up studies deciphering the molecular mechanisms of annexins within neurons. I have identified Annexin A2 as a substrate for CHIP and revealed other novel calcium-regulated membrane-binding CHIP targets. Thus, CHIP is likely to play a role in regulating membrane protein homeostasis and maintaining membrane integrity, which may help to explain the neuroprotective actions of CHIP. This is of relevance within the emerging field of impaired membrane integrity in the context of neurodegeneration.

# Lay Summary

Neurodegeneration is a progressive phenomenon where brain cells (neurons) become gradually worse in health and eventually die. Identifying early changes to their repertoire of proteins may shed light into disease-promoting events and provide promising therapeutic targets for disease modification. A key player in the regulation of proteins is an enzyme called CHIP, which is both capable of acting as a chaperone for misfolded proteins and signalling them for degradation. Its role in neurodegenerative diseases and the rapid ageing and cellular toxicity seen in mice lacking CHIP support its neuroprotective effects. How this happens mechanistically is largely unknown and understudied. This project aimed to identify the protein targets of CHIP in a brain cell model of disease.

To address this aim, I deleted the CHIP protein from stem cells derived from a Parkinson's patient with dementia (a type of neurodegenerative disease) and engineered them to become neurons similar to the ones found in the area of the brain affected in patients of dementia, the cortex. I did a deep analysis of the repertoire of proteins in these neurons (with and without CHIP), to identify CHIP-dependent changes. Of all the proteins identified, only 35 proteins seem to be changed between the neurons with and without CHIP. This supports the emerging school of thought that CHIP can regulate a tight subset of proteins in our model of disease, rather than affecting multiple proteins.

The protein levels of Annexin A2 are higher in neurons lacking CHIP. In different CHIP cell models, CHIP was shown to interact with Annexin A2. Furthermore, a CHIP-dependent addition to Annexin A2 protein was identified, and I have engineered antibodies targeting CHIP that stimulate this addition to Annexin A2, but not to other protein clients of CHIP.

Annexins are required for repairing and maintaining the integrity of a shielding structure that envelopes each cell (plasma membrane), as well as internal structures within the cell (intracellular membranes), to protect them from the environment. Given these functions, several experiments to induce membrane damage were conducted and suggested that CHIP KO cells are more sensitive to damage, despite retaining the ability to repair. This impairment in membrane resilience was also seen in cells lacking normal CHIP but expressing a form of CHIP that is not capable of targeting

proteins for degradation. However, this observation was reversed when cells have a form of CHIP that is not capable of being a chaperone to client proteins or when cells were re-introduced fully functional CHIP. Compromised interactions of proteins important for the membrane repair mechanism (Annexin A2 and S100-A11 proteins) and a different composition of lipids (present in membranes) between cells with and without CHIP could contribute to this phenomenon.

Although annexins have been reported to be dysregulated in some neurodegenerative diseases, there have been no follow-up studies deciphering the underlying mechanisms in neurons. We have identified Annexin A2 as a CHIP-regulated protein and have revealed other novel target proteins of the enzyme. Thus, CHIP is likely to play a role in regulating membrane-related proteins and maintaining membrane integrity, which might help to explain the neuroprotective actions of CHIP. This is of relevance within the emerging field of impaired membrane integrity in the context of neurodegeneration.

# Abbreviations

| | |
|---|---|
| **2DE** | Two-dimension electrophoresis |
| **3-MA** | 3-Methyladenine |
| **α-Syn** | α-Synuclein |
| **aa** | Amino acid |
| **Aβ** | Amyloid-β |
| **AD** | Alzheimer's disease |
| **ANOVA** | Analysis of Variance |
| **ANXA1** | Annexin A1 |
| **ANXA2** | Annexin A2 |
| **ANXA4** | Annexin A4 |
| **ANXA6** | Annexin A6 |
| **APS** | Ammonium persulphate |
| **ARCA** | Autosomal recessive cerebellar ataxia |
| **ATP** | Adenosine triphosphate |
| **BafA1** | Bafilomycin A1 |
| **BDNF** | Brain-derived neurotrophic factor |
| **bp** | Base pair |
| **BSA** | Bovine serum albumin |
| **C1P** | Ceramide-1-phosphate |
| **Cas9** | CRISPR associated protein 9 |
| **CASA** | Chaperone-assisted selective autophagy |
| **CDK5** | Cyclin-dependent kinase 5 |
| **cDNA** | Complementary DNA |
| **CDR** | Complementarity determining regions |
| **CER** | Ceramide |
| **CHIP** | C-terminus of Hsc70-interacting protein |
| **CID** | Collision-induced dissociation |
| **CMA** | Chaperone-mediated autophagy |
| **Cp** | Crossing point |
| **CRISPR** | Clustered regularly interspaced short palindromic repeats |
| **crRNA** | CRISPR RNA |
| **D** | Deuterium |
| **DAPI** | 4',6-Diamidino-2-Phenylindole |
| **DDA** | Data-dependent acquisition |
| **DHA** | Docosahexaenoic acid |
| **DIA** | Data-independent acquisition |
| **diGly** | Glycine-glycine |
| **DLB** | Dementia with Lewy bodies |
| **DMEM** | Dulbecco's Modified Eagle Media |
| **DMSO** | Dimethyl sulphoxide |
| **DNA** | Deoxyribonucleic acid |
| **dNTP** | Deoxyribonucleotide triphosphate |
| **DPA** | Docosapentaenoic acid |
| **dsDNA** | Double-stranded DNA |
| **DTT** | Dithiothreitol |

| | |
|---|---|
| **DUB** | Deubiquitinating enzyme |
| **E1** | Ubiquitin activating enzyme |
| **E2** | Ubiquitin conjugating enzyme |
| **ECL** | Enhanced chemiluminescence |
| **EDTA** | Ethylenediaminetetraacetic acid |
| **EPA** | Eicosapentaenoic acid |
| **ER** | Endoplasmic reticulum |
| **Fab** | Antigen-binding fragment |
| **FASP** | Filter-aided sample preparation |
| **FBS** | Fetal bovine serum |
| **FGF2** | Fibroblast growth factor 2 |
| **GDNF** | Glial-derived neurotrophic factor |
| **GFAP** | Glial fibrillary associated protein |
| **GFP** | Green fluorescent protein |
| **gRNA** | Guide RNA |
| **HBSS** | Hank's Balanced Salt Solution |
| **HCD** | Higher-energy collisional dissociation |
| **HDR** | Homology directed repair |
| **HDX-MS** | Hydrogen/deuterium exchange-mass spectrometry |
| **HEPES** | 4-(2-hydroxyethyl)-1-piperazineethanesulfonic acid |
| **HH** | Helix-turn-helix |
| **HLA-B** | Human leukocyte antigen B |
| **HNE** | 4-hydroxy-2-nonenal |
| **HPLC** | High Performance Liquid Chromatography |
| **HRP** | Horseradish peroxidase |
| **HSP** | Heat-shock protein |
| **IAA** | Iodoacetamide |
| **IC50** | Half maximal inhibitory concentration |
| **IF** | Immunofluorescence |
| **IGR1R** | Insulin-like growth factor 1 receptor |
| **iNOS** | Inducible nitric oxide synthase |
| **INSR** | Insulin receptor |
| **IP** | Immunoprecipitation |
| **IPG** | Immobilized pH gradient |
| **iPSC** | Induced pluripotent stem cells |
| **IPTG** | Isopropyl b-D-1-thigalactopyranoside |
| **IRF-1** | Interferon regulatory factor 1 |
| **ISS** | Insulin-like growth factor 1 signalling |
| **kDa** | Kilo Dalton |
| **KO** | Knock-out |
| **LB** | Lewy body |
| **LB** | Luria-Bertani |
| **LC** | Liquid Chromatography |
| **LC-MRM** | Liquid chromatography-mass spectrometric multiple reaction monitoring |
| **LC-MS/MS** | Tandem mass spectrometry |
| **LPA** | Lysophosphatidic acid |
| **LPC** | Lysophosphatidylcholine |

| | |
|---|---|
| **LPI** | Lysophoshphatidylinositol |
| **mAb** | Monoclonal antibody |
| **MAS** | Multiple systems atrophy |
| **MDM2** | Mouse double minute 2 |
| **MHC** | Major histocompatibility complexes |
| **MMEJ** | Microhomology-mediated end joining |
| **MOPS** | 3-(N-morpholino) propanesulfonic acid |
| **mRNA** | Messenger RNA |
| **MS** | Mass spectrometry |
| **MUFA** | Monounsaturated fatty acid |
| **MW** | Molecular weight |
| **NAC** | Non-amyloid β/A4 component |
| **NHEJ** | Non-homologous end joining |
| **OCT4** | Octamer-binding transcription factor 4 |
| **OD** | Optical density |
| **ORF** | Open reading frame |
| **OS** | Phosphatidylserine |
| **OTX2** | Homeobox protein OTX2 |
| **OUT** | Orthogonal ubiquitin transfer |
| **p53** | Tumour suppressor protein 53 |
| **PA** | Phosphatidic acid |
| **pAb** | Polyclonal antibody |
| **PaeI-R** | Parkin-associated endothelin receptor-like receptor |
| **PAM** | protospacer adjacent motif |
| **PAM** | Phosphatidic acid |
| **PAX6** | Paired box gene/protein 6 |
| **PBS** | Phosphate buffered saline |
| **PC** | Phosphatidylcholine |
| **PCA** | Principal component analysis |
| **PCR** | Polymerase chain reaction |
| **PD** | Parkinson’s disease |
| **PE** | Phosphatidylethanolamine |
| **PFA** | paraformaldehyde |
| **PI** | Phosphatidylinositol |
| **PI4P** | Phosphatidylinositol 4-phosphate |
| **PKC** | Protein kinase C |
| **PLA** | Proximity ligation assay |
| **PLD** | Phospholipase D |
| **PM** | Plasma membrane |
| **PQC** | Protein quality control |
| **PS** | Phosphatidylserine |
| **PTM** | Post-translational modification |
| **PUFA** | Polyunsaturated fatty acid |
| **qRT-PCR** | Quantitative reverse transcription PCR |
| **RE** | Restriction enzyme |
| **RF** | Replicative form |
| **RING** | Really interesting new gene |
| **RNA** | Ribonucleic acid |

| | |
|---|---|
| **rpm** | Revolutions per minute |
| **RT** | Retention time |
| **SCA** | Spinocerebellar ataxia |
| **SCAR16** | Spinocerebellar ataxia autosomal recessive type 16 |
| **ScFv** | Single chain variable fragment |
| **SD** | Standard deviation |
| **SDS-PAGE** | Sodium dodecyl sulphate–polyacrylamide gel electrophoresis |
| **SEC** | Size exclusion chromatography |
| **SEM** | Standard error of mean |
| **SFA** | Saturated fatty acid |
| **siRNA** | Short interfering RNA |
| **SM** | Sphingomyelin |
| **SNARE** | Soluble N-ethylmaleimide–sensitive factor attachment protein receptor |
| **SOD** | Superoxide dismutase |
| **SPH** | Sphingosine |
| **ssDNA** | Single-stranded DNA |
| **STUB1** | STIP1 homology and U-box containing protein 1 |
| **SWATH-MS** | Sequential window acquisition of all theoretical fragment ion spectra mass spectrometry |
| **tAIF** | Truncated apoptosis-inducing factor |
| **TBP** | TATA-binding protein |
| **TCEP** | Tris 2-carboxyethyl phosphine hydrochloride |
| **TEMED** | Tetramethylethylenediamine |
| **TFA** | Trifluoroacetic acid |
| **TPR** | Tetratricopeptide repeat |
| **TR-FRET** | Time-resolved fluorescence energy transfer |
| **tracrRNA** | trans-activating crRNA |
| **Tris** | 2-amino-2-hydroxymethyl-propane-1,3-diol |
| **Ub** | Ubiquitin |
| **UFA** | Unsaturated fatty acid |
| **UIM** | Ubiquitin-interacting motif |
| **UPR** | Unfolded protein response |
| **UPS** | Ubiquitin-proteasome system |
| **UV** | Ultraviolet |
| **$V_H$** | Variable heavy-chain |
| **$V_L$** | Variable light-chain |
| **WB** | Western blot/Western blotting |
| **WT** | Deuterium |

# Contents

## Chapter 3: Engineering iPSCs to generate isogenic neuronal cell models



## Chapter 4: Effect of CHIP on the proteome

## Chapter 6: Modulating the activity of CHIP using single-chain antibodies

## Chapter 7: Final discussion & Future work

# List of figures

# List of Tables

# Chapter 1: Introduction

The majority of neurodegenerative diseases are broadly classified as proteinopathies, being defective in protein homeostasis. This thesis focuses on α-synucleinopathy, as an example of such diseases, and a key protein in the regulation of the cellular proteome, the C terminus of Hsc70-interacting protein (CHIP).

## 1.1 Protein homeostasis

### 1.1.1 Regulation of protein homeostasis

Protein homeostasis ("proteostasis") refers to the preservation of proper concentration, distribution and functions of proteins. Its regulation is key for normal cellular physiology and is achieved through the safeguarding of protein synthesis and protein quality control (PQC) mechanisms mediating protein maturation, folding and degradation. The main proteolytic routes are ubiquitin-proteasome system (UPS) and the lysosome-autophagy pathway. The proteostasis network includes >1000 accessory factors and regulatory components[1], having more than 300 different members of chaperones, co-chaperones and adaptors[2]. One can easily appreciate the importance of PQC when considering the number of proteins involved and the functional redundancy between different PQC mechanisms, all with the same function: maintain proteostasis[3].

### 1.1.2 Proteostasis regulation in neurons

The UPS plays a critical role in the spatial and temporal control of protein turnover in the nervous system - important for the maintenance and modulation of neuronal and synaptic structures and signalling complexes. The regulation of proteostasis influences neuronal activity[4], plasticity[5], development and differentiation[6]. For example, at the post-synaptic terminal, ubiquitination ensures sustained density of neurotransmitter receptors upon neurotransmitter release, thus readily influencing synaptic activity[6]. However, the precise mechanism for how local degradation of proteins is achieved in non-dividing neurons remains unclear.

Molecular chaperones and ubiquitination enzymes are also important for regulation of proteostasis via the autophagy-lysosome pathway. Its main role is to mediate the turnover of defected and aggregated proteins, multimeric complexes and whole organelles, which cannot be handled by the proteasome. Autophagy can be non-selective (chaperone-mediated autophagy (CMA)) or selective (chaperone-assisted selective autophagy (CASA)) in the degradation of cargo[7]. The latter is ubiquitin (Ub)-dependent[8]. Under normal conditions, CASA is the preferred route for lysosomal degradation, whilst CMA is induced by proteotoxic stress. Both CMA and CASA have been implicated in the regulation of proteostasis during ageing[3,7].

### 1.1.2 Dysregulation of proteostasis

It is clear that neuronal health is maintained by tightly controlled and coordinated ubiquitin-proteasomal and autophagy-lysosomal degradative events. Not surprisingly, there is growing evidence to support the involvement of the UPS in the pathogenesis of neurodegeneration. Firstly, inclusion bodies (commonly seen across neurodegenerative diseases) contain Ub, ubiquitinated proteins and other components of the UPS and, the closely connected, molecular chaperone system. Secondly, post-mortem brains of patients with Parkinson's disease (PD) and Alzheimer's disease (AD) revealed an impairment in proteasomal activity. Thirdly, mutations in UPS proteins cause neurodegenerative diseases, e.g. the E3 ligase Parkin and the deubiquitinating enzyme (DUB) UCHL1 in PD, the DUB ATX3 in spinocerebellar ataxia (SCA)[9], and a mutation in Ub that is associated with AD (causing proteasomal inhibition[10] and impairment in axonal transport[11]). Accordingly, model organisms with compromised UPS have increased neurodegeneration, e.g. SCA1 mice with loss-of-function of the E3 ligase Ube3a have more severe neurodegeneration[12]. Likewise, loss-of-function mutations of CHIP cause a multisystemic syndrome with severe neurodegeneration[13] (see Section 1.4 CHIP and neurodegeneration), and CHIP knock-out (KO) mice have increased neurodegeneration[14,15].

A common pathogenic hallmark across neurodegenerative diseases is the progressive accumulation of misfolded/unfolded proteins – reflective of a proteostasis profile that reflects a state of stress. Here, PQC mechanisms to maintain cellular

health are compromised, failing to cope with the accumulated proteins and falling into a viscous cycle of increasing protein aggregation, which causes other proteins to become sequestered, dysregulated and dysfunctional (Figure 1.1)[8]. This can promote the switch from proteasomal to autophagy pathways for protein degradation (this phenomenon is seen during ageing)[16]. In fact, with increasing severity of neurodegenerative diseases, autophagy becomes more important as the UPS capacity becomes compromised, but eventually the autophagy-lysosome pathways also eventually fail[7,8]. This results in progressive loss of proteostasis.

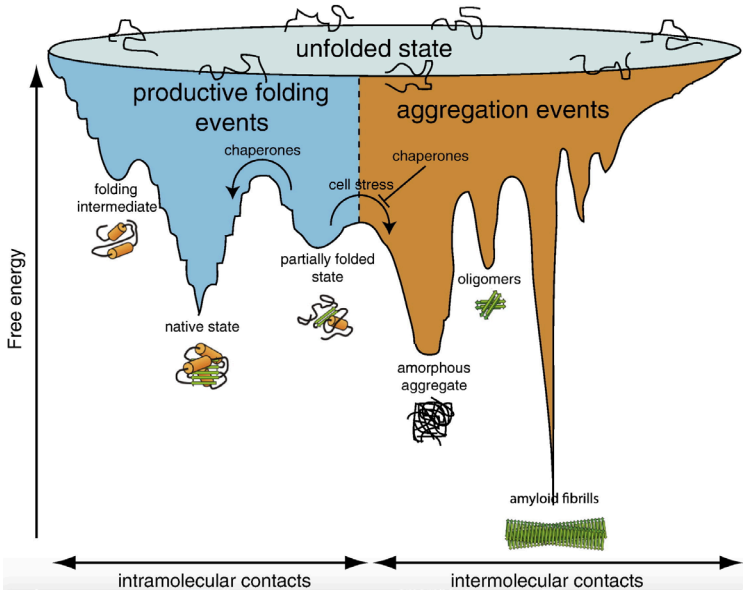


**Figure 1.1: Loss of proteostasis**
Proteins become kinetically trapped in conformations, having to overcome free-energy barriers to enter an energetically favourable folding path (with decreased free energy). These events are facilitated by chaperones. The aggregation process is biphasic: initially governed by intramolecular contacts and later by intermolecular interactions between folded proteins. Although PQC mechanisms counteract the aggregation process, eventually aggregates, toxic oligomers and amyloid fibrils form.

(Amm *et al.*[8])

The prevailing hypothesis is that aged organisms also have increased pressure on PQC mechanisms[1]. In fact, the quality of housekeeping processes dictates, at least partly, the "fitness" of cells, resulting in selective neurodegeneration and influencing the longevity of organisms. Hence, ageing is the greatest risk factor for neurodegenerative diseases.

For example, worms with increased proteasomal activity have decreased levels of polyubiquitinated proteins, a more rapid protein turnover and extended lifespan[17]. The opposite was observed in transgenic mice with decreased proteasomal activity[18] and in worm models of accelerated ageing (Figure 1.2)[19]. Thus, functionally, a decline in proteasomal activity may promote ageing[18], and has been detected in brains of AD patients[10]. Not only are proteostasis and ageing inextricably linked, they are associated to stress tolerance[1]. Worms with enhanced resistance to proteotoxic stress resistance have a longer lifespan[17]. Therefore, in the context of neurodegeneration, where cellular stress levels are high and PQC mechanisms are "aged", regulation of proteostasis is likely to be critical in the progression of disease and onset of progeria. This highlights the intimate relationship between stress, defence mechanisms, proteome status and ageing.

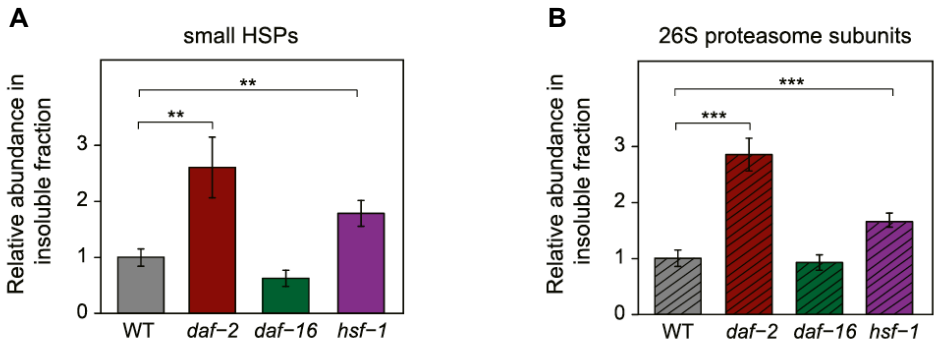


**Figure 1.2: Decline in PQC mechanisms in lifespan mutant worms**
The longevity of worms was manipulated by interfering with the insulin and insulin-like signalling pathway. Long-lived (the daf-2 mutant) and short-lived (the daf-16 and hsf-1 mutants) worms were studied. The longevity of daf-2 worms requires daf-16 activation and hsf-1 (a transcription factor of multiple chaperones and co-chaperones).
**A)** Abundance of small HSPs (6-11 different proteins) across worm models.
**B)** Abundance of proteasomal subunits (19-27 different proteins) across worm models, reflective of 26S proteasomal activity.

(Walther et al.[19])

To counteract cytotoxicity caused by misfolded proteins, multiple strategies come into play, including refolding or buffering of toxic misfolded proteins by molecular chaperones, different proteasomal and lysosomal degradative branches, and processing of aggresomes[20]. Independent of the PQC mechanisms employed to counteract proteotoxic stress during ageing and the course of neurodegenerative diseases, the end-effect is the same: despite the extensive proteome remodelling in attempt to maintain proteostasis, ultimately, a state of marketed proteome imbalance is reached.

Before reaching such state of chaos, early and more subtle changes in proteostasis are likely to be of significance in disease onset and progression – particularly when considering the need for tight regulation of proteostasis in neurons. There has been extensive investigation into the effect of UPS defects in the homeostasis of disease proteins, however how the proteostasis of other proteins is being affected, and in turn can result in proteotoxic stress, is much less understood.

# 1.2 Neurodegeneration

## 1.2.1 Synucleinopathy pathology

Synucleinopathies are a group of neurodegenerative diseases in which the pathology is driven by the abnormal accumulation of α-Synuclein (α-Syn). This includes PD, Dementia with Lewy bodies (DLB) and multiple systems atrophy (MSA)[21,22]. α-Syn favours the formation of insoluble, fibrillary aggregates in neurons and/or glial cells. These are referred to as Lewy bodies (LBs) and contain various nitrated, phosphorylated and ubiquitinated proteins at their granular core, which is surrounded by a filamentous halo primarily composed of neurofilament and α-Syn (Figure 1.3)[23,24]. The α-Syn aggregation process promotes the formation of β-sheet-rich structures, making LBs immunoreactive to thioflavin-S. Phosphorylation of α-Syn at serine 129 is also regarded as a pathogenic post-translational modification[23]. Interestingly, LBs also contain proteins involved in PQC mechanisms, including heat-shock proteins (HSP) and CHIP[25], the subject of this thesis.

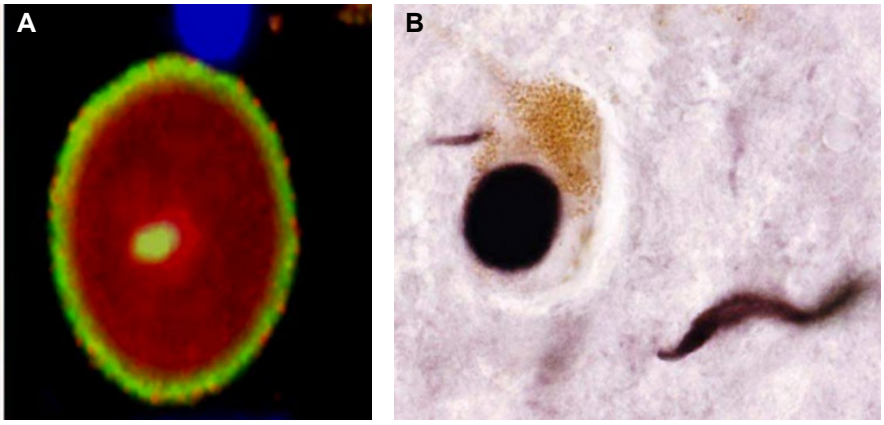


**Figure 1.3: Lewy bodies (LBs)**
**A)** Confocal image of a Substantia Nigra LB stained for Ub (red) and α-Syn (yellow). **B)** LB and Lewy nitrate in grafted dopaminergic neurons stained for α-Syn.
(Olanow and Brundin[23])

It is believed that, in healthy conditions, native α-Syn exists in equilibrium with different conformational and/or oligomeric states. However, in the absence of a higher molar ratio of monomers to the other species, or if partially folded α-Syn self-assembles, stable oligomers are formed, which undergo slow conversion into fibrils and eventually form LBs and Lewy neurites[26–28]. In disease, abnormal α-Syn homeostasis can be driven by an overproduction of α-Syn due to point mutations or multiplications (duplications or triplications) of the *SNCA* gene, for example, which disrupts the equilibrium and drives aggregation[27]. At a cellular level, this accumulation challenges housekeeping processes of the proteasome, lysosome, endoplasmic reticulum (ER), mitochondrion and the plasma membrane. These eventually fail due to the cumulative defects caused by α-Syn[23,27,29–31]. The net effect of increased α-Syn synthesis and inadequate clearance, promotes more aggregation and neuronal dysfunction. This is a viscous cycle leading to increasing toxicity and neurodegeneration.

The pathology is more severe in patients with *SNCA* triplications compared to duplications, supporting the hypothesis that synucleinopathies are α-Syn-dose-dependent[23]. Mixed diseases, such as cases of AD with α-Syn accumulation, are also more severe[28], causing a greater decline in cognitive function[32]. Mechanistically it has been proposed that this is ruled by the innate ability of the α-Syn species to self-aggregate and seed the formation of aggregates[22,33], following a "prion-like" behaviour[22]. Furthermore, α-Syn may have synergistic effects in causing dementia with other pathogenic proteins of AD, tau and amyloid-β (Aβ), by promoting accumulation of each other[32].

### 1.2.1 α-Synuclein

α-Syn is upregulated during development, in injury or other conditions that require neuronal plasticity, which explains the age-related accumulation of the protein. It is abundantly expressed by the *SNCA* gene and its name derives from its nuclear and cytoplasmic subcellular localisation. The cytosolic form of α-Syn (making up 1% of total cytosolic protein) is present mainly at presynaptic terminals, rather than in the soma[29]. A fraction (10-15%) is also membrane-bound[32].

α-Syn is a highly dynamic but intrinsically disordered protein. The ability of α-Syn to adopt diverse conformational states confer multifunctionality in health (although its main physiological role is still unknown) and help to explain why α-Syn species cause broad neuronal defects in disease. The N-terminus, non-amyloid β/A4 component (NAC) region and C-terminus of this 14 kDa protein[27] result in different structural properties (Figure 1.4)[34], which are also influenced by the abundance of α-Syn, interactions with proteins and lipids and the overall cellular homeostasis[27,35]. Interestingly, α-Syn was first identified by analysing the SDS-insoluble fraction from post-mortem AD brains, as it has the propensity to form β-sheet structures, thus promoting protein oligomerisation and fibrillogenesis[28]. On the other hand, the C-terminus of α-Syn is highly negatively charged and prone to remain unstructured[29], while the N-terminus acts as a hydrophobic core with lipid-binding motifs (several imperfect repeats of the lipid-binding, lysine-rich motif, KTKEGV) that drives towards a helical structure[26–29,34].

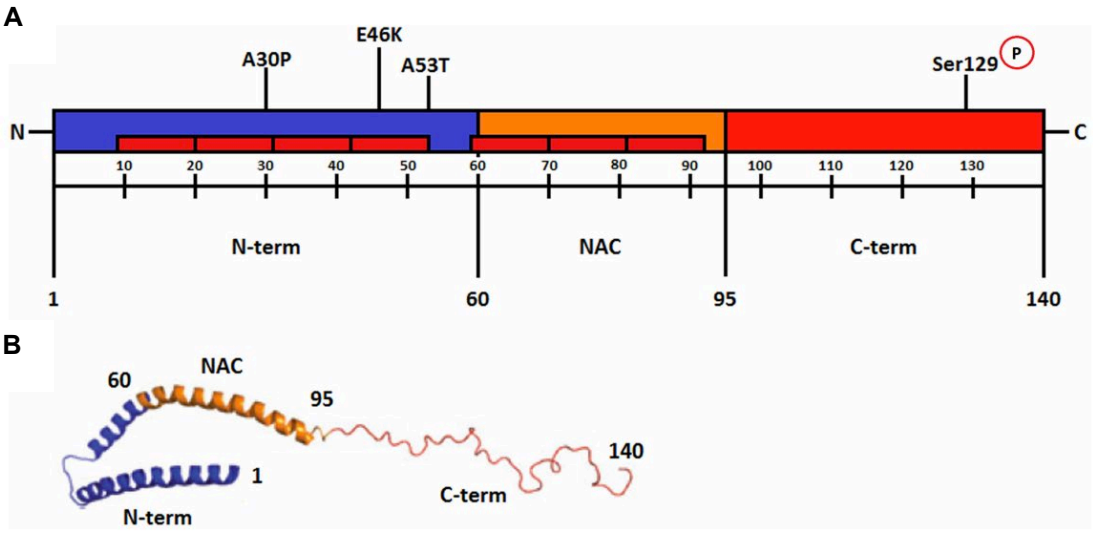


**Figure 1.4: Structure of α-synuclein**
**A)** The N-terminal, NAC and C-terminal domains of α-Syn, with some point mutations associated with familial PD indicated. The disease-associated phosphorylation occurs Serine at position 129. **B)** Schematic representation of micelle-bound α-Syn. Upon binding to the negatively-charged phospholipids (e.g. vesicles) α-Syn undergoes a large-scale disorder-to-helix transition forming two non-contacting antiparallel helices in the N-terminal (in blue).
(Gallegos *et al.*[34])

Rather simplistically, it is generally accepted that the α-helical form of α-Syn is associated with its physiological roles in synaptic plasticity and learning, neurotransmitter release and maintenance of synaptic pools, whilst its β-sheet conformation drives pathology. In support of this physiological functions, a model for α-Syn-dependent vesicle budding has been proposed, allowing α-Syn to mediate and sense both vesicle budding and docking and to regulate membrane remodelling processes (such as membrane curvature) (Figure 1.5)[26]. For such, α-Syn undergoes a large-scale disorder-to-helix transition upon binding to phospholipids, forming two non-contacting antiparallel helices in the N-terminus and, to a lesser extent, the more flexible C-terminal domain, which remains available for regulation via post-translational modifications and protein-protein interactions with vesicle proteins (Figure 1.4B)[26,34,36]. However, there is also a potential role for helical/lipid-induced intermediates during the aggregation process. Firstly, vesicles confine α-Syn into a small area, which increases the local concentration and drives aggregation through mass action. Secondly, lipid-induced α-helical conformation favour intermolecular interactions that lead to aggregation[26].

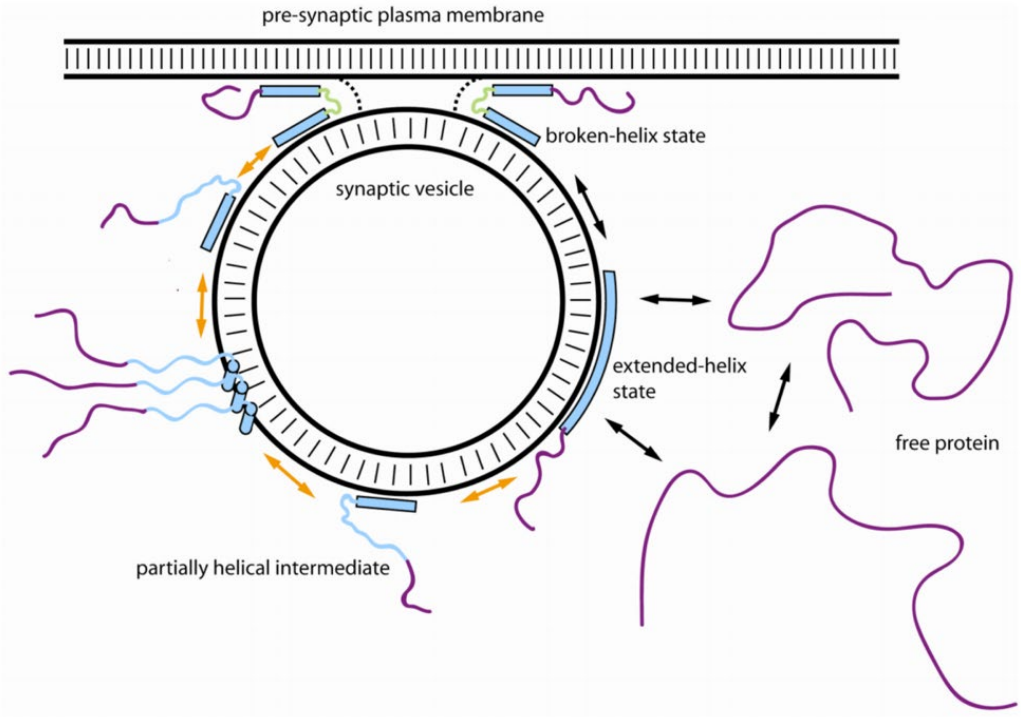


**Figure 1.5: Model of α-synuclein-dependent synaptic vesicle budding/docking**
In this schematic, poorly structured protein regions are represented as solid lines, while helical regions are filled bars or cylinders. The unbound, intrinsically disordered state of α-Syn is in dynamic equilibrium with the vesicle-bound extended-helix state. Upon vesicle binding, the later can convert to the broken-helix state. Physiological transitions between these states are depicted as black arrows. The pathogenic aggregation cascade can also be driven by intermolecular association of these intermediate states: the membrane-associated N-terminal helices may bring the disordered regions into close proximity, facilitating intermolecular β-sheet formation. This results in amyloid oligomer and fibril generation. This pathogenic behaviour of α-Syn is represented by the orange arrows.

(Dikiy & Eliezer[26])

Over the years β-sheet-rich structures have been regarded as the pathogenic species in synucleinopathies, however the focus has shifted from the large and insoluble fibrils within LBs to the smaller and soluble oligomeric species. The idea that the process of fibril formation *per se*, rather than the fibrils themselves, lead to cellular toxicity has been growing in popularity[27]. If this theory is correct, formation of LBs could be an active method to isolate and facilitate clearance of the toxic intermediate oligomeric species and to convert them into the more stable fibrils that exhibit reduced toxicity[23,27,28]. Alternatively, LB formation could be an epiphenomenon, which develops as proteins get trapped in the hydrophobic core. During the course of disease, LBs could become toxic by blocking neuronal trafficking and capturing critical neuronal components[28]. Anything from α-Syn monomers, oligomers or fibrils, either

soluble or insoluble, α-helical or β-sheet-rich in structure, has been given some degree of attention – illustrating the complex nature of the pathology.

## 1.3 C-terminus of Hsc70-interacting protein (CHIP)

With loss of proteostasis at the core of neurodegeneration, there is great interest in understanding the role of regulators of proteostasis in this disease context. Namely, the dual chaperone and E3 ligase enzyme, CHIP, has been studied across some neurodegenerative diseases, including α-synucleinopathies. Functional studies investigating CHIP have consistently described it as neuroprotective[13,14,25,37].

CHIP is encoded by the *STIP1 homology and U-box containing protein 1* (*STUB1*) gene. It is ubiquitously expressed and is especially important in tissues that are active with regards to metabolism and protein turnover, such as the brain, heart and skeletal muscle[38]. Its dual functions are intimately related to its complex structure.

### 1.3.1 Structure

To better understand its functions, efforts have been put into investigating the dynamic structure of CHIP. It contains a C-terminal U-box domain, a N-terminal tetratricopeptide repeat (TPR) domain and a linker domain (Figure 1.6A)[25,39,40]. The U-box domain is the most conserved[41]. It resembles the Really interesting new gene (RING)-finger domain, although it is stabilized by intramolecular hydrogen bonds and salt bridges rather than $Zn^{2+}$ ions. Functionally, it targets Ub-conjugates to protein substrates, consistent with the RING-finger type of E3 ligases[42]. These have been previously regarded as having a "passive" role in scaffolding E2 and Ub and bringing them into close proximity[42] (through its U-box hydrophobic groove[39]). However, crystallography data revealed the possibility of a more active role in determining E2 and Ub conformations, due to the folded-back position that Ub adopts as the E2 interacts with a protomer of the E3, which locks the C-terminal tail of Ub at the E2 active site[43,44]. This is expected to influence the type of ubiquitination pattern and the specificity of the enzymes involved in the ubiquitination process.

CHIP has three TPR domain units, generating three pairs of anti-parallel helices. This facilitates protein-protein interactions between TPR- and non-TPR-containing proteins[41]. TPR-containing proteins are involved in a diverse spectrum of cellular functions with the majority of them regulating proteostasis, including protein transport and protein folding[45]. The hydrophobic pocket of the CHIP's TPR domain allows binding to the C-terminus of Hsc70/Hsp70[46] and Hsp90[39]. The crystal structure of CHIP bound to either HSP proteins illustrates how CHIP adopts an unusual asymmetric homodimer in which each protomer has pronounced structural differences (Figure 1.6B)[39]. Furthermore, hydrogen/deuterium exchange-mass spectrometry (HX-MS) revealed that the TPR domain is very flexible and when bound to Hsp70/90 it becomes more stable and organised. This "locked" conformation can be modelled by mutating the lysine 30 to a structure favouring amino acid. The flexibility of the TPR domain also correlates with that of the U-box domain, indicating intramolecular allosteric regulation of the domains. The E3 ligase activity decreases significantly upon Hsp70/90 binding, possibly to ensure that one of its dual functions is predominant at any given time[47].

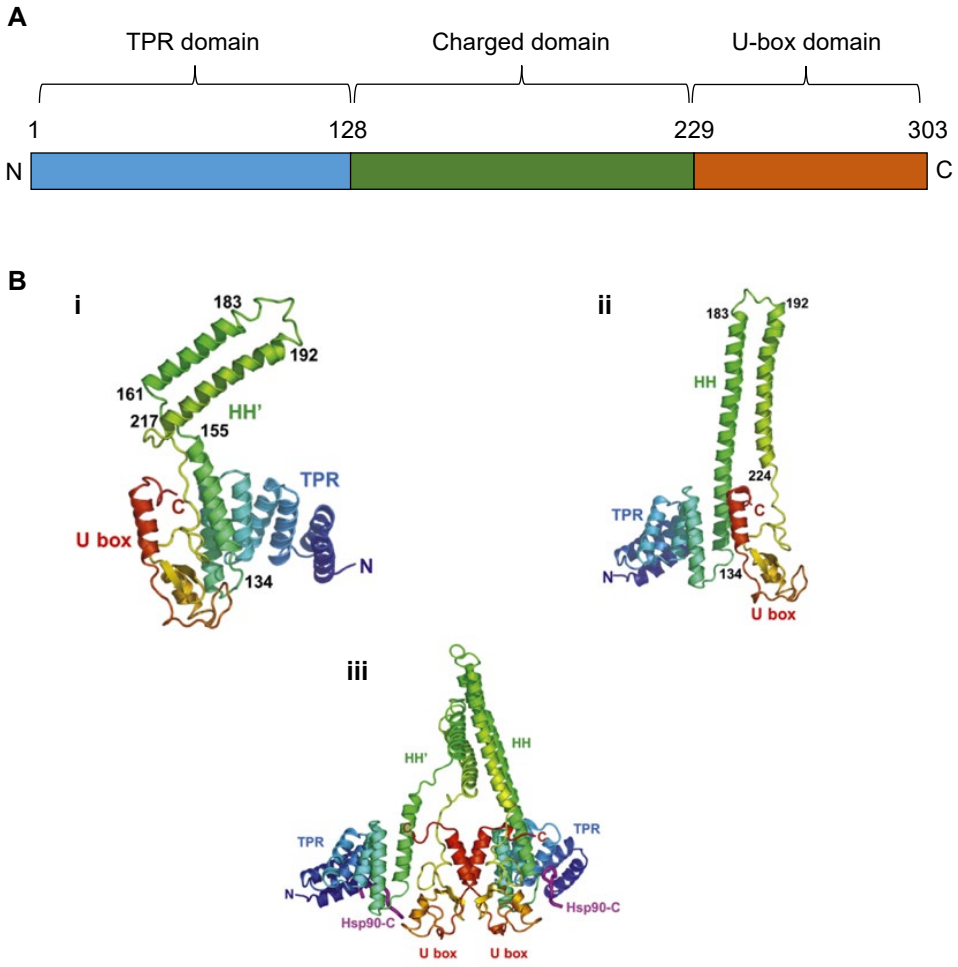


**Figure 1.6: Structure of CHIP**
**A)** Schematic of the functional domains of CHIP (numbers represent amino acid (aa) numbers). The TPR region includes TPR 1 (26-59 aa), TPR 2 (60-93 aa) TPR 3 (95-127 aa) domains.
**B)** Crystal structure of murine CHIP (PDB 2C2L) as monomers (**i** and **ii**) and an asymmetrical dimer (**iii**). In the latter conformation, one protomer (**ii**) has a hairpin structure formed by two straight helices, while this interaction is broken in the other protomer, having its helices separate (**i**).
(**A**: Information according to Nikolay *et al.*[40] and Zhang *et al.*[39]; **B**: Adapted from Zhang *et al.*[39])

Finally, the charged domain, also called coiled-coil/helix-turn-helix (HH) region, of CHIP is flanked by both enzymatic domains. This region is important for CHIP dimerization[39]. CHIP homodimers form asymmetrically, having an elongated protomer and a compact/bent one. Asymmetry in homo-oligomers is rare: 75% of the homodimers have global asymmetry scores of ≤ 0.4 (indicator of a highly symmetry homodimer) and 90% have ≤ 1, while CHIP has a score of 8.29 (i.e. high values reflect

a greater degree of asymmetry)[48]. Such rarity in structure is likely to be intimately linked to its complex functions and intricate auto-regulation.

### 1.3.2 Regulation of CHIP

The spatiotemporal control of CHIP functions in different conditions (unstressed and stressed) still need further attention. This includes understanding how its substrate specificities change depending on the cellular context[1] and how the activity of CHIP is regulated. Not only can interactions with chaperones[49] and other proteins and lipids[50] influence the activity of CHIP, intrinsic mechanisms of regulation have been proposed. Different oligomeric states (dimeric, tetrameric or even higher) of CHIP have been described, thus regulation could occur at a conformational level. *In vivo* it is believed that CHIP is largely dimeric, although this state could be in equilibrium with tetrameric CHIP, which is detected at higher concentrations[40]. Furthermore, our group has previously reported an allosteric regulation between the TPR and U-box domains via intra-molecular interactions[47].

A few studies have reported regulation of CHIP through post-translational modifications, including phosphorylation and ubiquitination. CHIP is phosphorylated by Cyclin-dependent kinase 5 (Cdk5) at serine 20, which negatively affects its neuroprotective functions. Cdk5 is a member of the cyclin-dependent kinases important in the regulation of post-mitotic processes in the nervous system and becomes dysregulated across neurodegenerative diseases. This post-translational modification inhibits CHIP's interaction with its substrate, truncated apoptosis-inducing factor (tAIF). As a result, tAIF does not get ubiquitinated and triggered for proteasomal degradation, causing tAIF-mediated neuronal cell death (via oxidative stress). Additionally, the negative regulation of CHIP by Cdk5 was also shown to inhibit CHIP-mediated ubiquitination and degradation of $\alpha$-Syn and p53[51].

CHIP is differentially ubiquitinated by E2 enzymes (the ubiquitination mechanism is explained in Section 1.3.3c). The UbcH5A E2 enzyme attaches Ub chains with non-specific linkages to CHIP[1]. While Ube2W directed-monoubiquitination was seen on a non-lysine N-terminal residue of CHIP[52] (abolishing its E3 ligase activity) and on lysine K2 (believed to enhance CHIP function)[53]. Furthermore, Ube2w-directed

monoubiquitination of CHIP may stimulate CHIP-Ataxin-3 complex formation, allowing this DUB to regulate the extent and duration of substrate ubiquitination by CHIP. It does so by limiting the length of Ub chains required on CHIP substrates to target them for degradation and by deubiquitinating ubiquitinated CHIP upon completion of substrate ubiquitination. Therefore, through their opposing activities, Ube2w and Ataxin-3 (and potentially other E2 and DUB enzymes) participate in initiating, regulating and terminating the CHIP ubiquitination cycle[53].

Another important mechanism for the regulation of Ub ligases, including CHIP, is through auto-ubiquitination. Analysis of *in vitro* ubiquitination assays by mass spectrometry (MS) identified two ubiquitination sites on Ub (K63 and K48) and one on CHIP (K22). This finding suggests that the auto-ubiquitination pattern of CHIP either consists of two types of polyubiquitination chains (with K63- and K48-linkages) coexisting or is formed by heteropolymers, including both modifications sites in the same chain[54]. While K63 polyubiquitin chains are associated with proteasome-independent pathways, both K48 and K48/63 polyubiquitin chains preferentially associate with the proteasome for degradation. Therefore, this may be a mechanism for CHIP regulation (auto-ubiquitination is discussed further in Section 6.3.2c)[55].

## 1.3.3 Canonical functions of CHIP

Arguing in favour of CHIP having important roles in cell biology is its strong conservation (having orthologues in plants, worms, flies, fish and mammals)[1]. Evident from its structural domains, CHIP functions as both co-chaperone and chaperone-dependent E3 ligase. These canonical functions will be reviewed in this order and, for a comprehensive understanding, an overview of both the chaperone and ubiquitination cascades will be included.

### a. Overview of the chaperone system

Despite being determined by the amino acid sequence and favoured by thermodynamics, protein folding is an energetically costly processes, relying on the adenosine triphosphate (ATP)-dependent action of chaperones to assist folding[8]. In fact, it is estimated that more than 30% of newly synthesised proteins are degraded

due to the inability to fold properly. Chaperones bind to hydrophobic regions exposed in unfolded/partially folded proteins or aggregation-protein proteins. The function of chaperones becomes especially important when stressors (including mutations, heat, oxygen radicals, heavy metal ions, etc) disturb proteostasis, compromising protein structure and function. It is not surprising that in response to stress cells upregulate HSPs, including the cytosolic chaperones Hsp70 and Hsp90, and small HSPs, Hsp40 and Hsp27[56].

Molecular chaperones refold damaged proteins and can accompany terminally misfolded proteins to their disposal machinery, a decision that is mediated by the protein triage network[8]. Both Hsp90[56] and Hsp70-Hsp40[8] are capable of targeting terminally misfolded proteins for proteasomal degradation. When in a complex with Hsp40 or Hsp104, the refolding capacity of Hsp70 is enhanced and it is capable to actively dissociate small and large aggregates, respectively[8,56,57]. Also, Hsp90 and Hsp70 can crosstalk regarding activity and target specificity. Hsp90 is able to bind denatured proteins who's folding is then finalised by Hsp70[8].

### b. CHIP as a co-chaperone

CHIP was discovered by the Patterson group as a binding protein for Hsc70[41] (as its name suggests) and, later, Hsp90[58] as well. These are highly conserved HSPs that function as molecular chaperones, binding to and orchestrating the folding of other proteins in association with co-chaperones that dictate their substrate affinity. This first study revealed CHIP:Hsc70 interaction but failed to detect chaperone activity. In fact, HSP-dependent substrate binding and refolding of luciferase was abolished in the presence of CHIP. Thus, CHIP was characterised as a co-chaperone that negatively regulates the chaperone functions of HSPs in vitro (Figure 1.7)[41].

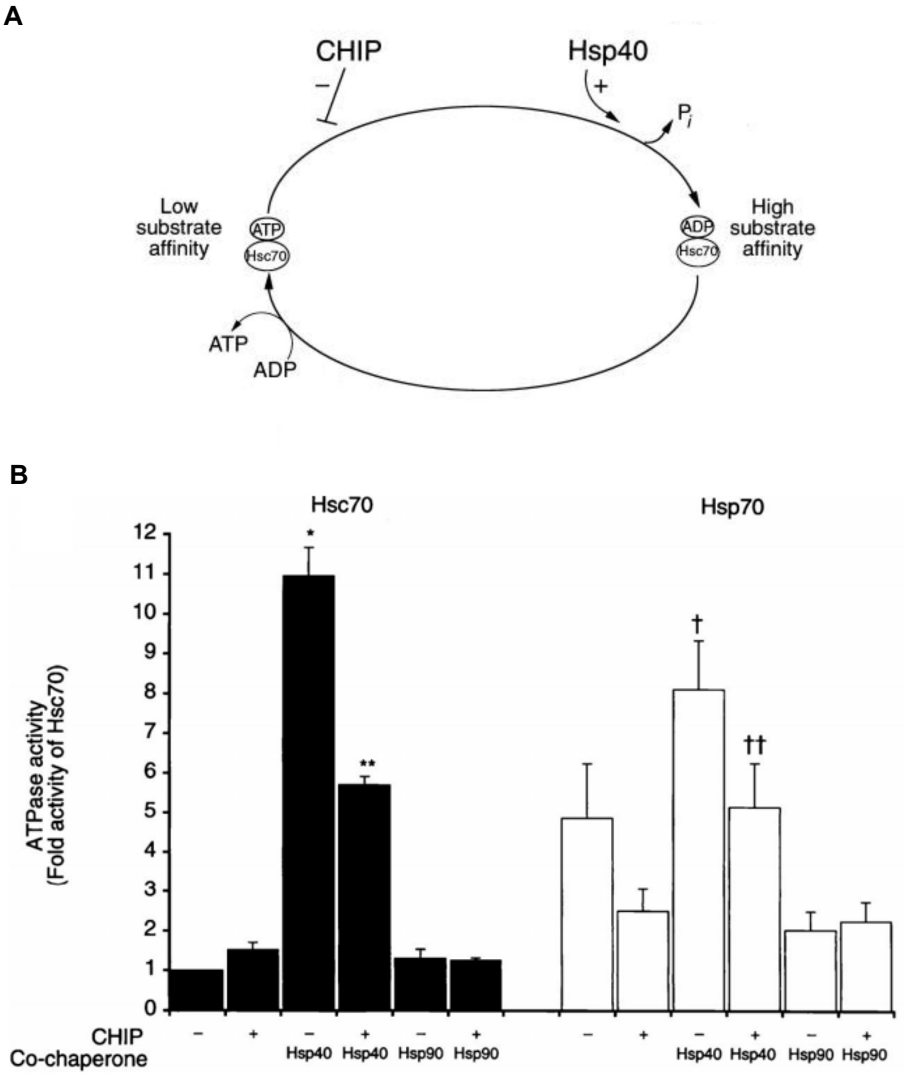


**Figure 1.7: CHIP as a negative regulator of the chaperone functions of HSPs and protein folding**

**A)** First mechanistic schematic of CHIP supporting that it inhibits the forward reaction of the Hsc70-Hsp70 substrate binding cycle. In the forward reaction, ATP is hydrolysed to release the substrate, which is promoted by Hsp40. Hsp40 stabilises the ADP-bound state, high-affinity conformation of Hsc70, enhancing its chaperone activity.

**B)** ATPase activities of Hs70/Hsp70 in the presence and absence of CHIP and/or other co-chaperones. CHIP compromises the ATPase activity of HSPs (by preventing ATP binding or inhibition ATP hydrolysis) and/or blocks the interactions of Hsc70/Hsp70-Hsp40 complex with the denatured substrate. Different between Hsc70/Hsp70 with/without Hsp40: * and † $P < 0.05$; difference between Hsc70/Hsp70 with Hsp40 in the presence and absence of CHIP: ** (or ††) $P < 0.05$. Six replicates for each condition.

(Adapted from Ballinger *et al.*[41])

Subsequently, the paper reporting the Hsp90:CHIP interaction, shed light into the dynamic and key function of CHIP: modulation of the cellular protein triage decisions that regulate the balance between protein folding and degradation. This capacity of the cell to determine the fate of a protein is achieved through the cooperation of chaperones with the degradation machinery. Upon Hsp90 binding to the TPR domain of CHIP, Hop and p23 dissociate from the Hsp90 heterocomplex. This CHIP-dependent remodelling of the Hsp90 heterocomplex disfavours substrate refolding and promotes its ubiquitination instead. For example, the glucocorticoid receptor (a Hsp90 substrate) has decreased steroid-binding activity in the presence of CHIP, due to misfolding, and becomes polyubiquitinated. This modification directs it for proteasomal degradation, explaining the decreased receptor steady-state levels in cells overexpressing CHIP[58]. Therefore, CHIP was able to shift the activity of Hsp90 from protein folding to degradation[58–61].

This hypothesis was then challenged by a study supporting the intricate nature of the protein triage and suggesting that this change from folding to degradation machinery induced by CHIP was not generally true for all Hsp70 substrates[57]. Unexpectedly, overexpression of CHIP enhanced protein refolding in stressed mammalian cells (after heat shock) (Figure 1.8A)[57], despite previously described as an inhibitor of Hsp70 ATPase and chaperone activity *in vitro*. Therefore, although features of the mechanism are shared (ATP- and Hsp70-dependent, but Hsp90-independent and mediated by the TPR domain of CHIP), the consequences differ, making it unclear what determines the fate of Hsp70-bound substrates. Clearly, the cellular state (e.g. stress) influences how proteostasis is regulated. More recently, there has been growing appreciation for the conformation of the substrates, which can be heavily influenced by stress, dictating their fate (i.e. refolding versus degradation)[47,62].

During the recovery from heat shock, luciferase refolding was increased in the presence of both Hsp70 and CHIP compared to Hsp70 alone, and this was dependent on the TPR domain of CHIP (Figure 1.8B)[57]. The increased luciferase refolding and Hsp70-luciferase interactions detected in cells overexpressing CHIP could have different explanations. Firstly, CHIP may increase Hsp70 folding activity by counteracting the inhibitory effect that excess Hsp40 levels has on Hsp70 activity (Hsp40 reduces Hsp70 recycling by stabilising the ADP-bound state of Hsp70 for longer, preventing other substrates from interacting). Secondly, CHIP may promote

ATP-bound Hsp70 by preventing ATP hydrolysis, having a higher substrate on-off rate (i.e. lower substrate affinity), which could lead to a better loading of denatured substrates to Hsp70[57]. Thus, the binding of Hsp70 to the TPR domain of CHIP could stabilise Hsp70-polypeptide complexes. The importance of ATP-bound conformation of chaperones for the refolding cycle is particularly important in conditions of cell stress[41] and underlies why CHIP-mediated increases in chaperone activity have been reported under conditions of stress[57]. However, stabilisation of the Hsp70 complex could also drive the assembly of the CHIP E3 ligase complex, favouring the degradative activity of CHIP[63].

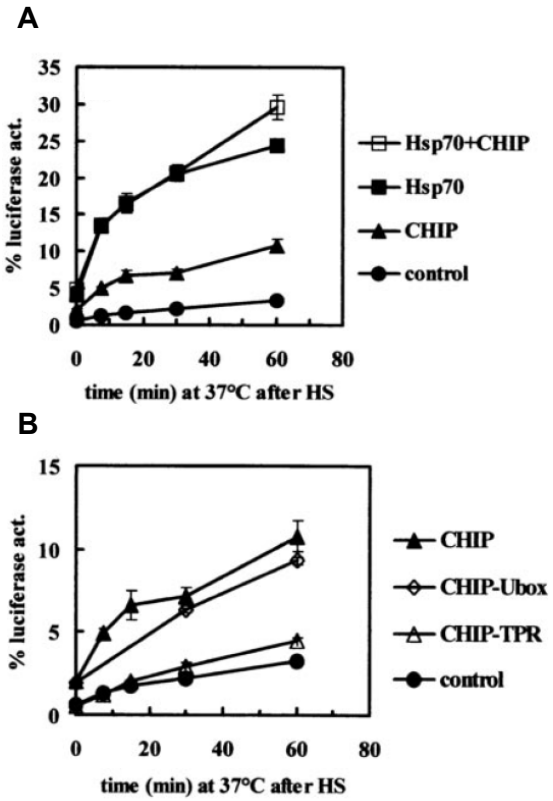


**Figure 1.8: CHIP as a positive regulator of HSP chaperone activity and protein folding**
Luciferase refolding in cells overexpressing CHIP, Hsp70 or Hsp70 and CHIP (**A**) and cells overexpressing different forms of CHIP: full-length and CHIP lacking the U-box or the TPR domains (**B**) during recovery from heat shock.

(Kampinga *et al.*[57])

### c. Overview of ubiquitination

Beyond the molecular chaperone network, the UPS also plays a crucial role in regulation of the proteome. The UPS is the primary means by which proteins are degraded, removing misfolded or damaged proteins and to regulating signalling pathways. It is a highly conserved system that plays a central role in cell proliferation, transcription, apoptosis, immunity, development and other cellular processes. Through a coordinated process relying on ATP and a cascade of enzymes, ubiquitin (Ub), a 76-amino acid protein, is added to substrates to create a ubiquitination signature that triggers different cellular fates. Each cycle involves, a Ub-activating enzyme (E1), a Ub-conjugating enzyme (E2) and a Ub ligase (E3). Initially, E1 forms a thio-ester bond with Ub, which allows Ub to then bind to E2. Finally, the formation of an isopeptide bond between the C-terminus of Ub and the ε-amino group of lysine residue of the substrate protein is catalysed by the E3 (Figure 1.9). Specificity of ubiquitination is largely controlled at the level of the E3 ligases. Over E3s of different domains, properties and activities have been identified and each is responsible for the ubiquitination a subset of proteins[9,64,65]. Furthermore, post-translational modifications on substrates that affect their interaction with ubiquitination enzymes[39]. Another degree of regulation is achieved through the action of DUBs, which reverse the isopeptide bonds connecting Ub molecules to the client protein. They replenish the pool of Ub by allowing Ub recycling, reverse the Ub status of proteins[66], and remove free Ub chains that would otherwise overwhelm the proteasome[3].

Ub itself has 7 lysine residues that allow for Ub chains to be formed with specific linkages when a certain lysine within Ub is linked to the C-terminal glycine of another Ub (K6, K11, K27, K29, K33, K48 and K63). The most common are K48-chains and, together with K63-chains, account for 80% of total mammalian linkages. Substrates can be mono-, multi-mono and poly-ubiquitinated, leading to specific cellular effects[9,67,68] (Figure 1.9). Although ubiquitination occurs predominantly on lysine residues on a substrate, other residues (cysteine, serine and threonine) have also been identified and these are believed to serve as proteasomal degradation signals[8].

Ubiquitinated proteins are targeted to the 26S proteasome, a highly abundant proteolytic complex. It consists of a 20S catalytic core particle capped at either end with the 19S regulatory particle. The latter contains Ub receptors and DUBs that

function in the recruitment and processing of ubiquitinated proteins, and ATPase subunits to unfold the substrate. The unfolded substrate is then exposed the chymotrypsin-like, trypsin-like and caspase-like activities of the core particle for degradation[9,39] (Figure 1.9).

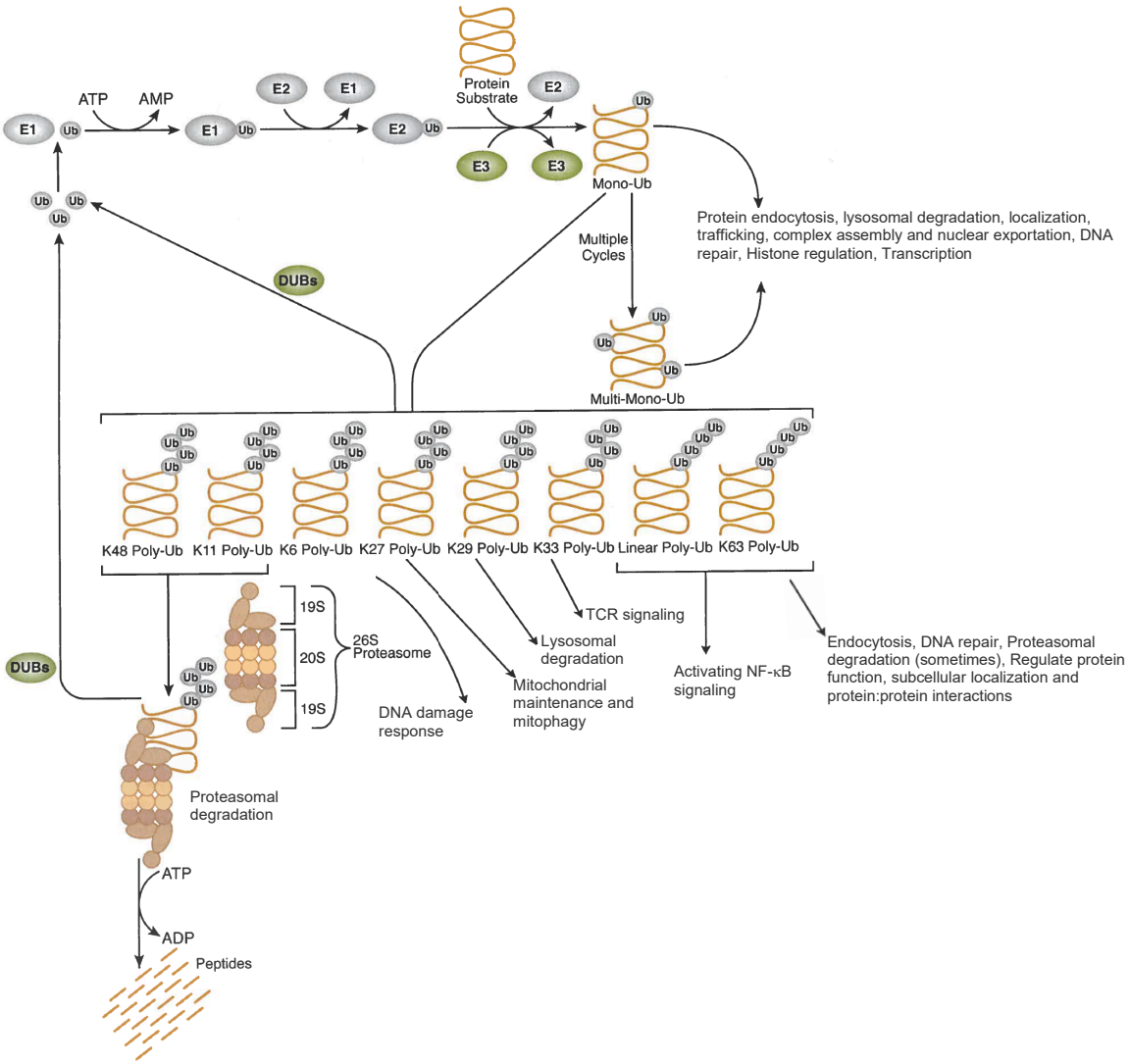


**Figure 1.9: Ubiquitination**
Illustration of the ubiquitination cascade. Depending on the ubiquitination profile, ubiquitinated proteins have different cellular fates[62,64,65].

(Adapted from Cell Signalling Technology[9])

### d. CHIP as a chaperone-dependent E3 ligase

After being studied as a co-chaperone involved in the refolding of proteins, the focus then shifted into investigating its role as a chaperone-dependent E3 ligase[61,65]. The turnover of unfolded Cystic fibrosis transmembrane conductance regulator[69] and the glucocorticoid receptor[58] are examples of such activity.

Interestingly, despite extensive functional redundancy in PQC components, these CHIP-mediated ubiquitination events were HSP- and substrate-specific[57]. Both HSP and CHIP substrate specificity is influenced by the conformation of the substrate[20]. CHIP preferentially degrades denatured luciferase compared to native, in a HSP-dependent manner (showing a 10-fold difference in an *ex vivo* Ub conjugation assay)[56]. This supported the school of thought that CHIP is primarily involved in ubiquitination and degradation of HSP-bound substrates, which tend to be misfolded/unfolded proteins[20,39].

The U-box of CHIP confers its ubiquitination activity for both its E3 and E4-like activities[65,70,71]. Through the cooperation of specific E2 enzymes, CHIP can ubiquitinate client proteins in different ways, leading to different cellular fates[39,65]. For example, Ubc13-Uev1a directs K63 polyubiquitin chains and UbcH5 can lead to K48 polyubiquitin chains added to the substrate and/or CHIP (auto-ubiquitination)[65]. CHIP catalyses the elongation of Ub chains attached to substrates that were previously initiated by another Ub ligase, targeting substrates for proteasomal degradation. For example, the Parkin-associated endothelin receptor-like receptor (Pael-R) is ubiquitinated by Parkin initially, but CHIP's association with Hsp70 dissociates the latter from Parkin, causing Parkin and Pael-R to become free. As a result, CHIP increasing the rate of Pael-R ubiquitination and clearance[65,71].

Since most of the chaperone-client interactions are driven by PQC pathways, there is strong evidence to suggest that CHIP plays an important role in maintenance of proteostasis, both in physiology (under resting conditions) and in pathology (under stress). However, in the latter, PQC pathways become challenged and response mechanisms come into play. This extends the repertoire of chaperone-mediated targets and, in turn, reflects CHIP as a promiscuous co-chaperone and E3 ligase. Nonetheless, it is unclear if this stress-responsive behaviour represents the main

function of CHIP, or if it emerges secondary, as a stress-induced function that diverts CHIP from its intrinsic cellular functions at basal conditions.

### e. Role of CHIP in the protein triage

Given its dual E3 ligase and chaperone functions, CHIP mediates PQC and plays an integral role in proteostasis. CHIP can influence decisions of the protein triage, where the fate of specific denatured protein is decided, promoting its refolding by the molecular chaperone network or degradation via the UPS or lysosome (). It remains unclear how these different PQC branches communicate with each other and favour a specific pathway. The functional relationship between molecular chaperones and the UPS is key for the protein triage and has been proposed to work either in a collaborative fashion or in a competitive manner[56].

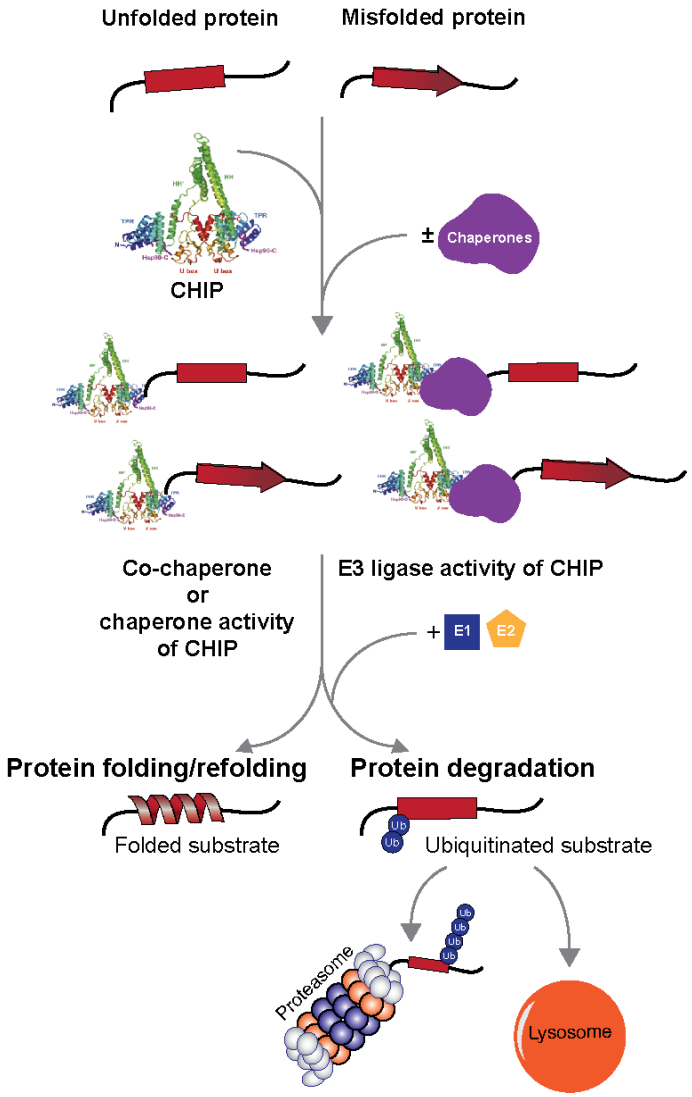


**Figure 1.10: CHIP at the protein triage**
At the point of triage, the fate of unfolded/misfolded proteins (or aggregated proteins – not shown in the schematic) is decided: promoting protein folding/refolding or degradation. CHIP interacts with the client protein in a chaperone-dependent or -independent manner. Likewise, CHIP-mediated folding of the client protein can be chaperone-dependent (where CHIP acts as a co-chaperone), or chaperone-independent (relying on CHIP's intrinsic chaperone activity – discussed in Section 1.3.4). Alternatively, CHIP can direct ubiquitination of the client protein to promote its degradation. Again, this mechanism can be chaperone-independent (as part of the non-canonical functions of CHIP discussed in Section 1.3.4) or not.

From a competitive perspective, the fate of the denatured protein may be dictated by the relative activities of the chaperone system versus the UPS. For example, addition of exogenous Hsp70 inhibited degradation of denatured luciferase and promoted refolding, whilst the opposite was observed when CHIP was added instead[56]. Alternatively, such competitive nature may arise from the affinity of a substrate for a chaperone or protease. A kinetic model for maintaining PQC has been proposed, in which the "decision" to degrade a substrate is determined by unproductive on and off cycling of substrate-chaperone interactions[58].

However, there is also evidence for a highly collaborative network of interactions between the molecular chaperone network and the UPS. First, both systems developed to be intrinsically able to recognise non-native proteins (including partially unfolded, misfolded and incorrectly modified proteins, as well as unassembled subunits of complexes), or proteins in the wrong cellular compartments, thus having substrates in common. Secondly, systems have common ATP-dependent methods of unfolding proteins and share certain components[56,58]. For example, Hsp90 and Hsp70, which apart from functioning independently as chaperones, are required for ubiquitination of a subset of proteins (mainly those highly hydrophobic)[61]. Finally, they work jointly and in a dynamic manner to maintain proteostasis and prevent protein aggregation. Under basal conditions both systems communicate with each other to ensure adequate regulation of protein homeostasis. For example, specific BAG-Hsp70 interactions favour CHIP-dependent substrate degradation by the proteasome or lysosome, or inhibit its ubiquitination activity[8]. Similarly, when the UPS is inhibited/compromised (seen in neurodegeneration, for example), cells respond by upregulating HSPs[56,58].

CHIP may work in this dynamic communication between the refolding and degradation branches. CHIP can convert clients of HSPs to the UPS for degradation. Artificial systems have provided some mechanistic insight into this regulation. For example, the refolding of denatured luciferase by HSPs (Hsp90 and Hsp70/Hsp40) is abolished when CHIP is introduced and, instead, the client protein becomes ubiquitinated[56]. Mechanistically, it was suggested that CHIP stimulates the release of the Hsp90 ATPase activity modulating cofactor p23, suppressing the affinity and folding activity of Hsp90, hence favouring ubiquitination[3]. Hsp90 and Hsp70 have been broadly described as having opposing effects: promoting refolding or

degradation of the target protein, respectively[72]. Another example is the competitive binding of CHIP and Hsp40 to Hsp70, where displacement of Hsp40 prevents the folding capacity of the chaperone complex[56,57].

At a cellular level it is likely that there is an attempt at chaperone-mediated refolding, as a first stage of triage. If successful, this allows the client protein to be removed from the triage system. However, if this fails, the co-chaperone CHIP comes into play to initiate chaperone-dependent ubiquitination[35,56], supporting a sequential mode of action for these PQC mechanism. The chaperone-directed recruitment of CHIP triggers an allosteric interaction between the TPR and U-box domains[3,47]. Both TPR and U-box domains are required for degradation of denature luciferase to be favoured over refolding, showing that both E3 ligase activity and chaperone-interaction capability is required[56]. Mechanistically, the TPR domain mediates interacts with the HSP-substrate complex, enabling CHIP-dependent ubiquitination of the hydrophobic substrate. Hypothetically, all clients of Hsp70 and Hsp90 are potential targets of CHIP, although not all CHIP substrates are recruited by chaperones[3] (evident from the non-canonical functions of CHIP – refer to Section 1.3.4 Non-canonical functions of CHIP). Studies using Hsp90 inhibitors supported such overlap in repertoire of client proteins. For example, the interferon regulatory factor 1 (IRF-1), which is positively regulated by Hsp90, becomes degraded upon Hsp90 inhibition possibly by CHIP (in the presence or absence of Hsp70)[73]. Likewise, CHIP was reported to be responsible for the degradation of aberrantly phosphorylated tau (a substrate of Hsp90) upon Hsp90 inhibition, in a Hsp70-dependent manner[35]. The canonical view is that CHIP is targeted to Hsp90-bound substrates by Hsp70 for ubiquitination[58,61]. However, it has been reported that loss of CHIP does not affect Hsp90 substrates, arguing that Hsp90-bound CHIP may not be exclusively involved in the ubiquitination of Hsp90 client proteins, as was previously concluded from experiments overexpressing CHIP[74]. This paved way to the hypothesis that CHIP may have other functions than those relying on its HSP-dependent ubiquitination and chaperone activity.

### 1.3.4 Non-canonical functions of CHIP

Historically, studies investigating the role of CHIP have focused on its functions as a co-chaperone and chaperone-dependent E3 ligase. However, this does not necessarily mean that these are the primary functions of CHIP, just that the data on CHIP is skewed towards these canonical functions. Looking at more recent literature, the non-canonical functions of CHIP are emerging, reporting intrinsic chaperone and E3 ligase properties[41,45,75,76].

There has been increasing evidence to support that CHIP has substrate specificity[69] and may be capable of substrate recognition and direct binding – a function that was previously reported to be undertaken by the HSPs. Therefore, under some conditions, CHIP might be able to bypass the requirement for a chaperone partner[77]. Although it is arguably a poor substrate of CHIP, identification of Hsp70 as a substrate was critical to pioneer investigation into the chaperone-independent E3 ligase activity of CHIP. Apart from being functionally regulated by CHIP as a co-chaperone and upregulated by CHIP-mediated transcriptional induction of HSF1 to protect against proteotoxic stress[3,78] (another non-canonical activity of CHIP), Hsp70 is also a direct ubiquitination substrate of CHIP. CHIP-mediated Hsp70 ubiquitination triggers its degradation and takes place in the aftermath of stress, to bring Hsp70 levels back to basal[3,79].

An elegant example of CHIP as a docking-dependent chaperone-independent E3 ligase is its interaction with IRF-1. CHIP binds directly to free IRF-1 by docking to the intrinsically disordered domain within the central region of IRF-1[77] and this causes site-specific ubiquitination[80]. Interestingly, this interaction is dependent on the cellular environment - under conditions of mild heat stress IRF-1 readily is ubiquitinated by CHIP, resulting in its degradation. However, in unstressed cells, CHIP acts as a chaperone of IRF-1, increasing its steady-state levels (Figure 1.11). CHIP:IRF-1 interaction can occur in a chaperone-independent manner[77].

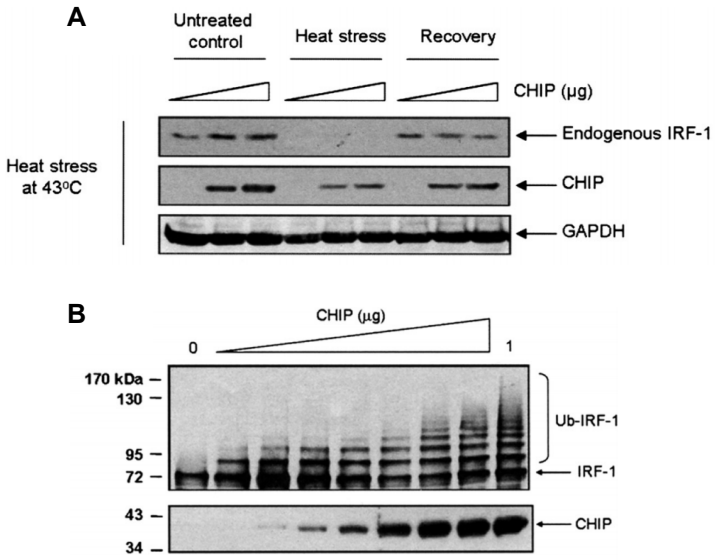


**Figure 1.11: Dual role of CHIP as chaperone and E3 ligase of IRF-1**
**A)** A375 cells transfected with a titration of Myc-CHIP were heat-shocked and harvested immediately (Heat stress) or allowed to recover for 1h (Recovery). SDS-PAGE/immunoblot using anti-IRF1, anti-Myc and anti-GAPDH mAbs.
**B)** *In vitro* ubiquitination assay with GST-IRF1 and a titration of His-CHIP (until 1mg). SDS-PAGE/immunoblot using anti-CHIP and anti-IRF1 mAbs.

(Narayan *et al.*[77])

Likewise, CHIP-mediated regulation of p53 has been reported to capitalise on both the intrinsic chaperone and E3 ligase properties of CHIP. Potentially via its chaperone activity, CHIP prevented wild-type (WT) p53 from thermal inactivation *in vitro* and restored the native-like conformation of p53 (capable of DNA-binding) in heat shocked cells. Furthermore, it was proposed that CHIP might be a direct chaperone of WT p53 for its translocation to the nucleus under heat shock conditions. As an E3 ligase, CHIP was reported to mediate the degradation of WT and mutant p53. These processes were chaperone-independent[81].

Rosser and colleagues[63] looked more closely into the intrinsic chaperone activity of CHIP. CHIP was able to refold denatured luciferase *in vitro* and in cells in a manner that was independent of Hsp70. The chaperone function was temperature-sensitive, increasing when exposed to heat shock. Interestingly, the group suggested that through its chaperone activity, CHIP was able to maintain heat-denatured luciferase in a foldable and ubiquitination-competent conformation. Indeed, following heat shock, CHIP was also capable of ubiquitinating the substrate, in the absence of

chaperones. Ultimately, the levels of luciferase ubiquitination increased and protein aggregation decreased[63].

The intrinsic E3 ligase activity of CHIP was supported by the CHIP-dependent ubiquitination of biologically relevant proteins in the absence of chaperones, including Smad1/5[82], the insulin receptor (INSR)[62] and Daxx[83]. Smad1/5 binds to the TPR domain of CHIP and competes with the binding of HSPs, which suppresses CHIP-mediated ubiquitination[82]. Likewise, CHIP-dependent ubiquitination of the INSR occurs in a chaperone-free *in vitro* reaction and the TPR domain is required for direct recognition of the substrate. Interestingly, the CHIP-dependent ubiquitination of Daxx is stress-induced and Ub chain formation utilises non-canonical lysine linkages that are associated with resistance to proteasomal degradation. Daxx binds to the charged domain of CHIP[83]. Although CHIP:substrate interaction could occur directly, as with IRF-1[77], this has not been addressed specifically (instead, only the structural domains necessary for the interaction were deduced from mutational analysis).

CHIP is not unique in possessing both intrinsic chaperone and E3 ligase activities. The mouse double minute 2 (MDM2) protein utilises these functions to regulate the proteostasis of p53 in cells. As observed with other chaperones, p53 undergoes MDM2-mediated folding-unfolding cycles to promote its folding to a conformation that has high affinity towards its promoter sequence. At the same time, MDM2 can trigger the degradation of p53 by ubiquitination. Such apparent contradictory mode of action (capable of both refolding and degrading protein targets)[84] is also seen for CHIP[77] and, similarly, is likely to be regulated by interactions with molecular chaperones (including Hsp90)[84].

The properties of CHIP allow it to regulate protein stability, turnover (including transcription and degradation), trafficking (e.g. ubiquitination renders proteins in insoluble cellular compartments[85]) and activity (e.g. ubiquitinated proteins may act as scaffolding proteins for signalling hubs[39,86]). CHIP has been associated with a wide and diverse array of substrates (including signalling molecules, receptors, kinases, etc) resident in different subcellular compartments (including the cytoplasm, plasma membrane, nucleus, ER and Golgi complex)[65,87]. Concomitantly, CHIP plays direct or indirectly roles in numerous cellular processes important in health and disease[65], such as quality control of the ER, response to stress (including heat stress and oxidative

stress), protection from stress-induced apoptosis, ageing and senescence, metabolism, proliferation, immunity (both potentiating and dampening inflammatory responses) and proteasomal and autophagy-lysosomal degradation[20]. CHIP has functions in disorders including PD, AD, Huntington's disease, Atherosclerosis, SCA1, hypogonadism and cancer[20,87].

Chaperones are highly promiscuous with regards to their client proteins. Therefore, when chaperones interact with CHIP, it is likely that the interactome of CHIP expands and the proteostasis of more proteins becomes influenced by CHIP. This can widen the scope of CHIP's functions, potentially activating more secondary functions (beyond its intrinsic functions). Given the intimate relationship of CHIP and molecular chaperones in the protein triage system, the main roles and mechanisms of action of CHIP may be confounded by the influence of the chaperones. Therefore, identification of direct substrates of CHIP (chaperone-independent) is likely to shed light into its inherent roles, which are much less understood.

# 1.4 CHIP and neurodegeneration

## 1.4.1 CHIP-related diseases

Across the literature, the neuroprotective properties of CHIP prevail and have been reported to be driven by both the canonical and non-canonical functions of CHIP. Perhaps the most compelling evidence to support the importance of CHIP in health comes from studies into CHIP-related diseases.

CHIP mutations are autosomal recessive and lead to a syndrome (referred to as Gordon Holmes syndrome[13]) with broad symptoms, including cerebellar ataxia. The syndrome can be grouped into five major classes[88]:

- Mitochondrial energy deficiencies (eg. Friedreich's ataxia),
- Ataxias with DNA repair defects (eg. Ataxia telangiectasia),
- Metabolic ataxias,
- Congenital ataxias,

- Degenerative ataxias (such as Autosomal recessive cerebellar ataxia, ARCA, including Spinocerebellar ataxia autosomal recessive type 16, SCAR16).

The effects of CHIP dysfunction are described as being gradual, eventually causing a multisystemic disease with severe dementia (Figure 1.12). This illustrates the importance of CHIP in cell survival of multiple cell types[13].

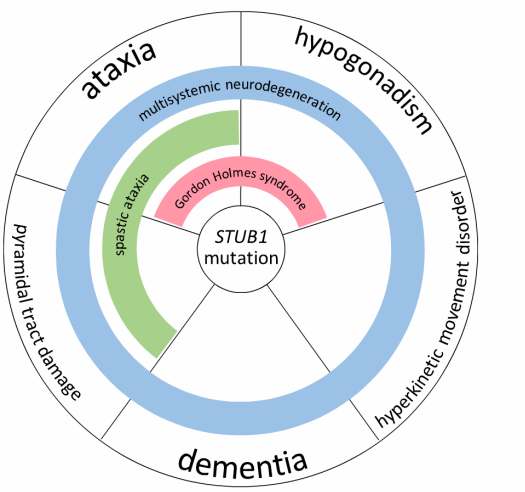


**Figure 1.12: Clinical spectrum of CHIP (*STUB1*) mutations**
Although single individuals may be missing some of these symptoms (eg. patients with Gordon Holmes syndrome), these are part of a continuum of CHIP-associated disease features, rather than in isolation.

(Hayer *et al.*[13])

Multiple *STUB1* mutations have been linked to the pathogenesis of SCAR16. Although their molecular and cellular consequences are still unclear, they support a loss-of-function disease mechanism. SCAR16 is an adolescent-onset, fate and rare form of neurogenerative disease characterized by ataxia, gait instability, loss of balance and discoordination, due to cerebellar degeneration, in addition to cognitive impairment. Apart from mutations that abort translation of full-length CHIP, 13 point mutations have been reported, spanning from the TPR domain (E28K, N65S, A79D/T and L123V), to the linker region (N130I, K145Q, W147C, L165F and M211I) and the U-box (S236T, M240T and T246M)[38,49]. These are biallelic *STUB1* mutations identified by screening ataxia patients with whole exome sequencing. The majority of these mutations are inherited in a compound heterozygotic manner and they affect its protein structure and folding. Some mutations impair CHIP's catalytic activities, while others destabilise the protein, or both. The end-effect is compromised CHIP activity as a chaperone and, possibly more severely, as an E3 ligase[13,38,49].

CHIP mutant were showed a severely compromised E3 ligase activity (namely N65S and L123V[38,49], and U-box mutants S236T, M240T and T246M (Figure 1.13))[49]. A possible explanation is the mutated residues are important for CHIP-substrate binding, thus directly diminishing CHIP's docking-dependent intrinsic E3 ligase activity. This is the case of the N65S CHIP mutant, which only poorly ubiquitinated Hsc70 whilst having an auto-ubiquitination pattern similar to WT CHIP[38]. However, an impaired CHIP-substrate binding may be caused indirectly: by a compromised interaction between CHIP and the previously formed chaperone-substrate complex (which facilitates ubiquitination of misfolded proteins). Indeed, some TPR mutant CHIP isoforms (N65S and L123V) showed a weakened affinity for chaperones by fluorescence polarization assay, which is likely to impair CHIP-chaperone interaction, being a possible pathogenic mechanism[49]. However, it is not the common biological consequence of all TPR mutant CHIP isoforms, since E28K showed similar ubiquitination activity as WT CHIP[38].

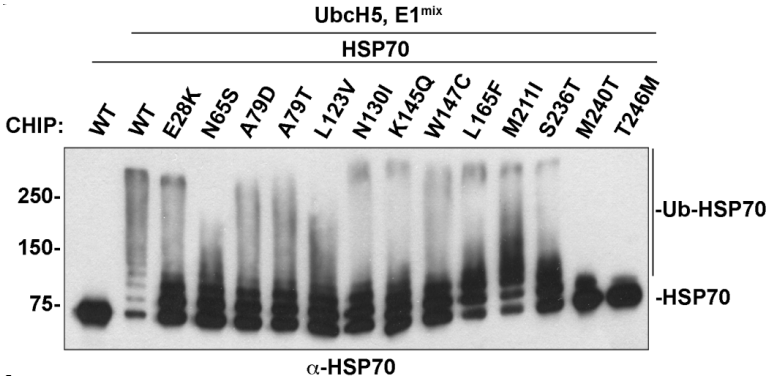


**Figure 1.13: E3 ligase activity of CHIP mutations**
*In vitro* ubiquitination assay of Hsp70 by WT and SCAR16 CHIP mutants performed for 1h at 37ºC.

(Kanack *et al.*[49])

A second hypothesis of the mechanism of action of CHIP mutants is that these fail to ubiquitinate substrates due to defects in E2 recruitment (preventing Ub chain formation) or structural defects preventing the anchoring of ubiquitination chains on the substrate[38,49]. Time-resolved fluorescence energy transfer (TR-FRET) revealed that mutations in the U-box and the TPR mutant N65S prevented E2 recruitment[49]. Hence, it is not surprising that the T246M mutant failed to ubiquitinate Hsc70 and to

auto-ubiquitinate[38]. The other mutations only formed free Ub chains due structural defects (causing a poor alignment between the E2 and the substrate)[49].

A third mechanism that is not mutually exclusive regarding mutations that impair the catalytic domains are mutation-driven changes in overall protein folding and oligomeric state that would also lead to loss-of-function. T246M CHIP, and other mutants, had a loss of secondary structure[38,49]. This structural instability explains its tendency to aggregate (from dimeric to mainly monomeric and higher-order oligomers[38]) both *in vitro* and in cells. In the latter system, a decrease in the steady-state levels of CHIP was also observed, which could have similar consequences to CHIP loss-of-function[38,49]. However, this mechanism does not apply to all mutations in enzymatic domains, since the TPR mutant E28K showed a 28% and 67% decrease in dimeric and monomeric conformations, respectively, while the N65S mutation increases the formation of highly stable dimers, having a similar biophysical profile as WT CHIP[38]. This mechanism of action seems to be particularly relevant for CHIP mutants with point mutations in the linker domain (e.g. M211I)[38]. Alternatively, rather than resulting in bulk structural changes in CHIP, mutations in the U-box directly or the TPR domain can alter the flexibility and molecular motions of the U-box domain, compromising the E3 ligase activity. Mutations and interactions to the TPR domain has been shown to allosterically regulate the U-box, including chaperone-binding[47]. Therefore, using Hsp70 as a read-out of the E3 ligase activity of the SCAR16 CHIP mutants is not ideal, since chaperone-binding itself allosterically inhibits the U-box.

## 1.4.2 Neuroprotective activity of CHIP

The association of CHIP loss-of-function mutations to neurodegeneration is strong proof-of-concept of its involvement in the maintenance of neuronal health. However, we lack mechanistic insight into its neuroprotective actions.

Age is the strongest risk factor for neurodegenerative diseases, thus indirect and direct effects of CHIP in the ageing processes could help to explain its actions. Furthermore, given the proteinopathic nature of most neurodegenerative diseases, CHIP could also help to prevent widespread protein accumulation or counteract the dysregulation of specific disease-associated proteins (such as $\alpha$-Syn in

synucleinopathies). These potential neuroprotective mechanisms will be reviewed. It is interesting to consider that advanced neurodegeneration mimics, to some extent, loss-of-function of CHIP, as WT CHIP can become trapped in the aggregates formed as a result of the pathomechanism[25]. In this scenario, CHIP losses its neuroprotective effects.

### a. Indirect role of CHIP in regulating longevity

The course of neurodegeneration is long and complex, having a cascade of events that unravel before aggregate formation, detection of disease biomarkers and manifestation of clinical symptoms. There extensive evidence to suggest that CHIP counteracts protein dyshomeostasis, preventing proteotoxicity, which is a known driver of ageing. This is largely due to its pivotal roles in PQC and stress responses. Furthermore, small changes in its expression and/or activity are likely to have pronounced effects in cell health, due to its dual actions and vast substrates.

CHIP KO mice and *Drosophila* have increased proteotoxic stress compared to age-matched WT - evident from the rapid age-dependent accumulation of oligomers (Figure 1.14)[14,62]. In parallel, CHIP KO mice have compromised 26S proteasomal activity[14] and extensive oxidative stress (both at protein and lipid levels) in the brain[15]. CHIP KO flies are also more sensitive to drug-induced oxidative stress[62]. Whether impairments in PQC mechanisms and redox homeostasis are a cause or consequence of the proteotoxic stress, they feed a viscous cycle that is commonly seen in ageing and, more severely, across neurodegenerative diseases. There is strong evidence to suggest that oxidative stress contributes to ageing[89]. However, the accelerated ageing phenotype observed in CHIP KO mice was more severe than in animals lacking enzymes directly involved in redox homeostasis (e.g. superoxide dismutase, SOD), supporting the role of CHIP in the regulation of different housekeeping processes[14].

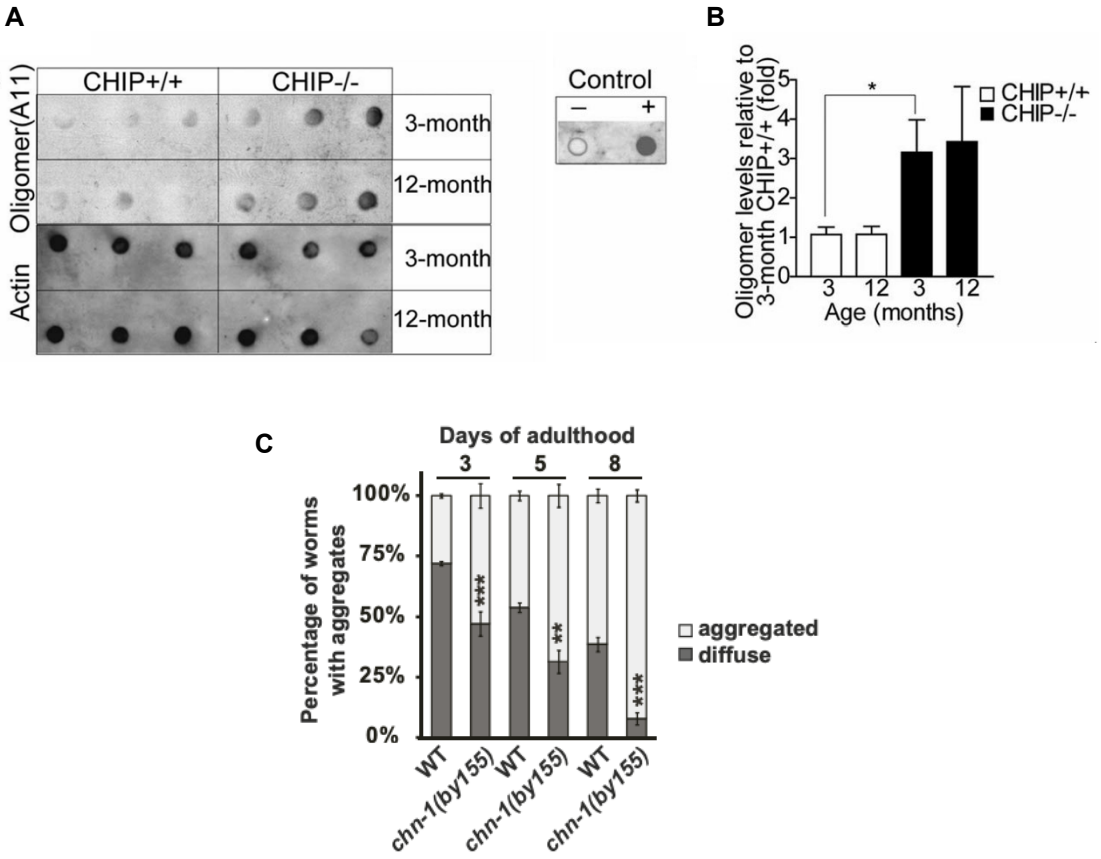


**Figure 1.14: Proteotoxic stress in CHIP KO mice and Drosophila**
**A)** Dot blot using an anti-oligomer antibody against cortical tissue lysate of CHIP KO and WT mice of 3 and 12 months old (left). R120G (α-R-crystallin) was used as a positive control (right). The antibody recognises soluble aberrantly folded oligomers.
**B)** Oligomer levels were 3-fold higher in both 3- and 12-month old CHIP KO mice compared to age-matched controls (right).
**C)** Loss-of-function allele *chn-1 (by155*) lack the single CHIP worm ortholog have increased age-dependent aggregation of a mutant polyglutamine protein and have decreased survival rates when treated with paraquat (drug-induced oxidative stress).
(**A-B**: Min *et al.*[14]; C: Tawo *et al.*[62])

Another mechanism by which CHIP has been implicated in the prevention of proteotoxic stress, is in the maturation of aggresomes. Cells lacking CHIP have increased protein aggregates that fail to form mature aggresomes, a process that is dependent on its E3 ligase activity[90]. These have been described as neuroprotective, as age-dependent aggregate load is believed to improve proteostasis and mitigate the effects of proteome imbalance. Aggregates in aged long-lived worms consist mainly of highly abundant and stable proteins (with lower intrinsic aggregation propensity), whilst aggregates in aged short-lived worms include more aggregation-prone proteins (highly instable, unstructured and more hydrophobic) (Figure 1.15).

The composition of the latter resembles inclusions detected across neurodegenerative diseases[19]. This supports the hypothesis that controlled sequestration of disease proteins may be a beneficial and active defence mechanism. Like small HSPs (Figure 1.15 B&C), CHIP may contribute to this active, proteome-wide mechanism in promoting protective aggregation[19,90]. CHIP-mediated aggresome maturation requires ubiquitination of inducible nitric oxide synthase (iNOS) by CHIP in a chaperone-dependent manner. Ubiquitinated iNOS becomes sequestered in aggregates and interacts with HDAC6, which is necessary for maturation of the aggresome. This mechanism is promoted in conditions of proteasomal overload. Therefore, by promoting healthy aggregation, CHIP indirectly prevents ageing.

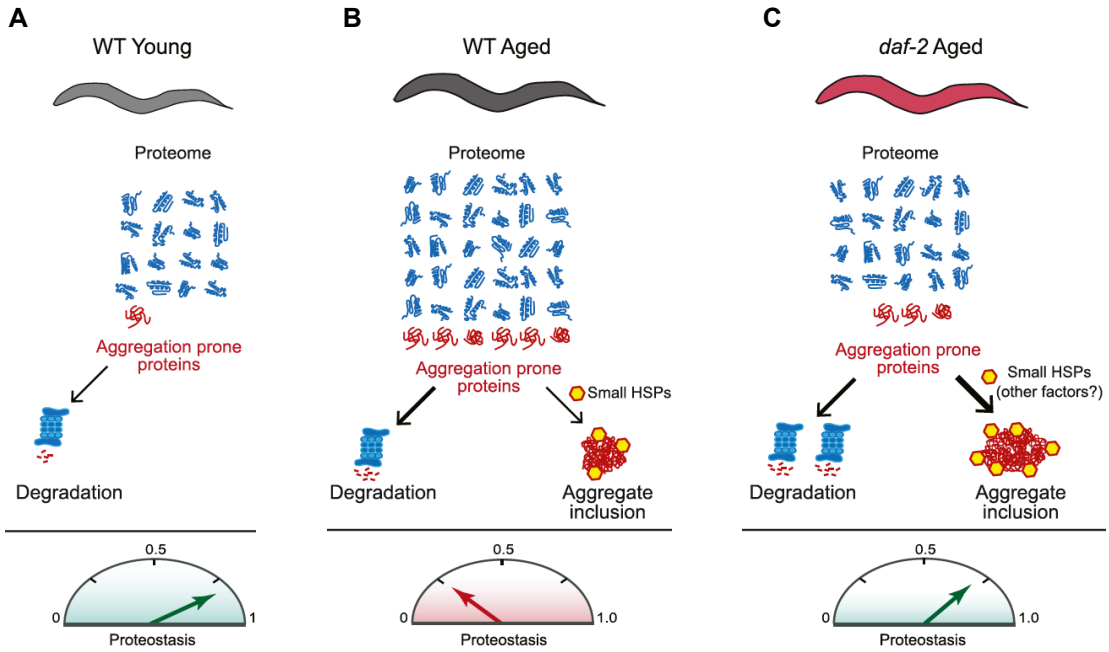


**Figure 1.15: Aggresome formation**
**A)** In young adult WT worms, proteostasis is maintained and soluble aggregates (*red*) are efficiently cleared.
**B)** In aged WT worms, accumulated aggregation-prone species associate with small HSPs. These may act to seed and concentrate aggregation material. However, mechanisms of protective aggregation are only partly active when proteostasis is strongly reduced.
**C)** In daf-2 mutant worms with increased longevity, mechanisms of protective aggregation formation are fully active, thus proteostasis collapse is delayed.
(Adapted from Walther *et al.*[19])

Signs of a progeria phenotype in CHIP KO models were observed at both cellular and organ levels. For example, tissues derived from CHIP KO cells had markers of senescence (including senescence-associated β-galactosidase and lower

proliferation rate compared to WT), compromised energy biogenesis and mitochondria homeostasis[14,15,78]. Therefore, if CHIP-mediated neuroprotective mechanisms are chronically or become gradually impaired during the course of disease, homeostatic defects build up and premature ageing is the end-result.

### b. Direct role of CHIP in regulating longevity

One way in which CHIP can influence the development of neurodegenerative diseases is by directly modulating proteins involved in the regulation of longevity, since ageing is intimately related with neurodegeneration. P53 is a key modulator of cell arrest, repair and death when stressed or damaged, by transcriptionally regulating genes involved in cell cycle control, DNA repair, apoptosis and cellular senescence (irreversible growth arrest). To remain responsive, p53 levels must be kept at low levels and accumulate upon stress, having its levels regulated by various post-translational modifications and Ub-dependent proteasomal degradation. The latter is chiefly mediated by the E3 ligase MDM2, but chaperone-dependent ubiquitination of p53 by CHIP has been reported[91], although the supporting data is weak and derived from overexpression systems.

However, it has been reported that p53 levels are increased in presenescent cells and then decreased in terminally senescent cells, which negatively correlates with CHIP levels and activity. This paved way to the hypothesis that CHIP-mediated degradation of p53 is important for a timely transition to arrest, whilst MDM2 regulates p53 at basal conditions[91]. As mentioned, CHIP KO mice have increased markers of senescence[14] and CHIP silencing in young fibroblasts results in premature senesecence[91]. Furthermore, in a senescence-accelerated mouse model, CHIP expression was abnormally decreased in the cerebral cortex and hippocampus[92]. Taken together, CHIP could regulate longevity via regulation of p53 and senescence.

More recently, CHIP has been reported to ubiquitinate the INSR and affect the lifespan of organisms. Not only does the insulin and insulin-like growth factor 1 signalling (IIS) influence longevity, it regulates innate immunity, stress response and proteotoxic stress resistance. CHIP loss-of-function worms have a reduced lifespan that is mimicked by RNAi-mediated downregulating daf-16 (a transcription factor

downstream of daf-2, the worm orthologue of INSR), and in turn the IIS. This phenotype was not further reduced by deleting the CHIP orthologue, chn-1 (Figure 1.16A), implying that CHIP might affect longevity through the IIS. Mechanistically, CHIP-mediated chaperone-independent mono-ubiquitination of INSR triggers endocytic-lysosomal turnover, under basal conditions. However, with increasing proteotoxic stress (i.e. during ageing), the capacity of CHIP to degrade the INSR is diminished (Figure 1.16B), leaving to its accumulation which is associated with the activation of pro-ageing genes[62]. Therefore, through PQC mechanisms, CHIP can regulate p53 and INSR, influencing longevity mechanisms directly.

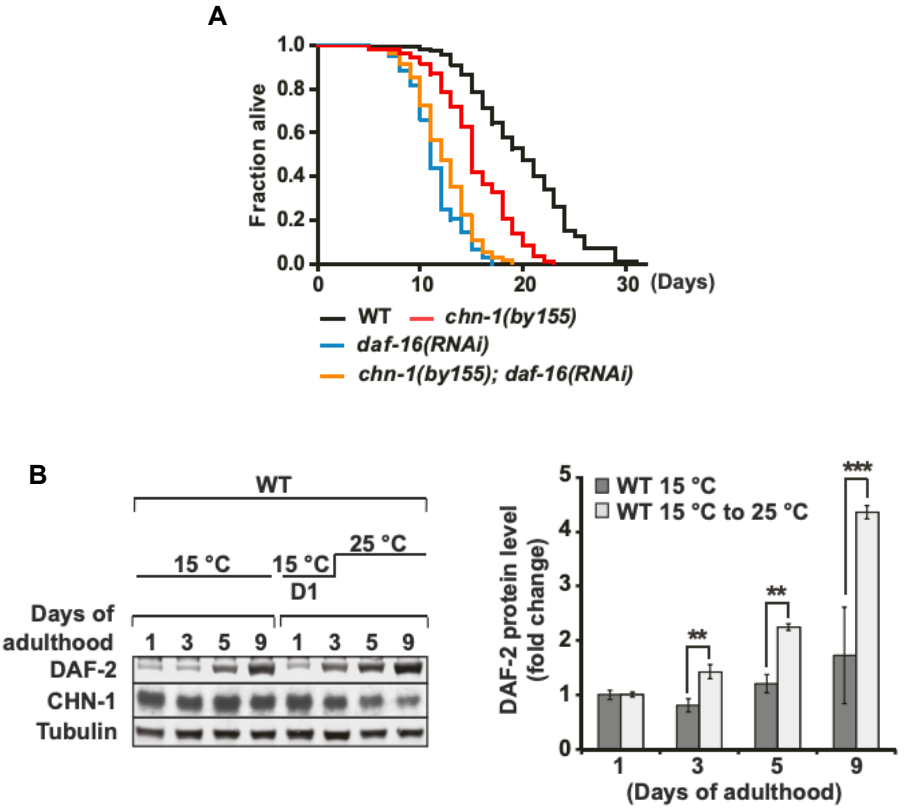


**Figure 1.16: CHIP modulates longevity pathways directly**
**A)** *C. elegans* chn-1 mutant (*by155*) exhibits a reduced lifespan compared to WT and in a similar manner as worms with depleted daf-16 (by RNAi). Daf-16 depletion in the chn-1 mutant worm did not reduce longevity further.
**B)** WT worms that were temperature-shifted (from 15ºC to 25ºC at day 1 of adulthood) show an age-related increase in daf-2 that was not significantly detected in controls worms.
(Tawo *et al.*[62])

### c. CHIP interactions with disease-specific proteins

The presence of CHIP within LB of patients with α-Synucleinopathies[25] and its ability to ubiquitinate α-Syn[25,93] supported its involvement in the pathology of PD and DLB[25]. Through its chaperone and E3 ligase activity, CHIP could counteract the accumulation of toxic misfolded, disease-associated proteins. Multiple studies have supported this hypothesis as a possible mechanism of action underlying CHIP's neuroprotective effects.

Although there are increasing studies reporting interactions between CHIP and α-Syn, the biochemical details and biological significance of such remain largely unknown, because assays tend to rely on overexpression systems and the use of tagged or modified proteins. Not only are these non-physiological systems, but the overexpression of CHIP is intrinsically fraudulent due to its expected pronounced effects on proteostasis. Nonetheless, the prevailing hypothesis regarding the role of CHIP in the context of synucleinopathy is that its neuroprotective effects are driven by CHIP-dependent regulation of α-Syn homeostasis.

*In vitro*[37] and *in vivo*[94] studies aimed at observing α-Syn aggregation in difference CHIP backgrounds, suggested that CHIP may play a role in suppressing α-Syn aggregation and inclusion formation. Overexpression of CHIP decreased the number and size of α-Syn aggregates (Figure 1.17) and significantly prevented neuronal loss, mitigating α-Syn-induced toxicity[94]. *In vitro* mutational strategies (using CHIPΔU and CHIPΔTPR) showed that this CHIP-mediated reduction in α-Syn oligomer formation occurs in an chaperone-dependent manner, involving Hsp70[37] or Hsp90[35]. This was contradicted by Shin *et al.*[25], who reported that either of CHIP's enzymatic domains independently were sufficient to achieve reduction of α-Syn-rich inclusions and change their morphology from large inclusions to diffuse micro-aggregates (Figure 1.18). Therefore, different pathways (non-degradative and/or degradative via the proteasome or lysosome) may be employed[25]. The biological significance of these changes is unclear.

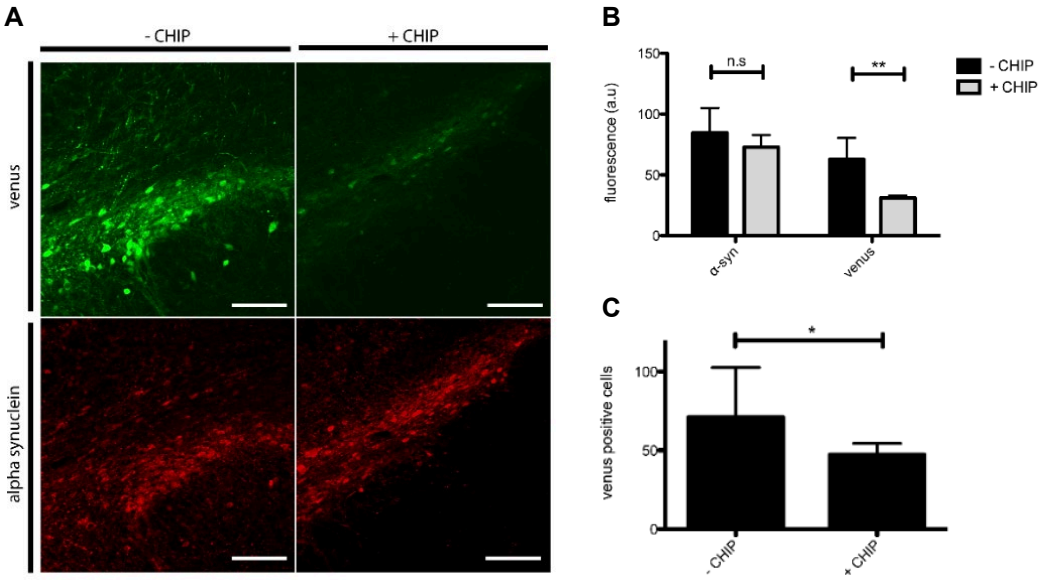


**Figure 1.17: Effect of CHIP on in vivo α-synuclein aggregation**
**A)** For the in vivo bimolecular fluorescence complementation (biFC) assay rats were co-injected AAV-venus1-synuclein and AAV-synuclein-venus2 ± AAV-myc-CHIP. Interaction of both tagged synuclein fragments results in venusYFP fluorescence (by reconstituting the fluorophore), hence regarded as a read-out of α-Syn aggregation. CHIP presence decreased fluorescence intensity by 50% (**B**) and venusYFP-positive cells by 35% (**C**).

(Dimant *et al.*[94])

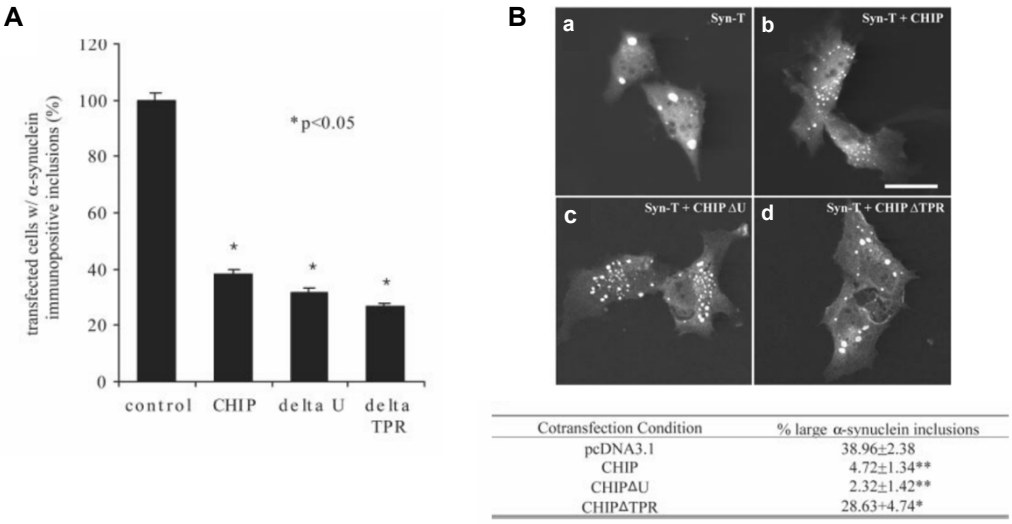


| Cotransfection Condition | % large α-synuclein inclusions |
|---|---|
| pcDNA3.1 | 38.96±2.38 |
| CHIP | 4.72±1.34** |
| CHIPΔU | 2.32±1.42** |
| CHIPΔTPR | 28.63+4.74* |

**Figure 1.18: Effect of CHIP on in vitro α-synuclein aggregation**
H4 cells cotransfected with Syn-T, synphilin-1, and either CHIP, CHIPΔU, or CHIPΔTPR were immunostained for α-Syn.
**A)** Quantification of the number of inclusions per cell.
**B)** Single cells immunopositive for inclusions in the different co-transfection conditions, together with the quantification of large inclusions present (*below*). CHIP (**b**) and CHIPΔU (**c**) transfection resulted in a reduction of the number of large inclusions compared to control cells (**a**), while CHIPΔTPR (**d**) cells had large inclusions with a similar morphology to those seen in cells without CHIP overexpression (**a**). Therefore, CHIP's effect on inclusions seems to be largely dependent on its chaperone functions.

(Shin *et al.*[25])

There is limited *in vitro* (Figure 1.19A) and *in situ* (Figure 1.19B) evidence to support that CHIP mono-, multi-mono- and/or poly-ubiquitinates α-Syn[68]. However, α-Syn ubiquitination tends to be studied under optimal conditions and in genetically manipulated models, thus direct evidence of CHIP-dependent ubiquitination of endogenous α-Syn in both healthy and synucleinopathy background is still lacking. This could be of biological significance, given the suggested negative correlation between α-Syn ubiquitination and aggregation. Overexpression of mutant α-Syn fragments that could not be ubiquitinated resulted in a 16% increase in oligomerisation compared to WT fragments. Oligomerisation was quantify using the bimolecular fluorescence complementation assay[68]. This approach is not only limited by the problems associated with overexpression, but also by the effects of introducing a fluorescent tag in a highly flexible and dynamic proteins such as α-Syn.

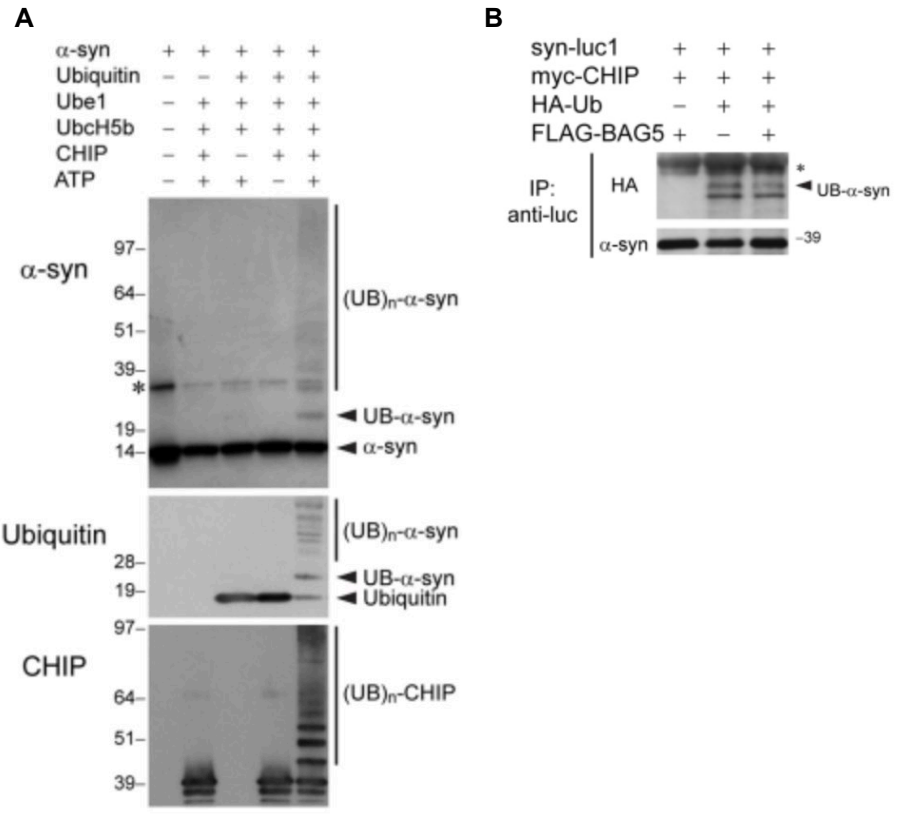


**Figure 1.19: CHIP-mediated ubiquitination of α-synuclein in vitro (A) and in cells (B)**
**A)** *In vitro* ubiquitination assay was performed by incubating purified recombinant human untagged WT α-Syn, Ub, Ube1, UbcH5b, CHIP, and Mg-ATP as indicated. Reactions were analysed by SDS-PAGE/immunoblot using anti-α-Syn and anti-Ub Abs. Mono- and polyubiquitinated α-Syn species were detected. The asterisk (*) indicates a non-specific band. **B)** H4 cells were transfected with syn-luc1, myc-CHIP, HA-Ub and FLAG-BAG5, as shown. Immunoprecipitations with anti-luc were performed and analysed by SDS-PAGE/immunoblot using anti-α-Syn and anti-HA Abs. The asterisk (*) indicates cross-reactivity of the secondary antibody with the immunoglobulin light chain.

(Kalia et al.[68])

Both chaperone and E3 ligase functions may cumulatively contribute to the regulation of α-Syn homeostasis, since reduction of CHIP levels caused a 35% increase in oligomerisation of WT α-Syn fragments[68]. Despite the limitations of the studies discussed, all of them support the direct relationship between of α-Syn homeostasis (e.g. by influencing the free pool of α-Syn) and oligomerisation/aggregation.

## 1.5 Objectives of this thesis

Although defects in protein homeostasis are regarded as early drivers of neurodegeneration, these tend to be studied in the context of aggregation (i.e. proteotoxic stress). However, aggregates are the consequence of years of disease and are rather late biomarkers of cellular stress. Early and more subtle changes in the proteome could shed light into disease-promoting events. These are also likely to be the most promising therapeutic targets to stop or slow down disease progression.

This project aims to investigate the protein targets of CHIP in a synucleinopathy background prior to pronounced proteome imbalances and neurodegeneration. Identification of protein targets of CHIP could help explain its early neuroprotective effects, which remain largely unknown. In contrast, several mechanisms have been proposed regarding its chaperone and E3-ligase functions in models with late biomarkers or symptoms of disease, where comprehensive and robust stress responses have been activated. This masks the intrinsic functions of CHIP, which could have the most biological significance in promoting neuroprotection.

For a comprehensive understanding of how CHIP regulates protein homeostasis in neuronal cells, this project focuses on the manipulation of endogenous CHIP. This will be accomplished using a combination of novel precision biologic tools and gene-edited authentic neuronal cell models. Chapter 3 describes the engineering of CHIP KO patient-derived induced pluripotent stem cells (iPSC) and subsequent differentiation into cortical neurons. The effect of the deletion on the proteome will be evaluated using an unbiased approach (Chapter 4).

Candidate protein targets identified will be further investigated in different CHIP cell models in attempt to obtain mechanistic insight into the underlying CHIP-mediated regulation and its possible cellular significance (Chapter 5). Finally, tools to modulate CHIP's activity *in vitro* and *in situ* will be produced and their effect evaluated in Chapter 6. The aim is to enrich our understanding of the biochemical properties and activity dynamics of CHIP.

# Chapter 2: Materials and Methods

## 2.1 Materials

### 2.1.1 Chemicals

All chemicals and solvents were obtained from commercial sources (Sigma, if not otherwise stated) and are Analar or molecular biology grade. Buffers were made up with deionized water.

### 2.1.2 Cell lines

**Table 2.1: Cell lines and culturing conditions**

| Cell line | Gene edit | Culturing conditions | Origin |
|---|---|---|---|
| SH-SY5Y | CRISPR control (CHIP WT) | DMEM (41965-039, Gibco), 10% fetal bovine serum (10270-106, Gibco), 37ºC, 5% $CO_2$ in a humidified atmosphere. | Human neuroblastoma line |
| | CHIP KO | | |
| | CHIP KO expressing H260Q mutant CHIP (stable transfection) | | |
| | CHIP KO expressing K30A mutant CHIP (stable transfection) | | |
| | CHIP KO expressing WT CHIP (stable transfection) | | |
| AST23 | Unedited | iPS-Brew XF (130-104-368, StemMACS, Miltenyi Biotech Inc.), 37ºC, 5% $CO_2$ in a humidified atmosphere. | iPSC derived from the fibroblasts of a synucleinopathy patient (carrying a *SNCA* triplication) |
| | Clone name: C1<br>CRISPR control (CHIP WT) | | |
| | Clone name: D3<br>CHIP heterozygous null | | |
| | Clone name: C6<br>CHIP KO (homozygous) | | |

The parental (unedited) cell lines were a kind gift from Dr Tilo Kunath.

The CHIP SH-SY5Y model was engineered by Erisa Nita[95].

## 2.1.3 Antibodies

**Table 2.2: Primary antibodies**

| Target | Class | Name/Reference | Source |
|---|---|---|---|
| CHIP | Mouse mAb | 3.1 | Gift by B. Vojtesek |
| α-Synuclein | Mouse mAb | 610787 | BD Biosciences |
| ANXA2 | Mouse mAb | Ab54771 | Abcam |
| ANXA2 | Rabbit pAb | Ab41803 | Abcam |
| S100-A11 | Rabbit pAb | 10237-1-ap | Proteintech |
| p53 | Mouse mAb | DO-1 | Gift by B. Vojtesek |
| LC3B | Rabbit pAb | Ab48394 | Abcam |
| p62 | Rabbit pAb | BML-PW9860 | Enzo Life Sciences |
| K48-specific chain linkage | Rabbit mAb | 4289S | Cell Signalling Technology |
| K63-specific chain linkage | Rabbit mAb | 5621S | Cell Signalling Technology |
| Ubiquitin | Mouse mAb | P4D1, sc-8017 | Santa Cruz Biotechology |
| Ubiquitin | Mouse mAb | F-11, sc-271289 | Santa Cruz Biotechology |
| Ubiquitin | Mouse mAb | FK2, PW8810 | BioMol |
| V5 | Mouse mAb (IgG2a) | Ab27671 | Abcam |
| V5 | Goat pAb | Ab9137 | Abcam |
| β(III)-tubulin | Mouse mAb IgG2b | Tuj, T8660 | Sigma |
| Pax6 | Mouse mAb IgG1 | AB_528427 | DSHB |
| Tbr1 | Rabbit pAb | ab31940 | Abcam |
| Ctip2 | Rat mAb | ab18465 | Abcam |
| Cux1 | Rabbit pAb | sc-13024 | Santa Cruz Biotechnology |
| HLA-B | Rabbit pAb | PA5-35345 | Invitrogen |
| HLA-A | Rabbit pAb | PA5-29911 | Invitrogen |
| HLA-C | Rabbit mAb | Ab126722 | Abcam |
| β-actin | Mouse mAb | A5441 | Sigma |
| GAPDH | Mouse mAb | 1650326 | Abcam |
| VGF | Mouse mAb | B-8 | Santa Cruz |
| VGF | Rabbit pAb | Ab69989 | Abcam |
| IFITM1/3 | Mouse mAb | MHK | Gift by B. Vojtesek |
| INSR | Mouse mAb | Ab69508 | Abcam |
| Hsp90 | Mouse mAb | SPA-830 | Stressgene Bioreagents Corp. |
| PARP | Mouse mAb | MAB3290 | Millipore |
| FLAG | Mouse mAb | F3165 | Millipore |

Table 2.3: Secondary antibodies

| Target | Class | Conjugate | Reference | Source |
|---|---|---|---|---|
| Mouse | Rabbit pAb | HRP-conjugate | PO260 | Dako |
| Rabbit | Swine pAb | HRP-conjugate | PO217 | Dako |
| Mouse (IgG1) | Goat pAb | A488 | A21121 | Invitrogen |
| Mouse (IgG1) | Goat pAb | A555 | A21127 | Invitrogen |
| Mouse (IgG2b) | Goat pAb | A647 | A21242 | Invitrogen |
| Mouse (IgG2b) | Goat pAb | A488 | A21141 | Invitrogen |
| Rat | Goat pAb | A630 | A11007 | Invitrogen |
| Mouse (IgG1) | Donkey pAb | A488 | A21202 | Invitrogen |
| Mouse (IgG1) | Donkey pAb | A594 | A21203 | Invitrogen |
| Rabbit | Donkey pAb | A488 | A21206 | Invitrogen |
| Rabbit | Donkey pAb | A555 | A31572 | Invitrogen |
| Mouse | Donkey pAb | PLA, minus probe | DUO92001 | Sigma |
| Rabbit | Donkey pAb | PLA, plus probe | DUO92005 | Sigma |

### 2.1.4 Plasmids

Table 2.4: Plasmids

| Plasmid | Description | Expression | Source |
|---|---|---|---|
| pSF-CMV (OG2) | Contains the pUC high-copy origin of replication. Ampicillin resistance. | Mammalian | Oxford |
| LentiV2 CRISPR plasmid | Contains two expression cassettes: hSpCas9 and the guide RNA: GGCCGTGTATTACACCAACC | Mammalian | Erisa Nita |
| pmaxGFP | Encodes GFP. | Mammanlian | Lonza |
| 16AAVZBP_scFv_11F_V5_pMA-T | Holder plasmid containing the V5-tagged scFv-encoding insert. Ampicillin resistance. | Bacterial | Invitrogen |
| 16AAVZBP_scFv_11F_FLAG_pMA-T | Holder plasmid containing the V5-tagged scFv-encoding insert. Ampicillin resistance. | Bacterial | Invitrogen |
| pET3a | Encodes His-tagged wild-type CHIP | Bacterial | Gift from Dr Vikram Narayan |
| pet15b -UbcH5$\alpha$ | Encodes the E2 conjugating enzyme, UbcH5$\alpha$. Ampicillin resistance. | | Gift from Dr Fiona Lickiss |

The glycerol stocks of BL21-DE3 bacteria expressing either 11F or 7A scFv antibodies were a kind gift from Mariana Santos[96].

## 2.1.5 Primers

### a. For polymerase chain reaction (PCR)

CHIP

Forward: AGAACGAGGGTGCGATGC

Reverse: GATGTCGTCCCCGAAGTTCA

Tm = 68ºC

### b. For quantitative reverse transcription PCR (qRT-PCR)

Primers for qRT-PCR (outlined in Table 2.5) were obtained from Sigma and designed using the Universal ProbeLibrary Assay Design Center (Roche).

**Table 2.5: Primers for qRT-PCR**

| Target gene | UPL Probe # | Primer (5' – 3') | | Efficiency |
|---|---|---|---|---|
| | | Forward sequence | Reverse sequence | |
| *hCDK6* | 85 | gaactaggcaaagacctacttctga | ggtgggaatccaggttttct | 2.161 |
| *hNanog* | 87 | tctccaacatcctgaacctca | ttgctattcttcggccagtt | 2.004 |
| *hOct4* | 78 | tgccgtgaaactggagaag | gcttggcaaattgttcgagt | 2.015 |
| *hVimentin* | 11 | agatggcccttgacattgag | cagggaggaaaagtttggaa | 1.844 |
| *hNestin* | 65 | acctgtgccagcctttctta | gccaaggtaggggtacgg | 2.154 |
| *hOtx2* | 86 | aacctcccatgaggctgtaa | ggtggacaggttcagagtcc | 2.007 |
| *hEmx1* | 25 | ctctccgagacgcaggtg | ttcttctgctcggactcagg | 2.015 |
| *hPax6* | 20 | tcaccatggcaaataacctg | cagcatgcaggagtatgagg | 1.980 |
| *hFoxG1* | 58 | tactaccgcgagaacaagca | tcacgaagcacttgttgagg | 2.075 |
| *hTbr2* | 69 | gagtcggcaggtgggtag | tcttccgaggggaaggtaa | 1.953 |
| *hTbr1* | 31 | ttcaaataacaatgggcagatg | gtctcagggaaagtgaacgtct | 2.156 |
| *hCtip2* | 82 | ccgccagagatagggttttt | ctggtcatgcacaacctcag | 2.032 |
| *hCux1* | 20 | agaggccactgccctattct | ctggagatgatggaaagcagt | 2.019 |
| *hBrn2* | 80 | ctttgcaggcgagtaaccag | ttctagctatcacacactctcctca | 1.967 |
| *hSNCA* | 68 | gagggagtggtgcatggt | tgctgtcacacccgtcac | * |
| *hStub1* | 70 | gttcgtgggccgaaagta | ggcccggttggtgtaata | 1.874 |
| *hTBP* | 87 | gaacatcatggatcagaacaaca | atagggattccgggagtcat | 2.005 |

*Published[97]

## 2.2 Microbiological techniques

All microbiological techniques were performed using aseptic conditions.

### 2.2.1 Growth of bacterial cultures

Bacterial cultures were grown in Luria-Bertani (LB) broth in an incubator-shaker at 37ºC and 220 rpm. To ensure adequate aeration, the sterile vessels used were at least 4-times the volume of the culture being grown. According to the resistance of the plasmid, selective antibodies were added to the culture (for ampicillin, a concentration of 100 μg/ml was used). When indicated, glucose was added to the LB broth.

LB broth
1% (w/v) Tryptone
0.5% (w/v) Yeast extract
1% (w/v) NaCl
Sterilised by autoclaving (121ºC, 20 min).

LB-agar plates were prepared by heating agar until liquid, cooling it to about 40ºC, adding the selective antibiotic (using the same final concentration as above) and pouring into 90 mm petri dishes. The plates are further cooled until the agar has solidified and were then allowed to dry at 37ºC for 1 h prior to use.

LB agar
1% (w/v) Tryptone
0.5% (w/v) Yeast extract
1% (w/v) NaCl
1.5% (w/v) Agar
Sterilised by autoclaving (121ºC, 20 min)

## 2.2.2 Glycerol stocks

For long time storage of bacterial cultures, glycerol stocks were prepared. For such, 800 µl of overnight culture was aliquoted into a sterile cryotube and 200 µl of 70 % (v/v) sterile glycerol was added and mixed gentle. Glycerol stocks were snap-frozen in liquid nitrogen and stored at -80ºC.

## 2.2.3 Preparation of competent cells

Bacteria (DH5a and BL21(DE3)) from glycerol stocks (Invitrogen) were inoculated into 3 ml of sterile, antibiotic-free LB broth and incubated overnight in a shaking incubator at 37ºC and 220 rpm. The overnight culture was diluted 1:200 in fresh LB media (e.g. 250 µl of the overnight culture into 50 ml of LB media) and grown until $OD_{600\ nm}$ (measured using Lambda Bio, Perkin Elmer) has reached 0.4 - 0.6. The culture was then cooled down on ice and then centrifuged at 4000 rpm for 15 min at 4ºC.

The pellet was resuspended in ice cold buffer I (16 ml when using the volumes mentioned above) and incubated for 10 min on ice. Cells were centrifuged again as above. The pellet was resuspended in ice cold buffer II (2 ml) and incubated for 10 min on ice. This was then aliquoted into pre-chilled sterile microcentrifuge tubes. The aliquots (containing 50 µl of competent cells) were snap-frozen in liquid nitrogen and stored at -80ºC.

Buffer I
60 mM $CH_3COOK$
10 mM RbCl
10 mM $CaCl_2$
40 mM MgCl
15 % (v/v) Glycerol
pH 5.8 with $CH_3COOH$
Sterilised by filtration (using a 0.22 µm filter).

Buffer II
10 mM MOPS

10 mM RbCl

75 mM $CaCl_2$

15 % (v/v) Glycerol

pH 6.5 with NaOH

Sterilised by filtration (using a 0.22 μm filter).

### 2.2.4 Transformation of competent cells by heat shock

DNA (100-200 ng of plasmid DNA or 10 μl of the ligation reaction) was added to a 50 μl aliquot of DH5α *E. coli* previously thawed on ice. The mixture was incubated for 30 min on ice and then heat shocked: incubated for 40 sec at 42ºC and then quickly cooled on ice for 2 min. LB broth (450 μl) was then added and the bacterial cells were placed in a shaking incubator for 1 h at 37 ºC and 220 rpm. Cells (100-150 μl) were plated onto 10-cm LB agar plates with the appropriate antibiotic and incubated upside down overnight at 37ºC.

## 2.3 Molecular biology techniques

### 2.3.1 Plasmid DNA amplification, extraction and quantification

As described, 5 ml or 250 ml overnight bacterial cultures were used for small (QIAprep Spin Miniprep Kit, Qiagen) or large (HiSpeed Plasmid Maxi Kit, Qiagen, or GeneJET Plasmid Maxiprep Kit, Invitrogen) scale plasmid DNA purification, respectively. DNA extraction was performed according to manufacturer's instructions. Plasmid DNA was eluted in nuclease-free water, quantified using a Nanodrop ND-1000 spectrophotometer and stored at -20ºC.

### 2.3.2 Agarose gel electrophoresis of DNA

Agarose gels were prepared by dissolving electrophoresis-grade agarose (Invitrogen) (1% w/v) in 1X TAE buffer. Once completely dissolved, the agarose was cooled down and SYBR®Safe DNA Gel Stain (1:10000; Invitrogen) was added prior to pouring the gel into the chamber. DNA samples were diluted in 6x loading dye (at a ratio of 5:1,

sample:dye) prior to loading onto the agarose gel. Alongside the samples, DNA ladders were loaded (either Quick-Load 100 bp DNA ladder or 1 kb DNA ladder, from New England Bioscience). The gel was run in 1x TAE buffer at 80-100 V for 45-60 min and visualised using an UV lamp imaging system a built-in camera.

1x TAE buffer
40 mM Tris
1 mM EDTA
pH 8 with glacial acetic acid.

DNA loading dye (6x)
0.25% (w/v) Bromophenol blue
0.25% (w/v) Xylene cyanol
15% (v/v) Glycerol

## 2.3.3 Polymerase chain reaction (PCR)

Gene amplification was performed using the high fidelity *Pfu* DNA polymerase, which possesses 3' to 5' exonuclease proof-reading activity, preventing errors, and has higher thermostability. Reactions were prepared as follows. When preparing multiple samples, master mixtures were made.

**Table 2.6: Components for PCR**

| Component | Volume/amount | Final concentration |
|---|---|---|
| 2x *Pfu* Master Mix (R551, Rovalab) | 25 μl | 1x |
| 100 μM Forward primer (Sigma) | 0.2 μl | 0.4 μM |
| 100 μM Reverse primer (Sigma) | 0.2 μl | 0.4 μM |
| DNA template | 100-200 ng | |
| DNAse-free water | Total volume of 50 μl | |

When using the PCR products for TOPO cloning, *Taq* DNA polymerase (M1661, Promega) was used instead.

For amplification of *STUB1* (CHIP), the following PCR cycling programme was used:

1. Initial denaturation (98ºC for 30 sec)
2. Denaturation (98ºC for 5 sec)

3. Annealing cycles x35 (68ºC for 10 sec)
4. Extension (72ºC for 2 min)
5. Final extension (72ºC for 2min)
6. Hold (4ºC forever).

PCR was performed using the Agilent SureCycler 8800 machine.

## 2.3.4 DNA sequencing

DNA Sanger sequencing was performed by Source Bioscience (LifeSciences) using their stock primers or either forward or reverse primers that were used for cloning.

## 2.3.5 RNA extraction

RNA extraction was performed using the Epicentre MasterPure™ Complete DNA and RNA Purification Kit (Epicentre, MC85200), according to the manufacturer's instructions. RNA was resuspended in RNAse-free water and riboguard RNAse inhibitor (Invitrogen, 10777019). To ensure contaminating DNA is removed, DNAse I (New England Biolabs) was added according to manufacturer's instructions. RNA concentration and purity were assessed using a Nanodrop spectrophotometer.

## 2.3.6 cDNA synthesis

Total RNA (1 μg) was used for cDNA synthesis. When such concentration of RNA yielded less than 12 μl, RNAse-free water was added to make up this volume. Next, samples were incubated with 1 μl of 10 mM dNTP mix (10297018, Invitrogen) and 1 μl of random primers (50 ng/μl) (PCR-545-020T, Invitrogen) at 65ºC for 5 min and then cooled on ice. After a brief centrifugation, 4 μl 5x First strand buffer (28025013, Invitrogen), 2 μl of 0.1M DTT (28025013, Invitrogen) and 1 μl riboguard RNAse inhibitor (10777019, Invitrogen) were added and incubated at 37ºC for 2 min. Note that when preparing multiple samples, master mixtures were made.

Then 1 μl M-MLV reverse transcriptase (200 units/μl) (28025013, Invitrogen) or 1 μl RNase-free water (for the control sample) was added per sample and mixed. Samples

were incubated for 10 min at room temperature, and then 60 min at 37ºC. For inactivation of the reserve transcriptase, samples were incubated for 10 min at 90ºC. The cDNA mix was then cooled on ice, 180 μl of RNase-free water was added and subsequently frozen.

### 2.3.7 Quantitative Reverse Transcription PCR (qRT-PCR)

Each reaction contained 2 μl of 2 μM primer mix (containing both forward and reverse) (Sigma), 0.1 μl of 10 μm UPL Probe (UPL61THRU70, Roche), 5 μl of 2x UPL Probe Master Mix (04707494001, Roche) were performed in 386-well plates, as described by the manufacturer's instructions. This was made up as a stock mix for all samples and replicates. In each well, 7 μl of this mix and 3 μl of cDNA was added. For each primer used, three technical replicates were included. Moreover, for each plate, expression of the housekeeping gene (TATA-binding protein, *TBP*) was quantified. The plate was sealed and centrifuged for 2 min at 1000 rpm. It was then analysed using the Roche LightCycler® 480 System with the Universal Probe Library (UPL) (Roche).

Primers were designed using the Roche UPL Assay design centre and, when possible, intron-spanning primers were designed. Prior to their use for the quantification of gene expression, primers were tested. For such, a dilution series of a positive control sample was made and a negative control (without reverse transcriptase) was included. Primers with efficiency close to 2 were selected.

Raw data includes the crossing point (Cp) value (the cycle at which fluorescence achieved the threshold) for each reaction. The average Cp of *TBP* expression per biological replicate was calculated. To determine the level of relative expression, the difference between this Cp value and that obtained for each sample (i.e. each replicate from all primer sets used) was analysed (ΔCp TBP – Cp Sample). Assuming a doubling of the target DNA during each cycle, $2^{\wedge\Delta Cp\ TBP\ -\ Cp\ Sample}$ was calculated, followed by the average and standard deviations of the technical replicates per gene analysed.

## 2.3.8 Cloning using restriction sites

### a. Designing V5- and 3xFLAG-tagged 11F scFv plasmids

Inserts were designed encoding either V5- or 3xFLAG-tagged 11F scFv antibody and subsequently sub-cloned into a high-copy number mammalian plasmid (pSF-CMV (OG2)). Inserts were optimised for *Homo Sapiens* and included the coding region for 11F. At the C-terminus, one plasmid encoded for the V5-tag and the other the 3xFLAG tag. A SGSG linker between the protein and tag was added to enhance flexibility and aid detection of the tag. An extra alanine was added as well to prevent methylation. Two restriction enzyme (RE) sequences were added at either end of the DNA (5' BamHI and 3' XbaI) although the REs that will be used are NcoI (C/CATGG) and XbaI, because the sequence for the former RE is created by the sequence for BamHI (GGATCC) together with the start of the coding region of 11F (ATGGCC) (underlined), thus preventing frameshift mutations. The 3' end RE site is just after the stop codon. The use of two different REs creates two different complementary ends in both the insert and vector, ensuring incorporation of the insert into the plasmid with the correct orientation (i.e. directional cloning). Inserts were extracted from host plasmids and added to the mammalian expression cassette, which includes the kozak consensus sequence to promote expression.

### b. Restriction digestion

Double digestion of the destination vector and holding plasmids (containing inserts encoding the V5- and 3xFLAG-tagged 11F scFv antibody) was performed using REs (New England Biolabs), NcoI_HF (C/CATGG) and XbaI (T/CTAGA) (enzyme activity: 10000 U/ml), and a compatible buffer, CutSmart Buffer (B7204S, New England Biolabs), according to manufacturer's instructions. Each reaction contains, 1 μg of the insert/vector DNA, restriction enzyme buffer (1x), 10 units of each restriction enzyme, making up a 20 μl solution. Digestion was performed for 2-3 hours at 37ºC in water bath. Control experiment with no/either restriction enzymes are included.

The digested products are analysed on a 1% agarose gel. Next, single bands corresponding to the double-digested vector and insert are excised from the gel under

UV light. The DNA is extracted using the QIAquick Gel Extraction Kit (Qiagen), following manufacturer's instructions.

### c. Ligation

Ligation of double-digested gel-extracted insert and vector was performed using T4 DNA ligase (M0202, New England Biolabs), following manufacturer's instructions. Per reaction (with a total volume of 20 μl), 10 units of the T4 DNA ligase was used, in addition to its buffer, 50-100 ng of vector and the appropriate amount of insert. The amount of insert used was calculated as follows:

$$\text{Amount of insert (ng)} = \frac{\text{Amount of vector (ng)} \times \text{Size of vector (kb)}}{\text{Size of vector (kb)}} \times \text{Molar ratio of } \frac{\text{insert}}{\text{vector}}$$

Different vector:insert ratios were tested (1:4 and 1:5) to increase the chance of a successful ligation reaction. Ligation reactions were prepared on ice and incubated overnight at room temperature.

As previously described, 5 μl of the ligation product was used to transform competent DH5α cells (as previously described). Single colonies were picked and used for making glycerol stocks. To verity the presence of the insert in the selected clones, they were double digested again with the same REs used for cloning – a band corresponding to the insert should be visible. Positive clones were further analysed by DNA sequencing to confirm that the insert is present, free of indels and in-frame with the open reading frame and tag.

## 2.3.9 Cloning using TOPO cloning kit

PCR products obtained using *Taq* DNA polymerase were suitable for sub-cloning into a vector (pCR 2.1-TOPO TA) optimised for high efficiency transformation, using the TOPO-TA Cloning Kit for Subcloning (450641, Invitrogen) according to the manufacturer's instructions. DH5α competent cells were transformed, as previously

described, and the DNA of single colonies was extracted using the QIAprep Spin Miniprep Kit (27104, Qiagen) and sequenced.

## 2.4 Biochemical techniques

### 2.4.1 Protein quantification

#### a. BCA assay

When the sample concentration is low, the Micro BCA Assay Kit (23235, Thermo Scientific) is used according to the manufacturer's instructions of the "microplate procedure". This method has a detection range of 2-40 μg/ml and the concentration of samples is compared to a dilution series of known concentrations of bovine serum albumin (BSA) (A9647, Sigma), ranging the detection limit and sample concentration. Samples and standards were loaded on a 96-well plate and analysed in triplicates. The plate is incubated shaking for 2 hours at 37ºC prior to being cooled down and analysed by a spectrophotometer (Spark Multiplate Reader, Tecan) in absorbance mode at 562 nm. The long incubation ensures that the reactions reach completion, achieving more accurate results and an increased linear working range at lower protein concentrations. However, the kit is incompatible with some sample buffers, thus compatibility is check prior to use.

#### b. Bradford assay

More routinely, Bradford assays were used to quantify protein concentrations, especially of cell lysates. Again, the concentration of samples is compared to a dilution series of known concentrations of BSA (A9647 Sigma), ranging the sample concentration (commonly from 0-2.5 mg/ml). The 5x Bradford reagent (5000006, Bio-Rad) was diluted with water to 1x prior to use, and 200 μl is added per well in a 96-well plate. The BSA standards and the protein-containing samples (e.g. 1 μl of cell lysate) are added to each well and mixed thoroughly. Each sample is quantified in duplicate/triplicate. Two negative control (lacking BSA) are added, one included the diluent of the BSA standards (water) and the other the buffer of the samples. The plate was promptly analysed using a spectrophotometer (Spark Multiplate Reader,

Tecan) in absorbance mode at 595 nm, seeing that this assay is time-dependent. The absorbance readings of known concentrations of BSA were plotted, yielding a linear standard curve that was used to deduce the concentrations of the unknown samples, based on their absorbance values.

### c. Sodium dodecyl sulphate-polyacrylamide gel electrophoresis (SDS-PAGE) compared with known BSA concentrations

The concentration of recombinant proteins is checked using SDS-PAGE and Coomassie blue. A dilution series of the sample, as well as the BSA (A9647, Sigma), is loaded onto a single gel. Once stained with Coomassie blue, the intensity of the bands can be quantified using Image Studio Lite (LI-COR Biosciences) and the concentration of the recombinant protein can be deduced from the linear standard curve of the BSA dilution series of known concentrations.

### d. Nanodrop

Again, the concentration of recombinant proteins can be readily analysed using a Nanodrop ND-1000 spectrophotometer. Again, concentration is calculated from the absorbance at 280 nm. To improve accuracy, the extinction coefficient of the protein, $\varepsilon$, (obtained from the ProtParam online tool: https://web.expasy.org/protparam/) should be included into the Beer's Law equation: $A = \varepsilon \times L \times c$, where *A* is absorbance (known), *L* is length (fixed) and *c* is concentration (unknown).

## 2.4.2 SDS-PAGE

### a. In-house polyacrylamide gels

Polyacrylamide gels were prepared in-house using the gel cast Mini-Protean 3 Cell apparatus (Bio-Rad) and either 1.0 mm or 1.5 mm gap glass plates (depending on the volume required to be loaded). Additionally, depending on the assay and number of samples, either 10- or 15-well combs were used. Stacking and resolving solutions were prepared as in Table 2.7, and higher percentage resolving gels were selected for analysis of proteins with small molecular weights. The appropriate resolving gel is

prepared and poured first onto the gel cast. It is then overlaid with isopropanol to ensure the gel solidifies in a straight manner and to prevent air bubbles. Once polymerised, the isopropanol is removed, and the stacking gel is prepared and poured into the cast.

**Table 2.7: Resolving and stacking gels for SDS-PAGE**

| **Reagents** | **Resolving gel** | | | **Stacking gel** |
|---|---|---|---|---|
| Acrylamide, 30% (w/v) and bis-acrylamide, 0.8% (w/v) (Protogel, National diagnostics) | **10%** | **12%** | **15%** | 5% |
| Tris pH 8.8 (Sigma) | 375 mM | 375 mM | 375 mM | - |
| Tris pH 6.8 (Sigma) | - | - | - | 125 mM |
| SDS (w/v) (Sigma) | 0.1% | 0.1% | 0.1% | 0.1% |
| APS (w/v) (Sigma) | 0.1% | 0.1% | 0.1% | 0.1% |
| TEMED (w/v) (Sigma) | 0.004% | 0.004% | 0.004% | 0.1% |

Generally, about 30 μg of cell lysate was loaded. The protein samples are diluted in sample buffer (2x) in a 1:1 ratio (v/v). The mix was heated for 3-4 min at 95ºC (unless otherwise stated) and subsequently loaded onto the gel. Pre-stained protein ladders were loaded in parallel as size markers. Gels were run in 1x Tris-Glycine-SDS running buffer and at 120 V for about 1h, until the dye front has reached the bottom of the gel, or a marker of a specific size has migrated until a position of interest.

Sample buffer (2x)
300 mM Tris (pH 6.8)
5% (w/v) SDS
25% (v/v) Glycerol
Bromophenol blue to desired colour
200mM DTT (unless otherwise stated), added freshly

Tris-Glycine-SDS running buffer (1x)
192 mM Glycine
25 mM Tris base
0.1% SDS (w/v)

### b. Precast gel protocol

Precast gradient gels (4-12% Bis-Tris Gels, Invitrogen) were run using MOPS buffer (1x) (Invitrogen) at 180 V for about 1 h.

## 2.4.3 Coomassie staining of SDS-PAGE gels

Once proteins were separated by SDS-PAGE, the gels are submerged in Coomassie blue stain solution for 30 min. Next, the gel is rinsed and then incubated overnight with destain solution shaking. Destained gels are scanned using a plate imager (Odyssey® SA Infrared Imaging System, Li-Cor Biosciences).

Coomassie blue stain solution
50% (v/v) Methanol
10% (v/v) Glacial acetic acid
0.2% (w/v) Coomassie brilliant blue R-250

Destain solution
7.5% (v/v) Methanol
10% (v/v) Glacial acetic acid

## 2.4.4 Western blotting (WB)

After SDS-PAGE, proteins were transferred onto 0.2 μM pore nitrocellulose blotting membrane (Advantec) using the Mini Trans-Blot® wet electroblotting systems (Bio-Rad). Transfer was carried out in tanks containing 1x transfer buffer for 1h30m at 100 V, or overnight at 30 mA. To prevent overheating, an ice pack was added in the tank (and replaced half way) or conducted at 4ºC (when overnight).

When indicated, membranes were overlaid with 0.4% or 4% paraformaldehyde (PFA) (Sigma), as indicated, and incubated for 30 min at room temperature. Subsequently, the membrane was thoroughly washed with PBS, three times for 5 min each, while shaking. Optionally, following transfer membranes were rinsed with phosphate

buffered saline (PBS) and stained with India ink (Pelican black) to confirm that proteins were transferred properly.

All membranes were washed briefly with PBS containing 0.1% (v/v) Tween-20 (PBS-Tween) and then blocked with PBS-Tween with 5% BSA (Sigma, A9647) for 1 h at room temperature or overnight at 4ºC. Next, primary antibodies (Table 2.2) were diluted in the blocking buffer and incubated for 1 h at room temperature or overnight at 4ºC in a humidified chamber, depending on the nature of the antibody. Blots were then washed with PBS-Tween, as previously. The appropriate horse peroxidase (HRP)-conjugated secondary antibodies (Table 2.3) were also diluted 1:2000 in blocking solution and added to membranes for 1 h at room temperature. This is followed by the same washing conditions. Finally, for antibody signal detection, enhanced chemiluminescence (ECL) reagents I and II were prepared in a 1:1 ratio (v/v) and overlaid on the membranes for 1 min. Excess solution was removed and blots were exposed to Hyperfilm ECL (Amersham) or X-Ray film (SLS) for the required period of time. The former is used when the expected signal is weak. Films were developed using a film processor (SRX-101A, Konica Medical).

Transfer buffer (1x)
24 mM Tris
191 mM Glycine
20% (v/v) Methanol

PBS-Tween
1x PBS
0.1% (v/v) Tween-20

Blocking buffer
1x PBS
0.1% (v/v) Tween-20
5% (w/v) Dried skimmed milk (Marvel)

ECL I
2.5 mM Luminol
0.4 mM p-Coumaric acid

0.1 M Tris pH 8.8

ECL II
0.02% (v/v) Hydrogen peroxide
0.1 M Tris pH 8.8

## 2.4.5 Two-dimension electrophoresis (2DE)

Two-dimension electrophoresis were performed in collaboration with Jitka Zakova†. On the first dimension, samples were analysed on immobilized pH gradient (IPG) strips (pH 3-10 NL). On the second dimension, samples were analysed on 12% polyacrylamide gels by SDS-PAGE. When gels were visualised by Coomassie blue staining, 200 μg of protein lysate was loaded, while when used for WB, 100 μg was loaded. For WB, PVDF membrane was used.

## 2.4.6 Protein purification

### a. Purification of His-CHIP

BL21(DE3) competent cells were transformed with pET15b-CHIP ($His_6$-tagged WT CHIP), as previously described. A colony was picked and used to inoculate a starter culture of 50 ml of LB broth supplemented with ampicillin, which was incubated overnight at 37ºC and 220 rpm. Next, 10 ml of this was used to inoculate 1 L of the same LB medium. Cells were incubated in the same conditions until $OD_{600}$ was 0.4-0.6 (mid-Log phase). Once reached, protein expression was induced with 1 mM isopropyl β-D-1-thigalactopyranoside (IPTG).

Protein expression was induced for 4 h at 30ºC and 220 rpm. An aliquot of cells (1 ml) before and after IPTG addition was taken to assess the induction of protein expression (the $OD_{600}$ was recorded for both). Cells were harvested by centrifugation (4000 g for 40 min at 4ºC) and the supernatant was discarded. The cell pellet was resuspended

† Department of Molecular Pathology and Biology, University Hospital Ostrava, Hradec Kralove, Czech Republic

with 5 ml of Lysis Buffer (without the components marked with an asterisks) and was then snap frozen in liquid nitrogen and stored at -80ºC.

To test the expression levels, all aliquots taken were centrifuged at 13000 rpm for 15 min at 4ºC and pellets were re-suspended in cold PBS or lysis buffer in an appropriate volume relative to the $OD_{600}$ readings. A fraction (20 μl) of each was isolated and the rest was sonicated 3 times for 5 seconds at amplitude 10 microns (MSE Soniprep 150 Plus ultrasonic disintegrator) with 5 second intervals resting on ice, or until samples become clear. Sonicated samples were centrifuged at 13000 rpm for 5 min at 4 ºC and the pellet formed was discarded. An aliquot (10 μl) of both sonicated samples (soluble protein) and both non-sonicated samples (total protein) was taken and analysed by SDS-PAGE stained with Coomassie blue.

If adequate protein expression is confirmed, the pellet was thawed on ice and 20 ml of cold Lysis Buffer was added (with all the components, resulting in the indicated final conentrations). Cells were resuspended by pipetting and incubated for 1 h on ice. Next, cells were sonicated three times for 15 sec each at an amplitude of 10 microns and with 30 second intervals, on ice.

The lysate was then centrifuged for 15 min at 16000 g and 4ºC and the supernatant was collected. It was filtered through a 0.22 μM filter to exclude cell particles and insoluble components and then mixed with $Ni^{2+}$-NTA agarose beads (1 ml, 50% slurry) (Qiagen) that have been previously washed with Wash Buffer I. For batch-binding, the mix was incubated for 1 h, at 4ºC on a rotating wheel. It was then transferred to a 10 ml disposable column (MoBiTec) and allowed to empty by gravity. The flow through was collected. The beads were then washed twice with 5 ml Wash Buffer I, twice with 5 ml Wash Buffer I + ATP and three times with 5 ml Wash Buffer II. Aliquots of each wash were collected. Finally, 2 ml of Elution Buffer was added to the beads and incubated for 30 min at 4 ºC while rotating. The eluate was collected and applied onto a buffer exchange column (Zeba Spin Desalting Column, Thermo Scientific) that has been pre-washed three times using 2.5 ml Protein Buffer. Buffer exchange was performed according to the manufacturer's instructions (the centrifugation step was performed for 2 min at 1000 g and 4ºC). The sample was aliquoted, snap frozen in liquid nitrogen and stored at -80ºC. The purity and concentration of the eluate was

assessed by SDS-PAGE stained with Coomassie blue and by Nanodrop, as previously described.

Lysis Buffer
20 mM Tris pH 8
300 mM NaCl
0.3% NP-40*
1 mg/ml lysozyme*
1 x Protease inhibitor mix*

Protease inhibitor mix (10x)
200 μg/ml Leupeptin
10 μg/ml Aprotinin
20 μg/ml Pepstatin
100 μg/ml Soybean trypsin inhibitor
10 mM Benzamidine
20 mM Pefabloc
10 mM EDTA

Wash Buffer I
20 mM Tris pH 8
300 mM NaCl
0.3% NP-40
2 mM Benzamidine
20 mM Imidazole

Wash Buffer I + ATP
Wash Buffer I
10 mM $MgCl_2$
5 mM ATP

Wash Buffer II
20 mM Tris pH 8
300 mM NaCl

0.3% NP-40
2 mM Benzamidine
40 mM Imidazole

Elution Buffer
20 mM Tris pH 8
150 mM NaCl
300 mM Imidazole

Protein Buffer
20 mM Tris pH 8
150 mM NaCl

### b. Purification of scFv antibodies

Glycerol stocks of BL21(DE3) competent cells transformed with either 11F or 7A scFv plasmids were used to inoculate 5 ml of LB supplemented with ampicillin and 0.1% glucose, which was incubated overnight 37 ºC and 220 rpm. Each starter culture was then used to inoculate 250 ml of LB with the same supplements and incubated at the same conditions until it reached $OD_{600}$ 0.4-0.6. Protein expression was induced with 1 mM IPTG and incubated overnight at 30 ºC and 220 rpm. Aliquots before and after induction of protein expression were taken, as previously described (in section a).

Bacterial cells were harvested by centrifugation at 4000 g for 40 min at 4 ºC and the supernatants was discarded. Cell pellets were re-suspended in 10 ml of cold, sterile PBS before being snap frozen in liquid nitrogen and stored at -80ºC.

If the expression was adequate, the bacterial cell pellets were thawed on ice and 100 μl triton-X100 was added. After a 30 min incubation on the rotating wheel at 4 ºC, pellets were sonicated four times for 15 s each at amplitude 10 microns, with 30 s intervals in between. Pellets were on ice the whole time during the sonication step and then were centrifuged at 13000 rpm for 10 min at 4 ºC. The supernatants were collected and filtered using a 0.22 μm membrane. In the meantime, for the purification of each scFv, 30 mg of Protein A Sepharose resin (CL-4B GE Healthcare) were

weighed and washed 3 times with 400 μl $ddH_2O$. Beads were allowed to settle sediment by gravity or with low speed centrifugation.

The beads were re-suspended in 400 μl $ddH_2O$ and mixed with the lysate. For batch-binding, the mixture was incubated for 1 h at 4ºC on a rotating wheel. It was then transferred into a 10 ml disposable column with a filter and the flow through was collected. Five washes with 1 ml PBS-1% triton X-100 were made and aliquots were collected as the solution left the column. Elutes were collected by added 500 μl of 0.2 M glycine pH 2 four times in total and these were collected into microcentrifuge tubes with 75 μl of 1 M Tris pH 9 previously added. For the last elute, another 500 μl of 0.2 M glycine pH 2 was added and the column was incubated rotating for 15 min at 4 ºC. The elute was collected in the same manner. The purification was performed either on ice or at 4 ºC. Samples were stored at 4 ºC.

A fraction of the total purified scFv (200 μl of each elute) was buffer exchanged. Exchange columns (Zeba Spin Desalting Column, Thermo Scientific) were prepared according to the manufacturer's instructions and washed with 2.5 ml of 1 M Hepes buffer with 150 mM NaCl. The concentration and purity of the Tris-Glycine elution fractions and the buffer exchanged sample was assessed by Nanodrop and by SDS-PAGE, as previously described.

## 2.5 *In vitro* assays

### 2.5.1 T7 endonuclease I assay

As part of the screening process to identify positive clones derived from Clustered regularly interspaced short palindromic repeats (CRISPR)/Cas9 gene-editing technology, the T7 endonuclease I assay (M0302, New England Biolabs) was used as an early detection method. It was used according to the manufacturer's instructions and required PCR products that were derived as previously described. The T7 endonuclease I assay reactions were analysed by using a 1% agarose gel.

### 2.5.2 *In vitro* ubiquitination assays

*In vitro* ubiquitination assays were performed with the following components unless otherwise stated: 3 μg His-CHIP (purified in-house), 1 μM UbcH5α, 100 nM Ube1 (E-305, Boston Biochem), 2 μg Ub (U-100H, Boston Biochem), 30 mM ATP (A7699, Sigma) and the reaction buffer (25 mM HEPES, 10 mM $MgCl_2$ and 0.5 mM DTT). Specifically, the UbcH5α was wither made in-house (purified in-house by Dr Fiona Lickiss) or, for the mapping of ubiquitination sites directly from the reaction, was commercially obtained (E2-616, Boston Biochem), due to the presence of the MS-incompatible glycerol in the former. When indicated, either 0.1 μg α-synuclein (purified in-house by Dr Vikram Narayan), 25 or 50 nM untagged or His-tagged Annexin A2 (ANXA2) (ab93005 and ab188455, respectively, Abcam) or 25 ng p53 (purified in-house from insect cells by Prof Kathryn Ball) were used as substrates. Each reaction volume was 24 μl and, when preparing multiple sample, a master mix was made. CHIP was added last. When indicated, 7A or 11F scFv antibodies were added at the concentrations specified. The reaction(s) was prepared on ice and then incubated at 30 ºC in a water bath for 45 min, unless otherwise stated. Samples were then snap frozen in liquid nitrogen or analysed by WB (the reaction was stopped by denaturing with heat and the loading dye).

### 2.5.3 Hydrogen-deuterium exchange (HDX)

The dynamics of the interaction between CHIP and 11F scFv antibody were monitored *in vitro* by hydrogen-deuterium exchange (HDX), in collaboration with Dr Lenka Hernychova and Dr Bořivoj Vojtesek[‡].

Human recombinant untagged CHIP (purified in-house by Dr Jia Ning) in 2 μM (final concentration) was diluted with 48 μl HEPES buffer (50mM HEPES, pH 7.5, 150mM NaCl, 1mM DTT) in $H_2O$ that was used for the preparation of the undeuterated control samples and for the peptide mapping. Deuterated samples containing CHIP either free or in complex with 11F scFv antibody in molar ratio 1:1 (protein:antibody) were

[‡] Regional Centre for Applied Molecular Oncology, Masaryk Memorial Cancer Institute, Brno, Czech Republic

preincubated for 60 min on ice. Then deuterium exchange was started by dilution with HEPES buffer in $D_2O$ (pD 7.1) carried out at room temperature. Deuteration was quenched at 30 s, 5 min, and 15 min by the addition 3.5 μl quench buffer (1 M glycine, 2 M HCl and 1 mg/ml pepsin), followed by a 3 min incubation and rapid freezing in liquid nitrogen.

## 2.6 Cell culture

### 2.6.1 Culturing of cell lines

All tissue culture disposables were from Greiner-Cellstar, unless otherwise stated. Cells were monitored daily using a bright-field inverted phase-contrast microscope and were confirmed to be mycoplasma-negative by periodic testing using the Luciferase-based MycoAlert™ detection kit (Lonza), following the manufacturer's instructions.

#### a. SH-SY5Y

SH-SY5Y cells were maintained in the appropriate medium, which was changed every 2-3 days. When 70-80% confluence, cells were washed briefly with PBS and passaged using trypsin (0.05% trypsin + 0.02% EDTA, Gibco, 15090), for a 10 $cm^2$ plate, 2 ml of trypsin was added. Cells were incubated for 3-4 min until detached. Trypsin was deactivated by dilution with the culturing medium (in 5:1, medium:typsin, ratio). Cell were plated at 1:10 or 1:5 (v/v) for routine culturing or counted and plated at specific densities for particular assays.

#### b. iPSC

To promote attachment, high survival and long-term maintenance self-renewal capacity, iPSC were plated on plastic previously coated with Laminin-521 (100 μg/ml, Biolamina). For such, Laminin-521 was diluted in dPBS with calcium and magnesium (14040083, Gibco) to a final concentration of 5 μg/ml. Enough to cover wells properly was added (e.g. 1000-1200 μl for a 6-well). Plates were sealed with parafilm and

incubated overnight at 4ºC or for 2 h at 37ºC. When using glass coverslips, coating with poly-L-ornithine is required prior to the addition of Laminin-521.

iPSC were maintained in the appropriate medium, which was changed daily or every 2 days. When 70-80% confluence, or when cells presented early signs of differentiation morphology, iPSC were passaged using 0.5 mM EDTA (UltraPure 0.5 M EDTA, pH 8, 15575020, Gibco), diluted in dPBS without calcium and magnesium (D8537, Sigma). Initially, cells were washed with 0.5 mM EDTA and then incubated with fresh solution for 15-20 min at 37ºC (i.e. until cells are partly detached but completely). This has been optimised for the iPSC AST23 parental line and CRISPR-derived clones. After the incubation, EDTA is discarded and cells are lifted by flushing with culturing medium (iPS-Brew XF medium). Cells were triturated by pipetting a maximum for four times, before being passaged onto a new plate. Ideally, cells are passaged as small clumps, to promote cell survival.

## 2.6.2 Cryopreservation

For long-term preservation of cell stocks, cells were cryopreserved in the appropriate solution and stored temporarily (for 24 hours) at -80ºC in a Mr. Frosty™ Freezing Container (Thermo Scientific) and then transferred to liquid nitrogen. For short-term storage, cryovials were maintained at -80ºC.

### a. SH-SY5Y

Cryopreservation solution was prepared containing 50% FBS (10270-106, Gibco), 10% DMSO (276855, Sigma) and 40% DMEM. SH-SY5Y were frozen at 70-80% confluency in a 10 cm plate, or equivalent. Cells were lifted with trypsin, as previously described. After centrifugation, the supernatant was discarded, and cells were resuspended with 3 ml of cryopreservation solution. Three aliquots were made and the cryovials were frozen.

### b. iPSC

Culturing medium (iPS-Brew XF medium) was supplemented with the ROCK inhibitor, Y27632 dichloride (1254, R and D, Tocris) for a final concentration to 10 μM, to promote cell survival. Previously, 10 mM stocks of Y27632 dichloride were made by diluting with PBS (D8537, Sigma).

iPSC were frozen when 70-80% confluent in a 6-well. Cells were lifted with EDTA, as previously described, and transferred to medium supplemented with Y27632 dichloride. After centrifugation (3 min at 800 rpm), the supernatant was discarded and the cell pellet was resuspended with 1.5 ml of Stem Cell banker (Stem-Cell Banker GMP grade, 11890, Amsbio). Two or three aliquots were made and the cryovials were frozen.

## 2.6.3 Cell recovery

### a. SH-SY5Y

Cryovials with frozen cells were quickly thawed at 37ºC (in the water bath) until partially thawed. Culturing medium (DMEM supplemented with FBS) was added and cells were transferred into a 15 ml centrifugation tube. A total of 9 ml of medium should be added to ensure removal of residual DMSO. Cells were centrifuged for 5 min at 1000 rpm and the supernatant was discarded. The cell pellet was resuspended with of fresh culturing medium and plated on 10 cm plates (with a total volume of 10 ml).

### b. iPSC

Cryovials with frozen iPSC were also quickly thawed at 37ºC (in the water bath) until partially thawed (~1 min). The supplemented medium (iPS-Brew XF medium with 10 μM Y27632 dichloride) was added (8 ml) and cells were centrifuged for 3 min at 800 rpm. The supernatant was discarded and cells were gently resuspended with fresh supplemented medium and plated on 6-well plates (with a total volume of 2 ml) or smaller. The medium was changed to fresh medium without Y27632 dichloride after 1 day, unless otherwise stated. This drives a morphological change from extended cells to round.

## 2.6.4 Transient transfection of DNA (SH-SY5Y cells)

### a. Electroporation

Cells were transfected with plasmids using a Nucleofector™ 2b Device and Amaxa Cell Line Nucleofector Kit V (VCA-1003, Lonza) according to manufacturer's instructions (2 μg of plasmid was used per transfection). Cells were platted onto 6-well plates and left to recover for 48 h before conducting any further analysis.

### b. Attractene

Transient transfections were more frequently done using Attractene transfection reagent (301005, Qiagen) according to the manufacturer's instructions. Cells were transfected at about 70% confluency and were harvested about 24 h post transfection.

## 2.6.5 Drug treatments

SH-SY5Y cells were treated with different inhibitors Ub-dependent pathways (Table 2.8) prior to cell lysis. Treatment conditions were based on the literature[62] and previous observations.

**Table 2.8: Principle effects and working concentrations of drugs used**

| Drug | Pathway inhibitor | Details | Reference | Treatment |
|---|---|---|---|---|
| Bafilomycin A1 (BafA1) | Autophagy | Inhibits fusion between autophagosome | B1793, Sigma | 150 nM for 16h |
| | Endosomal/ Lysosomal | Inhibits endosomal acidification | | |
| Chloroquine | Endosomal/ Lysosomal | Inhibits endosomal acidification | C6628, Sigma | 100 μM for 16h |
| | Autophagy | Inhibits lysosomal acidification, inactivating lysosomal enzymes and preventing lysosomal fusion | | |
| 3-Methyladenine (3-MA) | Autophagy | Inhibits type III PI-3K, which blocks autophagosome formation | M9281, Sigma | 3 mM for 16h |
| V34-2 | Endosomal | Inhibits dynamin I and II, blocking receptor mediated endocytosis | 324414 Merck | 10 μM for 16h |
| MG-132 | Proteasomal | Inhibitor of proteases and peptidase activity of the proteasome, in a reversible manner | 474790, Merck | 50 μM for 4h |
| Lactacystin | Proteasomal | Irreversible inhibitor of the 20S proteasome | 426100, Merck | 10 μM for 4h |

## 2.6.6 Cell counting

For consistency across experiments and to allow comparison between different conditions (eg. between CHIP KO cells and WT cells), cell plates were seeded with similar cell numbers. For such, once adherent cells were detached, an aliquot was taken, further triturated by pipetting to obtain single cells and cells were counted using a haemocytometer or an automated cell counter. When using the latter, a 15 μl aliquot containing single cells was diluted 1:1 with 0.4% Trypan Blue stain (T13001, Labtech) and added to a cell counting slide (L12001, Labtech). This was analysed in an automated cell counter (Luna BF cell counter, L10001, Labtech). The average of duplicate readings was considered.

## 2.6.7 Coverslip preparation

### a. Sterilization

For immunofluorescence-based assays, cells were plated on glass coverslips. Round glass coverslips of 13 mm (631-0149, VWR International) or 25 mm (631-0171, VWR International) were washed with 70% ethanol and autoclaved at 180ºC for at 30 min.

### b. Differentiated SH-SY5Y

Although undifferentiated SH-SY5Y cells do not need prior coating of coverslips, differentiated SH-SY5Y do. Poly-L-Ornithine (100 ug/ml, P4957, Sigma) was diluted with dPBS without calcium and magnesium (D8537, Sigma) to achieve a final concentration of 15 ug/ml, which was added on top of the coverslip placed in the 4 or 24-well plate or 12-well plate. The plate was sealed and incubated overnight at room temperature. Next, the coverslips were washed three times with dPBS.

### c. iPSC

Coverslips seeded with iPSC were coated primarily with poly-L-ornithine and then with Laminin-521, as previously indicated.

### d. Cortical differentiation

Coverslips seed with neural stem and progenitor cells and cortical neurons were coated primarily with poly-L-ornithine, as previously indicated, and then with Laminin-111 (100 ug/ml, Biolamina). Laminin-111 was diluted in dPBS with calcium and magnesium (14040083, Gibco) to a final concentration of 5 μg/ml. Enough to cover the coverslips properly was added (e.g. 1000-1200 μl for a 6-well). Plates were sealed with parafilm and incubated overnight at 4ºC.

## 2.6.8 Lipidomics analysis

### a. Preparation and harvesting of cells

SH-SY5Y WT and KO cells were grown in 10 cm plates in culturing medium containing DMEM and FBS. Prior to cell harvest (24 h before) the medium was changed to fresh, serum-free media (just DMEM). Cells were scraped in the medium and on ice and transferred to microcentrifuge tubes. They were centrifuged for 10 min at 2000 rpm and 4ºC. The condition medium (supernatant) was collected in a new microcentrifuge tube and snap frozen with liquid nitrogen prior to storage at -80ºC. The cell pellet was washed with PBS and centrifuged again at the same conditions. The buffer was discarded, and the cell pellet was snap frozen in liquid nitrogen and stored at -80ºC.

### b. Cell lysis and lipidomics

Cell lysis and lipidomics was conducted in collaboration with Dr Irena Dapic and Dr Laura Bindila[‖]. Lipid extraction and liquid chromatography-mass spectrometric multiple reaction monitoring (LC-MRM) assays were performed as described in Lerner *et al.*[98].

## 2.6.9 Harvesting cells

Cells were washed three time with PBS at room temperature. Next, enough cold PBS was added to overlay the plate/well (e.g. 1 ml for a 10 cm plate) and cells were scrapped on ice with a cell scrapper. Detached cells were transferred to a microcentrifuge, which was then centrifuged for 5 min at 4000-5000 rpm and 4ºC. The cell pellet was either lysed or snap frozen in liquid nitrogen and stored at -80ºC. Alternatively, cells were lysed on the plate using a urea-based buffer.

## 2.6.10 Mammalian cell lysis

Cells were either lysed with a triton-based or urea-based lysis buffer. When cells were scrapped, a volume of about three-times that of the size of the cell pellet was added.

[‖] Institute for Physiological Chemistry, University Medical Center Mainz, Germany

However, when cells were lysed on the cell culture plate, the minimum volume of buffer (just enough to overlay the well) was used (e.g. 80-100 μl for a 24-well plate). To aid lysis, the plate was placed on a shaking platform. When cells were lysed for MS, urea-based lysis buffer was added to the cell culture plate (i.e. cells were not scrapped) and MS-compatible detergent was used instead of triton.

After a 30 min incubation with the cell lysis at 4ºC (for the triton-based buffer) or room temperature (when using the urea-based buffer), cells we centrifuged for 20 min at 13000 rpm and 4ºC or 12ºC, depending on the buffer. The supernatant transferred into a new microcentrifuge tube and the protein concentration was assessed as previously described.

Triton-based lysis buffer
50 mM HEPES pH 7.5
0.2% (v/v) Triton X-100
150 mM NaCl
10 mM NaF
2 mM DTT
0.1 mM EDTA
1x Protease inhibitor mix

Urea-based lysis buffer
8 M Urea
50 mM HEPES pH 8
100 mM KCl
1 mM DTT
0.5% (w/v) n-Dodecyl-β-D-maltoside (for MS-compatible buffer) or 0.2% Triton X-100 (for non-MS-compatible buffer)

## 2.6.11 Differentiation of SH-SY5Y

SH-SY5Y were differentiated using retinoic acid. Cells were detached using trypsin and counted, as previously described, in order to be seeded at 11.8 x $10^3$ cells/$cm^2$. Cells plated on coverslips require poly-L-ornithine coating. Cells were maintained in

DMEM + FBS medium for 2 days and then switched to the differentiation media. Half of the media was replaced every 2-3 days with retinoic acid added freshly every time. Working stocks of the retinoic acid have been previously prepared by dilution with DMSO to a final concentration of 10 mM. These were stored at -80ºC (long-term) or -20ºC (short-term) and protected from light. The differentiation was maintained for 7-14 days, depending on desired end-point.

SH-SY5Y Differentiation media

1x DMEM/F12 (21331-020, Gibco)

1x Neurobasal (21103-049, Gibco)

1 mM L-glutamine (200 mM, 25030-024, Gibco)

0.5x N2 supplement (100x, 17502001, Gibco)

10 μM Retinoic acid (R2625, Sigma)

### 2.6.12 Differentiation of iPSC into cortical neurons

Please refer to Chapter 3: Engineering iPSCs to generate isogenic neuronal cell models.

## 2.7 Cell-based assays

### 2.7.1 Clustered regularly interspaced short palindromic repeats (CRISPR)/Cas9 gene editing technology

#### a. Nucleofection

iPSC were subjected to CRISPR/Cas9 technology. Both Geltrix matrix (A1413201, Gibco) and Laminin-521-coated plates were prepared (according to the manufacturer's instructions or as previously described) for the seeding of electroporated cells. Geltrex matrix was diluted in DMEM/F12 (21331-020, Gibco).

To promote single cell detachment, cells were washed with PBS and then incubated with Accutase (A6964, Sigma) for about 10 min (until detached). Lifted cells were transferred to a 15 ml centrifuge tube, counted and centrifuged for 3 min at 800 rpm.

The supernantant was discarded and cells were resuspended in culturing medium (iPS Stem-Brew XF) supplemented with 10 μM Y27632 dichloride.

For nucleofection, the Human Stem Cell Nucleofector (VPH-5012, Lonza) was used according to the manufacturer's instructions. Different conditions were tested: transfection with 3 μg of the LentiV2 CRISPR plasmid (encoding both Cas9 and the gRNA directed to the coding region of CHIP – kindly gifted by Erisa Nita[95]) and co-transfection with 2 μg of this plasmid and 1 μg of a GFP-encoding plasmid (pmaxGFP vector) (a 2:1 molar ratio). Electroporation was performed with the B-016 program in a Nucleofector™ 2b Device (AAB-1001, Lonza). Cells were plated at low density onto four 10 cm plates either coated with Laminin-521 or Geltrix-coated plates. Cell transfected with both plasmids were treated with different doses of puromycin, since the GFP-encoding plasmid contains a puromycin resistance gene. All electroporated cells were maintained in medium supplemented with Y27632 dichloride for 2 days to promote cell survival.

### b. Colony selection

Once single cells grew into small colonies they passaged onto individual wells within a 96-well plate. Prior to this, cells were treated for 2 h with culturing medium supplemented (iPS-Brew XF) with 10 μM Y27632 dichloride, to increase survival. Cells were then washed with HBSS containing calcium and magnesium (14025, Gibco) and then incubated with 250 U/ml of Collagenase Type IV (17104019, Gibco), diluted in the same HBSS, for 30 min to facilitate subsequent detachment from the matrix and improve survival. The solution was discarded, and the culturing medium was supplement with 0.5 U/ml Penicillin + 500 ng/ml Sreptomycin (15140122, Gibco) and 10 μM Y27632 dichloride.

For manual colony picking, an inverted phase contrast microscope with a camera and auxiliary screen was used. Small, isolated colonies within the 10 cm plates were selected by mechanical detachment (a combination of scrapping and aspirating, using a pipette with clipped tips). As they were transferred onto individual wells within a 96-well plate, they were gently triturated by pipetting to partially dissociate the colony.

They were grown in this supplemented medium for 2 days before fresh iPS-Brew XF was added.

### c. Validation of clones

Once clones grew from the 96-well plate, they were passaged into incrementally increasing plates. Two duplicate 96-well plates were used to screen positive clones by immunofluorescence (IF) using anti-CHIP mAb and to extract DNA for PCR. The latter was then used for direct sequencing from the PCR product and for TOPO cloning and subsequent sequencing (as previously described). Once clones occupied two duplicate 24-well plates, one was used for screening via WB and the other for mycoplasma testing and cryopreservation.

## 2.7.2 Subcellular fractionation

Cytoplasmic, membrane and nuclear fractions of from CHIP WT and KO SH-SY5Y cells were achieved using the Subcellular Protein Fractionation kit (78840, Thermo Scientific), according to the manufacturer's instructions. The fractions were analysed by WB. The expression of CHIP, ANXA2, Hsp90 and PARP were analysed. The latter two were used as positive controls for the cytoplasmic and nuclear fractions, respectively.

## 2.7.3 Immunoprecipitation (IP)

### a. Annexin A2 and CHIP co-IP

Two 10 cm of CHIP WT cells (80% confluent) were harvested by scrapping and incubated in lysis buffer. The lysate concentration was assessed by Bradford assay and 500 μg of lysate was used per IP/control condition, except for the condition lacking lysate. The following conditions were tested:

- Beads + lysis buffer + Ab
- Beads + WT lysate
- Beads + WT lysate + Ab

Of these aliquots, two were added 1 μg of anti-ANXA2 Rb pAb. All samples were incubated overnight at 4ºC and on a rotating wheel.

For the IP, columns (Mobicols with 2 different screw caps without filters, MoBiTec #M1002) with filters (35 μm pore size, MoBiTec #M513515) were used. Sepharose protein G beads (17-0618-01, GE Healthcare) were aliquoted (20 μl per IP/control condition) and were washed three times with PBS buffer containing 0.1% Tween-20 (PBS-Tween). Between washes, beads were allowed to pellet by gravity. Post-incubation, the lysate/control samples were added to the beads. The mixture was incubated for 1 h at 4ºC on a rotating wheel. Again, beads were pelleted by gravity. Three washes with PBS-Tween were the performed, allowing the beads to pellet between each wash. For the elution, 50 μl of SDS-PAGE sample buffer was added, and the samples were heated for 5 min at 95ºC.

The IP was analysed by WB, as previously described. Each sample (40 μl) was loaded on an SDS-PAGE 12% gels, in parallel to 30 μg of WT lysate. The immunoblot was first probed with HRP-conjugate anti-Mouse pAb (for 1 h at room temperature), to identify background bands derived from the beads and antibody itself. Next, the immunoblot was probed with anti-CHIP mAb (for 1 h at room temperature), to determine the expression of CHIP across the different samples. Finally, the immunoblot was probed with anti-ANXA2 pAb (overnight at 4ºC).

Of note, these were the optimised conditions for this ANXA2 and CHIP co-IP. Different conditions were tested, including IP with different anti-ANXA2 and anti-CHIP antibodies, buffers containing calcium (since part of the ANXA2 interactome is calcium-dependent) and different pre-clearing and blocking steps (data not shown).

Lysis buffer
0.2% Triton-X100
50 mM Tris pH 8
150 mM NaCl
5 mM EDTA
1x Protease inhibitor mix

### b. Recombinant scFv and endogenous CHIP IP

SH-SY5Y CHIP KO and WT cells grown in 10 cm plates were harvested and lysed, and the protein concentration was measured by Bradford assay, as previously described. Protein A Sepharose beads (17-0780-01, CL-4B GE Healthcare) were weighed into microcentrifuge tubes (10 mg each). They were washed three times with 600-700 μl of $ddH_2O$ and in between washes beads settled by gravity. Beads were then re-suspended with 50 μl of $ddH_2O$ (manufacturer's instructions suggest 1 g in an end volume of 4/5 ml), thus having a binding capacity of 1000 μg (according to the 20 mg/ml binding capacity).

Buffer exchanged 11F scFv or its buffer (25 mM HEPES + 150 mM NaCl) were added to the beads (30 μl), except for the control conditions. Subsequently, the mixture was incubated for 1 h at 4ºC on a rotating wheel. The 500 μg of lysate from WT cells or CHIP KO cells, or the equivalent volume of lysis buffer, were added to either 11F scFv or buffer-containing beads. Next, samples were incubated for 1 h at room temperature on a rotating wheel (previous data showed no different between these incubation conditions and overnight at 4ºC – data not shown).

After each incubation time, beads were transferred to a small column (Mobicols with 2 different screw caps without filters, MoBiTec #M1002) with filter (35 μm pore size, MoBiTec #M513515) and were washed 5 times with 200 μl of wash buffer. Beads were then re-suspended in 100 μl of wash buffer and all samples were transferred into new microcentrifuge tubes. Beads were let to settle and the supernatant was discarded.

SDS-PAGE sample buffer was added in a volume that was approximate to that of the beads, 40 μl. Samples were heated at 95 ºC for 3-4 min and loaded in a 12% gel for SDS-PAGE/WB. Cell lysates (20 μg) were also ran alongside to the IP samples. Membranes were probed with HRP-conjugate anti-Mouse pAb to assess non-specific binding. After this, membranes were incubated with anti-CHIP mAb and then the same secondary antibody.

Protocol optimisation was performed by introducing two different changes. Firstly, a blocking step was added, where beads were incubated for 1 h at 4 ºC on the rotating

wheel with 3% BSA in wash buffer, after batch-binding (incubation with 11F scFv) and before incubation with the lysate. Secondly, lysates were pre-cleaned by incubating with beads (2010 μg lysate: 50 μg beads, i.e. about 40:1) for 1 h, at 4 ºC on the rotating wheel. As before, 500 μg of lysate was added to 10 mg (50 μl) of beads with or without 11F.

## 2.7.4 Fixing cells

Independent of the fixation reagent(s) used, cells were rinsed with PBS prior to fixation. Enough fixative was added to submerge the coverslip thoroughly.

### a. 4% Paraformaldehyde (PFA)

The PFA solution was made in-house and stored for a maximum of 6 months at -20ºC. The desired amount of PFA to make a 4% solution was dissolved in 60ºC dd$H_2O$. 2N NaOH was added until the solution became clear. Then PBS tablets (Sigma) were dissolved to make a 1x solution. The pH was adjusted to 7.2 with HCl and the solution was filtered (Stericup Durapore 0.22μm PVDF, 5643, Millipore). Aliquots were stored at -20ºC.

Coverslips were incubated with 4% PFA for 15-min at room temperature and protected from light. Next, they were washed three times with PBS for 5 min each, while gently shaking.

### b. 4% PFA and methanol

Cells were fixed with 4% PFA, as previously described. After the 4% PFA was removed and cells were rinsed with PBS, cool methanol (M/400/17, Fisher Chemical) was added for 5-10 min (the plate should be on a flat surface at -20ºC). Next, cells were washed three times with PBS, while gently shaking.

### c. 10% Formalin

Cells were incubated with commercial 10% formalin for 15 min at room temperature and protected from light. Subsequently, three washes with PBS for 5 min each, while gently shaking, were performed.

### d. Methanol and acetone

Pre-chilled methanol (M/400/17, Fisher Chemical) and acetone (A/0600/15, Fisher Chemical), mixed at a 1:1 ratio, were added to cells. This was incubated on a flat surface at -20ºC for 20 min. Next, cells were washed three times with PBS, while gently shaking.

## 2.7.5 Immunofluorescence (IF)

For immunofluorescence (IF) assay, cells were plated on sterile coverslips at low density and incubated for at least 24h before analysis. Once about 50% confluent, cells were fixed in 4% PFA or another fixative, as indicated. Coverslip preparation and fixation methods have been previously described.

Once fixed and washed with PBS, cells were incubated with blocking solution for 1 h at room temperature, gently shaking. This prevents non-specific binding of the fluorophore-conjugated secondary antibody. The blocking solution is either 2% (v/v) donkey or goat serum (the same species as the origin of the secondary antibodies used), diluted in PBS with 0.1% Tween-20 (PBS-Tween). Cells were incubated overnight at 4ºC with the primary antibody(s) desired. Next, cells were washed three times for 5 min at room temperature, while gently shaking. In the meantime, fluorophore-conjugated secondary antibodies were diluted in the same blocking solution and added to cells for 1 h at room temperature, protected from light. Post-incubation, cells were washed three times with PBS-Tween and then incubated with DAPI (62248, Invitrogen) diluted in PBS (1:5000) for 5 min. Finally, they were washed and mounted.

For mounting, excess solution was removed from the coverslips and these were added to ~10 ml of mounting media (VECTASHIELD® Antifade Mounting Medium, H-

1000, Vector Laboratories) on the microscope slide (cells should become covered in mounting media). The coverslips were blotted to removed excess mounting media before being sealed with varnish. After 24h at 4ºC, the slides were imaged.

## 2.7.6 Proximity ligation assay (PLA)

The proximity ligation assay (PLA) was performed using the Duolink *In Situ* Detection Reagents Green kits (DUO92014, Sigma). Firstly, cells were plated on coverslips and fixed as previously described for IF. They were washed three times with PBS for 5 min, while gently shaking, and blocked with 2% donkey serum in PBS with 0.1% triton X-100 (PBS-Triton) for 1 h at room temperature. Two primary antibodies of a combination of mouse and rabbit species were diluted in the blocking solution and incubated overnight at 4ºC. Next, cells were washed again three times with PBS-Triton for 5 min each, on a slow shaking platform.

Per coverslip, 4 μl of anti-rabbit PLUS (DUO92005, Sigma) and 4 μl anti-mouse MINUS (DUO92001, Sigma) probes were diluted in 32 μl of Ab diluent. For this and all subsequent mixtures of PLA reagents, a master mix was prepared and then added to all coverslips simultaneously. The mixture was incubated for 20 min at room temperature. In the meantime, cells were washed three times for 5 min with PBS (about 80 μl each time). All washes were performed on a slow shaking platform. Once the probes were added to the coverslips, this was incubated at 37ºC for 1 h in a humidified chamber. Next, coverslips were washed three times for 5 min with Buffer A. The ligation mix was prepared by adding 8 μl of 5x ligation stock, 31 μl of $ddH_2O$ and 1 μl of ligase (per coverslip), which was then added to the coverslips and allows to incubate for 30 min at 37ºC in a humidified chamber.

Post-incubation, the coverslips were washed three times for 5 min with Buffer A. In the meantime, the amplification mix was made as follows: 8 μl of 5x amplification stock, 31.5 μl of $ddH_2O$ and 0.5 μl of polymerase (per coverslip). This was added to the coverslips and incubated for 2h at 37ºC in a humidified chamber, protected from light.

Coverslips were then subjected to a series of washes (each for 5 min with gentle shaking), as follows:

- Twice with Buffer A
- Three times with Buffer B
- Twice with 0.01x Buffer B

Then DAPI (62248, Invitrogen) was diluted in 0.01x Buffer B (1:2500) and added to each coverslip for 5 min, while protected from light. Coverslips were then washed twice with 0.01x Buffer B again before mounted onto microscope slides, as previously described.

Buffer A
150 mM NaCl
10 mM Tris pH 7.4 (adjusted with HCl)
0.05% Tween-20 μm

Buffer B
100 mM NaCl
250 mM Tris pH 7.5 (adjusted with HCl)
Filtered with 0.22 μm

## 2.7.7 Membrane assays

### a. Permeability assay

Cortical neurons were washed with HEPES-based buffer (10 mM HEPES diluted in HBSS containing 1-26 mM calcium and magnesium (24020117, Gibco)). Next, neurons were incubated with green cell-impermeable dye (lysine fixable 10-kD FITC dextran, D1820, Invitrogen) diluted 1:100 in the HEPES-based buffer, for 5 min at 37ºC. Neurons were rinsed with HEPES-based buffer and fixed with 4% PFA. In addition to assessing the degree of permeability (by the intensity of the intracellular dye), the expression of ANXA2 was also analysed in parallel by IF (performed as previously described), using anti-ANXA2 pAb and a secondary antibody with a different emission wavelength. The co-localisation of the green dye and ANXA2 was assessed using ImageJ.

### b. Membrane injury induced by glass beads

Most membrane-injury assays were done in collaboration with Dr Jesper Nylandsted[§] (except for the bead-rolling).

#### i. Bead rolling-induced injury

Cells were incubated with HEPES-based buffer (10 mM HEPES diluted in HBSS containing 1-26 mM calcium and magnesium (24020117, Gibco)). Coverslips were transferred to O-rings (Z503959 Sigma) on a 6-well plate. The green cell-impermeable dye (lysine fixable 10-kD FITC dextran, D1820, Invitrogen) was diluted 1:100 in the HEPES-based buffer and 30 μl was added per coverslip. Previously weighed glass beads (26 mg) (glass beads, acid-washed 425-600 μm, G8772, Sigma) were added per coverslip, except for the control coverslips, which were not subjected to injury. The plate containing the coverslips was manually inverted by 30º back and forward 8 times. Cells were allowed to recover for 5 min at 37ºC. The beads were removed by submerging the coverslips in a HEPES-based buffer and the cells were immediately fixed with 4% PFA, as previously indicated. Cells were then incubated with DAPI (62248, Invitrogen) diluted in PBS (1:5000) for 5 min. Next, they were washed and mounted, as previously described.

When indicated, instead of being fixed immediately after recovery, cells were incubated with red cell-impermeable dye (lysine fixable 10-kD FITC dextran, D1863, Invitrogen) was diluted 1:1000 in the HEPES-based buffer (30 μl) for 5 min at 37ºC. Next, cells were rinsed with HEPES-based buffer and fixed with 4% PFA, stained with DAPI and mounted.

The intracellular intensity of the dye(s) was asses by epifluorescence microscopy, both quantitatively and qualitatively. This is a read-out of increase permeability, since poor membrane integrity (e.g. glass bead-induced holes) favours intracellular incorporation of the dye.

[§] Danish Cancer Society Research Centre, Copenhagen, Denmark

### ii. Injury induced by mixing glass bead by vortex

SH-SY5Y were detached using trypsin and counted, as previously described. Cells were centrifuged for 5 min at 1000 rpm, the media was removed, and the pellet was resuspended in culturing media to obtain a solution with 200,000 cells/ml. A fraction (400 μl) was then added to microcentrifuge tubes containing 250 mg of glass beads each. These were mixed by vortex for 30 s, 60 s, 90 s, 120 s, 150 s and 180 s. Three controls were added: microcentrifuge tubes with cells and without beads were either not vortexed or vortexed for 180s, while another contained both cells and beads was not mixed by vortex.

After the injury, cells were plated in triplicates in 96-well plates (50 μl added to each well). Wells were incubated with 2.5 μg/ml Hoechst-33342 (H3570, Invitrogen) and 2 μg/ml propidium iodide (P4864, Sigma) diluted in HBSS (24020117, Gibco) for 2 min at 37ºC. Cells were imaged with a plate cytometer (Celigo cytometer, Brooks Life Science Systems) and analysed using Celigo Software Version 2.1.

## c. Membrane injury induced by digitonin

Digitonin is a membrane pore-forming detergent that wound cholesterol-rich membranes (Figure 2.1). For this membrane-wounding assay, SH-SY5Y and iPSC cells were plated into 96-well plates at 1 x $10^4$ and 1 x $10^5$ cells/well, respectively. Once wells are 90% confluent, they were treated with different concentrations of digitonin (0, 3, 5, 7, 10, 13, 15, 17, 20, 25 and 30 μg/ml), in triplicates. Digitonin stocks of 5 mg/ml were previously prepare and heated up to 97ºC for <5 min and vortexed briefly prior to use. Digitonin was diluted in either culturing media (DMEM with FBS or iPS-Brew media, depending on the cell line) or HBSS without calcium and magnesium. When repair is allowed (in the presence of calcium), digitonin was incubated for 10 or 20 min, as indicated. However, when repair is impaired (in the presence of HBSS without calcium), the incubation is reduced to 2 min. Incubations were performed at 37ºC.

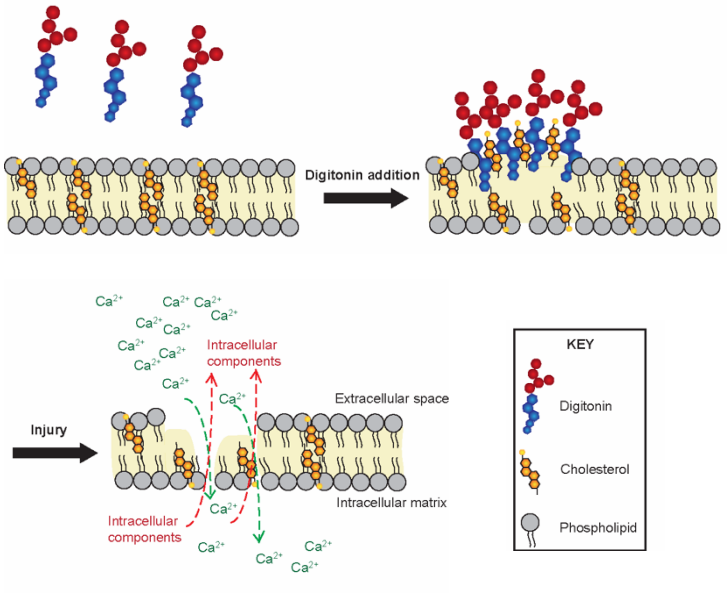


**Figure 2.1: Schematic of digitonin-induced membrane damage**

Post-incubation, wells were incubated with 2.5 μg/ml Hoechst-33342 (H3570, Invitrogen) and 2 μg/ml propidium iodide (P4864, Sigma) diluted in the same media as digitonin for 2 min at 37ºC. Cells were imaged with a plate cytometer (Celigo cytometer, Brooks Life Science Systems) and analysed using Celigo Software Version 2.1.

When indicated, digitonin treatment was also performed prior to PLA experiments. For such, cells were treated with 15 μg/ml digitonin for 15 min, before being washed with PBS and fixed.

### d. Membrane injury induced by UV laser

SH-SY5Y cells were plated in glass bottom wells. When 50-60% confluent, cells were incubated with HEPES-based buffer (10 mM HEPES diluted in HBSS containing 1-26 mM calcium and magnesium (24020117, Gibco)) and 1mg/ml of FM1-43 dye (T3163, Invitrogen). Injury was performed by irradiating a small region (1-2 $\mu m^2$) for <10-100 ms with a pulsed UV laser (Rapp OptoElectronic) close to cellular projections.

### 2.7.8 Microscopy

#### a. Live-imaging

Cells were imaged every 4-10 s starting before the injury and continuing for 3 min following injury, while maintained at 37ºC. The injury response was imaged with a 63x objective using the Nikon confocal microscope equipped with a PerkinElmer spinning disk. Microscope hardware was controlled by Volocity (PerkinElmer) and live-imaging data was analysed using the same software.

#### b. Epifluorescence microscopy

IF-based assays were visualised using the Axio Imager (Zeiss) with 63x, 40x and 20x objectives. Microscope hardware was controlled by Micromanager Software (μManager). Images were subsequently analysed using ImageJ.

## 2.8 Mass spectrometry (MS)-based assays

### 2.8.1 Sample preparation

Cells were lysed in a urea-based MS-compatible buffer and protein concentration was assessed using Micro BCA assay or Bradford assay, as previously described. For cortical neurons, specifically, biological replicates were imaged by phase-contrast, lysed on-plate and protein concentration was assessed using the Micro BSA assay. Two biological replicates per cell line that had similar morphology and confluency were pooled together to yield 80 μg samples. This was repeated twice, yielding three samples per cell line (each pooled from biological duplicates). The next steps of sample preparation and the MS analysis was performed in collaboration with Dr Jakub Faktor, Prof Ted Hupp and Dr Bořivoj Vojtesek‡.

‡ Regional Centre for Applied Molecular Oncology, Masaryk Memorial Cancer Institute, Brno, Czech Republic

### a. Filter-aided sample preparation (FASP)

FASP is a proteomic technique used for the preparation of samples for bottom-up MS analysis. Here, samples are subjected to on-column proteolysis to yield peptides. Firstly, each filter (Sartorius Stedim Biotech, #VN01H02 with a 10 kD cutoff) was incubated with 100 μl of a urea-based buffer (8M Urea + 0.1 M Tris, pH 8.5), to which 80-100 μg of the protein was then added. The mixture was centrifuged for 15 min at 14,000 g and 20ºC. Next, another 100 μl of the urea-based buffer was added, as well as 20 μl of 100 mM Tris 2-carboxyethyl phosphine hydrochloride, TCEP (a reducing agent) (C4706, Sigma). The reaction was incubated for 30 min on a shaking thermo-block at 37ºC and 600 rpm. This was followed by centrifugation for 15 min at 4,000 g and 20ºC. The sample was then alkylated by the addition of 20 μl of 300 mM iodoacetamide (IAA) (I6125, Sigma), together with 100 μl of the urea-based buffer. This was mixed on the thermo-block for 1 min at 600 rpm and 25ºC and then incubated for 20 min at room temperature (protected from light). After being centrifuged for 15 min at 14,000 rpm and 20ºC, the flow-through was discarded and 100 μl of 100 mM ammonium bicarbonate was added. Again, the sample was centrifuged for 20 min at 14,000 rpm, which was followed by another addition of 100 μl 100 mM ammonium bicarbonate and a centrifugation step. Next, 100 μl of 50 mM ammonium bicarbonate was added and, finally, trypsin (Promega) was added in a mass ratio 1:50 (w/w) (trypsin:protein). The sample was collected in a low-binding collecting tube (Axygen). The sample was mixed at 600 rpm for 1 h and then incubated overnight in a humidified chamber at 37ºC. The peptides were eluted by centrifugation at 14,000 rom for 15 min at room temperature. Samples within the same experiment were prepared simultaneously.

### b. Peptide quantification

Peptide concentration was measured using the Quantitative Colorimetric Peptide Assay, following the manufacturer's instructions (23275, Thermo Scientific). The absorbance of the reaction was measured using a TECAM spectrophotometer at 480 nm. A calibration curve was created and used to deduce the peptide concentration of samples. Based on this, 25 μg of peptides per sample were transferred into a new

low-binding microcentrifuge tube and dried in a SpeedVac at 35ºC for 1 h or until no residual liquid is present. Samples were stored at -80ºC.

## 2.8.2 Mapping of ubiquitination sites

### a. From reactions

Samples were processed by FASP and measured in data-dependent positive mode. The MS precursor mass range was set from m/z 400 Da up to m/z 1250 Da and from m/z 200 Da up to m/z 1600 Da in MS/MS. Cycle time was 2.3 seconds and in each cycle 20 most intensive precursor ions were fragmented. Subsequently, their corresponding MS/MS spectra were measured. Precursor exclusion time was set to 12 sec. Precursor ions with intensity below 50 cps were suspended from the IDA experiment. The extraction of mass spectra from chromatograms, their annotation and deconvolution were performed using Protein Pilot 4.5 (SCIEX, Toronto, Canada). MS and MS/MS data were searched using the Uniprot+Swissprot database restricted to *Homo sapiens* taxonomy. Fixed modification – alkylation on cysteine using iodoacetamide and digestion using trypsin was set for all searches. An emphasis on identification of GlyGly modification (ubiquitination) was selected in the software. FDR analysis was performed by searching the shotgun data against the decoy search database.

MS/MS spectra were inspected for evidence of product ions bearing the GlyGly modification. Ubiquitinated peptides identified by a set of product ions without GlyGly modification (less than 3 GlyGly modified product ions) were excluded from analysis and considered as false positive.

This was conducted in collaboration with Dr Jakub Faktor and Dr Bořivoj Vojtesek[‡].

‡ Regional Centre for Applied Molecular Oncology, Masaryk Memorial Cancer Institute, Brno, Czech Republic

### b. From polyacrylamide gels partly resolved by SDS-PAGE

*In vitro* ubiquitination assays with CHIP in the presence and absence of untagged ANXA2 were conducted as previously described. Upon completion, the reactions were diluted with loading dye and loaded an SDS-PAGE gel. Electrophoresis was performed until the dye front reach the interface between the stacking and resolving gels. Individual bands were the excised from the gel and stored at -20ºC.

Gel pieces were washed with 100 mM ammonium bicarbonate and acetonitrile and then incubated with 50 mM iodoacetamide for 30 minutes at room temperature in the dark. Gel pieces were washed again three times as before and then incubated overnight with 1:100 trypsin:protein at 37ºC in 100 μl 100 mM ammonium bicarbonate, 10% acetonitrile.

Excess liquid was removed and peptides were extracted from the gel with 2x 10 μl acetonitrile. Extracted peptides were then added to a fresh tube, before being diluted to 2% acetonitrile in 0.1% trifluoroacetic acid, and finally underwent solid-phase extraction on C18 stage-tips.

The acidified peptide solution was loaded onto an activated (15 μl methanol), equilibrated (50 μl 0.1% TFA) C18 StAGE tip, and washed with 50 μl 0.1% TFA. The bound peptides were eluted with 40 μl 80% ACN 0.1% TFA and concentrated to less than 8 μl in a vacuum concentrator. The final volume was adjusted to 15 μl with 0.1% TFA.

Online UPLC was performed using a Thermo Ultimate 3000 Nano. Following the C18 clean-up, 5 μl peptide solution were injected onto a C18 packed emitter and eluted over a gradient of 2%-28% acetonitrile in 40 min, followed by 76% acetonitrile for 6 min, with 0.5% acetic acid throughout. Eluting peptides were ionised at +1.7kV before data-dependent analysis on a Thermo Fusion Lumos. MS1 was acquired with mz range 350-1400 and resolution 60,000, and 2-second cycle for fragmentation with normalised collision energy of 28, and an exclusion window of 12 seconds. MS2 were collected with resolution 30,000 and AGC targets for MS1 and MS2 were $7e^5$ and $5e^4$ respectively.

Finally, the data were analysed using MaxQuant (v 1.6.3.3) in conjunction with Uniprot fasta database 2018_09, with match between runs (MS/MS not required), LFQ with 1 peptide required and normalization skipped. “GlyGly (K)” was added to the variable modifications. Modifications with a localization probability of >0.8 were considered.

This was conducted in collaboration with Dr Jimi Wills & Dr Alex von Kriegsheim[¶].

### 2.8.3 HDX-MS

HDX analysis by MS (HDX-MS) was conducted in collaboration with Dr Lenka Hernychova and Dr Bořivoj Vojtesek[‡]. HDX experiments were performed as previously described.

Mass spectrometric analysis was carried out using an Orbitrap Elite mass spectrometer (Thermo Fisher Scientific, Massachusetts, USA) with ESI ionization online connected with a robotic system based on the HTS-XT platform (CTC Analytics, Zwingen, Switzerland). The instrument was operated in a data-dependent mode for peptide mapping (high performance liquid chromatography (HPLC)-MS/MS). Each MS scan was followed by MS/MS scans of the top three most intensive ions from both collision-induced dissociation (CID) and higher-energy collisional dissociation (HCD) fragmentation spectra.

Tandem mass spectra were searched using SequestHT against the cRap protein database (ftp://ftp.thegpm.org/fasta/cRAP) containing the sequence of the CHIP protein with the following search settings: mass tolerance for precursor ions of 10 ppm, mass tolerance for fragment ions of 0.6 Da, no enzyme specificity, two maximum missed cleavage sites and no-fixed or variable modifications were applied. The false discovery rate at peptide identification level was set to 1%. Sequence coverage was analysed with Proteome Discoverer software version 1.4 (Thermo Fisher Scientific,

[¶] Institute for Genetics and Molecular Medicine, University of Edinburgh, Edinburgh, UK
[‡] Regional Centre for Applied Molecular Oncology, Masaryk Memorial Cancer Institute, Brno, Czech Republic

Massachusetts, USA) and graphically visualized with MS Tools application[99]. Totally 94.72% of CHIP protein sequence was covered by 294 identified unique peptides.

Analysis of deuterated samples was done in HPLC-MS mode with ion detection in the orbital ion trap. The MS raw files together with the list of peptides (peptide pool) identified with high confidence characterized by requested parameters (retention time, XCorr, and ion charge) were processed using HDExaminer version 2.2 (Sierra Analytics, Modesto, CA). The software analysed protein and peptides behaviour and created the uptake plots that showed peptide deuteration over time with calculated confidence level (high, medium confidence are accepted, low confidence is rejected). The results from peptide pool were displayed as graph showing the evolution of deuteration at individual parts of the protein at the same time and different protein states plotted using MS Tools application. Molecular structures were rendered using PyMOL[100].

## 2.9 Software and statistics

### 2.9.1 Analysis of DNA sequences

To identify indels in the *STUB1* gene in the clones derived from CRISPR/Cas9-based gene editing, the SnapGene software was used. Here, sequences obtained from PCR products and the DNA extracted from competent cells transformed using the TOPO cloning kit were aligned with the human WT *STUB1* gene.

### 2.9.2 Imaging analysis

Fluorescent images were analysed by ImageJ in multiple ways. Firstly, different channels were isolated and overlaid using this software to represent co-localisation signal. For some experiments, such co-localisation was quantified using the “Coloc 2” plugin, according to the software’s instructions, which resulted in a colocalization index (the Pearson’s colocalization number) that was compared across conditions/cell lines. Secondly, ImageJ was used to create maximal projections from z-stacks of images.

Additionally, the signal intensity of single images or maximal projections was quantified using this software. For such, colour channels were isolated and the brightness and contrast of the per channel was adjusted in a consistent manner across replicates within an experiment, to improve signal:background. When the signal of interest is localised to the cytoplasm or membrane, rather than restricted to the nucleus, the mean intensity of the channel of interest is recorded and normalised by that of DAPI (for normalisation purposes).

In the glass bead-rolling assay, the fluorescence of the intracellular dye was quantified per area of the nucleus (represented by the DAPI staining). For such, after splitting the different channels per image, the intensity of the green channel was adjusted to 1000-7500. Next, the DAPI channel was selected and a binary image was created using the default threshold. The different nuclei were highlighted using the "Analyse particles" plugin (using an arbitrary size that would identify nuclei, e.g. 20 to infinity), which was then manipulated manually to adequately detect the nuclei present in the image. The highlighted areas were added to the regions of interest (ROI) manager and overlaid on the adjusted fluorescence channel of interest (green). The mean intensity was measured and, if >2000 the cells was classified as injured (the arbitrary value was achieved by qualitative analysis of the images). The percentage of cells injured compared to the total cells analysed was calculated and compared across cell lines.

Finally, ImageJ was also used for the quantification of PLA signal. For the majority of the PLA experiments, the number of PLA puncta per field of view was counted manually and then this was divided by the number of nuclei (represented by DAPI staining) present. However, the quantification of the PLA analysing the interactome of ANXA2 and S100-A11, which resulted in abundant signal, was performed in a semi-automated manner. For such, the PLA channel was isolated, and the total integrated density was measured (i.e. ROI were not selected). This was then divided by 10000 and then normalised by the number of nuclei within each image (that was counted manually). The effect of slightly varying background intensities was proven to not change the results obtained significantly (data not shown). All quantifications were conducted using TIFF images.

### 2.9.3 Live-imaging analysis

The Volocity software (PerkinElmer) was used for live-imaging analysis. The kinetics of repair was measured by monitoring the uptake of FM1-43 dye as a change in fluorescence at regions of interest over the course of imaging. The software was also used to measure the distance migrated by cells upon laser-induced injury was quantified by measuring the length from the end of a single projection to the cell body both before and after injury, in projections that are close to the site of injury.

### 2.9.4 Quantification of immunoblots and polyacrylamide gels analysed by SDS-PAGE

Immunoblots and gels stained with Coomassie blue were scanned and specific bands were quantified using Image Studio Lite (using TIFF images). The background intensity was used to normalise the quantification of each band. Quantification takes into account the intensity and area occupied by the signal. Quantification of proteins of interest was normalised by that of the loading control.

### 2.9.5 Statistical analysis

Normality tests and statistical analysis were performed using Prism GraphPad. When datasets pass the D'Agostino-Pearson normality test (alpha=0.05), they were analysed using the student's *t*-test or One-way/Two-way Analysis of Variance (ANOVA) statistical tests with Holm-Sidak's multiple comparison post-hoc test, as indicated. When the data failed the normality test applied, a non-parametric statistical test was performed, Kruskal-Wallis test, with the Dunn's multiple comparisons post-test.

# Chapter 3: Engineering iPSCs to generate isogenic neuronal cell models

## 3.1 Introduction

### 3.1.1 Existing physiological models for studying CHIP function

Largely due to the lack of authentic models to study CHIP, cell biologists have relied on overexpression systems[25,57]. These are particularly inadequate when studying tightly-regulated enzymatic housekeeping pathways, such as ubiquitination and other PQC mechanisms, in which CHIP functions. Furthermore, overexpression of CHIP is likely to interfere with the interactome of other TPR-containing proteins.

Recently, iPSC lines have been engineered to model CHIP-related diseases[101,102], thus moving towards a more biologically relevant system. Regarding animal models, the first CHIP KO mouse model was reported in 2003[78]. Since then other groups have characterised it from different angles[14,15,103,104], but no new mouse models have been engineered. *Drosophila* and *C. elegans* CHIP models have also been derived, but their phenotype was not characterised in detail, except for their reduced longevity[62]. All these models support a robust neuroprotective role for CHIP, however, the underlying mechanisms are largely unknown.

#### a. Homozygous CHIP KO mice

CHIP KO mice were first established by the Patterson group[78]. The first three exons of the CHIP gene were replaced with a selection cassette (PGK-Neo for expression of neomycin resistance) by homologous recombination. CHIP homozygous KO mice have significant mortality in prenatal (5% has been reported[78]) and early postnatal periods (studies reported 20%[78] and 95%[103]). These mice had thymic atrophy, a characteristic non-specific response to abnormal stress tolerance[78]. Although the first report of CHIP KO mice did not observe obvious morphologic abnormalities in the surviving mice[78], two subsequent sutides[14,103] reported compromised bodyweights (Figure 3.1A). Additionally, the latter group observed severe neurological and

peripheral phenotypes in CHIP KO mice, which have profound gait impairment (dysbasia)[103].

Overall, the literature agrees with the severe progeria phenotype exhibited: CHIP KO mice have a 60% decrease in longevity compared to WT (Figure 3.1B) and a 31% gender-specific decrease in longevity, with male mice showing increased progeria[14,15]. Accordingly, CHIP KO mice had profound progressive reductions in bodyweight and age-related conditions, such as osteoporosis[14].

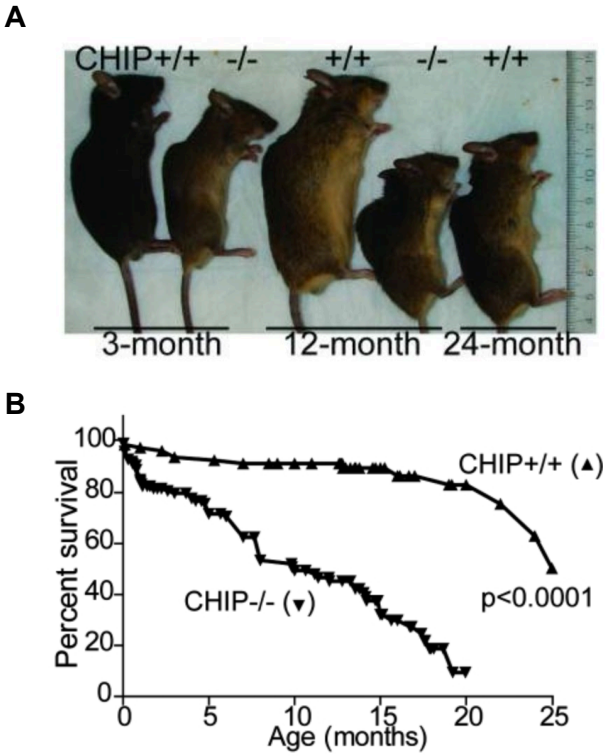


**Figure 3.1: CHIP KO mouse model**
**A)** CHIP KO mice have small body sizes and enhanced progressive kyphosis.
**B)** CHIP KO mice have significantly reduced lifespans. Cohort including male and female CHIP KO (*n* = 82) and WT (*n* = 128) mice.

(Min *et al.*[14])

Interestingly, both the CHIP KO mice and its isolated fibroblasts have compromised responses to stress. For example, Hsp70 upregulation in response to heat shock was reduced by 50-60% in fibroblasts (similar to that observed in cells lacking the inducer of HSPs, HSF-1) and severely impaired in multiple tissues, including the brain. In parallel, caspase-3 protein levels and activity were enhanced in CHIP KO mice, indicative of cell death. Accordingly, all CHIP KO mice subjected to heat stress died

rapidly, either during or immediately thereafter, compared to WT mice that only recorded 25% death during recovery[78].

### b. Heterozygote CHIP mutant mice

The extreme phenotype of CHIP homozygous KO mice can confound investigation into protein targets of CHIP KO mice. Heterozygote mice were generated from the established CHIP KO mouse model[78] and analysed by McLaughlin and colleagues[104]. Gross abnormalities, such as body and brain weights and muscle tone, which were seen in homozygous KO mice were normal in the heterozygous mice. However, cardiac dysfunction, brain dysfunction (detected by specific motor disturbances) and impaired response to environmental stress were maintained. Finally, the heterozygous CHIP mice are likely to be a better model to investigate human diseases, seeing that no total loss-of-function mutation in CHIP have been reported in humans[104].

### c. CHIP mutant iPSC

Recently, iPSCs were reprogrammed from fibroblasts of a 12-year-old patient with Gordon Holmes syndrome/SCAR16, having severe early-onset multi-systemic neurodegeneration. The cell line carries two heterozygous mutations in the *STUB1* gene, encoding for CHIP, leading to a premature stop codon at Arg119 and a point mutation (Ile294Phe) at the protein level. Cells express markers of pluripotency genes, including OCT4, and can differentiate into ectodermal cell lineages[101].

### d. CHIP KO iPSC

The same group established iPSCs from fibroblasts of a healthy 37-year old woman. These were then transfected with two tracrRNA ribonucleoprotein complexes targeting exon 2 and 3 of *STUB1* for CRISPR/Cas9 gene-editing. Sequencing confirmed that the homozygous KO line carries a deletion resulting in a protein with a frameshift mutation (p.Val94Alafs*5) leading to nonsense-mediated decay and loss of CHIP protein. Again, the iPSCs express markers of pluripotency and have differentiation potential[102].

### 3.1.2 CRISPR/Cas9-based gene-editing technology

Clustered regularly interspaced short palindromic repeats (CRISPR)/Cas is a defence mechanism of the microbial adaptive immune system that uses RNA-guided nucleases to cleave foreign genetic elements (e.g. virus or plasmid)[105]. In bacteria and archaea, the mechanism has three stages, adaptation/acquisition of CRISPRs to invaders, CRISPR RNA (crRNA) biogenesis and invader silencing[106–108]. This mechanism has been exploited to allow targeted nucleases to be used for genome alteration with high precision (Figure 3.2)[105,109]. There are three types of CRISPR/Cas systems identified, but type II from *S. pyogenes* is the most widely used system for genetic manipulation and utilizes the nuclease Cas9.

It has been suggested that Cas9 protein intrinsically interacts with nuclei acids in a non-specific manner, thus the RNA components confer specificity[105]. The crRNA array not only encodes the guide RNA for directing the nuclease to the DNA target, but also encodes an essential auxiliary trans-activating crRNA (tracrRNA)[105]. TracrRNA is complementary to the repeat sequences in pre-crRNA and forms an RNA duplex[107,109] (Figure 3.2A). The two RNAs complex with Cas9.

Both crRNA and tracrRNA are critical for Cas9-mediated targeted DNA cleavage[108]. Mechanistically, tracrRNA ensures target DNA recognition, possibly by directing the orientation of Cas9 on the complementary strand. The crRNA has a short high-affinity binding site (called the “seed” sequence) in its 3’ end, which is the protospacer-encoded portion of the crRNA and governs the efficiency of target binding[107]. The region of the crRNA is complementary to the seed sequence (8-12 bp) in the target DNA, thus directs the Cas9 to this site for subsequent cleavage[108,109].

For the CRISPR/Cas9 methodology, the crRNA and tracrRNA have been fused to create a chimeric, single-guided RNA (gRNA)[105] (Figure 3.2B[109]). It retained the hairpin structure and mimicked the dual-RNA structure required to guide Cas9[108]. This allows bypassing of the adaptation/acquisition and crRNA biogenesis steps and, by designing gRNAs, DNA sequences of interest can be targeted.

While the architecture of the gRNA used influences the efficiency of Cas9 activity for any given locus[109], the protospacer adjacent motif (PAM) dictates the cleavage

location[105,108]. The PAM conforms to an NGG consensus sequence within the target DNA, which occurs downstream of the crRNA binding sequence[108] (Figure 3.2C). This is the PAM requirement for Cas9, although it varies across different Cas proteins[105]. The PAM plays a role in the recruitment of the ribonucleoprotein (Cas9-tracrRNA:crRNA) complex to the correct target DNA site. Mutating a single G nucleotide compromised the interaction[108]. Therefore, specific recognition of the PAM sequence by Cas9 as a pre-requisite for target DNA binding[108].

For gene-editing, the expression of Cas9 and the requisite gRNA is induced in the model of interest. Commonly, the gRNA is engineered to specify the 20-nt targeting sequence (not including the PAM) (Figure 3.2C). Cas9 cleavage results in a double strand break, which can undergo repair by non-homologous end joining (NHEJ) or homology directed repair (HDR), resulting in genome editions (Figure 3.2D). NHEJ occurs in the absence of a repair template and is error-prone. Insertions/deletion (indel) mutations can result in gene KO, if they occur within a coding exon or within promoters/enhancers[105,109]. HDR, on the other hand, is a high-fidelity repair pathway that can generate precise and defined modifications at a target locus. Although it occurs less frequently than NHEJ, it can be driven by the presence of an exogenously introduced repair template. Templates contain homologous sequences flanking the insert sequence and are effective methods for making small edits (e.g. introduction of single nucleotide mutations)[105].

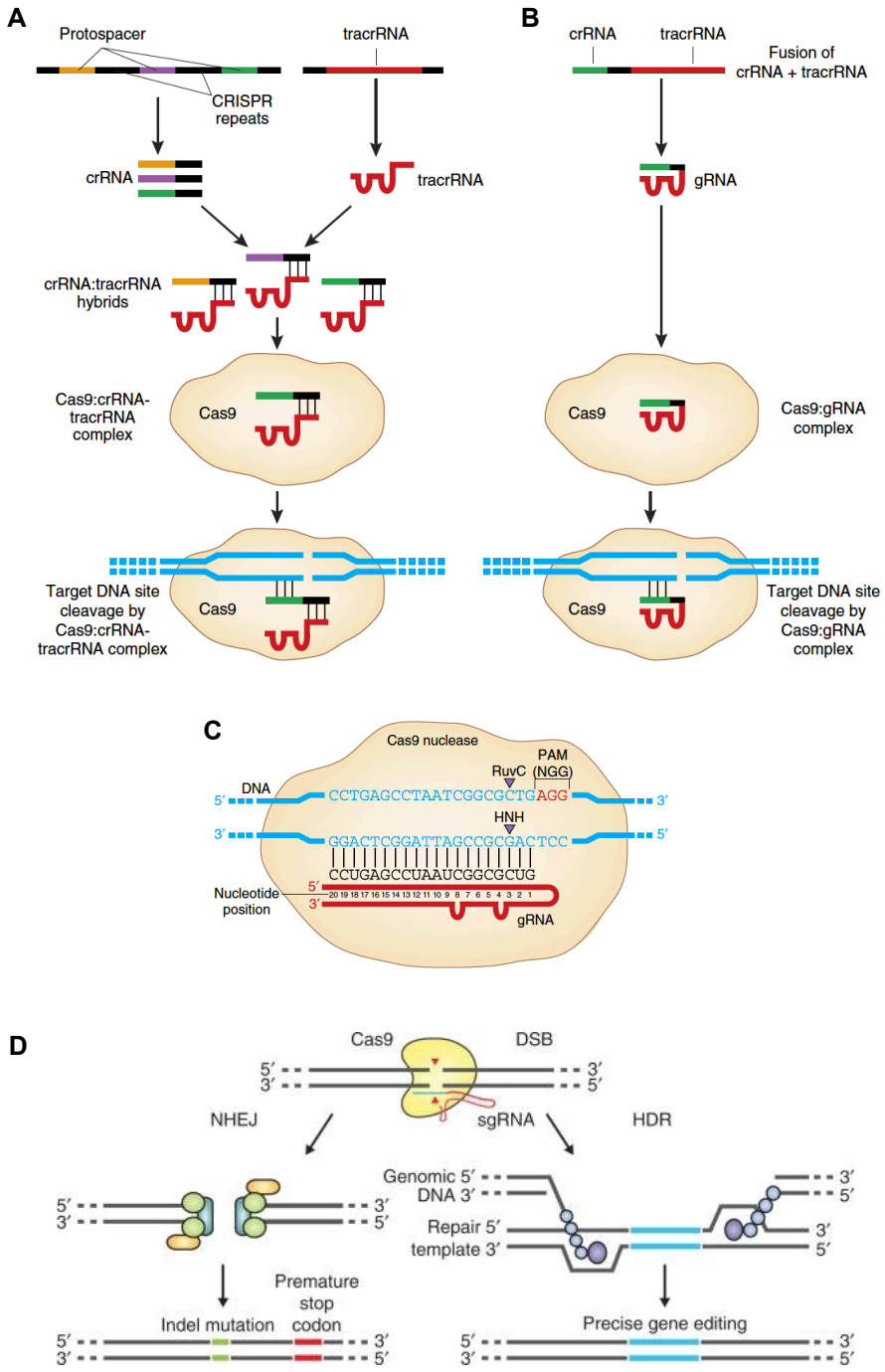


**Figure 3.2: Naturally occurring and engineered CRISPR/Cas9**
**A)** Naturally occur CRISPR/Cas system. TracrRNA hybridizes to the pre-crRNA repeat, forming a duplex RNA that is recognized and cleaved by the ribonuclease RNase III[13,14]. Such processing of crRNAs requires the presence of Cas9[13,14]. The pair of RNAs (crRNA-tracrRNA) complex with Cas9 allowing Cas9 to recognise and cleave foreign DNAs bearing the protospacer sequences.
**B)** Engineered CRISPR/Cas systems use a single gRNA to target Cas9 to the target DNA site.
**C)** Cas9 is a large protein that includes both HNH and RuvC-like nuclease domains[11,13]. Each domain cleaves the complementary and noncomplementary strands of the target DNA, respectively[14]. The gRNA mediates the cleavage of DNA sites that are complementary to the 5' 20nt of the gRNA and lie adjacent to a PAM sequence.
**D)** Once dsDNA is cleaved, repair can be mediated by non-homologous end joining (NHEJ) or homology directed repair (HDR).

(**A-C**: Sander *et al.*[109]; **D**: Ran et al.[105])

### a. Advantages of the CRISPR/Cas9 system

The extensive advantages of the CRISPR/Cas9 technology drove its rapid expansion from being a niche to mainstream method used by many researchers across different fields[109]. It allows the generation of modified cell lines, having enormous potential across basic science to medicine and biotechnology[105]. It aids in the investigating protein function, by deleting protein-encoding genes or altering functional domains, enabling more accurate disease modelling[109]. Compared to gene-editing technologies previous used (e.g. using zinc-finger nucleases and transcription activator-like effector nucleases), the system is easy to design, highly specific and customizable[105,109]. The use of single gRNAs also increased the editing efficiency rates, compared to double gRNA systems[109]. This contributed to the great potential of CRISPR/Cas technology for high-throughput and multiplex gene editing. By changing the gRNA, the nuclease can be targeted to any target within the vicinity of the PAM[105,108].

### b. Limitations of the CRISPR/Cas9 system

Despite advances compared to other methodologies, the main drawback of CRISPR/Cas9 is off-target mutagenesis. Potential off-targets include sites that differ by up to five positions within the protospacer region compared to the on-target site and/or have an alternative PAM sequence than ‘5-NGG (such as 5’-NAG)[105,109]. The occurrence of off-targets is influenced by enzyme concentration, the abundance of similar sequences in the target genome and, potentially, the accessibility of off-target sites (dictated by epigenetics)[105]. Beyond the problem of the presence of off-target mutagenesis, albeit at variable frequencies, is the challenge in predicting the off-targets[109]. Thus, development of unbiased strategies to globally assess the off-target effects is of great interest and will potentiate the use of CRISPR/Cas9[109].

### 3.1.3 Parkinson's induced pluripotent stem cells (iPSC)

A patient within the Iowa kindred with Familial Lewy Body Parkinsonism caused by a triplication of the *SNCA* locus (Figure 3.3A) had rapid and progressive motor and cognitive decline[97,110]. Fibroblasts from this patient were reprogrammed into iPSCs by transfecting the Yamanaka transcription factors (OCT4, SOX2, KLF4 and c-Myc) (Figure 3.3B). The underlying rational is its potential as a model of both familial and sporadic PD[97]. Familial PD has been reported from several duplication and triplication *SNCA* kindreds[111] and multiple GWAS studies have identified polymorphisms around *SNCA* as the most significant genetic risk factor for sporadic PD[112]. The iPSC lines engineered were able to differentiate into neuronal lineages. Patient-derived iPSC have four copies of the *SNCA* gene, causing a twofold increase in $\alpha$-Syn expression both in undifferentiated state and upon differentiation into dopaminergic neurons (Figure 3.3 C&D)[97].

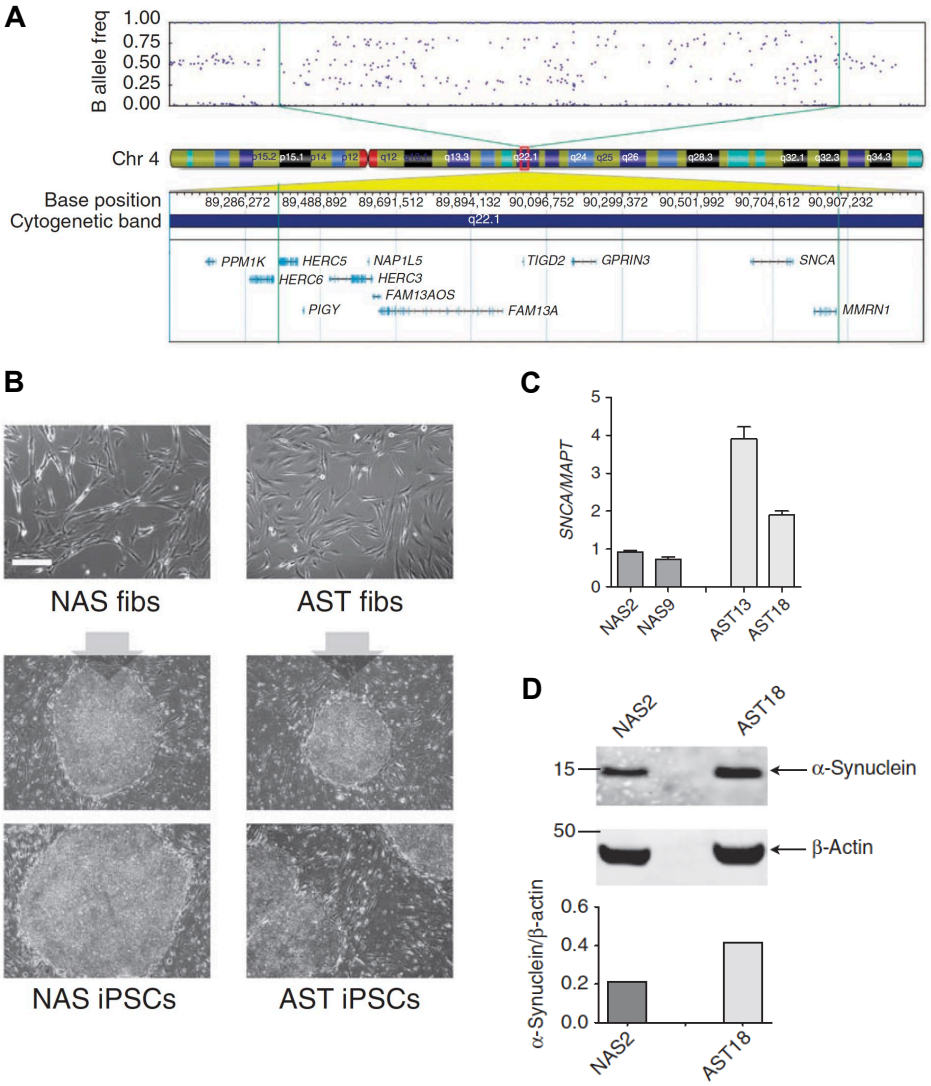


**Figure 3.3: Patient-derived iPSC**
**A)** The patient with Familial Lewy Body Parkinsonism due to a triplication locus spanning multiple genes, including SNCA.
**B)** Phase contrast images of AST (patient-derived) and NAS (derived from a healthy relative) fibroblasts and *de novo* iPSC colonies at day 20 post-viral transduction. Scale bar, 100 µm.
**C)** Quantitative RT-PCR analysis of SNCA expression normalised with a pan-neuronal marker (MAPT). Twofold or greater increase in SNCA expression in neurons derived from AST iPSC.
**D)** Western blot analysis of SNCA expression showing a doubling in AST-derived neurons.
(Devine et al.[22])

### a. Neural induction

Neural induction is the first step in neuronal differentiation from stem cells. Dual-SMAD inhibition is necessary and sufficient for neural induction of human pluripotent stem cells in culture[113–115]. Together with the high plating density, this biases

pluripotent stem cells to become Pax6$^{+}$ neural progenitors (an early marker of neuroectodermal differentiation). Dual-SMAD inhibition achieves complete neural conversion of >80% of stem cells (whilst the use of either inhibitor alone only yields <10%)[113].

However, for efficient cortical differentiation, inhibition of SMAD signalling in combination with retinoid-mediated pathways is critical[114,115]. The use of retinoic acid is reported to result in the conversion of >95% of stem cells into cortical stem and progenitor cells 15 days after neural induction[115]. *In vivo*, retinoids promote derivation of neural stem cells, regulate the transition from neural stem cell expansion into neurogenesis in the cerebral cortex and pattern cortical tissue to caudal and/or ventral identities in a concentration-dependent manner[113–115].

During neural induction, a process that lasts around 11 days, cells undergo multiple changes in morphological and expression profile. Between days 3 and 5 neural patterning takes place, with markers of pluripotency (e.g. *OCT4*) becoming silenced, achieving a population of Oct4$^{-}$/Pax6$^{+}$ intermediate cells. At day 5, epiblast markers (FGF5 and OTX2) are highly expressed. The protein expression of Pax6 gradually increases and becomes strong in the majority of the cells by day 7. The lineage of these early Pax6$^{+}$ neuroectodermal cells is biphasic. Initially, large numbers of neural crest-like cells form. This is followed by rosette neural stem cells (expressing the neural stem cell marker, Nestin), which drive rosette formation[113]. Cortical rosettes have an obvious apico-basal polarity, with many mitoses located at the apical, luminal surface of each rosette[115]. Spontaneously, rosette neural stem cells acquire anterior CNS markers (OTX2 and FOXG1B)[113].

### b. Cortical neurogenesis

To achieve successful cortical neurogenesis and differentiation *in situ*, one approach has been to recapitulate *in utero* development, thus generating all classes of cortical projection neurons in a fixed temporal order[115]. A key feature is the generation of both primary and secondary cortical stem and progenitor cells following neural induction. They mimic the main population of cortical stem cells (the neuroepithelial ventricular zone), as well as the secondary populations found in the inner and outer

subventricular zones (the basal progenitor cells and the outer radial glial cells) of the developing human cortex[115].

The primary cortical progenitor cells generated from pluripotent stem cells make up the major population of rosettes, these are $Pax6^+/OTX2^+/Ki67^+$ polarized cells with radial processes. These give rise to secondary progenitor cells, which are composed of two subpopulations: basal/intermediate progenitor cells and radial glial cells [114,115]. The former are $TBR2^+/Ki67^+/Pax6^-$ and lack basal processes. About half of the $Tbr2^+$ population are cycling stem and progenitor cells (co-expressing Ki67), whilst the rest are newly born, post-mitotic neurons. Expressing of secondary progenitors (FOXG1 and TBR2) increases over time. These progenitor cells are present at the periphery of each rosette and make up 10-15% of its cells[114,115]. The other subpopulation of secondary progenitor cells are radial glial cells, marked by $Pax6^+/TBR2^-$ expression and lengthy basal processes[115].

Following the establishment of cortical neural rosettes, fundamental principles of neural development govern the ability of these three critical classes of progenitors to generate complex populations of cortical projection neurons, in a cell-intrinsic manner. Around 2-3 weeks after initiation of neural indication, early-born deep-layer neurons ($TBR1^+$ and/or $CTIP2^+$) form and become the major population ~day 35[114]. From day 28, synaptic markers are detected, including the glutamatergic postsynaptic protein PSD-95, the major synaptic vesicle protein, synaptophysin, and the presynaptic protein, Munc13-1. These are detected in close proximity, likely to represent physical synapses, although still functionally inactive[114,115]. However, by days 45-50, physical and functional synapses are detectable and become more abundant over the subsequent weeks[114]. After around 70 days of cortical differentiation, late-born upper-layer neurons ($Stab2^+/Cux1^+/Brn2^+$ neurons) are detected[114,115]. Once all populations have developed, complex patters of spontaneous activity are detected (at day 80 and above). It was reported that functional cortical neural networks only emerge in culture after 2-3 months[114]. Although this protocol promotes the formation of cortical neurons, glial cells emerge from at a later stage. Heterogeneous astrocytes (both $GFAP^+/S100^+$ and $GFAP^-/S100^+$ populations) appear around day 60 and become more abundant over the next 40 days, making up approximately 1-7% of cells in culture[115].

By capturing the complexity of human cortical progenitor cell types found *in vivo*, the *in situ* system is able to achieve the diversity of projection neuron types in the human cortex[115]. Moreover, the time frame for cortical neurogenesis and emergence of functional cortical neural networks observed *in situ* is remarkably similar to that occurring during development[114]. Glutamatergic projection neurons destined for the six layers of the adult cortex are generated in a stereotyped temporal order, with deep-layer neurons being produced first and upper-layer neurons last. *In utero*, once these are generated, the different classes form local microcircuits between them. This is recapitulated in the cellular system by the gradually increasing complexity of neural circuits[115].

### c. Advantages

Methods of neuronal differentiation from stem cells allow the generation of disease-relevant cell types, establishing models to elucidate disease mechanisms and a platform to validate candidate drugs and therapies in target cell types. Cortical neuron differentiation, in specific, enabled functional studies of human cortex development, function in health and dysfunction in disease[114,115]. Furthermore, when combined with patient-derived iPSC technology, individual-specific cortical networks can be generated, carrying a genetic background of interest[115].

Beyond its potential applications, certain features make this protocol useful. Firstly, the use of dual-SMAD inhibition results in neural patterning response that can be achieved within a short period of time (~19d). Previously, neural induction was stromal feeder-mediated and would take 30-50 days[113]. Secondly, the purity and robustness of the protocol are great advantages, as they allow almost pure cultures of cortical stem and progenitor cells to be produced repeatedly. Finally, this system is likely to recapitulate cortex-specific mechanisms, as it generates cultures of both deep- and upper-layer excitatory neurons, which are electrically active and form functional circuits[114,115]. This contributes to the biological relevance its findings when used as a model. In fact, some argue that human iPSC-derived cortical neurons are a more adequate model than rodent-based ones due to intrinsic differences in cortical neurogenesis between the species. Cortical neurogenesis in rodents takes approximately 6 days and has reduced complexity and diversity in the stem cell

populations and neuron cell types derived (lacking primate-specific neuron types in deep layers)[114,115].

### d. Limitations

However, it is unclear whether all classes of cortical stem and progenitor cells are present and, as discussed, progenitor cell populations are key to achieve the full spectrum of neurons[114]. Furthermore, this protocol generates glutamatergic projection neurons, while GABAergic interneurons were not detected. This could be a limitation when modelling the cerebral cortex, as it consists of two major classes of neurons: excitatory, glutamatergic projection neurons (making up about 80%) and GABAergic interneurons. During development, glutamatergic neurons are derived from cortical stem and progenitor cells, whilst the GABAergic neurons are generated outside of the cortex and migrate[115].

Another significant drawback of across differentiation methodologies is clonal variation, which can arise from different sources. When differentiating iPSC that have been reprogrammed from mature cells, genetic and epigenetic changes introduced during the course of reprogramming may influence the ability of cells to differentiation. For example, the differentiation of iPSC clones that are epigenetically prone to source cell memory, become bias towards the source cell lineage. Also, the inherent variable and dynamic nature of the differentiation process *per se* can also introduce genetic and epigenetic changes that may potentially cause phenotypic changes during or in the aftermath of differentiation[97,116,117]. This makes it more challenging to achieve an isogenic set of iPSC lines with comparable differentiation potentials[116]. However, both Chambers *et al.*[113] and Shi *et al.*[114,115] have reported reproducible results in neural induction and cortical neurogenesis across cell lines, arguing that the robustness of the protocol surpasses clonal variability.

## 3.2 Results

### 3.2.1 CHIP KO iPSC using CRISPR/Cas9

Within our group, a neuroblastoma cell line, SH-SY5Y, capable of differentiating into neurons was previously engineered using CRISPR/Cas9 to ablate the expression of the CHIP-encoding gene, *STUB1* – work was conducted by Erisa Nita[95]. SH-SY5Y cells have been widely used in the field of neuroscience research due to its ease for genetic manipulation, low maintenance and cost, human origin and ability to differentiate into neuronal lineages[118]. Within the scope of my PhD project, the engineering of a CHIP SH-SY5Y model is viewed as proof-of-concept for the ability to ablate CHIP expression in cells using this system and without affecting cell viability.

Given its success, the same CRISPR/Cas9 system was used in a patient-derived iPSC line. The gRNA was designed to target downstream of ATG within the first coding exon (exon 1) of *STUB1*, increasing the likelihood of an indel mutation knocking out CHIP protein. The guide sequence used is GGCCGTGTATTACACCAACC GGG (PAM sequence underlined). According to the MIT software*, it has a quality score of 94% and predicted to have 30 off-target sites, of which 7 are located in genes. The gRNA was inserted into a LentiV2 backbone, containing the Cas9 gene, using the restriction enzyme BsmB1 (Figure 3.4A). SH-SY5Y were successfully electroporated with the LentiV2 vector containing the gRNA, along with a GFP-encoding plasmid, using Amaxa nucleofection (Lonza), achieving high transfection efficiency (94% $GFP^+$ cells) and CHIP KO clones (Figure 3.4B-D)[95]. Interestingly, the PCR product derived from genomic DNA of what was then characterised as a CHIP KO clone (labelled “KO1” in the agarose gel) shows two amplicons of different sizes, whilst the other lane (labelled “WT”) shows an amplicon of a single size (Figure 3.4B). This reflects the presence of pronounced indels in one of the alleles of the KO clone, which was confirmed by sequencing (Figure 3.4C). The other allele has a single nucleotide deletion, thus its PCR product is of a similar size as that from the WT clone (CRISPR negative control) (Figure 3.4B).

* http://crispr.mit.edu

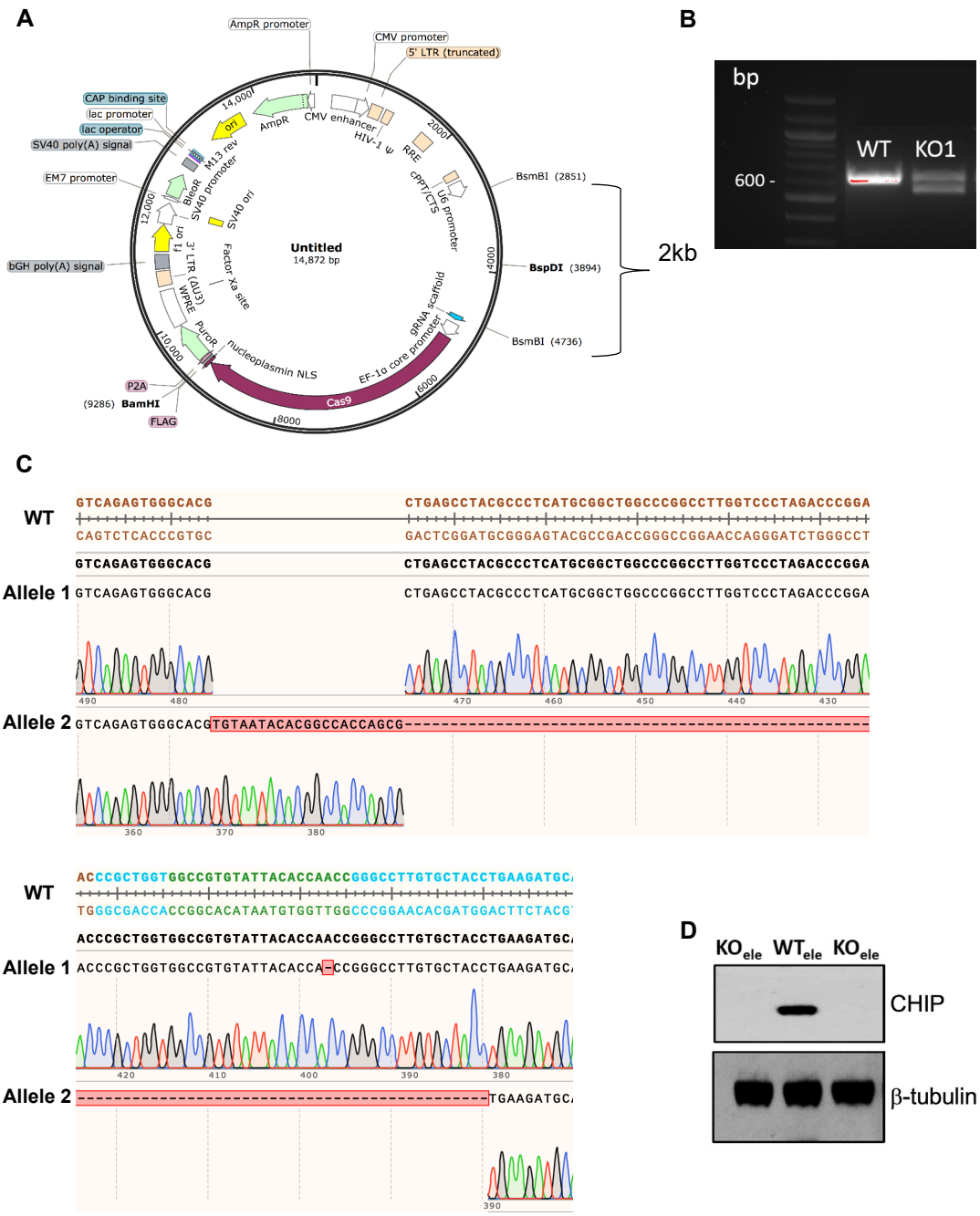


**Figure 3.4: CHIP KO SH-SY5Y cells**

**A)** Map of the LentiV2 plasmid and the restriction sites of the BsmB1 enzyme used. The gRNA was inserted into the vector. Digestion also yield a 2-kb product that contains another restriction site (BspD1) that was used for screening of successfully digested and ligated clones.

**B)** PCR products flanking the region of the *STUB1* gene where the gRNA sequence were made from genomic DNA of two different CRISPR clones and analysed using a 1% agarose gel.

**C)** The sequences of both alleles of the CHIP KO clone are shown aligned with the human WT *STUB1* gene. The *STUB1* exons (brown), coding regions (blue), forward and reverse primers (magenta) and gRNA (green) are indicated. One allele has a single nucleotide deletion, whilst the other has multiple deletions and insertions.

**D)** CHIP protein expression in the clones was analysed by SDS-PAGE/immunoblot. Both anti-CHIP and anti-β-tubulin mAbs were used.

(**A**, **B** and **C**: Adapted from Nita[95]; **C**: collaborative work with Erisa Nita)

Aiming to obtain a disease-relevant CHIP KO cell model, I genetically manipulated iPSC derived from a patient with triplication of α-Syn using CRISPR/Cas9. More specifically, the AST line was used for this project, not only because of its twofold increase in α-Syn mRNA and protein expression (Figure 3.3C&D), but also for its differentiation potential (previously, it was shown to successfully form dopaminergic neurons[97]). Once cells were electroporated, single colonies were picked manually, as single cell sorting tends to be too stressful for iPSCs. Cell survival was optimised by treating cells with the ROCK inhibitor Y-27632 and Collagenase Type IV, to partially detached cells from the underlying matrix prior to dissociation of the colony using mechanical force. Different matrices were also tested (Laminin-521, which we routinely use for iPSC culturing, and Matrigel) and colonies were obtained from both.

Once colonies became confluent in 24-wells, clones were screened by IF with anti-CHIP mAb and using the T7 endonuclease I assay. The former was unsuccessful (data not shown) given the difficulties in confidently classifying clones are immunopositive or negative, due to the characteristic high nucleus:cytoplasm ratio of iPSCs, in combination with the predominantly cytoplasmic expression of CHIP. Next, the DNA of each clone was extracted and the region flanking the gRNA target sequence in *STUB1* was amplified by PCR. The PCR products were annealed and subjected to the T7 endonuclease I assay. This enzyme recognises and cleaves non-homologous dsDNA, thus detecting indels. The reactions with and without the endonuclease were ran on an agarose gel (Figure 3.5). The following clones had extra bands from the incubation with the T7 endonuclease, hence were of interest: A1, F1, B2, D2, E3 and G3.

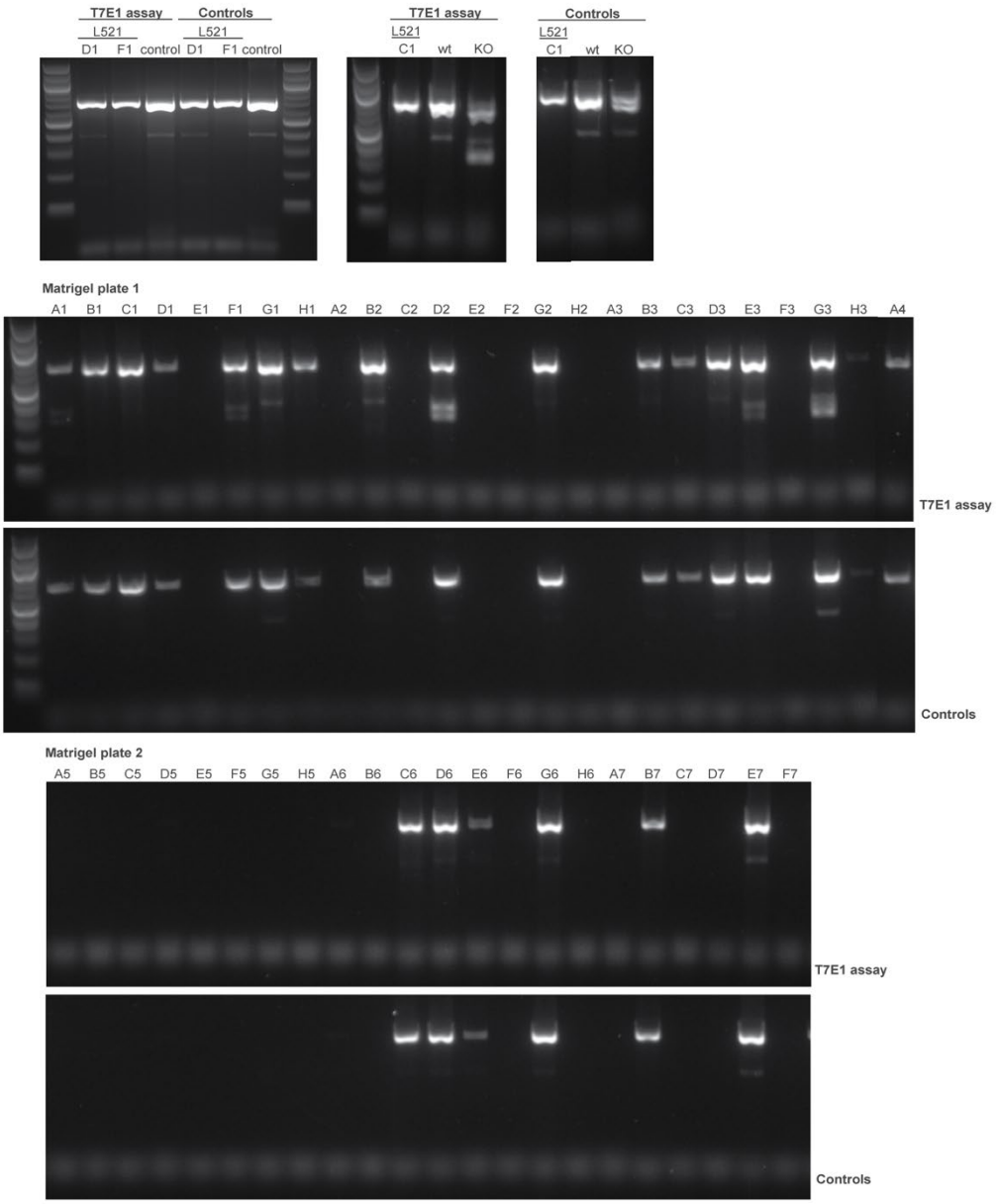


**Figure 3.5: T7 Endonuclease I assay of iPSC CRISPR clones**
Agarose gels (1%) containing the T7 endonuclease reactions (*top*) and controls (*bottom*) of the different CRISPR clones. CHIP KO and WT SH-SY5Y were included as positive and negative controls, respectively. Clones selected from Laminin-521 and Matrigel coated plates were tested.

Proliferating clones, including those of particular interest, were analysed by WB to assess the expression of the CHIP protein (Figure 3.6). While some clones had increased CHIP levels compared to WT iPSC and SH-SY5Y, clones D2 and D3 had about half the amount of CHIP, clone A7 had a negligible band and C6 had

undetectable CHIP levels. Clones D2, D3 and A7 could be heterozygote mutants for CHIP or, given the very low expression levels, A7 could be a KO clone with some degree of contaminant CHIP-expressing cells.

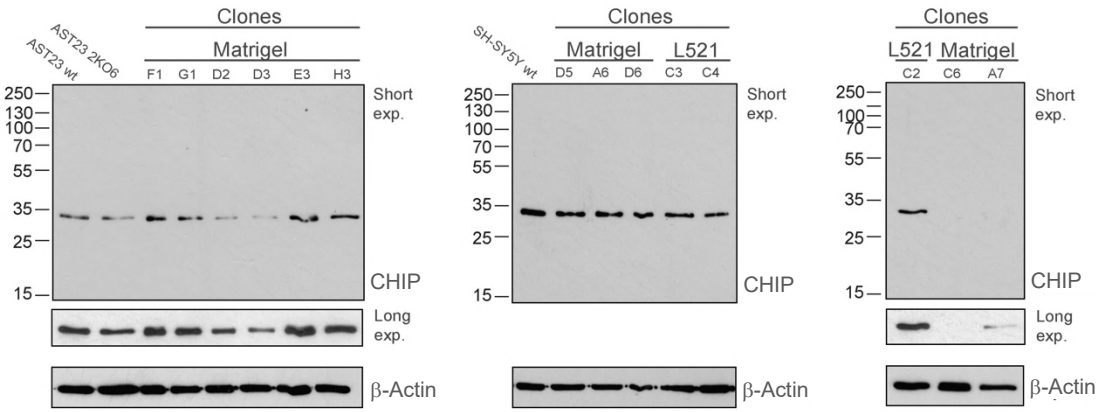


**Figure 3.6: Western blot analysis of iPSC CRISPR clones**
Cell lysate from CRIPSR clones were analysed by SDS-PAGE/immunoblot using anti-CHIP (1:10000) and anti-β-actin (1:5000) mAbs. Positive controls were included: the patient-derived iPSC parental line (AST23), its isogenic control line (AST 2KO6) and the WT SH-SY5Y cells. These immunoblots were ran and exposed simultaneously.

To confirm the CHIP genotype of clones of interest, PCR products flanking the gRNA sequence were generated and sent for sequencing (Figure 3.7). Firstly, the parental line (AST) and the C1 CHIP-expressing CRISPR clone were identical to the published sequence for the human *STUB1* gene (Figure 3.7B). Therefore, these cell lines encode WT CHIP protein (Figure 3.7C).

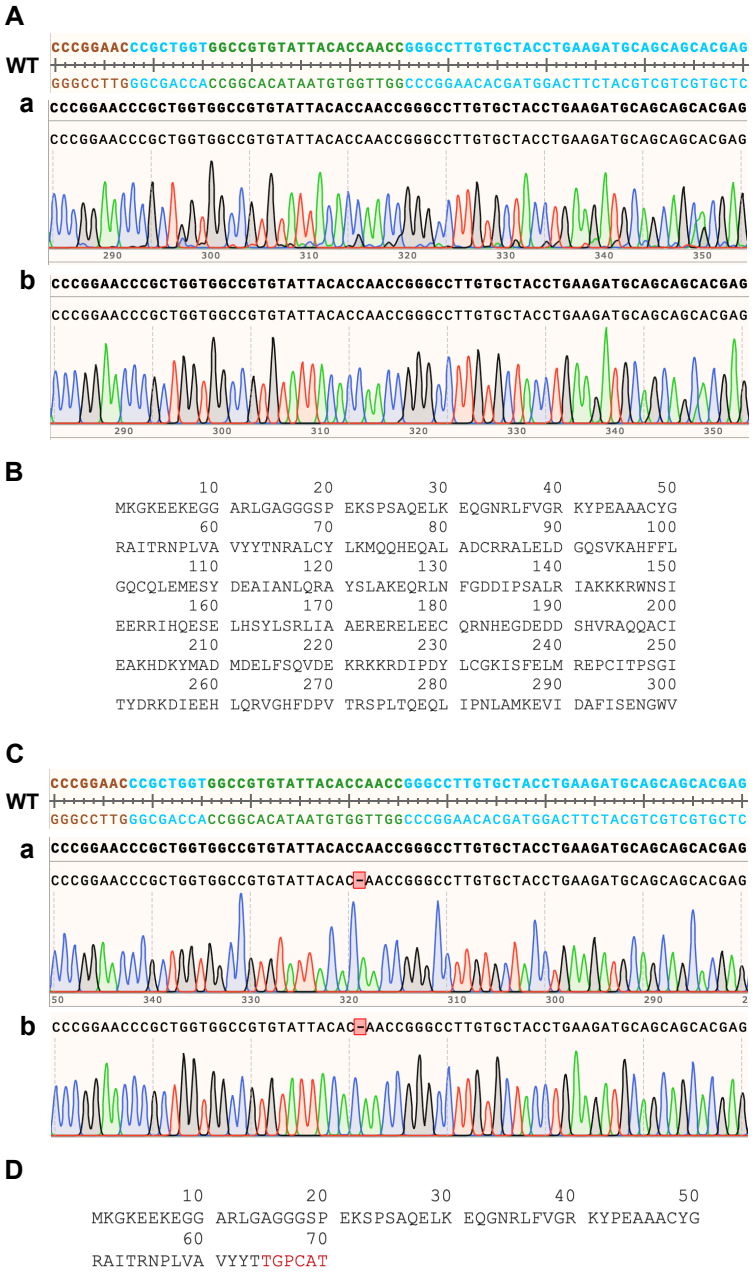


**Figure 3.7: CRISPR/Cas9-based editing of patient-derived iPSC**
Alignment of the sequences derived from the CRISPR clones with the human *STUB1* gene (**A & C**), and the predicted CHIP amino acid sequence (**B & D**). The *STUB1* exons (brown), coding regions (blue), forward and reverse primers (magenta) and gRNA (green) are indicated.
**A)** Sequencing of the PCR products derived from CHIP WT-expressing lines: the parental line (AST23) (**a**) and the C1 CRISPR clone (**b**).
**B)** Predicted CHIP protein sequence expressed from **A** is identical to WT CHIP.
**C)** Sequencing of plasmid DNA derived from the TOPO cloning using PCR product obtained from genomic DNA of the C6 CRISPR clone (**a**) is shown together with the sequencing of the PCR product (**b**)
**D)** Predicted CHIP protein sequence expressed from **C** has frameshift and nonsense mutations (p.N65TfsX7).

For the potential CHIP KO clone, C6, in addition to PCR product sequencing, PCR products were sub-cloned into the TOPO cloning vector and competent *E. coli* cells were transformed. The plasmid DNA from 25 *E. coli* colonies (from two independent experiments) was isolated and sequenced. All sequences from colonies harbouring an insert of the expected size and the PCR product were identical. CRISPR/Cas9 resulted in a single GC base pair deletion close to the PAM sequence, GGG (Figure 3.7C). This is predicted to cause a frameshift in the protein coding region, which eventually results in a premature stop codon (p.N65TfsX7). Therefore, the truncated mRNA is likely to be degraded by nonsense-mediated decay, yielding a homozygous CHIP KO line. Finally, sequencing identified D3 clone as a heterozygote for CHIP (data not shown).

## 3.2.2 Differentiation of CHIP KO iPSC into cortical neurons

Protocol development for efficient neural induction and cortical differentiation, and subsequent validation, was a significant part of my PhD. When successful, I was able to differentiate the parental line (AST) and CRISPR-edited clones (the CHIP-expressing control, C1, and the CHIP KO, C6) of the patient-derived iPSC into cortical neurons simultaneously and in three independent experiments (in two different laboratories).

The differentiation process is highly dynamic, passing through multiple gene expression and morphological changes – from a monolayer of cycling iPSCs to neural progenitors within rosettes, which then extend processes and generate functional, post-mitotic neurons. An overview of these changes is outlined in Figure S.1. Validation of the differentiation and assessment of cell identity was performed by qPCR and IF assays at multiple stages and by MS once mature (in Chapter 4: Effect of CHIP on the proteome).

### a. Neural induction

The neural induction protocol developed was based on the initial methodology proposed by Chambers *et al.*[113], as well as the optimisations conducted by Shi *et al.*[114,115] for efficient cortical differentiation. I optimised it further for our CHIP patient-

derived iPSC model. Development of an optimal neural induction protocol is critical, as it not only ensures efficient cortical induction and subsequent neuronal differentiation, but also promotes robust and reproducible differentiation[114].

Since both published protocols agreed that a high plating density is required (recommended 18,000 cells/cm$^2$ for plating[113] or enough to be confluent at day 1), I plated our iPSC lines at 80,000 cells/cm$^2$. In agreement with both protocols, cells were initially cultured with ROCK inhibitor Y-27632 to promote survival. In detail, after seeding and each passage, cells were treated with 10 μM Y27632 dichloride (1254, R and D, Tocris) for 48 or 24 hours, respectively.

In contrast to the original protocols, once iPSCs were seeded for differentiation they were maintain in differentiation media, rather than cultured in stem cell conditions until confluent (72h according to Chambers *et al.*[113] or when 95% confluent[115]). Additionally, while Shi *et al.* use CELLstart-coated plates for neural induction and later switch to Laminin-coated plates, I decided to use Laminin-111 (Biolamina) coated plates throughout the differentiation process. Laminin-111 brings together the favourable aspects of both matrices: promotes stem cell survival and proliferation and drives differentiation. Glass coverslips were pre-treated with poly-L-ornithine (P4957, Sigma).

The studies above mentioned[113–115] both suggest the use of 500 ng/ml Noggin (or 1 μm Dorsomorphin[114,115]), a BMP inhibitor, and 10μM SB431542, an inhibitor of Lefty/Activin/TGFβ pathways, for neural induction. However, they contrast in the temporal specificity of the treatments. Chambers *et al.*[113] removed SB431542 after 5 days of differentiation and used increasing amounts of N2 media (containing Noggin) until day 11[113], while Shi *et al.*[114,115] added both inhibitors during the first 8-11 days. Given the optimisation nature of the latter study, I developed a protocol that was primarily based on this. For 11 days, I treated iPSCs with 10 μM SB431542 (616461, Merck Chemicals, Calbiochem) and 100 nM LDN (130-103-925, Miltenyi Biotech) (a derivative of Drosomorphin that also inhibits BMP type I receptors, preventing activation of downstream SMADs).

These supplements were added to N2-containing differentiation media based on what Shi *et al.*[114] developed for optimal neural induction, neurogenesis and neuronal differentiation. This study used a 1:1 mixture of N2-containing media (DMEM/F12, 1x N2, 5 µg/ml Insulin, 1mM L-Glutamine, 100 µm non-essential amino acids, 100 µM 2-mercaptoethanol, 50 U/ml Penicillin and 50 mg/ml Streptomycin) and 1x B27-containing media (Neurobasal, B27 with retinoic acid, 200 mM Glutamine, 50 U/ml Penicillin and 50 mg/ml Streptomycin)[114,115]. I used the following media: DMEM/F12 (21331-020, Gibco):Neurobasal media (21103-049, Gibco) in 1:1 ratio, 0.5x B27 supplement with retinoic acid (50x, 17504044, Gibco), 0.5x N2 supplement (100x, 17502001, Gibco) and 2mM L-glutamine (200 mM, 25030-024, Gibco). From days 2-11, the media was changed daily and freshly supplemented with the SMAD inhibitors.

### b. Cortical neurogenesis

At day 11, I passaged neuroepithelial cells (that were a confluent monolayer at this point) to promote cortical neurogenesis and differentiation. According to Shi *et al.*[114], cells should be plated as clumps (300-500 cell aggregates), thus the group uses Dispase to dissociated cells. However, I decided to use Collagenase Type IV instead because the use of Dispase is associated with increased risk of degradation of the culture if residual Dispase persists, as it is not inhibited by the media. Cells were incubated with 250 U/ml Collagenase Type IV (17104019, Gibco) diluted in HBSS containing calcium and magnesium (14025, Gibco), for 30 min at 37ºC. They were triturated by pipetting several times (with 1 ml pipette tips) and then washed twice in wash media (1:1 DMEM/F12 and neurobasal media supplemented with 10 µM Y27632 dichloride) with centrifugation steps (3 min at 300 g) in between, to ensure removal of the enzyme. Cells were plated at a 1:1.5 and kept for 24 hours in differentiation media containing 10 µM SB431542, 100 nM LDN and 10 µM Y27632 dichloride. After this, the media was renewed daily or every 2 days. In line with Shi *et al.*[114], upon appearance of rosettes (that form around days 12-17) cultures were passaged as clumps. This was done at day 17, using Collagenase Type IV (instead of Dispase), and this time cells were plated at a 1:2 ratio and only Y27632 dichloride was added.

A final passage was suggested by Shi *et al.*[114], when neurons first begin to accumulate at the outside of rosettes, between days 25 and 30. At this stage the cells should be dissociated into single cells using Accutase and re-plated at 50,000 cells/cm$^2$. I used the same methodology at day 25 of differentiation and the plating density was dictated by the use of each culture: wells used for IF were plated at a low density, 35,000 cells/cm$^2$, and those for WB and MS analysis were plated at a higher density, 80,000 cells/cm$^2$. Incubation with Accutase (A6964, Sigma) was optimised to 10-15 min at 37ºC. To ensure single cells are obtained, after triturated several times in Accutase, cells were added to the wash buffer and filtered using a 40 μm cell strainer, prior to counting and plating. As previously, cells were cultured with 10 μM Y27632 dichloride for 24h after plating.

Cells were then fed routinely until mature. To promote neuronal survival, I supplemented the medium with 20 ng/ml BDNF (450-02-100, Peprotech) and 20 ng/ml GDNF (450-10-100, Peprotech) neurotrophic factors. These human recombinant proteins were reconstituted in 0.1% BSA (Bovine Albumin Fraction V, 7.5% solution, 15260037, Gibco) in PBS (D8537, Sigma). After a full media change (to remove the Y27632 dichloride at day 26), half of the media was exchanged twice a week until day 80, or otherwise stated, with fresh differentiation media containing BDNF and GDNF.

### c. Validation of cortical differentiation

As with cortical neurogenesis *in utero*, the differentiation process *in situ* can be monitored through markers arising with temporal specificity. A schematic of the differentiation and the different markers of cell types arising during the course of differentiation is shown in Figure 3.8.

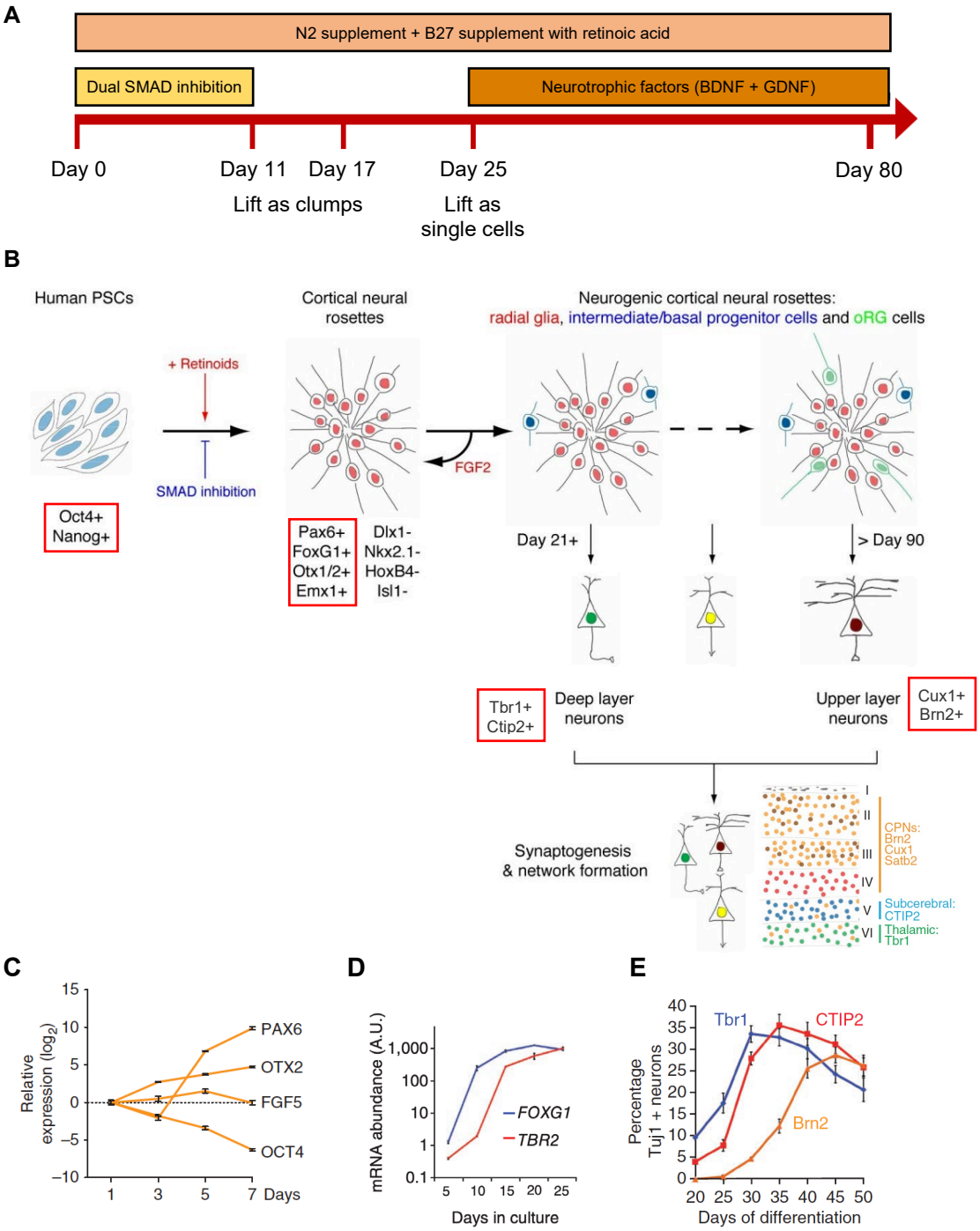


**Figure 3.8: Overview of the cortical differentiation**
**A)** Overview of methodology.
**B)** Schematic of the cortical differentiation from human pluripotent stem cells (PSCs). Different progenitor and neuronal markers arise throughout the differentiation. Cell identity was characterised using the markers outlined by the red boxes. Classes of cortical projection neurons (CPN: callosal projection neurons) in the layers of the adult cortex.
**C)** Quantitative RT-PCR for markers of pluripotency and neuronal lineage. Pax6 is a neuroectodermal marker, while Otx2 and FGF5 are epiblast markers and Oct4 is a stem cell marker.
**D)** Quantitative RT-PCR for the expression of cortical stem cell transcription factor *FOXG1* and the marker of secondary progenitor cells and newly-born neurons, *TBR2*.
**E)** Neurons (Tuj1$^{+}$) express TBR1, CTIP2 and Brn2 with temporal specificity.
(**B**: Adapted from Shi *et al.*[115]; **C**: Chambers *et al.*[113]; **D&E**: Shi *et al.*[115])

Quantitative RT-PCR was performed at day 0, 11, 25, 45 and 80, which are key time-points during the differentiation that reflect changes in cell identities. Figure 3.9 shows a decline in pluripotency and stem-renewal markers (*CDK6*, *NANOG* and *OCT4* genes) from day 0 to day 11. On the contrary, markers of the primary cortical stem and progenitor cells (including the *VIM, NES, OTX2, EMX1* and *PAX6* genes) increase from day 0 to 11 (Figure 3.10). The second differentiation experiment (referred to as "differentiation 2"), which is aimed for MS analysis, has a more promising profile at day 11. Markers of the secondary progenitors (the *FOXG1* and *TBR2* genes) increase at day 25 (Figure 3.11). However, the expression of *TBR2* was very low relative to *TBP*, making the levels detected not reliable. The transcription of the *TBR1* and *CTIP2* genes, markers of early-born, deep-layer neurons, was assessed at day 0, 25, 45 and 80 (Figure 3.12). Again, *TBR1* expression is low but showed a slight increase from day 0 to day 25. *CTIP2* expression, on the other hand, clearly peaks at day 45 across the time-point analysed. Next, the transcription profile of markers of late-born, upper-layer neurons (*CUX1* and *BRN2* genes) was analysed (Figure 3.13). Although *CUX1* expression seemed to be relatively unchanged between days 25 and 45 (but higher than the qRT-PCR results of undifferentiated cells), *BRN2* expression clearly peaks at day 25. Finally, *SNCA* shows a modest increasing trend throughout the course of differentiation, while *STUB1* expression seems to be unchanged (Figure 3.14).

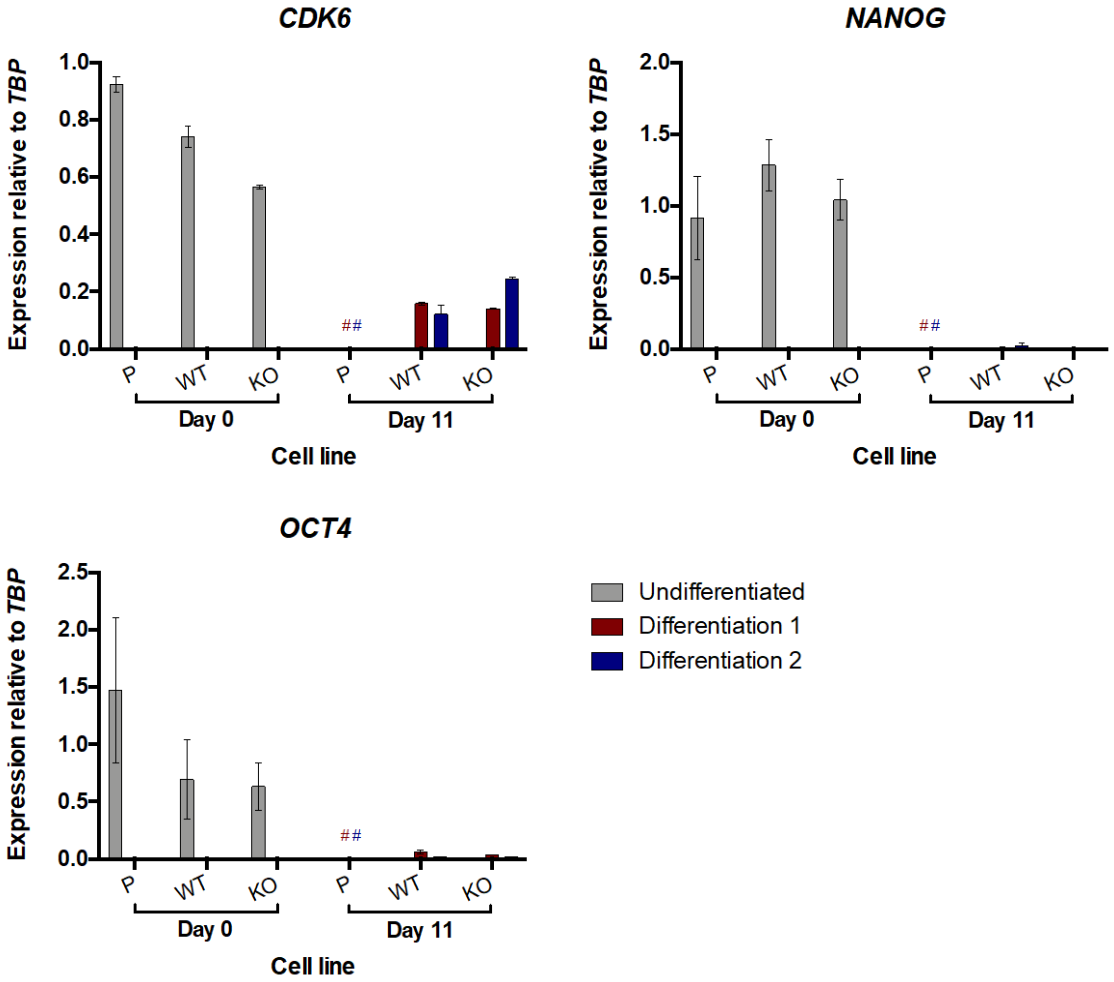


**Figure 3.9: Decline in pluripotency and stem-renewal markers upon neural induction**
RNA was extracted from neurons of the CHIP KO line (KO) and two CHIP-expressing lines (the parental line (P) and the CRISPR control (WT)) at the indicated days of differentiation and qRT-PCR was performed. The expression of *CDK6*, *NANOG* and *OCT4* was assessed. The latter two are strong markers of pluripotency and they are virtually unexpressed at day 11 of differentiation. *CDK6* is a cycling marker, which is expected to decrease but still be present in the cortical stem cells, as they proliferate to expand and generate progenitors. Results were normalised to TATA binding box protein (*TBP*) gene expression and bars represent averages. Two independent differentiation experiments were included in this assay. Error bars represent standard deviation of three technical replicates. The colour-coded hash (#) indicates that the particular cell line, at the specific time point and from a specific differentiation experiment was not assayed.

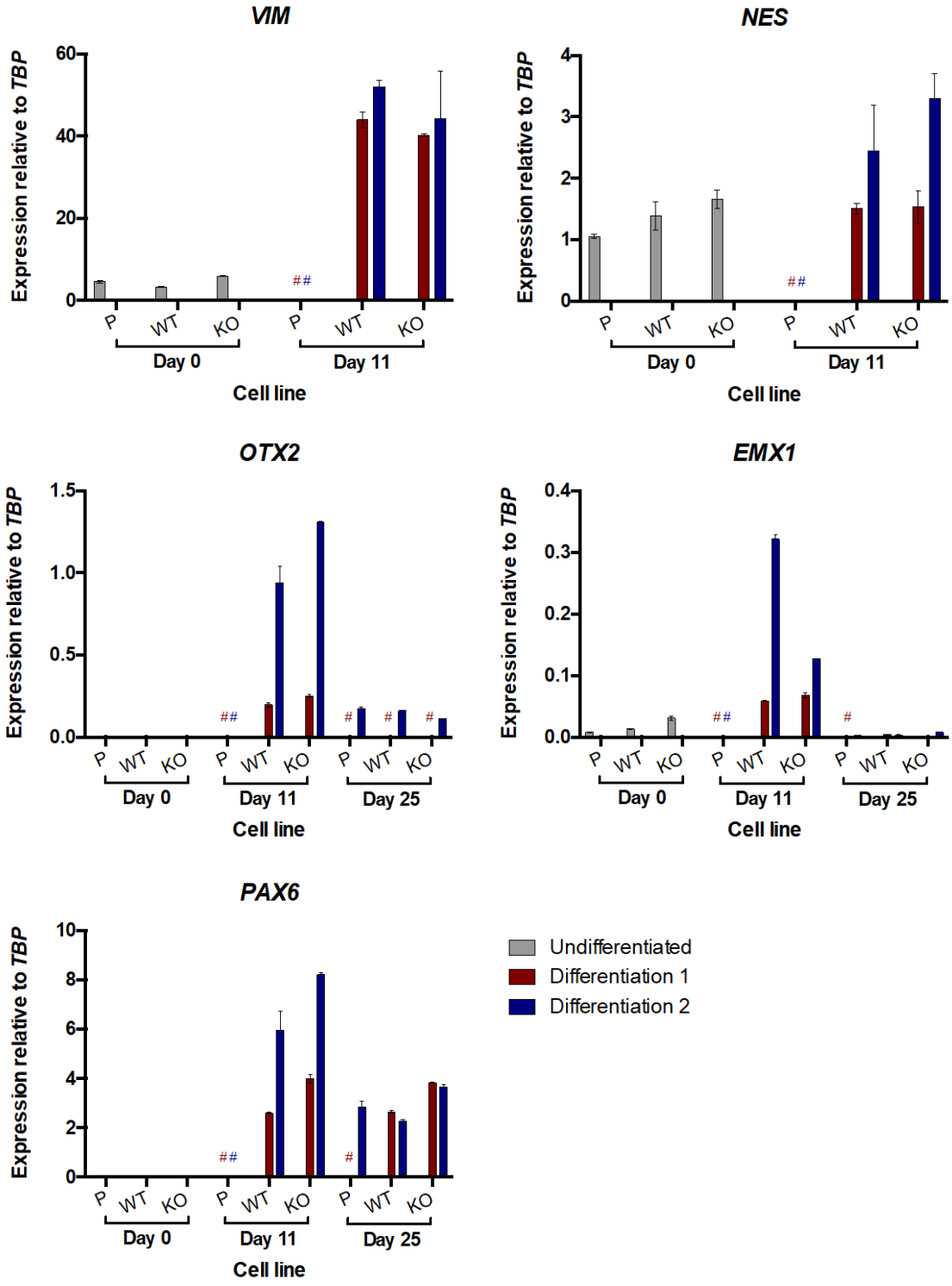


**Figure 3.10: Increase in markers of cortical stem and progenitor cells**
RNA was extracted from neurons of the CHIP KO line (KO) and two CHIP-expressing lines (the parental line (P) and the CRISPR control (WT)) at the indicated days of differentiation and qRT-PCR was performed. The expression of *VIM*, *NES*, *OTX2*, *EMX1* and, the commonly used marker of neuroectodermal differentiation, *PAX6* was assessed. Results were normalised to TATA binding box protein (*TBP*) gene expression and bars represent averages. Two independent differentiation experiments were included in this assay. Error bars represent standard deviation of three technical replicates. The colour-coded hash (#) indicates that the particular cell line, at the specific time point and from a specific differentiation experiment was not assayed.

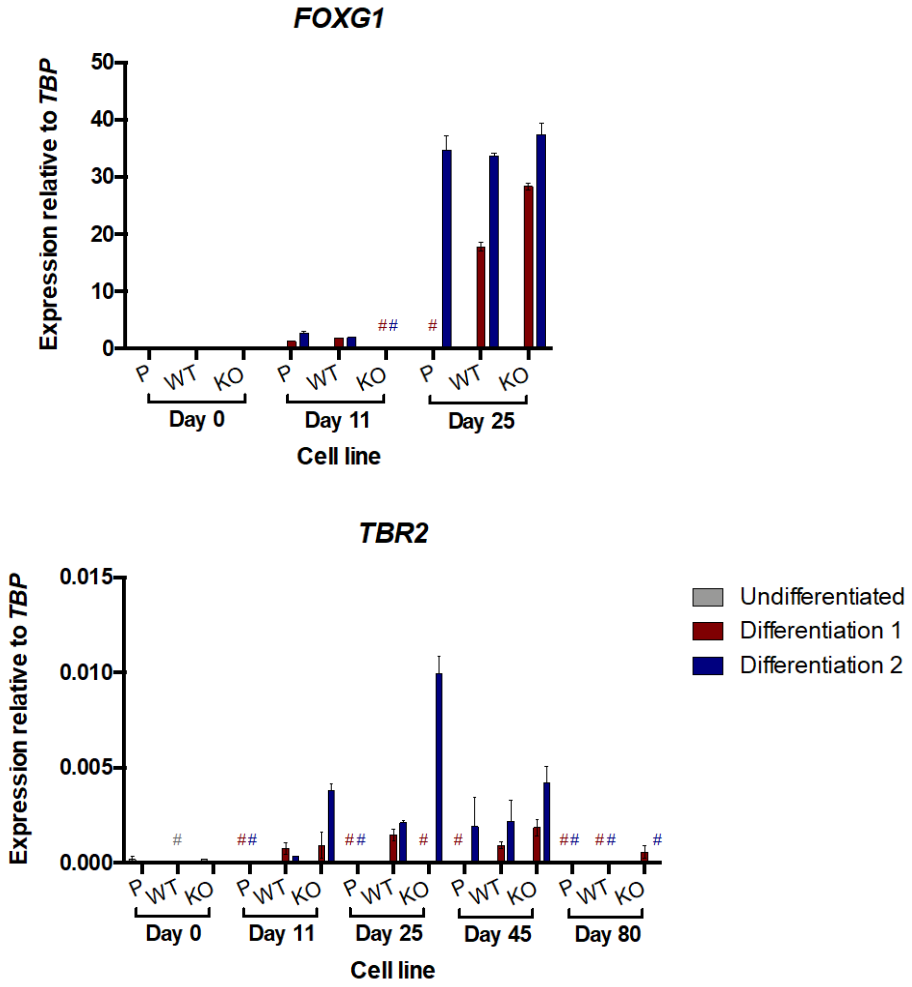


**Figure 3.11: Markers of secondary cortical progenitor and stem cells**
RNA was extracted from neurons of the CHIP KO line (KO) and two CHIP-expressing lines (the parental line (P) and the CRISPR control (WT)) at the indicated days of differentiation and qRT-PCR was performed. The expression of *FOXG1* and *TBR2* was assessed. The levels of the latter were very low. Results were normalised to TATA binding box protein (*TBP*) gene expression and bars represent averages. Two independent differentiation experiments were included in this assay. Error bars represent standard deviation of three technical replicates. The colour-coded hash (#) indicates that the particular cell line, at the specific time point and from a specific differentiation experiment was not assayed.

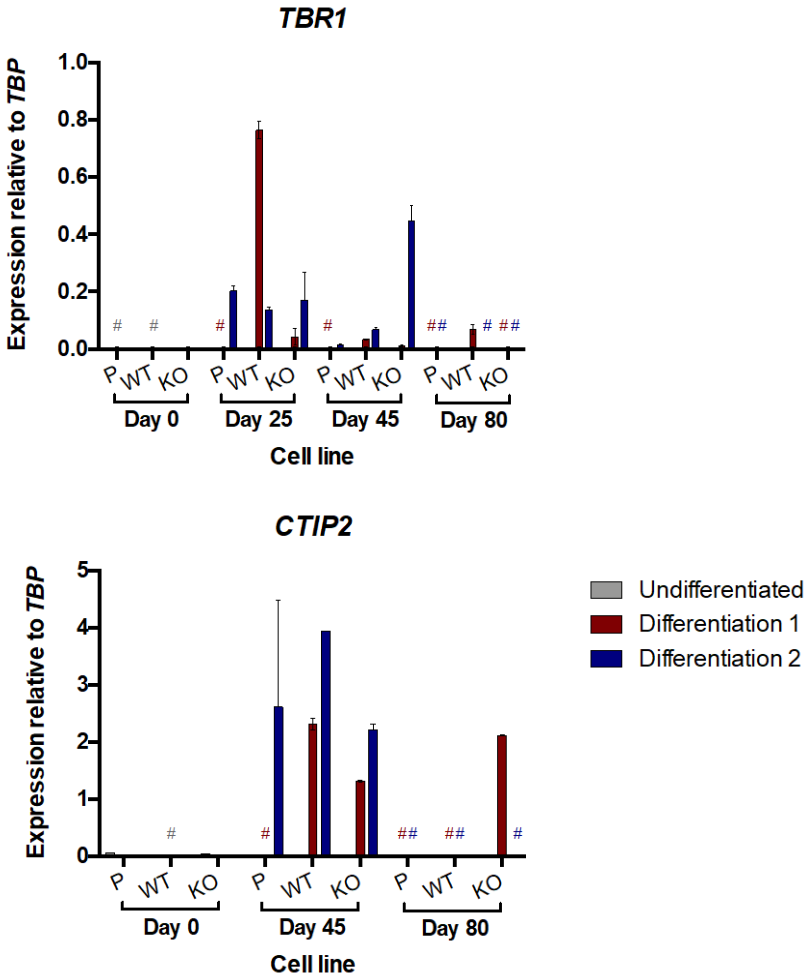


**Figure 3.12: Markers of early-born deep-layer neurons**
RNA was extracted from neurons of the CHIP KO line (KO) and two CHIP-expressing lines (the parental line (P) and the CRISPR control (WT)) at the indicated days of differentiation and qRT-PCR was performed. The expression of *TBR1* and *CTIP2* was assessed. These are markers of early-born and deep-layer neurons. Both markers increased with neural induction and cortical differentiation. Results were normalised to TATA binding box protein (*TBP*) gene expression and bars represent averages. Two independent differentiation experiments were included in this assay. Error bars represent standard deviation of three technical replicates. The colour-coded hash (#) indicates that the particular cell line, at the specific time point and from a specific differentiation experiment was not assayed.

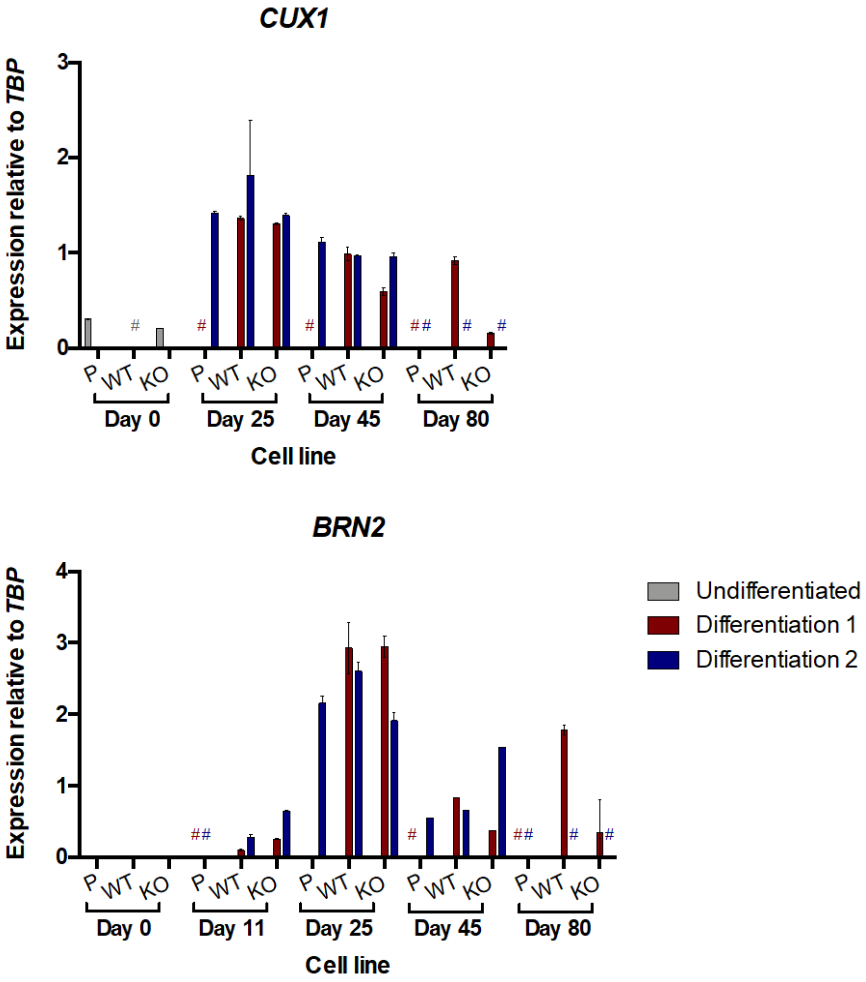


**Figure 3.13: Markers of late-born upper-layer neurons**
RNA was extracted from neurons of the CHIP KO line (KO) and two CHIP-expressing lines (the parental line (P) and the CRISPR control (WT)) at the indicated days of differentiation and qRT-PCR was performed. The expression of *CUX1* and *BRN2* was assessed. These are commonly used markers of upper-layer neurons. The expression of both *BRN2* and, to a lesser extent, *CUX1* peaked at day 25, but had a sustained expression later in the course of differentiation, compared to the lack of expression in undifferentiated cells. Results were normalised to TATA binding box protein (*TBP*) gene expression and bars represent averages. Two independent differentiation experiments were included in this assay. Error bars represent standard deviation of three technical replicates. The colour-coded hash (#) indicates that the particular cell line, at the specific time point and from a specific differentiation experiment was not assayed.

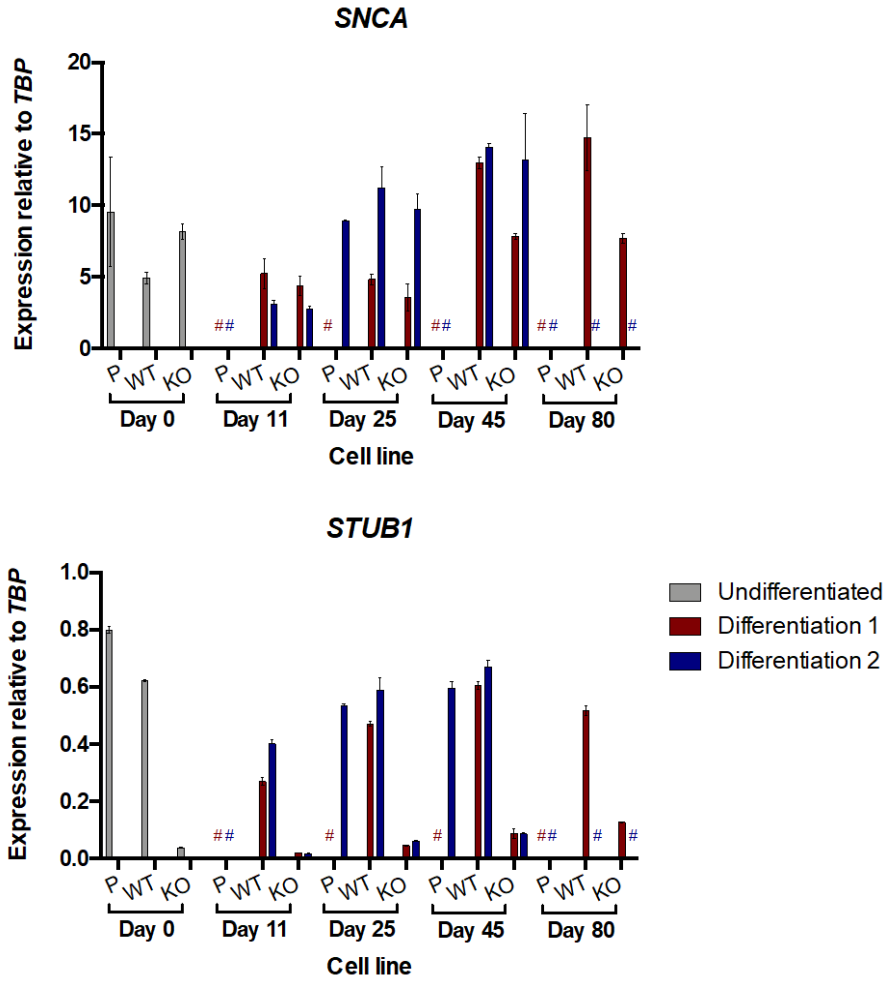


**Figure 3.14: Expression of *SNCA* and *STUB1***
RNA was extracted from neurons of the CHIP KO line (KO) and two CHIP-expressing lines (the parental line (P) and the CRISPR control (WT)) at the indicated days of differentiation and qRT-PCR was performed. The expression of *SNCA* and *STUB1* was assessed. The results were normalised to TATA binding box protein (*TBP*) gene expression and bars represent averages. Two independent differentiation experiments were included in this assay. Error bars represent standard deviation of three technical replicates. The colour-coded hash (#) indicates that the particular cell line, at the specific time point and from a specific differentiation experiment was not assayed.

As described in the literature[113–115], formation of a homogenous neuroepithelial monolayer of Pax6$^+$ progenitor stem is critical for successful differentiation. At day 11, Pax6 expression was widespread and strong across cell lines and rosette structures begin to emerge (Figure 3.15). Although some β(III)-tubulin expression is observed, the structures are still small and do not show the characteristic branching of neuronal processes. However, by day 25 long and interconnecting processes are visible and the majority of cells retain Pax6 expression (Figure 3.16). Additionally, some TBR1

staining was detected in both $Pax6^+$ and $Pax6^-$ cells. In attempt to characterise neuronal identity, markers of deep-layer neurons (CTIP2 and TBR1) were analysed at a protein level at day 50 (Figure 3.17). At this timepoint Shi *et al*.[115] describe around 25% and 20% CTIP2 and TBR1-expressing neurons, respectively. Our cultures exceed these numbers both as single- and co-expressing markers. Furthermore, no significant difference was observed between CHIP KO and WT neurons. By day 80, when neurons are considered mature and harvested for proteomic analyses, these deep-layer neurons are still present (Figure 3.18), along with Cux1-expressing upper-layer neurons (Figure 3.19). In these mature neurons, $\alpha$-Syn is expressed across nuclei, cell bodies and processes, correlating well with the $\beta$(III)-tubulin staining.

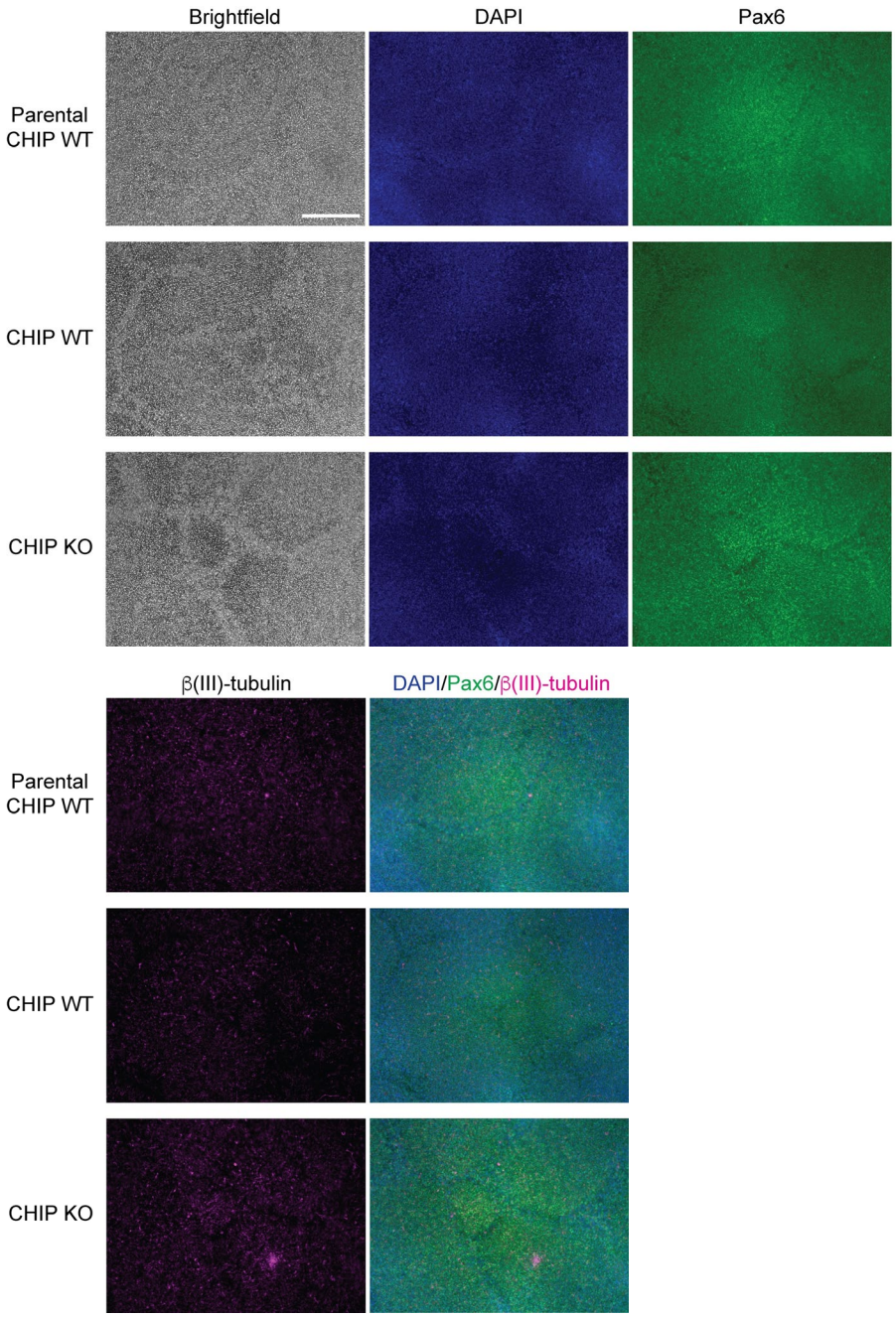


**Figure 3.15: Neural induction**
Neurons of the CHIP KO line and two WT CHIP-expressing neurons (the parental line and the CRISPR control) were fixed with 4% PFA at day 11 of differentiation. IF was performed using anti-Pax6 mAb (IgG1; 1:40), anti-β(III)-tubulin mAb (IgG2a; 1:1000) and DAPI. Phase contrast and fluorescent images were taken. Pax6 is an early ectodermal marker and β(III)-tubulin is a neuron-specific marker. These samples alabre from the second differentiation experiment. Scale bar, 200 μm.

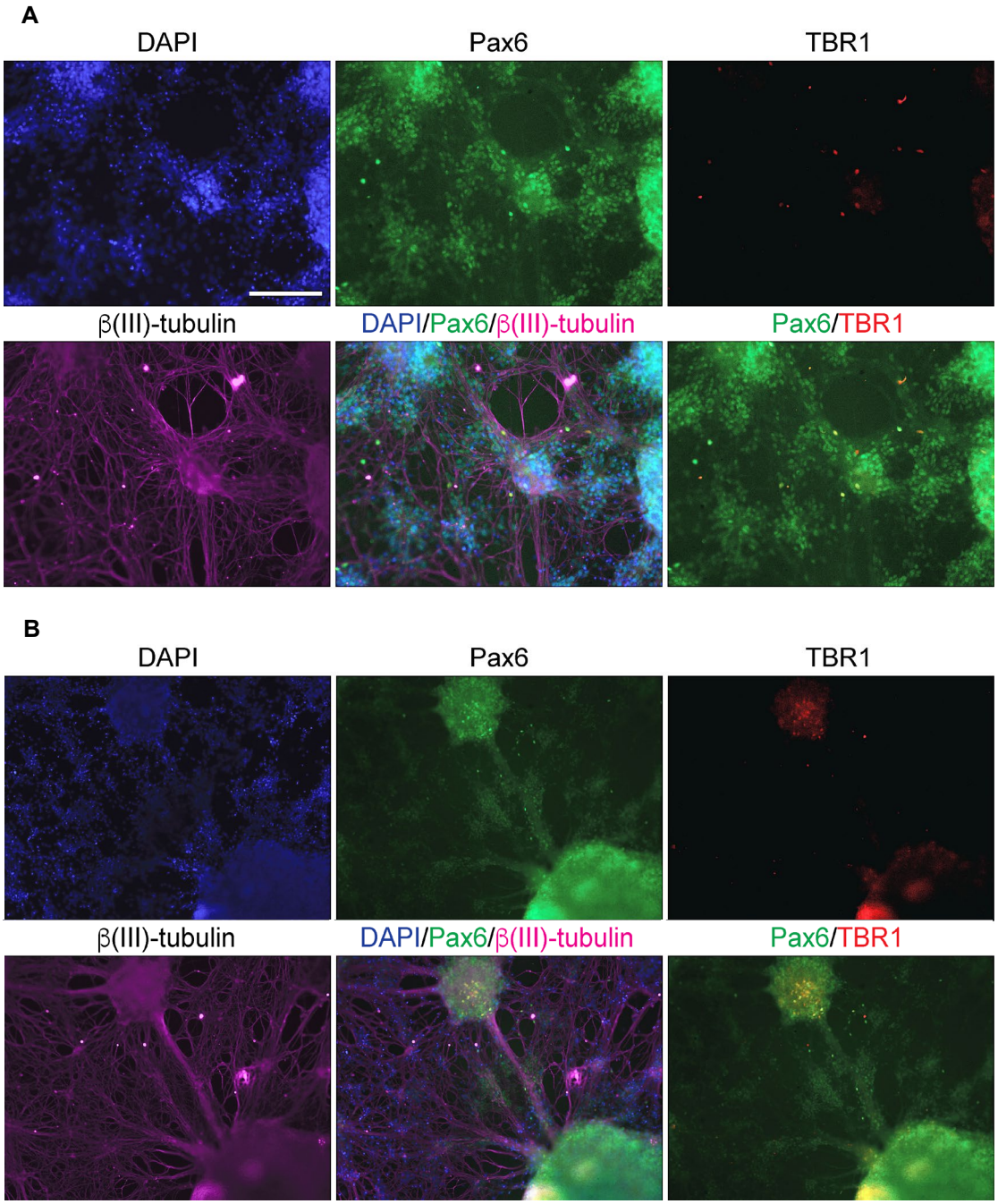


**Figure 3.16: Cortical neurogenesis and differentiation in CHIP WT and KO neuronal cultures**

CHIP WT (**A**) and KO (**B**) neurons were fixed with 4% PFA at day 25 of differentiation. IF was performed using anti-Pax6 mAb (IgG1; 1:40), anti-Tbr1 pAb (1:200) anti-β(III)-tubulin mAb (IgG2a; 1:1000) and DAPI. Phase contrast and fluorescent images were taken. The former two markers are expressed by cortical progenitor and stem cells and β(III)-tubulin is neuron-specific. Pax6 staining is heterogenous, with some cells have strong expression, while have weaker expression. Tbr1 expression is less prominent, with a minority of the cells being $Tbr1^{+}$. The projection of processes and the three-dimensional architecture acquired by neurons at this stage is evident. Moreover, cells are seen both in clumps and more diffuse. These samples are from the first differentiation experiment. Scale bar, 100 μm

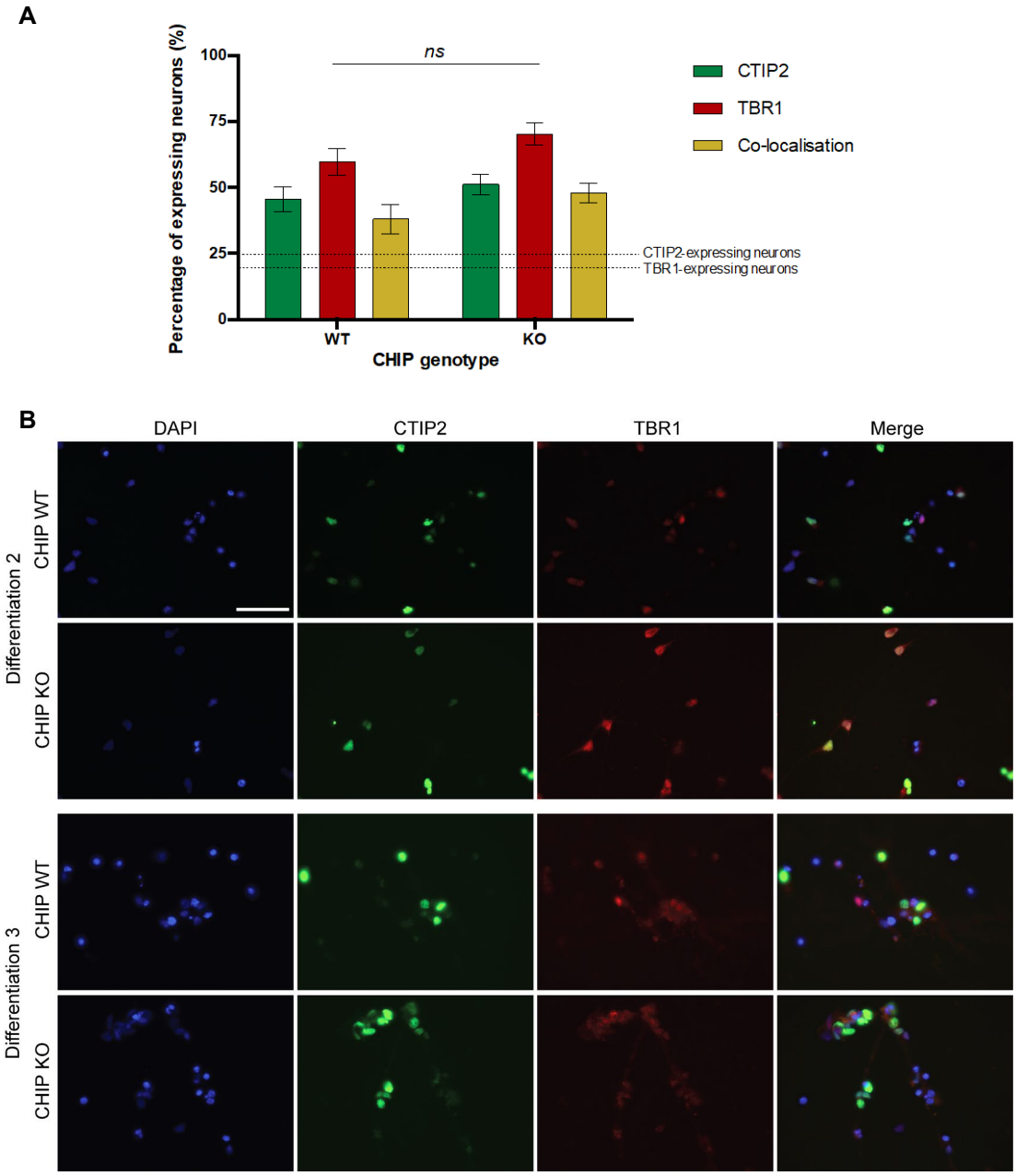


**Figure 3.17: Quantification of early-born deep-layer neurons at day 50**
CHIP WT and KO neurons were fixed with 4% PFA at day 50 of differentiation. Corticothalamic projection neurons of layer 6 express both TBR1 and CTIP2, while corticospinal motorneurons of layer 5 only express CTIP2. Expression of these markers was analysed by IF and, for the second differentiation experiment ("Differentiation 2") quantified (**A**). Cells were incubated with anti-CTIP2 mAb (1:500), anti-TBR1 pAb (1:400) and DAPI.
**A)** Dashed lines represent the percentage of TBR1 and/or CTIP2 expressing cortical neurons that Shi *et al.*[115] reported in their cultures at this timepoint. The percentage of neurons expressing TBR1 and/or CTIP2 was compared across CHIP genotypes using a paired *t*-test. Differences were not significant (*ns*).
**B)** The TBR1 and CTIP2 expression was similar across differentiation experiments and cell lines. Scale bar, 100 μm.

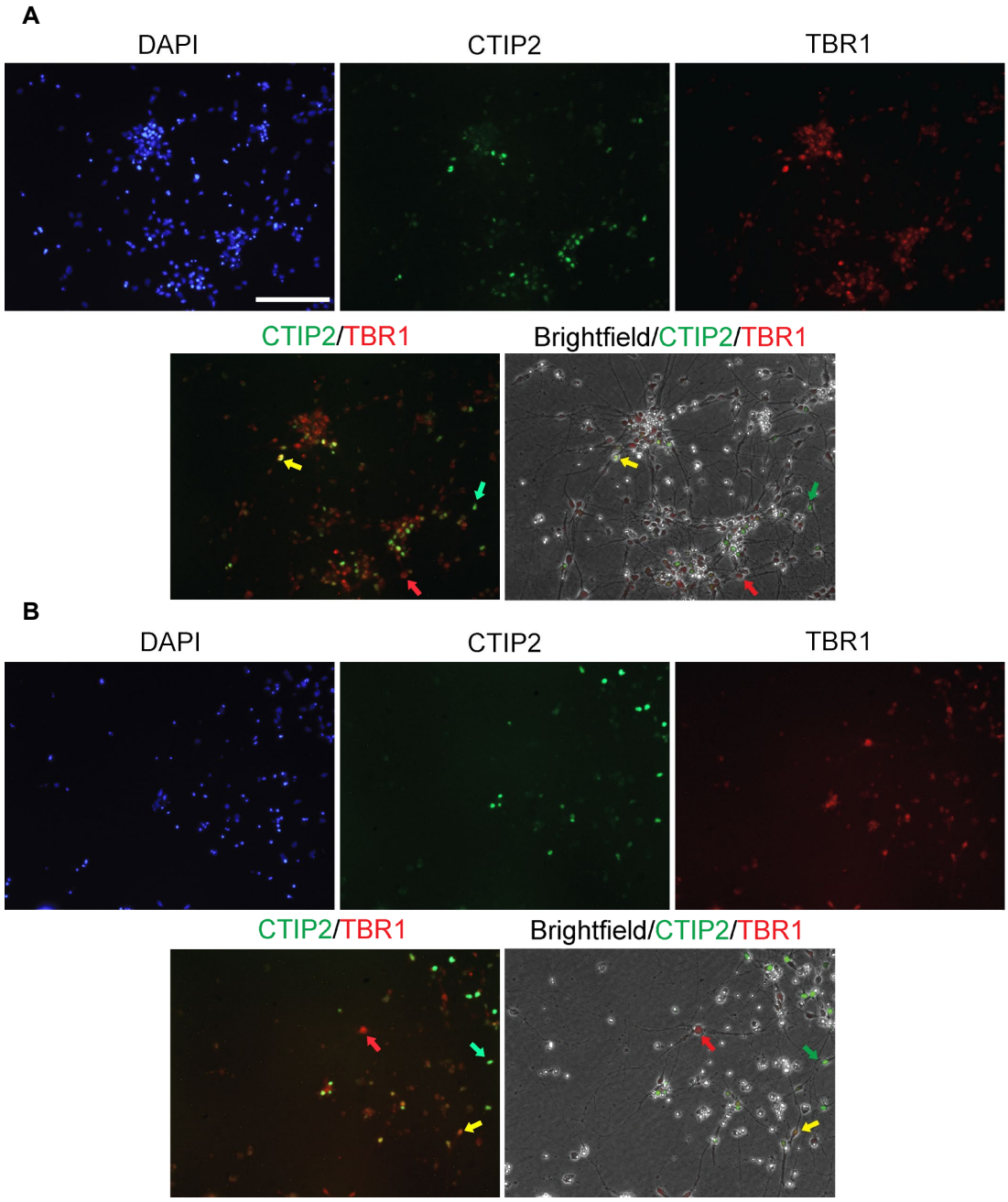


**Figure 3.18: Early-born deep-layer neurons at day 80**
CHIP WT (**A**) and KO (**B**) neurons were fixed with 4% PFA at day 80 of differentiation. IF was performed by incubating neurons with anti-Ctip2 mAb (1:500), anti-Tbr1 pAb (1:400) and DAPI. Phase contrast and fluorescent images were taken. Across cultures, neurons expressing Tbr1 only (red arrows), Ctip2 only (green arrows), or both (yellow arrows) were present. These samples are second differentiation experiment ("Differentiation 2"). Scale bar, 100 μm.

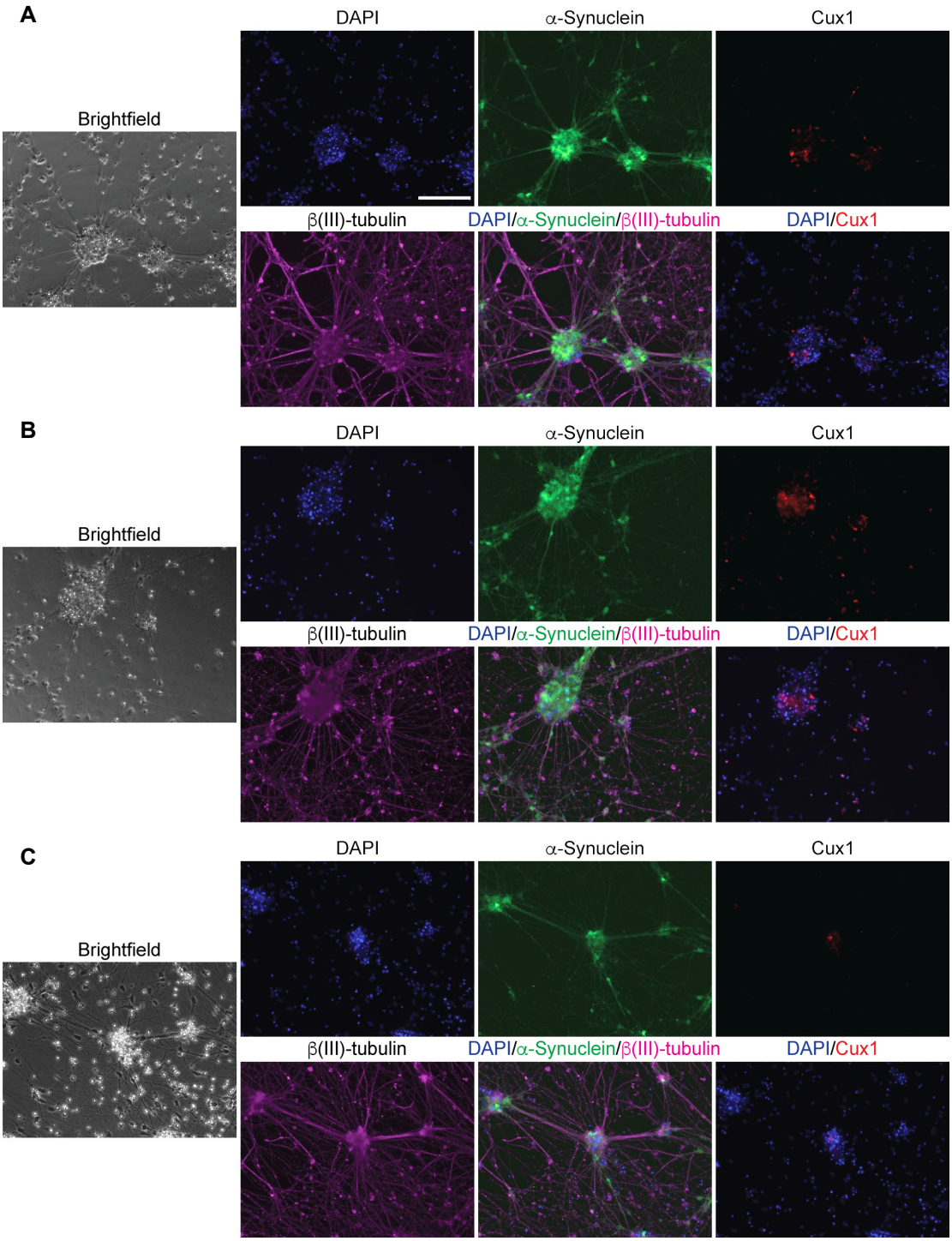


**Figure 3.19: Late-born upper-layer neurons at day 80**
Neurons derived from two CHIP-expressing iPSC lines (the parental line (**A**) and the CRISPR control (**B**)) and a CHIP KO iPSC line (**C**) were fixed with 4% PFA at day 80 of differentiation. IF was performed by incubating neurons with anti-α-Syn mAb (IgG1, 1:500), anti-β(III)-tubulin mAb (IgG2a; 1:1000) anti-Cux1 pAb (1:200) and DAPI. Phase contrast and fluorescent images were taken. Low Cux1 expression, a marker of late-born, upper-layer neurons, is observed. In contrast, α-Syn and β(III)-tubulin staining is widespread and shows the interconnecting network between neurons. Scale bar, 100 μm.

Finally, although the majority of the cells differentiate from the neuroepithelium monolayer into more structured neural rosettes and neural networks, a journey that gains three-dimensional structure and complexity, some cells fail to differentiate properly. These can be detected within cultures by the distinctive flat morphology (Figure 3.20). Furthermore, they are slowly proliferating, thus competing in space with the post-mitotic neurons. “Flat cells” were observed in about 11% of the differentiating cultures and they tend to emerge late in the differentiation process (being observed around day 45). Possibly due to clonal variation or other reasons, the CHIP KO line seemed to have a higher propensity for having some “flat cells” within cultures. These were either discarded or used for assays, such as immunofluorescence, where “flat cells” can be isolated from the neurons and excluded from findings.

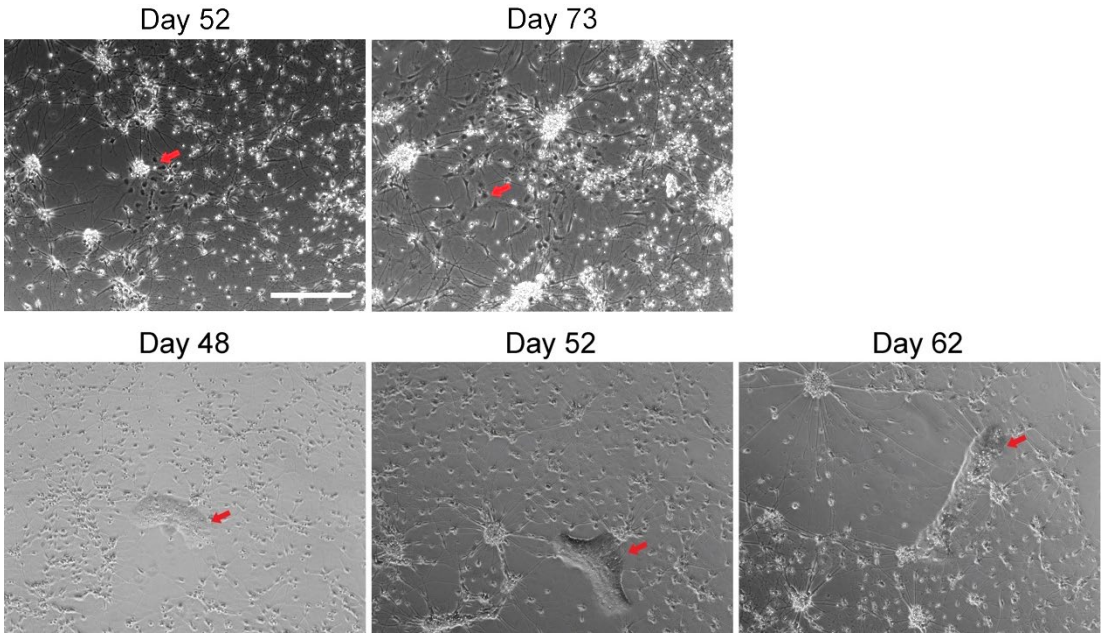


**Figure 3.20: “Flat cells” in neuronal cultures**
A minority of the cells in our neuronal cultures are cycling and have a characteristic “flat” morphology. Two areas (*top and bottom row*) with “flat cell” populations (bearing different morphologies) were observed over time. “Flat cells” (*red arrows*) grow over time. These phase contrast images were obtained from cultures of the CHIP KO line. Scale bar, 200 μm.

## 3.3 Discussion

### 3.3.1 Engineering patient-derived iPSC

#### a. Advantages, limitations and use of iPSC technology

Prior to iPSC technology, the field of neurodegeneration relied on transgenic models of synucleinopathy that do not fully replicate the phenotype of human disease. Primary neuronal cultures from rodent models were also popular, although these are difficult to maintain *in vitro* and do not self-renew. Also, rodent α-Syn has an amino acid change at position 53 that is pathogenic in humans. Different cell lines were also transformed to engineer models of synucleinopathy, but these are limited by their genetic background and manipulations can disrupt cell signalling pathways[97]. Also, overexpression of poorly controlled transgenes, such as *SNCA*, has its own problems, especially in the context of synucleinopathies, which are dose-dependent[111].

Undoubtedly, iPSC technology made the generation of patient-specific stem cells feasible and readily accessible[117]. The potential uses of iPSC are extensive. These cells can be used as a platform for drug screening and for cell-replacement therapies. Of particular interest, iPSC can be used to probe disease mechanisms[97,117] and study early disease-promoting events in a mechanistic manner. These are likely to be pathogenic, rather than the changes that occur at later stages of the disease, which may be protective[97]. Furthermore, they are likely to have increased therapeutic potential. Although the use of iPSC may be limited when modelling diseases that arise from complex interplays between environment and multiple genes[116], this is not the case for the *SNCA* triplication is monogenic and fully penetrate.

Despite the compelling advantages of the use of iPSC models, its limitations should also be considered. The major drawback of the use of iPSC is clonal variability[97,116,117]. It can confound our ability to distinguish disease-associated features, limiting the use of iPSC for disease modelling[116]. During the production, selection and culturing of iPSC, variability can arise from three levels:

1. The inconsistency in criteria that define iPSC lines as pluripotent;
2. The inherent variability between the cell lines derived from different donors (inter-individual variability), i.e. due to different genetic backgrounds;

3. The variability in the cell lines derived from the same donor (inter-clonal variability), i.e. due to the stochastic nature of the reprogramming method[116,117].

Additionally, clonal variability in our CHIP iPSC can arise from the genetic engineering using CRISPR/Cas9. The inherent mutational nature of the system can result in off-targets[105,109], which could drive variability between sets of isogenic CHIP models that would otherwise be regarded as identical (except the *STUB1* genotype). Such inter-clonal variability can affect the self-renewal and differentiation capacity of edited clones, if off-targets occur at critical genes. In fact, while maintaining edited clones, some lost their pluripotency and self-renewal abilities, while others were highly unstable and differentiated spontaneously into unknown lineages.

Therefore, following CRISPR/Cas9, cell lines may no longer fulfil all pluripotency criteria, introducing another level of variability[116,117]. However, both the parental line before CRISPR/Cas9 and the clones derived had the expected morphology of iPSC, self-renewal ability resembling embryonic stem cells, expressed pluripotency genes (including Oct4 and Nanog) and were able to differentiate – meeting the criteria that define iPSC[116]. It has been proposed that when iPSC lines fulfil stringent pluripotency criteria, their clonal variability is low[116]. This supports the use of iPSC technology for investigating subtle-disease associated changes[116].

### b. CHIP KO patient-derived iPSC

Patient-derived iPSC were subjected to a CRISPR/Cas9 system aimed at introducing indels in the coding region of *STUB1* to abolish CHIP expression in a homozygous manner. As seen from the WB (Figure 3.6), clone C6 does not expressed CHIP, and sequencing confirmed the presence of identical biallelic genetic mutations (Figure 3.7). Interestingly, the T7 endonuclease I assay was negative for the C6 clone, supporting that its DNA is perfectly match at the amplified *STUB1* locus (targeted by the CRISPR/Cas9 system).

Theoretically, the DNA strand that is complementary to the target-binding sequence in the crRNA/gRNA (spanning 20 bp) is cleaved 3 bp upstream of the PAM[105,108].

Although such editing signature was observed in the CHIP KO SH-SY5Y clone, having a single base-pair deletion at this position (work performed in collaboration with Erisa Nita), this indel occurred at 5 bp upstream of the PAM in our CHIP KO iPSC clone. The non-complementary strand, on the other hand, is reported to be commonly cleaved at one or more sites within 3-8 bp upstream of the PAM[108]. Indeed, multiple indels were observed in the non-complementary strand in CHIP KO SH-SY5Y cells, but not in the CHIP KO iPSC line. It is important to stress that both SH-SY5Y and iPSC cell lines were edited using the same CRISPR/Cas9 system (including the same gRNA).

Differences in gene-editing signature could be due to differential properties between the cell lines or differences in cell cycle status. When compared to cancer cell lines, iPSC are notoriously more challenging to edit. This is mainly due to their lower DNA repair efficiency (0.1-1% HR efficiency) after Cas9-induced double strand breaks compared to cancer lines, which have abnormally high rates (5- to 20-fold higher)[119–121]. Also, differences in chromatin structure due to intrinsic differences in cell cycle could also affect the activity of the Cas9[121,122] and DNA repair mechanism employed[123].

Interestingly, in our CHIP KO iPSCs, the non-complementary strand was identical to the complementary strand, thus occurring within the 3-8 bp range. Recent studies have argued that CRISPR/Cas9-based gene-editing has highly-preferred indels and is not random. Recently, Chakrabarti and colleagues[122] found that CRISPR/Cas9 technology can achieve high precision in DNA editing, driven by intrinsic preference for specific indels at target sites. The class (insertion or deletion) and size of the indel can be predicted by the target site. Nucleotides at positions 4 and 5 before the PAM sequence are particularly influential in the editing signature. When position -4 is an adenine, which is the case of our gRNA, this correlated with a precision indel frequency of 0.42 and 77% likelihood of repair mediated by insertions versus deletions. Such precision index was increased to 0.53 when the nucleotide at position -5 was a cytosine, as found in our gRNA. Therefore, the design of our CRISPR/Cas9 system would statically favour precise genome editing and such was observed. Furthermore, the group also found that precise targets displayed a strong bias towards single-nucleotide indels, which was seen in both alleles of the iPSC CHIP KO line and one allele of the SH-SY5Y. Nevertheless, although repair occurred in a

precise manner, it created deletions rather than insertions, which were reported to be less probable. Importantly, this contradicts the assumption that, based on the stochastic nature of NHEJ, CRISPR/Cas9-based gene editing is random. The indels detected in our CHIP KO iPSC argue for canonical NHEJ repair pathway, rather than microhomology-mediated end joining (MMEJ), seeing that small indels rather than larger deletions were observed[122].

The identical bilallelic single base-pair deletion is predicted to cause a frameshift mutation, eventually causing a premature stop codon. Ultimately these mutations result in nonsense-mediated decay, abolishing CHIP expression. Interestingly, the pattern of indels yielded by this CRISPR/Cas9 system was similar to one allele of the SH-SY5Y CHIP KO cell line (having a single nucleotide deletion as well) (refer to Figure 3.4C).

### 3.3.2 Differentiation potential

During cortical differentiation cells are subjected to multiple morphogenic factors and undergo substantial changes in their proteome and cell identity. It is not surprising that differentiation is associated with some degree of variability, as cell-intrinsic differences influence their response to the factors, in addition to the inherent variability associated with long culturing of cells. However, similarities in cell morphology and expression profile were observed across iPSC lines of different CHIP genotypes throughout the course of differentiation. This suggests that these iPSC lines have similar differentiation potentials and dynamics – key criteria to allow adequate comparative proteomics.

The three iPSC lines (P, WT and KO) have similar stem cell signatures (including *NANOG* and *OCT4* gene expression), thus deletion of CHIP expression does not affect pluripotent properties. These markers are rapidly lost by day 11, in parallel to a decrease in proliferating rate (evident from the decrease in *CDK6* expression) (Figure 3.9). Importantly, at day 11, the monolayer of neuroepithelial cells undergoing rosette formation express Pax6 and OTX2 proteins, as detected by IF (Figure 3.15) and/or qPCR (Figure 3.10). These cells are the primary cortical progenitor cells and become the main population of rosettes (Figure 3.8C)[113–115]. The secondary progenitor cells

are mainly characterised by TBR2[114,115]. However, despite observing an increase from day 0, the relative gene expression of *TBR2* was low (Figure 3.11). Arguing in favour of the success of the differentiation is the high expression levels of FOXG1 mRNA of neural stem cell cultures (Figure 3.11), which has been described to precede *TBR2* expression (Figure 3.8D)[115]. Therefore, in agreement with previously characterised markers of cortical stem and progenitor cells[115], our cultures expression key transcription factors of neural induction: FOXG1, Pax6, Vimentin, OTX1/2 and TBR2.

At day 25, the expression of Pax6 has decreased when compared to day 11 (indicated by both qPCR and IF) but remains strong (Figure 3.10). This was expected since the subpopulation of secondary progenitor cells that are $Pax6^-$ (the basal/intermediate progenitor cells) only make up around 10-15% of the cells within each rosette[114,115]. These Pax6-expressing cells are likely to be radial glial cells (characterised by $Pax6^+/TBR2^-$ expression and long processes[115]). It was reported that from around day 35, early-born deep-layer neurons ($TBR1^+$ and/or $CTIP2^+$) are the main population of cells (Figure 3.8E)[114]. This was consistent with our observation at days 45-50 (Figure 3.12 & Figure 3.18). Moreover, late-born upper-layer neurons would be expected by day 70[114] and indeed were observed at day 80 ($Cux1^+/Brn2^+$) (Figure 3.13 & Figure 3.19). The mRNA expression profile of Brn2 over time, however, was not expected, having a peak at day 25. Although the cortical differentiation protocols[114,115] have not included the Brn2 transcription profile over the course of differentiation, the percentage of $Brn2^+$ neurons increases from day 25 to 50 (Figure 3.8E) and is maintained at day 70 (analysed by IF). Therefore, the increase in Brn2 mRNA expression at day 25 may promote its protein expression from this timepoint onwards.

The identity of different types of cortical projection neurons was defined by their combinatorial expression a core set of transcription factors: TBR1, CTIP2, Cux1 and Brn2[114]. At the end of the course of differentiation (day 80), co-cultures of mature deep-layer (Figure 3.18) and upper-layer neurons (Figure 3.19) were achieved. Since the majority of the changes observed were consistent with those reported by Shi *et al.*[114,115] and Chambers *et al.*[113], including in its temporal specificity, we are confident that our iPSC-derived neurons adequately model cerebral cortex neurons. By day 80, mature neurons are likely to function in cortical neural networks[115]. The increase in the synaptic protein $\alpha$-Syn at the later stages of differentiation (Figure 3.14 & Figure 3.19) may reflect this. Importantly the expression of *STUB1* remained largely

unchanged throughout differentiation (Figure 3.14). Therefore, subsequent proteomic differences identified between CHIP genotypes at different differentiation states are not likely to be due to a change in CHIP expression. Furthermore, we can conclude that CHIP does not affect the differentiation potential of the iPSC lines.

Although CHIP KO and WT patient-derived iPSC were able to differentiate with similar kinetics and yield comparable neuronal co-cultures, the CHIP KO line was more variable, have an increased propensity to form “flat cells” (Figure 3.20). These have been described as fibroblast-like cells – a mitotic cell population, with a characteristic wide-spread cytoplasm and flat morphology[124]. They express Nestin, collagens, collagen fibre crosslinking proteins and synthesizing enzyme, the extracellular matrix protein fibronectin and platelet-derived growth factor receptors[124,125]. Although fibroblast-like cells are phenotypically similar to neural progenitor cells, these are distinct populations. “Flat cells” tend to emerge late in adult neural progenitor cells culture and, despite their high degree of plasticity and tendency towards a neuroectodermal lineage, are incapable to give rise to neurons or astrocytes. They do not express markers of the neuronal lineage (β(III)-tubulin and GFAP)[124]. Therefore, the occurrence of fibroblast-like cells within neuronal cultures suggests heterogeneity and diminished differentiation efficiency, as these cells have a greater proliferative capacity and can dominate long-term cultures[124]. Although it is unclear what drives the appearance of these cells, the increased propensity of the CHIP KO line to have “flat cells” would argue for a restricted differentiation potential compared to the other iPSC lines. However, given the detection of fibroblast-like cells across all iPSC-derived cultures and the low frequency of these cells (in <11% of CHIP KO differentiation cultures), this does not limit the potential use of this CHIP KO iPSC line.

### 3.3.3 Neuronal CHIP models

Given the variability between iPSC clones, the variable responses to the neural differentiation protocol, and the heterogeneity of neural differentiation[97], it is challenging to obtain a set of cell lines (WT and KO) that are similar in cellular state for comparative proteomics. As these patient-derived iPSC lines display similar pluripotent and self-renewal capacities and comparable differentiation potentials, we

have engineered a cell model that is valid and robust for investigating the protein targets of CHIP in a disease-relevant background and cell-type.

However, the cumulative potential variability from both the generation of iPSC and differentiation into neurons emphasizes the need to generate multiple iPSC lines and neuronal cultures[97]. This increases the likelihood of achieving iPSC lines of identical states, capable of complete differentiation and able to form matching isogenic sets with equivalent differentiation efficiency[97,116]. This is particularly applicable to the field of age-related diseases, as using older tissues for iPSC generation is associated with increased inherent clonal variability, when compared to using embryonic or juvenile tissue[117]. Also, enough clones are required in order to surpass biological variability and identify disease-related phenotypes[116]. Therefore, by having multiple CHIP KO lines, findings can be thoroughly investigated across lines. In the future, the A7 clone that had low CHIP expression could be further analysed and, if a mixed population of cells are present (both CHIP-expressing and not), the CHIP KO cells can be isolated.

Although another CHIP KO iPSC line was not achieved, any findings from the comparative proteomics study will be also investigated in our SH-SY5Y CHIP KO model. If molecular and cellular phenotypes and underlying mechanisms are maintained across the different cell lines this increases the robustness and validity of conclusions drawn.

# Chapter 4: Effect of CHIP on the proteome

## 4.1 Introduction

### 4.1.1 Studying the proteome

Proteomics is a large-scale and comprehensive study of the proteins of a cell or organism (i.e. the proteome). It aims to analyse the homeostasis and function of proteins at a given time[126]. The biggest challenge of proteomics is the complexity of the proteome[126,127]. Due to alternative splicing and post-translational modifications, the approximate 22,000 human genes translate to ~400,000 proteins[126]. Its dynamic nature drives a vast array of qualitative and quantitative protein changes in response to differences in the extracellular and intracellular environment. Thus, by comparing the proteome of two or more different states of a cell or organism (e.g. diseased versus non-diseased), mechanistic insight underlying the change of state can be achieved[126,127]. Changes in protein expression levels and major post-translational modifications (PTMs) have been associated with disease mechanisms. PTMs regulate protein folding, stability, subcellular localization and function[128].

At present, proteomics often analyses the proteome as a static snapshot within its dynamic continuum. Ultimately, the aim is to resolve the proteome with temporal specificity and to decipher signalling cascades responsible for the changes observed. Despite multiple human proteins identified by proteomic methodologies, it is estimated that only 5-10% of pair-wise interactions of the human interactome have been characterised[128].

Fundamental advances within the mid-1990s promoted proteomic research. Firstly, 2DE technology became a robust method to separate proteins. Secondly, MS-based methods were developed and allowed the identification of proteins with high degree of sensitivity and specificity. And thirdly, the growing large-scale genomic research constantly contributed to the number of sequences catalogued in databases. These became the basis for bioinformatic tools, allowing databases to be queried to aid in proteome identification[127].

## 4.1.2 Two-dimensional electrophoresis (2DE) technology

2DE technology was first introduced in the early 1970s. It exploited the structural and biophysical diversity of proteins within the proteome to achieve high-resolution separation[127]. In the first dimension of 2DE, proteins are separated on a gel based on their isoelectric point (pI), *i.e.* charge, a technique called isoelectric focusing[126,127]. The pI is the pH at which the protein carried no net charge, hence does not migrate within an electric field[126]. In the second dimension, proteins are separated by SDS-PAGE according to their molecular weight[127]. Following separation, proteins in the 2D gel are visualised by staining. Different staining methods have varying sensitivity, reproducibility, detection limits and may or not be compatible with subsequent MS analysis[127,128]. Finally, the stained gel can be digitalised for qualitative and quantitative analysis. Software programs can be used to quantify specific spot patterns (representative of proteins/isoforms) within a single or across multiple gels[126,127]. They have been designed for spot detection, matching, normalization and quantification, thus determining meaningful features[128].

### a. Advantages of 2DE

This is a useful separation technique that despite being established years ago is still routinely used. 2DE technology is also technically and financially more accessible than MS[127]. It allows a global view of a sample proteome by simultaneously resolving thousands of proteins on a single gel[127,128]. Importantly, comprehensive data can be derived from 2DE gels including biochemical properties of proteins (pI and MW), relative quantification (based on the density of the staining) and presence of isoforms (including PTMs)[126,127]. Proteins with PTMs can be readily detected by 2D gels due to their horizontal/vertical clustering pattern[127]. Furthermore, 2DE immunoblotting with specific antibodies can confirm the presence of isoforms and screen for possible PTMs (e.g. phosphorylation)[128].

### b. Limitations of 2DE

Beyond being labour-intensive and having relatively low throughput[127], there are fundamental drawbacks that prevent its widespread application. Firstly, protein

separation is limited by spatial resolution when analysing complex proteomes. This can result in differential protein processing (when a single protein produces multiple spots), co-migrating spots (multiple proteins with similar properties represented by the same spot) and spots migrated outside of the detection limit. The end-effect is compromised protein detection, identification and quantification[127,129]. Resolution can be optimized by using a series of narrow overlapping immobilised pH gradient strips[127,128] or by introducing a pre-fractionation step (e.g. sequential extraction of proteins based on solubility or subcellular localisation) prior to 2DE separation[127].

Secondly, its intrinsic bias towards proteins with specific characteristics means that only a subset of the proteome is analysed by 2DE-based proteomics. Highly abundant proteins tend to be more readily detected, while low-abundance proteins are not detected by staining limitations and are masked by the high-abundance proteins. These low-abundance proteins include regulatory proteins and receptors and isoforms with PTMs, which play key roles in cellular processes and might be of interest[127–129]. Increasing sample load promotes the detection of low abundance proteins[129]. Moreover, very small/large proteins and proteins with extremely basic/acidic pI values are unsuitable for the gel limits. Hydrophobic proteins, such as membrane proteins, are also disfavoured by 2DE, due to their poor solubility in extraction solutions[127,128].

Thirdly, the problems associated with the staining techniques for protein visualisation also compromise the quantification accuracy and sensitivity of the 2DE. These include: the narrow dynamic range of stains, the bias of the stain for certain protein characteristics, and the low staining reproducibility and sensitivity of some staining methods[127].

However, the biggest drawback in 2DE technology was the inability to identify unknown 2DE-separated proteins. This was largely answered by combining 2DE with MS, where separated bands representative of proteins of interest were excised from the gel and identified and quantify by MS[127].

### 4.1.3 Mass spectrometry (MS)

MS developed from the drive to discover unknown proteins of interest[130]. Over 10,000 proteins have been detected from whole-cell lysate, contributing to the human proteome drafts[130]. There are efforts to characterise at least one protein product of all protein-coding genes (20,300 genes)[131].

MS has been described as the most powerful method in terms of throughput and proteome coverage[130]. However, its high technical complexity and cost of instrumentation and limited dept of proteomic databases have restricted its impact[131]. MS can be performed with labelling techniques or as a label-free method. Labelling is often done using stable isotopes and yields more precise and accurate quantitative proteomics data. However, labelling has its own disadvantages: its complex, expensive, bias towards proteins with higher turnover and limits the sample number and type analysed[130,132]. Label-free methods, on the other hand, are easy to use and have no sample limitations, but can have low quantification precision and accuracy[130].

MS-based proteomics can be broadly grouped into “bottom-up” and “top-down” strategies. The former is widely used and analyses small peptides for protein identification and quantification, whilst the latter approach investigates native proteins. “Bottom-up” experiments are initiated by cleaving proteins into peptides (commonly using trypsin that cleaves at lysine and arginine residues) and the first separation is achieved using liquid chromatography (LC). Once peptides are separated based on hydrophobicity, having different retention times (RTs), they become ionized and enter the mass spectrometer. The first MS measurement determines the masses of all peptides, referred to as peptide-mass fingerprinting and obtaining the first dimension of analysis ($MS^1$)[127].

#### a. Tandem mass spectrometry (LC-MS/MS)

$MS^1$ is not sufficient for accurate protein identification because the same ionized peptides can be achieved from different proteins, given the redundancy in amino acids. Tandem MS (referred to as $MS^2$ or MS/MS) solves this problem by enabling identification and characterisation of isomeric precursor ions by adding another dimension of data, their unique fragmentation profile (i.e. the set of product ions

derived). Furthermore, it improved the quantification capacity of the method and allowed for structural information to be deduced from selected ions.

Specific peptides (parent/precursor ions) are isolated in the first quadrupole of the mass spectrometer. They are fragmented in the second quadrupole, where precursor ions are converted into product ions of different mass-to-charge (m/z) values. Usually this involves energetic collisional dissociation of the ion to cause fragmentation with gases, such as nitrogen. Mainly *b* and *y* product ions are produced from the cleavage of peptide bonds during fragmentation (Figure 4.1). Product ions are then detected in an analyser (either a third quadrupole or a Time-of-flight, TOF, detector), yielding $MS^2$ spectra[133].

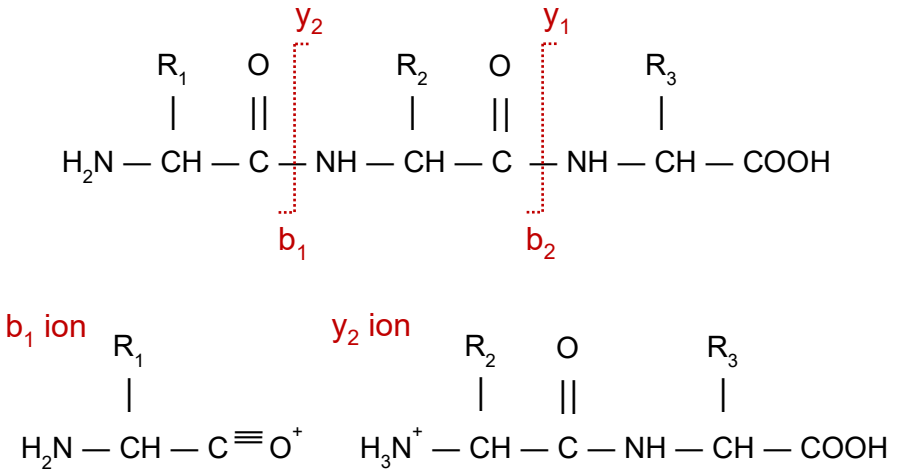


**Figure 4.1: *b* and *y* ions from fragmentation of peptide bonds**
The dotted line represents the fragmentation of the precursor ion, yielding product ions (*b* and *y* ions).

### b. Data-dependent acquisition mass spectrometry

Data-dependent acquisition (DDA) MS (also targeted/shotgun proteomics) is bias towards proteins with higher relative abundance within the sample. It does so by selectively isolating and fragmenting peptides with higher intensities at a given chromatographic elution time[130] (Figure 4.2). Alternatively, user-defined transitions (combination of precursor peptide and fragment ion) can be selected for individual analysis, which is referred to as selected acquisition monitoring. This can extend to

the consecutive analysis of multiple product ions from one or more precursor peptide[130,134].

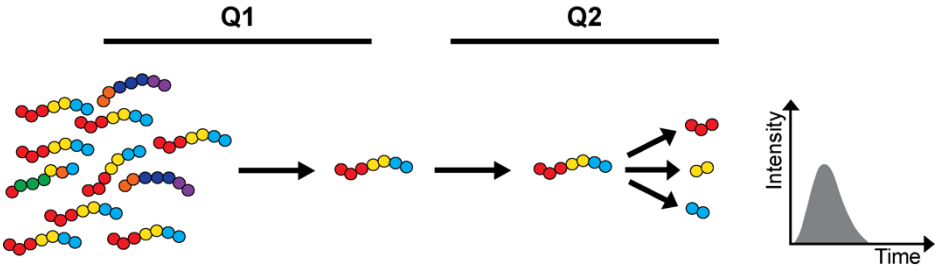


**Figure 4.2: Data-dependent acquisition mass spectrometry**
Peptides are ionized into ions (referred to as precursor ions), specific precursor ions are selected in the first quadrupole (Q1), fragmentated in the second quadrupole (Q2) into product ions and analysed in the last section of the mass spectrometer. For DDA, the criteria to select the precursor ion is based on abundance.

Although shotgun proteomics have made remarkable progress in deconvoluting complex proteomes[131], its application was limited by the relative low number of proteins (50-100) that could be identified and quantified in a single injection. This was improved by distributing sample complexity among several instrument injections using fractionation techniques (e.g. strong anion exchange or off-gel electrophoresis) prior to LC-MS/MS[131]. Additionally, this is also limited by the need to specify target proteins for each sample prior to data acquisition, thus requiring prior knowledge of the sample and potentially compromising the depth of proteomics[131].

### c. Data-independent acquisition mass spectrometry

Data-independent acquisition (DIA) MS (also untargeted proteomics) improved the reproducibility, sensitivity, accuracy and increased the dynamic range of MS-based proteomics[130,133]. When compared to DDA, it greatly increased the information acquired from a sample. DIA is a group of methods in which ions within a selected m/z range are fragmented and analysed in tandem MS/MS.

Sequential window acquisition of all theoretical mass spectra (SWATH-MS) vastly extended the throughput of proteins that can be targeted in a sample, using a large-scale multiple acquisition monitoring. It combines data-independent acquisition and

targeted data extraction and requires a high-resolution spectrometer and a peptide spectral library match[130,131]. SWATH-MS continuously fragments all the peptides (precursor ions) within consecutive *m/z* windows, termed swathes[133]. In the TOF accelerator, product ions are exposed to a known voltage and fly over a known length, thus the time of flight is recorded, and the mass can be deduced from this data (Figure 4.3). Spectra for all peptides belonging to different mass intervals for each RT point is recorded, obtaining 3-dimensional data (Figure 4.4A). This can be represented as both precursor ion relative intensity against time (chromatograph) and product ion relative intensity against m/z (spectrum) for all the RTs analysed (Figure 4.4B)[131,135].

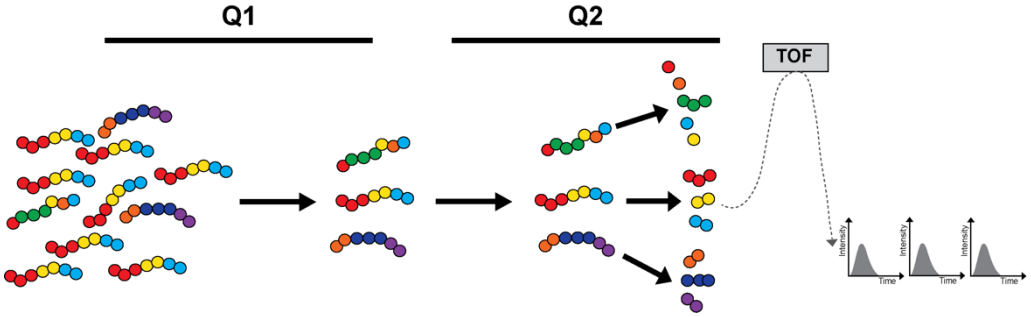


**Figure 4.3: Data-independent acquisition mass spectrometry**
Peptides are ionized into ions (referred to as precursor ions), specific precursor ions within a selected m/z range are selected in the first quadrupole (Q1) for fragmentation in the second quadrupole (Q2) into product ions. The Time-of-Flight (TOF) of the ions is then recorded, achieving mass spectra for all product ions of selected precursor ions.

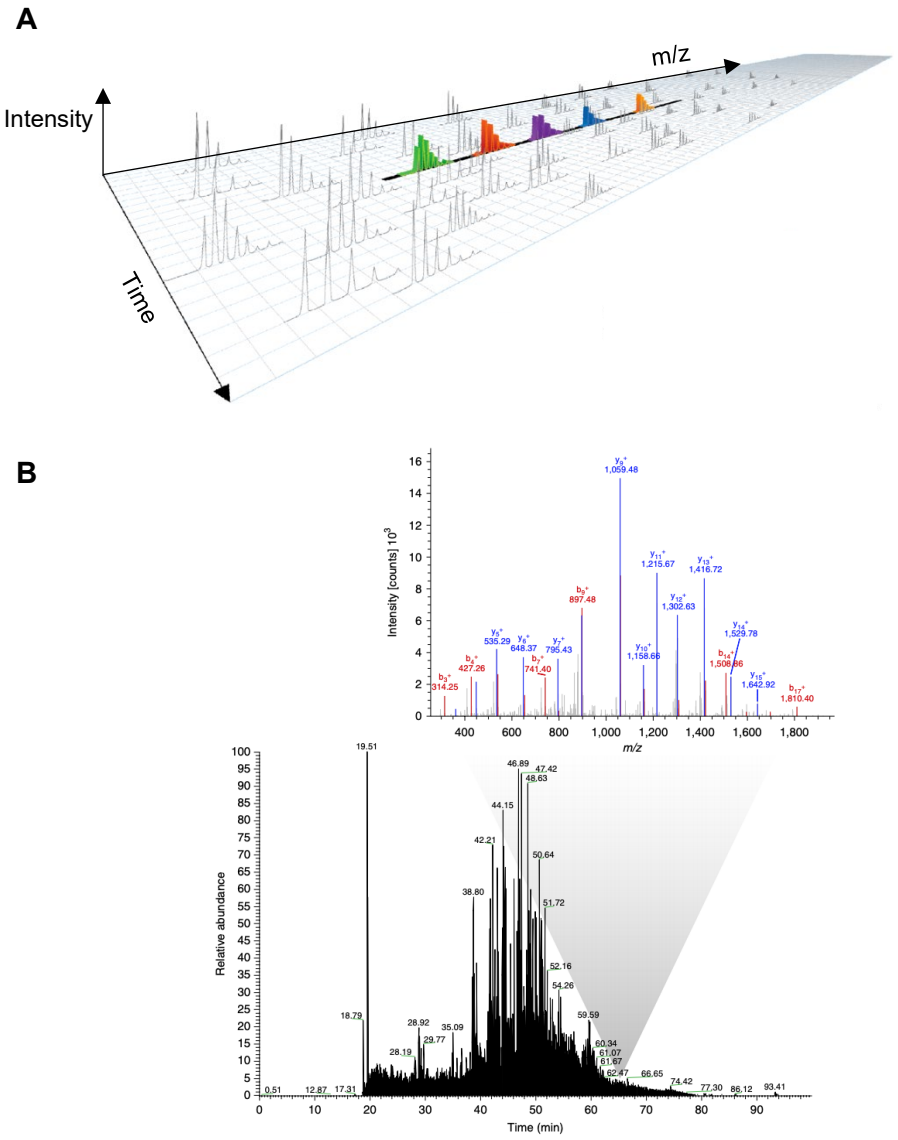


**Figure 4.4: SWATH-MS**
**A)** SWATH-MS analyses multiple proteins in samples in three dimensions (retention time, precursor and product ion intensities and mass/charge ratio).
**B)** Ionized peptides (precursor ions) are identified throughout the chromatogram (relative abundance/intensity over time) for a specific swath (selection window). At a particular retention time, product ions and their intensities are analysed and represented as a mass spectrum.
(**A**: Adapted from Hunter[135]; **B**: Adapted from Mohammed *et al*.[134])

Peptides, and in turn ion products, belonging to a single protein have similar RT, thus can be overlapped and normalised. The most abundant peptides and ion products are used for the identification of a protein, through sequence prediction. The theoretical peptide library to which the recorded spectra is compared to contains fragment ion

spectra known peptides and retention time data, and therefore is used as a reference to identify unknown proteins. This is possible because peptides tend to have a reproducible RT and fragmentation pattern. The library has been generated from fractionated or enriched samples previously analysed in the DDA mode[131]. Nowadays, this database can be used to generate a theoretical identification library *in silico*.

### i. Advantages of SWATH-MS

Arguably, SWATH-MS does not go deeper into the proteome compared to DDA-based MS *per se*[130]. Its throughput potential, however, enables greater proteome coverage for a single experiment. Theoretically, no data is discarded during acquisition by SWATH-MS, achieving a deeper proteome coverage[133]. This is an advantage over selected acquisition monitoring, where target peptides need to be determined prior to data acquisition[131]. SWATH-MS datasets are recorded independently can be re-mined subsequently using targeted analysis strategy[131].

Another advantage of SWATH-MS is the high quantification accuracy and the precision it offers[130,131]. This label-free quantification strategy is capable of spectral counting, where the number of fragment spectra of the peptides derived from a given protein is counted[132]. Quantification is possible due to the linear relationship between signal intensities and sample loading amounts (i.e. the number of acquired spectra is an indicator of the amount of the protein)[131,132]. The spectral counting approach yields a relative quantification of protein abundance. Quantification accuracy is greater when protein abundance ratios are about 1:1 (i.e. when fold changes are moderate) and decreases substantially when protein abundances differ greatly (e.g. by more than 4-fold)[130,136], although it can detect large changes[132]. Fold changes tend to be an underestimation of the real value due to limitations in ionization and ion detection, which affect ion with high concentrations to a greater extent[130]. Nevertheless, for most biological studies, the exact fold change is not necessary to determine its biological significance[130]. This is particularly true for chaperones and E3 ligases, as they have a wide interactome and can influence the homeostasis of multiple proteins, thus a fold change of 2, for example, can have pronounce cellular effects. Although less common, SWATH-MS can also be used for absolute quantification using peptide

chromatographic peak intensity measurements[130,132,133]. Here, the chromatographic peak area of all transition ions belonging to a specific protein is measured[130,132].

### ii. Limitations of SWATH-MS

The main drawback of SWATH-MS used to be the requirement for a peptide spectral library. However, large-scale human proteomic studies have greatly contributed to an extensive library[130,131]. Nowadays, the main limitation of SWATH-MS is sample complexity[133]. Previously SWATH-MS was used to study less complex systems (e.g. enriched peptide mixtures)[131], but increasingly it is used for proteome scale analysis of complex samples with PTMs[130]. For example, SUMO and Ub-derived isopeptides have been detected using SWATH-MS[133]. However, given the nature of "bottom-up" proteomics, PTMs may be cleaved from the peptide upon trypsinization (such as Ub chain linkages), limiting the use of MS for PTM identification[133].

Furthermore, obtaining in-depth coverage of the complex human proteome remains a challenge. The great range of abundance levels of proteins (with copy numbers from tens of millions to single digits) not only compromises quantification accuracy but can also mask the detection of low abundance peptides. Also, mass spectrometers have limited dynamic ranges of detection[136]. This can affect the analysis of a complex proteome containing proteins with high and low expression levels and both unmodified and modified PTMs. Fractionation steps (e.g. SDS-PAGE separation prior to MS) improve the limit of detection. This is particularly relevant when studying ubiquitination substrates in unstressed cells, where the levels of ubiquitinated species are kept low[136]. However, SWATH-MS can achieve a useful proteome coverage, having identified and quantified 3600 proteins without prefractionation[130].

## 4.2 Results

### 4.2.1 Preliminary proteomics of CHIP cell models using 2DE

As a first approach to investigate whether *STUB1* gene deletion (ablation of CHIP protein expression) resulted in bulk changes in the proteome, we focused on two models with isogenic *STUB1* deletions: iPSC and undifferentiated SH-SY5Y. The former cells were generated as described in Chapter 3. However, the SH-SY5Y CHIP model was previously made by Erisa Nita[95] in our group using CRISPR/Cas9 technology (with the same Cas9 and gRNA-encoding plasmid as that I used to generated CHIP KO iPSC) (Figure 3.4). This cell line was chosen because of its neuroblast-like phenotype (with non-polarized cell bodies, few truncated processes and the expression of immature neuronal markers) (Figure S.2), low maintenance and cost, human origin and ability to differentiate[118]. It is a neuroblastoma line that was originally derived from a metastatic bone tumour biopsy.

As a preliminary approach to assess the overall effect of loss of CHIP on the cellular proteome, 2D gels of cell lysates derived from isogenic CHIP KO and WT cells of two cell lines, SH-SY5Y and iPSC, were performed (Figure 4.5), in collaboration with Jitka Zakova†. Interesting, similar patterns were seen across CHIP genotypes, suggesting that CHIP deletion likely results in specific changes in the proteome with relatively minor differences in steady state levels rather than grossly changing the intensity and distribution of most proteins (represented as spots).

† Department of Molecular Pathology and Biology, University Hospital Ostrava, Hradec Kralove, Czech Republic

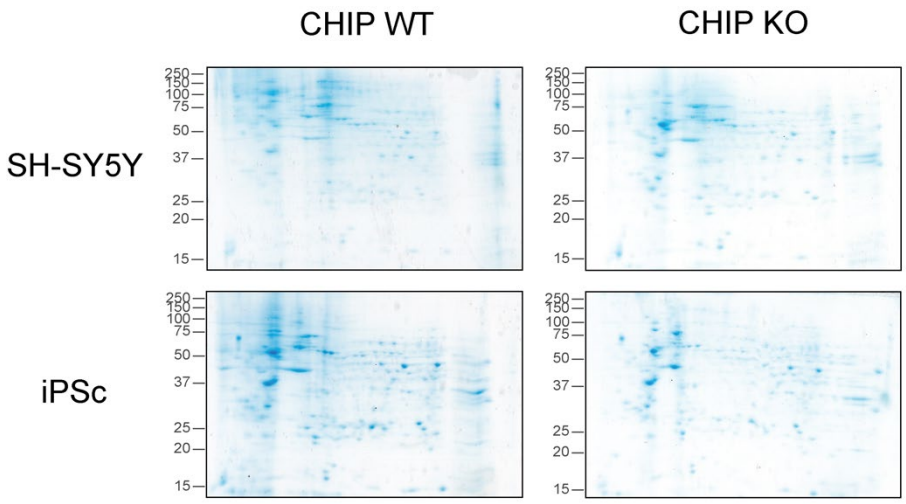


**Figure 4.5: 2D gels of different CHIP cell models**
Undifferentiated iPSC and SH-SY5Y CHIP KO and WT cells were lysed with urea-based lysis buffer and analysed by 2D gels (pH 3-10NL strips). For each gel, 200 μg of lysate was loaded, and gels were stained with Coomassie blue.

## 4.2.2 Proteomics of the CHIP cortical neuron model using SWATH-MS

### a. Overview of the changes in the proteome

Once mature cortical neurons were generated and validated (see section 3.3.3) they were harvested (at day 80 of the differentiation) for protein quantification using proteomics methodologies and analysed in collaboration with Dr Jakub Faktor and Dr Bořivoj Vojtesek‡. Label-free SWATH-MS was used to identify proteins and their relative abundance between sample pairs. Each sample was pooled from 2 wells of differentiated cells and triplicates were analysed. Different analyses were performed comparing neurons derived from the non-engineered parental line (referred to as P) and from CRISPR clones, both $CHIP^{+/+}$ (WT) and $CHIP^{-/-}$ (KO). In an attempt to account for the inherent variability of the cortical differentiation, the KO cells were compared to both control cell lines (P and WT). SWATH-MS data was compared between and within conditions to assess inter- and intra-heterogeneity by principal

‡ Regional Centre for Applied Molecular Oncology, Masaryk Memorial Cancer Institute, Brno, Czech Republic

component analysis (PCA) (Figure 4.6). The biological replicates of the WT samples grouped together on the positive scores of PC1, while the KO biological replicates were found in the negative range. This supports the existence of genotype-specific proteomic changes between KO and WT cells. Overall, the intra-heterogeneity between biological and technical replicates was restricted.

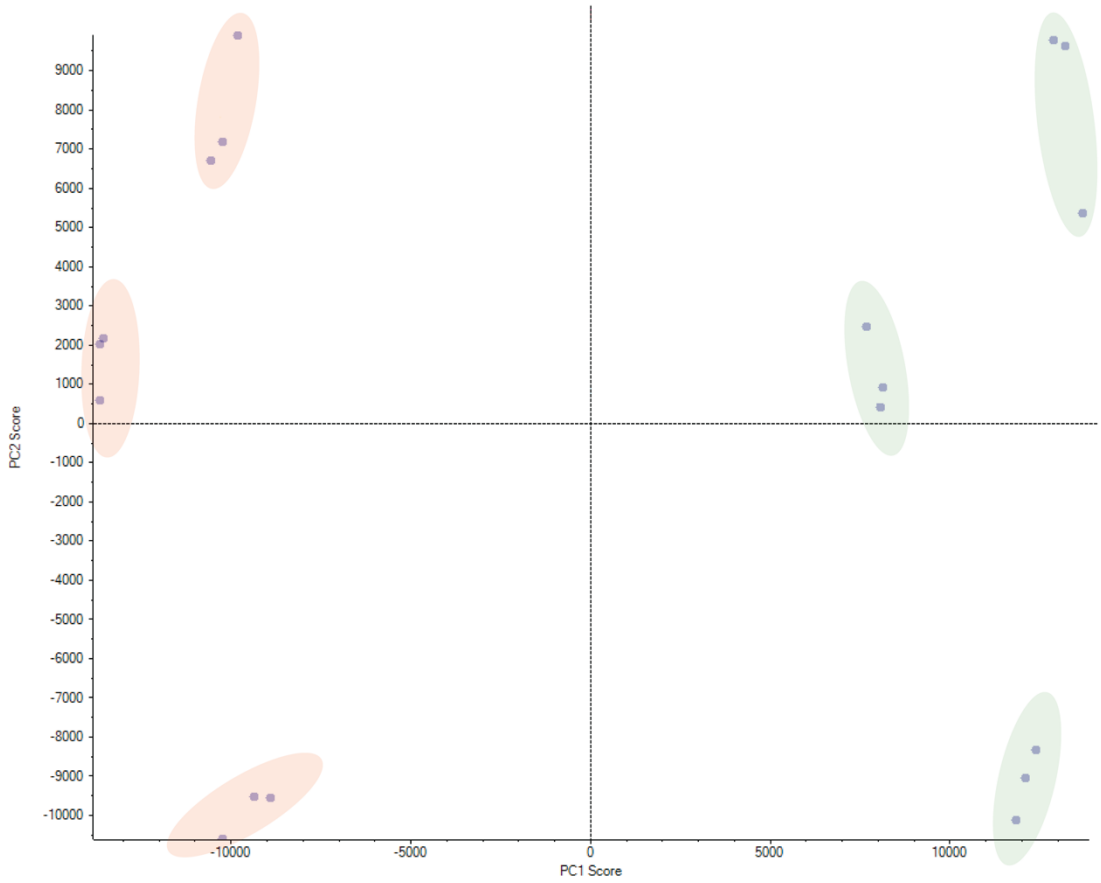


**Figure 4.6: Principal component analysis of the proteomics analysis of cortical neurons of different CHIP genotypes**
CHIP KO cortical neurons (red clusters) segregate between scores 0 to -14,000 on PC1, while CHIP WT cortical neurons (green clusters) are found between scores 0 to 14,000 on PC1. Each colour-coded cluster represents a biological replicate (3 of each genotype). Three technical replicates for each biological replicate cluster together and are represented by the dots within each individual cluster.

When the SWATH-MS data comparing CHIP KO neurons with CHIP-expressing neurons was analysed using the Ingenuity Pathway Analysis software, pathways associated with neurodegenerative diseases (PD and AD) where identified as being

related to the data set (Figure S.3). This suggests that the proteome of our patient-derived neurons models, to some extent, disease-associated pathways.

The comparative proteomics analysing CHIP KO neurons with CHIP-expressing neurons (P, Figure 4.7, and WT, Figure 4.8) are represented as volcano plots. These show that the vast majority of the proteins identified were not changed with regards to fold change (dots coloured in grey), while the outliers of the graph (dots in red) are potential proteins of interest. Over-represented proteins have increased fold change (in terms of ion products) in CHIP KO cells compared to WT cells, and the opposite trend is seen for under-represented cells. The most changed significant proteins identified in P vs KO and WT vs KO comparative proteomics are listed in Table S.1 & Table S.2 and Table S.3 & Table S.4, respectively. SWATH-MS data comparing P with WT neurons is also represented in Figure 4.9 and Table S.5 & Table S.6.

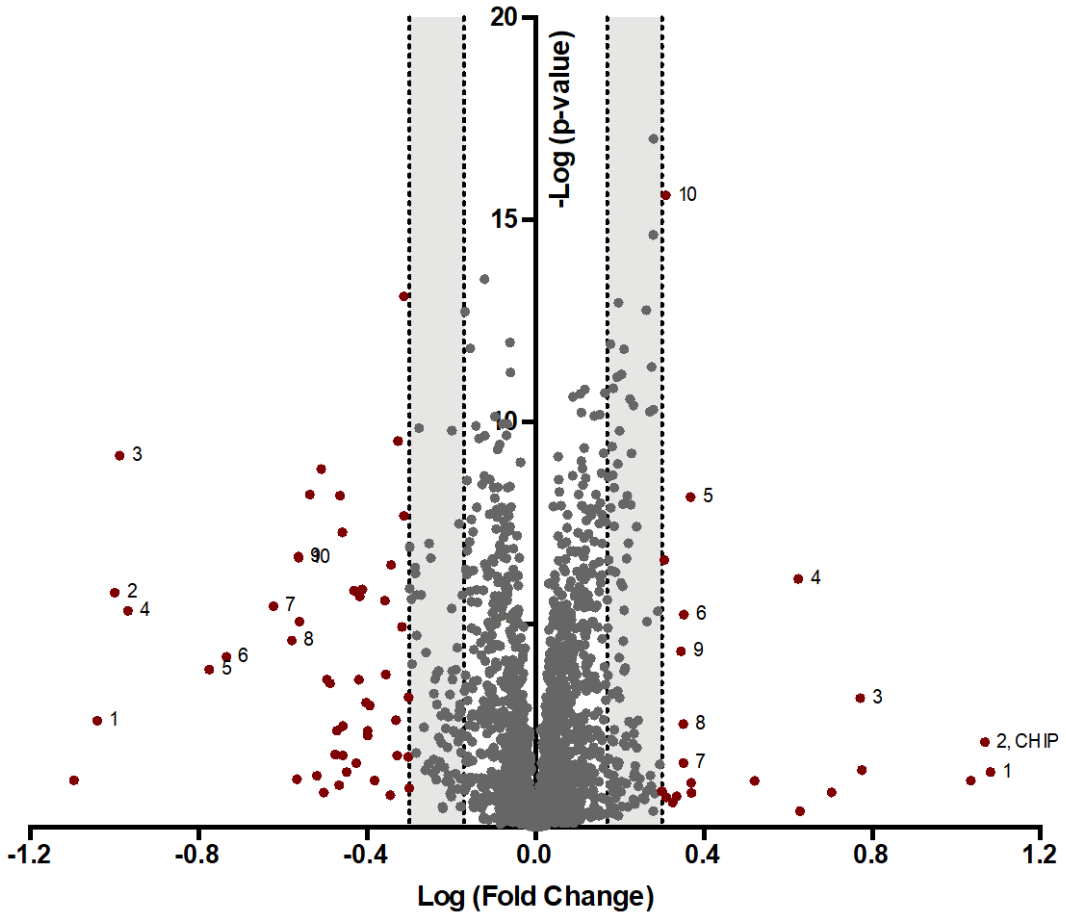


**Figure 4.7: Comparative proteomics of mature cortical neurons derived from the parental and CHIP KO iPSC lines**

SWATH-MS analysis of the parental line compared to CHIP KO cortical neurons. Cut off criteria (≤0.5 and ≥2 or ≤0.67 and ≥1.5 fold change) are represented by the dotted lines and shaded areas. Proteins (dots) that do not meet this fold change criteria are colour-coded in grey and does that do are in red. Over-represented proteins in the CHIP KO sample compared to WT have negative log (fold change), while under-represented proteins have positive values. The top 10 most under- and over-represented proteins that were significantly changed ($P < 0.05$) are numbered. The dot representing CHIP is indicated.

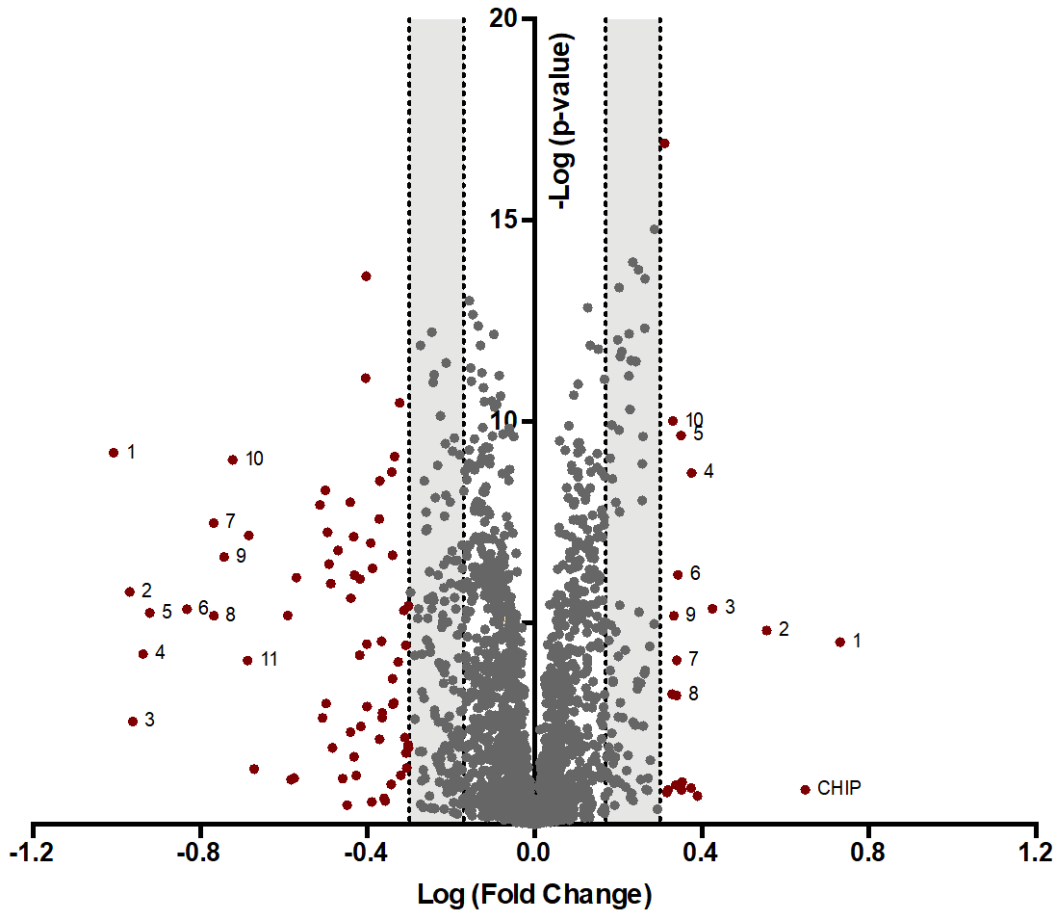


**Figure 4.8: Comparative proteomics of mature cortical neurons derived from the CHIP WT and CHIP KO iPSC lines**

SWATH-MS analysis of the CHIPS WT (CRISPR control) compared to CHIP KO cortical neurons. Cut off criteria (≤0.5 and ≥2 or ≤0.67 and ≥1.5 fold change) are represented by the dotted lines and shaded areas. Proteins (dots) that do not meet this fold change criteria are colour-coded in grey and does that do are in red. Over-represented proteins in the CHIP KO sample compared to WT have negative log (fold change), while under-represented proteins have positive values. The top 10 most under- and over-represented proteins that were significantly changed ($P < 0.05$) are numbered. S100-A11 was also included in the over-represented list of proteins ($11^{th}$ position) as it shares functional overlap with the most changed proteins. The dot representing CHIP is indicated.

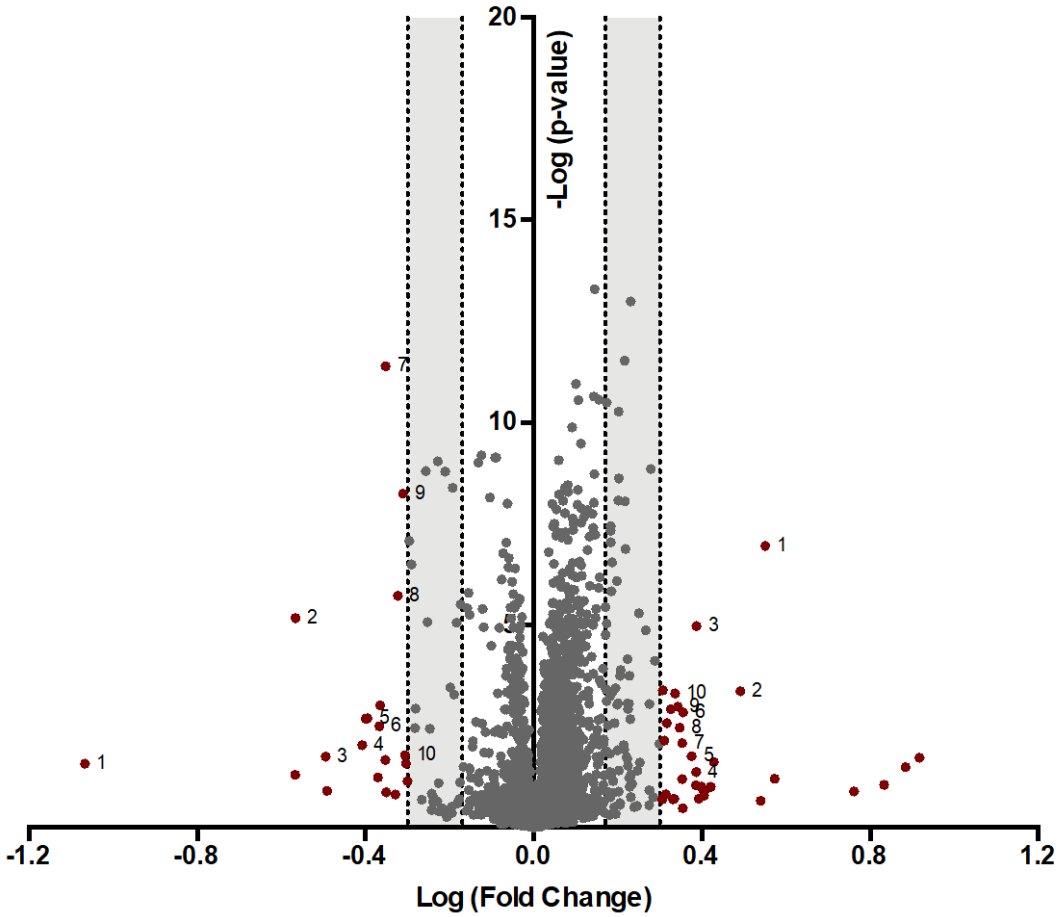


**Figure 4.9: Comparative proteomics of mature cortical neurons derived from the parental and CHIP WT iPSC lines**
SWATH-MS analysis of the parental line compared to CHIP WT (CRISPR control) cortical neurons. Cut off criteria (≤0.5 and ≥2 or ≤0.67 and ≥1.5 fold change) are represented by the dotted lines and shaded areas. Proteins (dots) that do not meet this fold change criteria are colour-coded in grey and does that do are in red. Over-represented proteins in the CHIP WT sample compared to P have negative log (fold change), while under-represented proteins have positive values. The top 10 most under- and over-represented proteins that were significantly changed ($P < 0.05$) are numbered.

### b. Similarities across the comparative proteomics data of cortical neurons of different CHIP genotypes

The majority of proteins identified in each comparative proteomics analysis (e.g. CHIP KO vs WT) were also present in the other analyses across the different cell lines (e.g. parental line vs CRISPR control), account for a 97.8% overlap (Figure 4.10A). When applying cut-off criteria (Figure 4.10B&C), the majority of the proteins shared in common are between the two analyses comparing different CHIP genotypes (113 and 40 proteins, depending on the stringency of the cut-off criteria) and are excluded from the P vs WT analysis. When removing proteins that are unlikely to be affected by CHIP, such as proteins changing significantly between P and WT and keratin, 110 and 35 proteins could be of interest (Figure 4.10D&E). These under- and over-represented proteins may be changing in CHIP KO cortical neurons compared to CHIP-expressing neurons.

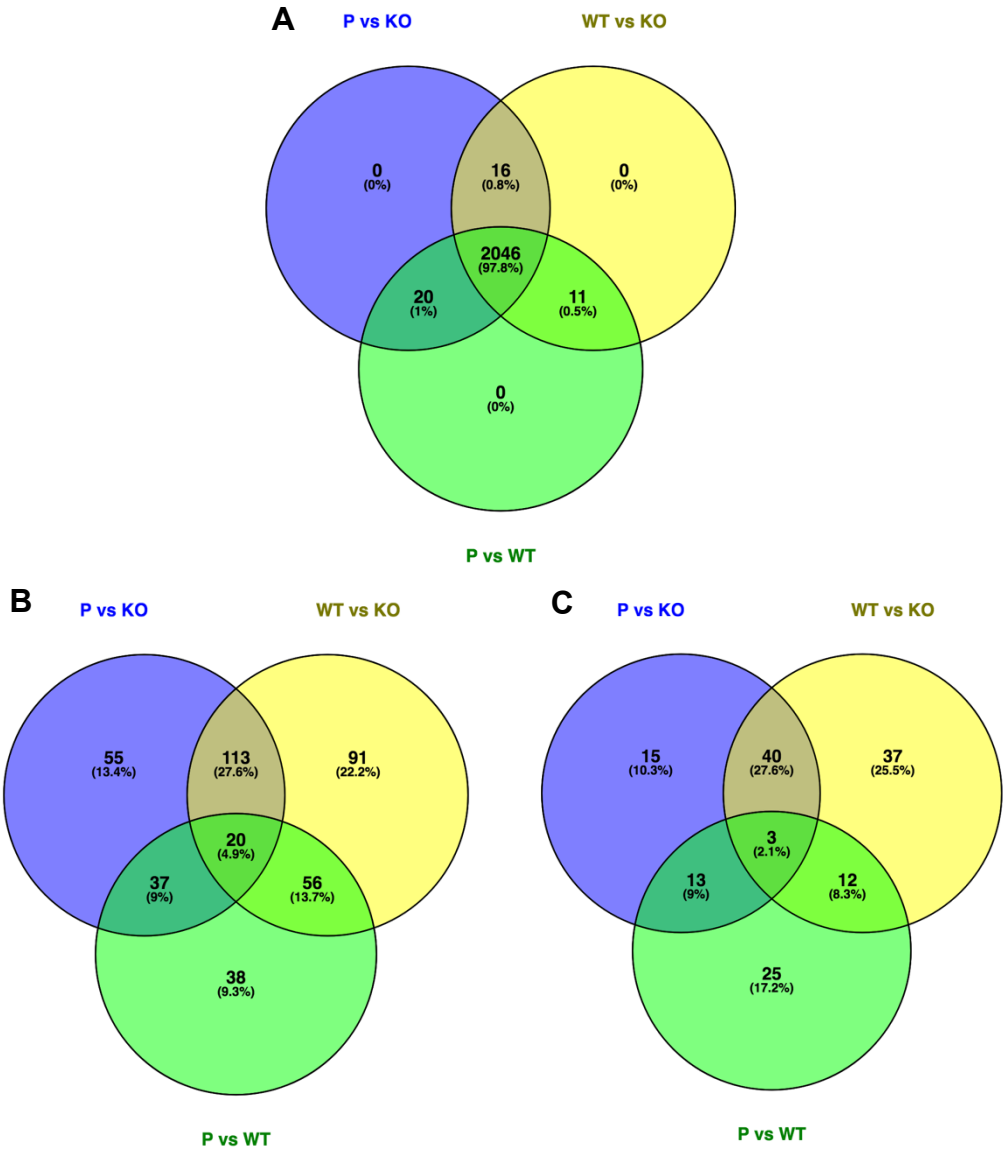


**Figure 4.10: Venn diagrams showing the overlap of proteins identified by SWATH-MS across CHIP cell models**
Comparisons between the parental line (P), the CHIP WT CRISPR control (WT) and CHIP KO cortical neurons are shown.
**A)** Total proteins identified, independent on p-value and fold-change.
**B)** Proteins identified with fold changes of ≤ 0.67 and ≥ 1.5.
**C)** Proteins identified with fold changes of ≤ 0.5 and ≥ 2.

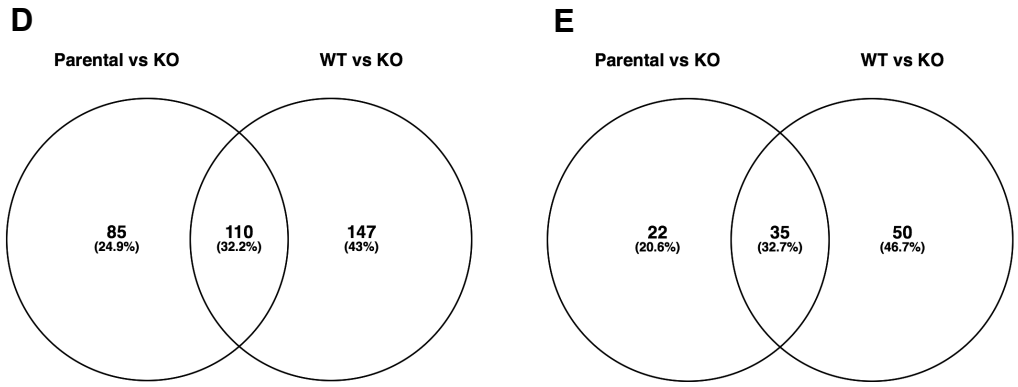


**Figure 4.10** *(continued)*
Comparisons between the parental line (P), the CHIP WT CRISPR control (WT) and CHIP KO cortical neurons are shown.
**D)** As B but with keratin and proteins found in P vs WT removed.
**E)** As C but with keratin and proteins found in P vs WT removed.

### c. Proteins of interest

When selecting candidate proteins that are likely to be affected by the expression of CHIP (i.e. proteins of interest), proteins that are significantly changed in both P vs KO and WT vs KO screens were favoured, as these are less likely to be changed due to CHIP-independent factors (e.g. differences in differentiation status). Under- or over-represented proteins in the P vs KO and/or WT vs KO analyses that were excluded from or unchanged in P vs WT are of interest, as these could be affected by CHIP genotype (Table 4.1 & Table 4.2). These two SWATH-MS analyses are compared in Figure 4.11 and show a positive linear relationship ($r = 0.7305$ and $r^2 = 0.5337$ with *P* value < 0.0001[#]), with proteins under- and over-represented in both experiments. Proteins of particular interest (with roles in neuronal health, membrane homeostasis and innate immunity) are colour-coded.

[#] Pearson correlation:
r quantifies the direction and magnitude of the correlation (ranges from -1 to 1).
$r^2$ is the coefficient determinant and is the proportion of the variance in the two sets of data that is shared (ranges from 0 to 1).
*P* value: probability of the null hypothesis (that the population correlation coefficient for the pair of variables is zero).

**Table 4.1: Proteins identified by SWATH-MS that are over-represented in CHIP KO cortical neurons compared to the control lines**

Control lines are the CRISPR control, WT, and the parental line, P. Fold changes ≤ 0.05. Keratin was excluded from this list.

| Proteins | WT vs KO | | P vs KO | | P vs WT | |
|---|---|---|---|---|---|---|
| | Fold change | p-value | Fold change | p-value | Fold change | p-value |
| Glial fibrillary acidic protein | 0.091 | 2.38E-03 | 0.109 | 2.78E-03 | - | - |
| Interferon-induced transmembrane protein 2 | 0.103 | 6.72E-10 | 0.098 | 5.84E-10 | - | - |
| Neuroblast differentiation-associated protein AHNAK | - | - | 0.328 | 0.01 | - | - |
| Protein S100-B | 0.470 | 0.02 | - | - | - | - |
| Annexin A2 | 0.107 | 1.66E-06 | 0.100 | 1.61E-06 | 0.964 | 0.86 |
| Caldesmon | 0.116 | 5.89E-05 | 0.168 | 1.30E-04 | 1.704 | 0.05 |
| Galectin-3 | 0.120 | 5.51E-06 | 0.108 | 4.56E-06 | 0.664 | 0.20 |
| Transgelin-2 | 0.148 | 4.49E-06 | 0.275 | 8.41E-06 | 1.845 | 1.37E-05 |
| Annexin A1 | 0.171 | 3.25E-08 | 0.274 | 2.09E-07 | 1.603 | 1.80E-04 |
| HLA class I histocompatibility antigen, B-78 alpha chain | 0.171 | 6.51E-06 | 0.264 | 2.46E-05 | 1.544 | 0.07 |
| PDZ and LIM domain protein 5 | 0.181 | 2.27E-07 | 0.382 | 1.99E-06 | 2.117 | 1.20E-03 |
| Clusterin | 0.190 | 8.83E-10 | 0.291 | 6.09E-09 | 1.535 | 2.82E-07 |
| Protein S100-A11 | 0.206 | 8.47E-05 | 0.184 | 6.19E-05 | 0.800 | 0.26 |
| Guanine nucleotide-binding protein G(I)/G(S)/G(O) subunit gamma-12 | 0.207 | 6.63E-08 | 0.274 | 2.23E-07 | 1.321 | 0.18 |
| Prelamin-A/C | 0.257 | 6.47E-06 | 0.238 | 3.48E-06 | 0.928 | 0.75 |
| Cat eye syndrome critical region protein 5 | 0.266 | 0.07 | 0.452 | 0.16 | 1.701 | 0.18 |
| Transgelin | 0.311 | 2.27E-03 | 0.337 | 4.18E-03 | 1.042 | 0.92 |
| Serpin H1 | 0.316 | 5.00E-09 | 0.343 | 6.52E-09 | 1.086 | 0.07 |
| Gelsolin | 0.320 | 5.53E-08 | 0.347 | 5.25E-08 | 1.093 | 0.26 |
| Filamin-A | 0.323 | 3.42E-07 | 0.388 | 1.35E-06 | 1.203 | 1.40E-04 |
| Serine protease HTRA1 | 0.326 | 1.03E-06 | 0.371 | 1.43E-06 | 1.140 | 0.27 |
| CD99 antigen | 0.339 | 1.56E-07 | 0.503 | 1.28E-06 | 1.485 | 3.90E-04 |
| HCG2042749, isoform CRA_d | 0.348 | 0.07 | 0.302 | 0.05 | 0.871 | 0.68 |
| Annexin A6 | 0.382 | 6.20E-05 | 0.441 | 1.70E-04 | 1.156 | 8.22E-06 |
| Tubulin beta-6 chain | 0.395 | 2.41E-14 | 0.487 | 7.60E-14 | 1.233 | 5.50E-04 |
| Integrin beta-1 | 0.397 | 3.32E-05 | 0.507 | 2.34E-06 | 1.279 | 0.31 |
| Annexin A5 | 0.406 | 1.02E-07 | 0.454 | 3.33E-07 | 1.121 | 0.01 |
| Midkine | 0.426 | 2.57E-08 | 0.310 | 1.42E-09 | 0.728 | 2.49E-03 |
| Polypyrimidine tract binding protein 1, isoform CRA_b | 0.427 | 2.94E-09 | 0.471 | 2.92E-10 | 1.106 | 0.33 |
| Parkinson disease 7 domain-containing protein 1 | 0.436 | 0.22 | 0.271 | 0.07 | 0.622 | 0.56 |
| Heat shock protein beta-1 | 0.456 | 1.76E-09 | 0.503 | 1.20E-07 | 1.104 | 0.18 |
| Palladin (Fragment) | 0.457 | 2.40E-04 | 0.500 | 6.30E-04 | 1.094 | 0.52 |
| Alpha-actinin-1 | 0.461 | 9.60E-04 | 0.380 | 2.30E-04 | 1.026 | 0.65 |
| Probable ubiquitin carboxyl-terminal hydrolase FAF-X | 0.487 | 4.80E-06 | 0.439 | 2.55E-06 | 0.902 | 0.65 |
| T-box brain protein 1 | 0.498 | 0.01 | 0.400 | 5.50E-03 | 0.803 | 0.60 |

**Table 4.2: Proteins identified by SWATH-MS that are under-represented in CHIP KO cortical neurons compared to the control lines**

Control lines are the CRISPR control, WT, and the parental line, P. Fold changes ≤ 0.05. Keratin was excluded from this list.

| Proteins | WT vs KO | | P vs KO | | P vs WT | |
|---|---|---|---|---|---|---|
| | Fold change | p-value | Fold change | p-value | Fold change | p-value |
| Heat shock 70 kDa protein 12A | 1.504 | 0.01 | 1.692 | 5.90E-10 | 1.126 | 0.29 |
| AMP deaminase 2 (Fragment) | 1.512 | 0.07 | 1.537 | 0.07 | 1.018 | 0.91 |
| Dynamin-1 | 1.517 | 1.50E-04 | 1.683 | 1.10E-08 | 1.127 | 0.07 |
| Syntaxin-1B | 1.531 | 1.20E-10 | 1.531 | 1.44E-11 | 1.001 | 0.96 |
| Clavesin-1 | 1.539 | 2.70E-04 | 1.740 | 3.80E-08 | 1.131 | 0.11 |
| Type I inositol 3,4-bisphosphate 4-phosphatase | 1.542 | 0.03 | 1.701 | 8.71E-03 | 1.103 | 0.03 |
| Ras-related protein Rab-3C | 1.565 | 9.98E-09 | 1.570 | 1.07E-09 | 1.004 | 0.87 |
| Prolyl endopeptidase-like | 1.587 | 0.01 | 1.556 | 0.02 | 0.981 | 0.83 |
| Synapsin-2 | 1.594 | 1.61E-10 | 1.538 | 3.75E-08 | 0.966 | 0.30 |
| Neurexin-3 | 1.595 | 1.72E-08 | 1.514 | 4.59E-07 | 0.950 | 0.20 |
| V-type proton ATPase subunit C 1 | 1.599 | 3.58E-06 | 1.549 | 5.03E-07 | 0.970 | 0.64 |
| Mitochondrial import inner membrane translocase subunit Tim9 | 1.604 | 9.40E-04 | 1.584 | 6.50E-04 | 0.988 | 0.85 |
| 4-aminobutyrate aminotransferase, mitochondrial | 1.604 | 2.38E-12 | 1.623 | 1.57E-12 | 1.013 | 0.51 |
| Calcium-dependent secretion activator 1 | 1.617 | 1.77E-12 | 1.521 | 4.00E-10 | 0.941 | 7.23E-03 |
| Microtubule-associated protein | 1.652 | 0.12 | 1.634 | 1.20E-04 | 0.990 | 0.97 |
| C2 domain-containing protein 2-like | 1.660 | 0.05 | 1.722 | 0.05 | 1.038 | 0.80 |
| Fructose-bisphosphate aldolase C | 1.672 | 0.02 | 1.567 | 0.03 | 0.938 | 0.71 |
| Synaptophysin | 1.682 | 7.18E-12 | 1.538 | 4.08E-09 | 0.915 | 5.84E-03 |
| Neurosecretory protein VGF | 1.685 | 6.54E-13 | 1.562 | 7.72E-12 | 0.928 | 4.54E-03 |
| Synaptic vesicle glycoprotein 2A | 1.703 | 3.00E-12 | 1.602 | 6.53E-12 | 0.941 | 1.20E-04 |
| Pyruvate dehydrogenase protein X component, mitochondrial | 1.742 | 3.40E-03 | 1.669 | 2.47E-03 | 0.959 | 0.74 |
| Synaptogyrin-1 | 1.748 | 3.16E-12 | 1.584 | 1.62E-10 | 0.907 | 1.40E-04 |
| Neural cell adhesion molecule L1 | 1.761 | 4.30E-04 | 1.531 | 7.78E-03 | 0.889 | 0.17 |

**Table 4.2** *(continued)*

| Proteins | WT vs KO | | P vs KO | | P vs WT | |
|---|---|---|---|---|---|---|
| | Fold change | p-value | Fold change | p-value | Fold change | p-value |
| Neural cell adhesion molecule 1 (Fragment) | 1.764 | 2.80E-04 | 1.752 | 2.31E-03 | 0.994 | 0.97 |
| Succinate-semialdehyde dehydrogenase, mitochondrial | 1.774 | 1.67E-14 | 1.574 | 1.11E-13 | 0.888 | 8.61E-07 |
| Limbic system-associated membrane protein (Fragment) | 1.778 | 5.32E-06 | 2.024 | 2.50E-07 | 1.084 | 0.32 |
| V-type proton ATPase subunit d 1 | 1.794 | 3.10E-04 | 1.540 | 3.95E-03 | 0.860 | 0.18 |
| Metallo-beta-lactamase domain-containing protein 2 | 1.808 | 8.97E-09 | 1.662 | 9.68E-08 | 0.920 | 8.89E-05 |
| Tumor protein D53 | 1.811 | 1.11E-09 | 1.646 | 2.35E-07 | 0.910 | 0.05 |
| Visinin-like protein 1 | 1.834 | 4.69E-13 | 1.711 | 3.81E-11 | 0.934 | 6.93E-03 |
| Guanine nucleotide-binding protein G(I)/G(S)/G(O) subunit gamma-7 | 1.836 | 2.80E-14 | 1.886 | 4.30E-12 | 1.028 | 0.28 |
| Nicotinamide phosphoribosyltransferase | 1.862 | 0.14 | 1.597 | 0.14 | 0.921 | 0.79 |
| Isochorismatase domain-containing protein 2 (Fragment) | 1.870 | 0.07 | 1.743 | 0.01 | 0.933 | 0.79 |
| Ras-related protein Rab-3B | 1.887 | 3.77E-05 | 1.954 | 4.61E-06 | 1.037 | 0.57 |
| Caseinolytic peptidase B protein homolog | 1.894 | 0.03 | 2.243 | 2.86E-03 | 1.185 | 0.41 |
| 6-phosphogluconate dehydrogenase, decarboxylating | 1.935 | 1.66E-15 | 1.907 | 9.78E-18 | 0.986 | 0.45 |
| Vesicular inhibitory amino acid transporter | 2.047 | 1.21E-17 | 1.905 | 2.34E-15 | 0.931 | 1.02E-05 |
| Phospholipid-transporting ATPase IA | 2.135 | 5.80E-04 | 1.713 | 0.06 | 0.803 | 0.16 |
| Caytaxin | 2.179 | 0.10 | 2.344 | 0.08 | 1.077 | 0.84 |
| Synaptotagmin-5 | 2.187 | 8.34E-05 | 2.247 | 0.03 | 1.028 | 0.90 |
| Metallophosphoesterase MPPED2 | 2.203 | 6.30E-07 | 2.337 | 7.08E-09 | 1.062 | 0.32 |
| Synaptosomal-associated protein 29 | 2.254 | 0.09 | 1.577 | 0.03 | 0.700 | 0.33 |
| F-box only protein 2 | 2.667 | 4.37E-06 | 2.217 | 4.62E-05 | 0.832 | 4.66E-03 |
| Sclerostin domain-containing protein 1 | 3.594 | 1.51E-05 | 4.213 | 7.46E-07 | 1.173 | 0.18 |
| E3 ubiquitin-protein ligase CHIP | 4.444 | 0.14 | 11.699 | 7.98E-03 | 2.636 | 0.10 |
| Corticoliberin | 5.385 | 2.98E-05 | 5.913 | 6.60E-04 | 1.099 | 0.70 |

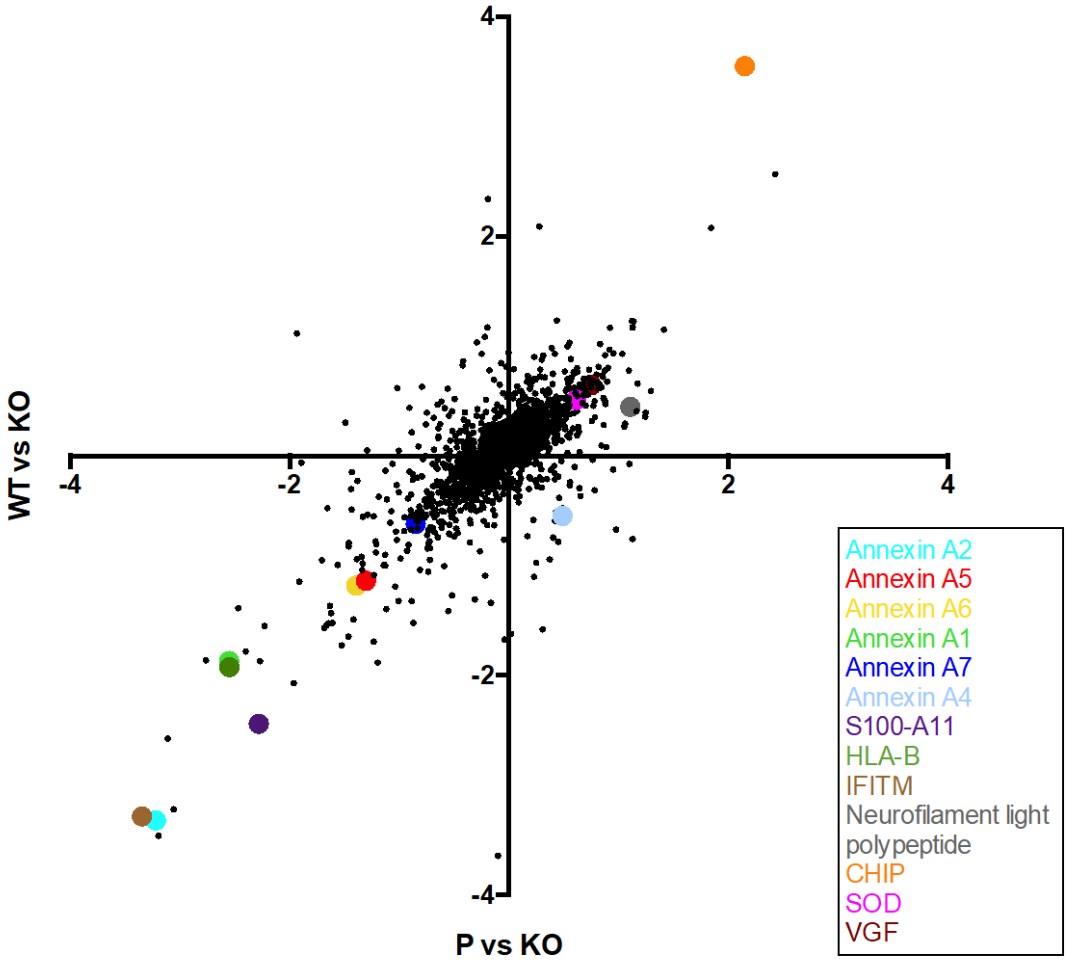


**Figure 4.11: Comparing the proteomic differences between cortical neurons derived from two CHIP-expressing iPSC lines and the CHIP KO line.**
The two CHIP-expressing lines are the CRISPR control line, WT and the parental line, P. $Log_2$ fold changes of proteins identified in both SWATH-MS experiments are plotted. Proteins of particular interest are colour-coded. Pearson correlation: $r = 0.7305$, $r^2 = 0.5337$ and $P$ value (two-tailed) < 0.0001 (****).

### 4.2.3 Proteomics of the other CHIP KO models

Aiming to better understand how CHIP affects the proteome of different non-neuronal and neuronal cell lines, the proteome of CHIP KO and WT iPSC and differentiated SH-SY5Y cells was also analysed by SWATH-MS. This data was compared to the SWATH-MS analyses from the patient-derived cortical neurons to obtain insights into the degree to which *STUB1* deletion changes the proteome, and whether proteins previously characterised as being of interest are neuronal-specific or even disease-specific.

#### a. iPSC

As previously, the SWATH-MS data obtained from CHIP WT vs KO iPSC was represented as a volcano plot (Figure 4.12) and shows that the majority of proteins are unchanged. The most under- and over-represented proteins are listed in Table S.7 & Table S.8. Some of the proteins identified are likely to be responsible for its pluripotency and self-renewal ability.

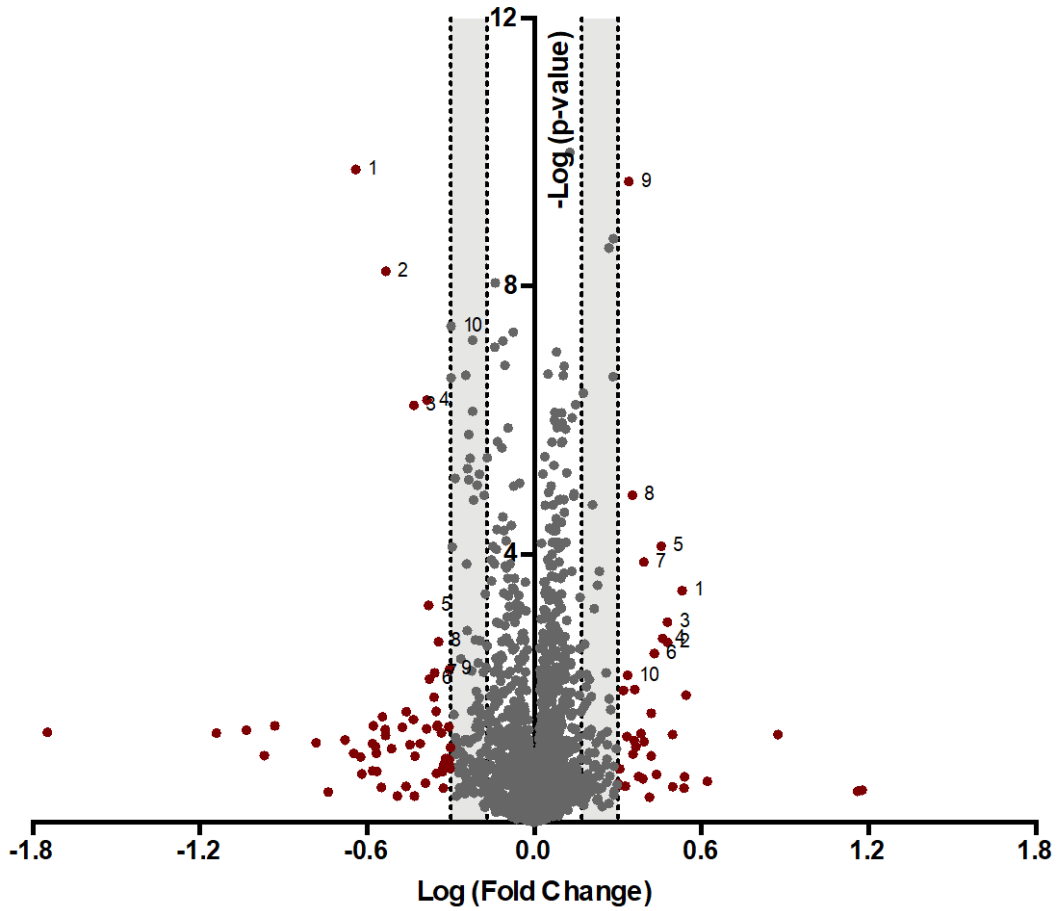


**Figure 4.12: Comparative proteomics of CHIP WT and CHIP KO iPSC lines**
SWATH-MS analysis of the CHIPS WT (CRISPR control) compared to CHIP KO iPSC lines. Cut off criteria (≤0.5 and ≥2 or ≤0.67 and ≥1.5 fold change) are represented by the dotted lines and shaded areas. Proteins (dots) that do not meet this fold change criteria are colour-coded in grey and does that do are in red. Over-represented proteins in the CHIP KO sample compared to WT have negative log (fold change), while under-represented proteins have positive values. The top 10 most under- and over-represented proteins that were significantly changed ($P < 0.05$) are numbered.

### b. Differentiated SH-SY5Y cell lines

The proteome of undifferentiated SH-SY5Y was previously analysed by SWATH-MS[95] (work performed by Erisa Nita and Jakub Faktor), using the same methodology and instrumentation as for the analysis of cortical neurons. Although some SH-SY5Y lines express immature neuronal markers in its basal state, differentiation drives the expression of mature neuronal markers and a more complex neuron-like morphology. It has been reported that during the course of differentiation, cells become post-mitotic, neuritic processes form and extend, there is increased excitability of the plasma membrane, formation functional synapses and induction of neuron-specific enzymes, neurotransmitters and receptors[118].

To investigate the effect of CHIP on the proteome of a different neuronal-like model, differentiated SH-SY5Y cells were used. Markers of neuronal identity were detected in the proteomic analysis, such as multiple transporters (e.g. sodium/potassium-transporting ATPase and various amino acid transporters), synaptic markers (e.g. synaptogyrin, synpatophysin and synaptic vesicle proteins) and other neuronal markers (e.g. cell cycle exit and neuronal differentiation protein 1 and the neuron-specific β(III)-tubulin, which was also validated by IF, Figure S.4). These features confirm the neuronal-like identity of the neurons and the fact that the majority had similar fold changes in CHIP KO and WT cells suggests that their differentiation state was comparable. Nevertheless, the type of the neurons obtained is unclear and likely to have some degree of variable due to the genomic instability of the SH-SY5Y cell line. Markers of adrenergic, cholinergic and dopaminergic neurons have been reported for differentiated SH-SY5Y lines using retinoic acid[118]. However, this line differentiates into tyrosine hydroxylase-negative neurons (supported by our SWATH-MS data and previous results, not shown), thus it is unlikely that the neurons are dopaminergic nor adrenergic. Additionally, the absence of dopamine transporters and markers of dopaminergic progenitors from the SWATH-MS data supports this. The presence of multiple acetyltransferase enzymes and components would suggest the samples have some cholinergic identity. The comparative proteomic analysis of differentiated SH-SY5Y WT versus CHIP KO cells is represented in Figure 4.13 and mostly changed proteins are listed in Table S.9 & Table S.10. Again, the vast majority of proteins identified have similar fold changes.

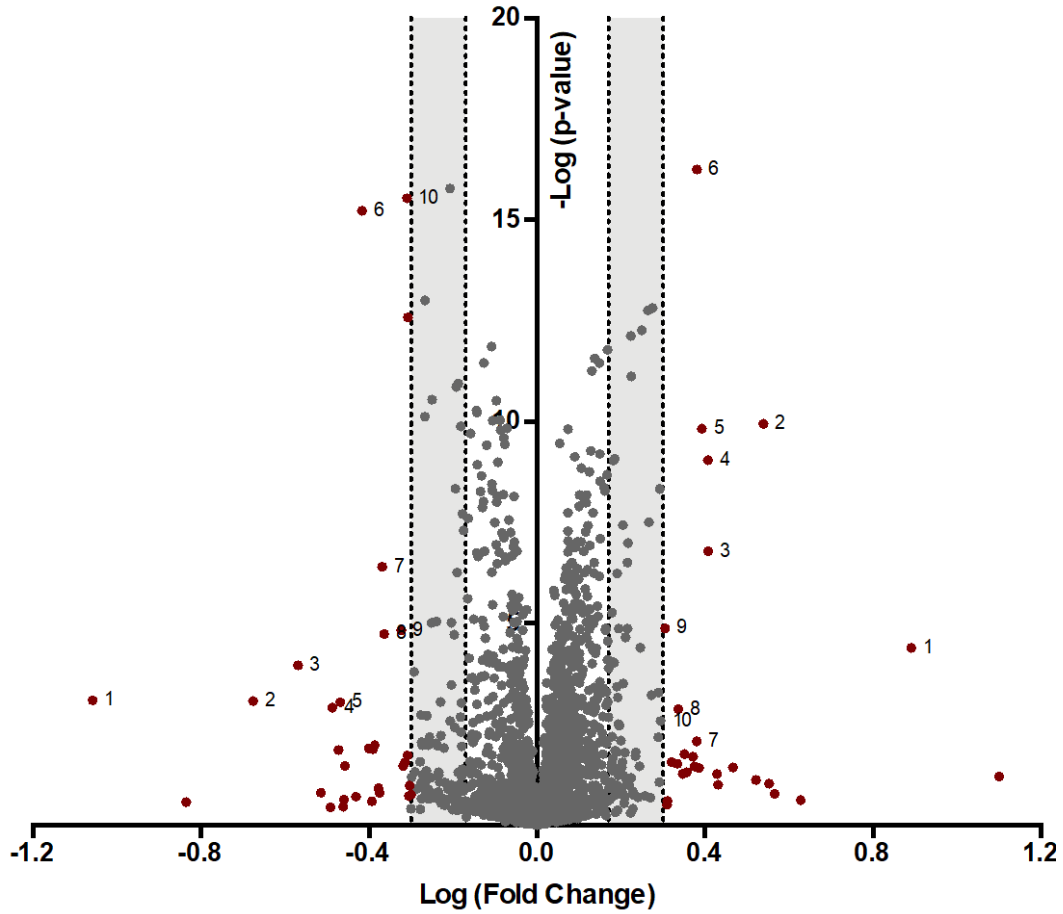


**Figure 4.13: Comparative proteomics of CHIP WT and CHIP KO differentiated SH-SY5Y cells**

SWATH-MS analysis of the CHIPS WT (CRISPR control) compared to CHIP KO differentiated SH-SY5Y cells. Cut off criteria (≤0.5 and ≥2 or ≤0.67 and ≥1.5 fold change) are represented by the dotted lines and shaded areas. Proteins (dots) that do not meet this fold change criteria are colour-coded in grey and does that do are in red. Over-represented proteins in the CHIP KO sample compared to WT have negative log (fold change), while under-represented proteins have positive values. The top 10 most under- and over-represented proteins that were significantly changed ($P < 0.05$) are numbered.

### c. Comparing the SWATH-MS analyses of different CHIP KO models with the cortical neuron model

All SWATH-MS experiments (iPSC WT vs KO, differentiated SH-SY5Y WT vs KO and both WT vs KO and P vs KO of cortical neurons) were compared to each other (Figure 4.14). When assessing all proteins identified, 1240 proteins overlapped across all comparative proteomic screens. This reduces to 5 proteins (Table 4.3) when applying cut-off criteria (fold changes <0.67 and >1.5).

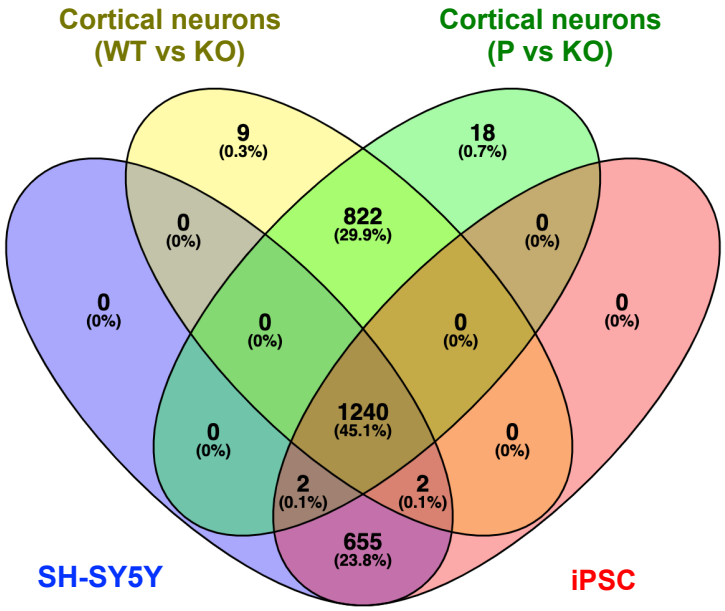


**Figure 4.14: Overlap of comparative proteomics of different CHIP models**
SWATH-MS analyses comparing CHIP WT with CHIP KO across different cell lines in both undifferentiated state (iPSC and cycling SH-SY5Y) and differentiated state (cortical neurons and neuronal-like SH-SY5Y cells). SWATH-MS experiments of cortical neurons include two control cells lines (derived from the CRISPR control, WT, and the parental line, P, iPSC lines). All proteins identified were included.

**Table 4.3: Potential proteins of interest shared between cortical neurons, differentiated SH-SY5Y and iPSC**

| Proteins | Cortical (WT vs KO) | | Cortical (P vs KO) | | Differentiated SH-SY5Y | | iPSC | |
|---|---|---|---|---|---|---|---|---|
| | Fold change | p-value | Fold change | p-value | Fold change | p-value | Fold change | p-value |
| Galectin-3 | 0.120 | 5.51E-06 | 0.108 | 4.56E-06 | 2.019 | 1.33E-05 | 2.748 | 1.93E-01 |
| Gelsolin | 0.320 | 5.53E-08 | 0.347 | 5.25E-08 | 1.502 | 3.84E-02 | 0.559 | 1.29E-01 |
| 2,4-dienoyl-CoA reductase, mitochondrial | 0.661 | 8.13E-03 | 0.656 | 1.93E-03 | 0.503 | 6.60E-02 | 0.475 | 1.55E-01 |
| Histone H2A type 2-A | 2.185 | 6.30E-04 | 0.592 | 2.47E-02 | 7.783 | 4.07E-05 | 1.825 | 1.14E-01 |
| Glutaredoxin-related protein 5, mitochondrial | 2.452 | 1.94E-01 | 1.507 | 4.08E-01 | 0.602 | 3.23E-01 | 1.856 | 5.23E-01 |

Focusing on significantly changing proteins, some are shared between the proteomics of cortical neurons and iPSC (Table 4.4). Therefore, these proteins could be influenced by the presence of CHIP and might be independent of the differentiation statues of cells. Furthermore, a few proteins were shared in common between the both SWATH-MS analyses of the cortical neurons and differentiated SH-SY5Y (Table 4.5). These could be influenced by CHIP expression and be dependent on a neuronal-like phenotype. Alternatively, proteins shared in common are related it the differentiated state of the cell lines.

**Table 4.4: Potential proteins of interest shared between cortical neurons and iPSC**

| Proteins | Cortical (WT vs KO) | | Cortical (P vs KO) | | iPSC | |
|---|---|---|---|---|---|---|
| | Fold change | p-value | Fold change | p-value | Fold change | p-value |
| Caldesmon | 0.116 | 5.89E-05 | 0.168 | 1.30E-04 | 0.502 | 3.92E-08 |
| Transgelin-2 | 0.148 | 4.49E-06 | 0.275 | 8.41E-06 | 0.583 | 7.74E-06 |
| Annexin A1 | 0.171 | 3.25E-08 | 0.274 | 2.09E-07 | 0.229 | 1.81E-10 |
| Prelamin-A/C | 0.257 | 6.47E-06 | 0.238 | 3.48E-06 | 0.588 | 3.69E-06 |
| Transgelin | 0.311 | 2.27E-03 | 0.337 | 4.18E-03 | 0.582 | 1.63E-06 |
| Neuroblast differentiation-associated protein AHNAK | 0.328 | 1.24E-02 | 0.349 | 1.72E-02 | 0.420 | 7.29E-03 |
| CD99 antigen | 0.339 | 1.56E-07 | 0.503 | 1.28E-06 | 0.469 | 1.60E-01 |
| Calponin-3 | 0.382 | 7.98E-07 | 0.521 | 1.85E-05 | 0.545 | 3.64E-03 |
| Galectin-1 | 0.363 | 5.10E-03 | 0.320 | 2.30E-04 | 0.412 | 5.01E-07 |
| Probable ubiquitin carboxyl-terminal hydrolase FAF-X | 0.487 | 4.80E-06 | 0.439 | 2.55E-06 | 0.662 | 1.32E-05 |
| Neural cell adhesion molecule L1 | 1.761 | 4.30E-04 | 1.531 | 7.78E-03 | 0.282 | 3.01E-01 |
| 6-phosphogluconate dehydrogenase, decarboxylating | 1.935 | 1.66E-15 | 1.907 | 9.78E-18 | 2.186 | 2.71E-10 |
| F-box only protein 2 | 2.667 | 4.37E-06 | 2.217 | 4.62E-05 | 0.601 | 6.32E-08 |

**Table 4.5: Potential proteins of interest shared between cortical neurons and differentiated SH-SY5Y**

| Proteins | Cortical (WT vs KO) | | Cortical (P vs KO) | | Differentiated SH-SY5Y | |
|---|---|---|---|---|---|---|
| | Fold change | p-value | Fold change | p-value | Fold change | p-value |
| Midkine | 0.426 | 2.57E-08 | 0.310 | 1.42E-09 | 0.661 | 2.64E-01 |
| Heat shock protein beta-1 | 0.456 | 1.76E-09 | 0.503 | 1.20E-07 | 0.621 | 1.68E-16 |
| Plectin | 0.457 | 2.04E-07 | 0.535 | 1.86E-06 | 0.545 | 2.15E-01 |

SWATH-MS analysis of undifferentiated SH-SY5Y was previously conducted by Erisa Nita in collaboration with Dr Jakub Faktor and Dr Bořivoj Vojtesek[‡95]. When comparing the proteomes of undifferentiated and differentiated SH-SY5Y (WT vs KO) cells (Figure 4.15A), the majority of the proteins identified in common are unchanged in both comparative proteomics. Some proteins are over- and under-represented in both SWATH-MS experiments, such as the neurofilament light polypeptide. However, most of the proteins of interest derived from the analysis of cortical neurons (the Annexin proteins, S100-A11 and superoxide dismutase) are unchanged in these cell lines.

Figure 4.15B-D assess how comparable the proteomes of the undifferentiated and differentiated SH-SY5Y and iPSC models with isogenic *STUB1* deletions are to the cortical neurons, respectively. In these two-dimensional comparative proteomics plots (comparing two CHIP WT/KO conditions), the majority of the proteins detected in common show no change (i.e. fold changes close to 1) in both conditions. These accumulate at the *xy* intersection (as $Log_2$ fold changes are plotted). Moreover, proteins have a stochastic distribution and do not fit into a linear regression (evident from the Pearson coefficient close to 0), as fold changes tend to have varying magnitudes and directions in the paired conditions analysed. However, when focusing on the potential proteins of interest, these are more similar in the comparisons of either undifferentiated SH-SY5Y cells or iPSC with cortical neurons. In these plots, some proteins of interest are found in quadrants II and III, being under-represented in the SH-SY5Y or iPSC and under-/over-represented in cortical neurons. In contrast to the differentiated SH-SY5Y cells compared to cortical neurons, where proteins of interest tend to be close to the *x*-axis (i.e. changing in the cortical neurons only).

[‡] Regional Centre for Applied Molecular Oncology, Masaryk Memorial Cancer Institute, Brno, Czech Republic

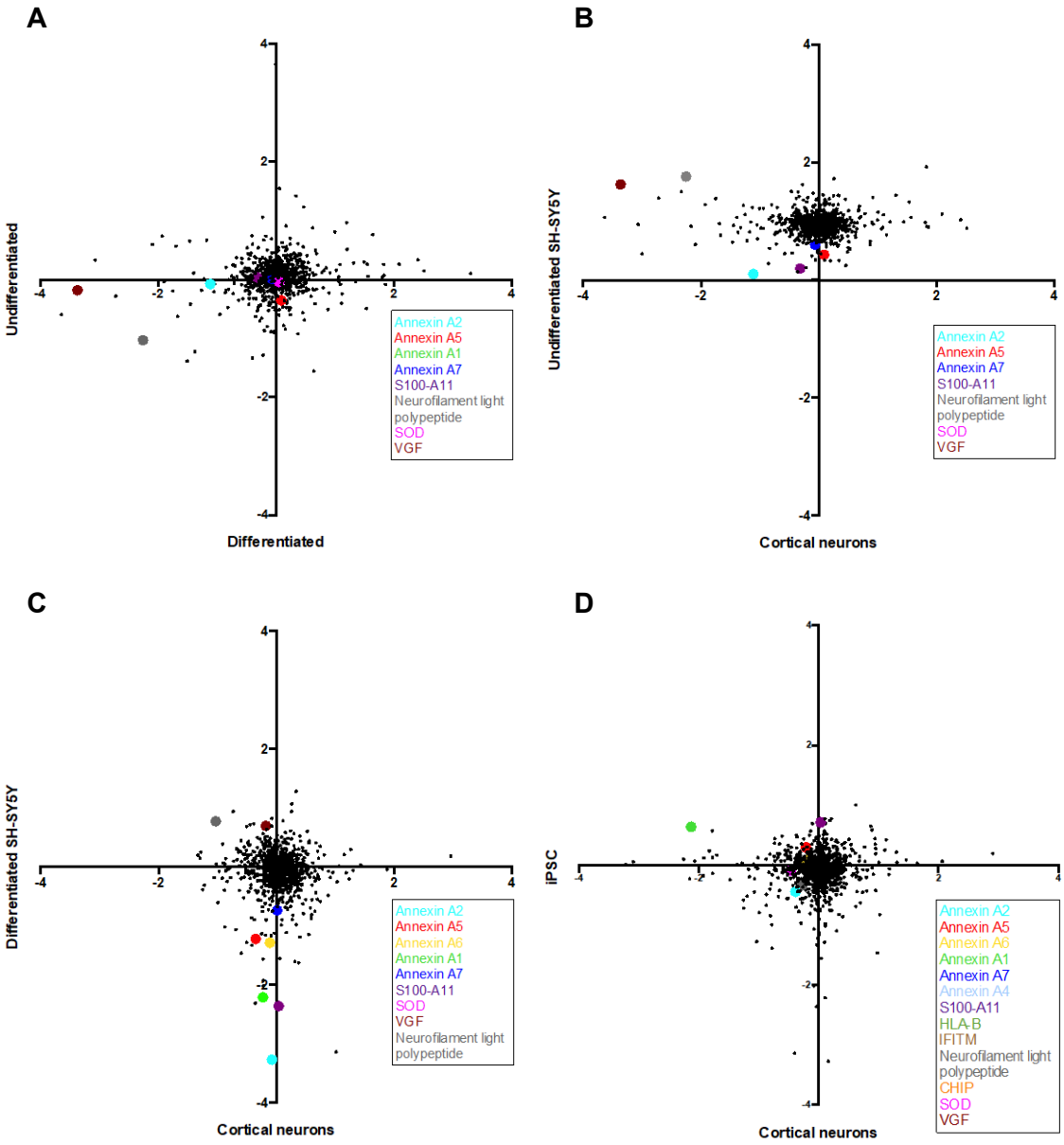


**Figure 4.15: Comparing the proteomic differences between CHIP WT and KO across different cell lines and differentiation statuses**

$Log_2$ fold changes of proteins identified in both SWATH-MS experiments are plotted. Proteins of particular interest are colour-coded.

**A)** Undifferentiated and differentiated SH-SY5Y cells. Pearson correlation: $r$ = 0.1339, $r^2$ = 0.0180 and $P$ value (two-tailed) < 0.0005 (***).

**B)** Undifferentiated SH-SY5Y cells and cortical neurons. The average of the WT/KO and P/KO comparative proteomics of cortical neurons was plotted. Pearson correlation: $r$ = 0.017, $r^2$ = 0.0003 and $P$ value (two-tailed) = 0.6275 (*ns*).

**C)** Differentiated SH-SY5Y cells and cortical neurons. The average of the WT/KO and P/KO comparative proteomics of cortical neurons was plotted. Pearson correlation: $r$ = -0.0397, $r^2$ = 0.0016 and $P$ value (two-tailed) = 0.1958 (*ns*).

**D)** iPSC and cortical neurons. The average of the WT/KO and P/KO comparative proteomics of cortical neurons was plotted. Pearson correlation: $r$ = 0.0321, $r^2$ = 0.0010 and $P$ value (two-tailed) = 0.2958 (*ns*).

## 4.2.4 Validation of proteomic analysis

The variability of proteins of interest across the comparative proteomics of cortical neurons (with same and different CHIP genotypes) was plotted in Figure 4.16 (taking into account fold changes and statistical significance). For the majority of the proteins, WT vs KO and P vs KO data converges in one quadrant, separate from the P vs WT data. Annexins, S100-A11, HLA-B and IFITM are over-represented in CHIP KO, while VGF, SOD and, as expected, CHIP are under-represented.

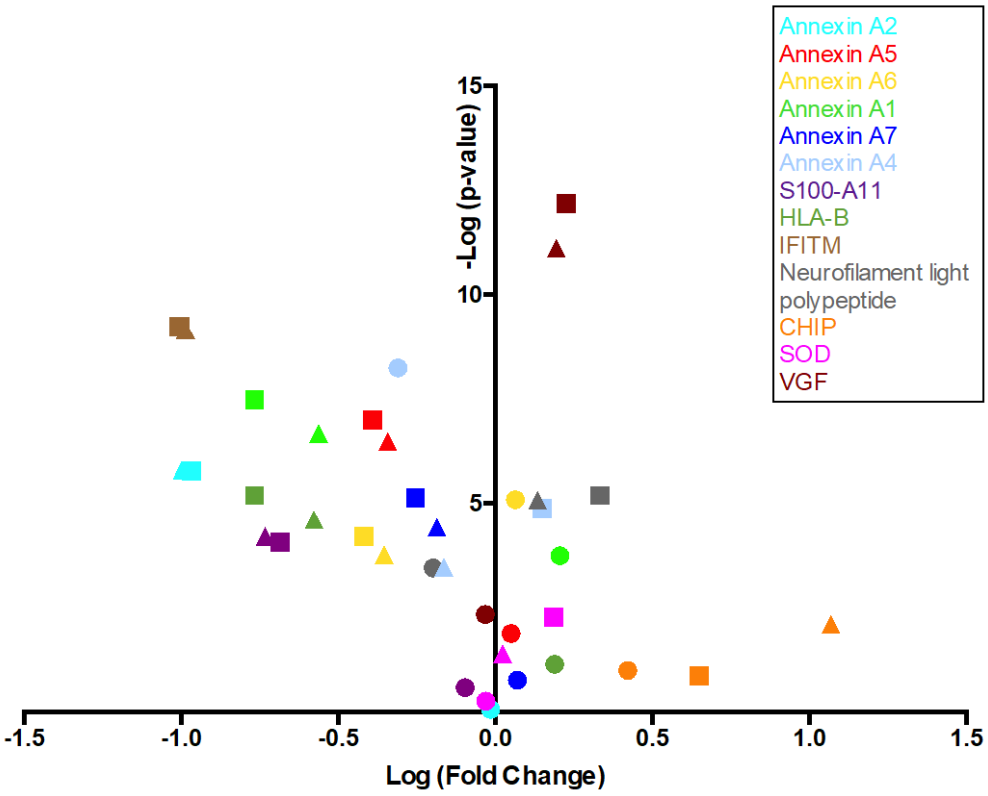


**Figure 4.16: Proteins of interest identified across the comparative proteomic analyses of cortical neurons of different CHIP genotypes**
Data from the SWATH-MS comparing CHIP-expressing (P and WT) neurons to KO are represented as triangles and squares, respectively, while the proteins from the comparative proteomics of CHIP-expressing neurons (P/WT) are displayed as circles. Proteins of interest are colour-coded and meet the cut-off criteria for at least one comparative proteomics analysis of cells with different CHIP genotypes.

It is important to take into account that the intensities of the peptides detected by MS are affected by a combination of factors including the post-translational modifications and inter-molecular interactions (including the degree of aggregation, which is particularly relevant for α-Syn), which can affect how proteins are cleaved by trypsin during sample preparation for MS. Additionally, peptides have different compatibilities with MS detection, in terms of ionization and fragmentation potential[137]. For all these reasons, whether a protein seems to be over- or under-represented in the CHIP KO relative to the control samples needs to be taken with caution and validation is required.

Thus, preliminary validation of the MS data was performed by analysing a selection of both under and over-represented proteins with different cellular functions, particularly those that have not been previously linked to CHIP. Furthermore, preliminary experiments investigating the same proteins of interest in different CHIP models, suggest whether these can be used for supporting experiments in parallel to cortical neurons.

### a. Human leukocyte antigen B

Human leukocyte antigen B (HLA-B) was over-represented in the MS analysis in CHIP KO neurons. This protein was selected for further validation given the previously reported CHIP-dependent regulation of IRF1, supporting its role in immunity[77], and the emerging link between cellular proteostasis and innate immunity[138].

The expression of HLA-B in the cortical neurons was evaluated using both WB (Figure 4.17A) and IF (Figure 4.17B). Although the former showed an increase in HLA-B expression in CHIP KO neurons that was above the level of detection of this assay for this line only, the most striking phenotype was observed by IF. HLA-B was highly expressed the nucleus, cytoplasm and axons of the CHIP KO neurons and had only faint puncta in the nucleus in WT cells. The difference in homeostasis of HLA-B between CHIP KO and WT cells was not seen in iPSC (Figure 4.18), thus it may be cell-type specific or the overexpression observed in CHIP KO cortical neurons is not due to the presence of CHIP.

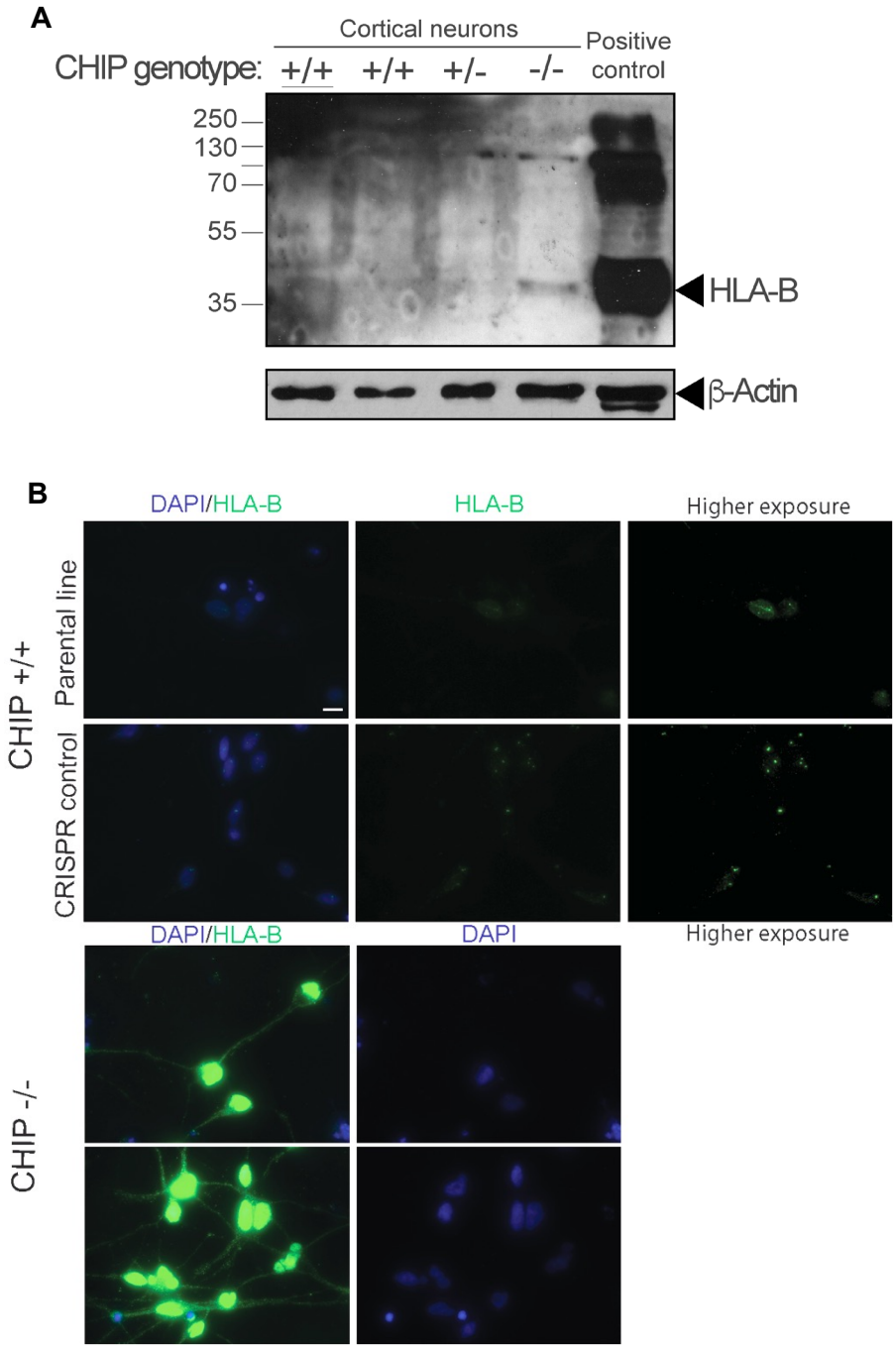


**Figure 4.17: Expression of HLA-B in CHIP KO and WT cortical neurons**
**A)** Mature iPSC-derived cortical neurons (harvested at day 80 of differentiation) were lysed with urea-based lysis buffer (the same as that used for SWATH-MS). CHIP homozygous (-/-) and heterozygous (+/-) KO neurons, as well as two CHIP-expressing lines (the parental line (+/+) and the CRISPR control (+/+)) were analysed. For each sample, 18 µg of lysate was loaded per 12% gel for SDS-PAGE/WB and two gels were ran together (in the same apparatus). Lysate from IFNγ-treated SiHa cells was also included as positive control. One immunoblot was probed with a mix of anti-HLA-A pAb, anti-HLA-B pAb and HLA-C mAb (each 1:500) and the other with anti-b-actin mAb (1:5000).
**B)** Mature iPSC-derived cortical neurons of different CHIP genotypes were fixed with 4% PFA (harvested at day 80 of differentiation). Neurons were stained with anti-HLA-B pAb (1:100) and DAPI (nuclear stain). Images are z-projections (maximal projection) from stacks. Axio Imager, Zeiss. Scale bar, 10 µm.

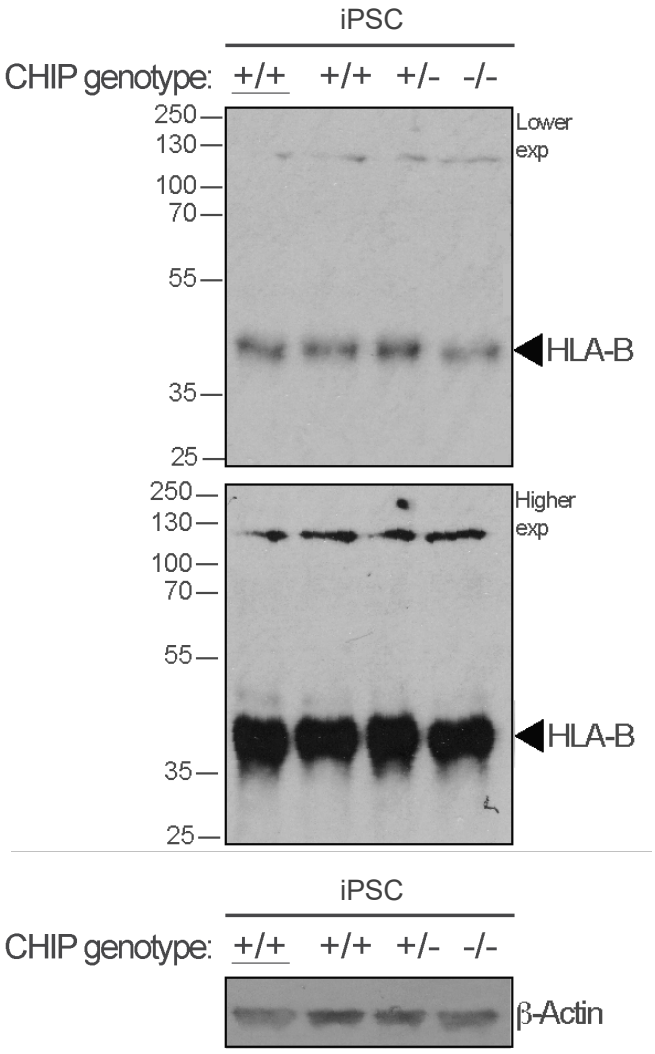


**Figure 4.18: Expression of HLA-B in CHIP KO and WT iPSC lines**
iPSC were lysed with urea-based lysis buffer (the same as that used for SWATH-MS). CHIP homozygous (-/-) and heterozygous (+/-) KO neurons, as well as two CHIP-expressing lines (the parental line (+/+) and the CRISPR control (+/+)) were analysed. For each sample, 20 µg of lysate was loaded per 12% gel for SDS-PAGE/WB and two gels were ran together (in the same apparatus). Lysate from IFNγ-treated SiHa cells was also included as positive control. One immunoblot was probed with a mix of anti-HLA-A pAb, anti-HLA-B pAb and HLA-C mAb (each 1:500) and the other with anti-b-actin mAb (1:5000).

HLA-B was identified by SWATH-MS by 3 unique peptides. One of these peptides (FIAVGYVDDTQFVR) has 100% sequence homology to HLA-A and HLA-C, while another peptide (THVTHHPVSDHEATLR) has 88% and 100%, respectively. Therefore, although the software assigned HLA-B to this peptide fingerprint, HLA-A and HLA-C should not be excluded. Only HLA-C was identified in the proteomics of iPSC and differentiated SH-SY5Y cells, although it was unchanged between CHIP genotypes (with fold changes of 0.990 and 0.534, respectively, and non-significant *P* values).

### b. VGF

Neurosecretory VGF, on the other hand, lies within the list of protein under-represented in the CHIP KO cortical neurons. The protein showed no significant change in cortical neurons by WB (Figure 4.19), but a significant decrease by IF in CHIP KO compared to CHIP-expressing neurons (Figure 4.20). Therefore, the SWATH-MS and IF data correlate with each other.

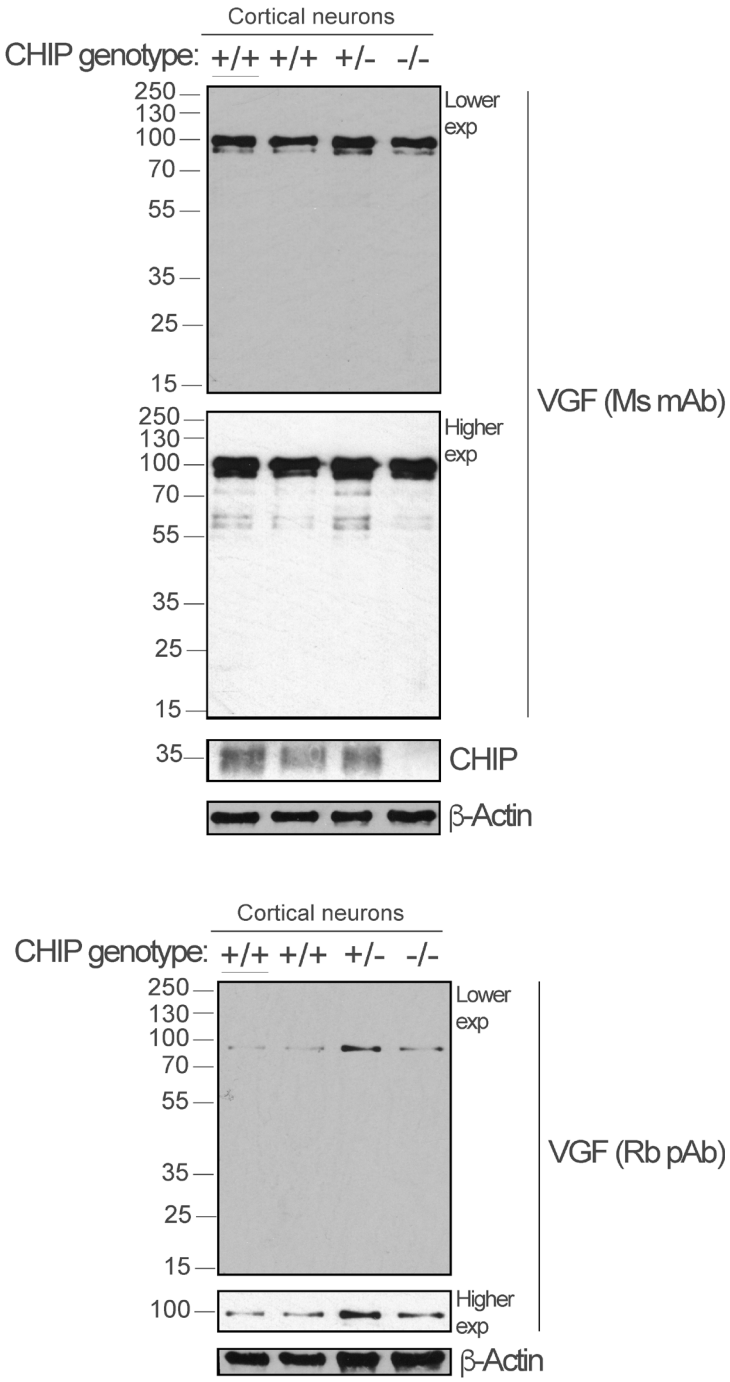


**Figure 4.19: Expression of VGF in CHIP KO and WT cortical neurons by WB**
Mature iPSC-derived cortical neurons (harvested at day 80 of differentiation) were lysed with urea-based lysis buffer (the same as that used for SWATH-MS). CHIP homozygous (-/-) and heterozygous (+/-) KO neurons, as well as two CHIP-expressing lines (the parental line (+/+) and the CRISPR control (+/+)) were analysed. For each sample, 20 µg of lysate was loaded per 12% gel for SDS-PAGE/WB and two gels were ran together (in the same apparatus). An immunoblot was probed with anti-VGF Ms mAb (1:500) and the other immunoblot with anti-VGF pAb (1:5000). The former immunoblot was then incubated with anti-CHIP mAb (1:10000). Finally, both immunoblots were probed with anti-β-actin mAb (1:5000).

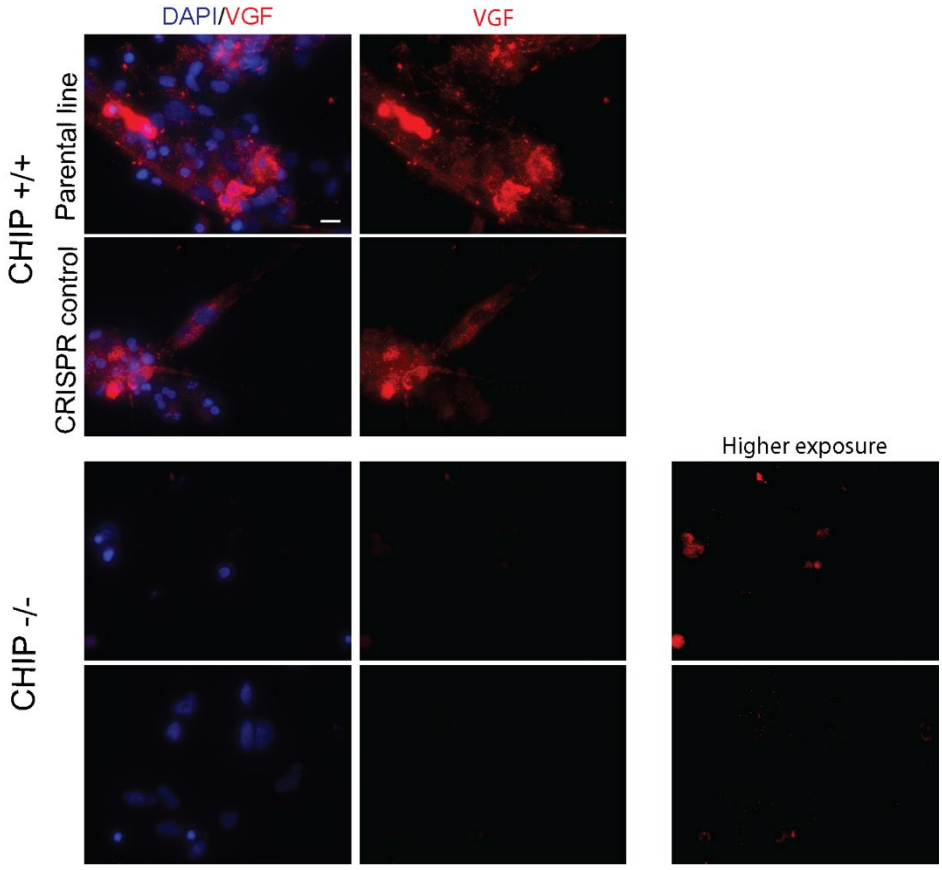


**Figure 4.20: Expression of VGF in CHIP KO and WT cortical neurons by IF**
Mature iPSC-derived cortical neurons of different CHIP genotypes were fixed with 4% PFA (harvested at day 80 of differentiation). Neurons were stained with anti-VGF mAb (1:1000) and DAPI (nuclear stain). Images are z-projections (maximal projection) from stacks. Axio Imager, Zeiss. Scale bar, 10 μm.

Previously, VGF was the single protein significantly changing across SWATH-MS experiments of multiple SH-SY5Y CHIP KO clones (work by Erisa Nita[95]). It is overexpressed in CHIP KO undifferentiated SH-SY5Y and showed increased processing into smaller fragments (Figure 4.21). This over-expression is also seen in CHIP KO differentiated SH-SY5Y. However, these cells display a decrease in lower MW isoforms and an increase in higher MW ones (Figure 4.21). Given the complex homeostasis of VGF in SH-SY5Y cells, it is unclear how it compares to cortical neurons.

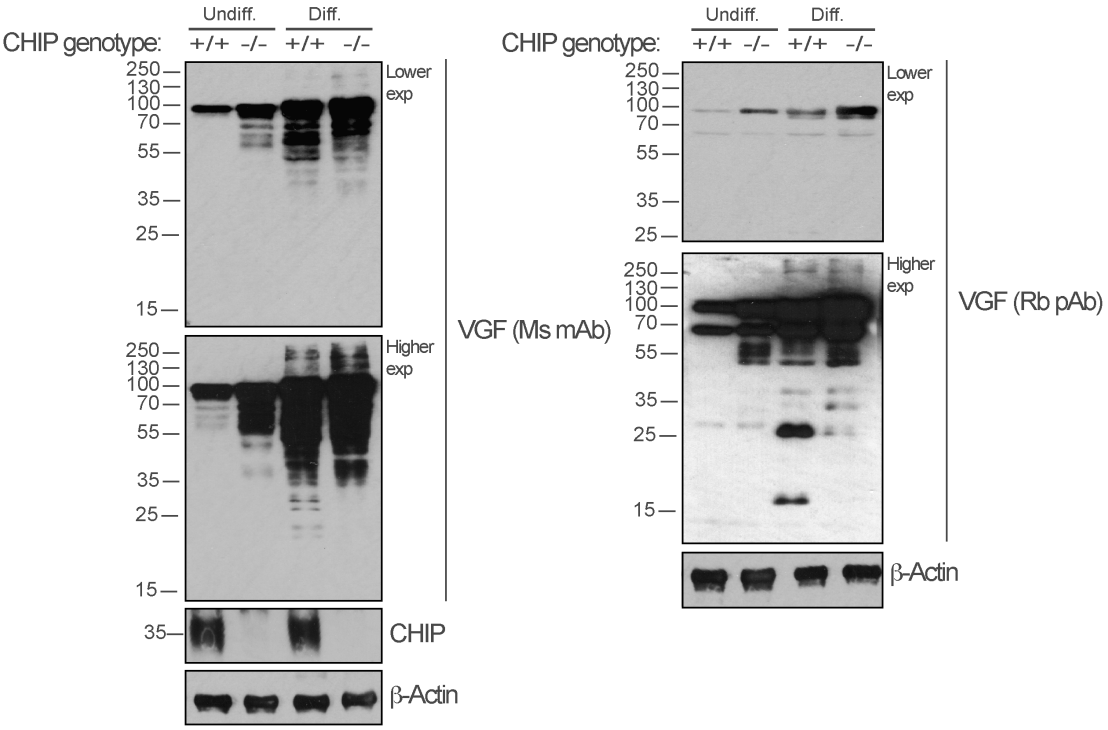


**Figure 4.21: Expression of VGF in CHIP KO and WT undifferentiated and differentiated SH-SY5Y cells**
Undifferentiated and differentiated CHIP KO and WT SH-SY5Y cells were lysed with urea-based lysis buffer (the same as that used for SWATH-MS). For each sample, 20 µg of lysate was loaded per 12% gel for SDS-PAGE/WB and two gels were ran together (in the same apparatus). An immunoblot was probed with anti-VGF Ms mAb (1:500) and the other immunoblot with anti-VGF pAb (1:5000). The former immunoblot was then incubated with anti-CHIP mAb (1:10000). Finally, both immunoblots were probed with anti-β-actin mAb (1:5000).

### c. Membrane proteins

Interestingly, multiple Annexin proteins and other proteins with known roles in maintenance of membrane integrity and repair reported in the literature, were detected in the MS analysis. These tend to be over-represented in the CHIP KO neurons and are largely unchanged when comparing the CHIP-expressing lines with each other, as seen in Figure 4.22. As evidence that of their detection and relative abundance in CHIP WT and KO cells, the mass spectra of a subset of these proteins, namely Annexin A2 (ANXA2) (Figure 4.23) and S100-A11 (Figure 4.24), was analysed closely. The *b* and *y* ions from unique peptides that identify ANXA2 and S100-A11 were greatly increased in the CHIP KO cortical neurons compared to WT. The steady state levels of ANXA2 and S100-A11 were also evaluated by IF (Figure 4.25) and WB (Figure 4.26A), respectively. By this validation method, the over-representation of ANXA2 by SWATH-MS was not observed. Thus, different pools of ANXA2 are being detected by the different methods. The WB to assess S100-A11 protein levels, on the other hand, following the trend observed by SWATH-MS, being enriched in the CHIP KO cortical neurons. Chapter 5 focuses on membrane proteins in the presence and absence of CHIP.

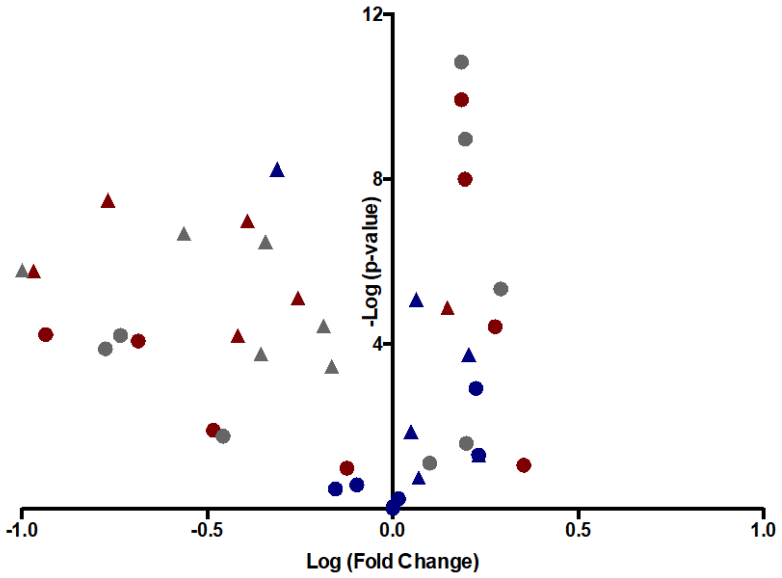


**Figure 4.22: Identified proteins with known roles in maintenance of membrane integrity** Proteins include: Annexin A1, A2, A4, A5, A6 and A7, protein S100-A11, Caldesmon, Syntaxin-1B, Synaptosomal-associated protein 29, Neuroblast differentiation-associated protein AHNAK and Ras-related proteins Rab-3C, 3B and 5C. Proteins from the Annexin family are represented as triangles. Data from the SWATH-MS comparing CHIP-expressing (P and WT) neurons to KO are represented in grey and red, respectively, while the proteins from the comparative proteomics of CHIP-expressing neurons (P/WT) are displayed in blue.

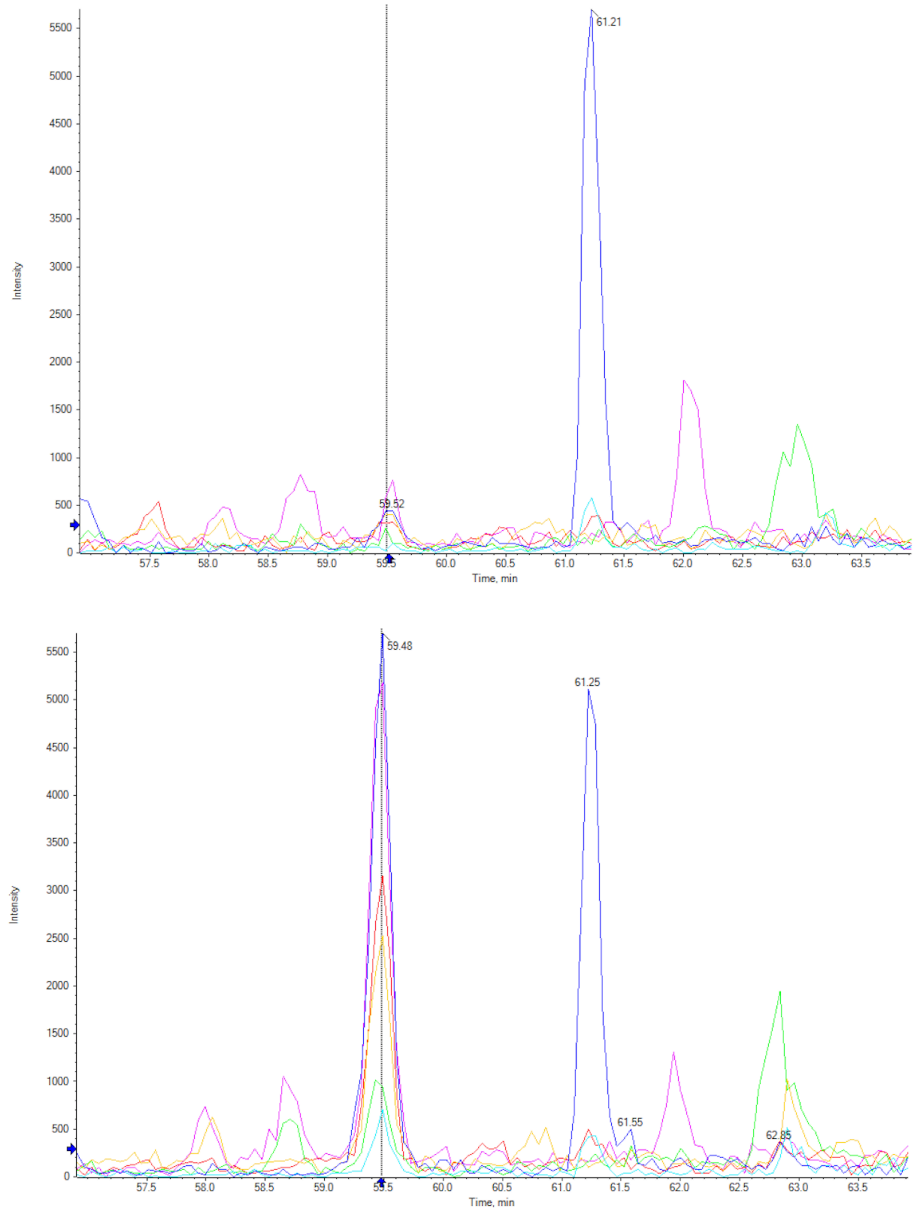


**Figure 4.23: Mass spectra of product ions detected that identified and quantified Annexin A2 in WT** *(top)* **and CHIP KO** *(bottom)* **cortical neurons by SWATH-MS**
The product ions of the unique peptide of Annexin A2, TPAQYDASELK, were detected in the *m/z* swath of 603-616 (normalised to 611.80) and RT = 60.43 min. Product ions detected: *y9* (indigo), *y7* (magenta), *y8* (red), *y6* (yellow), *b9* (green) and *y10* (cyan). One biological and technical replicate for each cell line is represented, but other biological and technical replicates (each *n*=3) are similar.

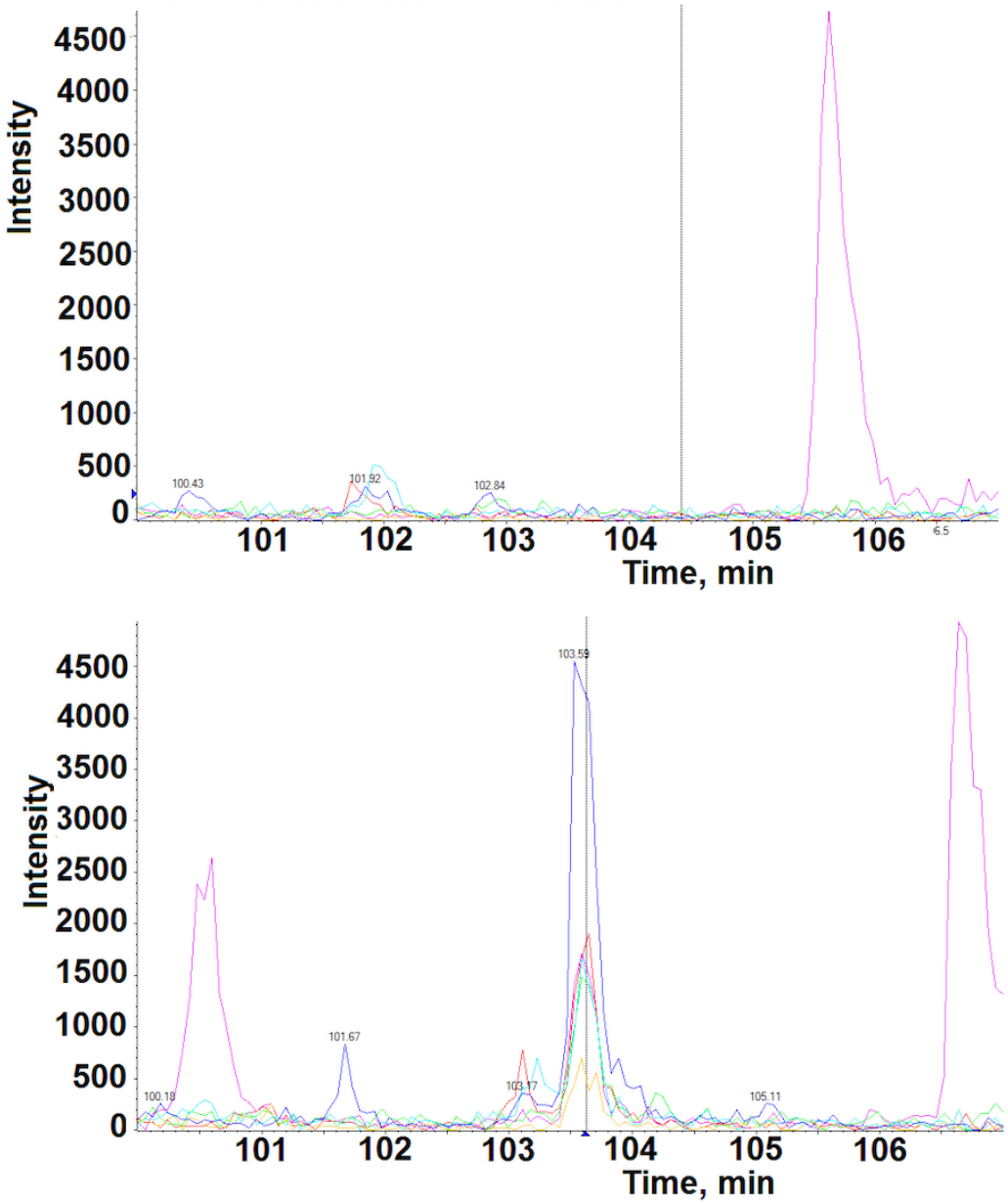


**Figure 4.24: Mass spectra of product ions detected that identified and quantified S100-A11 in WT** *(top)* **and CHIP KO** *(bottom)* **cortical neurons by SWATH-MS**
The product ions of the unique peptide of S100-A11, CIESLIAVFQK, were detected in the *m/z* swath 651-664. Product ions detected: *y9* (indigo), *y8* (magenta), *y6* (red), *y7* (yellow), *y5* (green) and *y3* (cyan). One biological and technical replicate for each cell line is represented, but other biological and technical replicates (each *n*=3) are similar.

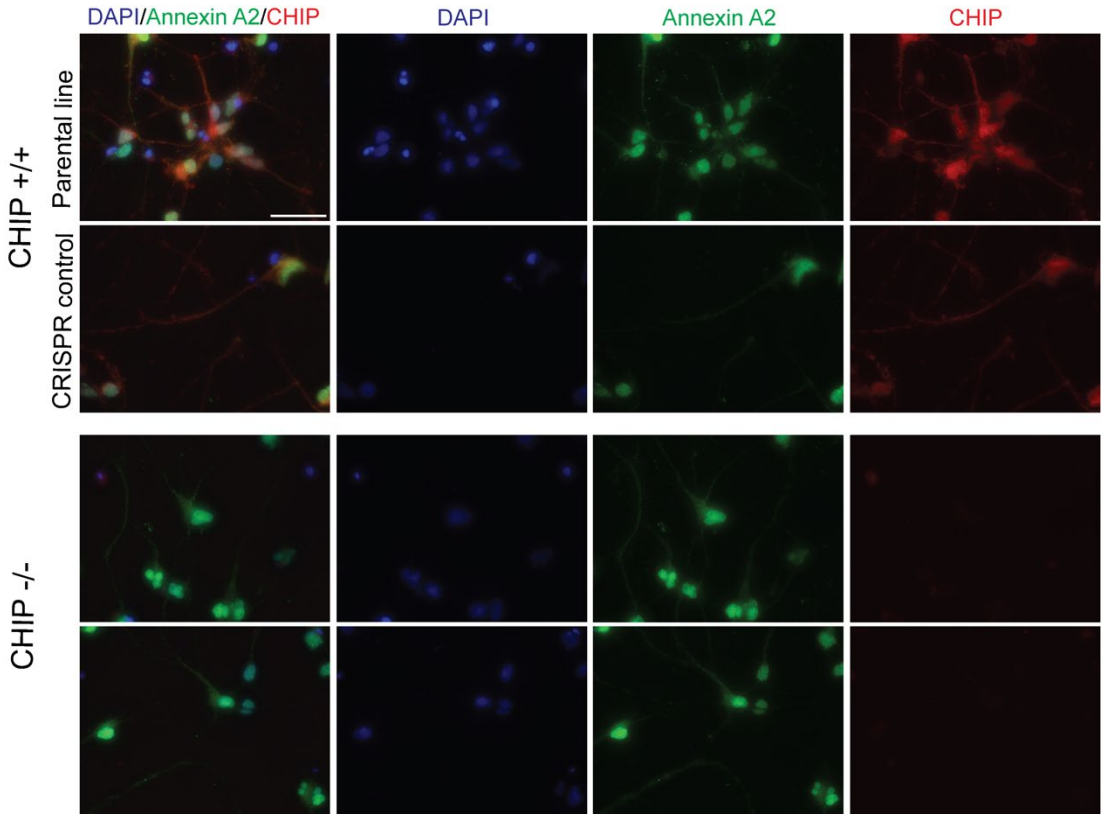


**Figure 4.25: Expression of ANXA2 in CHIP WT and KO cortical neurons**
Mature iPSC-derived cortical neurons of different CHIP genotypes were fixed with 4% PFA (harvested at day 80 of differentiation). Neurons were stained with anti-Annexin A2 pAb (1:500), anti-CHIP mAb (1:1000) and DAPI (nuclear stain). Images are z-projections (maximal projection) from stacks. Axio Imager, Zeiss, 63x objective. Scale bar, 100 μm. Images are representative of at least three biological replicates.

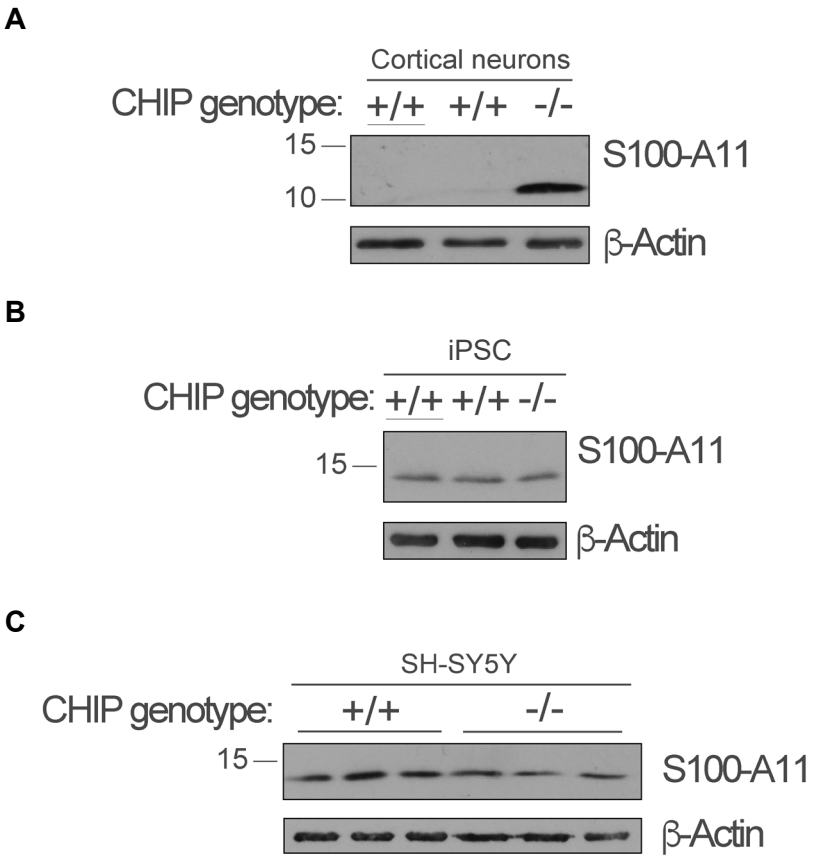


**Figure 4.26: Expression of S100-A11 in different CHIP cell models**
Mature iPSC-derived cortical neurons (harvested at day 80 of differentiation) **(A)**, iPSC **(B)** and undifferentiated SH-SY5Y cells **(C)** of different CHIP genotypes were lysed with urea-based lysis buffer (the same as that used for SWATH-MS). For each sample, 20 µg of lysate was analysed by 12% gel for SDS-PAGE/WB. The immunoblot was cut and probed with anti-S100-A11 pAb (1:1000) and anti-β-actin mAb (1:5000). Immunoblots are representative of at least two independent experiments.

Some of the membrane-related proteins identified in cortical neurons (in Figure 4.22) were also found in SH-SY5Y and iPSC. Their relative WT/KO fold changes were plotted together in Figure 4.27 for comparative purposes. S100-A11, for example, was also found to be expressed in these cell lines but its steady state level was not dependent on CHIP expression, as supported by the SWATH-MS data (Figure 4.27) and WB (Figure 4.26B&C). Once again, this validates the reliability of the SWATH-MS approach. Furthermore, this difference in S100-A11 proteostasis compared to cortical neurons suggests the existence of proteomic differences between cycling and differentiated cells.

However, there are also some similarities in the SWATH-MS data between cortical neurons and cycling cells. As in cortical neurons, ANXA2 is over-represented in CHIP KO undifferentiated SH-SY5Y cells (having a fold change of 0.460 compared to 0.104). Likewise, ANXA1, caldesmon-1 and AHNAK are over-represented in iPSC (0.229, 0.503 and 0.420, respectively, compared to the average fold changes of cortical neurons: 0.222, 0.142 and 0.339) (Figure 4.27). Therefore, in the context of membrane proteins of interest, it seems that the proteomes of undifferentiated SH-SY5Y cells and iPSC are similar to that of cortical neurons. Surprisingly, the proteostasis of these proteins of interest in differentiated SH-SY5Y cells seem to be the most different from cortical neurons.

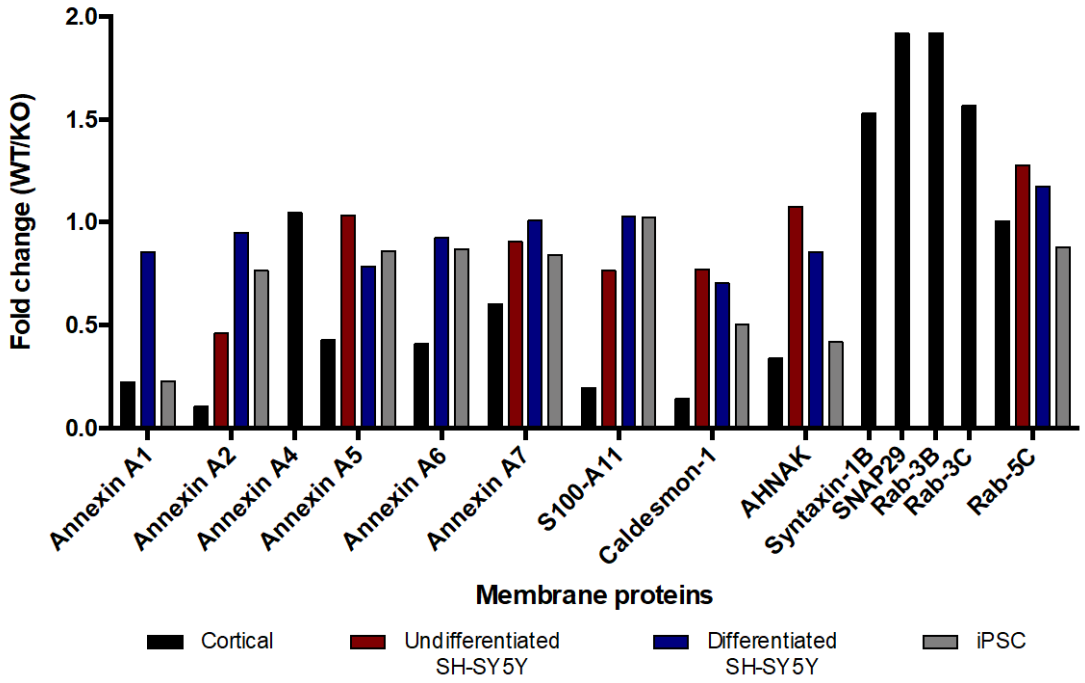


**Figure 4.27: Identified proteins with known roles in maintenance of membrane integrity across CHIP cell models**
Proteins known to have roles in membrane homeostasis identified across the comparative proteomics of different CHIP cell models were compared with regards to WT/KO fold changes.

## 4.3 Discussion

### 4.3.1 Proteomics to identify targets of chaperones and E3 ligases

Previous proteomic studies have investigated the effect of particular chaperones and E3 ligases on the proteome of cells. This includes deciphering their role in the maintenance of protein homeostasis and the size of its interactome (whether they regulate multiple or specific aspects of the proteome). By critically evaluating methods used we have decided to conduct an unbiased proteome-wide study to decipher the effects of this dual function, chaperone and E3 ligase, CHIP.

The identification of substrates of E3 ligases is particularly challenging. This is due to the low abundance of ubiquitinated species[139] (it is estimated that only 0.1-3% of substrates appear to be ubiquitinated[140] at any given time[141]) and the often transient interaction between a particular E3 ligase and its substrate. Consequently, studies have relied on the use of tagged proteins, overexpression systems or proteasomal inhibitors.

Traditional approaches to identify E3 substrates are based on the identification of interacting proteins[132]. For example, Galligan and his group[142] transfected cells with tagged fragments of the E3 ligase HERC for immunoprecipitation, followed by analysis by LC-MS/MS. This led to the identification of nearly 300 potential interactions. Although this approach has had some success for monomeric E3s, it is limited by the ability to successfully purify interacting proteins[132]. Furthermore, is not ideal for multimeric E3s due to the weak affinity that each subunit may have independently for the substrate[132]. We hypothesise that CHIP functions both as a monomer and multimer, having different substrate specificities (discussed in Chapter 6), thus may not be suitable for this assay. Furthermore, the use of tags and the overexpression *per se* may influence the biochemical properties of proteins, including their structure, function, regulation and interactome.

Another method in attempt to maximise the chances of identifying ubiquitinated proteins, has been the use of proteasome inhibitors to stabilise ubiquitinated proteins. Simplistically, the proteasome can be inhibited by various drugs leading to the accumulation of ubiquitinated proteins that have been destined to the UPS for

degradation[141,143,144]. The majority of the proteins that accumulate are regulatory proteins with short half-life and a signal-dependent turnover[141]. This introduces bias to the proteomics data derived. Furthermore, proteasomal inhibition results in proteome-wide effects beyond blocking substrate degradation, due to the complex feedback loop. Proteasome inhibition-induced unfolded protein response (UPR) blocks translation and stimulates other degradation pathways, such as autophagy[144]. Therefore, methods based on proteasomal inhibition are bias for the detection of certain ubiquitinated species and cause proteome-wide effects.

Despite the availability of multiple targeted approaches to detect ubiquitination substrates, their potential is hampered by inherent limitations. The use of tagged and overexpressed proteins and inhibitors alter the finely tuned dynamics of ubiquitination[145], thus are not representative of the *in vivo* scenario[140]. An unbiased proteome-wide investigation of E3 ligases may circumvent some of the challenges of identifying substrates. Here, the endogenous cellular environment is maintained, hence promoting the identification of targets with physiological significance. For these reasons, we decided to investigate the protein targets of CHIP using an unbiased proteome-wide mass spectrometry technique, SWATH-MS.

Although ubiquitinated proteins destined for degradation tend to have rapid destruction rates when these are not stabilised (e.g. with degradation inhibitors), the high sensitivity of proteomics (in particular DIA methods, such as SWATH-MS), in some cases, is enough to detect candidate substrates. Similarly, proteins ubiquitinated with non-canonical moieties (e.g. K63-linked Ub chain) can also be detected by SWATH-MS. In fact, protein-wide MS-based studies at basal conditions prevent bias towards the identification of canonical ubiquitination substrates. Substrates of non-canonical ubiquitination that are not destined for degradation are less known, as they tend to be missed in assays using proteasomal inhibitors, for example. Therefore, although proteome-wide SWATH-MS is an indirect approach to identify ubiquitinated proteins, it is likely to be informative.

To study the effect of CHIP on the proteome using an unbiased proteome-wide approach, we performed comparative proteomics on CHIP cell models in the presence and absence of CHIP. Such indirect manner to identify ubiquitinated species has been used in the past. The underlying rational is that in E3 ligase loss-of-function

assays the relative abundance of proteins ubiquitinated by the particular enzyme and destined for degradation may increase. For example, by analysing the proteome of cells expressing WT or an E3 ligase-defective mutant of a member of the cullin-RING ligase family (ASB2), filamin A and B were identified as substrates[132]. In the case of CHIP, we believed that such loss-of-function approach is less invasive to the cellular proteostasis compared to its overexpression. Overexpression of the TPR domain of CHIP, responsible for its chaperone activity, *per se* is likely to influence the interactome of chaperones and TPR-containing proteins, interfering with multiple cellular processes and masking the effect of its differential E3 ligase activity on the proteome.

### 4.3.2 CHIP is a docking-dependent, chaperone-independent E3 ligase with tight specificity

#### a. General effects of CHIP deletion on the proteome

The MS analysis of our iPSC-derived cortical neurons displayed similarities in neuronal-specific markers (e.g. synaptic vesicle proteins) across different samples, which can be regarded as an internal control, suggesting that samples have similar neuronal identities. Interestingly, the comparative proteomic analysis of patient-derived cortical neurons with and without CHIP expression demonstrated that only a few proteins (35 or 110 depending on the selection criteria, representing about 1.7% and 5.4% of the proteome analysed, respectively) could be directly or indirectly regulated by CHIP (Figure 4.10). Likewise, when comparing the proteomics data of the different CHIP cell models (cortical neurons, undifferentiated and differentiated SH-SY5Y and iPSC), out of the 1240 proteins identified in common (Figure 4.14), only 5 proteins (0.4%) were significantly changed (under- or over-represented) in all cell lines (Table 4.3). Visually, this is clear from the volcano plots of these SWATH-MS experiments, where the vast majority of proteins are unchanged (in grey) and the proteins of interest are outliers (in red) (including Figure 4.7 & Figure 4.8). Therefore, across different CHIP WT and KO cell lines, the deletion of this protein did not result in bulk changes to the proteome.

The predominant idea within the field describes CHIP as being like other chaperone-dependent E3 ligases with a broad range of substrates, thus capable of global

changes in the proteome. In agreement, Bhuripanyo and colleagues[146] identified 226 candidate E3 ligase substrates of CHIP. This includes previously reported CHIP substrates (including p53, BAG proteins and Hsp70), in addition to new substrates (kinase MAPK3, methyltransferase PRMT1, phosphatase PPP3CA, β-catenin and CDK4). Interestingly, this was achieved from an affinity-purified based MS assay with a functional component: using an orthogonal Ub transfer (OUT) assay in combination with the isolation of Ub-conjugates and MS analysis. For such, OUT ubiquitination enzymes and a modified His-Ub (used exclusively by the OUT enzymes and not native ubiquitination enzymes) were transfected into cells. Here, substrate identification is based on the transfer of Ub from a particular E3 to its ubiquitination targets, rather than on E3:substrate interactions, which tend to be transient. To our knowledge, this was the first proteomic analysis of CHIP to identify its E3 substrates. However, the system relies on the overexpression of Ub and ubiquitination enzymes, which compromises the reliability of the substrates identified with regards to its physiological significance.

The chaperone functions of CHIP have also contributed to the hypothesis of CHIP having a wide interactome. Chaperones are highly promiscuous, interacting transiently with thousands of substrate proteins and promoting their folding, trafficking and degradation[147]. The broad nature of its interactome was evident from a study conducted by Taipale *et al*.[147]. Here, 54 chaperones, cochaperone or quality-control factors were tagged with 3xFLAG and following affinity purification-MS, 486 high-confidence interactions were identified. This was organised into two tiers, the first containing Hsp70 and Hsp90 chaperone complexes and bridged by cochaperones including CHIP, and the second tier is its cochaperone-client interactions. The broad network of protein-protein interactions includes proteins involved in unrelated cellular processes (e.g. spindle assembly, DNA replication and mRNA decapping)[147]. Since CHIP was identified as a co-chaperone, some of its substrates might overlap with substrates of chaperones, such as Hsp70. However, it is unclear if, under basal conditions, CHIP shares the same broad interactome as chaperones and co-chaperones.

In fact, there is growing evidence suggesting that CHIP may have tight specificity and the ability to mediate direct recognition of its targets (in a chaperone-independent manner), under specific conditions. For example, under healthy conditions, CHIP

ubiquitinates the INSR and not the closely related insulin-like growth factor 1 receptor (IGF1R). However, upon accumulation of damaged proteins the dynamic equilibrium of quality-control networks is challenged and CHIP switches to protein degradation pathways, to counteract proteotoxicity. As a result, the INSR accumulates, which significantly shortens lifespan[62]. In line with this, the Ball group have reported that in unstressed cells CHIP acts as a positive regulator of IRF-1 levels, while stress leads to CHIP-dependent down-regulation of IRF-1. This highlights the importance of the cellular environment in regulation of proteostasis[77]. As a docking-dependent, chaperone-independent E3 ligase it would be expected that only a few proteins would be influenced by the deletion of CHIP. The data presented in this chapter supports this mode of action.

### b. Identification of candidate proteins

The MS analysis of cortical neurons revealed proteins of interest that could be regulated directly or indirectly by CHIP in the disease context under investigation. These meet the standard cut off criteria, are found in both comparative proteomics of CHIP-expressing versus KO neurons and are excluded/unchanged between the control lines (P vs WT) (Figure 4.16). The P vs WT SWATH-MS analysis helps to accounts for differences in differentiation status or proteins that could be changed due to off-targets of the CRISPR/Cas9 system used. Furthermore, by comparing these candidate proteins to those also under- or over-represented in the other CHIP cell models analysed (iPSC, undifferentiated and differentiated SH-SY5Y) proteins that are more likely to be directly influenced by CHIP can be identified. This comprehensive approach also provides some insight as to whether these proteins are disease-specific or neuronal-specific, and how conserved this CHIP-mediated proteomic change is across different cell lines. Although candidate protein identification is primarily based on our disease-relevant CHIP model (patient-derived cortical neurons), the use of other cell lines can aid the search for mechanistic insight into the role of CHIP in the regulation of proteins.

From the proteins that were consistently under- or over-represented in the SWATH-MS analysis of cortical neurons, we focused on a subset of proteins. Given the identification of numerous proteins from the Annexin family, Annexins A2, A4, A5, A6

and A7 were all given some degree of attention. ANXA2 was of particular interest as it was consistently detected in the top over-represented proteins in CHIP KO cortical neurons and unchanged in the CHIP-expressing neurons. Also, given its functions in the same membrane homeostasis pathways, the ANXA2-interacting protein[148], S100-A11 was also included in this list. Finally, HLA-B was also found to be overexpressed across the comparative CHIP KO vs WT proteomics.

VGF, SOD and the neurofilament light polypeptide were some of the under-represented proteins in both WT vs KO and P vs KO. Firstly, VGF had been previously detected in proteomic analyses of the undifferentiated SH-SY5Y cells in our group[95], hence was validated in the cortical neuron model. Secondly, CHIP has been associated with prevention of oxidative stress[149], thus alteration of enzymes such as SOD, would be expected. Finally, neurofilament light polypeptide was significantly changed in most SWATH-MS analyses (cortical neurons, undifferentiated and differentiated SH-SY5Y). Neurofilament light polypeptide increases with ageing and is believed to be linked with different neurodegenerative diseases, including AD and PD[150]. Therefore, the change in homeostasis of neurofilament light polypeptide could reflect a change in overall cell health.

### 4.3.3 Possible targets of CHIP

We have previously described the vast interactome and cellular effects of CHIP in age-related diseases[87], based on the literature. In line with this, the identification of a greatly distinct subset of proteins potentially regulated by CHIP, presented in this chapter, may suggest that CHIP functions in a wide range of cellular processes.

#### a. CHIP and innate immunity

There is compelling preliminary evidence to support an upregulation of HLA-B in the CHIP KO neurons. This was very striking by IF (having high expression throughout the neurons) (Figure 4.17B) and by MS (HLA-B was consistently detected in the top most over-represented proteins) (Figure 4.11). On the other hand, iPSC show no difference in the steady state level of HLA-B (Figure 4.18). HLAs are major histocompatibility complexes (MHC) class I proteins and have been reported to be

expressed by neurons (Figure 4.28)[151]. However, to our knowledge, there is no evidence that neurons express HLA-B, specifically.

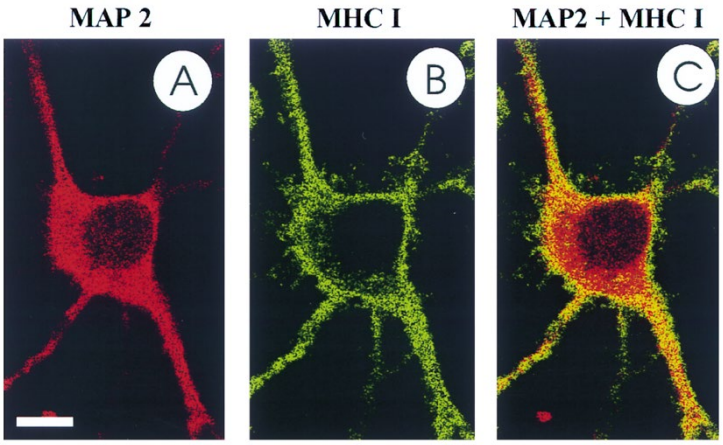


**Figure 4.28: Neurons express MHC-I**
Expression of a combination of MHC-I proteins in neurons treated with IFNγ. Expression is not detected when untreated. Scale bar, 10μm.

(Neumann *et al*.[151])

Although the field of immunity in terms of neurodegeneration gained popularity over the years, the role of neuronal innate immunity in neurodegenerative disease is still understudied. MHC-I proteins function to present antigens at their surface for the ability to distinguish self from non-self[152]. Other than its role in the initiation of antigen receptor signalling, HLA proteins play roles in synaptic plasticity during development and may regulate the ability of neurons to maintain synapses[152]. A GWAS study by Hamza and colleagues[112] reported HLA-DRA (MHC class II protein expressed by antigen-presenting cells including microglia) as a strong predictor in sporadic and late-onset PD (Figure 4.29). This supported the involvement of immunity in PD. The group suggested that chronic immune activation (possibly due to α-Syn accumulation) could result in neuroinflammation, leading to neuronal death[112]. Although supporting data is required, it is possible that, in a synucleinopathy background, the absence of CHIP directly or indirectly contributes to the over-activation of the immune system, manifested as HLA-B upregulation. Thus, one can hypothesize that, along with MHC-II proteins, MHC-I proteins may also contribute to the chronic immune activation seen in neurodegeneration. In fact, HLA-A2 and HLA-B7 have been linked to AD[153,154].

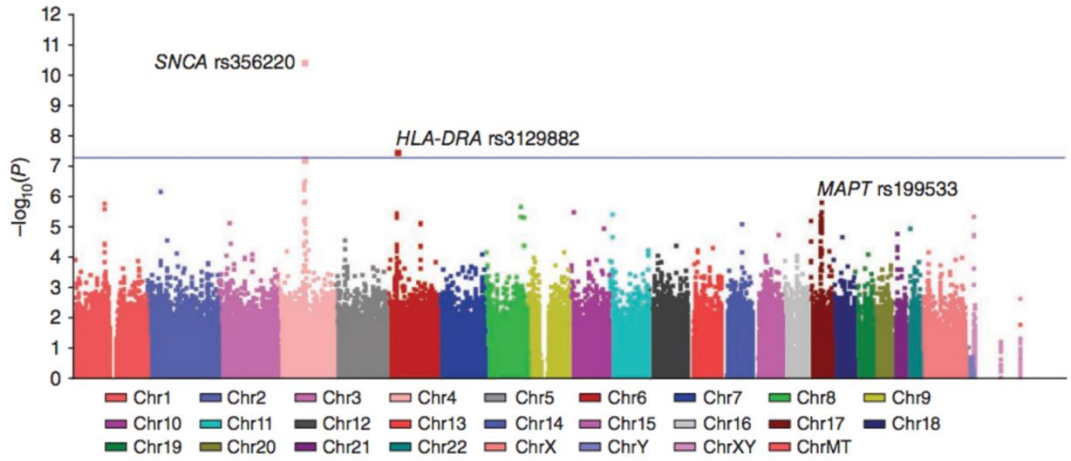


**Figure 4.29: *HLA-DRA was identified as a risk gene for sporadic and late-onset PD***
Manhattan plot showing the *P* values for the association of 811,594 SNPs with PD. SNPs that surpassed genome-wide significance (*P* < 5 x 10-8) were SNCA and HLA-DRA.
(Hamza *et al.*[112])

Furthermore, since alterations in cellular redox state are communicated to the immune system through antigen presentation, HLA proteins may also be affected by oxidative stress. Supporting evidence includes the increase in neuronal MHC-I proteins observed under stress[152] and the presentation of oxidised proteins in the immunopeptidome, which can hinder interactions between T-cells and MHC-I[155]. Therefore, changes in proteotoxic and/or redox state of cells as a consequence of CHIP deletion could underlie this change in HLA, although these conditions of stress would probably have wide effects on the proteome, which were not seen.

CHIP, as an integral component of proteostasis, has been suggested to play a role in regulating antigen presentation (of endogenous and foreign material) on MHCI-I proteins for immune recognition. Here, defective proteins become ubiquitinated and accumulate transiently to form aggregates (aggregsome-like induced structures). These are then cleared by the proteasome or chaperone-assisted selective autophagy to promote antigen presentation. CHIP is believed to aid this process[156]. Our preliminary findings relating HLA-B to CHIP function, together with previous evidence of CHIP-dependent regulation of IRF-1[77], contributes to a possible role for CHIP in innate immunity.

### b. CHIP in synaptic function and energy metabolism

The neurosecretory protein VGF was also analysed further due to its detection in independent MS experiments investigating the effect of CHIP in the proteome of different cell lines. These included the cortical neurons and differentiated SH-SY5Y cells investigated during the course of this project, and undifferentiated SH-SY5Y previously studied by Erisa Nita[95]. VGF is a 68kD polypeptide that is expressed by a neurotrophin-induced gene responsive to BDNF[157]. It is synthesized by neurons (including cortical[150]) and endocrine cells[157]. Its processing post-translationally by prohormone convertases into numerous smaller peptides that have been studied in a mouse model (Figure 4.30), although translational studies to humans have not been reported. These peptides and full-length VGF are found in dense core vesicles, which are released in response to depolarization signals[157].

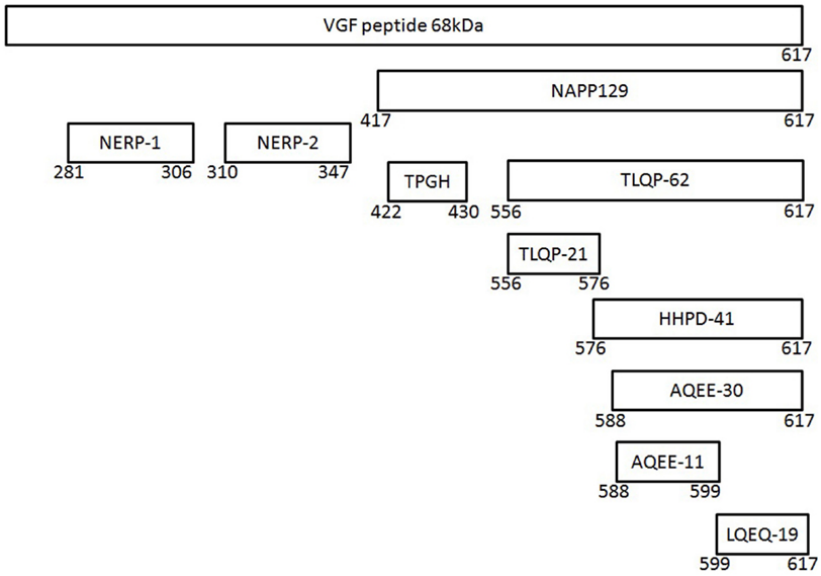


**Figure 4.30: Post-translational processing of VGF in a mouse model**
Several proteolytic cleavages process the full-length VGF protein (at the top) into several smaller peptides.

(Lewis *et al.*[157])

Patient-derived CHIP KO cortical neurons show a pronounced decrease in VGF by MS and IF (Figure 4.20), but no/little change by WB (Figure 4.19). The discrepancy of VGF phenotype could be due to extractability differences, hence detecting different pools of VGF. Cortical neurons show a slight decrease in the abundance of a doublet at around 58 and 62 kDa in CHIP KO cells (by WB using a monoclonal Ab). This

doublet is also decreased in CHIP KO differentiated SH-SY5Y cells but increased in undifferentiated cells of this genotype compared to WT (Figure 4.21). Therefore, this difference could be related to the neuronal-like phenotype of SH-SY5Y and cortical neurons.

The deletion in differentiated SH-SY5Y also caused a decrease in lower MW forms of VGF (<35 kDa), but an increase in higher MW species (>100 kDa). Although this question was not address further, it is possible that CHIP is involved in the processing of full-length VGF and its preforms (the high MW species) to its smaller peptides, possibly through proteolytic cleavage (that has been described for other E3 ligases[158]). Such processing may also be neuron specific. What undifferentiated and differentiated KO cells have in common is an increase in 100 kDa VGF, which is not seen in cortical neurons. This would also argue for a role of CHIP as an E3 ligase of VGF to mediate its degradation. Clearly, the homeostasis of VGF in these cell lines is very different, thus underlying mechanisms are likely to differ.

VGF and its neuropeptides have multiple roles in the brain. TLQP-62 and AQEE-30 increase synaptic activity, potentiation, plasticity and neurogenesis[150,157], while TLQP-21 prevents neuronal apoptosis[157] and regulates pain mechanisms[159] and NERP-1 and NERP-2 peptides regulate water balance[160]. VGF and its neuropeptides are upregulated in pain models[159] and in neurodegeneration. A post-mortem study revealed that the parietal cortex of PD patients showed a reduction in TPGH and NERP-1 peptides specifically, while all VGF peptides were reduced in AD. This suggests the involvement of VGF in physiological or pathological mechanisms during neuronal health and disease[157,160].

Interestingly, a 62 kDa peptide was reduced in CHIP KO differentiated SH-SY5Y. This could represent the TLQP-62 peptide, although validation is required. Reduced expression of this peptide (seen in AD) has been related to impaired memory acquisition and consolidation through a BDNF-dependent pathway that modulates synaptic structure and function[150]. In fact, it has been hypothesised that the decrease in VGF may correlate with loss of BDNF[160]. Interestingly, BDNF was also under-represented in the CHIP KO cortical neurons by MS.

VGF deficits are not only related to cognitive impairment defects but also severe metabolic abnormalities. VGF KO mice consume twice as much oxygen at rest, along with impaired learning and memory[157]. Accordingly, patients harbouring *STUB1* mutations and CHIP KO mice have cognitive and metabolic defects[13,14,88], thus it is possible that VGF partially mediates the neuroprotective properties of CHIP.

### c. CHIP and membrane integrity

When analysing the proteins identified using MS, the amount of calcium and membrane-binding proteins detected is striking. The majority of the Annexin family proteins were detected in our SWATH-MS analyses and a few were significantly and consistently over-represented in the proteomics comparing CHIP-expressing to CHIP KO cortical neurons (Figure 4.22). ANXA2 (Figure 4.23) is of particular interest. Annexin are involved in maintenance of membrane homeostasis through multiple strategies. They regulate the formation of a repair cap[161] and mediate repair mechanisms such as membrane excision[162]. Interesting, S100 proteins are also heavily involved in these pathways[162] and S100-A11 was consistently detected in the top over-represented proteins in the CHIP KO cortical neurons in our proteomics (Figure 4.24), which is consistent with upregulation of its steady state levels in these neurons (Figure 4.26A).

Accordingly, other proteins involved in membrane repair were also found to be under- or over-represented in the CHIP KO neurons (Figure 4.22). This includes caldesmon-1, which plays a role in the modulation of the actin cytoskeleton, an essential step during repair[148,163]. As well as proteins involved in exocytosis-mediated plasma membrane repair, such as the large membrane protein AHNAK[164], tSNARE proteins (including SNAP and syntaxin) and Rab proteins[162]. Interestingly, ANXA2 has been reported to regulate exocytosis-mediated plasma membrane repair by promoting the fusion of enlargeosomes (characterised by the presence of the large membrane protein AHNAK)[164] and lysosomes (a mechanism that relies on the action of tSNARE proteins such as SNAP-23 and syntaxin 4)[162]. Some of these proteins were also found to be changing in the other CHIP cell models analysed (Figure 4.27). Therefore, we question whether the membrane repair pathway is enhanced in CHIP KO cells.

Given how the homeostasis of multiple proteins involved in the regulation of membrane integrity are being affected by CHIP deletion, we hypothesise that CHIP might play a role in the maintenance of membrane integrity. This biological significance of membrane homeostasis in the context of neurodegeneration is largely unknown and understudied. For this reason and given the robust ANXA2 phenotype observed, we decided to focus on this protein as a potential target of CHIP, important for its neuroprotective role. CHIP dependent regulation of ANXA2, its interaction dynamics with S100-A11 and its cellular consequences are discussed in Chapter 5.

### d. CHIP-regulated cellular pathways

Whether the effect of CHIP on the candidate proteins discussed (including HLA-B, VGF, ANXA2 and S100-A11) is direct or indirect is still unclear. Factors such as oxidative stress could contribute to the phenotypes seen. Therefore, future work would investigate the effect of the cellular environment (including oxidative stress and proteotoxicity, which have been reported in CHIP KO mice) on CHIP-dependent regulation of its protein targets. It seems that CHIP-mediated differences in the proteostasis of some proteins of interest could be exacerbated in the disease context under study.

Our CHIP KO cortical neurons of a synucleinopathy model show changes in specific proteins involved in a broad spectrum of functions, including immunity, metabolism and membrane integrity. Interestingly, although multiple pathways could be influenced by CHIP, gross changes in the proteome were not detected. This supports the hypothesis that CHIP affects the proteostasis of specific proteins and these, either individually or cumulatively, could play a role in the molecular mechanisms underlying the neuroprotective effects of CHIP, which remain largely unknown.

# Chapter 5: The possible role of CHIP in regulating the homeostasis of Annexin A2 and membrane integrity

## 5.1 Introduction

### 5.1.1 Annexin A2 at a protein level

Annexins are a conserved family of calcium-regulated phospholipid-binding proteins that are required for membrane repair and the regulation of membrane proteins and fusion events[165]. They are widely expressed in plants and animals[166], and humans have more than 23 different Annexin family members with a common core domain. This consists of a conversed 70-amino acid sequence that is repeated four times (and eight for Annexin A6, ANXA6)[167], each repeat features five $\alpha$-helices, which together form a slightly curved disc[162,165,168,169]. At its convex side is the membrane attachment sites and the type II calcium-binding sites[162]. The N-terminal region is unique to each of the Annexin members and is susceptible to post-translational modifications[165,170]. This region is also responsible for self-association properties[162]. Annexins are localised in the plasma membrane, early and late endosomes, multivesicular bodies, phagosomes, Golgi, mitochondria and nucleus[170]. Despite the inherent lipid-binding properties, Annexin members display different spatio-temporal and calcium-sensitive kinetics, thus influencing their functions within the cell[167]. This is further regulated by protein interactions, pH and lipid interactions (including ceramide, $PI(4,5)P_2$, and cholesterol)[167].

Annexin A2 (ANXA2) is a 36kDa protein[168] that is widely distributed and abundantly expressed in endothelial cells, monocytes, macrophages and tumour cells[167]. It has low calcium requirements for phospholipid binding[170]. ANXA2 tends to favour binding to negatively charged phospholipids, including phosphatidylinositol ($PI(4,5)P_2$), phosphatidic acid (PA) and phosphatidylserine (PS)[167]. Interaction with different proteins is mediated by binding sites located throughout the ANXA2 protein. The N-terminal region binds to tissue plasminogen activator and S100 proteins, the core domain to phospholipids and calcium (having two or four annexin-type calcium-binding sites) and the C-terminal region to F-actin, herapin and plasminogen[171]. The flexible and disordered N-terminal domain is buried within repeat III of the core region

in the absence of calcium[172]. However, upon binding to calcium, the conformational change induced exposes its hydrophobic amino acids within the N-terminal domain, allowing interaction with S100 proteins[171] and other lipids[169].

Annexins, such as ANXA2, regulate lipid segregation (including $PI(4,5)P_2$ domain formation mediated by the $PI(4,5)P_2$-binding sites, lysine residues 279 and 281, on ANXA2). This allows the formation of membrane indentations to promote membrane deformations and remodelling – a mechanism possibly underlying annexin-mediated membrane trafficking[169]. As monomers, ANXA2 can adopt two conformations, anti-parallel and parallel, bringing together two membrane structures or inducing membrane indentation, respectively (Figure 5.1A&B), mechanisms that rely on its core domain. The N-terminus has been proposed to be required for ANXA2-mediated membrane aggregation by conveying a second membrane binding site[169].

The N-terminal domain of ANXA2 also mediates binding to S100 proteins. This occurs in the presence of calcium or as a result of post-translational modifications on the S100-binding site of annexins[166,169,172]. The S100 family consists of small dimeric, EF-hand-type calcium-binding proteins. S100-A10 has lost its ability to bind to calcium, thus is constitutively in its active conformation and ready to interact with Annexins[172]. S100 proteins exert both intracellular and extracellular functions and can form symmetrical noncovalent homodimers[163].

ANXA2:S100 heterotetramer complex formation, with a 1:1 stoichiometry[171], induces a shift in subcellular localisation of ANXA2 which, as a monomer, is mainly cytoplasmic and on early endosomes[166,169,172]. The complex can adopt different conformations, having secretory, membrane-bound, cytoplasmic and nuclear forms[168]. Underlying this change is the increased affinity of the heterotetramer for lipids[168,169]. Consequently, phospholipid binding and vesicle aggregation also occur at significantly lower calcium concentrations[171]. Other than the S100-induced conformational change in ANXA2 (favouring lipid-binding), S100 may enhance the lipid segregating properties of ANXA2 by physically linking two membrane binding ANXA2 moieties (Figure 5.1C)[169].

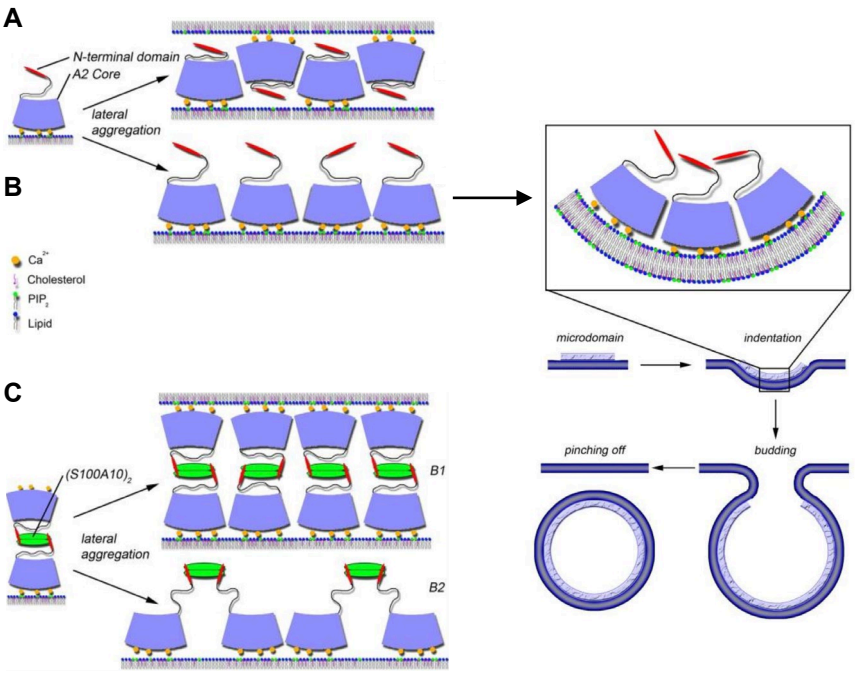


**Figure 5.1: Dimeric forms of Annexin A2 on membranes**
**A)** In the zipper-like mechanism (N-terminal-independent), ANXA2 monomers adopt an anti-parallel conformation. Here, each ANXA2 core domain binds to the $PI(4,5)P_2$ head group on the membrane and adjacent ANXA2 monomers face opposite membranes. This results in a rigid scaffold that binds together two membrane surfaces, promoting membrane aggregation. **B)** ANXA2 monomers can also adopt a parallel (side-by-side) conformation, where the $Ca^{2+}$/lipid-binding sites are exposed on the convex side, which attaches a membrane surface. This induces membrane bending, resulting in indentation and budding (*right*), due to the intrinsic curvature of the core domain. This is also a N-terminal-independent mechanism. **C)** Lateral aggregation of the ANXA2:S100 heterotetramer can adopt two conformations: each core domain of ANXA2 can face opposite membrane surfaces, inducing membrane interconnections (*top*), or in can orientate in a parallel manner (*bottom*), promoting microdomain formation/raft clustering and eventually membrane indentation.
(Adapted from Drucker *et al.*[169])

## 5.1.2 Annexin A2 at a cellular level

Annexins have been described as membrane fusogens, calcium sensors, cytoskeletal- and membrane-associated proteins and signal transducers[166,168,170,173]. At a cellular level, these functions allow annexins to mediate membrane remodelling events (including intracellular vesicular trafficking, endocytosis and exocytosis) (Figure 5.1), lipid raft formation and/or stabilisation, segregation of lipid domains, turnover of ion channels/receptors, regulation of membrane-actin interface, intracellular calcium homeostasis and membrane repair (discussed in Section 5.1.4 The role of Annexins, S100 proteins and other membrane proteins in membrane integrity). Its non-canonical functions include regulation of inflammatory processes,

proliferation, mRNA transport, DNA replication and repair, and redox regulation[165,168–173]. Its activities dependent on the cell type and metabolic state of cells[170].

In general, ANXA2 is regarded as an important component of the protein network that is involved in the maintenance of cell health. Despite the functional redundancy within the Annexin family, deletion of ANXA2 leads to endosomes with an abnormal morphology and turnover[165,174]. Regulation of endosomes is dependent on the activity of ANXA2:S100-A10[174], since the recruitment of ANXA2 to membranes is promoted by S100 proteins[171]. Not only can the heterotetramer link two membrane surfaces (Figure 5.1B), allowing aggregation of lipid vesicles[169], it can modulate actin dynamics, thus regulating trafficking and intracellular vesicle fusion events[163,166].

ANXA2 also regulates cell signalling and has added protective roles in response to stress. It associates with cholesterol- and PI(4,5)$P_2$-rich domains, called 'lipid rafts', where ANXA2 serves as a scaffolding protein, mediating the recruitment of signalling components to these platforms[167]. This allows extracellular cues (including stressors) to communicate with the inside of the cell, activating intracellular signalling pathways accordingly. Nuclear ANXA2 is believed to be cell-cycle dependent[168] or induced by reactive oxygen species signalling, where ANXA2 nuclear aggregation prevents genomic damage. This ANXA2-mediated defence mechanism has been observed following injury or stress[175]. ANXA2 also regulates stimuli-induced apoptosis[176] and can rapidly translocate to the plasma membrane for maintenance of membrane integrity and response to injury[163].

## 5.1.3 Regulation of Annexin A2

### a. Selective degradation of Annexin A2

Some members of the Annexin family, including ANXA2 and ANXA6, can be selectively degraded by CMA. Chaperones partially unfold these substrates to expose the buried the KFERQ-like motif that favours protein clearance by CMA via the lysosome[170]. This selective degradation contributes to the control of the homeostasis of specific Annexin proteins, thus it is likely to have physiological relevance[170]. For example, ANXA2 degradation correlates with cellular apoptosis induced by p53-mediated pathways[168].

### b. Regulation by phosphorylation

Both *in vitro* and *in vivo* experiments suggest that ANXA2 is a substrate of various classic calcium-activated protein kinase C (PKC) isozymes. These are activated by DAG in a calcium-dependent manner and bind to negatively charged phospholipids, in particular PS[167]. PKC-mediated phosphorylation of Annexins is a two-way regulatory mechanism, since Annexins A1, A2, A5 and A6 provide scaffolding functions to modulate PKC localisation and signalling[167].

The major phosphorylation site on ANXA2 phosphorylated by PKC isozymes is the serine residue at position 25[166,168,177]. This triggers a change in subcellular localisation from the nucleus to the perinuclear region, becoming associated with membranes and cytoskeletal elements, which intrinsically changes its interactome and function. pSer25ANXA2 has been implicated in exocytosis, recycling of lipid rafts and recruitment of PKC to $PI(4,5)P_2$-rich membrane domains[173]. Interestingly, phosphorylation at Ser25 prevents ANXA2-mediated aggregation of membranes[168,178] (illustrated in Figure 5.1A), but stimulates the fusion of pre-aggregated vesicles/granules/endosomes with the plasma membrane for exocytosis[167].

PKC-mediated phosphorylation of ANXA2 at serine 11 has been proposed to promote nuclear entry of monomeric ANXA2 and, importantly, to abolish the interaction with the heterotetrameric conformation with S100 proteins[166]. Such dissociation exposes S100-A10 to degradation by the UPS[167] and can result in accumulation of ANXA2 monomers, which are unable to organize membranes. On the contrary, phosphorylation of Annexin at tyrosine 23 induces membrane translocation[167] and may promote ANXA2 homodimer formation (devoid of S100 proteins) given the reduction in affinity of ANXA2 for S100 proteins[177,179]. Such phenomenon was observed for ANXA1 in the brain, where monomers dimerised when associated with the membrane and may play a role in neurotransmitter release at the synaptic plasma membrane[179].

Tyrosine phosphorylation of ANXA2 might become important in mediating cellular response to stress. During heat stress, ANXA2 translocates from the cytoplasm to the plasma membrane (resulting in a 2 to 3-fold increase at the cell surface) (Figure 5.2A). This is dependent on the expression of S100-A10 (Figure 5.2B) and on tyrosine

phosphorylation of ANXA2 (Figure 5.2C). Mechanistically, ANXA2 may be directed to the inner face of the plasma membrane by S100-A10, where it becomes phosphorylated by membrane-associated pp60 Src kinase. As a result, phospho-ANXA2 couples more avidly with the inner leaflet PS and could undertake a conformational change that might potentiate its insertion into the plasma membrane[180]. Pp60 Src kinase becomes rapidly activated in response to oxidative stress, heat stress, hypoxia, shear stress and increases in intracellular calcium[180].

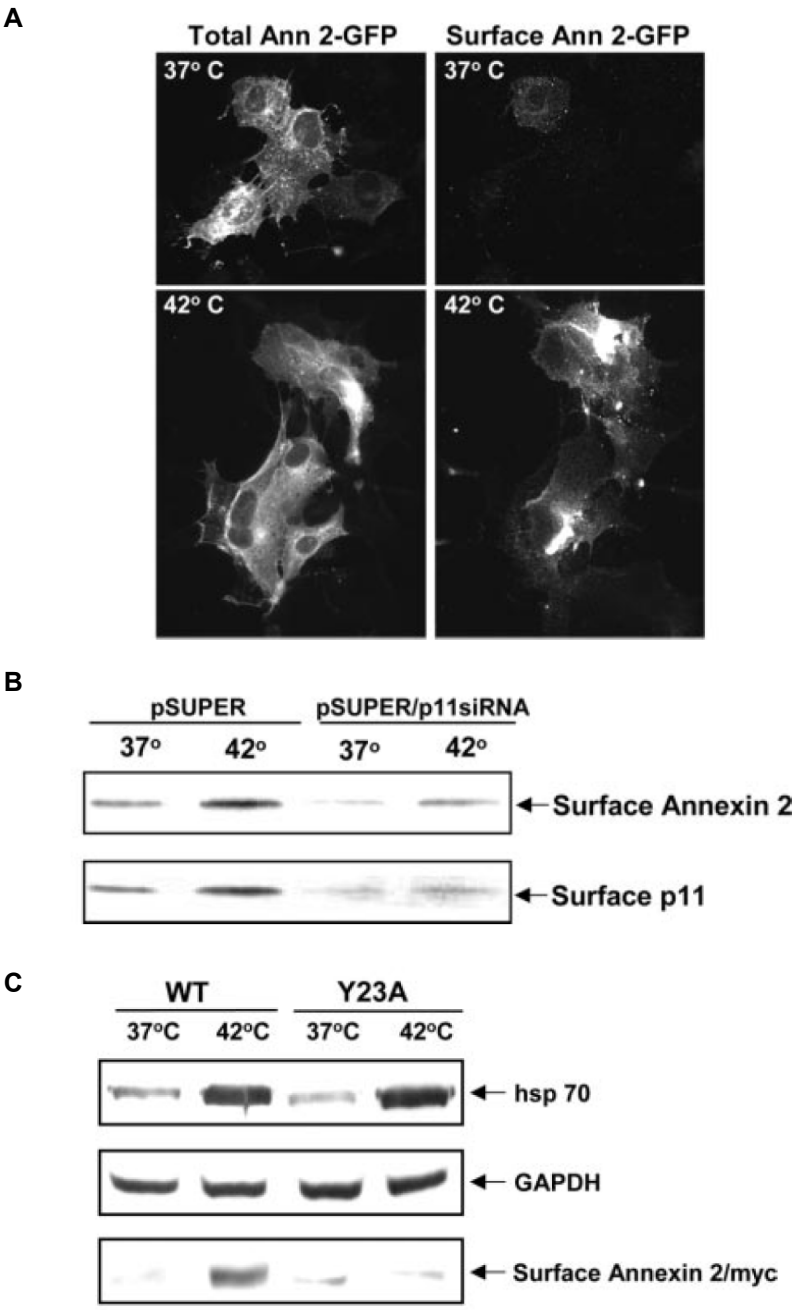


**Figure 5.2: Stress-induced translocation of Annexin A2 to the cell surface is dependent on phosphorylation and interaction with S100 proteins**
**A)** Translocation of ANXA2 to the cell surface was observed in cells transfected with ANXA2-GFP (Ann-2-GFP) were exposed to heat shock (42ºC for 3h). The relative fluorescent intensity of surface-associated ANXA2-GFP (immunostained with anti-GFP antibody) to total ANXA2-GFP (direct GFP fluorescence) was measured.
**B)** Knockdown of S100-A10 (pSUPER/p11siRNA) prevented ANXA2 translocation that is seen in cells transfected with the empty vector (pSUPER).
**C)** Cells stably transfected with myc-tagged WT or the phospho-mutant Y23A ANXA2. The latter failed to show heat shock-induced surface ANXA2 expression.

(Deora *et al.*[180])

### c. Regulation by ubiquitination

Although ANXA2 has been found to be ubiquitinated, the ubiquitination sites, the cellular fates of ubiquitinated species and the ubiquitination enzymes responsible for this are unknown. Sequence analysis revealed a single Ub-interacting motif in domain II of the core region of ANXA2, although this was not confirmed experimentally[181]. With regards to enzymes involved in ubiquitination of Annexins, UBE3A, an E3 Ub ligase involved in the UPS, has been implicated in the regulation of both ANXA1 and ANXA2. UBE2A gene knockdown results in a downregulation of ANXA2. It is unlikely that UBE2A-dependent ubiquitination regulates the degradation of ANXA2, but instead may regulate its activity or subcellular localisation. On the contrary, ubiquitination-mediated degradation of S100-A10 is commonly seen in the unbound state, since the N-terminus of ANXA2 masks the autonomous ubiquitination signal on S100-A10 when they interact[173].

Ubiquitination of different pools of ANXA2 has been reported. Firstly, both pSer25ANXA2 and pTyr23ANXA2 are differentially ubiquitinated by an unknown E3 ligase(s) (Figure 5.3A)[173]. Phosphorylation at Ser25 could induce subsequent ubiquitination and/or sumoylation, since a phosphomimic of ANXA2 (ANXA2-Ser25Glu) readily forms ubiquitinated species. Secondly, a cytoskeletal-associated pool of ANXA2 was shown to be both mono- and poly-ubiquitinated (Figure 5.3B)[181]. Again, the cellular consequence of ANXA2 ubiquitination are not likely to be degradation, given the extended half-life of cytoskeleton-bound ANXA2 (15 h)[181]. Instead, ubiquitination may regulate internalisation of plasma membrane proteins by endocytosis destined to the endosomal/lysosomal pathway (commonly seen for monoubiquitination)[173,181]. Alternatively, such ubiquitination may be associated with ANXA2's function as an actin-binding protein[181]. Thirdly, total ANXA2 was upregulated and ubiquitinated (both monoubiquitinated and polyubiquitinated) in cancer tissue, associating Annexin dysregulation to disease[182].

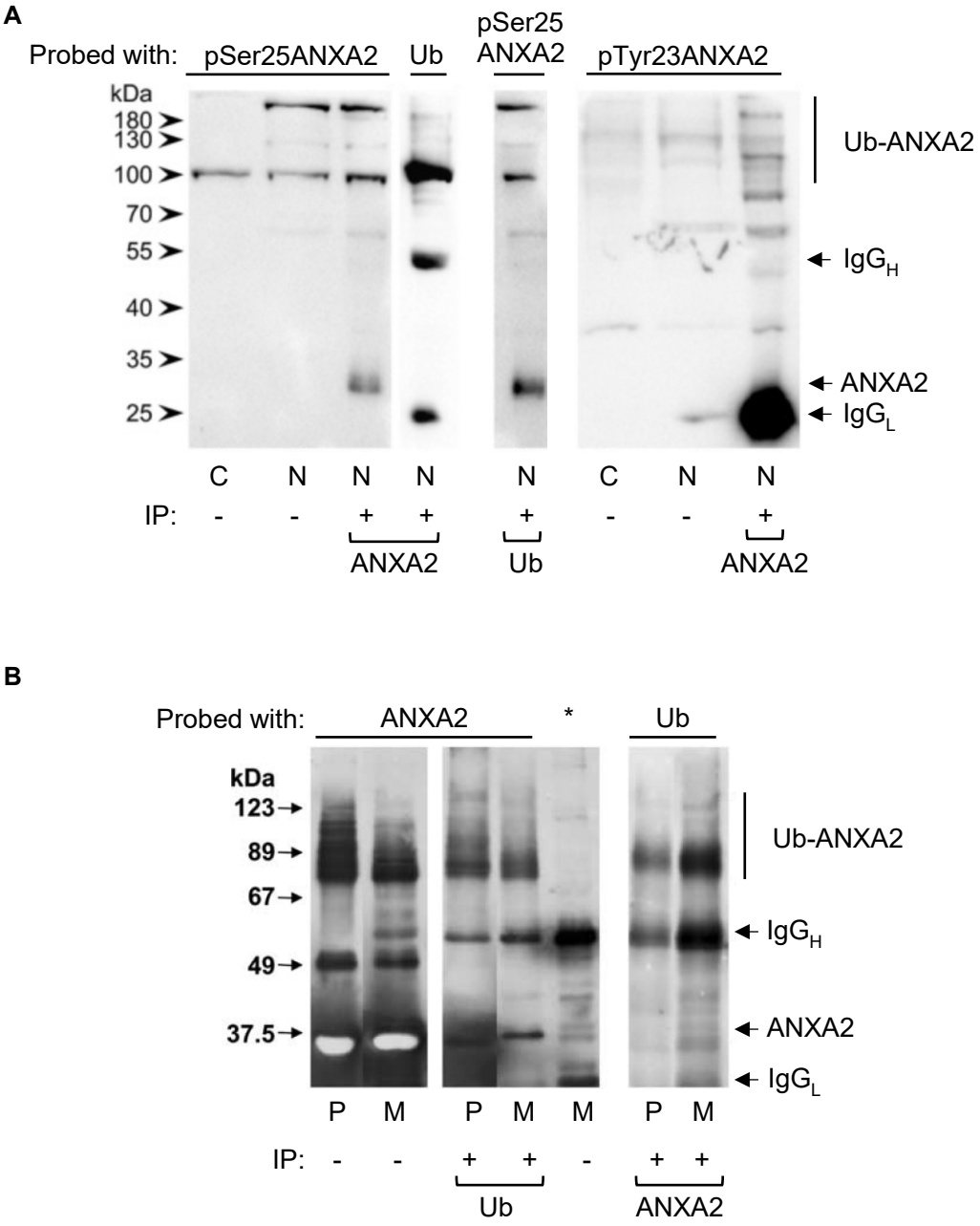


**Figure 5.3: Ubiquitination of Annexin A2**

**A)** Lysate (100 μg) from the cytoplasm (C) and nuclear (N) fractions of PC12 cells and immunoprecipitations from nuclear fractions (IP) using anti-ANXA2 or anti-Ub antibodies were analysed by SDS-PAGE/immunoblot and probed with anti-pSer25ANXA2 or anti-pTyr23ANXA2 antibodies as indicated.

**B)** Lysate (30 μg) of ANXA2 preparations purified from porcine intestinal mucosa (P) and mouse Krebs II cells (M) were analysed by SDS-PAGE/immunoblot probed with anti-ANXA2 antibody. Preparations were immunoprecipitated with anti-Ub and anti-ANXA2 antibodies and also analysed by SDS-PAGE/immunoblot using anti-ANXA2 and anti-Ub antibodies, respectively. Incubation with the HRP-conjugated secondary antibody in the absence of primary antibodies (*) detected heavy and light chain IgG subunits.

(Adapted from **A**: Aukrust *et al.*[173]; **B**: Lauvrak *et al.*[181])

### 5.1.4 The role of Annexins, S100 proteins and other membrane proteins in membrane integrity

Annexins and S100 proteins are particularly important in regulation of membrane homeostasis and maintenance of membrane integrity, of both intracellular and plasma membranes (PM)[163]. Although in the past PM repair used to be regarded as a passive process, relying on the spontaneous re-organisation of phospholipids (i.e. self-sealing), a highly dynamic and complex repair machinery associated with an active repair mechanism has now been elucidated[162].

Experimentally, the study of membrane repair replies on lesions induced by mechanical stress (including microneedle puncture, glass beads, cell scraping or laser irradiation) or by toxins (pore-forming bacterial toxins)[162]. Repair of small lesions caused by the latter is mediated by microparticle/ectosome shedding, blebbing or endocytosis. For greater lesions (e.g. laser-induced damage) repair is mediated by exocytosis, endocytosis or excision-based mechanisms (Figure 5.4)[162,163]. Importantly, these mechanisms are not mutually exclusive and potentially collaborate in the repair process[162]. This functional redundancy illustrates the importance of maintenance of membrane integrity, since repair deficiency results in membrane disruptions, cell death and tissue inflammation[163,183].

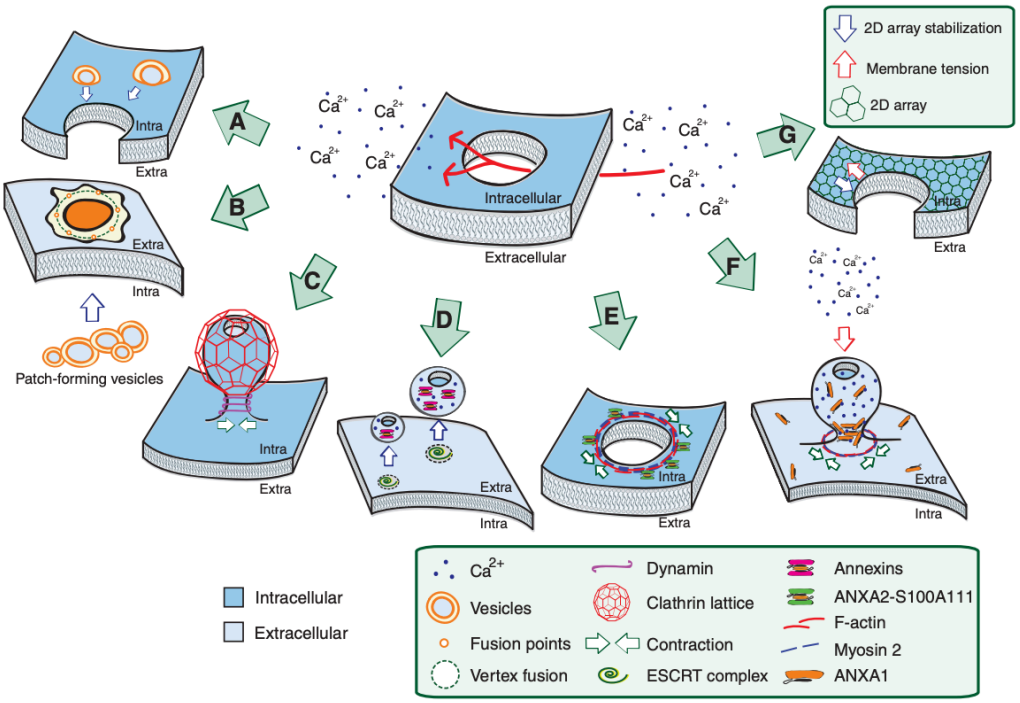


**Figure 5.4: Mechanisms of membrane repair**
**A)** Exocytosis-mediated PM repair following the tension reduction model. Here, vesicles fuse around the wound perimeter to decrease membrane tension and promote re-sealing.
**B)** Exocytosis-mediated PM repair following the patch-mediated membrane fusion model. Homotypic fusion of intracellular vesicles form a patch on the injured membrane.
**C)** Endocytosis-mediated PM repair. For such, clathrin coats the newly formed vesicles and dynamin can then self-associate into rings around the clathrin-coated vesicles for constriction and subsequent vesicle scission. Repair can be clathrin- and dynamin-dependent or independent. Annexins A1, A2, A6 and A8 have been implicated in this form of repair.
**D)** Microparticle shedding-mediated PM repair. Annexins mediate the shedding of ectosomes containing the damaged membrane.
**E)** Contractile actomyosin pulse string contraction.
**F)** PM repair by bleb formation. Once the permeability barrier is disrupted, the influx of calcium triggers phosphorylation of myosin II via $Ca^{2+}$/calmodulin-dependent myosin light chain kinase. This induced myosin-driven contraction of the cortical cytoskeleton generates hydrostatic pressure, causing herniation of the plasma membrane (i.e. plasmalemmal protrusion) to form a bleb containing the damaged membrane. If the cell is able to repair the membrane lesion, the elevated intra-bleb calcium is pumped out and the bleb retracts. If not, Annexins are recruited, eventually forming a plug.
**G)** Formation of 2D arrays by self-assembly of Annexins.

(Nylandsted & Boye[162])

Although PM lesions can be repaired by individual Annexin proteins, the concerted action of annexins is instrumental for efficient repair of multiple, simultaneously occurring lesions[184]. The influx of calcium from the site of injury triggers a change in the conformation of Annexins, promoting their sequential recruitment from the cytosol to the repair site[162,163]. Annexins (including ANXA6, ANXA1 and ANXA2) bind strongly to negatively charged phospholipids, such as PS, that became exposed by the injury. They self-aggregates into a tight structure, the “repair cap” (i.e. forming a protein lattice), within 6 seconds after injury (Figure 5.5A)[161,184]. Such fast-wound healing response counteracts the influx of calcium and efflux of cytoplasmic components, and facilitates subsequent healing[161]. The inherent properties of oligomerisation and phospholipid-binding across Annexins contribute to the redundancy in cap formation, which can be composed of multiple annexins. Similarly, ANXA2, and potentially others, can self-aggregate to form intracellular 2D arrays around the wound perimeter (Figure 5.4G & Figure 5.5B)[162,163]. This tension prevents wound expansion and brings the wound edges together to encourage fusion and membrane resealing[163]. In fact, a common trait among the Annexin family of proteins is their ability to induce membrane curvature, which appears to be important during PM repair to bring together the wound edges[185].

**A**

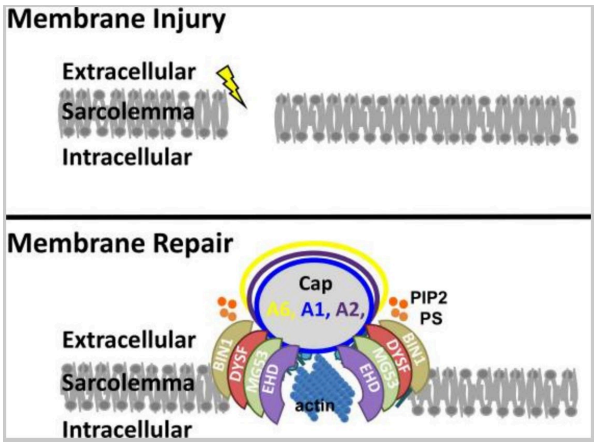


**B**

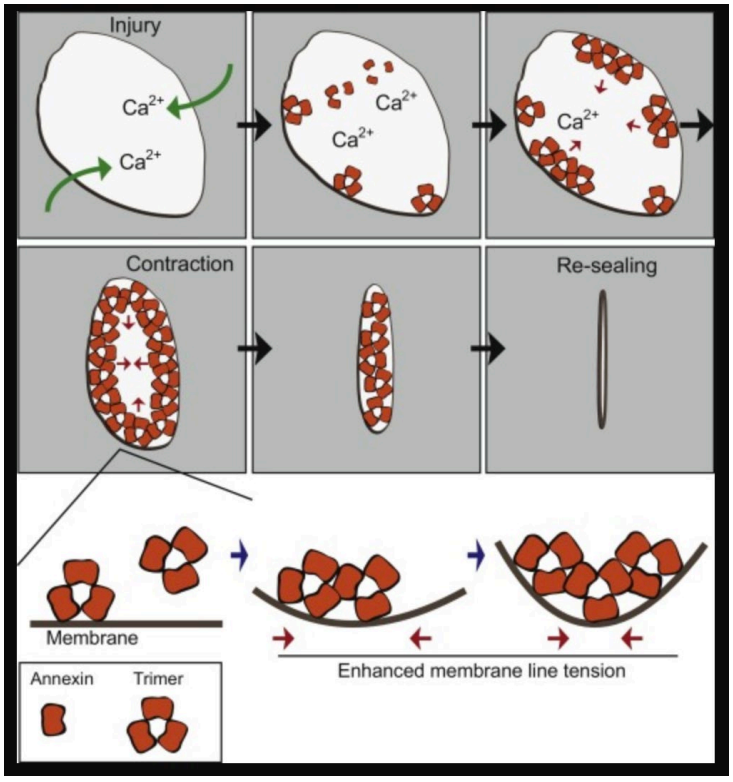


**Figure 5.5: Self-oligomerisation of Annexins**
**A)** Model of membrane repair by forming a repair cap at the site of damage consisting of ANXA6, ANXA1 and ANXA6. Other proteins are form he shoulder of the repair cap, while PIP2 and PS localise adjacent to the repair cap.
**B)** Disruption of the PM results in $Ca^{2+}$-triggered formation of a 2D ordered protein array consisting of Annexin trimers that are further ordered in dimers and trimers. This activity has been well documented for ANXA5, ANXA2 and ANXA1. These 2D structures restrict wound expansion, as they enhance the tension at the membrane wound edges, promoting re-sealing.
(**A:** Demonbreun *et al.*[161]; **B:** Lauritzen *et al.*[163])

Annexins have also been implicated in PM repair by different mechanisms. ANXA2 regulates both endocytosis- and exocytosis-mediated PM repair. For the repair of small lesions, ANXA2 promotes $Ca^{2+}$-dependent endocytosis of the pore-containing or damaged membrane region to restore membrane integrity (Figure 5.4C)[162]. In the context of exocytosis-mediated PM repair, ANXA2 promotes the fusion of lysosomes and enlargosomes with the PM either to reduce membrane tension around the wound perimeter to promote sealing (following the tension-reduction model) or by direct fusion to form a continuous membrane over the injury site (patch model) (Figure 5.4A)[162]. The ability of Annexin proteins to aggregate vesicles is key to this process[148,162].

The majority of repair mechanisms have been found to be regulated by more than one member of the Annexin family of proteins. Simplistically, such evolutionary conserved proteins display extensive functional redundancy to ensure maintenance of membrane integrity (relying on compensation between members if needed). However, the seemingly subtle biochemical differences between annexins seem to have cellular significance, at a mechanistic level, arguing for Annexin-specific roles within the family, rather than all members contributing to the overall functional redundancy *per se*. As Potez and colleagues[184] concluded, by expressing several annexins with different calcium sensitivities, a cell is able to mount an adequate response to a spatiotemporally restricted injury and to withstand a sustained lesion. For example, repair of a single pore occurring within a thin cellular protrusion (e.g. neuronal axon), which results in a pronounced influx of calcium, relies on its most calcium-sensitive annexins (e.g. ANXA6). Here, annexins with low calcium sensitivity (e.g. ANXA1) are ineffective during the early stages of injury[184]. Instead, these serve as a “strategic reserve” and are indispensable in sustained injury. By having annexin proteins with different, but overlapping, calcium sensitivities, cells are able to continuously fine tune its repair response. This contributes to the temporal specificity of the repair machinery (Annexin members and other proteins) and allows for different levels of regulation of the repair cascade. Moreover, changes to the expression profiles of Annexins allows for a dynamic and cell-specific calcium tolerance limit, which can be adjusted depending on physiological requirements[184].

## 5.2 Results

### 5.2.1 Increased expression of Annexin A2 in CHIP KO cortical neurons and other CHIP cell models

SWATH-MS revealed a consistent and significant over-representation of ANXA2 in the CHIP KO cortical neurons (0.107- and 0.100-fold change of the CRISPR control or parental line compared to CHIP KO, respectively). Considering that over-representation of an ionised peptide detected by MS does not directly correlate with protein steady state levels at a cellular level, being influenced by factors including protein post-translational modifications and differential ionisation potentials of proteins, it is necessary to validate this further.

The steady state levels of ANXA2 in cortical neurons from independent differentiation experiments were assessed by WB (Figure 5.6). A consistent and robust increase in CHIP KO neurons was observed. Interestingly, this phenotype was dependent on the neuronal status of these cell lines, as no difference in ANXA2 levels was detected in CHIP KO and WT iPSC (Figure 5.7). Undifferentiated SH-SY5Y cells, on the other hand, showed a modest increase in ANXA2 in CHIP KO cells (Figure 5.8), while differentiated SH-SY5Y cells shown no change (Figure 5.9).

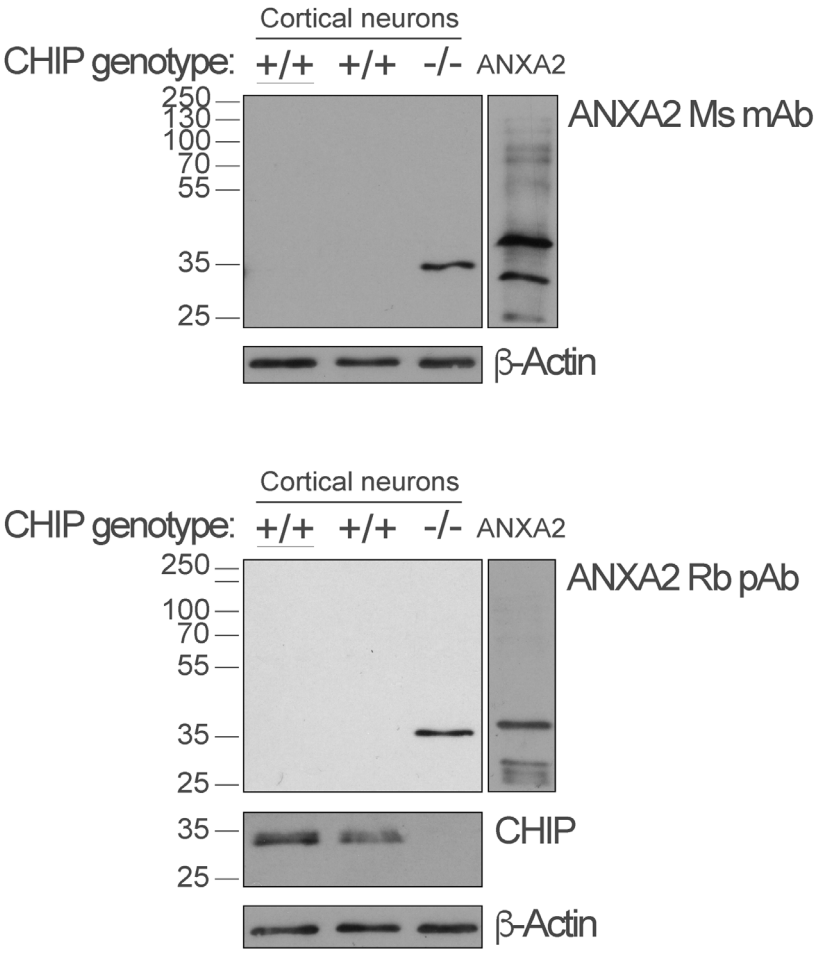


**Figure 5.6: Annexin A2 expression in cortical neurons of different CHIP genotypes**
Mature iPSC-derived cortical neurons (harvested at day 80 of differentiation) were lysed with urea-based lysis buffer (the same as that used for SWATH-MS). CHIP KO neurons (-/-) as well as two CHIP-expressing lines (the parental line (+/+) and the CRISPR control (+/+)) were analysed. For each sample, 20 μg of lysate was loaded per 12% gel for SDS-PAGE/WB and two gels were ran in parallel (in the same apparatus). In parallel, 25 ng of human recombinant ANXA2 (Abcam, ab93005) was loaded as a positive control. Each immunoblot was probed firstly with either anti-ANXA2 Ms mAb (1:500) or anti-ANXA2 Rb pAb (1:1000), then with anti-β-actin mAb (1:5000) and finally the immunoblot probed with anti-ANXA2 Rb pAb previously was incubated with anti-CHIP mAb (1:10000). These immunoblots are representative of at least 5 biological replicates from independent cortical differentiation experiments.

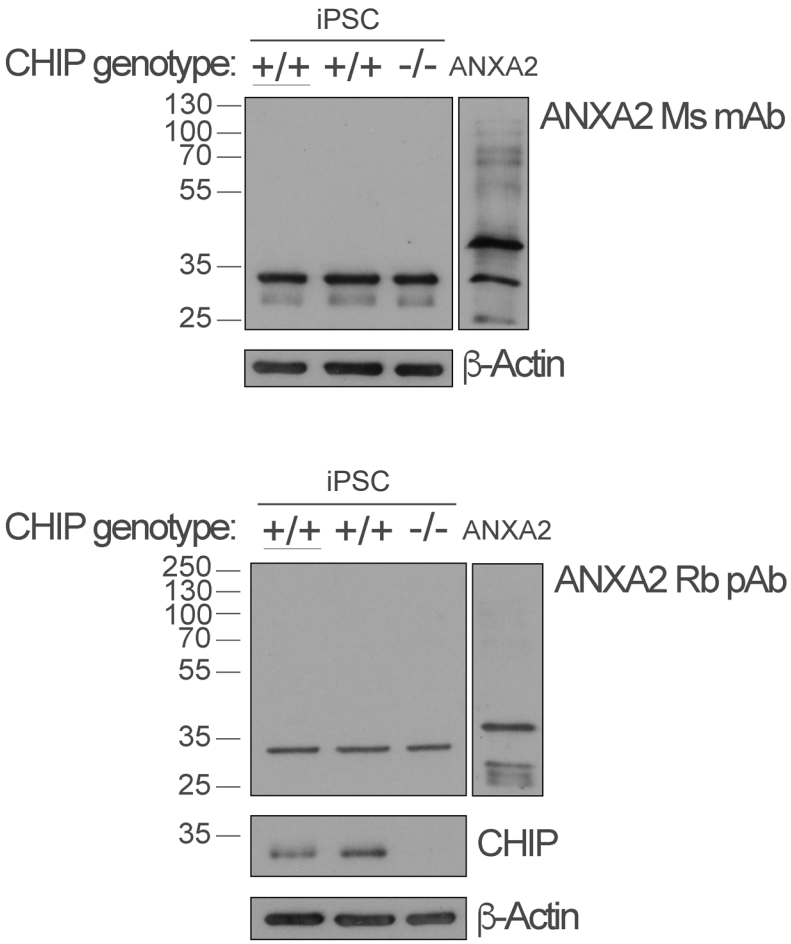


**Figure 5.7: Annexin A2 expression in iPSC of different CHIP genotypes**
iPSC were lysed with urea-based lysis buffer (the same as that used for SWATH-MS). CHIP KO cells (-/-) as well as two CHIP-expressing lines (the parental line (+/+) and the CRISPR control (+/+)) were analysed. For each sample, 20 μg of lysate was loaded per 12% gel for SDS-PAGE/WB and two gels were ran in parallel (in the same apparatus). In parallel, 25 ng of human recombinant ANXA2 (Abcam, ab93005) was loaded as a positive control. Each immunoblot was probed firstly with either anti-ANXA2 Ms mAb (1:500) or anti-ANXA2 Rb pAb (1:1000), then with anti-β-actin mAb (1:5000) and finally the immunoblot probed with anti-ANXA2 Rb pAb previously was incubated with anti-CHIP mAb (1:10000). These immunoblots are representative of at least 5 biological replicates.

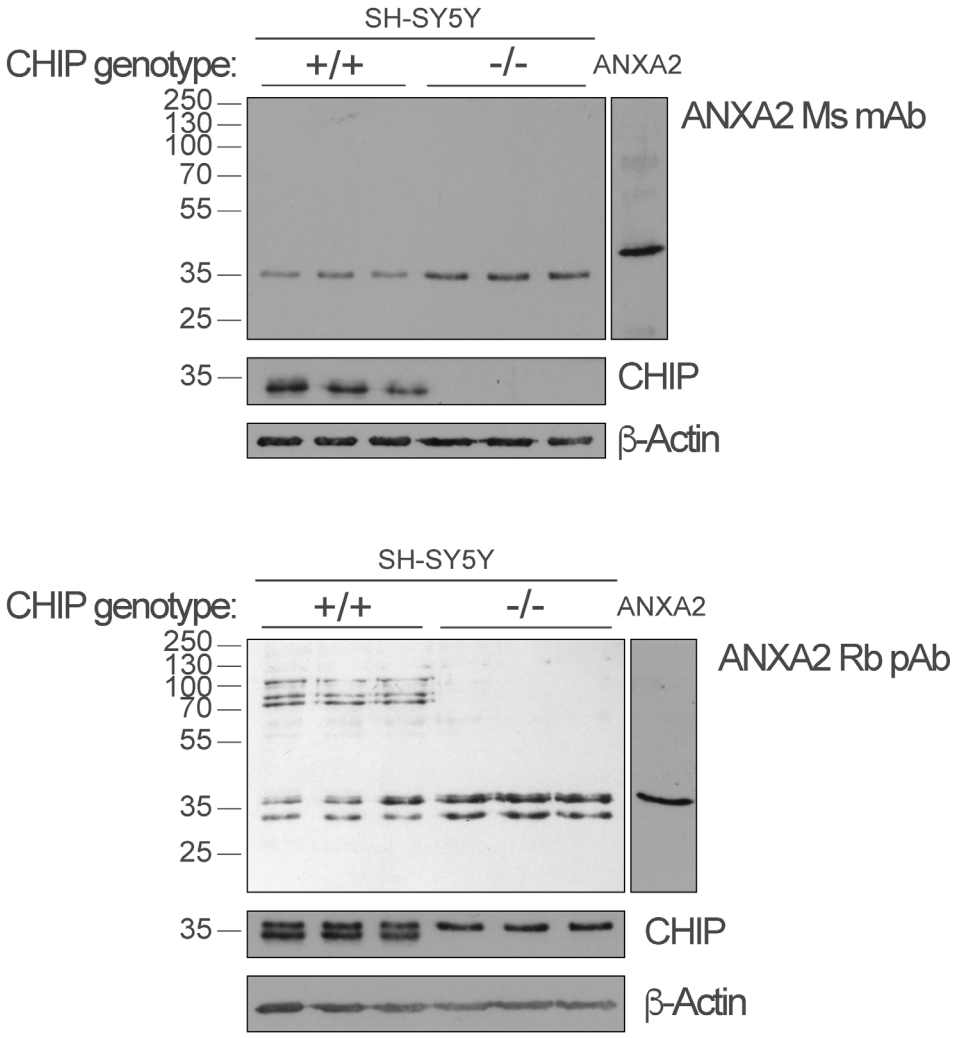


**Figure 5.8: Annexin A2 expression in undifferentiated SH-SY5Y CHIP KO and WT cells** Undifferentiated SH-SY5Y CHIP KO and WT cells were lysed with urea-based lysis buffer (the same as that used for SWATH-MS). For each sample, 20 μg of lysate was loaded per 12% gel for SDS-PAGE/WB and two gels were ran in parallel (in the same apparatus). In parallel, 25 ng of human recombinant ANXA2 (Abcam, ab93005) was loaded as a positive control. Each immunoblot was probed firstly with either anti-ANXA2 Ms mAb (1:500) or anti-ANXA2 Rb pAb (1:1000), then with anti-β-actin mAb (1:5000) and finally the immunoblot probed with anti-ANXA2 Rb pAb previously was incubated with anti-CHIP mAb (1:10000). In undifferentiated cells, a band detected by anti-ANXA2 pAb runs in close proximity to the band representing CHIP (indicated by the asterisk). These immunoblots are representative of at least 6 (A) biological replicates.

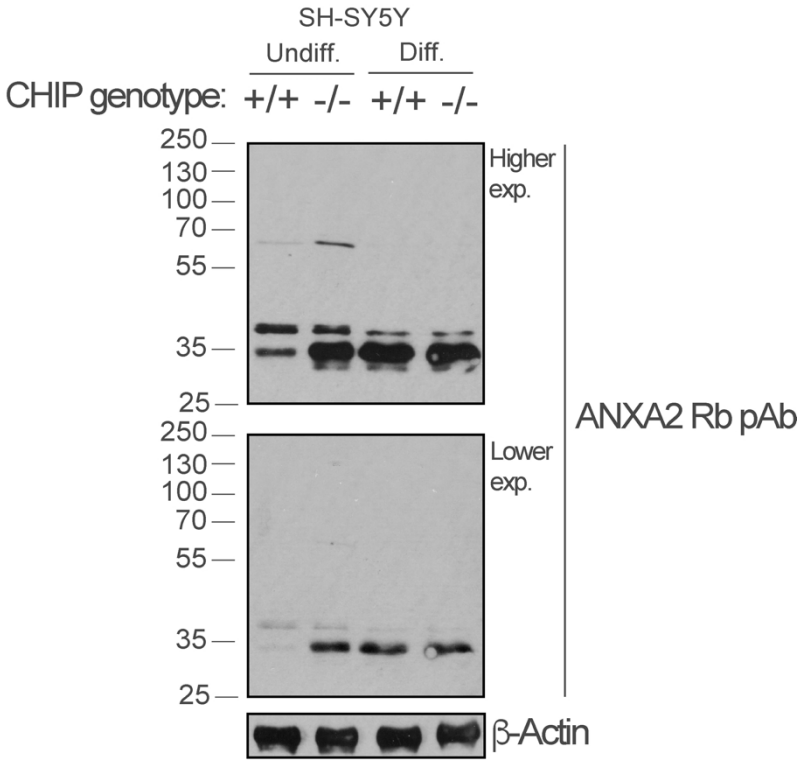


**Figure 5.9: Annexin A2 expression in differentiated SH-SY5Y CHIP KO and WT cells**
Undifferentiated and differentiated SH-SY5Y CHIP KO and WT cells were lysed with urea-based lysis buffer (the same as that used for SWATH-MS). For each sample, 20 μg of lysate was loaded per 12% gel for SDS-PAGE/WB. The immunoblot was probed with anti-ANXA2 Rb pAb (1:1000) and then with anti-β-actin mAb (1:5000). This immunoblots is representative of at least 3 biological replicates.

## 5.2.2 Subcellular localisation of Annexin A2 in CHIP models

According to the literature[168], a small subpopulation of ANXA2 is nuclear, while some is membrane-bound and the majority is cytoplasmic. While we do not detect nuclear ANXA2 by subcellular fractionation, the cytoplasmic and, to a lesser extent, the membrane-bound fractions are present in undifferentiated SH-SY5Y CHIP KO and WT cells (Figure 5.10). IF conditions were optimised to detect these pools of ANXA2 (Figure 5.11). While ANXA2 was largely nuclear when samples were fixed with 4% paraformaldehyde, membrane and cytoplasmic staining was seen when fixed with the other reagents. Clearly, the various fixation methods cause different protein epitopes to become exposed to the antibodies. Fixation with 4% PFA & methanol seems to be optimal – allowing detection of all subcellular populations of ANXA2 (nuclear, membrane-bound and cytoplasmic).

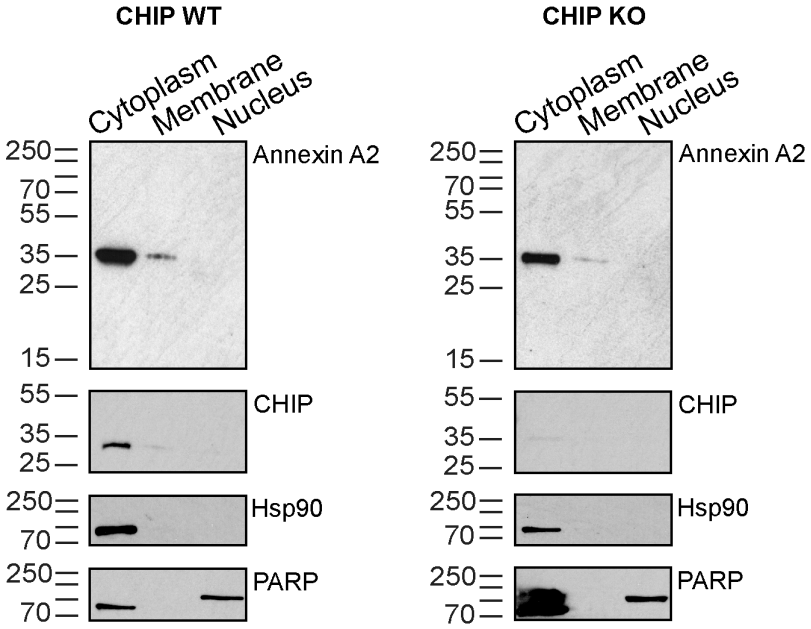


**Figure 5.10: Subcellular localisation of Annexin A2 and CHIP**
Differentiated SH-SY5Y CHIP KO and WT cells were harvested and lysed using a subcellular protein fractionation kit. Cytoplasmic, membrane and nuclear fractions were analysed by 15% SDS-PAGE/immunoblot. Immunoblots were probed with anti-ANXA2 pAb (1:1000) and anti-CHIP mAb (1:10000), as well as anti-Hsp90 (1:1000) and anti-PARP (1:1000) antibodies as controls. Sample loading between different fractions and cell lines was based on volume, rather than cell count or protein concentration (due to protocol limitations). Immunoblots representative of 2 biological replicates.

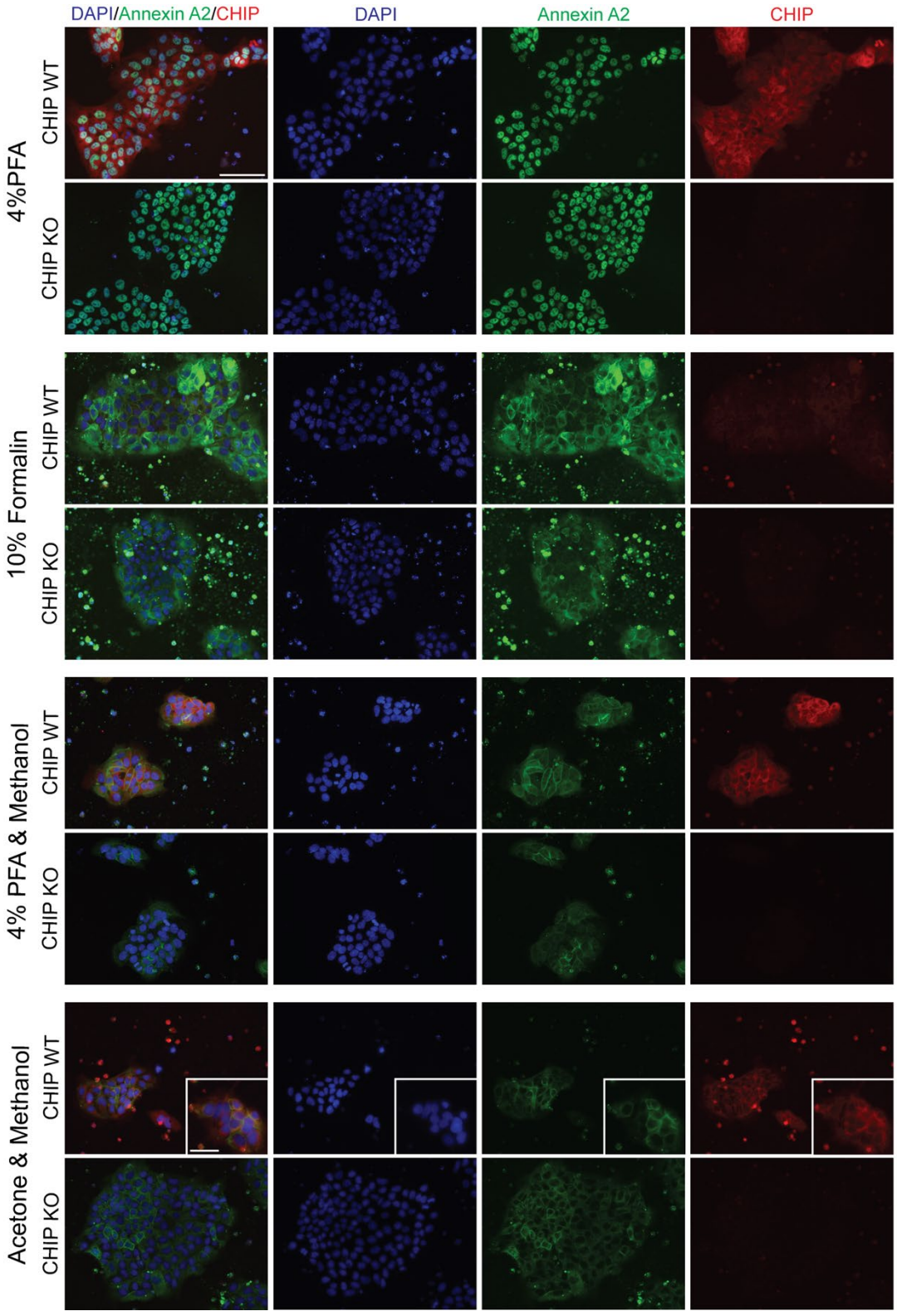


**Figure 5.11: Effect of fixation method on the staining of Annexin A2**
Immunofluorescence assay of CHIP WT and KO iPSC fixed with different fixation reagents (as indicated) and incubated with anti-ANXA2 pAb (1:500) and anti-CHIP mAb (1:1000). Nuclei were stained with DAPI. Axio Imager, Zeiss, 20x and 63x objectives. Scale bars, 100 mm and 20 mm (inlet images), respectively. Images obtained from cells fixed with 4% PFA are representative of at least 3 biological replicates and those fixed with 4% PFA & methanol are representative of at least 7 biological replicates from different independent experiments.

As previously observed in cortical neurons (Figure 4.25), there is no difference in the ANXA2 staining by IF in undifferentiated SH-SY5Y CHIP KO and WT cells, independent of the fixation reagent used. Findings from this assay contradict those obtained by SWATH-MS and WB, despite the use of the same antibody for the latter assay. Possible explanations could be differential epitope exposure and varying degrees of lysate solubilization obtained by the different methods. Potentially the pool of ANXA2 readily detected by IF is unchanged between these CHIP cell models. However, this does not exclude the existence of CHIP-mediated regulation of ANXA2, possibly at a post-translational level. In favour of such emerging hypothesis, as with most protein binding partners, CHIP and ANXA2 are present within the same subcellular compartment (cytoplasm).

### 5.2.3 Annexin A2 interacts with CHIP

Being present in the same subcellular compartment, CHIP and ANXA2 could interact directly or within a complex conformation. Following optimisation of the IP conditions, endogenous ANXA2 was seen to co-immunoprecipitate with endogenous CHIP (Figure 5.12). Unfortunately, given the “sticky” nature of self-aggregating and membrane-binding proteins, residual ANXA2 bound to the beads without anti-ANXA2 antibody (lane 3). A band for CHIP was also detected in lane 3, but it is weaker than that in the IP (lane 4).

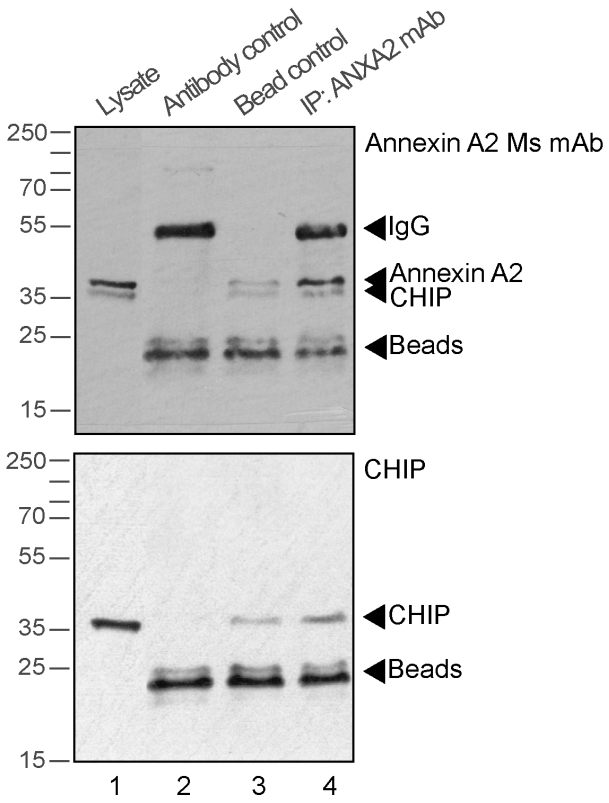


**Figure 5.12: Co-immunoprecipitation of endogenous Annexin A2 and CHIP**
Lysate from CHIP WT undifferentiated SH-SY5Y (1 mg total protein/reaction) was incubated with protein-G beads alone (lane 3) or with protein-G beads that had been cross-linked to anti-ANXA2 Ms mAb (IP: ANXA2 mAb, lane 4). A reaction of antibody with beads and without lysate was also included (lane 2) showing the IgG band from the antibody (in lanes 2 and 4). Each reaction was analysed by WB. The immunoblot was firstly probed with HRP-conjugate anti-Ms pAb (secondary antibody), to identify the background noise derived from the beads and the antibody itself (not included). It was then probed with anti-CHIP mAb (1:10000), exposed and then with anti-ANXA2 mAb (1:1000). This immunoblot is representative of 2 co-IP experiments using different anti-ANXA2 antibodies (mAb and pAb).

Taking into account the limitations of the IP, it was important to validate this interaction using a different method and, moving forward, question whether it occurs in cells. For such, PLA detecting CHIP:ANXA2 interaction was conducted in mature cortical neurons (Figure 5.13). Indeed, some PLA signal was seen in CHIP WT neurons (in the two control lines), but not in CHIP KO neurons. Furthermore, the PLA signal detected is likely to be an underestimation, since these neurons were fixed with 4% paraformaldehyde (where ANXA2 is likely to be mostly nuclear, while CHIP is essentially absent from the nucleus).

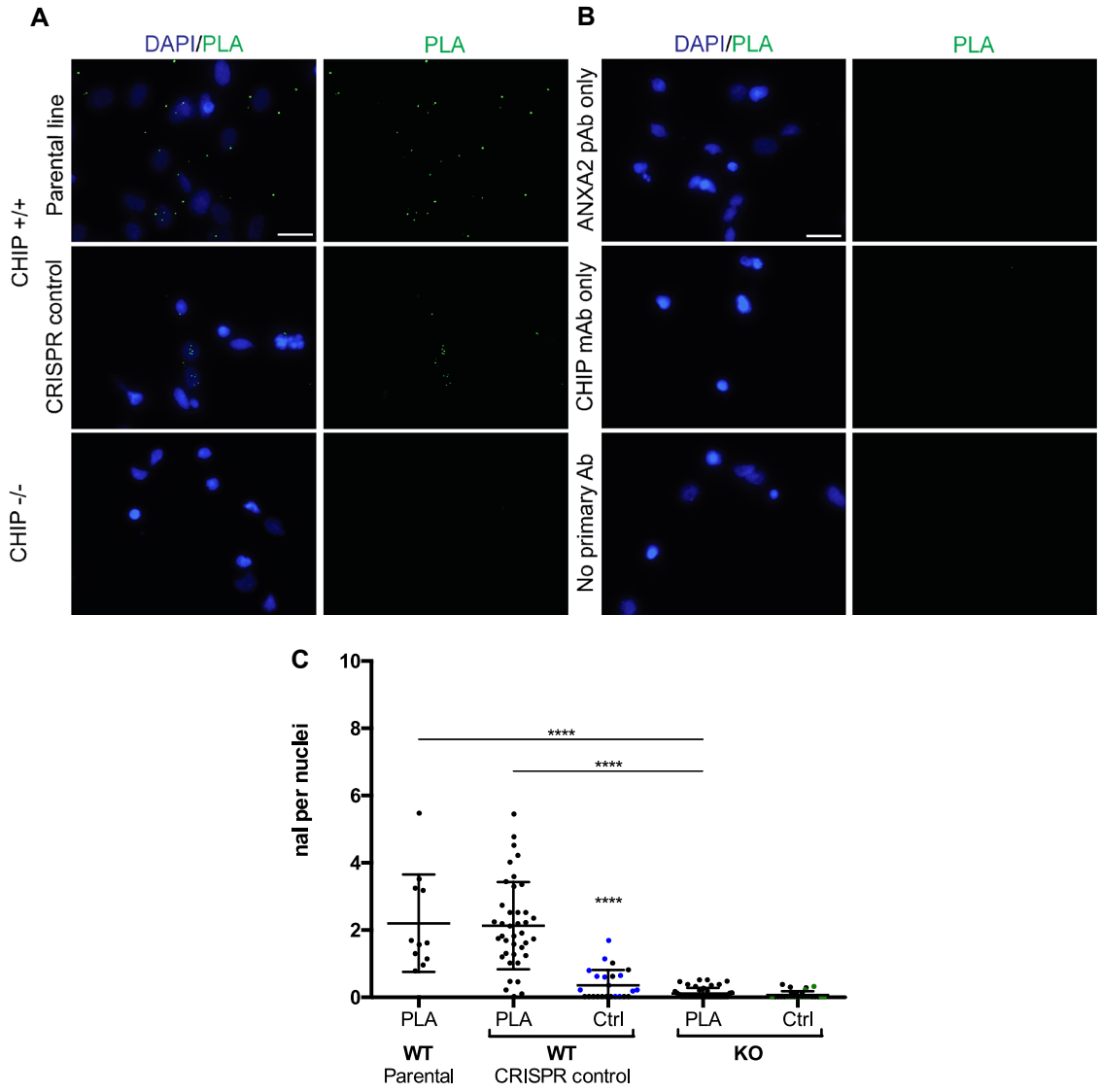


**Figure 5.13: Annexin A2 & CHIP interaction by PLA in cortical neurons**
**A)** CHIP KO and WT mature cortical neurons were fixed with 4% PFA. A single well of the parental line and triplicate wells of the CRISPR control and CHIP KO line were stained with anti-ANXA2 pAb (1:500) and anti-CHIP mAb (1:1000) antibodies (referred to as "PLA" in **C**). PLA signal (puntae in green) were quantified using ImageJ and normalised by the number of nuclei (stained with DAPI) within a field of view.
**B)** In parallel, two wells of CHIP WT (CRISPR control) (for CHIP only and no primary Ab conditions) and CHIP KO (for ANXA2 only) were used for control conditions (grouped under "Ctrl" in **C**): wells were incubated with either antibodies alone (ANXA2 only in green and CHIP only in blue) or with no primary antibodies (in black).
**A-B)** Axio Imager, Zeiss, 63x objective. Scale bar, 20 μm.
**C)** Quantifications of PLA signal per nuclei of different cell lines were represented in the dot plot as mean ± SD. Kruskal-Wallis test and Dunn's multiple comparisons post-test (comparisons between PLA and Ctrl conditions per cell line is indicated above each Ctrl), ****$P < 0.0001$, $n \geq 12$ images per biological triplicate and $n \geq 12$ images per control condition per cell line.

To investigate whether this interaction is consistent in other CHIP cell models, the same PLA conditions were used in undifferentiated SH-SY5Y (Figure 5.14A-C). The same trend was observed. In addition to CHIP KO and WT cells, cell lines derived from the CHIP KO cell line stably expressing the E3 ligase dead mutant H260Q (CHIP KO + H260Q) or wild-type CHIP (CHIP KO + WT) were also analysed. The former mutation lies within the U-box prevents its interaction with the E2, thus inhibiting the ubiquitination cascade[47,186]. Both these lines rescued the CHIP:ANXA2 interaction that was absent from the CHIP KO line. It is important to note that, as shown in Figure S.5, the KO+H260Q line has increased CHIP expression compared to endogenous CHIP (compared to CHIP WT cell line) and that not all cells of the KO+WT line express CHIP, and the CHIP-positive ones have increased intensity compared to cells of the CHIP WT line. This disparity within the CHIP KO+WT line probably gives rise to the variability seen in the PLA quantification. However, considering that the KO + H260Q line has much higher CHIP expression compared to endogenous WT CHIP, increases the confidence of these results.

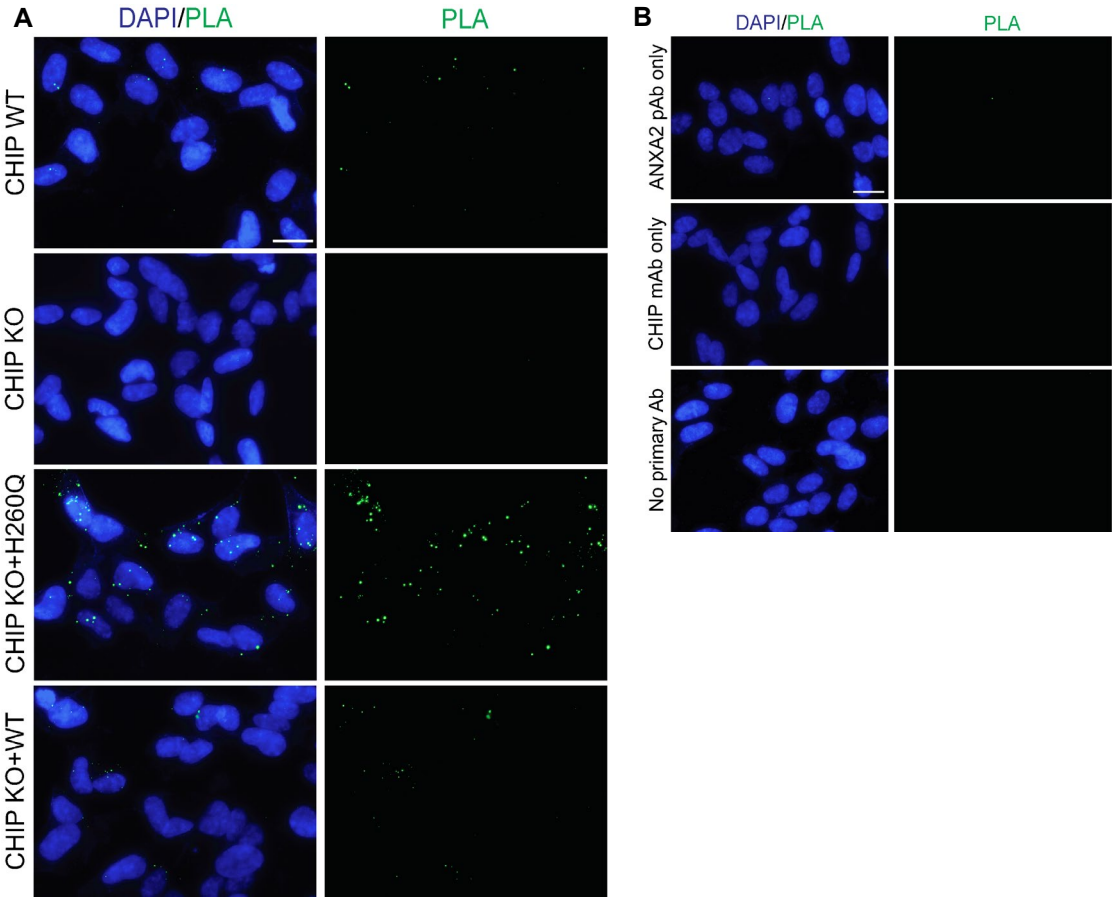


**Figure 5.14: CHIP & Annexin A2 interaction by PLA in undifferentiated SH-SY5Y**
**A&B)** Undifferentiated SH-SY5Y cells of different CHIP genotypes (WT, KO and the stable cell lines KO+H260Q and KO+WT) were fixed with 4% PFA and then methanol.
**A)** For each cell line, duplicate wells were stained with anti-ANXA2 pAb (1:500) and anti-CHIP mAb (1:1000) antibodies (referred to as "PLA" in **C** and biological duplicates are colour-coded with black or green dots). PLA signal (puntae in green) were quantified using ImageJ in a semi-automated manner and normalised by the number of nuclei (stained with DAPI) within a field of view.
**B)** In parallel, three controls were included (grouped under "Ctrl" in **C**): wells containing CHIP WT cells were incubated with either antibodies alone (ANXA2 only in green and CHIP only in blue) or with no primary antibodies (in black).
Axio Imager, Zeiss, 63x objective. Scale bars, 20 μm.
Representative data of at least 2 independent PLA experiments.

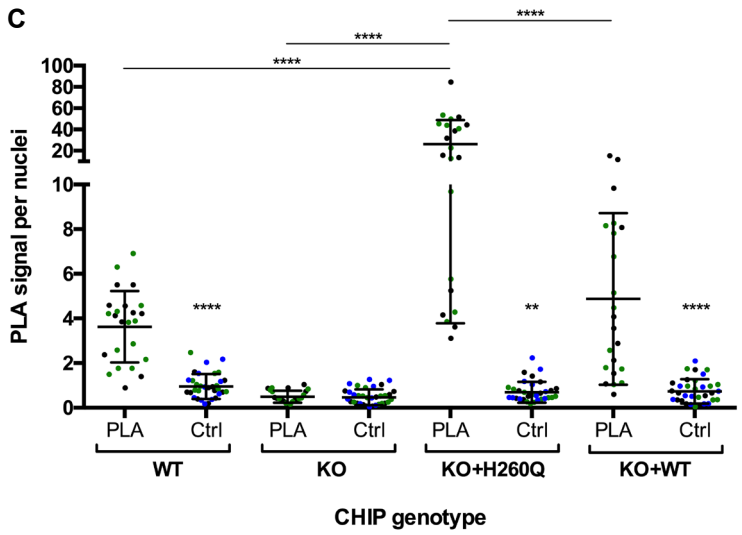


**Figure 5.14** *(continued)*
**C)** Quantifications of PLA signal per nuclei of different cell lines represented in the dot plot as mean ± SD. All PLA datasets passed the D'Agostino Pearson normality test. One-way ANOVA with Holm-Sidak's multiple comparisons post-test (comparisons between PLA and Ctrl conditions per cell line is indicated above each Ctrl), $^{**}P < 0.005$, $^{****}P < 0.0001$, $n \geq 11$ images per biological duplicate and $n \geq 10$ images per control condition per cell line.

## 5.2.4 CHIP-dependent changes in Annexin A2 profile in CHIP models

As a preliminary and gross approach to assess the existence of CHIP-dependent species of ANXA2, the global profile of the steady state levels and form(s) of ANXA2 in different CHIP cell models was analysed by 2D-gel WB in collaboration with Jitka Zakova[†] (Figure 5.15). Under un-optimised conditions, both undifferentiated SH-SY5Y and iPSC showed similar forms of ANXA2. The CHIP KO lysates show novel higher-MW forms of ANXA2, that ran at around 75 kDa in SH-SY5Y cells and 50 kDa in iPSC (indicated by the red arrows). Beyond this predominant feature, there are other differences in the ANXA2 species detected when comparing CHIP WT to KO cells. This supports the existence of post-translational modifications of ANXA2. Further optimisation of the conditions and MS analysis of individual bands could be informative.

[†] Department of Molecular Pathology and Biology, University Hospital Ostrava, Hradec Kralove, Czech Republic

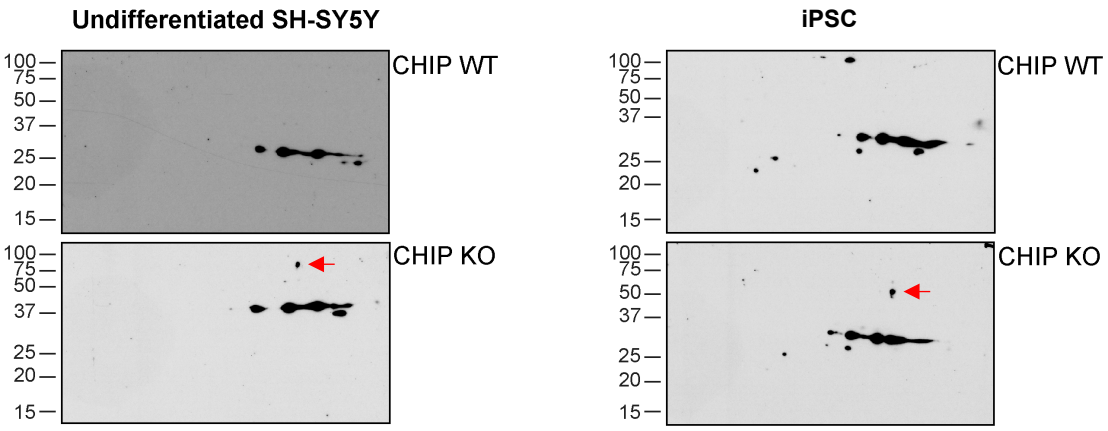


**Figure 5.15: Annexin A2 protein profile in CHIP KO models**
Undifferentiated SH-SY5Y and iPSC CHIP KO and WT cells were harvested with urea-based lysis buffer and loaded (100 μg) onto separate 2D gels for SDS-PAGE/WB (gels ran in parallel). Immunoblots were probed with anti-ANXA2 pAb (1:1000).

## 5.2.5 CHIP-dependent ubiquitination of Annexin A2 *in vitro*

Given this CHIP:ANXA2 interaction and the E3 ligase functions of CHIP, we sought to investigate whether CHIP could ubiquitinate ANXA2. Once the *in vitro* ubiquitination assay was optimised (Figure 5.16 A,B&D), both ubiquitinated ANXA2 species (Figure 5.16A&D) and auto-ubiquitination of CHIP (Figure 5.16 A&B) were readily detected. The higher MW ANXA2 isoforms were detected with different anti-ANXA2 and anti-Ub antibodies (Figure 5.17). These were both CHIP- and ATP-dependent (Figure 5.17).

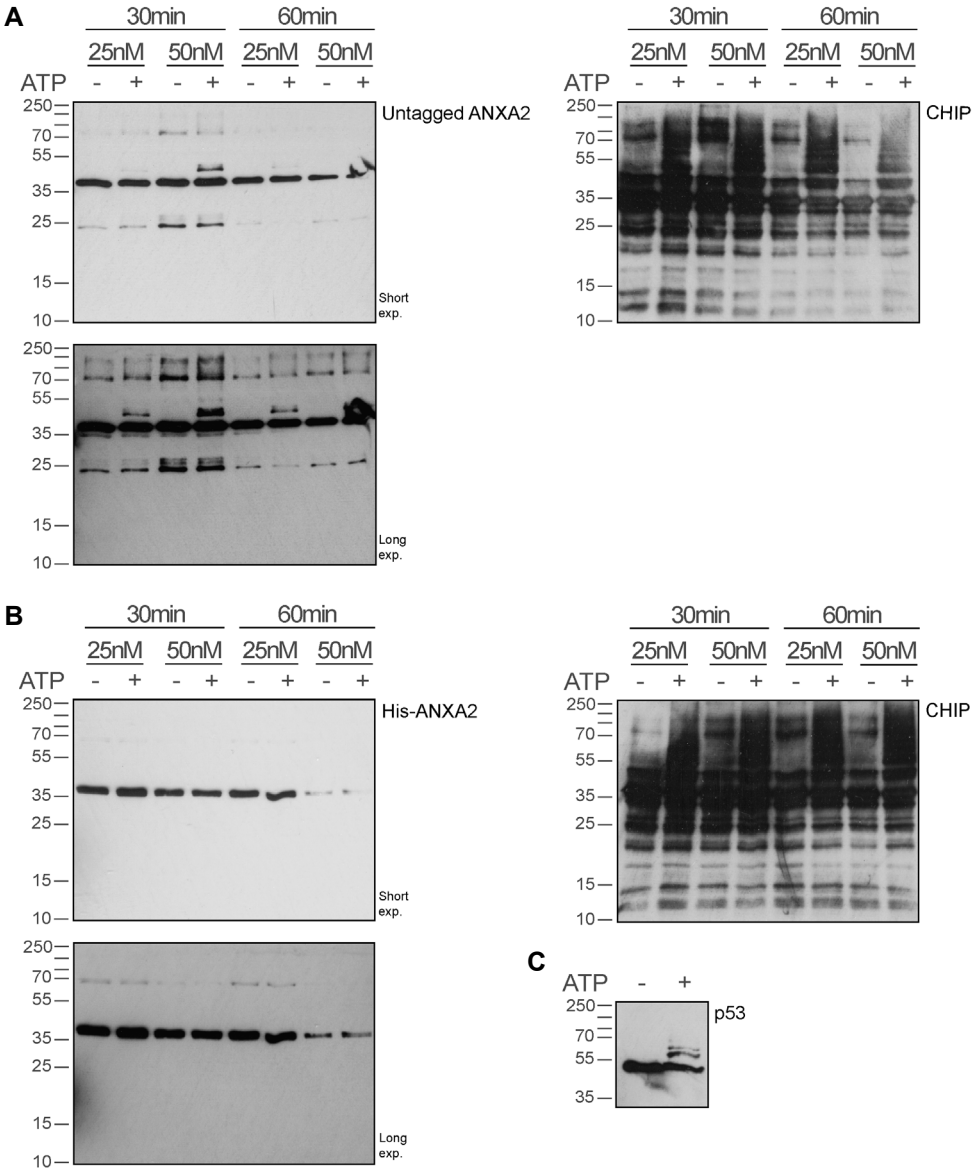


**Figure 5.16: Optimisation of CHIP-dependent *in vitro* ubiquitination of Annexin A2**
*In vitro* ubiquitination assays using untagged human recombinant ANXA2 (**A**) or His-tagged (**B**) at the concentrations and react times indicated. Each reactions was analysed by two 15% SDS-PAGE/WB gels ran in parallel. One immunoblot was probed with anti-ANXA2 Rb pAb (1:1000) and the other anti-CHIP mAb (1:10000). The in vitro ubiquitination of p53 was conducted as positive control and stained using anti-p53 mAb (1:500) (**C**).

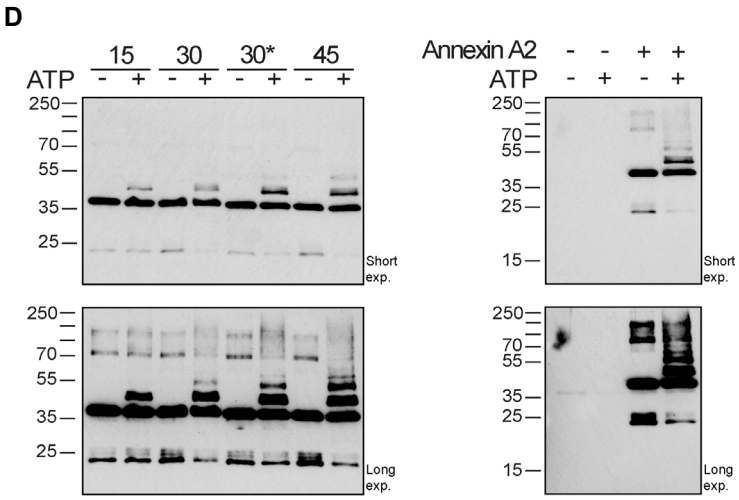


**Figure 5.16** *(continued)*
**D)** Time-course of *in vitro* ubiquitination assay using the untagged ANXA2 from 15 min to 60 min (immunoblots on the right). *Refers to a sample that was denatured with 1:4 DTT:loading dye, compared to the 1:2 ratio used for the other reactions. These immunoblots were also probed with anti-ANXA2 Rb pAb (1:1000).

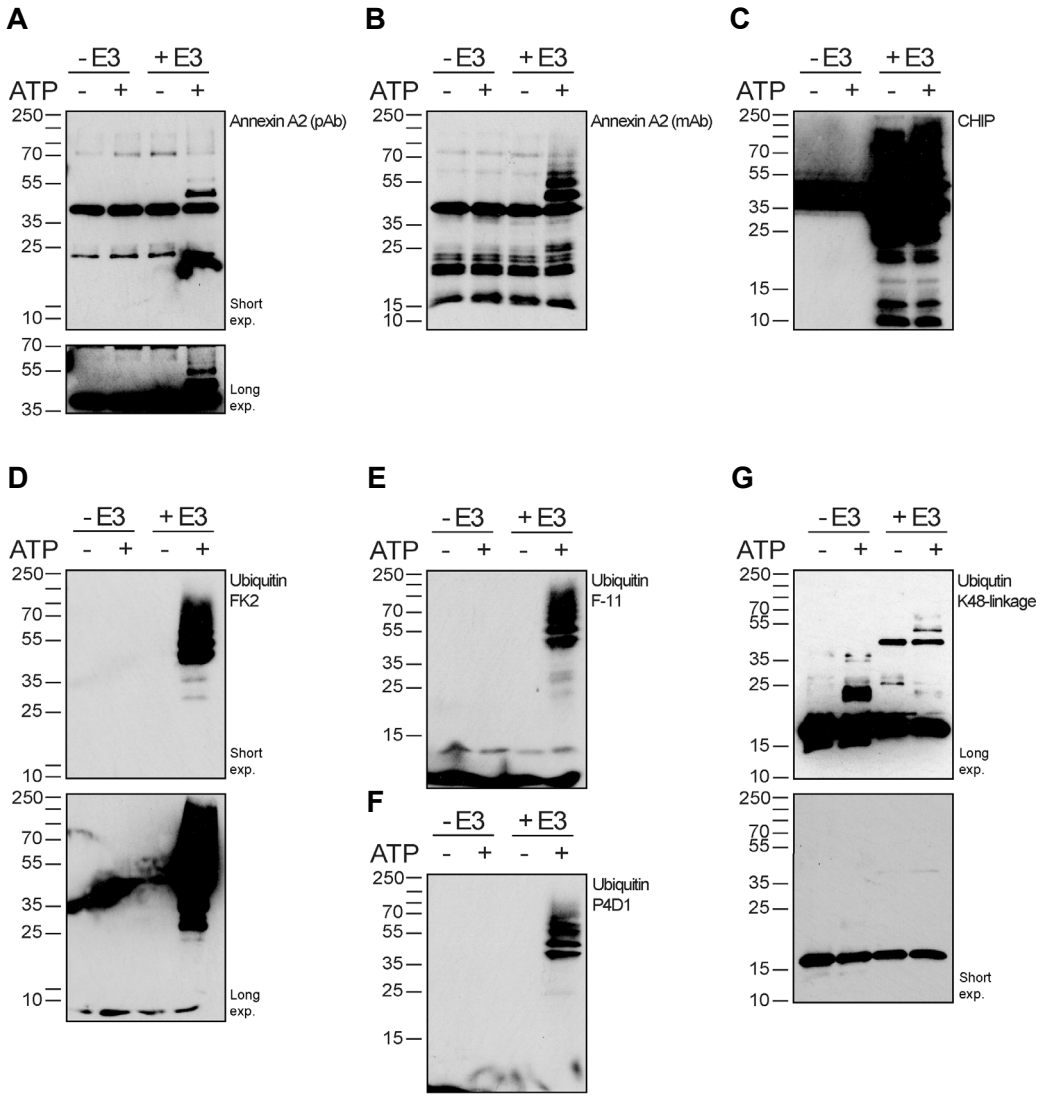


**Figure 5.17: CHIP-dependent *in vitro* ubiquitination of ANXA2**
*In vitro* ubiquitination assays using untagged human recombinant ANXA2 in the presence and absence of CHIP and ATP for 1h. Reactions were made in batch and loaded onto different gels for SDS-PAGE/WB. Immunoblots were probed with two anti-ANXA2 antibodies (1:1000 Rb pAb, **A**, and 1:500 Ms mAb, **B**), anti-CHIP mAb (1:10000), **C**, and three anti-Ub antibodies (FK2, **D**, F-11, **E**, P4D1, **F**, and the K48-linkage specific antibody, **G**, each used at 1:1000).

### 5.2.6 CHIP-dependent ubiquitination of Annexin A2 *in situ*

In attempt to detect endogenous ANXA2 ubiquitination, PLA using anti-ANXA2 and anti-Ub antibodies was conducted. Prior to this, the fixation methods and antibody conditions were optimised (Figure S.6). The PLA revealed that ANXA2 is in close proximity with Ub (within 40 nM) in CHIP WT SH-SY5Y cells, but not KO cells. Interestingly, cells expressing the E3 ligase-dead CHIP mutant (CHIP KO + H260Q) had a similar PLA signal to that of KO cells and was statically different from WT cells. The cell line re-expressing fully functional CHIP (CHIP KO + WT), rescued this ANXA2-Ub interaction, having a PLA signal similar to that of WT cells and statistically different from the other lines (Figure 5.18). In parallel to the PLA, an IF was conducted using the same antibodies (Figure S.7). Together with the findings from the *in vitro* ubiquitination assay, this would suggest that ubiquitination of ANXA2 is CHIP-dependent.

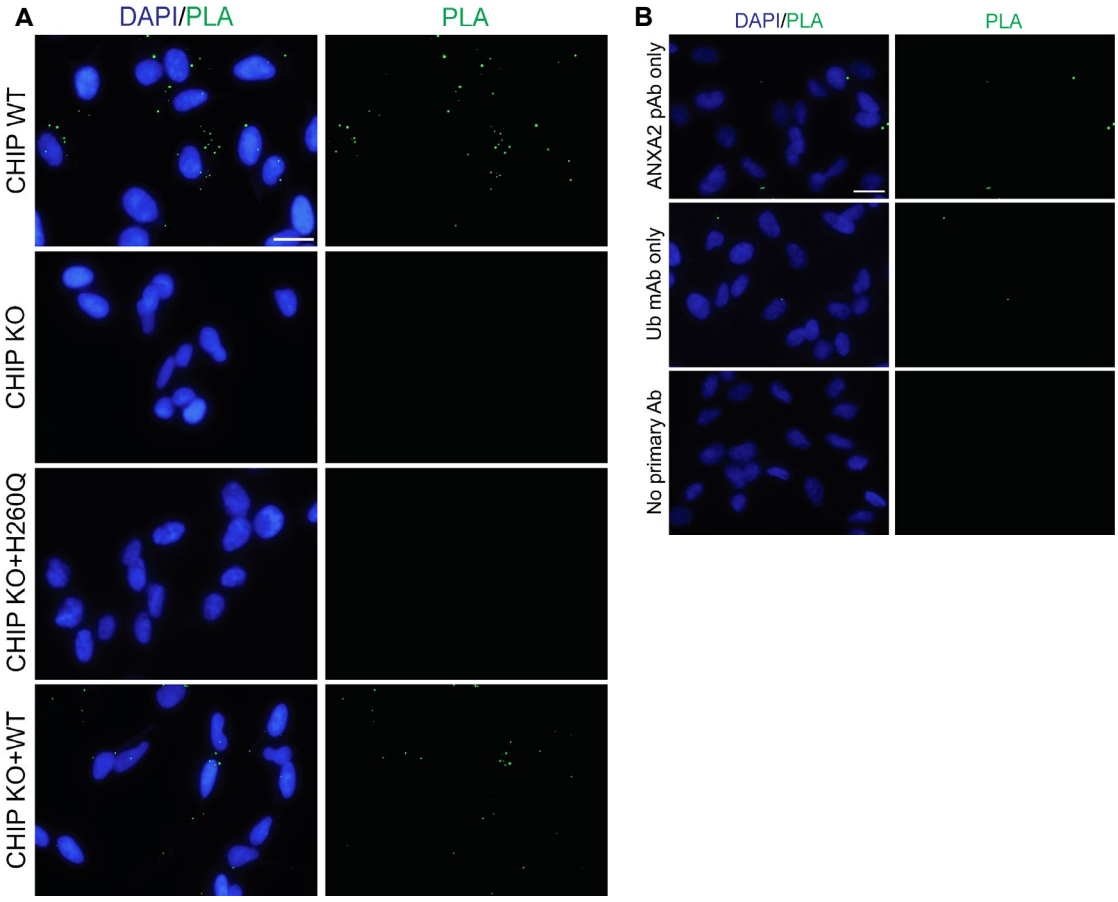


**Figure 5.18: Ubiquitin & Annexin A2 interaction by PLA in undifferentiated SH-SY5Y**
**A&B)** Undifferentiated SH-SY5Y cells of different CHIP genotypes (WT, KO and the stable cell lines KO+H260Q and KO+WT) were fixed with acetone and methanol.
**A)** For each cell line, duplicate wells were stained with anti-ANXA2 pAb (1:500) and anti-Ubiquitin mAb (P4D1) (1:100) antibodies (referred to as "PLA" in **C** and biological duplicates are colour-coded with black or green dots). PLA signal (puntae in green) were quantified using ImageJ in a semi-automated manner and normalised by the number of nuclei (stained with DAPI) within a field of view.
**B)** In parallel, three controls were included (grouped under "Ctrl" in **C**): wells containing CHIP WT cells were incubated with either antibodies alone (ANXA2 only in green and Ubiquitin only Axio Imager, Zeiss, 63x objectives. Scale bars, 20 μm.

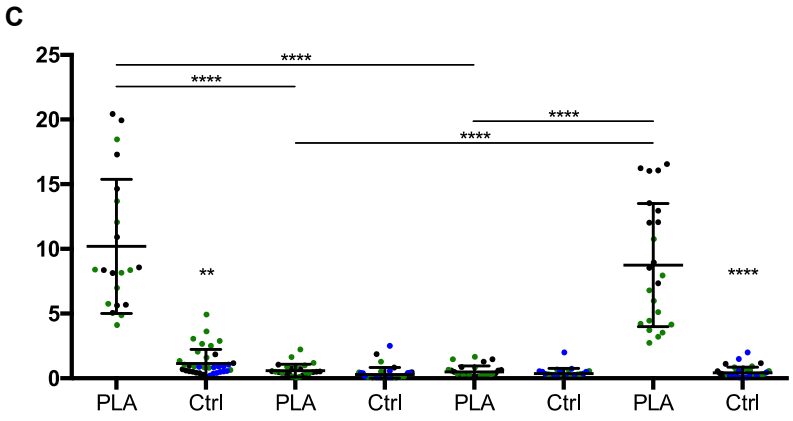


**Figure 5.18** *(continued)*
**C)** Quantifications of PLA signal per nuclei of different cell lines represented in the dot plot as mean ± SD. Kruskal-Wallis test and Dunn's multiple comparisons post-test (comparisons between PLA and Ctrl conditions per cell line is indicated above each Ctrl), $^{**}P < 0.005$, $^{****}P < 0.0001$, $n \geq 10$ images per biological duplicate and $n \geq 11$ images per control condition per cell line.

Since different polyubiquitination chains drive ubiquitinated proteins to different cellular fates, we next tried to elucidate what Ub chain linkages were in close proximity with ANXA2. PLA using an anti-ANXA2 antibody and either K63 or K48 Ub-linkage specific antibody was performed in CHIP WT, KO and rescue cell lines (Figure 5.19). As previously observed in the Ub-ANXA2 PLA, the interaction of ANXA2 with the different Ub chain types was more frequent in WT cells compared to CHIP KO cells. The SH-SY5Y stable cell lines expressing either the E3 ligase-mutant CHIP (KO + H260Q) or a chaperone-dead mutant CHIP (KO + K30A) were also included in this assay. While the PLA signal obtained from the KO + H260Q line was not statistically different from that of CHIP KO cells, the KO + K30A line was able to partly rescue the PLA signal. The same trends were seen in both K48 and K63 Ub chain specific PLAs.

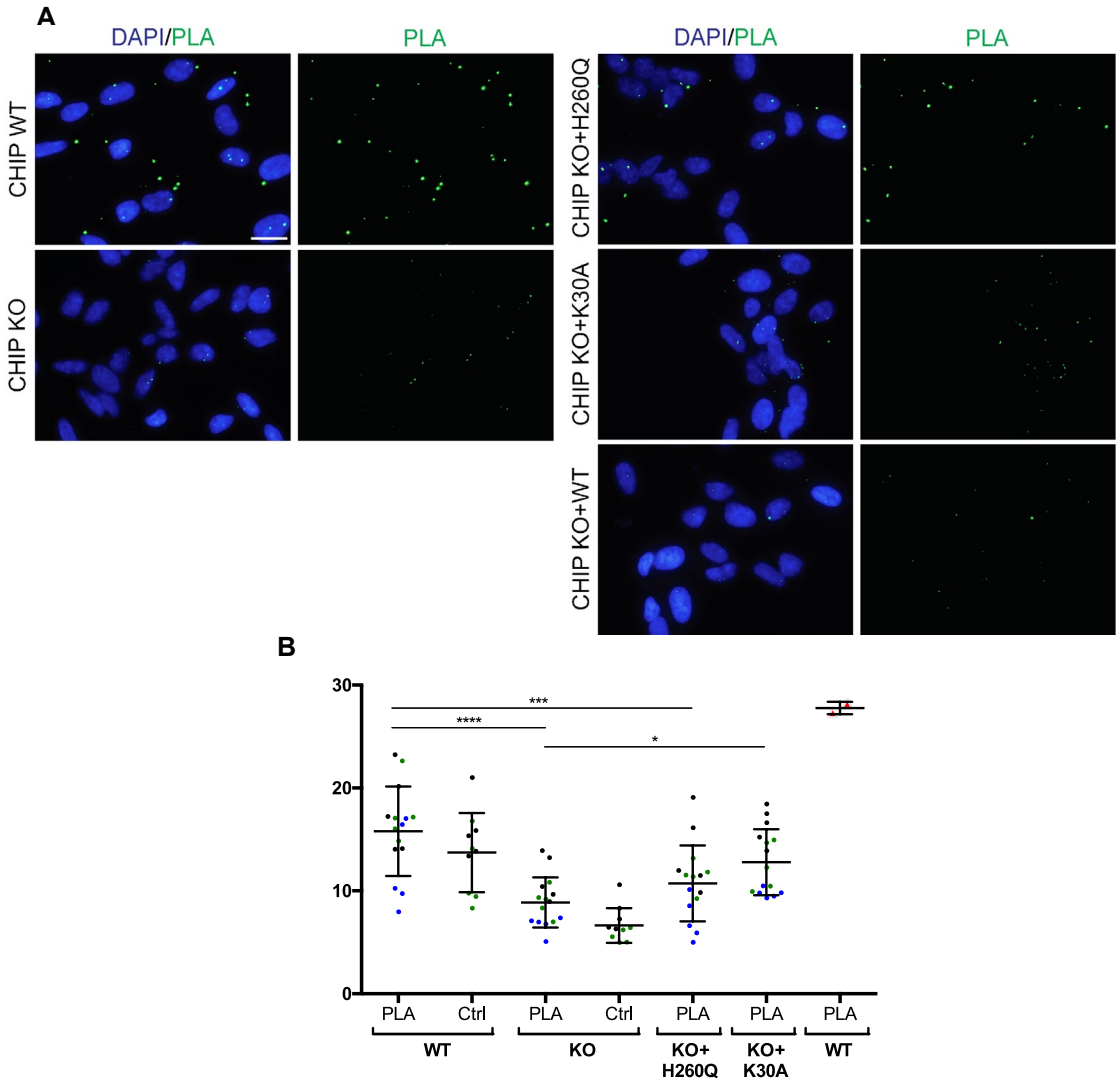


**Figure 5.19: Annexin A2 & Ubiquitin-linkage specific interaction by PLA in undifferentiated SH-SY5Y**

**A,C,E)** Undifferentiated SH-SY5Y cells of different CHIP genotypes (WT, KO and the stable cell lines KO+H260Q and KO+K39A) were fixed with 4% PFA and then methanol.

**A)** For each cell line, triplicate wells were stained with anti-ANXA2 pAb (1:500) and anti-K48-linkage specific Ub chain antibody (1:100) (referred to as "PLA" in B and biological replicates are colour-coded with black/blue/green dots). As a positive control, the anti-Ub antibody (same as in Figure 5.18) was used instead of the Ub chain-specific linkage antibody was used in a sample. PLA signal (puntae in green) were quantified using ImageJ in a semi-automated manner and normalised by the number of nuclei (stained with DAPI) within a field of view.

**B)** Quantifications of PLA signal per nuclei of different cell lines represented in the dot plot as mean ± SD. One-way ANOVA with Holm-Sidak's multiple comparisons post-test (comparisons between PLA and Ctrl conditions per cell line is indicated above each Ctrl), *$P$ < 0.05, ***$P$ < 0.0005, ****$P$ < 0.0001, $n$ ≥ 5 images per biological duplicate (except for the single positive control) and $n$ ≥ 5 images per control condition per cell line (and 2 images for the positive control).

Axio Imager, Zeiss, 63x objective. Scale bar, 20 μm.

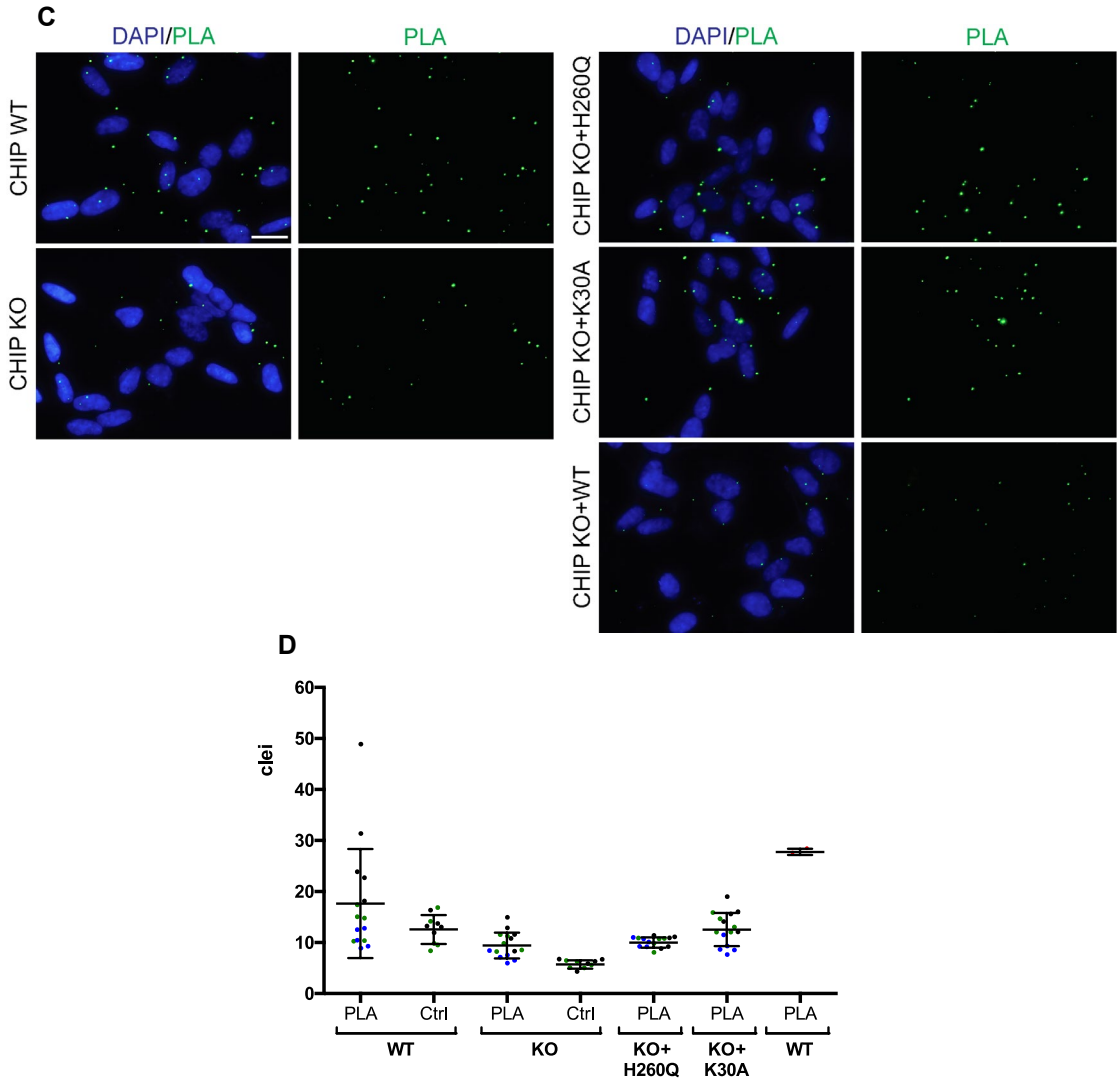


**Figure 5.19** *(continued)*
**C)** For each cell line, triplicate wells were stained with anti-ANXA2 pAb (1:500) and anti-K63-linkage specific Ub chain antibody (1:100) (referred to as "PLA" in **D** and biological replicates are colour-coded with black/blue/green dots). As a positive control, the anti-Ub antibody (same as in Figure 5.17) was used instead of a Ub chain-specific linkage antibody. PLA signal (puntae in green) were quantified using ImageJ in a semi-automated manner and normalised by the number of nuclei (stained with DAPI) within a field of view.
**D)** Quantifications of PLA signal per nuclei of different cell lines represented in the dot plot as mean ± SD. Kruskal-Wallis test and Dunn's multiple comparisons post-test (comparisons between PLA and Ctrl conditions per cell line is indicated above each Ctrl), $n \geq 5$ images per biological duplicate (except for the single positive control) and $n \geq 5$ images per control condition per cell line (and 2 images for the positive control).
Axio Imager, *Zeiss*, 63x objective. Scale bar, 20 μm.

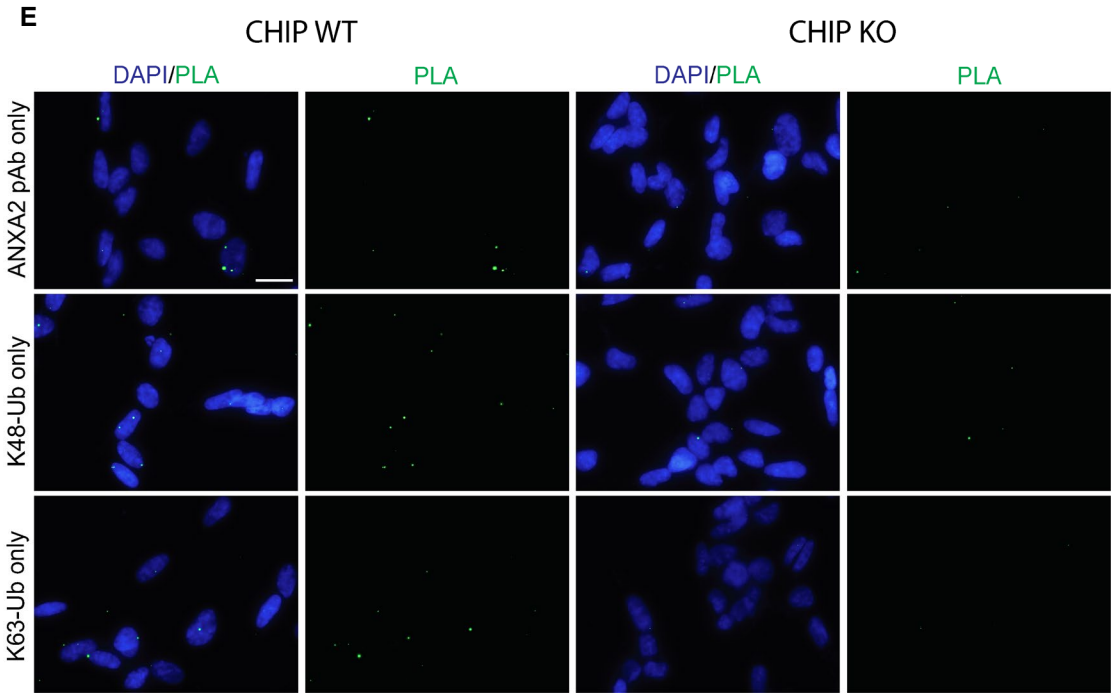


**Figure 5.19** *(continued)*
**E)** In parallel, controls were included (grouped under "Ctrl" in **B&D**): wells containing CHIP WT and KO cells were incubated with antibodies alone (ANXA2 only in green and either anti-Ubiquitin antibodies only in blue).
Axio Imager, *Zeiss*, 63x objective. Scale bar, 20 μm.

CHIP expressed in the latter line carries a mutation in the TPR of CHIP, which prevents its binding to Hsp90 and Hsp/Hsc70[186]. Interestingly, K30A CHIP also has an intrinsic defect in E3 ligase activity (severely restricted auto-ubiquitination and reduced substrate ubiquitination, both *in vitro* and in cells) (Figure 5.20A[47]). This functional defect can be explained by structural changes. K30A CHIP has reduced structural flexibility, which "mimics" binding of Hsp70/90 to the ligase (Figure 5.20B&C[47]). The transition from a highly flexible to a more structured TPR domain allosterically modulates the E3 ligase activity of CHIP. It does so by attenuating the correlated motions between the two U-box domains of the dimer and the anticorrelated motions between these and one of the TPR domains. This impairs the nature of the U-box, rather than altering the accessibility of either U-boxes at any given time[47]. The E3 ligase activity across these cell lines is as follows: WT > K30A > H260Q[47]. This helps to explain why only a partial rescue was achieved with the KO + K30A.

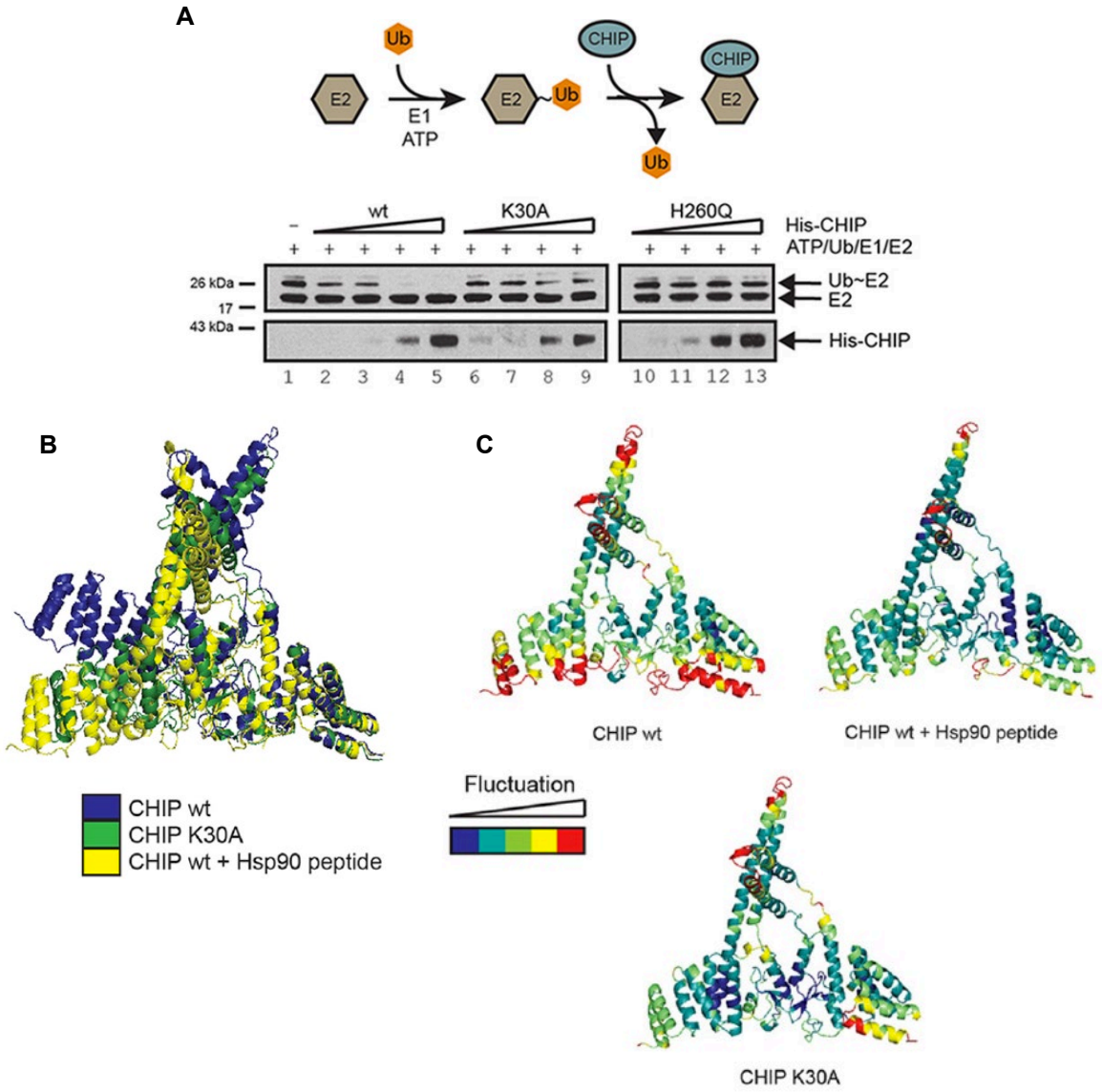


**Figure 5.20: Activity and conformation of CHIP mutants**
**A)** In vitro Ub discharge assay using WT, K30A and H260Q CHIP. Firstly, the E2 His-UbcH5a was charged with Ub by incubating with the E1 UBE1, Ub and ATP. The Ub discharge from the E2 to His-CHIP (WT and mutants) was monitored. Reactions were analysed by SDS-PAGE/immunoblot using antibodies against CHIP and the E2. H260Q CHIP was not able to discharge E2 and the activity of K30A was also impaired compared to WT CHIP, which showed a clear dose-dependent effect.
**B)** Molecular dynamic (MD) stimulations of unliganded dimers of CHIP K30A (green) and CHIP WT in the absence (blue) and presence (yellow) of a Hsp90 peptide.
**C)** Positional fluctuation analysis across the structure of unliganded dimers of CHIP K30A and CHIP WT ± Hsp90 peptide. The root mean square fluctuations obtained from the stimulations were averaged over amino acids and colour-coded on the crystal structure.
(Narayan *et al.*[47])

We have identified pronounced changes in the proteostasis of ANXA2 in CHIP KO cortical neurons and, to a lesser extent, undifferentiated SH-SY5Y. Beyond affecting steady state levels, the expression of CHIP induces changes in the isoforms of ANXA2 across cell lines, which could reflect post-translational modifications. Namely, CHIP-dependent ubiquitination of ANXA2 was detected *in vitro* and is likely to occur in cells. The cellular consequence of this event and what drives it remains unknown.

### 5.2.7 Expression of Annexin A2 in cortical neurons correlates with poor membrane permeability

Aiming to elucidate the possible significance of the increased ANXA2 levels observed in CHIP KO neurons and given the role of Annexins in membrane homeostasis, membrane integrity was assessed. For such, a cell-impermeable dye (FITC dextran) was added extracellularly to cells. Internalisation of the dye is a short-term marker of poor membrane integrity. The correlation between membrane permeability and endogenous ANXA2 was evaluated (Figure 5.21). ANXA2 co-localised more with intracellular dye in CHIP KO neurons compared to WT, at basal conditions. However, interpretation of dextran uptake into cells requires caution, as the dye is also endocytosed within minutes, thus intracellular dextran would eventually be affected by both the leakiness of the membrane (i.e. passive transport) and endocytosis velocity. Although preliminary, this observation paved way for assays addressing membrane integrity in a quantitative and more sensitive manner.

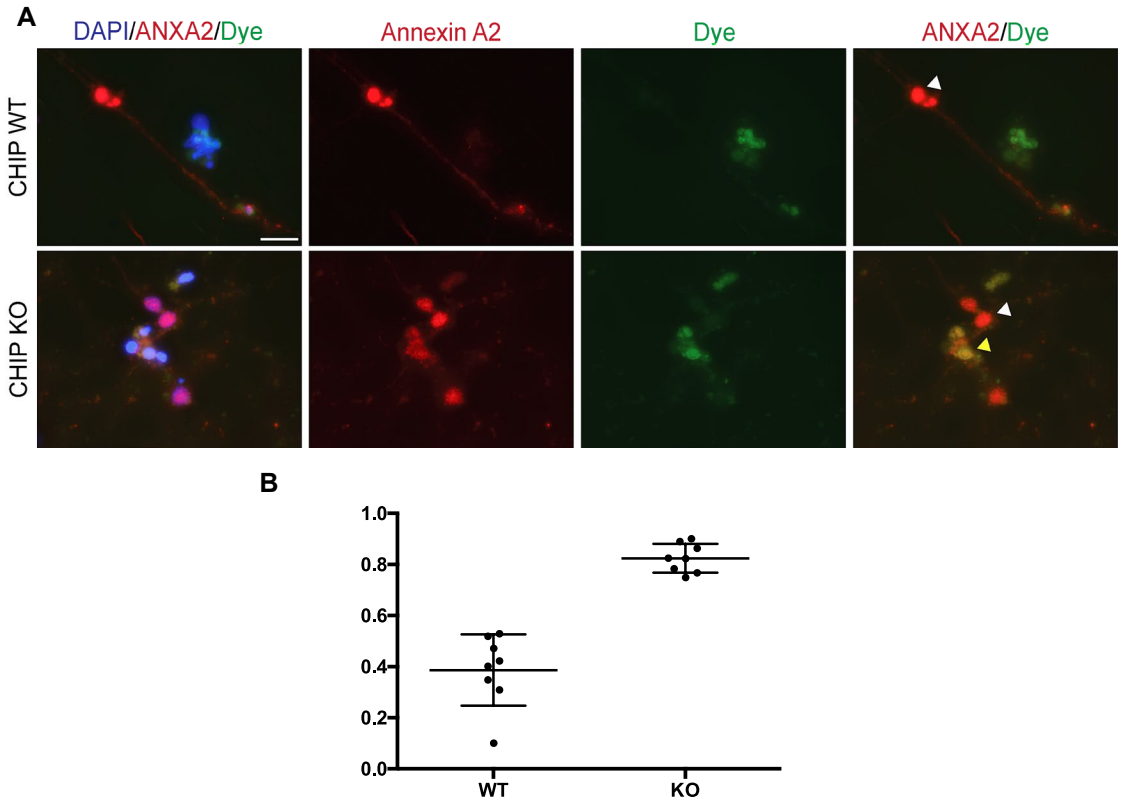


**Figure 5.21: Annexin A2 correlates with increased membrane permeability in CHIP KO cortical neurons**

**A)** Mature cortical neurons of CHIP WT and KO genotypes were treated with the cell impermeable dye FITC dextran at basal conditions prior to fixation with 4% paraformaldehyde. IF using anti-ANXA2 pAb (1:500) was performed and images were taken (*n* = 8 fields of view per cell line). Endogenous ANXA2 was seen colocalising with the dye (yellow arrows) in some cells, while others displayed a negative correlation (white arrows). Axio Imager, Zeiss, 63x objective. Scale bar, 20 μm.

**B)** The colocalization index between the ANXA2 fluorescence and the dye was quantified using ImageJ. The mean ± SD colocalization index is plotted.

## 5.2.8 CHIP KO cells are more sensitive to membrane injury

The overall membrane integrity of CHIP cell models and their resilience to damage was investigated by subjecting cells to different membrane injury assays. These included using glass beads (both rolled and vortexed), digitonin and UV laser. The majority of this work was carried out by me in the laboratory with Dr Jesper Nylandsted[§].

### a. Bead rolling-induced injury

Undifferentiated SH-SY5Y were incubated with glass beads and a cell-impermeable dye (FITC dextran). Beads were rolled over the cells manually and then fixed immediately for imaging. The percentage of cells that have internalised the dye (i.e. damaged cells) was quantified (Figure 5.22). Although no difference was observed in the percentage of damaged cells at basal conditions between CHIP genotypes, CHIP KO cells were significantly more sensitive to membrane injury. Given the nature of this assay, the majority of the injured cells lift off the plate before imaging and the reproducibility across fields of view is quite low. Therefore, this difference is likely to be an underestimation.

[§] Danish Cancer Society Research Centre, Copenhagen, Denmark

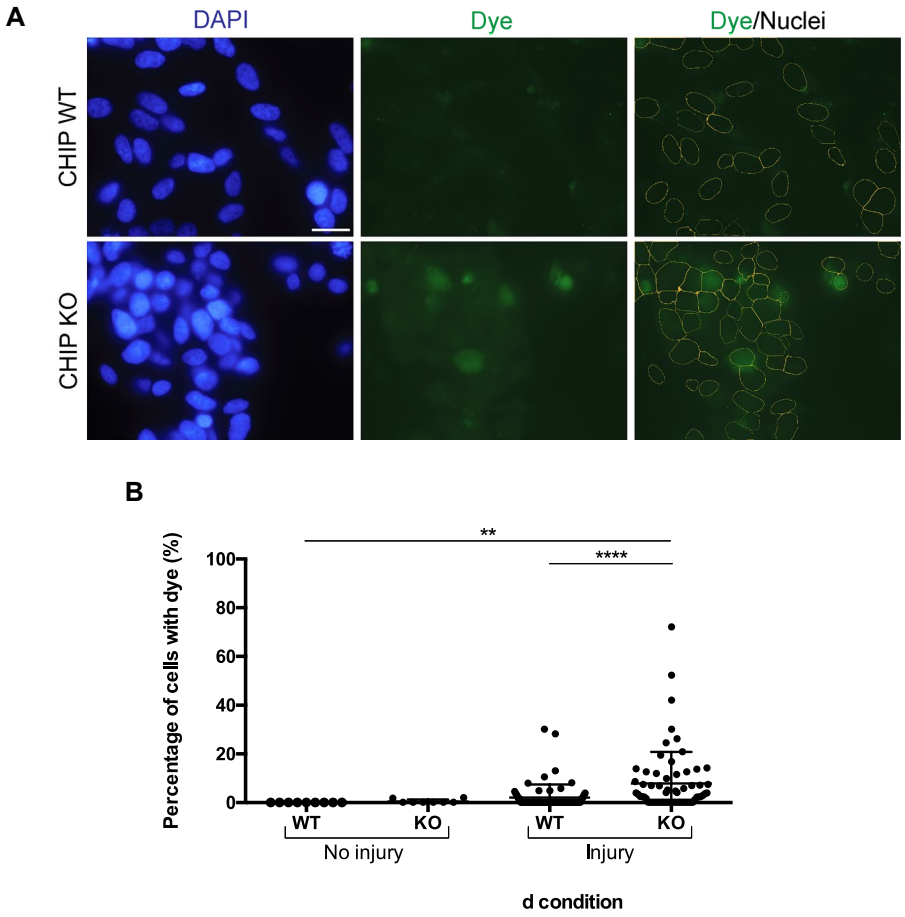


**Figure 5.22: SH-SY5Y CHIP KO cells are more sensitive to membrane injury induced by glass bead-rolling**

**A)** Undifferentiated SH-SY5Y cells were incubated with the cell-impermeable FITC dextran dye and injured by rolling glass beads. Cells were then fixed and fluorescence was imaged. Axio Imager, Zeiss, 63x objective. Scale bar, 20 μm.

**B)** Fluorescence within the nucleus of cells was quantified and an arbitrary cut-off score was applied to determine whether a particular cell incorporated or not the cell. The percentage of cells with dye was per image per cell line was plotted (represented as mean ± SD). Kruskal-Wallis test and Dunn's multiple comparisons post-test. $^{**}P < 0.005$, $^{****}P < 0.0001$, $n \geq 11$ images per biological duplicate ($n = 3$ per cell line for the "injury" condition and $n = 1$ for "no injury") and $n \geq 21$ images per control condition per cell line. Representative data of at least 3 independent experiments.

### b. Bead-induced injury by vortex

To overcome the limitations of membrane damage induced by rolling glass beads, SH-SY5Y cells were detached from the plates and incubated with glass beads and mixed by vortex. Subsequently, cells were incubated with PI (impermeant to live cells) and Hoechst (permeant to live cells) to obtain a count of live and dead cells and obtain the cell death percentage (Figure 5.23). Although there were some small differences between CHIP KO and WT cells, the trends were not consistent. This method might have been too invasive for cells and/or was not favourable in elucidating differences between CHIP KO and WT.

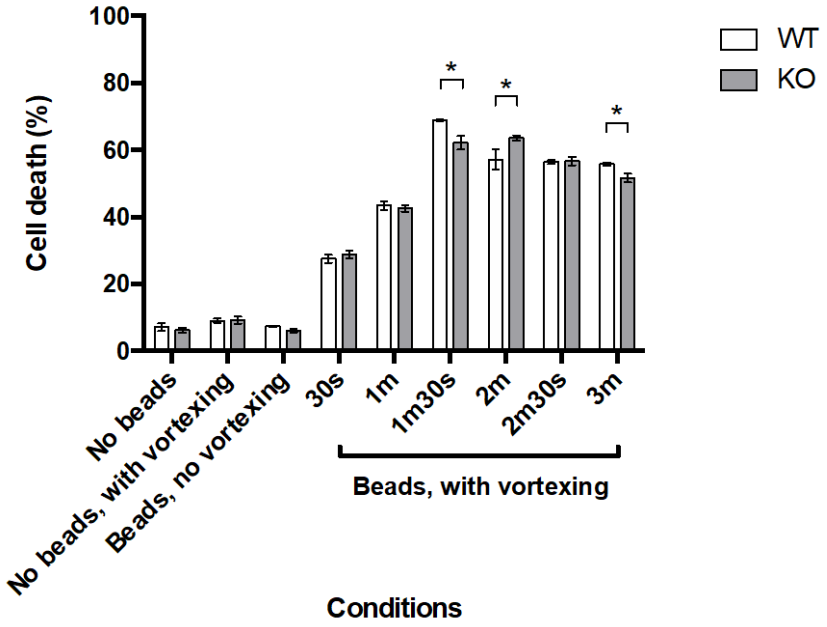


**Figure 5.23: Membrane damage induced by mixing glass beads (by vortex) injures CHIP KO and WT SH-SY5Y cells to a similar extent**
Undifferentiated SH-SY5Y CHIP WT and KO cells were passaged and incubated with glass beads and mixed by vortex for the indicated times. Damaged and controls cells were incubated with Propidium iodide (impermeant to live cells) and Hoechst (permeant to live cells), allowing quantification of cell death, which is presented as mean ± SD. Three measurements were taken from cells incubated in each condition. Student's *t-test*, $*P < 0.05$.

### c. Digitonin-induced injury

Digitonin, a mild non-ionic detergent, is routinely used to permeabilize cellular and nuclear membranes. It specifically interacts with cholesterol, creating holes and rendering cells permeable[187]. By optimising the concentration of digitonin used, the window showing differences between CHIP WT and KO can be widened, overcoming the problem associated with inducing injury by mixing glass bead with cells by vortex. As before, cells were incubated with PI and Hoechst following damage and then imaged using a cytometer. Both CHIP KO SH-SY5Y cells and iPSC showed a consistently higher cell death than WT cells (Figure 5.24). As expected, at higher digitonin concentrations or following longer incubation times, the percentage of cell dead between CHIP genotypes was similar.

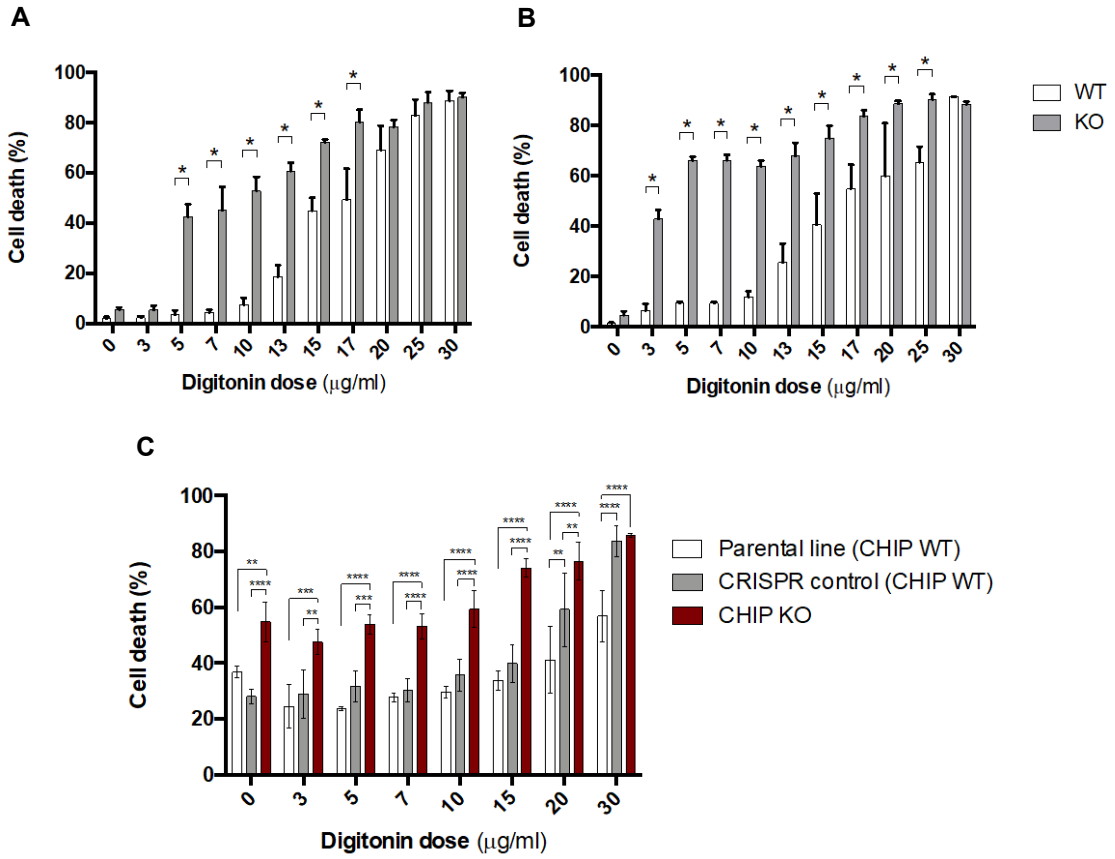


**Figure 5.24: CHIP KO cells are more sensitive to membrane damage induced by digitonin**

**A&B)** Undifferentiated SH-SY5Y CHIP WT and KO cells incubated with increasing concentrations of digitonin for 10 min (**A**) and 20 min (**B**). Damaged and controls cells were incubated with Propidium iodide (impermeant to live cells) and Hoechst (permeant to live cells), allowing quantification of cell death, which is presented as mean ± SD. Three biological replicates were included per condition and cell line. t-test, **P* < 0.05. The same trends were seen when cells are incubated for 15 min with digitonin.

**C)** iPSC with different CHIP genotypes were incubated with increasing doses of digitonin for 10 min. Three biological replicates were included per condition and cell line. Data from two independent experiments was combined and represented as Mean ± SD. Two-way ANOVA, *P* < 0.05, ***P* < 0.005, ****P* < 0.0005, *****P* < 0.0001.

To provide insight into whether the activity of CHIP could be important for the sensitivity/resilience of cells to digitonin-induced injury, the stable cell lines re-expressing mutant CHIP we also included in this assay (Figure 5.25). Both WT and CHIP KO + K30A cells behaved in a similar way and were more resistant to digitonin treatments, while KO and KO + H260Q cells were much more sensitive to injury.

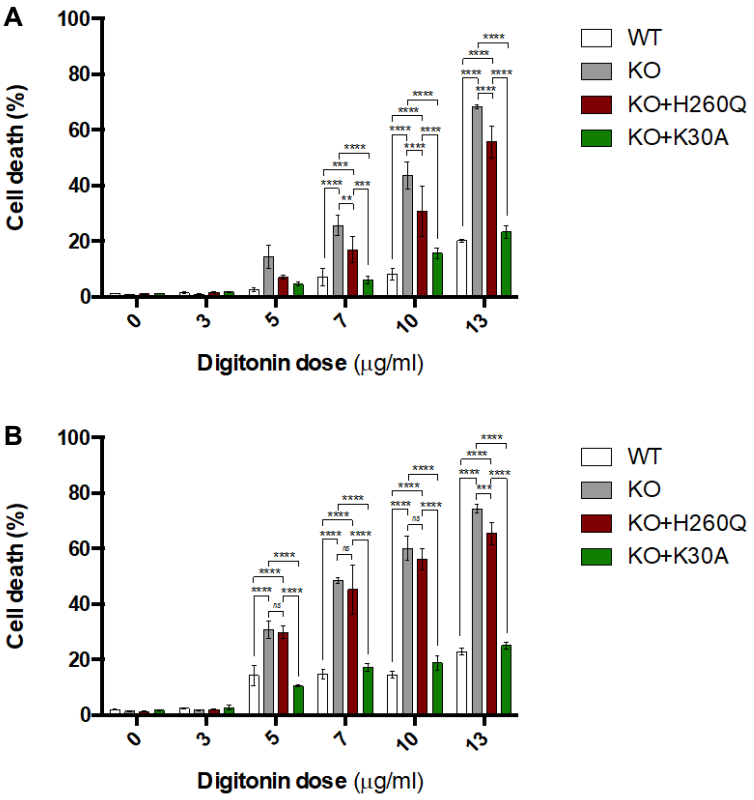


**Figure 5.25: Membrane damage induced by digitonin is more severe in CHIP KO and CHIP KO + H260Q cell line**

Undifferentiated SH-SY5Y cells of different CHIP genotypes (WT, KO and the mutant stable cells lines) were incubated with increasing concentrations of digitonin for 10 min (**A**) and 20 min (**B**), as in Figure 5.23. Damaged and controls cells were incubated with Propidium iodide (impermeant to live cells) and Hoechst (permeant to live cells), allowing quantification of cell death, which is presented as mean ± SD. Three biological replicates were included per condition and cell line. Two-way ANOVA, $^{**}P < 0.005$, $^{***}P < 0.0005$, $^{****}P < 0.0001$. The same trends were observed in two repeated experiments with increased digitonin concentrations (data not included).

### d. UV laser-induced injury

Undifferentiated SH-SY5Y cells incubated with an impermeable dye (FM1-43 dye) and were imaged before and after being subjected to injury induced by UV laser (Figure 5.26). The cell bodies were outlined and the fluorescence intensity within the cell bodies were quantified as a function of time. As shown by the representative images (Figure 5.26A), on average, CHIP KO cells incorporate more FM1-43 dye intracellularly compared to WT cells (Figure 5.26B). Interestingly, the positioning of the CHIP WT cell bodies is similar in both pre- and post-injury scenarios, whilst CHIP KO cells show pronounced changes in positioning (Figure 5.26A). It seems that CHIP

KO show increased migratory patterns in response to laser-induced injury (Figure 5.26D). Moreover, during repair, three phenomena were observed: cell projections were either not, partly or fully retracted into the cell bodies (Figure 5.26C). The predominant repair strategy adopted by both CHIP KO and WT cells was partial retraction of their damaged projections. These preliminary results indicate that CHIP KO cells show a pronounced increase in the extent of cell body movement during repair, when their projections are not retracted or only partially (Figure 5.26D).

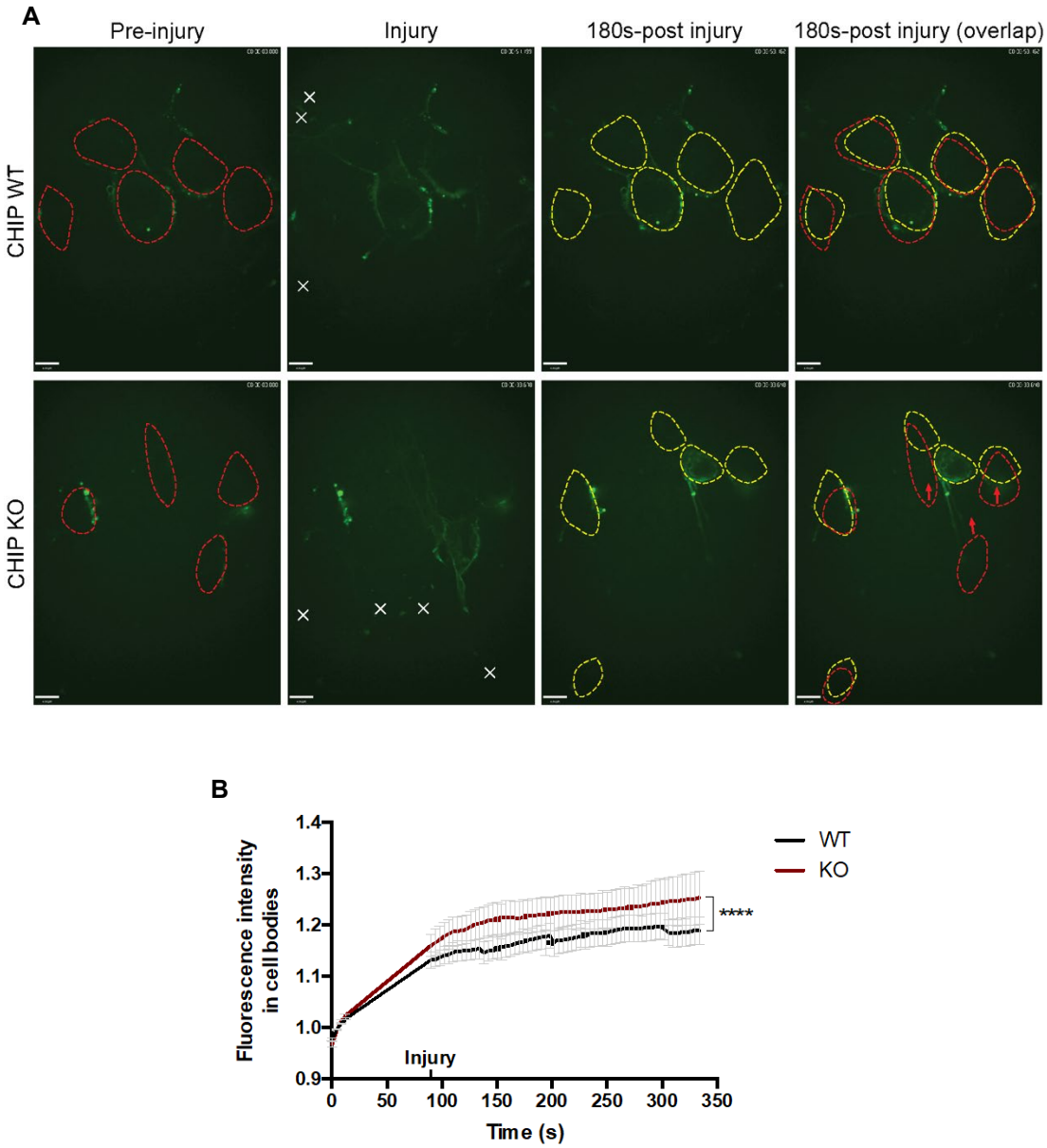


**Figure 5.26: CHIP KO SH-SY5Y cells are more sensitive to laser-induced membrane damage and retract to a greater extent**

**A&C)** Undifferentiated SH-SY5Y cells were incubated with the cell impermeable dye FM1-43 (Life technologies, 1mg/ml) and injured using UV laser (at sites indicated by the white crosses). Live cell imaging was performed before and after the injury (cells were imaged every 4-10 s). Representative images of CHIP WT and KO cells at pre-injury, injury and 180s-post injury are shown. **A)** The cell bodies before (red) and after (yellow) injury are outlined (the outlines were obtained from brightfield images taken in parallel – not shown). The fluorescence intensity over time within the cell bodies were quantified (refer to **B**). The overlap of the outlines of the cell bodies before and after injury show whether cells have moved in the aftermath of the injury (the red arrows indicate cells that have moved significantly). The distances migrated by the cell bodies are quantified in **D**.

Nikon confocal microscope equipped with a PerkinElmer spinning disk (Rapp OptoElectronic pulsed UV-laser) with a 63x objective. Scale bar, 9 μm.

**B)** The fluorescence intensity (F) within cell bodies was quantified over time and normalised by the pre-injury fluorescence (FΔ/F0). Averages were plotted. Data shows that CHIP KO cells incorporate more dye following injury, reflecting compromised repair kinetics. Student's *t-test,* ****$P < 0.0001$, $n \geq 16$ cell bodies. Quantifications were performed using the Volocity software.

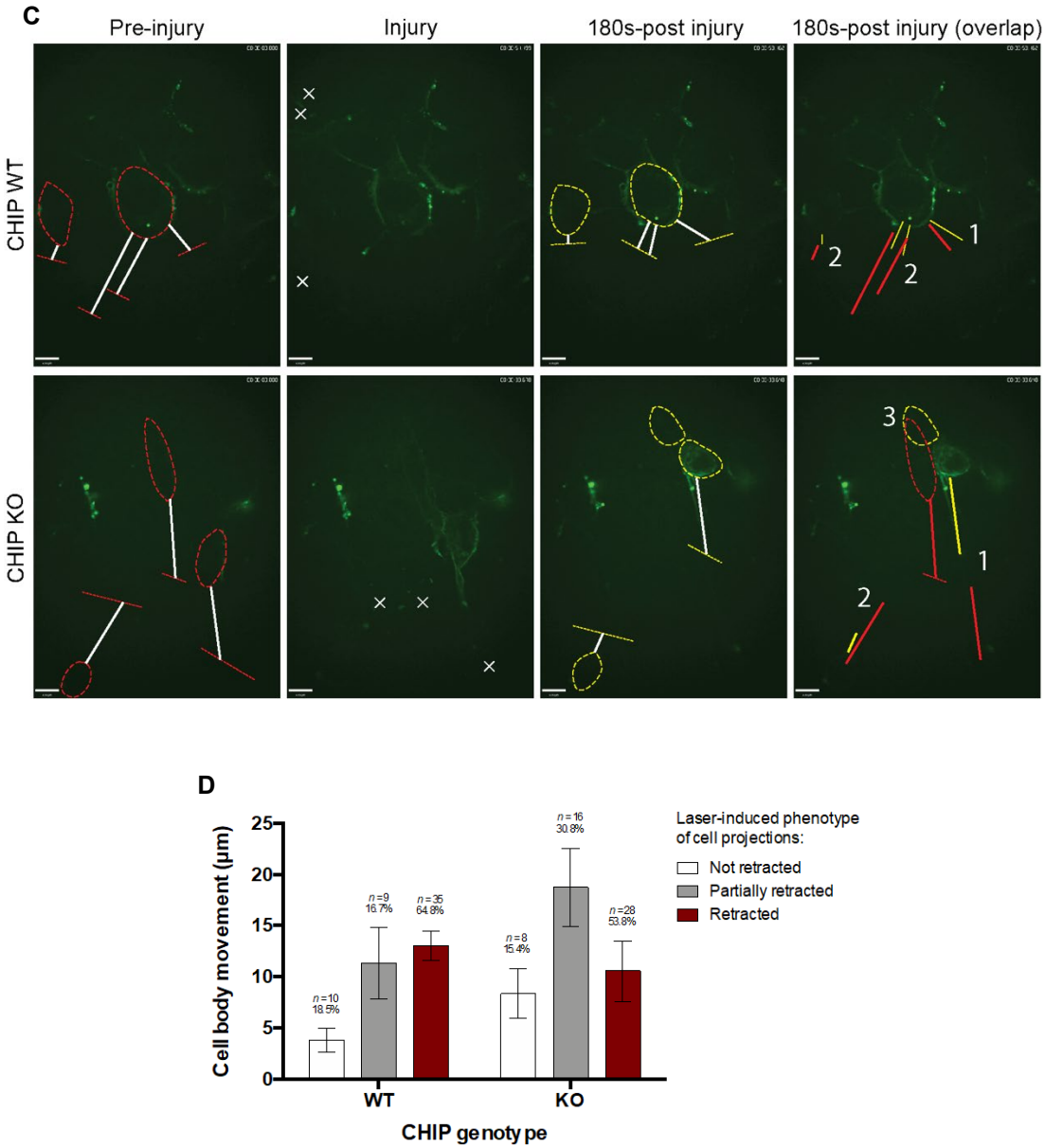


**Figure 5.26** (*continued)*

**C)** The same representative images as those in **A** have the cell bodies and tip of the cellular projections outlined in red (before injury) or yellow (after injury) (the outlines were obtained from brightfield images taken in parallel – not shown). The distance between both structures is marked with a white line (representing the length of the cellular projection). These are then marked on the repeated 180-post injury images and colour-coded as pre-injury (red) or post-injury (yellow).

Projections showing no change in length are labelled 1 (despite potential changes in positioning). Those showing partial reductions in length in post-injury (i.e. representing partial retractions) are labelled 2. Finally, projections that have been completely retracted post-injury are labelled 3.

**D)** Distance migrated by cells upon laser-induced injury was quantified by measuring the length from the end of a single projection at pre-injury to the cell body both before and after injury, in projections that are close to the site of injury. The mean difference (in µm) was plotted. Error bars represent SEM. Projections analysed were classified according to their phenotype upon injury: not retracted (i.e. projection remained), partially retracted (i.e. projection reduced in length upon injury or part of the projection remained upon cell repair forming a tail-like structure) or retracted (i.e. the projection was internalised by the cell body). Examples of these phenotypes are shown in **C**. The occurrence of each phenomena per cell line is represented as a percentage above each bar. Quantifications were performed using the Volocity software.

## 5.2.9 CHIP KO cells do not show significant repair defects

The increased membrane damage observed could reflect enhanced membrane sensitivity to injury and/or inability to repair damage. To investigate whether damaged cells are capable of repairing, cells were incubated with glass beads in the presence of a green impermeable dye (FITC dextran), then washed and incubated with a red impermeable dye (Texas dextran) during repair. Cells were fixed and imaged (Figure 5.27). Cells damaged by the beads become permeable to the green dye. Those that repair do not internalise the red dye (remaining green), while cells that fail to repair become red (having both dyes co-localise). Both CHIP KO and WT SH-SY5Y cells were capable of repair (indicated by the white arrow).

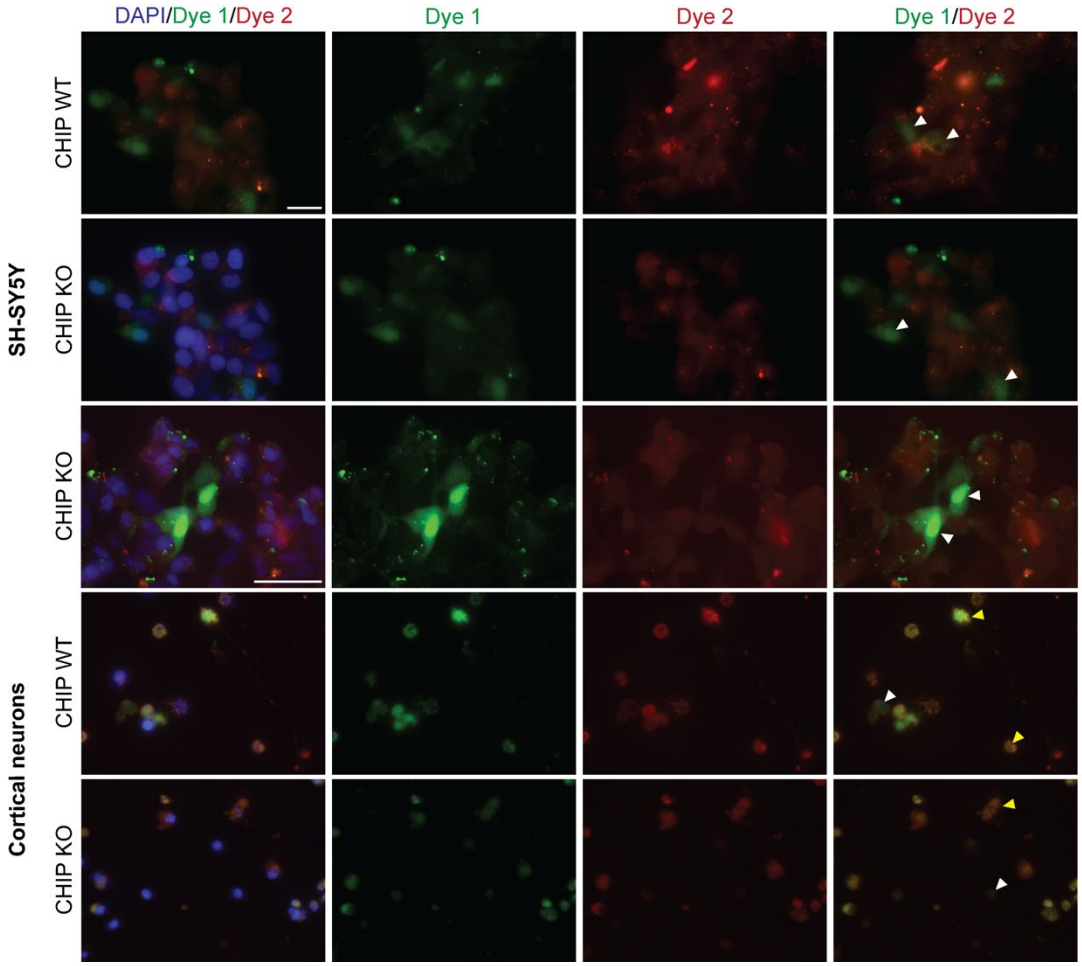


**Figure 5.27: CHIP KO and WT cells are able to repair after membrane damage**
Undifferentiated SH-SY5Y and cortical neurons were incubated with the FITC dextran (green) dye followed by glass bead-induced injury. Cells were then washed and the Texas dextran (red) dye was added. Cells were allowed to recover for 5 min, followed by fixation with 4% paraformaldehyde. IF images show cells that were injured but have repair (green only, indicated by the white arrows) and those that have not repaired (incorporated both green and red dyes, yellow arrows). Axio Imager, Zeiss, 63x objective. Scale bar, 20 μm (exclusively for images in the third row: scale bar, 50 μm). Images of SH-SY5Y cells are representative of at least 3 independent experiments and images of cortical neurons are representative of biological duplicates.

In an attempt to quantify the ability of CHIP KO and WT cells to repair, iPSC (Figure 5.28A) and undifferentiated SH-SY5Y (Figure 5.28B) were treated with digitonin in the absence of calcium, which is necessary for repair. Although all cell lines tested were sensitive to calcium withdrawal, there was more cell death recorded for CHIP KO iPSC compared to WT in the absence of digitonin. This could mean that CHIP KO cells are more dependent on efficient repair at basal conditions, although this would have to be validated further. Addition of digitonin increased the cell death in both CHIP KO and WT iPSC, thus the difference between the cell lines was maintained. However, such difference between CHIP genotypes is subtle (particularly when the data is normalised by the cell death observed in the absence of digitonin treatment for each cell line) and is unlikely to explain the pronounced differences observed when both sensitivity and repair are assayed (Figure 5.24 & Figure 5.25). SH-SY5Y were extremely intolerant to the calcium withdrawal in conjunction with digitonin treatment, resulting in significant cell death across the CHIP genotypes tested.

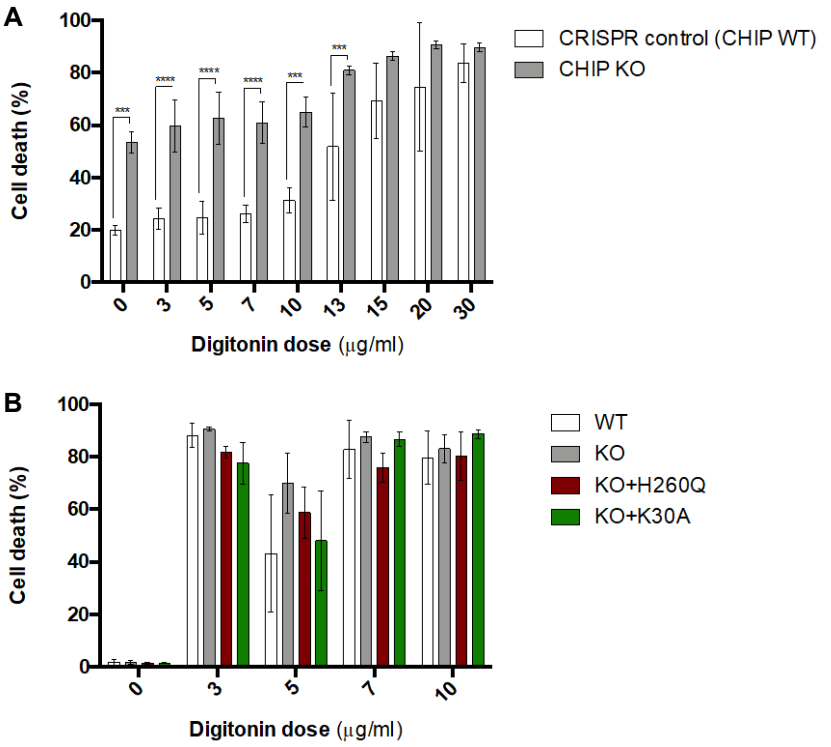


**Figure 5.28: CHIP KO cells are more sensitive to membrane damage induced by digitonin when repair is inhibited (in the absence of calcium)**
As in Figure 5.23, iPSC (**A**) and undifferentiated SH-SY5Y (WT, KO and the mutant stable cell lines) (**B**) were subjected to digitonin-induced injury (with increasing concentrations). However, instead of diluting digitonin in DMEM ($Ca^{2+}$-containing medium), here digitonin was diluted in HBSS without calcium. Damaged and controls cells were incubated with Propidium iodide (impermeant to live cells) and Hoechst (permeant to live cells) immediately after the injury to prevent cell death associated with calcium withdrawal. Cell death was quantified and is presented as mean ± SD. Biological triplicates were represented as mean ± SD. Student's *t*-test, ***$P < 0.0005$, ****$P < 0.0001$. The experiment was repeated a second time and the same trends were observed. Note that due to the scanning order, cells treated with 3 μg/ml digitonin were scanned after the 5 μg/ml conditions.

### 5.2.10 Injury-induced changes in Annexin A2 dynamics and interactome

With the aim to understand the underlying molecular mechanisms contributing to the poor membrane integrity of CHIP KO cells, the dynamics and interactions of the key protein in membrane homeostasis, ANXA2, were investigated. We believed that changes in ANXA2 proteostasis (including levels, subcellular localisation and protein:protein interactions) could influence membrane integrity either directly or indirectly – helping to explain, at least partly, the cellular phenotype observed. At present, we cannot exclude the possibility that these changes in ANXA2 proteostasis could be unrelated to membrane homeostasis and, instead, a separate CHIP-dependent molecular event.

#### a. Annexin A2 dynamics

As previously seen in Figure 5.21, the FITC dextran dye penetrates into cortical neurons at basal condition and its intracellular presence correlated with expression of ANXA2 more closely in CHIP KO than WT neurons. Upon injury by bead rolling, a positive correlation between damaged cells and ANXA2 expression was observed for both CHIP KO and WT neurons (Figure 5.29). ANXA2 is known to respond to increases in permeability by upregulating and becoming recruited to the site of injury[163]. The increase in correlation index in CHIP WT upon damage compared to basal condition supports such responsive nature. Phenotypically, ANXA2 also seems to accumulate around the nuclear staining, forming ring-like structures, in these cells. In contrast, in CHIP KO neurons appear to lack this dynamic response and the ANXA2 staining might be localised more diffusely within permeable (i.e. injured) cells.

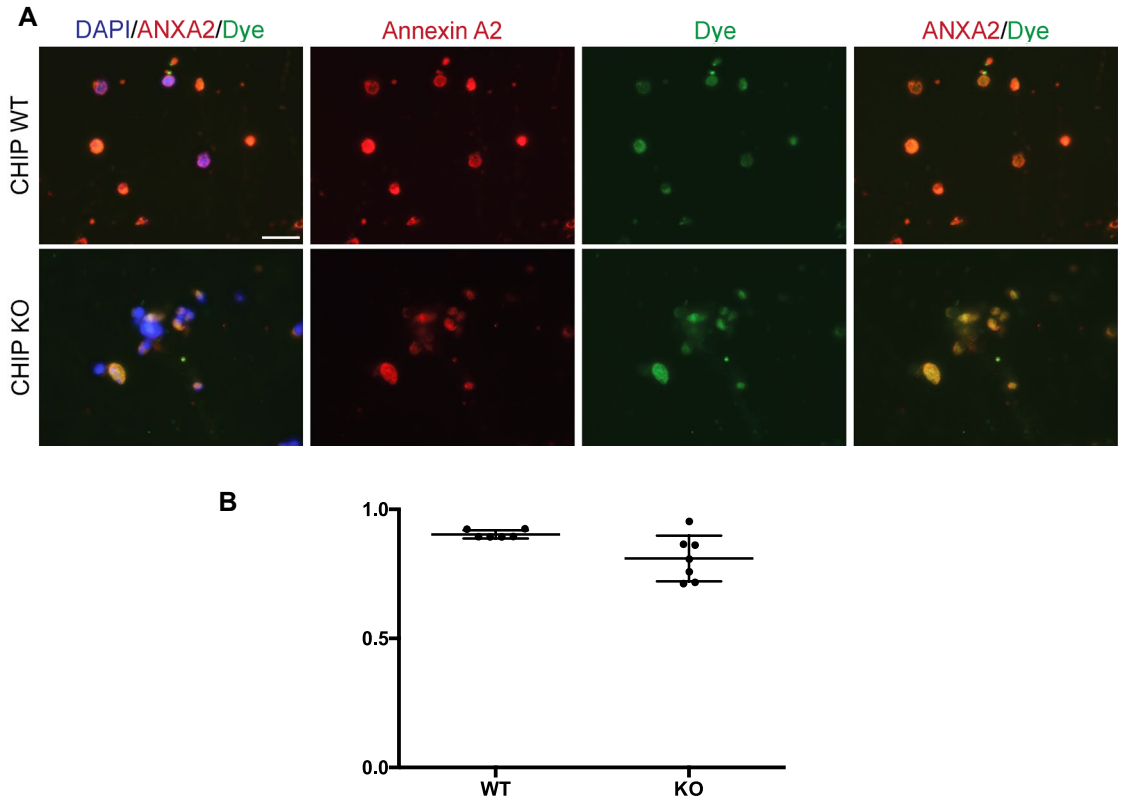


**Figure 5.29: Upon damage, ANXA2 colocalises with the impermeable dye**
**A)** Mature cortical neurons of CHIP WT and KO genotypes were treated with the cell impermeable dye FITC dextran and injured by rolling glass beads. Immediately following injury, cells were fixed with 4% paraformaldehyde. The expression of endogenous ANXA2 was analysed by IF using anti-ANXA2 Rb pAb (1:500). Images were taken ($n \geq 6$ fields of view per cell line). Axio Imager, *Zeiss*, 63x objective. Scale bar, 20 μm.
**B)** The colocalization index between the ANXA2 fluorescence and the dye was quantified using ImageJ. The mean ± SD colocalization index is plotted.

The damaged-induced response of endogenous ANXA2 was monitored in undifferentiated SH-SY5Y. A dose-time-response assay of digitonin was performed where the read-out was the fluorescence intensity of ANXA2 per cell (Figure 5.30). Importantly, the increase in ANXA2 following injury is not CHIP-dependent. However, the kinetics of this phenomenon could be influence by the presence of CHIP. In CHIP KO cells, ANXA2 intensity took slightly longer to increase following injury (refer to the 15 minutes time-point using the 15 μg/ml dose), recorded higher fluorescence intensities and reached its maximum intensity later than control cells (Figure 5.30B). Qualitatively, with increasing digitonin treatment, ANXA2 staining in CHIP KO cells is predominantly within the PM initially, and then becomes nuclear. In contrast, control

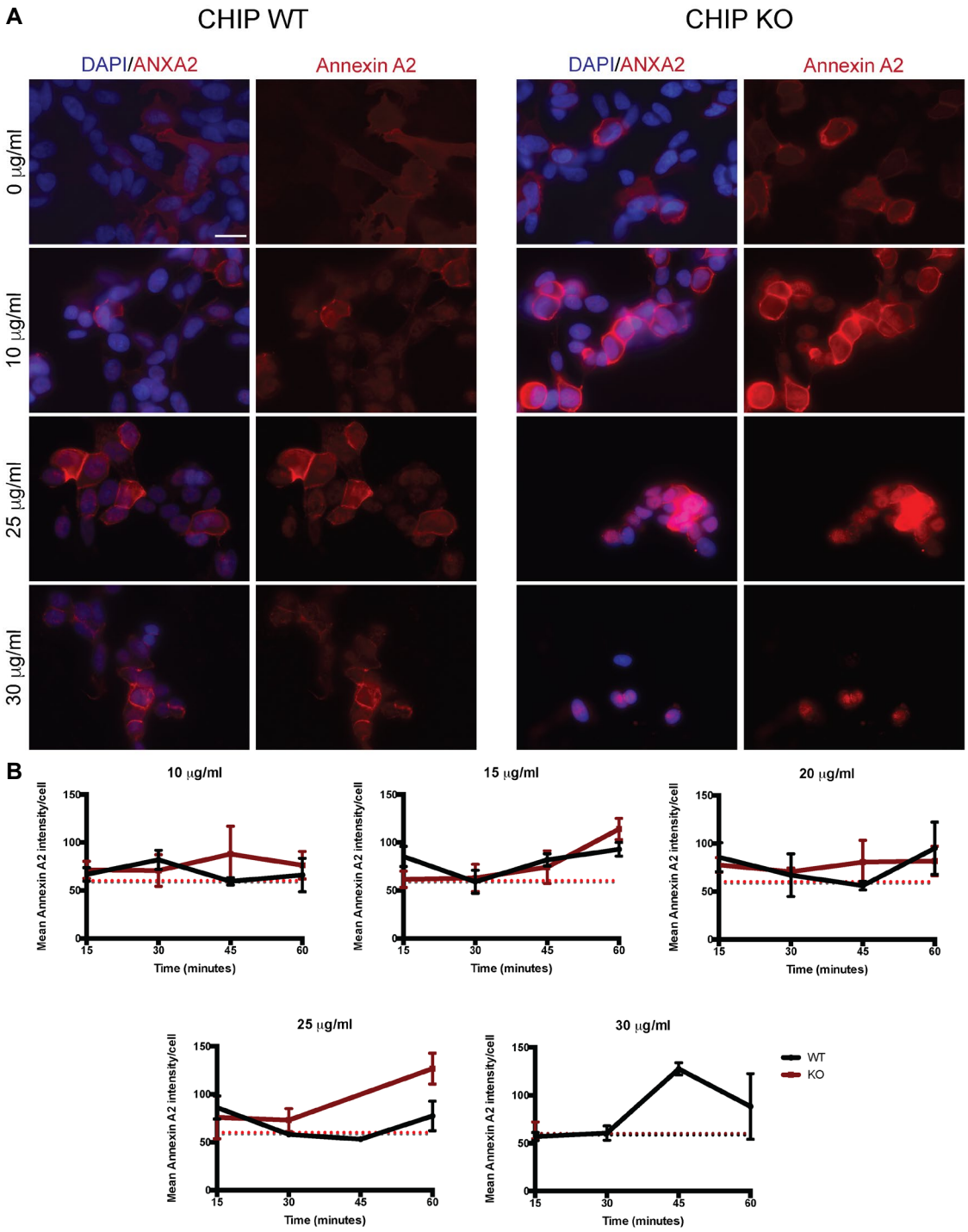


**Figure 5.30: Upon damage, ANXA2 levels increase in both CHIP KO and WT undifferentiated SH-SY5Y cells**

**A)** Undifferentiated SH-SY5Y CHIP WT and KO cells were treated with different concentrations of digitonin (0, 10, 15, 25 and 30 μg/ml. Cells were fixed with acetone & methanol. The endogenous expression of ANXA2 was analysed using anti-ANXA2 pAb (1:500). Representative images are shown of untreated cells and treated with 10 μg/ml (for 15 min), 25 μg/ml (for 30 min) and 30 μg/ml (for 30 min). Differences in ANXA2 subcellular localisation and expression are evident between CHIP KO and WT treated cells. Axio Imager, Zeiss, 63x objective. Scale bar, 20 μm.

**B)** The mean fluorescence intensity per cell line per condition was quantified using ImageJ software and plotted. Dotted line represents the average ANXA2 expression at basal conditions. Quantification of CHIP KO cells treated with 30 μg/ml was only possible until the 15 min time-point due to substantial cell death.

### b. Annexin A2:S100-A11 interactome

Given the difference in ANXA2 dynamics detected and the known injury-induced ANXA2:S100-A11 interaction that promotes its membrane-related functions, the dynamics of such interaction were evaluated. PLA revealed that such interaction is more frequent in CHIP-expressing cells compared to KO undifferentiated SH-SY5Y cells at basal conditions (Figure 5.31 and Figure S.8, where data from independent experiments was quantified either in a semi-automated or manual manner, and the control IF is represented in Figure S.9), despite the increased ANXA2 levels in CHIP KO cells. S100-A11 levels, on the other hand, are unchanged in this CHIP SH-SY5Y model (Figure 4.26). Since the complex has been implicated in the maintenance of membrane homeostasis, this could help to explain the poor membrane integrity observed.

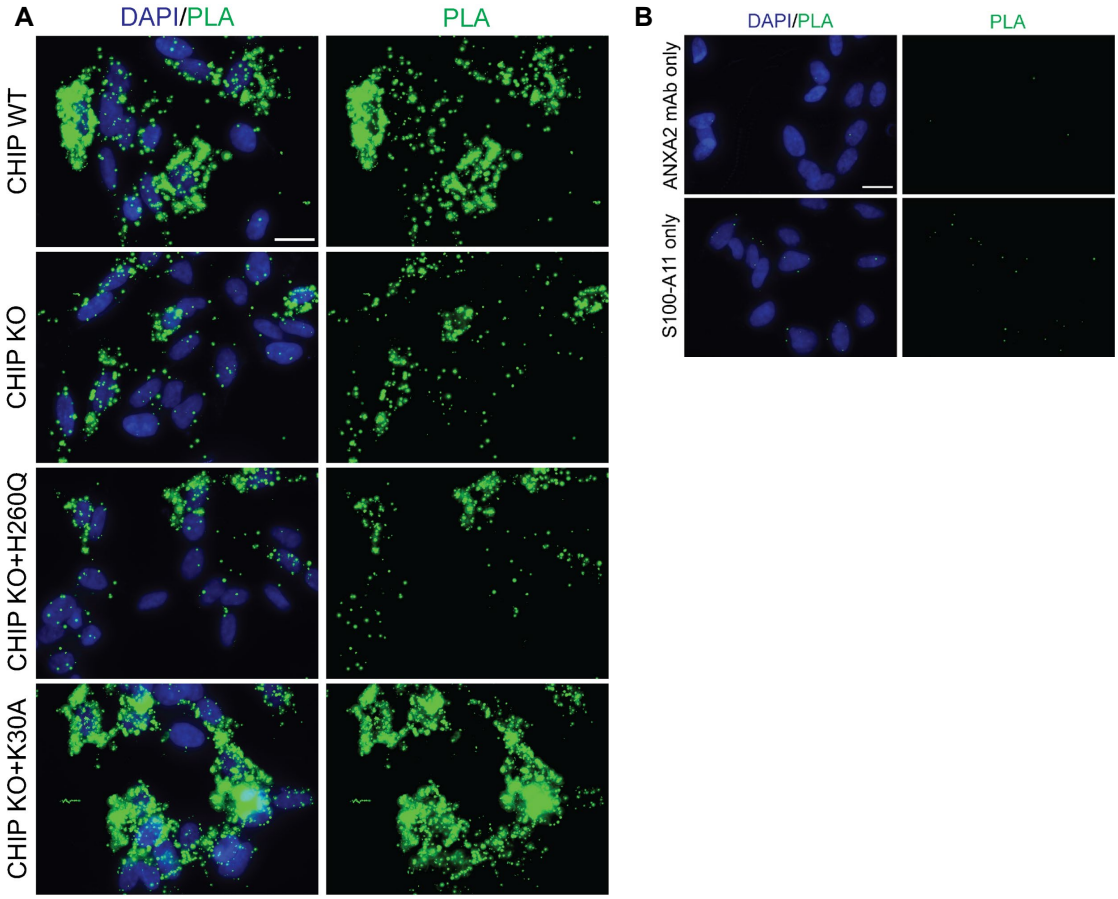


**Figure 5.31: Annexin A2 & S100-A11 interaction by PLA in undifferentiated SH-SY5Y**
**A&B)** Undifferentiated SH-SY5Y cells of different CHIP genotypes (WT, KO and the stable cell lines KO+H260Q and KO+K30A) were fixed with acetone & methanol.
**A)** For each cell line, duplicate wells were stained with anti-ANXA2 mAb (3:500) and anti-s100-A11 pAb (1:500) antibodies (referred to as "PLA" in C and biological duplicates). PLA signal (puntae in green) were quantified using ImageJ in a semi-automated manner and normalised by the number of nuclei (stained with DAPI) within a field of view.
**B)** In parallel, two controls were included (grouped under "Ctrl" in **C**): wells containing CHIP WT cells were incubated with either antibodies alone or with no primary antibodies.
Axio Imager, *Zeiss*, 63x objective. Scale bars, 20 μm. Representative data of at least 4 independent experiments. Representative data of at least two independent PLA experiments.

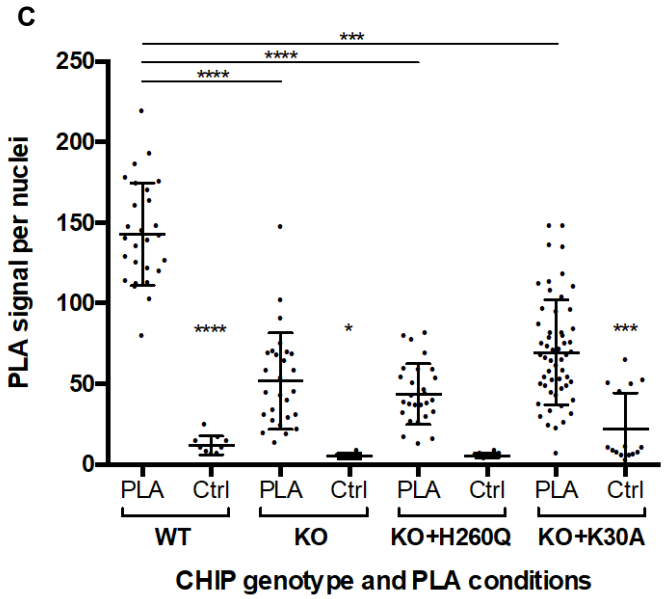


**Figure 5.31** *(continued)*
**C)** Automated quantifications of PLA signal per nuclei of different cell lines represented in the dot plot as mean ± SD. Two CHIP KO+K30A clones were pooled into the quantification. Kruskal-Wallis test and Dunn's multiple comparisons post-test (statistical significance indicated above each Ctrl). **P* < 0.05, ****P* < 0.0005, *****P* < 0.0001, *n* ≥ 12 images per biological duplicate and *n* ≥ 11 images per control condition per cell line.

Furthermore, the ANXA2:S100-A11 interaction seems to be influenced by the E3 ligase activity of CHIP. While the line expressing a E3 ligase-dead mutant CHIP (KO + H260Q) was similar to KO cells, the chaperone-dead mutant CHIP (KO + K30A) partially rescued the ANXA2:S100-A11 interaction. Importantly, the steady state levels of ANXA2 and S100-A11 are similar in both stable cell lines (Figure S.10).

Although the ANXA2:S100-A11 interaction is compromised in CHIP KO cells compared to WT at basal conditions, upon injury the difference between WT and KO cells ceases to be statistically different (Figure 5.32). However, the PLA signal for the KO damaged cells remains much lower than the control cells, illustrating that even upon injury the interactome of ANXA2 remains defective. Interestingly, WT cells had a similar PLA signal when subjected to digitonin treatment (compared to untreated cells), while KO cells showed a slight increase (not significant) of this interaction when damaged. Of note, CHIP was also found to interact with S100-A11 by PLA (Figure S.11). CHIP- and S100-A11-containing complexes were detected in WT cells but not in CHIP KO cells, *in situ*, pointing to a direct or indirect interaction between these proteins.

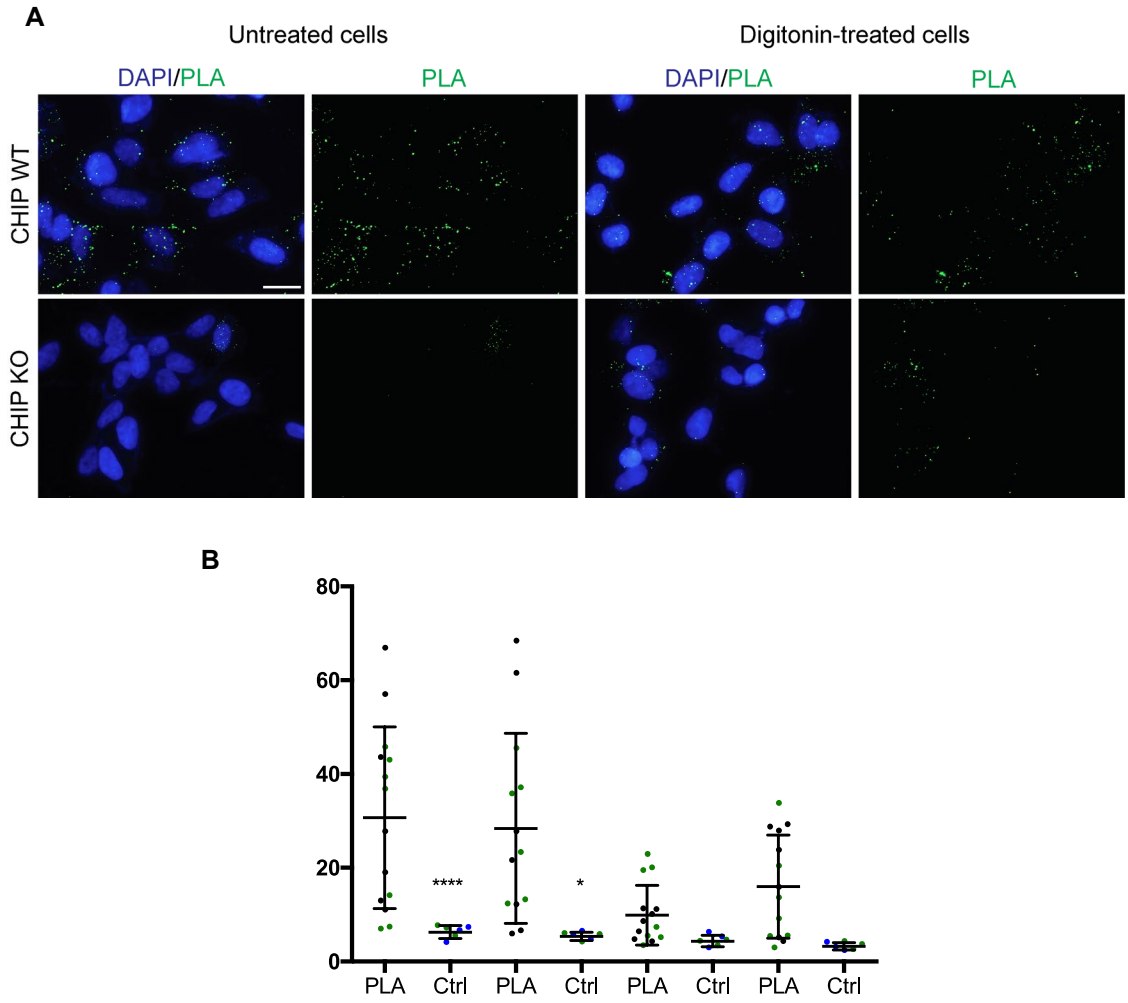


**Figure 5.32: Annexin A2 & S100-A11 interaction by PLA in untreated and digitonin-treated undifferentiated SH-SY5Y**

**A)** Undifferentiated SH-SY5Y CHIP KO and WT cells were fixed with acetone & methanol. For each cell line, duplicate wells were stained with anti-S100-A11 pAb (1:500) and anti-ANXA2 mAb (3:500) (referred to as "PLA" in **B** and biological replicates are colour-coded with black/green dots). PLA signal (puntae in green) were quantified using ImageJ in a semi-automated manner and normalised by the number of nuclei (stained with DAPI) within a field of view. In parallel, two controls were included (images not shown, grouped under "Ctrl" in **B**): wells containing cells of both genotypes were incubated with either antibodies alone (S100-A11 only in green and ANXA2 only in blue). Axio Imager, Zeiss, 63x objective. Scale bar, 20 μm.

**B)** Quantifications of PLA signal per nuclei of different cell lines represented in the dot plot as mean ± SD. One-way ANOVA with Holm-Sidak's multiple comparisons post-test (comparisons between PLA and Ctrl conditions per cell line is indicated above each Ctrl), $*P < 0.05$, $**P < 0.005$, $****P < 0.0001$, $n = 7$ images per biological duplicate and $n = 3$ images per control condition per cell line.

### c. Annexin A2:CHIP interactome

The dynamics of the interaction of CHIP with ANXA2 under basal conditions and upon membrane damage were also investigated (Figure 5.33). The PLA signal reflecting ANXA2:CHIP complexes showed a slight increase in interaction in CHIP WT cells following injury compared to basal conditions, although this was not significant. No change was seen in CHIP KO cells treated with digitonin compared to untreated.

The observed differences in ANXA2 dynamics and interactome in our CHIP models at both basal conditions and in response to membrane damage opens several questions. It would be interesting to investigate further how the ANXA2:CHIP interaction changes under these conditions. For example, by immunoprecipitating CHIP and analysing its interacting proteins by MS other interacting proteins, possibly within the same complex as ANXA2 and CHIP, could be identified. Beyond this, the effect of the ANXA2-binding on CHIP's structure and function (both directly, due to the protein:protein interaction, or indirectly, caused by the lipid-rich environment of membrane-bound ANXA2 – which is of importance in response to damage) would be informative.

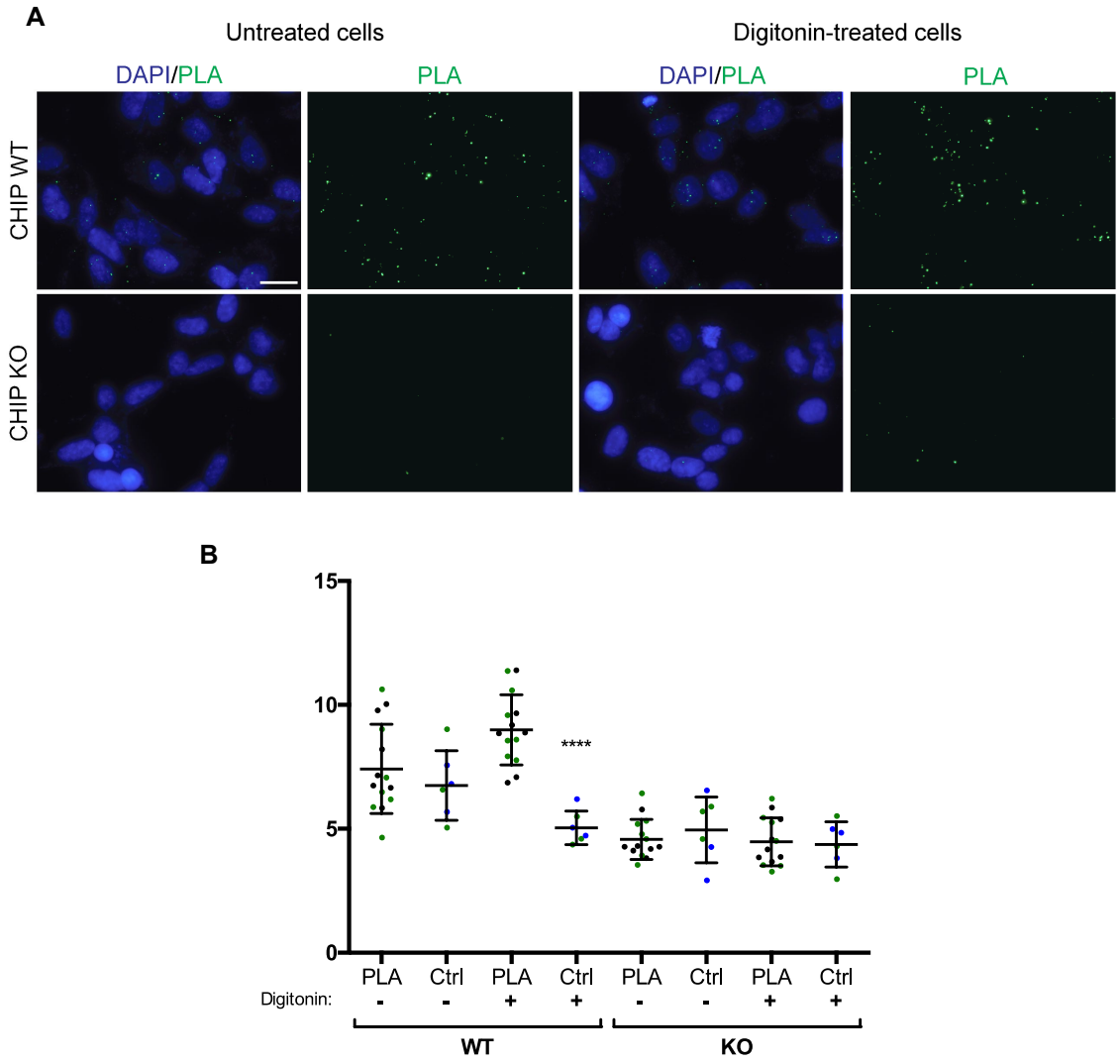


**Figure 5.33: Annexin A2 & CHIP interaction by PLA in untreated and digitonin-treated undifferentiated SH-SY5Y**

**A)** Undifferentiated SH-SY5Y CHIP KO and WT cells were fixed with 4% PFA and then methanol. For each cell line, duplicate wells were stained with anti-CHIP mAb (1:1000) and anti-ANXA2 pAb (1:500) (referred to as "PLA" in **B** and biological replicates are colour-coded with black/green dots). PLA signal (puntae in green) were quantified using ImageJ in a semi-automated manner and normalised by the number of nuclei (stained with DAPI) within a field of view. In parallel, two controls were included (images not shown, grouped under "Ctrl" in **B**): wells containing cells of both genotypes were incubated with either antibodies alone (CHIP only in green and ANXA2 only in blue). Axio Imager, Zeiss, 63x objective. Scale bar, 20 μm.
**B)** Quantifications of PLA signal per nuclei of different cell lines represented in the dot plot as mean ± SD. One-way ANOVA with Holm-Sidak's multiple comparisons post-test (comparisons between PLA and Ctrl conditions per cell line is indicated above each Ctrl), ****$P < 0.0001$, $n = 7$ images per biological duplicate and $n = 3$ images per control condition per cell line.

### 5.2.11 Lipids inhibit CHIP-dependent ubiquitination of Annexin A2 *in vitro*

In parallel to studying the proteostasis of ANXA2 in our CHIP models, lipid composition and CHIP-lipid interactions were investigated as other possible underlying mechanisms contributing to the poor membrane homeostasis observed in CHIP KO cells. The effect of CHIP-lipid interactions (occurring either as a by-product of ANXA2:CHIP or unrelated to ANXA2) on CHIP's function was assessed.

The ANXA2-binding lipid, PA, was titrated into the *in vitro* ubiquitination assay containing ANXA2 and CHIP (Figure 5.34A). With increasing PA (from 1mM to 5mM) the ubiquitination of ANXA2 was inhibited and the auto-ubiquitination of CHIP was slightly impaired. Above 7mM, the concentration of PA buffer itself interfered with the ubiquitination reaction (both of ANXA2 and the auto-ubiquitination of CHIP). To rule out the possibility of the buffer used to reconstitute the lipid driving the suppression of ubiquitination, different buffers (HEPES- and Ethanol-based) were tested (Figure 5.34B). The inhibitory effect of PA was observed when diluted in both buffers. Such inhibition did not correlate with the extent of CHIP's auto-ubiquitination detected. Next, the effect of the CHIP-binding lipid, phosphatidylinositol 4-phosphate (PI4P) was also analysed (Figure 5.34C). With increasing PI4P, both the ubiquitination of ANXA2 and auto-ubiquitination of CHIP decreased.

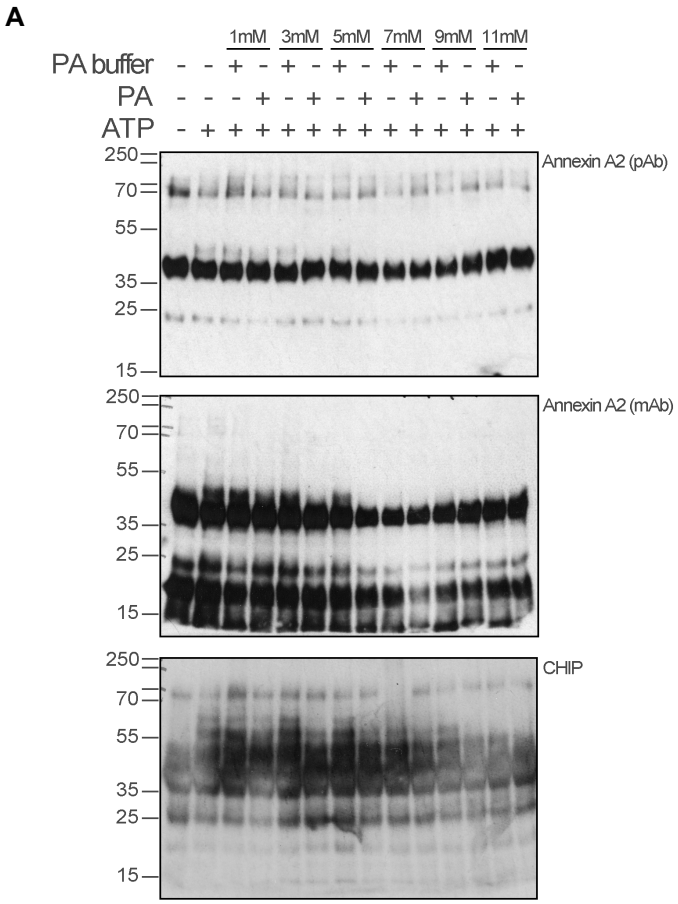


**Figure 5.34: Effect of lipids on CHIP-dependent ubiquitination of ANXA2, *in vitro***
*In vitro* ubiquitination assays using untagged recombinant human ANXA2 and CHIP were performed in the absence and presence of lipids. PA diluted in ethanol (**A**) or in HEPES-based buffer (**B**) was added to the ubiquitination reactions at different concentrations. PI4P was also tested (**C**). Reactions were analysed by 12% SDS-PAGE/WB. Immunoblots were probed with anti-CHIP mAb (1:10000) and anti-ANXA2 antibodies (mAb, 1:500, and/or pAb, 1:1000).

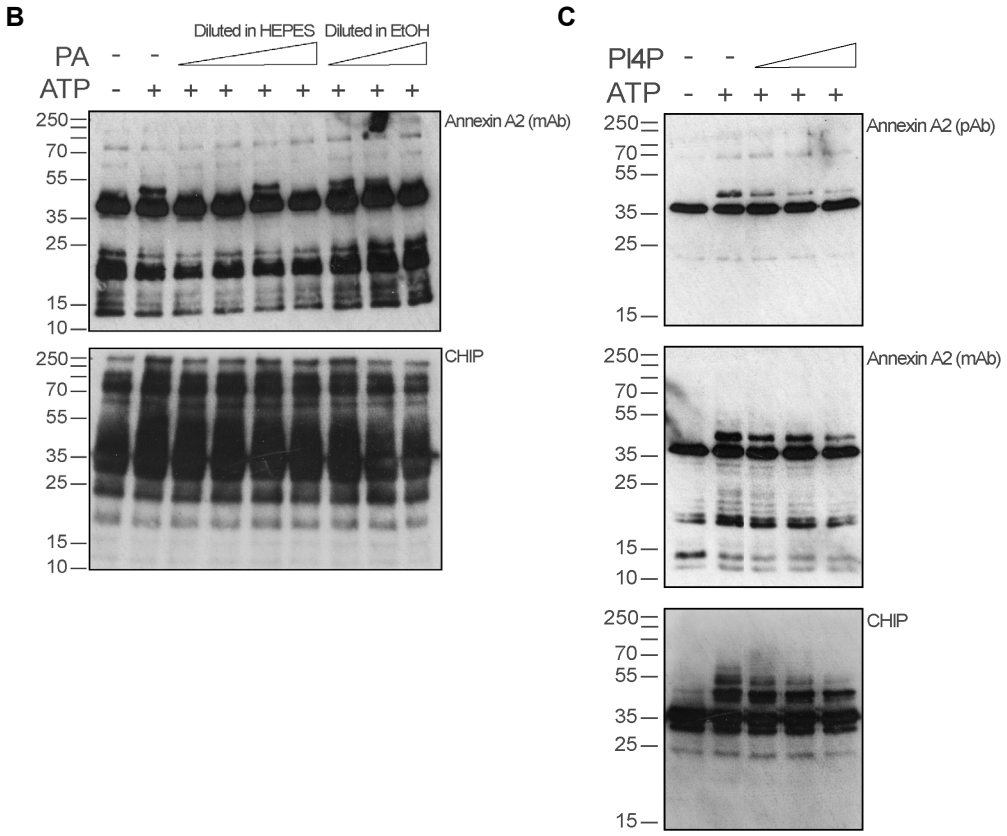


**Figure 5.34** *(continued)*
*In vitro* ubiquitination assays using untagged recombinant human ANXA2 and CHIP were performed in the absence and presence of lipids. PA diluted in ethanol (**A**) or in HEPES-based buffer (**B**) was added to the ubiquitination reactions at different concentrations. PI4P was also tested (**C**). Reactions were analysed by 12% SDS-PAGE/WB. Immunoblots were probed with anti-CHIP mAb (1:10000) and anti-ANXA2 antibodies (mAb, 1:500, and/or pAb, 1:1000).

## 5.2.11 Lipids inhibit CHIP-dependent ubiquitination of Annexin A2 *in vitro*

Given the effect of lipids on the activity of CHIP, we sought to investigate possible changes in lipidomic profile of the CHIP SH-SY5Y model. The relative abundance of some classes of phospholipids were plotted (Figure 5.35). Although the majority of phospholipid groups assayed did not seem to differ significantly between CHIP WT and KO (e.g. phosphatidylethanolamine, PE, lysophosphatidylcholine, LPC, and sphingomyelin, SM), some showed 1.5 to 2.5-fold change in WT compared to KO cells (including PA, lysoPA, LPA, and PS). This work was done in collaboration with Dr Irena Dapic and Dr Laura Bindila[‖].

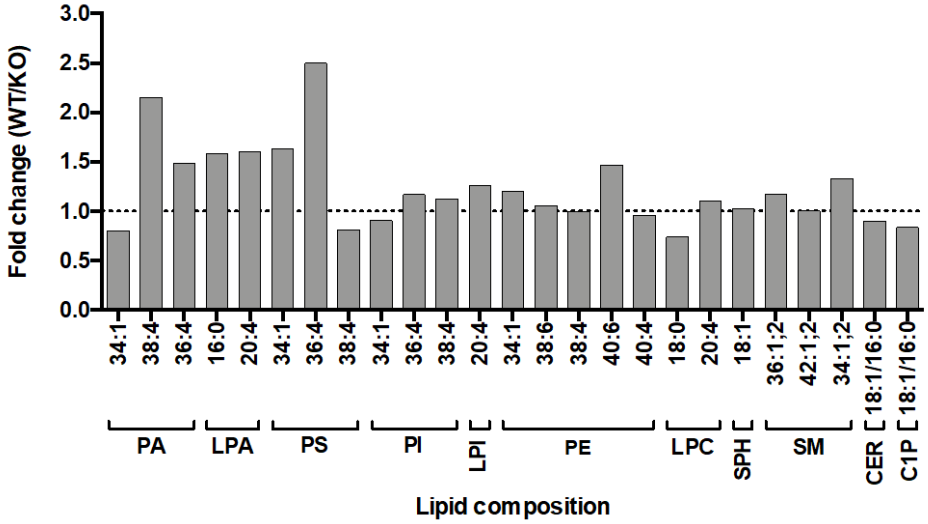


**Figure 5.35: Lipidomics of CHIP KO and WT undifferentiated SH-SY5Y cells**
Undifferentiated CHIP KO and WT SH-SY5Y cells were harvested for lipidomics analysis of phospholipids. Phosphatidic acid (PA), lysophosphatidic acid (LPA), phosphatidylserine (PS), phosphatidylinositol (PI), lysophosphatidylinositol (LPI), phosphatidylethanolamine (PE), lysophosphatidylcholine (LPC), sphingosine (SPH), sphingomyelin (SM), ceramide (CER), ceramide-1-phosphate (C1P).

[‖] Institute for Physiological Chemistry, University Medical Center Mainz, Germany

## 5.3 Discussion

### 5.3.1 Annexinopathy in CHIP KO models

Using an unbiased approach to identify protein changes in the CHIP KO cortical neurons (i.e. possible substrates of CHIP), ANXA2 was the most striking. The over-representation detected by SWATH-MS reflected an upregulation of the protein levels of ANXA2 in CHIP KO cortical neurons (Figure 5.6). This was consistently seen in independent cortical differentiation experiments, thus accounting for the variability of the neuronal differentiation. The increase in ANXA2 levels is either a direct CHIP-related phenomenon or a conserved compensatory mechanism, which could be relevant in the maintenance of cellular health.

Interestingly, this phenotype seems to be dependent on the differentiation status and cell type. Undifferentiated CHIP KO iPSC do not share this increase in ANXA2 steady state levels, evident from both the WB (Figure 5.7) and SWATH-MS data (having a WT/KO fold change of 0.764). In contrast, cycling SH-SY5Y show an increase in ANXA2 levels by WB (Figure 5.8) and SWATH-MS (fold change of 0.764), although the difference between CHIP KO and WT tends to be less pronounced compared to that of cortical neurons. Commonly, metastatic cancer cells upregulate ANXA2[163,168] and this neuroblastoma cell line was derived from a metastatic bone tumour biopsy[118]. However, this increase seems to be dependent on CHIP genotype, which could be explained by the relationship between CHIP and the neuronal-like background of these cells or their cancerogenic nature (CHIP has been implicated in cancer[87]). Their differentiated counterparts, on the other hand, do not show a CHIP-dependent change in ANXA2 steady state levels by WB (Figure 5.9) nor SWATH-MS (having a fold change of 0.948). However, these differentiated SH-SY5Y cells and iPSC-derived cortical neurons are intrinsically different. As previously mentioned, the neuronal identity of differentiated SH-SY5Y is unclear and likely to be mixed (i.e. not cortical) and these cells lack the neurodegeneration-prone genetic background of our iPSC CHIP model and derived cortical neurons.

Taken together, the effect of CHIP on the steady state levels of ANXA2 is clearly observed in our CHIP cortical neuron model from a disease-relevant background. More broadly, CHIP may affect the expression of ANXA2 in other cell lines, although this seems to be dependent on the cellular status and type (e.g. potentially promoted

by the synucleinopathy background). Whether this CHIP-dependent regulation of ANXA2 is direct or not remains unclear although supporting data favours CHIP-dependent post-translational modifications of ANXA2.

"Annexinopathy" was first used in 1999 and describes the involvement of Annexins in human diseases[165]. High expression of ANXA2 has been associated with more aggressive gliomas and increased severity of muscular dystrophy. In the latter, ANXA2 promotes sarcolemma wound healing by aggregating intracellular vesicles that fuse to form patches at sites of plasma membrane defect[165].

Whilst mechanistic roles of annexins in cancer progression and muscle diseases have been investigated, their involvement in neuron homeostasis and neurodegeneration is largely unknown and understudied. The first study investigating the expression of Annexins reported that ANXA2 and ANXA4 were present in glia but absent from neurons, whilst ANXA1 and ANXA6 were neuronal[188]. ANXA1 and ANXA2 were found in the PM of neuronal synapses (purified from pig cerebral cortices)[179] and reactive astrocytes[188], respectively. More recently, ANXA2 was detected in the cell body and processes of neurons, showing enrichment in the distal tips (Figure 5.36)[189]. The association of Annexins with the PM of neurons drove its proposed role in neurotransmitter release by exocytosis[179].

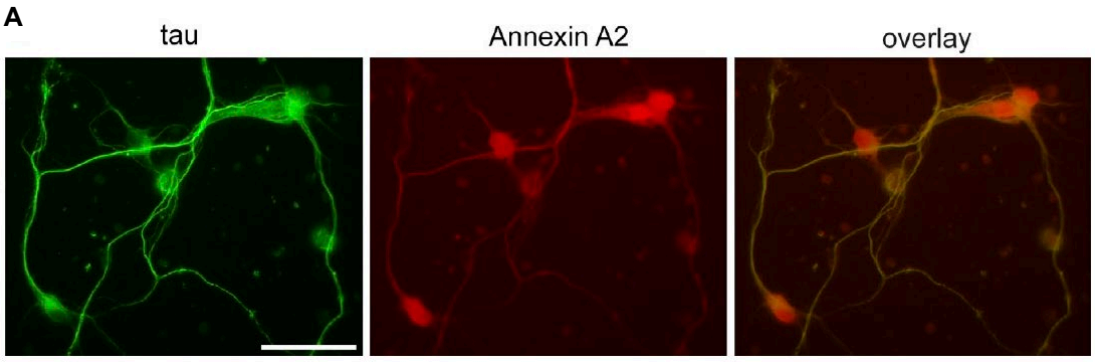


**Figure 5.36: Annexins in neuronal health and disease**
Neuronally differentiated PC12 cells stably expressing PAGFP WT tau were subjected to a combined detergent extraction-fixation protocol to reveal the cytoskeletal fraction. The expression of endogenous ANXA2 and transfected tau was analysed by immunofluorescence using anti-GFP and anti-ANXA2 antibodies. ANXA2 is enriched in the distal tips (in growth cones). Scale bar, 50 μm.

(Gauthier-Kemper *et al.*[189])

There is some degree of appreciation that the patterns of expression of annexins throughout the brain change during development and in pathological states. This led to the hypothesis that annexins may be involved in neuronal and glial responses to acute and chronic injury[188]. In 1994, Eberhard and colleagues[188], reported alternations in the distribution of ANXA6 in affected neurons and the upregulation of ANXA1, ANXA2 and ANXA4 in reactive astrocytes in post-mortem brains of patients with acute CNS damage or chronic degeneration. Later, ANXA2 was found to be overexpressed in patients with Frontotemporal dementia with Ub and TDP-43 positive inclusions by 11.3-fold and with motor neuron disease (lacking a significant number of frontal cortex inclusions) by 2.3-fold compared to controls. Thus, increase of ANXA2 appeared to correlate with the presence of inclusions (i.e. proteinopathy)[190]. Likewise, when a key component involved in the regulation of the proteome (CHIP) is removed, ANXA2 steady state levels increase, especially in a neurodegeneration-prone genetic background.

Although annexins have been reported to be overexpressed in frontotemporal dementia, AD and PD, this has not translated into comprehensive studies investigating regulation of the proteostasis of Annexins and its molecular mechanisms and cellular significance within neurons - despite the availability of tools and techniques largely established using models of cancer and muscle injury. Data presented in this chapter contributes to this gap in our understanding.

## 5.3.2 CHIP-mediated regulation of Annexin A2 homeostasis

ANXA2 is a highly dynamic protein that regulates membrane remodelling events at basal conditions and repairs membrane injuries. Upon injury, ANXA2 is rapidly recruited to the site of injury and becomes upregulated[148]. Such prompt response is only possible with tight control of the steady state levels of ANXA2 and an orchestrated regulation of ANXA2 in the aftermath of membrane repair. We propose ANXA2 as a novel target of the E3 ligase CHIP. Such regulatory event could be important both at basal conditions and upon membrane-induced damage.

Work on the cortical neurons pioneered the hypothesis of CHIP-induced changes in the homeostasis of ANXA2. Going beyond assessing bulk protein levels, which are

likely to be tightly controlled and the final read-out of a regulatory cascade(s), we sought to investigate the ANXA2 isoform profile. This could elucidate potential PTMs across CHIP cell lines, which could influence protein stability, turnover, subcellular localisation and interactome. Indeed, an unbiased analysis using 2D-gel SDS-PAGE/WB shed light into differences in ANXA2 isoforms in the presence and absence of CHIP (some consistent across cell lines) (Figure 5.15). Therefore, CHIP-induced changes in ANXA2 might occur at a post-translational level.

When lacking CHIP, cells form a higher-order ANXA2 isoform. This novel ANXA2 species is conserved across iPSC and undifferentiated SH-SY5Y lines and could be an aggregated form of ANXA2, which is important in membrane repair[162,163,169]. It is unclear if the CHIP KO-specific higher MW isoform arises due to a lack of CHIP-dependent regulation directly (i.e. CHIP is a negative regulator of such isoform), or as a consequence of how the absence of CHIP shapes the cellular status.

CHIP may influence the homeostasis of ANXA2 by acting in close proximity in a direct (via CHIP:ANXA2 interaction) or indirect manner (interacting with ANXA2 within a complex containing other protein(s) or through a third party). In these scenarios, when CHIP is ablated, the interaction is abolished and ANXA2 would become dysregulated. Alternatively, the effect of CHIP on ANXA2 dynamics may be secondary to an altered intracellular environment (e.g. absence of CHIP could lead to proteotoxic stress, which could affect ANXA2). Our investigation then pursued into studying the underlying mechanism of CHIP-dependent changes in ANXA2.

Different methods suggest that CHIP and ANXA2 could interact in cells. Firstly, IF (Figure 5.11) and a subcellular fractionation assay (Figure 5.10) revealed that CHIP and ANXA2 have similar subcellular localisations (cytoplasmic), a requirement for direct protein:protein interaction. Moreover, the ANXA2 distribution observed in cells of different CHIP genotypes was comparable, being found in the cytoplasm, membrane and nucleus of cells – in line with the literature[168,170]. Secondly, PLA revealed that endogenous CHIP and ANXA2 are within <40 nm of each other *in situ*, thus direct protein:protein interaction is a possible mechanism of action in different CHIP cell models (Figure 5.13 & Figure 5.14). Finally, endogenous CHIP co-immunoprecipitated with endogenous ANXA2 (Figure 5.12). At present we cannot conclude whether CHIP:ANXA2 interaction occurs directly and independently or

within a complex. Commonly, the CHIP interactome has been assessed in a chaperone-dependent manner, where chaperones mediate the direct interaction with the substrate. At least *in vitro*, I have found that CHIP:ANXA2 interaction does not require chaperones (Figure 5.16 & Figure 5.17). This is the first account of this interaction. In fact, to our knowledge, there is no published evidence of the interaction of ANXA2 with an E3 ligase enzyme.

Given the E3 ligase functions of CHIP, the possibility of ANXA2 being an ubiqitination substrate of the enzyme was explored. CHIP-dependent ubiquitination of ANXA2 was readily detected *in vitro* using untagged ANXA2, forming both mono- and multimono- or poly-ubiquitinated species (Figure 5.17). In attempt to detect endogenous ubiquitinated ANXA2 in situ, PLA using anti-ANXA2 and anti-Ub antibodies was performed. Punctae (PLA signal) would implicate that ANXA2 is in close proximity with Ub, thus ANXA2 could be covalently bound to Ub (either one Ub, forming mono-ubiquitinated ANXA2, or multiple, yielding multimono- or poly-ubiquitinated species). The PLA with both Ub and Ub-linkage specific antibodies suggested that WT cells might have more ubiquitinated ANXA2 species than CHIP KO cells (Figure 5.18 & Figure 5.19).

In attempt to further validate CHIP as an E3 ligase responsible for the ubiquitination of ANXA2 in cells, stable cell lines expressing an E3 ligase- or chaperone-dead mutant CHIP (KO + H260Q and KO + K30A, respectively) were also included in this assay. Only the latter was capable of partly restoring the PLA signal, while CHIP KO + H260Q cells was not statistically different from CHIP KO cells. Importantly, the levels of ANXA2 remained unchanged between the KO + H260Q and KO + K30A cell lines, increasing the confidence of the results presented. In parallel, the PLA addressing the CHIP:ANXA2 interaction showed a pronounced increase in signal in CHIP KO + H260Q cells compared to WT cells (Figure 5.14), thus the mutation does not abolish ANXA2-binding.

Enzymatic kinetics together with the decreased ANXA2:Ub PLA in the KO + H260Q cell line might explain the observed increase in ANXA2:CHIP interaction in these cells. The interaction between an E3 and its substrate is weak and/or transient[145] and substrates are tuned to dissociate with a few seconds ($k_{off}$ tends to be about 0.4 $s^{-1}$)[191]. Ubiquitin ligase trapping techniques counteract this[145] and the dissociation rate,

rather than the Ub transfer, becomes the rate-limiting step[191]. Expression of mutant E3 ligase variants 'trap' putative ligase substrates, thus changing the kinetics of the ligase-substrate interaction by decreasing the off-rate[145]. Therefore, it seems that ANXA2 binds to H260Q mutant CHIP and, because the enzyme is catalytically dead, Ub is not added to the substrate. As a result, instead of substrate detachment from the complex, ligand-induced intermediates become stabilised – direct evidence for an induced-fit mechanism¶[192]. Taken together, this data reveals ANXA2 as a novel substrate for the E3 ligase CHIP.

The fate of ubiquitinated ANXA2 is dictated by characteristics of the PTM, including the length of the Ub chain and the lysine residues of Ub used for chain formation. Attachment of a polyubiquitin chain consisting of at least 4 Ubs linked together through their K48 residue destines the substrate for proteasomal degradation. A chain using K63 drives endocytosis, DNA repair and initiates signalling cascades[9]. CHIP-dependent ubiquitination of ANXA2 might use different Ub chains (K48 and K63), since the PLA signal detected as similar in all experiments in CHIP WT cells. Therefore, we can conclude that ANXA2 regulation via ubiquitination is complex.

### 5.3.3 Membrane integrity in CHIP KO models

There is robust evidence implying that the main function of ANXA2 is in maintenance of membrane integrity[162,163]. Accompanying the increase in ANXA2 detected in CHIP KO cortical neurons, is an increase in intracellular co-localisation of endogenous ANXA2 with the incorporation of a dye into cells, a marker of increased cell permeability (Figure 5.21). Therefore, despite the increase in ANXA2 in CHIP KO cells, like WT cells, they are permeable to this dye. This discards the linear correlation between increased ANXA2 and better membrane integrity, at least in terms of permeability, in our model. Such hypothesis could be deduced from the pathogenic mechanism of cancer cells to upregulate Annexins and, in turn, enhance membrane resilience during formation of metastasis[163].

¶ Induced-fit mechanism: Ligand binding induces a conformational change in the ligand and enzyme, resulting in a precise complex orientation for the enzymatic reaction. This differs from the "lock-and-key" and selected-fit models, where either the conformational of unbound and bound proteins are similar or conformational change precedes ligand binding, respectively[192].

However, two main questions remain unanswered by this assay: is ANXA2 actively recruited to areas rich in the intracellular dye and/or upregulated in attempt to restore membrane homeostasis (i.e. a protective response of ANXA2 to restore membrane integrity)? Or is the increase in co-localisation simply the result of increase membrane permeability in a background with increased ANXA2 (i.e. an epiphenomenon)? A compensatory mechanism of increased ANXA2 expression has been reported for neurons in the context of neurodegeneration[188–190].

It has been suggested that the overexpression of ANXA2 in acute/chronic injury of in neurodegeneration is a protective response to limit damage. Several deleterious conditions (including hypoxia ischemia, excitotoxin exposure, seizures and chronic neurodegeneration) result in phospholipase-mediated membrane degradation, which can be inhibited, at least *in vitro*, by Annexins. In fact, under these conditions, ANXA6 is consistently increased in hippocampal neurons, which are more resistant to injury than others in this region. These findings support a neuroprotective role for annexins in promoting neuronal survival or recovering from injury[188].

Our preliminary experiment showing increased colocalization of endogenous ANXA2 with the intracellular dye can be regarded as proof-of-concept that even if the ANXA2 increases in CHIP KO cortical neurons a secondary, protective response, it seems to fail to restore membrane integrity to the extent seen in control cells.

Given the differences in membrane integrity observed in cells with different CHIP genotypes at basal levels, we hypothesised that CHIP could also influence membrane resilience to injury. Underlying mechanisms that could be somewhat compromised at basal conditions could be exacerbated when the membrane dyshomeostasis phenotype is enhanced by membrane-induced damage. Although injury assays are not physiological *per se*, the signalling cascades activated are likely to be relevant in the context of maintenance of cell health, given the extensive redundancy in the proteins recruited across repair mechanisms[162] (independent of the type of stressor)[148,180].

Most methods employed supported CHIP KO cells having a weaker membrane. In particular, digitonin-induced damage revealed robust and reproducible differences across cell models of different CHIP genotypes (Figure 5.24 & Figure 5.25). When the

stable cell lines expressing CHIP mutants were subjected to digitonin-induced injury, CHIP KO+H260Q cells resulted in similar cell death percentages as CHIP KO cells, while CHIP KO+K30A cells were similar to WT (Figure 5.25).

Beyond supporting this difference in membrane resilience, UV laser-induced injury monitored by live-imaging revealed differences in the repair dynamics (Figure 5.26). Upon injury, CHIP KO cells tend to migrate more when their damaged projections are retained or partially retracted (showing increased cell body movement and "elasticity"). This could translate to a different repair mechanism being employed.

Cell health is likely to be influenced by both the sensitivity to damage and ability to repair. To decipher which of these factors is mainly affected in CHIP KO cells, we first analysed whether these cells can repair following injury. Our CHIP cell models indicate that both WT and KO cells are able to repair following membrane injury (Figure 5.27) with similar kinetics (Figure 5.28). Therefore, it is likely that the increased membrane damage observed in KO cells reflect a sensitivity, rather than repair, phenotype.

The exact molecular mechanisms underlying the poor membrane integrity in CHIP KO cells specifically are unknown. However, we have explored several potential CHIP-mediated mechanisms that could contribute to the phenotype observed in a mutually non-exclusive manner. Namely, changes in membrane proteomics and lipidomics (including phospholipid composition) in the presence and absence of CHIP were studied.

## 5.3.4 Could CHIP-dependent effect(s) on membrane proteomics contribute to differences in membrane integrity?

### a. Dynamics of Annexin A2

The canonical function of ANXA2 is in regulation of membrane-related events and in response to membrane damage[162], thus having roles in normal physiological conditions and upon stress. As discussed, dysregulation of ANXA2 proteostasis under basal conditions in CHIP KO cells (either directly or indirectly by CHIP) could influence its physiological function and result in detrimental cellular effects (i.e. membrane

dyshomeostasis) or the CHIP KO background may stimulate the stress-induced behaviour of ANXA2. Different studied have reported that stress (mechanical and chemical) triggers an upregulation of ANXA2 protein levels[176,180]. Therefore, one possibility is that deletion of CHIP expression mimics such conditions of stress.

We sought to investigate whether ANXA2 in CHIP KO cells retain the ability to respond to injury, considering its altered proteostasis at basal conditions. Our preliminary data not only supports the known stress-induced behaviour of ANXA2 but identifies some differences between CHIP KO and WT cells. Whilst at basal conditions ANXA2 correlated poorly with dye incorporation in CHIP-expressing neurons (Figure 5.21), such correlation increased substantially with injury (Figure 5.29). This could be due to an overall upregulation of ANXA2 levels or its recruitment to damage – mechanisms that have been reported for ANXA2[148,163,176,180]. This change between uninjured and injured conditions was not seen in CHIP KO neurons.

In agreement is a preliminary experiment analysing the effect of digitonin on the levels and localisation of endogenous ANXA2 in a dose- and time-dependent manner by IF (Figure 5.30). An increase in ANXA2 fluorescence intensity could reflect recruitment, upregulation of the protein or change in epitope exposure at the site of injury. The fact that the increase in ANXA2 was detected later in CHIP KO cells following injury could imply a delay in the response to damage. Also, the maximum intensity of ANXA2 reached through the injury assay was higher in KO cells (despite showing no change in basal ANXA2 fluorescence between CHIP KO and WT cells). This difference in ANXA2 dynamics could reflect a compromised ability to mount an adequate response to injury and/or be the consequence of exacerbated damage due to the enhanced sensitivity of these cells to injury.

Beyond quantitative changes in ANXA2 levels in injury, the subcellular distribution of ANXA2 might differ between CHIP-expressing and KO cells. With digitonin treatment, ANXA2 staining becomes gradually more prominent and associated with the plasma membrane, rather than diffuse in the cytoplasm. When extensive damage occurs, translocates to the nucleus. This dynamic behaviour seems to be enhanced in CHIP KO cells (Figure 5.30A). The cytoplasm-to-membrane translocation during injury has been reported[163], while nuclear ANXA2 in the context of stress has only been observed in stimuli-induced apoptosis[176] and during oxidative stress to protect from

genomic damage[175]. Likewise, in conditions of extensive PM damage, ANXA2 might migrate to the nucleus to protect from genomic damage and/or induce apoptosis. This dynamic distribution of ANXA2 in injury could reflect a protective mechanism that is triggered more extensively in CHIP KO cells, due to their increased sensitivity to damage compared to controls. At present, we cannot exclude the existence of other underlying mechanisms for nuclear translocations, such as PTMs, which have been shown to mediate nuclear entry of ANXA2[166]. These findings support the enhanced sensitivity of CHIP KO cells to membrane-induced damage.

### b. Dynamics of Annexin A2:S100-A11 interactome

Multiple membrane-related functions of ANXA2 are S100-dependent. The dynamics of ANXA2:S100 interaction under basal conditions and following injury were analysed in attempt to elucidate the molecular mechanism underlying the increased permeability of CHIP KO cells and their enhanced sensitivity to injury.

CHIP KO cortical neurons and SH-SY5Y cells show poor membrane integrity. The ANXA2:S100-A11 heterotetramer forms in response to calcium influx (a consequence of increased membrane permeability) to restore membrane integrity[148,163]. PLA revealed that this interaction is less frequent in CHIP KO cells at basal conditions, despite the increase in ANXA2 levels. Moreover, CHIP KO + H260Q cells were not significantly different from the CHIP KO line, while CHIP KO + K30A partially rescued this molecular phenotype (Figure 5.31). Since CHIP interacts with ANXA2 (Figure 5.13 & Figure 5.14), as well as S100-A11 (Figure S.11), CHIP could act as a mediator of the ANXA2:S100-A11 interaction, which is not CHIP-dependent but seem greatly promoted by the presence of CHIP. Alternatively, CHIP-induced changes to ANXA2 or S100-A11 homeostasis (e.g. PTMs) could promote such interaction.

Although further experiments would be necessary to reach a robust conclusion, it is interesting to entertain the hypothesis that the ANXA2:S100-A11 interaction seems to be dependent on the E3 ligase functions of CHIP. These protein:protein events correlate with the ubiquitination activity of CHIP (H260Q < K30A < WT CHIP[47]). Alternatively, changes in the interactome of ANXA2 could be a secondary effect of the overexpression system *per se*. Overexpression of a TPR-containing protein such

as CHIP can affect the pool and interactome of TPR-containing proteins. This is particularly applicable to the KO+H260Q, which expresses very high levels of CHIP harbouring a functional TPR domain. Additionally, it has been reported that the H260Q mutant associates more strongly with Hsp90[186] and Hsp70[193] compared to WT CHIP.

Given the well-documented formation of ANXA2:S100-A11 complexes upon injury[148], the effect of injury on this interaction in our CHIP model was also analysed (Figure 5.32). Upon injury, ANXA2:S100-A11 PLA was unchanged in WT cells. CHIP KO cells, on the other hand, recorded a subtle increase in this interaction, but the difference between untreated and treated cells was not significant. This increase could be an attempt to counteract the damage, which is expected to occur when incubating CHIP KO cells with this treatment (while CHIP WT cells should be relatively unaffected, given their increased resistance). Despite such increase, treated CHIP KO cells remain with less ANXA2:S100-A11 puncta than untreated control cells. Therefore, as in basal conditions, formation of the ANXA2:S100-A11 complex is compromised in CHIP KO even in the presence of external stressors. Alternatively, the extent of injury was too mild to induce this interaction, or this mechanism is not required for repair in the SH-SY5Y cells, or the interactions come into play at a later stage (during repair or its resolution). Future work would entail a time-course analysis (using PLA and live-imaging) of the interaction dynamics following digitonin-induced injury.

The interaction of ANXA2 with CHIP shares the same positive trend as ANXA2:S100 in response to injury (Figure 5.33). Although statistical significance was not reached, when the PLA signal was for each cell line and conditions was subtracted by their background noise (the mean of each “Ctrl” group), the difference between untreated and treated CHIP WT cells is significant ($P < 0.05$) (data not shown). This suggests that injury may induce the interaction of ANXA2 with the active E3 ligase CHIP, which is not seen in KO cells. The functional significance of this interaction under cellular stress is unknown. Further studies should investigate whether the consistent correlation between ANXA2:S100 and CHIP:ANXA2 in uninjured and injured cells is biologically related and causative in nature. The interaction of CHIP with ANXA2 (i.e. the binding *per se* or PTMs derived) could be important for the heterotetramer formation with S100-A11.

S100-A11 is known to enhance the capacity of cells to complete the Annexin-mediated repair process. As a complex they promote repair and membrane-remodelling events in multiple ways. S100-A11 mediates the recruitment of ANXA2 to the membrane, hence accumulation of these proteins at the membrane mutually dependent and occurs within 15-45 seconds post-injury[148]. The heterotetramer promote different PM repair mechanisms[162], including by endocytosis (Figure 5.4A)[162,174] and membrane excision (Figure 5.37)[163]. For the latter, ANXA2:S100-A11 is recruited to the restoration zone of the lesion, rather than the injury site (that is delineated by ANXA1 in a S100-independent manner). This allows actin polymerisation to occur in the area where cells choose to cut off the damaged part of the membrane (Figure 5.37A)[148,162]. Annexins and S100 proteins contribute to cytoskeletal remodelling. ANXA2:S100-A11 not only helps to nucleate actin polymerisation, but it also binds to F-actin to decrease its depolarization rate, preserving and allowing new build-up of F-actin locally[163]. The F-actin build-up pulls the membrane edges of the wound together for resealing[162].

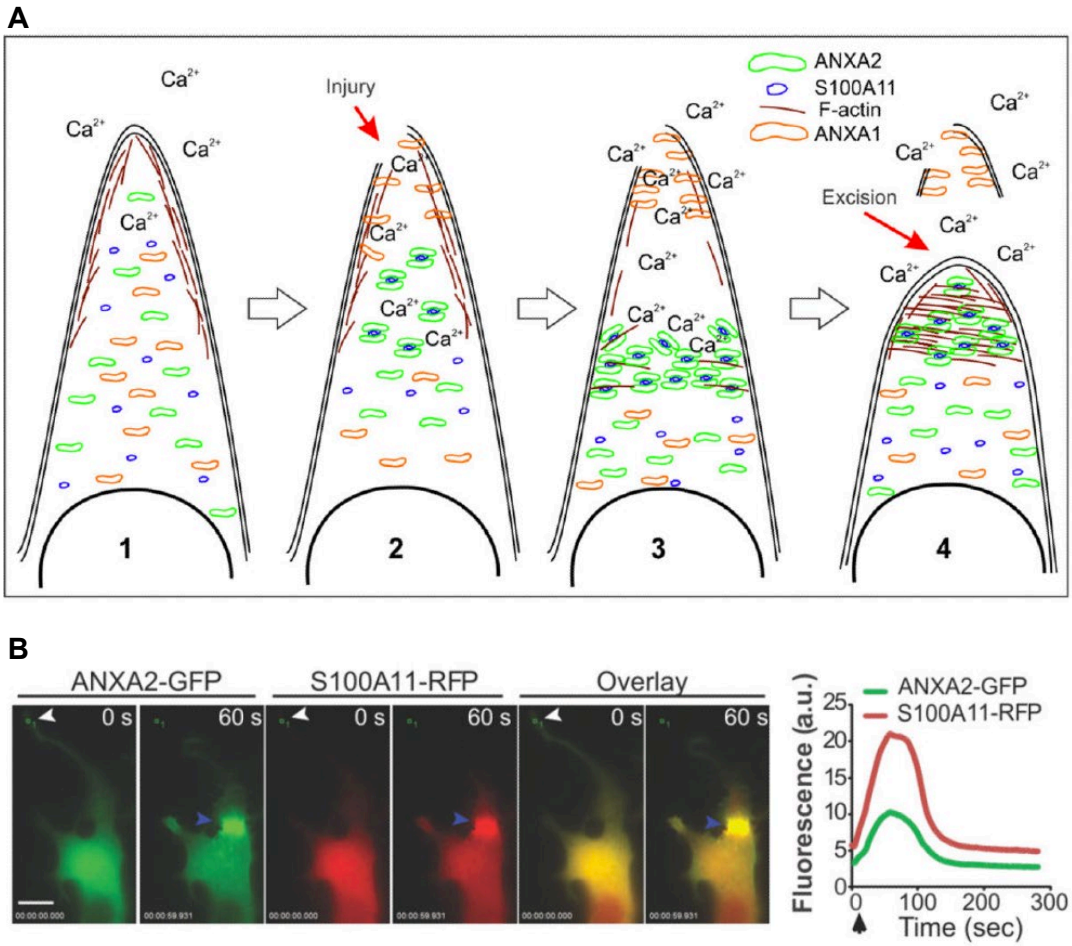


**Figure 5.37: Annexins and S100 proteins in membrane repair**
**A)** Proposed model: **1**) In the uninjured cell, membrane tension is maintained by the cortical cytoskeleton and repair proteins are diffuse in the cytosol. **2**) Injury. **3**) The increase in cytosolic $Ca^{2+}$ results in depolymerisation of F-actin and accumulation and the accumulation of ANXA1 at the site of injury and ANXA2:S100-A11 adjacent to it. **4**) The wounded membrane surrounding the site of injury detaches. ANXA2:S100-A11 initiates F-actin polymerisation at the site of injury, which aids membrane re-sealing and the restoration of membrane tension.
**B)** The kinetics and localisation of ANXA2-GFP and S100-A11-RFP following laser-induced damage.

(Jaiswal *et al.*[148])

## 5.3.5 Could CHIP-dependent effect(s) on lipidomics contribute to differences in membrane integrity?

### a. Effect of lipids on CHIP activity

Membrane recruitment of ANXA2 and formation of the heterotetramer with S100 proteins is promoted by the influx of calcium. Therefore, at basal conditions, the majority of ANXA2 is expected to be cytoplasmic (in agreement with our subcellular fractionation, Figure 5.10, and IF data, Figure 5.11). In this scenario, it is easy to imagine that the interaction between ANXA2 and CHIP is likely to occur within the cytoplasm. However, once ANXA2 is recruited to the site of membrane injury and becomes membrane-bound, interaction with CHIP could be ablated. However, our PLA data contradicts the possibility of ANXA2 and CHIP becoming separate (by > 40nm). Digitonin treatment rather than abolishing this interaction even promoted it (Figure 5.33). Can ANXA2 and CHIP interact at the membrane in our model? The hypothesis that CHIP can translocate to the membrane was recently pioneered by Kopp and colleagues[50]. They reported membrane-bound CHIP under conditions of stress[50]. Moreover, CHIP was shown to ubiquitinate the INSR, which like ANXA2 is also a membrane-binding protein[62]. Although we could not capture CHIP at the membrane by IF with different fixation methods (possibly due to specific epitope exposure or due to the transient nature of the interaction) nor live-imaging (data not shown), its direct contact or close proximity with such lipid-rich environment could influence its activity. CHIP could also migrate to the membrane independent of Annexin A2, although membrane-related functions for CHIP have not been previously identified.

It was reported that CHIP binds specifically to PA and PI monophosphates, in particular PI4P[50]. PIs constitute 10-20% (mol%) of total phospholipids, are synthesised in the ER and recruited to the cytoplasmic leaflet of cell membranes. They are converted to PI3P in early endosomes or PI4P in the Golgi, PM, and early and late endosomes. PI4P make up 2-5% of total PI and a substantial fraction is likely to be present in the PM. PA is also a component of cellular membranes, although its abundance is low[194,195]. It is generated from the phospholipiase D (PLD)-regulated hydrolysis of the most abundant membrane glycerophospholipid, phosphatidylcholine (PC). Interestingly, various PLD enzymes have been implicated in Alzheimer's disease[196]. PA can be hydrolysed by phospholipase A to generate LPA[196]. Within the

cell, PA can regulate phospholipid biosynthesis, as it is a common precursor of glycerophospholipid (such as PS, PI and PE)[195]. Functionally, PA also regulates membrane vesicle trafficking (i.e. promotes membrane vesicle formation and fusion), by inducing membrane curvature driven by its negatively charged headgroup[195,196].

Through binding to PA or PI4P, potentially CHIP could become membrane-bound and interact with ANXA2 at this compartment. Although supporting data for this is still required, we sought to investigate the effect of these lipids on the E3 ligase activity of CHIP. Our *in vitro* ubiquitination data suggests that both PA and PI4P inhibits CHIP-dependent ubiquitination of ANXA2, while the latter also prevents CHIP's auto-ubiquitination (Figure 5.34), thus the underlying mechanism for compromised ubiquitination of ANXA2 may be different. This contradicts the reported enhancement of auto-ubiquitination of CHIP and slight impairment of CHIP-dependent formation of free polyubiquitin chains in the presence of PA-containing liposomes[50]. The importance of PA and PI4P in the homeostasis of CHIP (both localisation and activity) is still unknown.

Kopp and colleagues[50] reported that CHIP mutant K30A resides in the PM (detected by live-imaging). The explanation proposed suggests that, given the competitive nature of both lipid and chaperones for the TPR domain, by abolishing chaperone interaction, CHIP becomes membrane-bound[50]. However, it has been shown that the inherent biophysical properties of K30A CHIP are highly similar to the chaperone-bound WT protein (Figure 5.20B). Therefore, lipid-binding, like chaperone-binding, may induce structural rigidity (Figure 5.20C), which has been shown to allosterically inhibit U-box activity[47]. This could explain the reduced auto-ubiquitination of CHIP in the presence of specific lipids.

There has been growing evidence supporting lipid-dependent regulation of proteins by different functional principles (Figure 5.38)[197]. Given the reported specificity of CHIP for PA and PI4P, the distribution of these lipids can regulate the recruitment of CHIP to specific membrane locations (illustrated by *mechanisms i-iii* in the figure), acting as lipid-anchors[196,197]. Furthermore, lipid-protein binding can initiate/modulate the functional activity of the protein by altering its conformation and electrostatic interactions (e.g. through allosteric regulation, *mechanism iv*). This lipid-induced regulation can be direct (e.g. PA-mediated activation of phosphatidylinositol kinases)

or indirect (e.g. activated as a downstream consequence of signalling cascades initiated by PA as a lipid secondary messenger[194]). Therefore, the spatial and temporal specificity of lipids might influence protein activity[197].

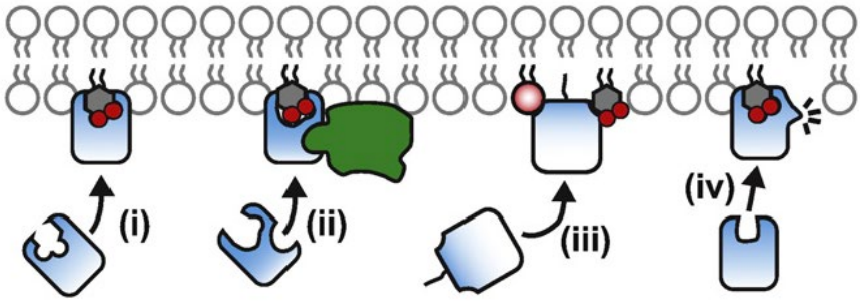


**Figure 5.38: Functional principles of lipid-regulated protein function**
**i)** Direct recruitment of a protein to the membrane by high affinity binding
**ii)** Phospholipids cooperate with other local molecular interactions for protein recruitment (e.g. small G-protein provides the avidity necessary for membrane binding)
**iii)** The anionic lipid environment drives protein binding by electrostatic interaction
**iv)** Lipid binding induces allosteric activation of the protein through a conformational change
(Adapted from Hammond *et al.*[197])

## b. Lipidomics of a CHIP KO model

The differences in lipidomic profile across cells expressing and lacking CHIP (Figure 5.35) could be informative when studied from different angles: in the context of lipid-dependent modulation of protein activity and with regards to membrane composition (affecting membrane integrity). These will be reviewed.

### i. Lipid-dependent modulation of proteostasis

Given the *in vitro* observations of lipid-induced changes in CHIP activity and growing field of how lipid composition influences protein and membrane homeostasis, we sought to evaluate how the lipidomic profile of the CHIP SH-SY5Y model could influence protein activity at a cellular level. Our preliminary results revealed that, although the concentration of the majority of phospholipid groups assayed did not change, PA, LPA and PS showed an increase of 1.5 to 2.5-fold change (WT/KO).

ANXA2 binds preferentially to PS, as well as other negatively charged phospholipids, including PA[167]. PS is also an important component of the cellular membrane, residing mainly in the inner leaflet[198]. PS can be synthesised from pre-existing PC or PE[199]. Accumulation of PS has been shown to improve hippocampal synaptic efficiency, possibly by enhancing the activity of membrane-bound enzymes involved in neurotransmitter release and promoting long-term potentiation. Phenotypically, this prevented age-related decline in cognitive ability and memory[200,201]. Increased PS also promotes neuronal survival via PI3K/Akt signalling pathway[199,202].

Following identification of ANXA2 as a disease-relevant potential protein target of CHIP, we investigated the dynamics of ANXA2 proteostasis (alone and as a complex with S100-A11), the lipidomic profile and membrane integrity of our CHIP model(s). However, the relationship between these is unknown and different questions have been opened. One hypothesis is that ablation of CHIP expression could lead to the dysregulation of lipids important for the homeostasis of ANXA2 (e.g. PS or PA). This would be suggestive of a role for CHIP in the regulation of membrane composition, which has not been previously reported. The increased WT/KO fold changes favour CHIP as a positive regulator of specific phospholipid classes. If CHIP proves to be a regulator of phospholipid composition, this could have significance in research and clinical settings, since PS levels in mammalian cells have been difficult to modulate[202].

Alternatively, CHIP could function as a direct negative regulator of ANXA2 homeostasis, thus deletion of CHIP would lead to ANXA2 accumulation (the same phenotype as that observed in CHIP KO cortical neurons). Lipid changes could rise secondary to this: dysregulation of the lipid-binding protein ANXA2 could in turn compromise the membrane homeostasis, in particular the levels of the lipids to which it binds to (PA, PS and PI – the latter two were found to be decreased in CHIP KO). A third hypothesis positions changes in lipid composition as an early event, as these would interfere with CHIP activity (as seen from the *in vitro* ubiquitination assay), eventually leading to changes in ANXA2 indirectly. Future work would investigate the strength of these correlations and possible underlying mechanisms to understand whether this correlation implies causation.

### ii. Implications for membrane integrity

A change in lipid composition could also help to explain the membrane-related phenotype observed across our CHIP models. Saturation and length of the acyl chains of phospholipids are important features to dictate membrane properties. Typically, fatty acids are attached to the *sn1* position of glycerol backbone (within the head of the phospholipid) are predominantly saturated (SFA), while those esterified to *sn2* tend to be mono- (MUFA) or polyunsaturated (PUFA), together referred to as unsaturated fatty acids (UFAs)[195]. The relative distribution of these in membranes is around 40:60 (SFAs:UFAs)[203]. Within the core of the lipid bilayer, acyl chains are tightly packed but remain highly mobile. Short lipid tails and unsaturated chains contributes to a more fluid membrane with high structural stability[198].

Fluidity influences membrane tension and bending rigidity and, in turn, membrane plasticity[198]. Seeing that repair mechanisms require extensive membrane remodelling, this flexibility is likely to be important in promoting membrane repair[195]. The nature of lipids reflects the flexibility and resistance of membranes, which is essential for the constant remodelling conducted without interfering with its barrier function and overall structural stability[198].

As proof-of-concept that particular changes in membrane composition can affect membrane integrity, lipidomic changes observed in Duchenne muscle dystrophy were compared to our CHIP model. In this progressive condition, breakdown of plasma membrane is the earliest detectable abnormality preceding muscle fibre loss[204]. Lipid composition is believed to be responsible for the abnormal membrane properties (Table 5.1)[205,206]. Overall, there is an increase in MUFAs (18:1) across phospholipid classes and a decrease in PUFAs (22:6) in PE and, possibly, in PC classes of phospholipids. Muscle membranes, like Duchenne muscle fibres, with increased saturation were shown to be more sensitive to eccentric-induced damage[207].

**Table 5.1: Lipidomics of Duchenne muscle fibres**
Saturated phospholipids are indicated in black, mono-unsaturated in red and poly-unsaturated in blue. Meta-analysis based on Pearce & Kakulas[205] and Kunze *et al.*[206].

| Lipid class | Fatty acid | Trend in Duchenne muscle |
|---|---|---|
| **PC** | 16:0 | Large decrease[55] |
| | 18:0 | Increase[54] |
| | 18:1 | Increase[54,54] |
| | 18:2 | Increase[54]/decrease[55] |
| **PE** | 16:0 | Large decrease[54] |
| | 18:0 | Increase[54] |
| | 18:1 | Increase[54] |
| | 22:6 | Decrease[54] |
| **SM** | 16:0 | Increase[54] |
| | 23:0 | Increase[54] |
| | 24:1 | Increase[54] |
| | 18:0 | Decrease[54] |
| | 18:1 | Decrease[54] |
| **LPC** | 18:0 | Increase[54,55] |

Likewise, our CHIP KO model showed an overall increase in SFAs analysed in this preliminary study (Table 5.2). However, MUFAs, which make up a greater fraction of fatty acids analysed, were decreased in the CHIP KO cells. Of significance, PS 34:1 was particularly decreased in KO cells compared to controls (Figure 5.35). This does not follow the observed increase in MUFAs seen across phospholipid classes in Duchenne muscle. However, the reported decrease in PUFAs is consistent with our observations in CHIP KO cells. The WT/KO fold change recorded for PA 38:4 and PS 36:4 was of >2 and for PA 36:4 and LPA 20:4 was 0.5 (Figure 5.35). The changes in PUFAs were restricted to a few phospholipids, thus the overall concentration was similar between CHIP KO and control cells (Table 5.2). The decrease in phospholipid unsaturation (and possibly the increase in saturation, although to a less extent) could to increased membrane rigidity. This is associated with increased permeability and susceptibility to membrane injury[207], thus could contribute to the poor membrane integrity observed in our CHIP KO cell models. Nonetheless, it is important to take into account that this was a preliminary lipidomic analysis of this CHIP model and that conclusions are limited by the spectrum of phospholipids analysed.

**Table 5.2: Concentration of phospholipid saturation classes identified by lipidomics of CHIP KO and WT undifferentiated SH-SY5Y cells**
Data presented are averages (nmol/g,ml).

| CHIP genotype or fold change | More saturation | | Less saturation |
|---|---|---|---|
| | SFAs | MUFAs | PUFAs |
| **WT** | 0.157 | 22.010 | 25.969 |
| **KO** | 0.207 | 17.548 | 23.660 |
| **WT/KO** | 0.756 | 1.254 | 1.098 |

Data in this chapter supported the role for CHIP in the regulation of the membrane proteins, ANXA2 and S100-A11, as well as their complex formation. Such regulation could occur post-translationally and possibly via ubiquitination, as ANXA2 was identified as an E3 ligase substrate of CHIP. In parallel, CHIP seems to influence lipid composition, which has not been previously reported. Whether the CHIP-mediated changes in membrane proteins and lipids are independent, yet related molecular events, or not, is unclear. However, these could be two mechanisms driving the same key cellular function of CHIP: regulation of proteostasis.

# Chapter 6: Modulating the activity of CHIP using single-chain antibodies

## 6.1 Introduction

### 6.1.1 Structure and function of CHIP

#### a. Folding of the CHIP dimer

WT CHIP has been described as predominantly dimeric[38,49], but monomeric[38] and other high multimeric forms[38,49] have been reported. The elongated protomer of the asymmetrical dimer is the most stable, having its HH extended and its C-terminal residues wedged between the TPR domain and the U-box. In the compact protomer the TPR domain packs directly on the U-box (residues 256-265), having the E2-binding site buried[39,208]. The CHIP dimer assembly pathway has been defined as consisting of symmetrical dimerization followed by an activation step that causes the dimer to break the symmetry[208] (Figure 6.1A). This gives rise to an asymmetrical dimer (Figure 6.1B) with intra-protomer packing of the TPR domain against the U-box of one of the protomers. As a result, one E2-binding site on the U-box is exposed, changing the stoichiometry of its binding with E2 enzymes[39,48,208].

The folding of the asymmetric dimer has been modelled. The HH-domain dimerization triggers rapidly partial symmetric U-box dimerization by positioning the U-boxes of the protomers within interaction range (Figure 6.1Aa). More specifically, HH dimerization brings together five consecutive basic amino acids within the linker region ($_{221}$KRKKR$_{227}$) between the HH and U-box of each protomer (Figure 6.1B). At this stage, repulsive interactions grow between the positively charged linker and the extended helix ($_{153}$RRIH$_{158}$ in H7). This electrostatic repulsion is eventually revealed by breaking H7 of one protomer, causing its bending and breaking dimer symmetry (Figure 6.1Ab). This snapping of the helix in one protomer forces the opposite protomer to insert its C-terminal through its own TPR and U-box domain interface (Figure 6.1Ac). Finally, the partial U-box dimer assumes a native-like conformation, forming a high-affinity complex with half-of-sites active (only one E2-binding site exposed)[208].

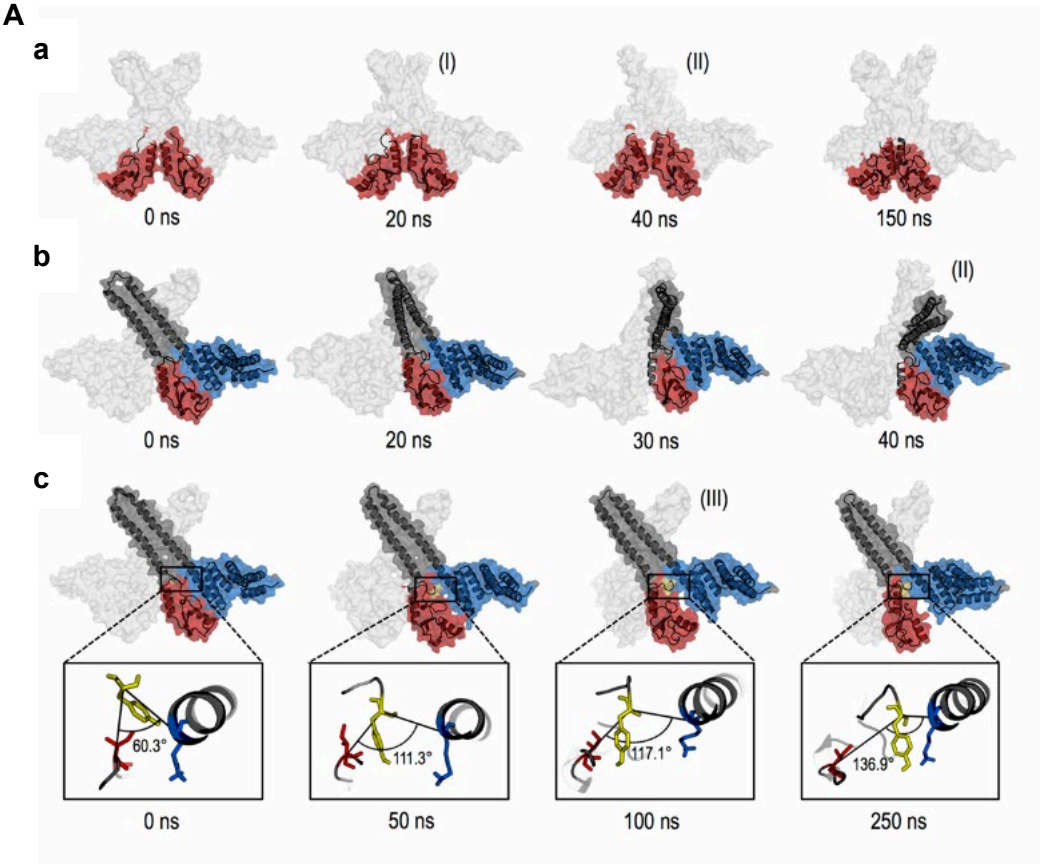


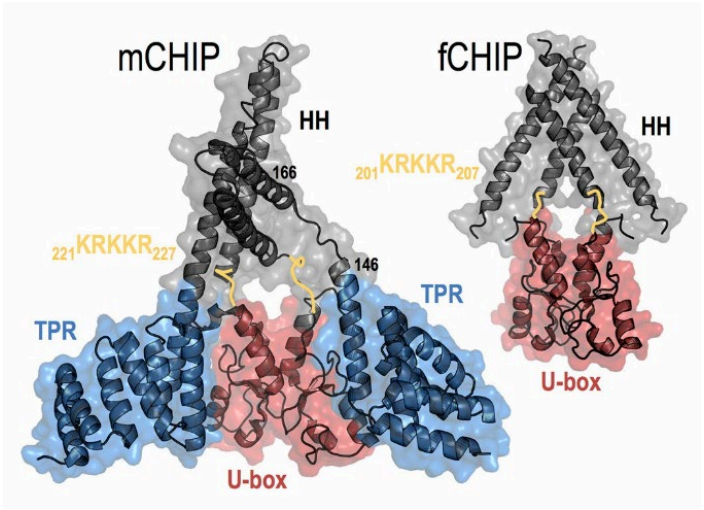


**Figure 6.1: Folding of dimeric CHIP**
**A)** Folding of the asymmetric dimer. The progressive molecular dynamics of the U-boxes (**a**), the bent/compact protomer (**b**) and the extended protomer (**c**) are represented. Folding starts with U-box dimerization (**I** in **a**), followed by the breaking of the helix H7 (**II**) to yield the bent protomer (**b**). The final events (**III**) are the TPR-U-box separation and the insertion of the C-terminus (involving the interaction between the C-terminal a-helix of the TPR domain in blue with the C-terminus in yellow, and the latter with the U-box in red) in the extended protomer (**c**).
**B)** Crystal structures of the dimeric asymmetric CHIP (mouse) and symmetric fCHIP (Zebrafish). The latter lacks the TPR domains. The $_{221}$KRKKR$_{227}$ residues link the TPR and the U-box domains.

(Ye *et al.*[208])

Although the formation of an asymmetrical dimer is usually associated with energy frustration and structural instability, snapping of the helix is transduced into mechanical force that kinetically activates the CHIP dimer by disrupting a stable domain-domain interaction. Thus, kinetic forces generated by opposing interactions control conformational activation (i.e. an induced-fit process) rather than thermodynamics[208].

### b. Function

The inherent and dynamic property of CHIP to form homodimers allows an elegant interplay between a dimeric chaperone and a single ubiquitination system[39,48]. The advantages of an asymmetric structure are clear: tight regulation of CHIP activity and prompt switching from chaperone-mediated protein folding to proteasome-mediated degradation[39]. Additionally, asymmetry may also contribute to the regulation of the steady-state levels of CHIP. The asymmetry of the monomers limits the availability of E2-binding sites, thus it may also function to prevent premature CHIP degradation until assembly of the fully formed dimer[208].

### c. Symmetric versus asymmetric

Both symmetric[209] and asymmetric[208] dimer conformations have been described for human CHIP in solution and crystallized from zebrafish and mouse, respectively[208,209] (Figure 6.1B). In principle, symmetric dimers formed by two bent protomers would be inactive with regards to E3 ligase function. Here, there is no extended H7 helix to disrupt the TPR-U-box domain interface, thus the E2-binding site would remain buried. However, the elongated-dimer model could yield, theoretically, an active dimer that could bind two E2 enzymes. In this scenario, snapping of the extended helix does not occur and the TPR-U-box domains never interact. Here, the U-boxes do not dimerise[208].

The bent-dimer conformation can be achieved solely by deleting six C-terminal residues of CHIP, responsible for TPR-U-box separation. The elongated-dimer is formed when CHIP lacks the TPR domain (as in Zebrafish)[208]. Only the asymmetric crystal structure of mouse CHIP has been published. However, based on HDX-MS

data, Graf and colleagues[209] reported that CHIP is a highly flexible symmetric dimer in solution with dynamic regions, capable of E2 binding. Structural flexibility has been directly linked to CHIP activity[47].

## 6.1.2 Single chain variable fragment (scFv)

### a. Structure and function

The use of antibodies in molecular biology takes advantage of the nature of the immune system: to detect and defend our body against non-self-agents[210]. They have proven to be efficient as high-affinity, protein-based binding reagents[211]. The IgG antibody contains a unique variable region (Fv) within the antigen-binding fragment (Fab) (Figure 6.2A). The antigen-binding sites, the paratopes, are located at the Fab tips[210]. Antibodies have been manipulated to improve their binding affinity, pharmacokinetics, stability and expression levels[212]. They have been engineered into monovalent (including Fab and single chain Fv fragments, scFv) and bivalent fragments (e.g. $F(Ab')_2$)[211] (Figure 6.2B)[96].

ScFv (Figure 6.2Bc) are heterodimeric recombinant antibodies consist of one Fv region (the smallest functional unit) of the classic IgG antibody, having a variable light-chain ($V_L$) and a variable heavy-chain ($V_H$) connected by a flexible linker[210,211,213]. They have the same specificity and affinity for antigens as a full IgG antibody containing such Fv region, in a monovalent manner[213]. The variable regions contain both hypervariable and framework sequences. In total, scFv contain six hypervariable sequences that make up the antigen-binding site and referred to as the complementarity determining regions (CDRs). The framework sequences, on the other hand, ensure correct β-sheet folding of the $V_L$ and $V_H$ domains, allowing interdomain interactions. The flexible linker also contributes to proper folding[213]. It contains hydrophilic residues (preventing intercalation of the linker between the variable domains during protein folding) together with stretches of residues that enhance flexibility (Gly and Ser) and solubility (Glu and Lys)[210,212]. Linker length is also an important factor[210].

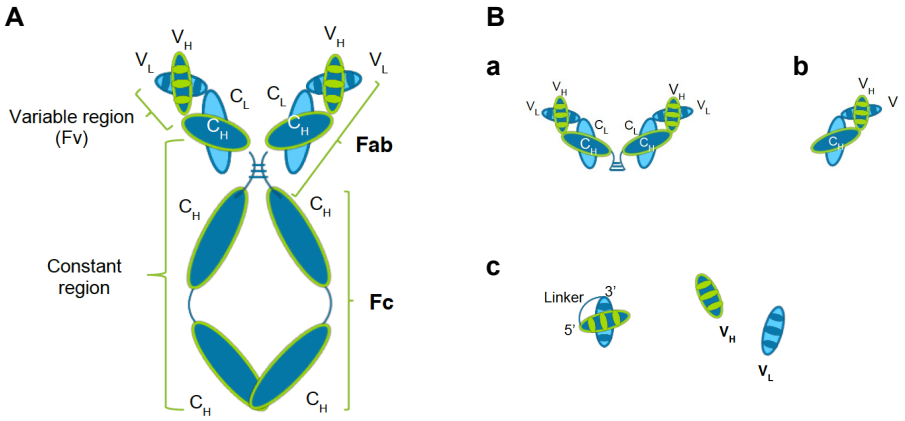


**Figure 6.2: Antibodies**
**A)** IgG antibody is a Y-shaped four polypeptide unit containing two heavy (H) and two light (L) chains held together by disulphide bonds. It has conserved constant regions (*in blue*) are located in both the fragment crystallizable, Fc, at the stem, and the antigen-binding fragment, Fab region, at the arms. The unique variable region, making up the Fv within the Fab region, is illustrated with stripes, representing the complementarity determining regions. This structure allows its bivalent activity, which increases the functional affinity (avidity) of the antibody for its antigen.
**B)** Recombinant Ab fragments: $F(Ab')_2$ (**a**), Fab (**b**) and scFv (**c**).
(Information based on Ahmad *et al.*[210] and Holliger & Hudson[211].
Schematic adapted from Dos Santos[96])

## b. ScFv antibodies engineered by phage display technology

Early methods for the generation of small recombinant antibodies were based on proteolysis[212,214], for example Fab was digested to obtain the Fv region only (in 1971). Later, the first scFv antibodies were cloned by Bird *et al.*[213], Huston *et al.*[215] and Skerra *et al.*[216] in 1988 by expressing scFv genes in *E. coli* and purifying them using acid-based or affinity-based purification. Common problems faced included loss of affinity for antigens compared to the parent antibody, poor solubility and stability and aggregation.

Phages are viruses that accommodate segments of "foreign" DNA. The most common phage-displayed vectors used in scFv production are filamentous phage strains. Phage infect *E. coli* by attaching its coat protein pIII to the bacterial host, which causes the coat protein to dissolve and allows the phage-displayed vector (ssDNA) to enter the cytoplasm. Next, the vector (containing the foreign insert) replicates in the host by having the host machinery synthesis a complementary DNA strand, forming a double-

stranded replicative form (RF) that makes progeny RF. Beyond the normal delivery of the vector, phage-display vectors cause the foreign DNA to be expressed as a protein in the host. For such, the host machinery is recruited to synthesize a foreign peptide (encoded by the DNA insert). Because the foreign gene sequence is spliced into the gene encoding one of the coat proteins, the foreign peptide synthesised is fused to the coat protein. The hybrid coat protein is then incorporated into phage particles ("virions") as they are released from the host cell. The extensive secretion of progeny virions (several hundred per cell per division cycle) does not kill the host. Phage harbouring the surface peptide infect fresh bacterial host to repeat this process and multiply. Variation in the peptides displayed by the phages arises from possible mutations in the peptide encoding DNA, which can result in a different amino acid sequence and/or structure and would pass on to phage progeny. This highlights two key characteristics of phage that make phage display technology attractive in the generation of scFV: replicability and mutability[217].

### i. Phage libraries

Phage-display libraries are heterogenous mixtures of phage clone harbouring different foreign DNA insert, hence displaying different peptides on its surface. Libraries can be 'genomic' (having fragments potentially representing the entire genome) or derived from mRNA (cDNA libraries)[217]. Furthermore, phage display libraries can be immune, naïve or synthetic[210], depending on the nature of the antigen of interest. While immune libraries utilise B cells from immunized animals, naïve libraries do not. Thus, the latter carry a broad pool of genes encoding the variable domains of antibodies, are not bias towards any antigen and are more successful for the selection of phage against a large repertoire of different antigens. Synthetic libraries are prepared through recombination of CDRs responsible for antigen binding[210]. Libraries promote the generation of high-affinity and high-specificity scFv[211].

### ii. Phage display biopanning

The method for generation of phage recombinants displaying antibodies at their surface was paired with affinity selection methodologies, referred to as biopanning

step (Figure 6.3). This enabled *in vitro* selection of scFv from large phage libraries, circumventing the need for expression systems[210]. For such, immobilized antigen-bearing peptide/protein is used to capture phage displaying different peptides that have affinity for the antigen. Unbound non-specific phages are washed off, while the fraction of bound phages is eluted. This artificial selection yields a subpopulation that is enriched in phages harbouring scFv that may be of interest (having increased "fitness" according to the selection criterion).

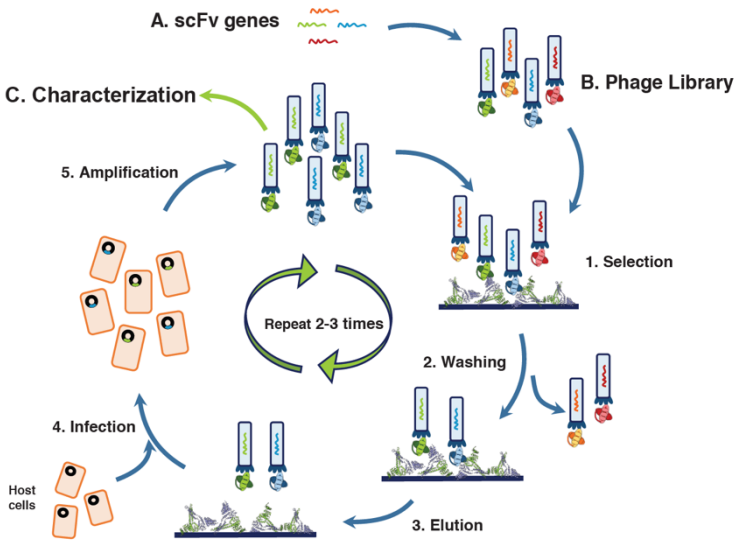


**Figure 6.3: Phage display biopanning**
Summary of the phage display rounds of selection to obtain several antibodies with high specificity for a particular protein. For such, there were multiple rounds of probing against the recombinant protein of interest interspaced with washing steps to remove non-specific phage clones.

(Dos Santos[96])

This is followed by an amplification step, where the eluted phages infect fresh bacterial host cells. The yielded amplified stock contains millions of copies of progeny derived from each potential phage of interest. This can be used as input for another round of affinity selection and the final eluate is typically achieved following 2-3 rounds. Given the mutability feature of phage, the phage-display peptides are subjected to subtle changes that culminate in an ever-fitter subset of the starting peptides. By periodically introducing mutations and a tight selection pressure on the phage population, the pool of epitopes displayed widens (surpassing that present in the initial phage-display library) and at the same time becomes bias towards the epitope of interest[217].

Ultimately, the aim is to generate phage that bind to the antigen of interest with high affinity from a large number of non-specific phage[210]. For such, biopanning incorporates two pivotal parameters: stringency and affinity. Some degree of stringency is necessary in order to discard the vast majority of nonspecific phages present in libraries, thus ensuring successful biopanning. However, stringency favours high fitness peptides at the cost of a decrease in yield. This parameter cannot be set too high at selection to make sure higher fitness phages are represented in subsequent rounds. This criterion is especially important in the first round of selection, when potential phage of interest have not been amplified. With subsequent rounds, yield can be compromised in favour of higher stringency[217]. Phage binding affinity is another common selection pressure applied to ensure functional scFv are later retrieved. This is possible because scFv displayed on phage surfaces retain active antigen-binding capability[210].

Phage recovered from the final round of biopanning are characterised individually[210,217]. Cloning techniques can be used to sequence the viral DNA and hence obtain the amino acid sequence of the phage-displayed peptide. Additionally, the DNA encoding the peptide can be cloned into expression systems for subsequent scFv purification and different expression formats[218].

### iii. Advantages and limitations

The use of phage display also bypasses the problems associated with hybridoma technology and immunization[210,217]. Furthermore, it is a highly scalable method. Rich and diverse antibody libraries with hundreds of unique antibodies per target can be generated using this technology, favouring the concept of genome-wide antibody generation[218].

ScFv are stable, easily manipulated and produced in a rapid and inexpensive manner. As a research tool, the small size of scFv is favourable when targeting epitopes that may be poorly accessible by other antibodies, such as cryptic epitopes, enzyme active sites and other protein domains[211]. Once generated, scFv can be delivered in multiple, non-mutually exclusive ways:

1. Using viruses, such as the adeno-associated virus,
2. As chimeric antibodies fused to proteins that aid delivery, e.g. the blood brain barrier receptor for transport into the brain[212],
3. As intrabodies, where scFv are designed to be expressed in-frame and intracellularly to modulate specific molecular interactions *in situ*, leading to changes in the activity of the target proteins[219].

However, there are some limitations in the use of scFV antibodies that have been challenged by some groups. Firstly, monovalent scFv (antibodies with a single antigen-binding domain), may have limited avidity and low dissociation rates, which can compromise its functions. The generation of multivalent scFv antibodies largely circumvented this problem[211,212]. Secondly, given the requirement for both high levels of scFv and adequate epitope binding (i.e. affinity) intracellularly for cellular outcomes to be elicited, can limit the use of scFv as nanobodies[220].

### iv. ScFv applications

ScFv antibodies have wide applications in both the fields of research and therapeutics. In fact, in 2013, scFv accounted for 35% of antibody fragments in clinical trials[212]. They are invaluable tools for the study of proteins and to modulate their activity and interactome (e.g. by targeting specific domains). A loss-of-function experiment used neutralizing scFv antibodies against Pax6 to decipher its functions during development[212].

As intrabodies, scFv have also been used to target disease proteins. For example, a scFv targeting an epitope on APP adjacent to its β-secretase cleavage site, prevented generation of the disease protein, Aβ. This supported the rational that targeting substrates rather than enzymes could modulate detrimental molecular mechanisms with greater specificity[221]. Another scFv nanobody against the NAC (aggregation-prone) region of α-syn[222] and effectively reduced aggregation and prevented toxicity[220]. Both studies showed that high steady-state expression levels and correct conformation epitope binding (i.e. stability and affinity in the cellular environment) were critical properties for intrabody efficiency, being more important than their *in vitro* affinity[220,222]. Importantly, given its success, anti-NAC can be regarded as deliverable

therapies to mimic gene deletions, which could disfavour disease progression and be useful in a disease-modelling context.

The use of scFv nanobodies has translated into animal models of disease, being useful as biomarkers and/or aggregation-modifiers[223–225]. For example, scFv antibodies engineered against Aβ resulted in a reduction in the number of amyloid plaques (by 25-50% compared to controls)[224], the levels of insoluble Aβ and hyperphosphorylated tau and improved cognitive function[225] in AD mouse models. The exact mechanisms of action are unknown, although hypotheses include:

1. Antibody-mediated disaggregation of pre-formed fibrils, preventing toxicity,
2. Antibody-induced immune responses, such as activation of microglia,
3. ScFv-mediated clearance of extracellular Aβ in an Fc-indepedent mechanism,
4. The “sink hypothesis”, where antibodies sequester soluble Aβ and thus prevent oligomerisation[224,225].

## 6.1.3 Hydrogen-deuterium exchange (HDX)

### a. HDX development and applications

HDX is a quantitative method for measuring the structural and biophysical properties of single protein or interacting complex[226]. Insulin was the first protein analysed by HDX in the mid-1950s and led to the understanding that amides engaged in hydrogen bonding for maintenance of secondary structures have slower HDX rates. In 1991, HDX was coupled with mass spectrometry (HDX-MS) and later paired with enzymatic digestion[227,228]. Previously, MS could only inform on primary protein structure, rather than protein conformation[227]. Therefore, the ‘gentle’ structure-dependent labelling approach of the HDX together with the detection sensitivity of MS resulted in a method with considerable analytical power[229].

Since then, HDX has contributed to our understanding of how biophysical properties relate to protein structure-function, interactions, dynamics and energetics[226–228]. Thus, HDX is commonly used in the study of protein conformation and conformational dynamics in the context of modifications, mutations, unfolding/refolding, protein-ligand or protein-protein interactions and protein aggregation[227,228]. This includes the assessment of antigen-antibody interactions (including the effect on protein folding,

stability and function) and identification of binding sites[227–229]. When a protein complex forms, the interface between the binding partners is protected from HDX, due to the steric exclusion of the deuterium-containing solvent (concept is explained below). To aid data interpretation, HDX experiments on the free antigen are performed in parallel. This reference experiment is then compared with the HDX behaviour of the antigen-antibody complex to identify regions that display different exchange kinetics (i.e. potential epitopes)[227]. Nevertheless, the use of HDX for epitope mapping needs to be undertaken with caution since binding can induce changes in protein dynamics and conformation in regions distant from the actual binding site/interface due to allosteric effects[227,228]. Furthermore, binding can enhance the thermodynamic stability of a protein, causing the overall protein complex to be more strongly protected from HDX[227,230]. Commonly, HDX-MS is combined with computational analysis and/or site-directed mutagenesis for validation of epitopes and to further our understanding of the mechanism of action and the structure-function relationship in question[227].

### b. HDX technique

HDX-MS allows for biophysical properties to be monitored in proteins in solution[227,230]. HDX takes advantage of the natural phenomena of hydrogen exchange[228] (hydrogen atoms in O-H, N-H and S-H groups are labile and exchange with surrounding water[230]). By exposing a protein to deuterium-containing environment, HDX occurs and deuterium replaces hydrogen, particularly at sites that are more exposed[230]. This can be detected by MS because each exchange event increases the mass of the protein (because deuterium has a greater mass than hydrogen)[227,229,230].

HDX occurs at protein amide, hydroxyl, or thiol hydrogens[229], thus takes place at side chains and the protein backbone. However, for multiple reasons, only the protein backbone is typically used for analysis to obtain information regarding protein conformation and dynamics[227]. Firstly, side-chains and N-terminal hydrogens undergo rapid back-exchange (i.e. loss of previously incorporated deuterium) during the quenching step[229]. Secondly, since the majority of residues (except prolines and the first amino acid of the chain) possess an amide group, HDX behaviour can be observed throughout virtually the entire protein. Thirdly, since the dynamics of HDX

of backbone amides correlate with protein structure, data can inform on regional conformational dynamics[230].

Isotope exchange of backbone amides (N-H to N-D) is influence by several factors and can range from seconds to hours[229]. Exchange is fastest in solvent-exposed amides (i.e. located at the surface of the protein), which are not or weakly involved in hydrogen bonding (e.g. for maintenance of secondary structure)[227,228,230]. In contrast, amides involved in hydrogen bonding or sequestered from the solvent (i.e. buried in the interior of the protein) take longer to exchange[227–229]. Additionally, the flanking side chains also affect the exchange[230]. All these factors influence the chemical exchange rate constant ($k_{ch}$) of each amide, which is dictated by the primary sequence in the absence of structure or sequestration[229,230]. Together, this data distinguishes regions of the protein that are more ordered (have increased intramolecular hydrogen bonds and shielded by larger side chains) and are protected from HDX, from unfolded or intrinsically disordered elements that lack stable hydrogen bonding, incorporating more deuterium[226,228,230]. Therefore, the level of deuteration tends to correlate with structural flexibility[47].

Eventually, even protected amides undergo HDX. This is driven by conformational fluctuations of the protein, where amides transition transiently to an "open" conformation, which is susceptible to isotope labelling[230]. A series of opening/closing events ($k_{op}$ and $k_{cl}$) may occur prior to isotope exchange[228,230], thus every amide group has a unique combination of criteria ($k_{ch}$, $k_{op}$, $k_{cl}$) dictating its rate of HDX[230]. The exchange mechanism is as follows[229,230]:

$$\mathrm{N-H_{closed}} \underset{k_{cl}}{\overset{k_{op}}{\rightleftharpoons}} \mathrm{N-H_{open}} \xrightarrow[\mathrm{D_2O}]{k_{ch}} \mathrm{N-D_{open}} \underset{k_{op}}{\overset{k_{cl}}{\rightleftharpoons}} \mathrm{N-D_{closed}}$$

Increasing opening/closing events occur as the protein unfolds to expose backbone amides within isolated regions (localised unfolding) or the entire protein (global unfolding)[228,230]. Such protein motions may result from localised or global structural events (e.g. induced by protein-protein interactions)[228–230]. This allows HDX-MS to be used for measuring mass shifts of individual protein segments, indicating where changes in behaviour occur[226,230]. Given enough time, addition of deuterium induces complete unfolding of the proteins due to protein motion and 'protein breathing' (the

alternative structures adopted naturally and transiently by proteins that differs from their native conformation)[228,230].

### c. Continuous and pulse HDX labelling techniques

There are two main approaches for HDX-mediated protein labelling: continuous and pulsed labelling[227] (Figure 6.4A&B). Continuous labelling consists of taking several aliquots of the protein sample and incubate in deuterated buffer for certain periods of time followed by quenching. This strategy reveals deuterium incorporation into the protein structure as a function of exposure time (i.e. the increase in protein mass over time)[227,228,230]. This informs on conformational dynamics because tightly folded regions tend to be less dynamic, spending less time in open conformations, hence taking longer to exchange compared to unfolded domains[227,230]. This approach is the most common and simple to perform[228]. Pulse labelling consists of inducing conformational changes (e.g. by the addition of a chemical denaturant or by changing pH or temperature) prior to a brief exposure to deuterated buffer (typically for ≤10s), referred to as the pulse time[227,229]. This method is useful in the identification of protein folding mechanisms and characterisation of short-lived folding intermediates, since the initially denatured protein will initiate protein refolding once transferred to the solvent environment[228,230].

### d. Mass spectrometry analysis of HDX experiments

Once the HDX experiment is completed, the protein sample is quenched to inhibit further HDX events. This is followed by MS-based detection, using either 'bottom-up' (Figure 6.4C) or 'top-down' (Figure 6.4D) approaches[228,230]. The former is more commonly used and consists of proteolytic cleavage (typically by pepsin) after quenching using acidic conditions, followed by peptide fragment separation by HPLC and mass analysis by MS[226,230]. The greatest advantage of using this approach is the increased spatial resolution, since the level of deuterium incorporation into different protein fragments is coupled with peptide mapping, providing information about local protein structure and motions[228].

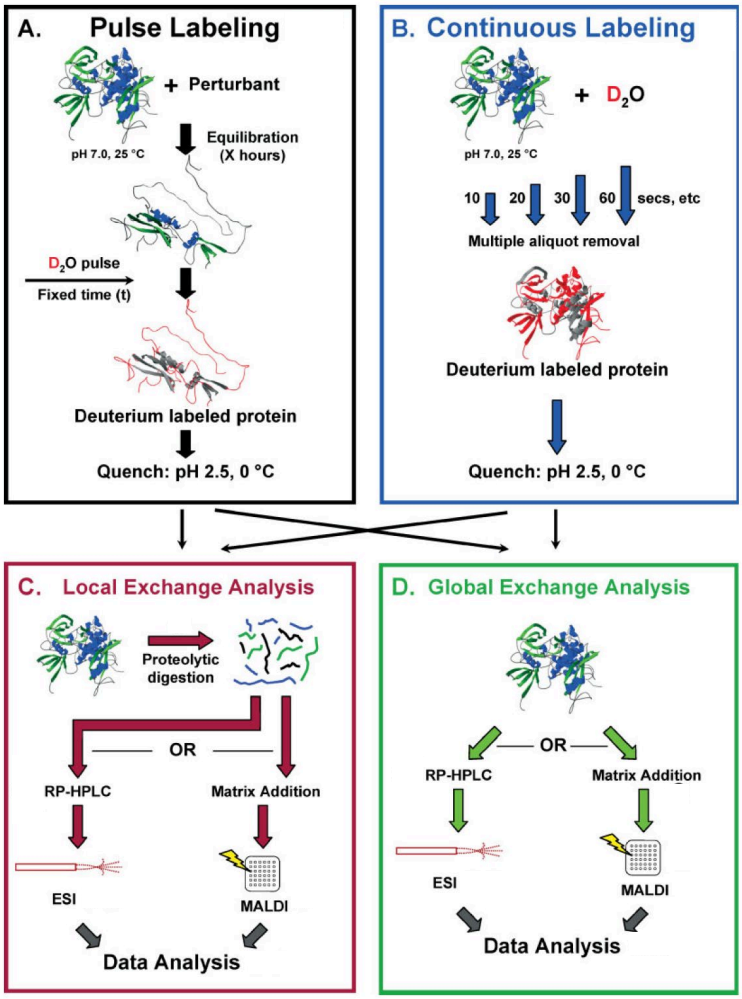


**Figure 6.4: HDX-MS**
**A)** Pulse labelling method: a protein is exposed to a perturbant that induces unfolding (regions *in grey*), becoming labelled with deuterium (*in red*).
**B)** Continuous labelling method: deuterium is gradually incorporated into a protein sample (*red*), which is quenched after subsequent labelling times.
**C)** Deuterated samples from either **A** or **B** are digested by pepsin or another acid protease. The resulting peptides are separated by HPLC and analysed by ESI-MS or by MALDI-MS (different ionization methods). This yields information about the local deuterium exchange across the peptide backbone. This is a "bottom-up" approach.
**D)** Samples from **A** and **B** can also be analysed using a "top-down" approach, which bypasses the proteolytic step, hence fragmentation of intact proteins only takes place in the gas phase of the MS. This method is useful for the evaluation of global changes in protein structure and stability, for thermodynamic measurements and analysis of noncovalent protein-ligand interactions.

(Adapted from Wales & Engen[228])

### e. Advantages and disadvantages of HDX

Compared to other analytical techniques, HDX is not limited by the crystallization properties and the size of the proteins of interest[227,229,230]. It only requires small amounts of sample (in the picomole range)[226–229] and confers unparalleled sensitivity[228–230], detecting subtle structural changes[227] and higher order protein structures[228–230]. This robust and powerful technique has been used to study complex protein systems[226,227].

However, the potential of HDX is limited by some challenges. Firstly, the method requires the addition of deuterium into the sample, which tends to result in dilution of the sample and may render it incompatible with sample quantity requirements for MS[228]. Secondly, back-exchange may occur during sample preparation due to the introduction of protiated solvents[228]. Finally, standard HDX can also be limited by spatial resolution, informing on region-specific HDX behaviour rather than at the amino-acid level. The later can be achieved by obtaining HDX data of several overlapping and sequential fragment ions derived from deuterated peptic peptides in order to cover the experimental protein with confidence[226–228]. Advances in HDX-MS are paving for direct protein structural information at single amino acid resolution[226,228].

## 6.1.4 Mapping ubiquitination sites

Throughout the years there has been considerable efforts to study the Ub-modified proteome, often referred to as the ubiquitome[141]. Pinpointing ubiquitination sites on substrates is not only essential for the understanding of ubiquitination, but it the ultimate proof that a putative substrate is indeed ubiquitinated[139]. Furthermore, as more ubiquitination substrates are identified, the focus has shifted into investigating the dynamics of this phenomenon, addressing questions such as when, where, how and why proteins are ubiquitinated *in vivo*[140]. Understanding characteristics of specific ubiquitination sites (including Ub chain length and linkages and whether the modification occurs constitutively or is driven by a signal) informs on the diverse cellular fates of the PTM and how it is regulated[143]. Ultimately the aim is to understand how protein function is regulated in both physiological and pathological contexts[139–141], given that ubiquitination pathways often fail in neurodegenerative diseases[140].

Advances in enrichment strategies (e.g. affinity-based) to isolate ubiquitinated substrates coupled with MS/MS have been successful in the identification of ubiquitination substrates and the mapping of ubiquitination sites[141,143]. These include the use of epitope-tagged Ub, tandem Ub-binding domains, Ub-specific antibodies, and ubiquitination remnant antibodies (represented in Figure 6.5)[139].

The most promising enrichment strategy is the use of an antibody against the ubiquitination remnant, glycine-glycine (diGly) (Figure 6.5D). The diGly signature on ubiquitinated peptides is yielded during proteolytic digestion of the sample – a critical step in sample preparation for bottom-up MS. The C-terminus of Ub (consisting of Arg-Gly-Gly followed by the substrate) is cleaved after the Arg residue, leaving a diGly remnant on the previously ubiquitinated peptide (usually attached to a lysine residue)[143]. Prior to the analysis of the diGly-containing peptides by MS, affinity purification using an anti-diGly antibody can be performed to enrich for these species[139,141,143]. The antibody is believed to be specific, recognising diGly sequences present as an adduct on the ε-amine of lysine and not internal diGly sequences. It has been reported that the antibody results in selective enrichment of diGly peptides by >50%[143]. Using this assay, Xu and colleagues[143] have identified 236 ubiquitinated proteins and 374 ubiquitination sites.

In the presence or absence of the enrichment strategy using the anti-diGly antitbody, ubiquitination (via the diGly remnant) is detected by MS by a mass shift of 114.043 Da, where the mass of the lysine residue without and with the diGly signature is 128.09 Da and 242.14 Da, respectively[139,143]. The protein sequence database is manipulated to yield the library of peptides following tryptic cleavage and with the addition of the mass of the diGly remnant on particular amino acids, typically lysine residues. Such theoretical protein database is compared to the MS data of the sample[139].

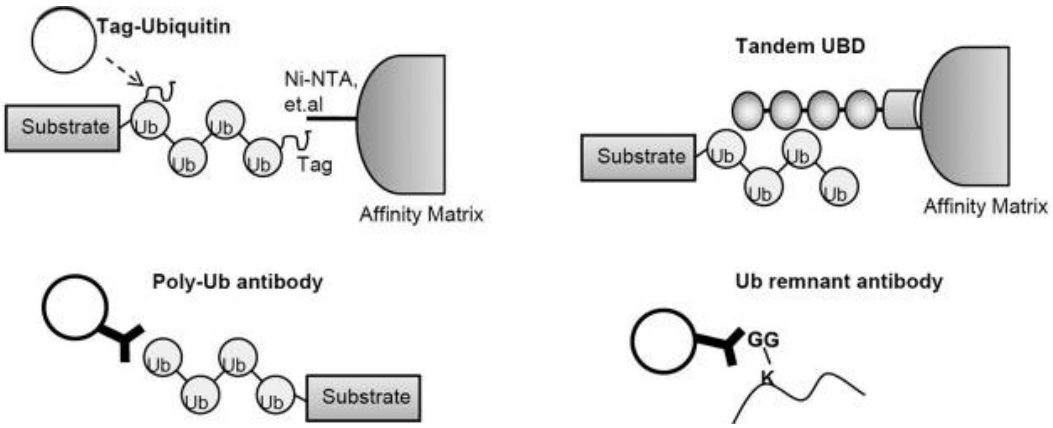


**Figure 6.5: Strategies to isolate ubiquitinated species**
**A)** Epitope-tagged Ub. The use of tagged-Ub for the purification of ubiquitinated proteins.
**B)** Ubiquitin-chain specific antibodies. Ub chain-linkages can inform of the fate of different ubiquitination events. However, it is still unclear whether these antibodies can efficiently purify linkage-specific substrates to be analysed by MS.
**C)** Tandem Ub-binding domains (UBD). Given the inherent low affinity of endogenous UBDs for Ub, which limits the purification of substrates, tandem UBDs have been engineered with antibody-like affinity. However, purification cannot be done under denaturing conditions, thus contaminant proteins are likely and might disfavour the identification low abundant substrates. Moreover, UBDs are bias towards the capture of polyubiquitinated versus monoubiquitinated substrates.
**D)** Ubiquitination remnant antibody (anti-diGly antibody). When ubiquitinated proteins are digested by trypsin, a signature motif is achieved. Peptides harbouring diGly motifs can be enriched using an anti-diGly antibody.
All these enrichment techniques can be performed prior to analysed by MS.
(Adapted from Shi *et al.*[139])

## 6.2 Results

### 6.2.1 Bacterial expression and purification of scFv

ScFv antibodies against CHIP (11F and 7A) previously engineered using phage display (Figure 6.6 & Figure 6.7) were expressed in competent bacterial cells using IPTG to induce expression. To ensure that induction was successful, a fraction of the bacterial lysate prior and subsequent to IPTG addition was analysed by SDS-PAGE (Figure 6.8A). IPTG resulted in protein overexpression and a strong band around 30 kD became visible, which could possibly represent the scFv of interest. The scFv antibodies were then purified as described in Section 2.4.6b (for elute 5, specifically) and with shorter incubation times with the elution buffer (Figure 6.8B-G). The latter optimisation step favour protein activity (as it prevents denaturation of the scFv by the acidic conditions) but at the cost of a lower yield.

Another optimisation step added was the buffer exchange step of scFv from Tris-Glycine to Hepes-based buffer. For such, a fraction of the elutes were pooled and buffer exchanged. Unfortunately, this fraction was more diluted (Figure 6.8F&G, lanes labelled “Hepes”). In attempt to quantify the concentration of scFv antibodies in each fraction, these were analysed by SDS-PAGE along with known concentrations of BSA (Figure 6.8D-G). Quantification of the bands (using Image Studio Lite) was used for a standard concentration curve and approximate concentrations of elutes were calculated (Table 6.1).

**Table 6.1: Approximate concentration of the eluted single chain antibodies**

| **7A scFv** | **Concentration** (μg/ml) | **11F scFv** | **Concentration** (μg/ml) |
|---|---|---|---|
| **E1** | 19.53 | **E1** | 22.75 |
| **E2** | 545.53 | **E2** | 467.42 |
| **E3** | 483.74 | **E3** | 294.33 |
| **E4** | 46.57 | **E4** | 32.91 |
| **Buffer exchanged** | 53.63 | **Buffer exchanged** | 32.91 |

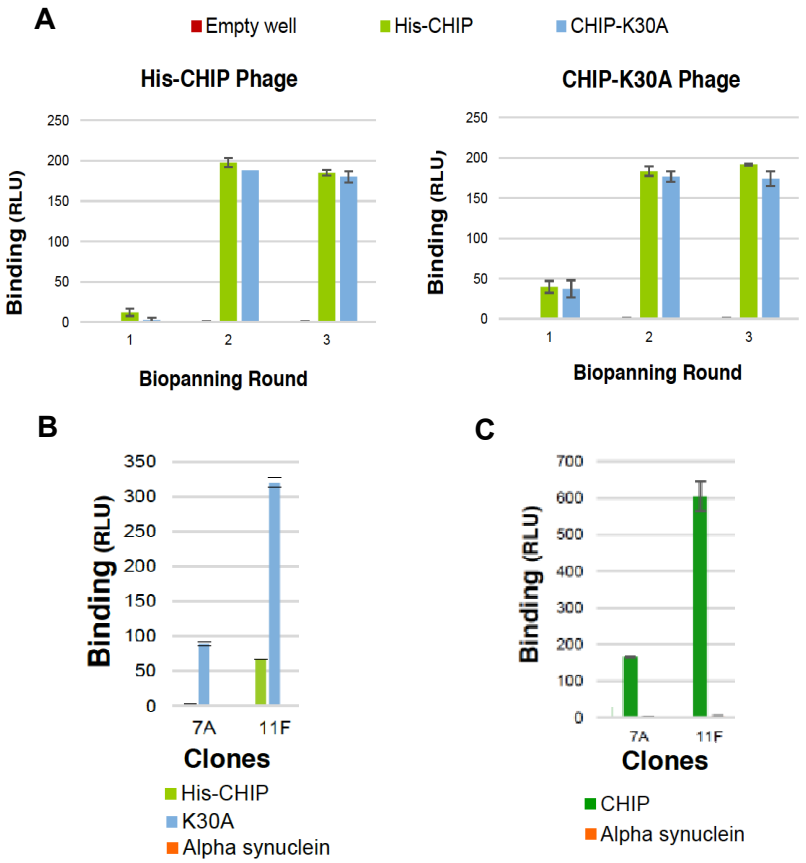


**Figure 6.6: Production and validation of scFv antibodies 7A and 11F**
Binding activities were quantified by polyclonal phage ELISA using an anti-M13 phage polyclonal antibody (**A**) or anti-Protein A polyclonal antibody (**B** and **C**), both conjugated with horseradish peroxidase (HRP). Binding is expressed in relative light units (RLU), mean ± SD of duplicates.
**A)** Enrichment of CHIP and CHIP-K30A binding phages by rounds of biopanning: the binding of CHIP and CHIP-K30A phages against CHIP, CHIP-K30A and uncoated wells.
**B)** Binding activity of 7A and 11F against 0.1 mg/ml wt CHIP, CHIP-K30A and, the negative control, α-Syn.
**C)** Binding activity of 7A and 11F against 0.1 mg/ml untagged-wt CHIP and, the negative control, α-Syn.

(Dos Santos[96])

```
                FR1                          CD1          FR2                CD2
7A   MAEVQLVESGGDLVKPGGSLRLSCVASGFTFS SYYMY WVRQAPGKGLQWVA RISSDGTDTFYADAVKG

11F  MAEVQLVESGGDLVKPGGSLRLSCVASGFTFS SYYMY WVRQAPGKGLQWVA RISSDGTDTFYADAVKG

                FR3                          CD3          FR4          LINKER
7A   RFTISRDNAKNTLYLQMNSLRAEDTAVYYCA TAI-------GSD WGQGTLVTVSS EGKSSGASGESKVDD

11F  RFTISRDNAKNTLYLQMNSLRAEDTAVYYCA SRVV------GAD WGQGTLVTVSS EGKSSGASGESKVDD

                FR1                  CD1          FR2                CD2
7A   ASYELTQPTSVSGSLGQRVTISC SGRTNDIGIVGAS WYQQFPGKAPKLLVY SNGNRPS

11F  AQSMLTQPASVSGSLGQKVTISC TGGNSNIGGNGVG WYQQLPGMGPRTVIY GDHYRPS

                FR3                          CD3          FR4
7A   GVPDRFSGSYSGDSATLTITGLQAEDEADYYC QPFYTTFDSHV FGGGTHLTVL GAAAEQKLISEED

11F  GVPDRFSGSKSGSSATLTISGLQAEDEAEYYC SSWDGSLGRHV FGGGTHLTVL GAAAEQKLISEED
```

**Figure 6.7: Alignment of the predicted amino acid sequences of the 7A and 11F scFv clones**
Sequences follow the following directionality: heavy chain ($V_H$) – linker (L) – light chain ($V_L$). Framework regions (FR, in black), complementary determining regions (CDR, in red or green) and linker (Linker, in blue). Within the CDR regions, different sequences are represented with different colours and changes.

(Adapted from Dos Santos[96])

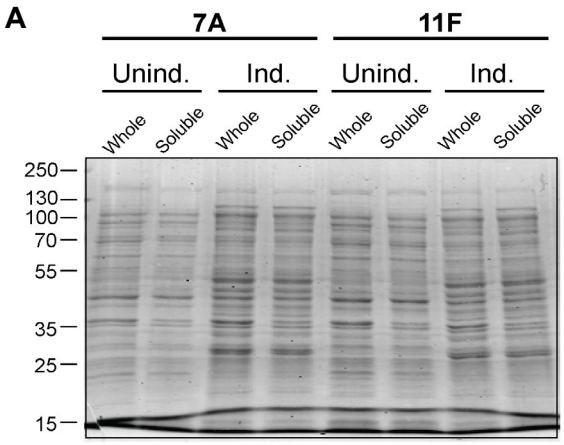


**Figure 6.8: Expression and purification of 7A and 11F scFv antibodies**
**A)** Bacterial lysates with protein expression uninduced (Unind.) and induced (Ind.) by IPTG were analysed. A fraction of each sample was sonicated and centrifuged and the supernatant (i.e. soluble proteins) was loaded on the gel.
Gel used for SDS-PAGE was 12% acrylamide and was stained with Coomassie blue.

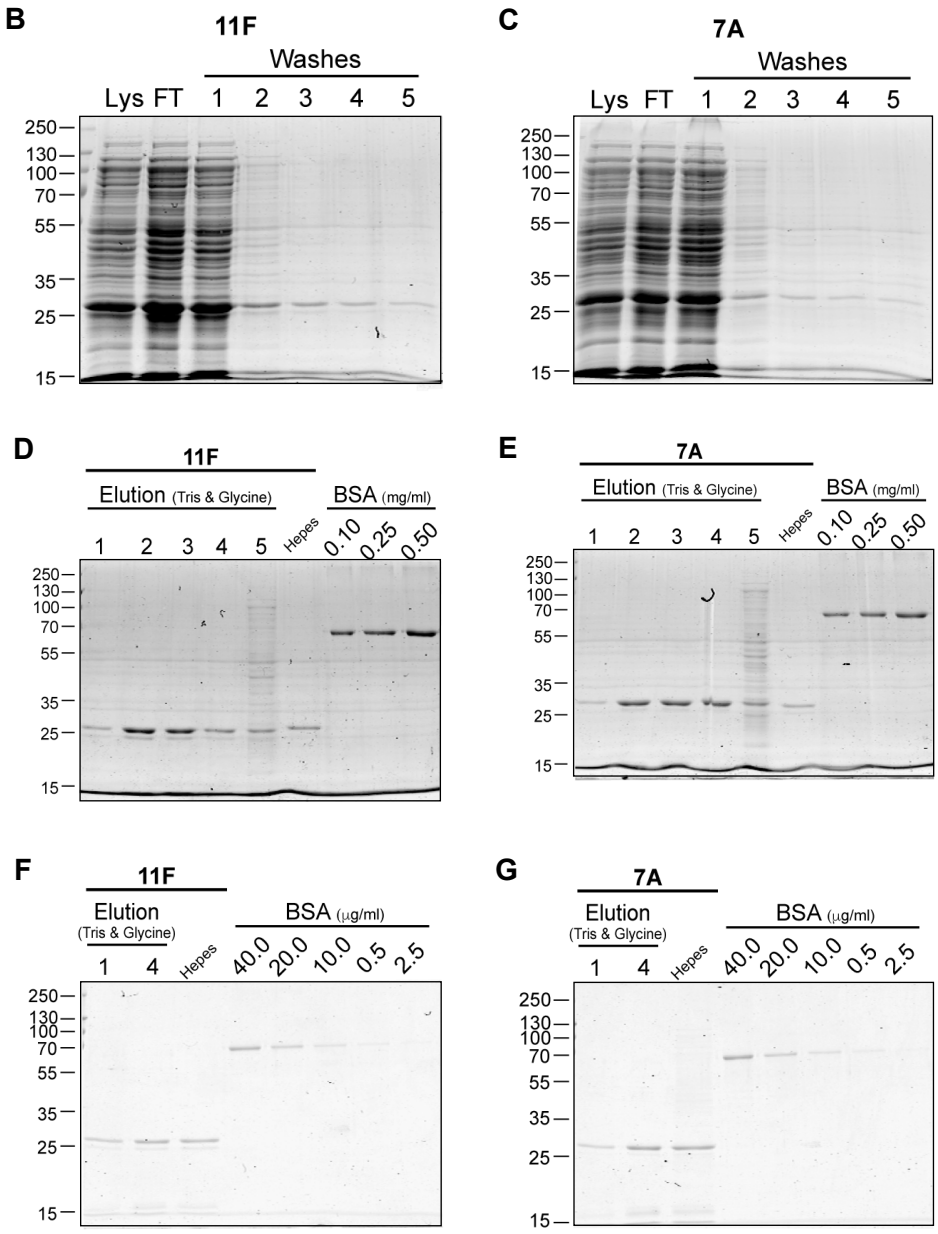


**Figure 6.8** *(continued)*
**B&C)** Samples from all the purification steps until elution of 11F (**B**) and 7A (**C**) scFv antibodies were analysed by SDS-PAGE. The lysate (Lys), flow through (FT) and washes show that the Protein A beads had greater affinity for the scFv (band at about 30 kDa) than the other proteins present in the lysate, although a small fraction was lost during the washes.
**D-G)** 11F (**D&F**) and 7A (**E&G**) antibody elutes (including the fraction that was buffer exchanged) were resolved on gels alongside with known BSA concentrations to assess the purity and concentration of the elutes (constant volumes were loaded, 5 μl). For the 11F scFv, elutes 2 and 3 had the highest antibody concentration, while for the 7A antibody, fractions 2-4 were more concentrated. Note that elute 5, which was kept in acidic conditions for longer during the elution step, had more proteins eluted from the column, decreasing its purity, and later displayed increased protein precipitation (**D&F**, lanes 5).
All gels used for SDS-PAGE were 12% acrylamide and were stained with Coomassie blue.

## 6.2.2 Effect of scFv on CHIP-dependent *in vitro* ubiquitination assays using different substrates

### a. Optimisation of *in vitro* ubiquitination assay conditions

Previous observations in our group have suggested that the ubiquitination of α-Syn is challenging to detect compared to other substrates, due to the weak binding of ubiquitinated α-Syn species to the nitrocellulose membrane. Therefore, the conditions of the *in vitro* ubiquitination assay were optimised using this substrate. Optimal denaturing conditions were investigated by changing denaturing temperature and incubation time (Figure 6.9A) and the reducing reagents used (Figure 6.9B). No ubiquitinated α-Syn (higher molecular weight above the monomeric form at 14 kDa) species were seen when samples were heated at 85ºC compared to 95ºC, where ubiquitinated species were detected after 3-10 min. Furthermore, 1:2 DTT to loading buffer ratio with samples incubated at 95 ºC for 3-4 min were clearly the best denaturing conditions to detect ubiquitinated α-Syn by WB, compared to others tested. Finally, the effect of using different crosslinking conditions on the membrane (subsequent to blotting and prior to the blocking step) was also evaluated (Figure 6.9C). Compared to using 0.4% PFA, which was previously used in our group, 4% PFA seemed to result in more ubiquitinated species detected.

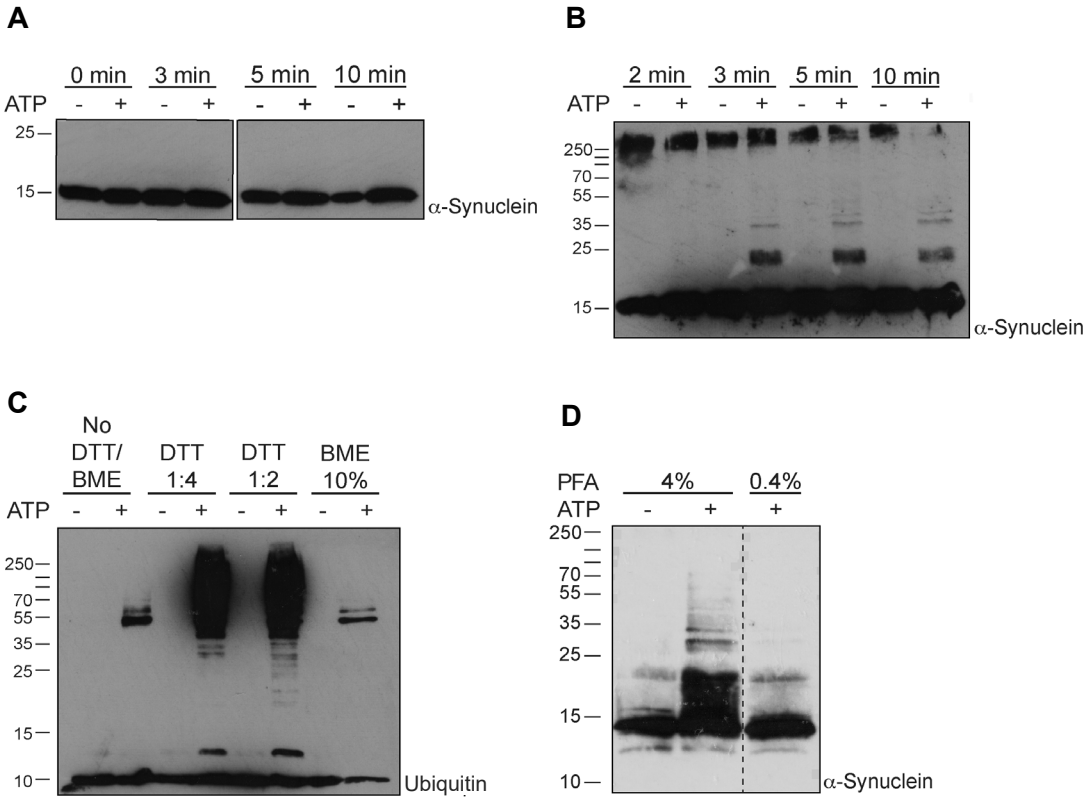


**Figure 6.9: Optimisation of *in vitro* ubiquitination assays with CHIP**

*In vitro* ubiquitination assays using CHIP as the E3 ligase and α-Syn as the substrate were analysed by SDS-PAGE/WB using 12% gels. Immunoblots were probed with anti- α-Syn mAb (1:1000) or anti-Ubiquitin mAb (P4D1, 1:1000), as indicated. Sample preparation and the immunoblotting technique was optimised as follows:

**A&B)** Samples were diluted in DTT and sample loading buffer (in a 1:4 ratio) and were denatured at 85 ºC (**A**) or 95 ºC (**B**) for the time indicated.

**C)** Samples were diluted in sample loading buffer alone or supplemented with DTT (in a 1:4 or 1:2 dilution) or with 10% β-mercaptoethanol (BME). Once mixed, samples were heated to 95ºC for 3-4 min.

**D)** Samples were denatured in optimal conditions (diluted in sample loading buffer with DTT in a 2:1 dilution and heated to 95ºC for 3-4 min) and analysed by SDS-PAGE/WB. The same sample from the *in vitro* ubiquitination assay in the presence of ATP was loaded twice on the same gel. The immunoblot was cut (dashed line) and incubated with 4% or 0.4% PFA for 30 min immediately after the transfer. Immunoblots in **A-C** were treated with 4% PFA.

### b. ScFv antibodies do not affect the auto-ubiquitination of CHIP

It is known that CHIP activity is regulated by auto-ubiquitination[54]. Thus, the effect of scFv on the auto-ubiquitination of CHIP was assessed by immunoblot (Figure 6.10). No apparent differences were observed and strong bands representing auto-ubiquitination were readily detected. This suggests that any effects of scFv antibodies on the ubiquitination of CHIP substrates are not likely due to differences in its intrinsic E3 ligase activity.

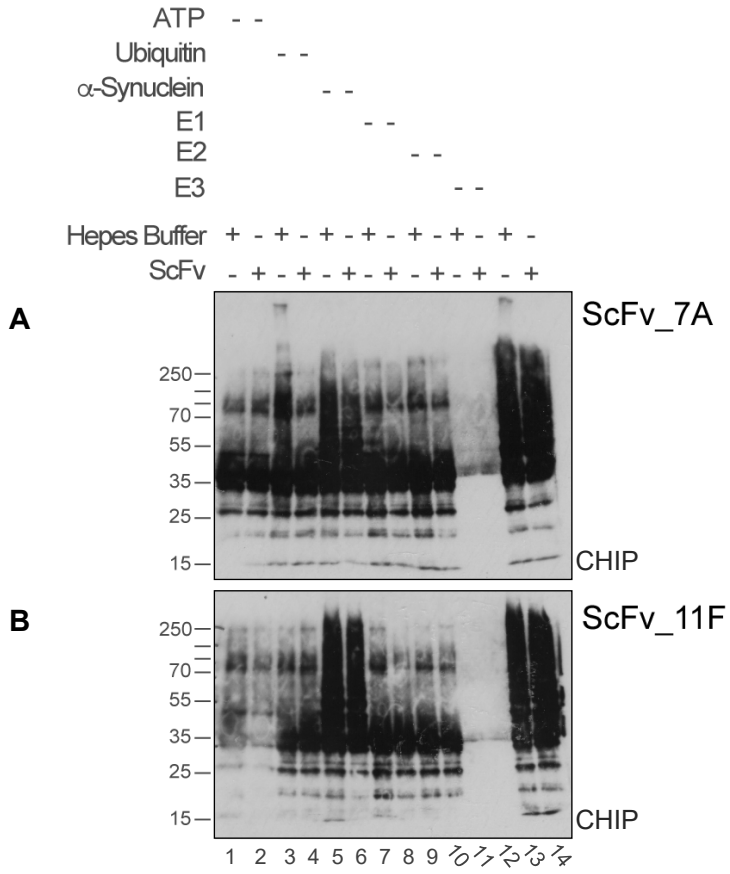


**Figure 6.10: Controls of *in vitro* ubiquitination reactions with and without scFv antibodies**
*In vitro* ubiquitination reactions missing single components or in the presence of all reagents were performed. These were analysed by 12% SDS-PAGE/WB and immunoblots were probed with anti-CHIP mAb (1:10000). Full auto-ubiquitination was only detected when all components of the ubiquitination cascade were added (ATP, Ub, E1, E2 and CHIP). The effect of the presence of 7A (**A**) and 11F (**B**) scFv antibodies (10 nM per reaction) on the auto-ubiquitination of CHIP was also assessed.

### c. Effect of scFv on CHIP-dependent ubiquitination of α-synuclein

#### i. *In vitro* ubiquitination of α-synuclein

Prior to assessing the effect of the scFv antibodies on the *in vitro* ubiquitination of α-Syn, experiments to determine whether such modification is CHIP-dependent were conducted, given the reported phenomenon of E2-mediated ubiquitination[231]. For this, the effect of each component in the *in vitro* assay on the ubiquitination of α-Syn was assessed (Figure 6.11). The same samples were loaded onto different SDS-PAGE gels to obtain immunoblots probed for α-Syn, CHIP and Ub. Importantly, there is a dominant α-Syn-positive band (possibly a doublet) at around 22 kDa, which is also Ub-positive (lane 7 in Figure 6.11 and lane 2 in Figure 6.12A&B). In fact, in the immunoblot probed with anti-Ub (Figure 6.11D), there are more bands lower than the MW of unmodified CHIP in lane 7 compared to lane 3, which are likely to represent ubiquitinated forms of α-Syn. Together, these blots show that α-Syn can be ubiquitinated, but only when all the components of the ubiquitination reaction are present. Moreover, E2-dependent and E3-independent ubiquitination was not seen in the conditions tested, thus ubiquitinated α-Syn is CHIP-dependent. Both mono- and poly-ubiquitination were observed (the latter is more clearly observed in lane 2 of the immunoblot in Figure 6.12A). Ub-positive bands were seen when the substrate, α-Syn, was not present due to the auto-ubiquitination of CHIP and, potentially, free polyubiquitin chains.

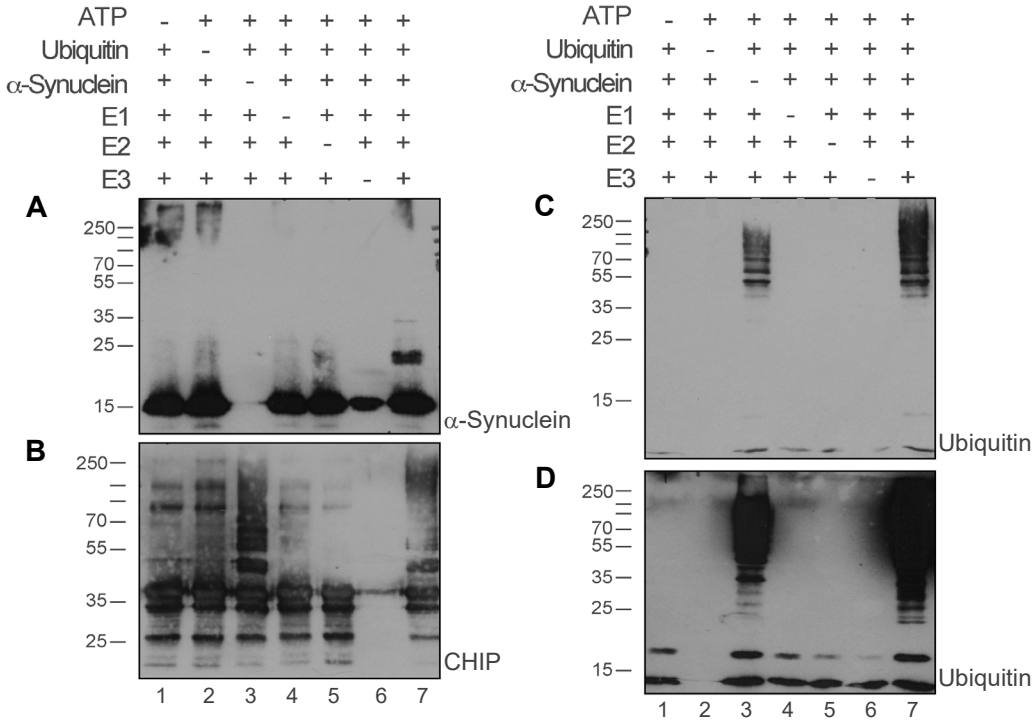


**Figure 6.11: Controls of in vitro ubiquitination assay**
*In vitro* ubiquitination assays using CHIP and α-Syn. The same samples were loaded in a 15% gel and three 12% gels for SDS-PAGE/WB. All samples were denatured in 1:2 DTT to loading buffer ratio and at 95 ºC for 3-4 min. Membranes were fixed with 4% PFA. Immunoblots were probed with either:
**A)** Anti-α-Syn mAb (1:1000),
**B)** Anti-CHIP mAb (1:10000) (specifically the 12% immunoblot),
**C)** Anti-Ub mAb FK2 that recognises mono- and poly-Ub but not free Ub (1:1000), or
**D)** Anti-Ub mAb P4D1 that recognises all forms of Ub (1:1000).

### ii. Effect of scFv on the *in vitro* ubiquitination of α-synuclein

There is a range of scFv concentrations where 11F potently inhibits ubiquitination of α-Syn while 7A has no/little inhibitory effect (Figure 6.12A). This effect was evident from the lack of higher MW bands (greater than 14 kDa) in the immunoblot probed for α-Syn in *in vitro* ubiquitination reactions conducted in the presence of 11F scFv. The half maximal inhibitory concentration (IC50) of the 11F antibody is estimated to be 12.41 nM to reduce by 50% the detection of monoubiquitinated α-Syn by immunoblot (calculated from Figure 6.12C). The higher MW ubiquitinated α-Syn species are below the detection limit of the immunoblot when only 0.28 ng/μl of 11F scFv is added. As observed in Figure 6.12C, the 7A scFv is also capable of partially inhibiting ubiquitinated α-Syn when present at a higher dose (lanes 5&6). The estimated IC50 of monoubiquitinated α-Syn (~22kDa) is 116.18 nM (calculated from Figure 6.12C). Of note, at lower concentrations (15.07 nM or less), 7A scFv promoted ubiquitination of α-Syn (lanes 3&4 of Figure 6.12C). This positive effect on ubiquitination is gradually abolished with increasing dose and ubiquitination of α-Syn becomes inhibited by the scFv, supporting a biphasic response (evident when comparing lanes 3 and 6 in Figure 6.12C). It seems that higher MW ubiquitinated α-Syn species are more readily inhibited by administration of the scFv antibodies (this is more clearly observed with the less potent 7A scFv antibody). More extensive dose-response experiments would be required for more accurate IC50 values and would be informative of the kinetics of the scFv antibodies. The higher MW Ub-positive bands observed (Figure 6.12B) are likely to represent auto-ubiquitination of CHIP, which does not seem to be affected by the presence of the scFv antibodies, as previously observed.

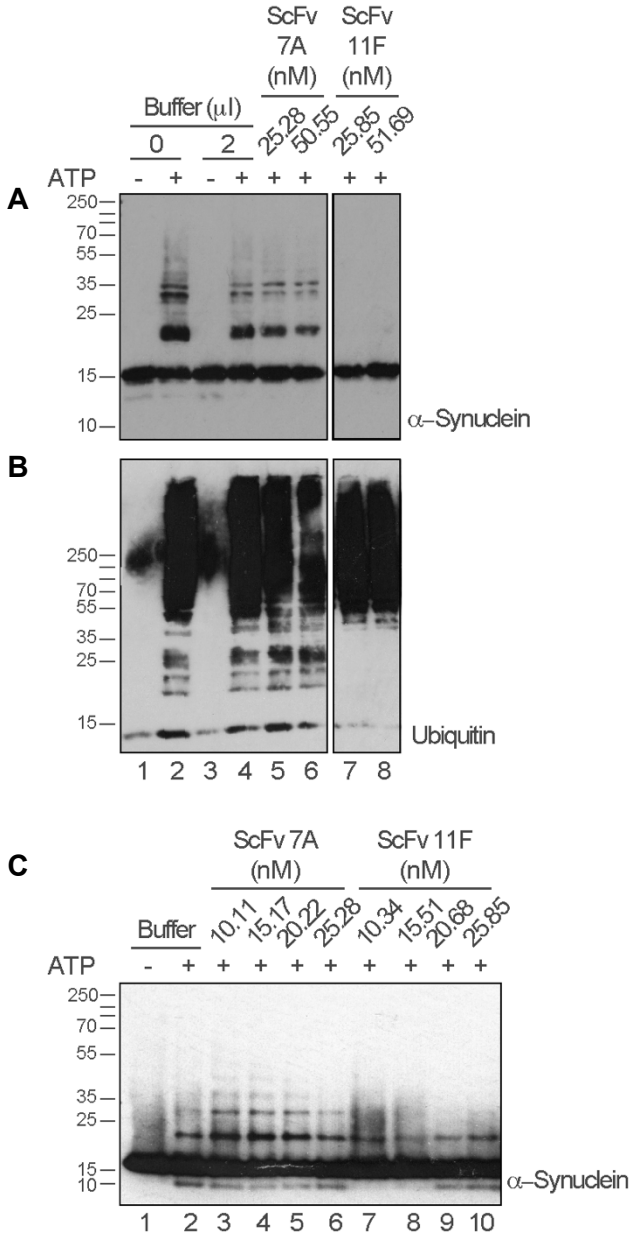


**Figure 6.12: Effect of scFv antibodies on the *in vitro* ubiquitination of α-Syn**
*In vitro* ubiquitination assays using CHIP and α-Syn were performed in the presence of HEPES-based buffer alone, 7A or 11F scFv antibodies, as indicated. A dilution series of each scFv was tested and the final volume of scFv/buffer added to the reaction remained constant (**A&B**: 2 µl, **C**: 1 µl). Samples were denatured in loading dye (with DTT in a 2:1 dilution) and at 95 ºC for 3-4 min. Samples were loaded onto both 15% (**A&C**) and 12% (**B**) SDS-PAGE and immunoblots were fixed with 4% PFA prior to blocking. Immunoblots were probed with either anti-α-Syn mAb (1:1000) (**A&C**) or the anti-Ub mAb PD41 (1:1000) (**B**). The effect of the scFv antibodies on the ubiquitination of α-Syn is representative of at least 4 independent experiments.

### d. Effect of scFv on CHIP-dependent ubiquitination of ANXA2

As seen in Chapter 5, CHIP ubiquitinates ANXA2 both *in vitro* and *in situ*. Given the ladder of ANXA2- and Ub-positive bands detected by WB, it seems that ANXA2 is monoubiquitinated and multi-monoubiquitinated or polyubiquitinated by CHIP. The effect of scFv antibodies on its in vitro ubiquitination was also investigated (Figure 6.13). Interestingly, scFv 11F enhanced the ubiquitination of ANXA2.

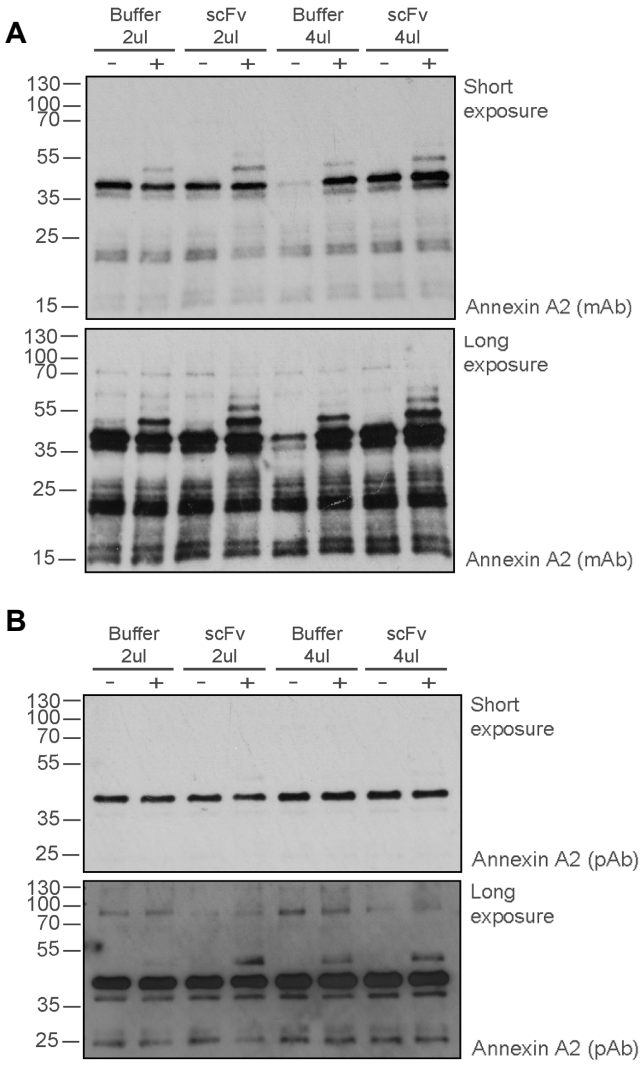


**Figure 6.13: Effect of scFv antibody on the *in vitro* ubiquitination of ANXA2**
*In vitro* ubiquitination assay using untagged human recombinant ANXA2 and CHIP and, when indicated, 11F scFv antibody (referred to as "scFv") or its HEPES-based buffer (referred to as "buffer"). Two concentrations of scFv were tested (95.49 nM and 161.28 nM) and the volumes of scFv solution added to these reactions (2 μl and 4 μl, respectively) were matched by control reactions where only the buffer was added to the *In vitro* ubiquitination assay. Reactions were analysed by 12% SDS-PAGE/WB using two different anti-ANXA2 antibodies: mAb (1:1000, **A**) and pAb (1:500, **B**). The effect of the scFv antibody on the ubiquitination of ANXA2 is representative of at least 3 independent experiments.

### 6.2.3 Mapping of ubiquitination sites on α-Synuclein, Annexin A2 and CHIP

Samples from *in vitro* ubiquitination assays were sent for MS analysis for validation and mapping of the ubiquitination sites on both substrates and the E3 ligase CHIP. This aids our understanding of the nature of the ubiquitination modifications and possible implications to the structure/function of the substrate. Mapping was achieved by detecting diGly remnant peptides following digestion with trypsin (no affinity-purification step was included) using MS. The ubiquitination of α-Syn was mapped to lysine 60, which lies at the interface between the N-terminal domain and the NAC region[34] (Figure 6.14A). This was done in collaboration with Dr Jakub Faktor and Dr Bořivoj Vojtesek‡. ANXA2, on the other hand, becomes ubiquitinated by CHIP on two lysine residues, 115 and 157 (Figure 6.14B), according to our preliminary data produced in collaboration with Dr Jimi Wills & Dr Alex von Kriegsheim¶. These sites lie on domain II of the core structure of ANXA2[232].

CHIP auto-ubiquitination on lysine residues (Figure 6.15) was readily detected in the presence, but not the absence, of ATP. Interestingly, multiple residues are ubiquitinated throughout the protein when no substrates were present in the *in vitro* ubiquitination assay mixture. However, in the presence of α-Syn, the majority of these residues were no longer ubiquitination sites and only K221 and K234 remained. When this is compared to the auto-ubiquitination signature of CHIP detected in the presence of ANXA2, it is clear that the ubiquitination signature is more complex, having 6 lysine residues involved in such modification. Nevertheless, it is important to note that the ubiquitination mapping obtained with ANXA2 as the substrate is only preliminary and was achieved independently from the other mapping experiments (with α-Syn and without substrates), which were conducted in parallel. The auto-ubiquitination sites mapped on CHIP in the presence of ANXA2 was a collaborative work with Dr Jimi Wills & Dr Alex von Kriegsheim¶, while the other experiments were performed with Dr

‡ Regional Centre for Applied Molecular Oncology, Masaryk Memorial Cancer Institute, Brno, Czech Republic

¶ Institute for Genetics and Molecular Medicine, University of Edinburgh, Edinburgh, UK

¶ Institute for Genetics and Molecular Medicine, University of Edinburgh, Edinburgh, UK

Jakub Faktor and Dr Bořivoj Vojtesek‡. Of note, although different MS services were used, some ubiquitination sites were detected in common.

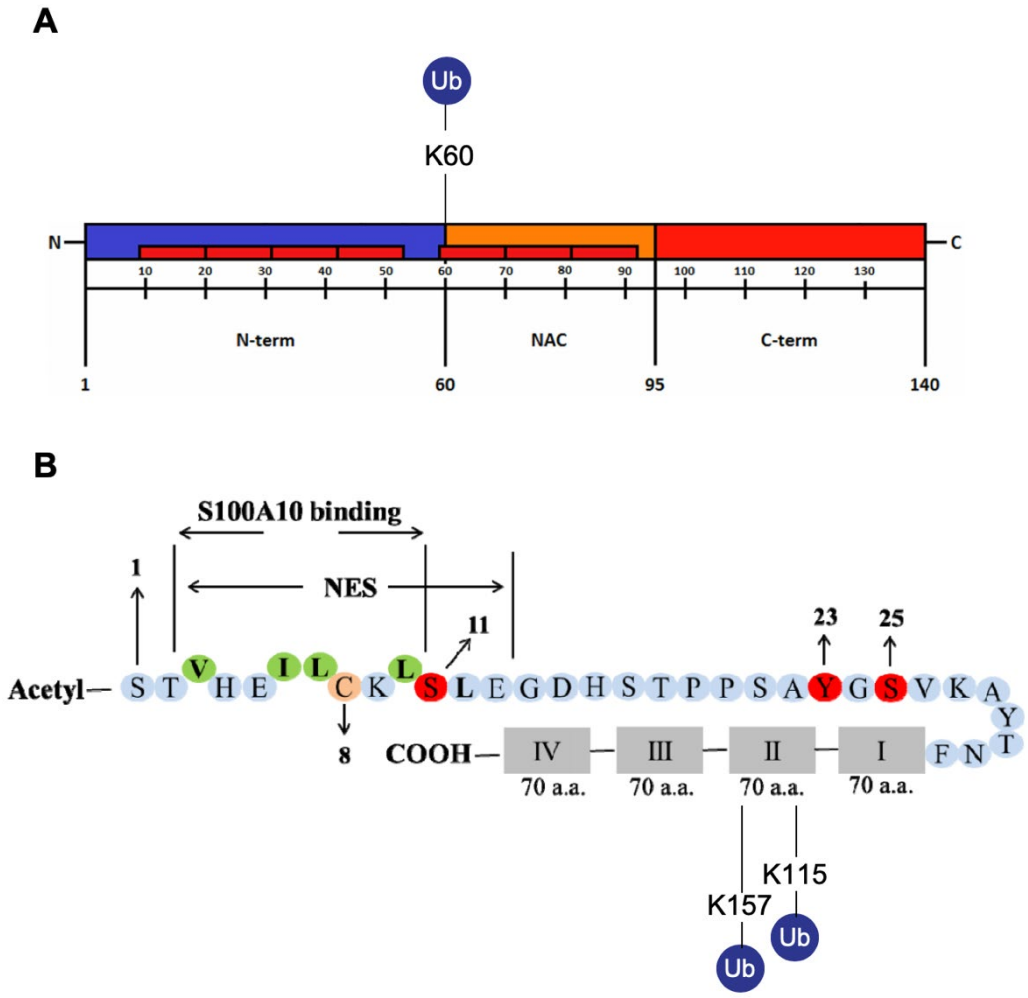


**Figure 6.14: Mapping of CHIP-dependent ubiquitination sites on α-synuclein and ANXA2**
*In vitro* ubiquitination reactions were digested with trypsin, yielding diGly signature motifs on ubiquitinated species. These were detected by MS/MS.
**A)** The mapped K60 ubiquitination site was added to the primary structure of α-Syn presented by Gallegos *et al.*[34].
**B)** Preliminary data suggesting K115 and K157 sites on ANXA2 are ubiquitinated by CHIP. These sites were illustrated on the schematic of the primary structure of ANXA2 from Bharadwaj *et al.*[232].

‡ Regional Centre for Applied Molecular Oncology, Masaryk Memorial Cancer Institute, Brno, Czech Republic

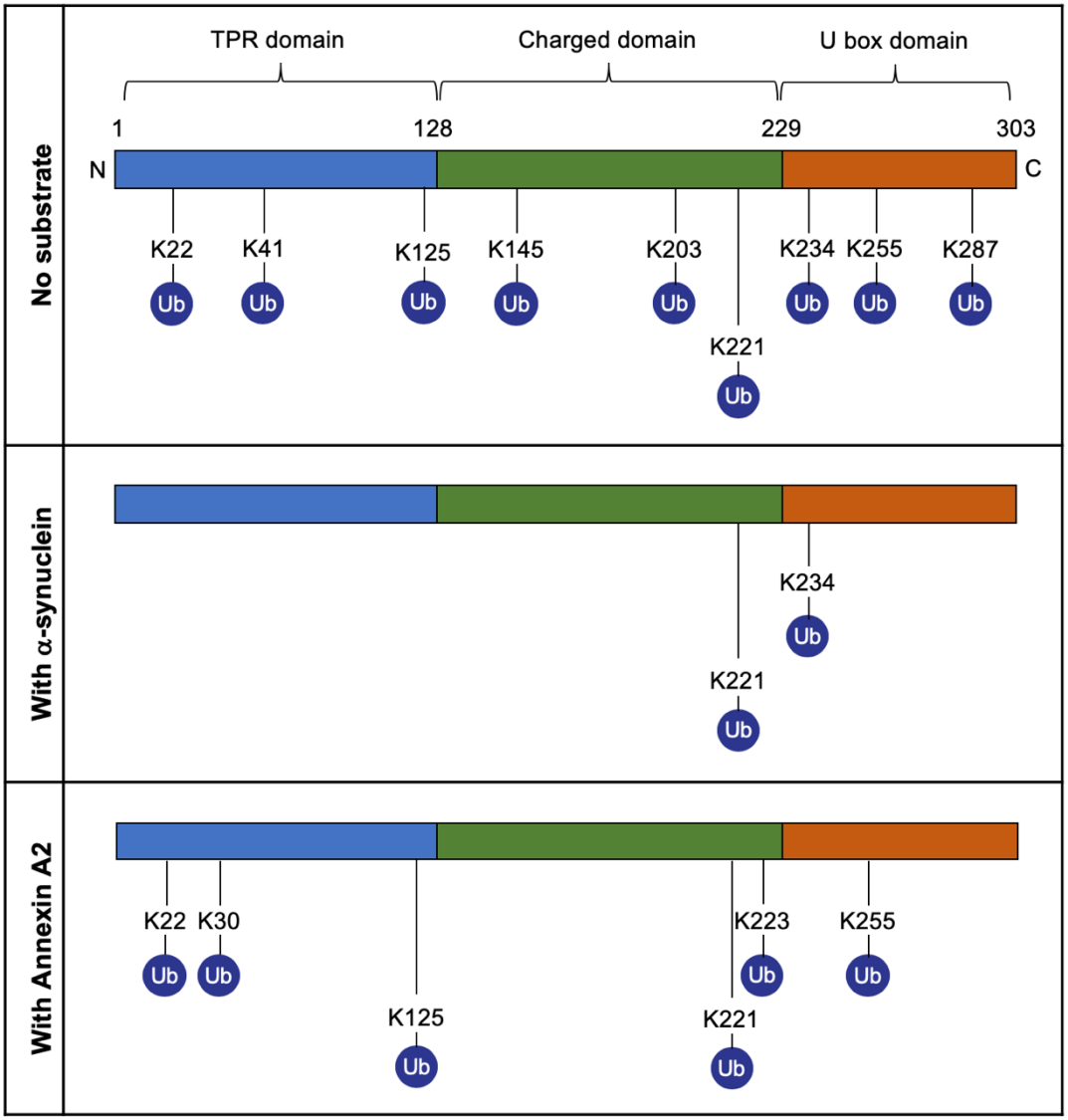


**Figure 6.15: Mapping of auto-ubiquitination sites on CHIP alone and in the presence of different substrates**

Schematic representation of CHIP domains with the auto-ubiquitination sites at lysine residues detected by MS/MS based on the presence of the diGly motif. Results were obtained from in vitro ubiquitination assays in the presence of ATP and with or without substrates (α-Syn or ANXA2).

### 6.2.4 Modulating CHIP with the scFv antibody

The structural flexibility of CHIP has been intimately linked to its function[47]. Thus, we sought to conduct biophysical analysis of the structure of CHIP when alone and in the presence of the purified 11F scFv antibody. HDX-MS analyses the solvent accessibility for residues within CHIP as a measure of dynamic conformational changes. Twenty unique peptides were identified (83.5% coverage of the protein) and characterised across a time course. The degree of deuteration at the amino acid level after 300s incubation was mapped onto the crystal structure of the murine CHIP (2C2L)[39,40], as there is over 97% identity between mouse and human CHIP[41].

HDX-MS of CHIP alone showed that the N-terminal tail and distal segments of the U-box displayed much greater incorporation of deuterium compared to the rest of the protein (Figure 6.16A&B). Increased exchange is indicative of a less rigid structure with more flexibility. We[47] (Figure 6.16C) and others[209] (Figure 6.16D) have previously analysed the structure of CHIP by HDX-MS. Although Graf and colleagues[209] have also observed most deuteration occurring at the N-terminal tail of CHIP, both studies agree that most exchange occurred at the flexible TPR domains, which is not so pronounced in our data.

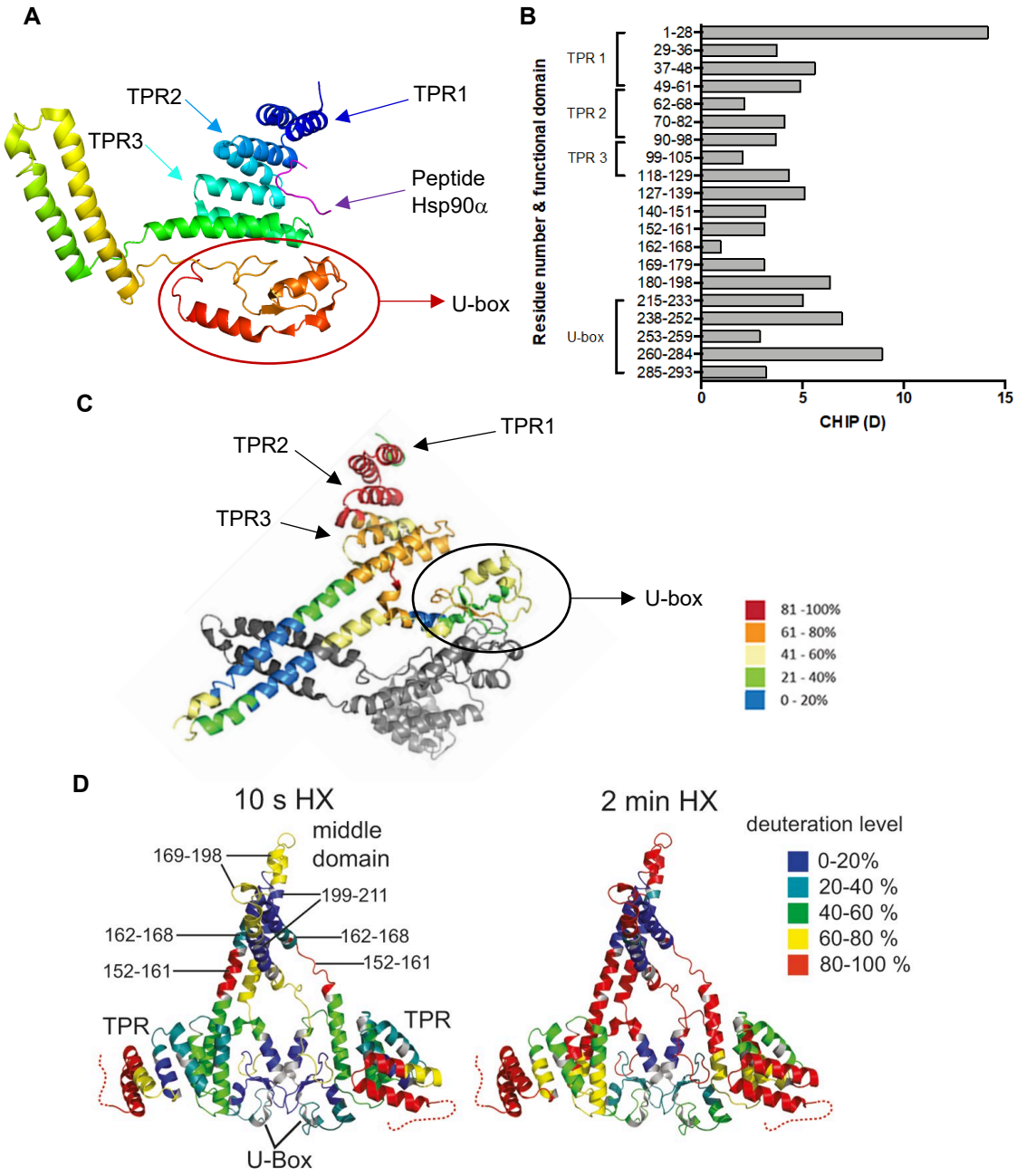


**Figure 6.16: HDX of unliganded CHIP**

**A)** Schematic representation of the functional domains of CHIP. TPR1 (26-59 aa), TPR2 (60-93 aa) TPR3 (95-127 aa), coiled-coil region (128-228 aa) and U-box (229-300 aa) (according to Nikolay *et al.*[40] and Zhang *et al.*[39] 2005).

**B)** HDX-MS data of unliganded human recombinant untagged CHIP after 300s incubation in deuterated buffer mapped onto the crystal structure of murine CHIP (PDB 2C2L). The deuteration level across the peptic peptides is represented as exchanged deuterons, D.

**C)** Published HDX-MS data of the percentage of deuteration of the analysed CHIP peptides after 60s incubation in deuterated buffer that was mapped onto the crystal structure of murine CHIP (PDB 2C2L).

**D)** Published HDX-MS data of the percentage of deuteration of the analysed CHIP peptide after 10s or 2min incubation in deuterated buffer that was mapped onto the crystal structure of murine CHIP (PDB 2C2L). The dashed line represents the 24 N-terminal residues missing in the crystal structure.

(**C**: Modified from Narayan *et al.*[47], 2015; **D**: Graf *et al.*[209])

By comparing the level of deuterium exchange on the structure of CHIP when alone and in the presence of scFv, we can understand the dynamic conformational changes induced by the antibody (Figure 6.17 & Figure 6.18). The scFv protects the U-box from deuterium exchange, indicative of its binding site on CHIP. Moreover, possibly due to allosteric effects, scFv binding to CHIP induced slight changes in the TPR region. The TPR 1 domain, for example, became more exposed and liable to deuterium incorporation. Therefore, beyond showing that scFv can bind to CHIP, the dynamic conformational changes observed can help to explain how scFv-binding modulates the E3 ligase activity of CHIP differentially, in a substrate-dependent manner. These HDX-MS experiments were performed in collaboration with Dr Lenka Hernychova and Dr Bořivoj Vojtesek‡. The binding of the scFv antibody to endogenous CHIP was also confirmed by immunoprecipitation (Figure 6.19).

To capitalise on the effect of scFv on the structure and function of CHIP observed *in vitro*, I have engineered nanobodies for cell delivery and the manipulation of the activity of endogenous CHIP (refer to Appendix II). Plasmids encoding tagged isoforms of the 11F scFv antibody were made for mammalian expression (Figure S.12 & Figure S.14) using conventional cloning (Figure S.13). SH-SY5Y cells were transfected and the expression of the intrabodies was confirmed (Figure S.15).

Although the effect of these intrabodies on CHIP homeostasis and the cellular proteome is left to be investigated, the potential applications of these intrabodies are extensive. For example, the intrabody can be used in the context of chemical genetics[233] as a tool to enhance our ability to manipulate the activity of CHIP and the pathways in which it is implicated. Recently, Shi and colleagues[234] have elucidated the importance of manipulating CHIP activity rather than studying its function from a null background. Modulation of the E3 ligase activity of CHIP specifically may be of interest, since mice expressing the SCAR16-related CHIP mutant T246M (lacking E3 ligase functions only) were phenotypically different from the CHIP KO mice[234].

‡ Regional Centre for Applied Molecular Oncology, Masaryk Memorial Cancer Institute, Brno, Czech Republic

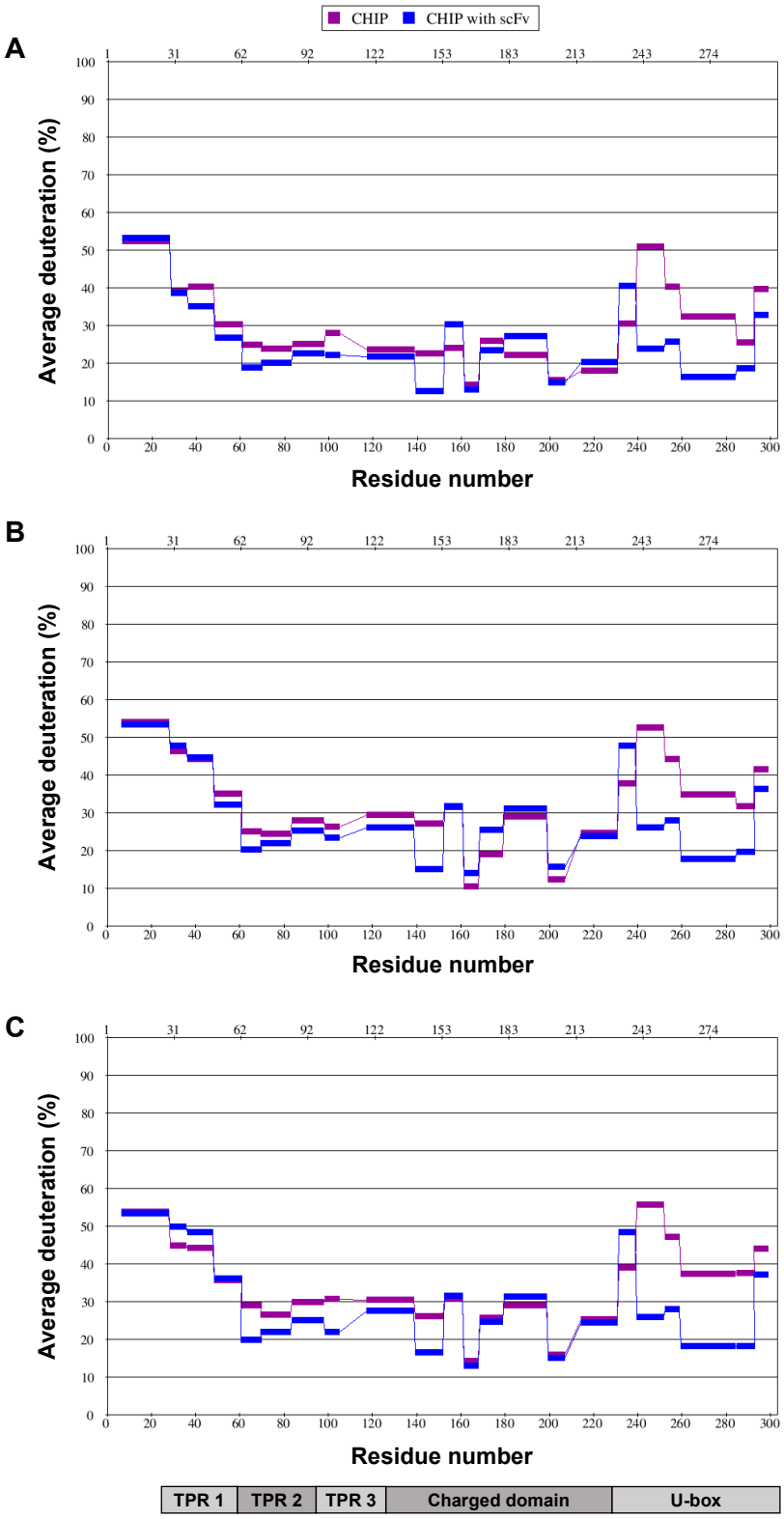


**Figure 6.17: HDX-MS of CHIP in the absence and presence of 11F scFv antibody**
Graphs showing the average deuteration (%) of peptic peptides as a function of primary amino acid sequence of scFv-bound and free CHIP after 30s (**A**), 300s (**B**) and 900s (**C**) incubation deuterated buffer. The functional domains of CHIP are indicated at the bottom.

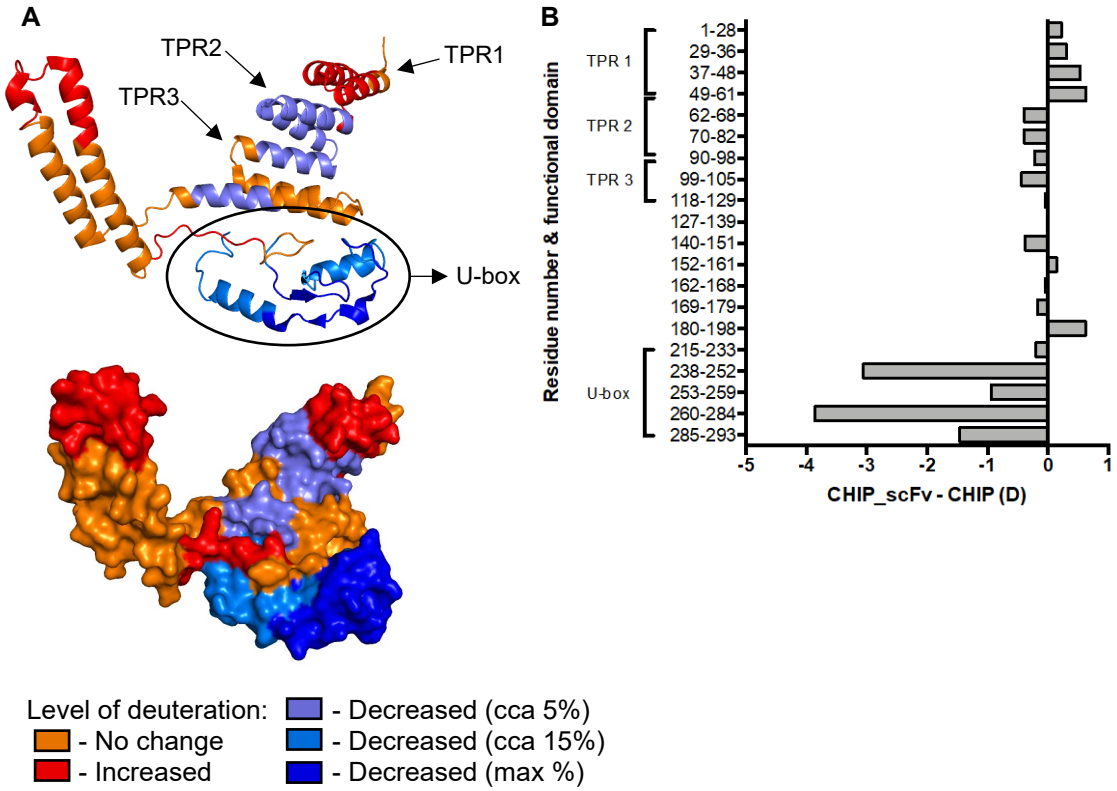


**Figure 6.18: HDX differences between CHIP alone and in the presence of scFv**
Difference in the level of deuteration between the human recombinant untagged CHIP in the presence and absence of the 11F scFv antibody after 300s incubation in deuterated buffer. This is represented schematically (mapped onto the crystal structure of murine CHIP (PDB 2C2L); **A**) and graphically (the deuteration level across the peptic peptides is represented as exchanged deuterons, D; **B**).

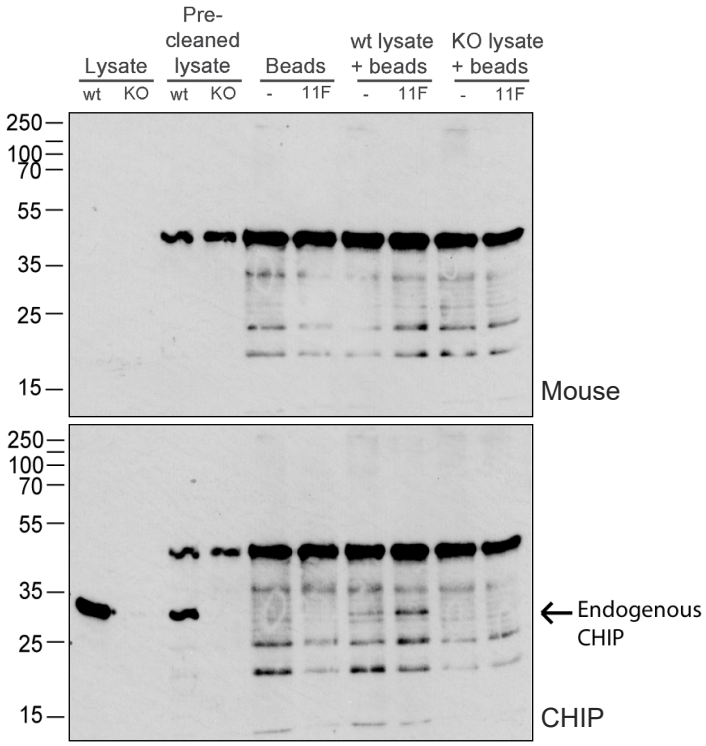


**Figure 6.19: 11F scFv antibody immunoprecipitates with endogenous CHIP**
The 11F scFv antibody was conjugated to Protein A beads and incubated with cell lysate from WT and CHIP KO SH-SY5Y cells. As negative control, lysate was added to unconjugated beads. For optimal results, cell lysates were subjected to pre-clearing with unconjugated protein A beads prior to incubation with 11F-conjugated beads. Cell lysates and the IP fractions were analysed by SDS-PAGE/WB. Secondary antibody (anti-mouse pAb) controls were performed prior to probing each membrane with anti-CHIP mAb.

## 6.3 Discussion

### 6.3.1 Identification of ubiquitination sites

#### a. The challenge

Studying the ubiquitome has proven to be very challenging. Despite advances in methodologies, large-scale analysis of ubiquitination sites have been largely unsuccessful[139] and the number of ubiquitination events identified is small when compared to that of other PTMs, such as acetylation and phosphorylation[141]. In fact, only around 255 mammalian proteins reported to be ubiquitinated according to experimental evidence[143]. The field is especially scarce in the quantitative aspects and pathway-mapping of ubiquitination events, including linkage quantification and linking substrates to individual Ub pathway enzymes (e.g. E3 ligase)[139,141]. Matching substrates to specific ubiquitination enzymes is difficult given the vast array of machinery (around 600 ligases are encoded by the eukaryotic genome)[139,141].

The low relative abundance of ubiquitinated species and the low signal derived from the ubiquitination moiety in a particular substrate, considering that only a few lysine residues are typically modified in an ubiquitinated protein[143], makes the detection of endogenous substrates challenging. Therefore, for the identification of substrates and mapping of ubiquitination sites, studies often use overexpression of either Ub or substrate[141], or include an enrichment step to allow identification by MS methods[139]. Finally, studying the dynamics of ubiquitinated proteins is also challenging, since it is hard to decipher the fate of ubiquitinated proteins, and how individual ubiquitination sites on a particular protein are independently regulated and influence the overall homeostasis of the protein[139–141].

#### b. Method used to map ubiquitination sites

All affinity-based purification techniques are limited by the presence of contaminant proteins in purification assays, which arise from non-specific binders to the solid matrix of the affinity reagent, precipitated proteins, and specific binders to Ub and Ub chains[139]. An increase in background noise can mask the detection of proteins of interest by MS-based techniques. Alternatively, the diGly motif can be detected by MS without the need for an enrichment step. The mapping of the ubiquitination sites

of α-Syn and ANXA2 in this project was achieved without the enrichment strategy. Here, the high sensitivity of DIA proteomics (SWATH-MS) was capable of identifying the ubiquitinated species.

## 6.3.2 CHIP-dependent ubiquitination

From our unbiased proteome-wide MS screen in CHIP WT and KO cortical neurons, ANXA2 was identified as a possible protein target of CHIP. Subsequent experiments identified ANXA2 as a candidate substrate of this E3 ligase. To confirm ANXA2 as a ubiquitination substrate and better understand the biochemical characteristics of this PTM, its ubiquitination sites were mapped *in vitro*. For comparative purposes, another E3 ligase substrate of CHIP, the disease protein, α-Syn, was also analysed, as it is structurally distinct from ANXA2 (α-Syn is intrinsically disordered, while ANXA2 is folded). Future work would assess whether these findings translate to a cellular model, although mapping of endogenous proteins has proven to be very challenging.

### a. CHIP-dependent ubiquitination of substrates

*In vitro* ubiquitination assays in the presence of CHIP and α-Syn or ANXA2 were analysed both by WB and MS. Using MS we have revealed that i*n vitro* ubiquitination of α-Syn is detected at a single residue, K60 (Figure 6.14A). It is likely that this site is involved in the mono- and poly-ubiquitination of α-Syn, which is evident from the ladder of α-Syn- and Ub-positive bands detected by immunoblot (Figure 6.11). However, it is unclear whether this is the only site involved in CHIP-dependent ubiquitination of α-Syn, or whether other diGly-containing remnant peptides exist but were below the detection limit of the mass spectrometer or have poor ionization potential[140]. The Ball group have previously reported both CHIP-dependent mono- and poly-ubiquitination of another intrinsically disordered protein, IRF-1, also in the presence of the E2 enzyme, UbcH5α[77].

ANXA2, in contrast, is ubiquitinated at K115 and K157 (Figure 6.14B) and has two clear bands above the MW of unmodified ANXA2 that are readily detected (Figure 5.17). These could represent monoubiquitinated (at either lysine residues), which

seems to be the especially prominent band on the immunoblot, and multi-monoubiquitinated (with both lysine residues modified) ANXA2. However, we cannot exclude the possibility of polyubiquitinated ANXA2 without further experiments.

Although it is generally accepted that ubiquitination specificity arises from the pair of E2-E3 employed[9,231] and the docking of E3 on the substrate[9,47,65,80], some groups have tried to decipher sequences of preference on substrates for ubiquitination. It has been reported that ubiquitination has a slight tendency to occur at regions enriched in small hydrophobic residues, including Ala, Leu, Ile, Gly, Pro and Val. In fact, K*XL was suggested as a potential motif for ubiquitination, as it is found 1.8-fold more often in ubiquitinated compared to unmodified lysines[139]. Some small hydrophobic residues were indeed seen close to the ubiquitination sites on ANXA2 (highlighted in red) and K157, specifically, lied within a K*XL motif (underlined):

111 ASELKASMK 119

153 TDLEKDIIS 161.

However, these trends were not seen in the region harbouring the ubiquitinated K60 on α-Syn, having small hydrophobic residues more distant from K60:

56 AEKTKEQVT 64.

Additionally, lysine residues that undergo ubiquitination tend to be more exposed (on the surface of the protein), hence more liable to modifications (by 6.5% compared to unmodified lysines)[139]. The ubiquitination sites identified on ANXA2 lie close to the beginning and end of the ANX core domain II. The domain is made up of 5 α-helices and these lysines are within the 1st and 4th helices[34,235–237] (Figure 6.20A). Within its globular structure, these lysine residues seem to be exposed at its surface, rather than buried in highly hydrophobic regions (Figure 6.20B). Furthermore, when analysing this highly conserved core region also present in ANXA1 Figure 6.20C[235], it seems that the ubiquitination sites lie close to the convex side of the protein in its calcium-bound state, which is important for its attachment to membranes. It would therefore be interesting to consider whether ubiquitination affects its lipid-binding activity and related functions.

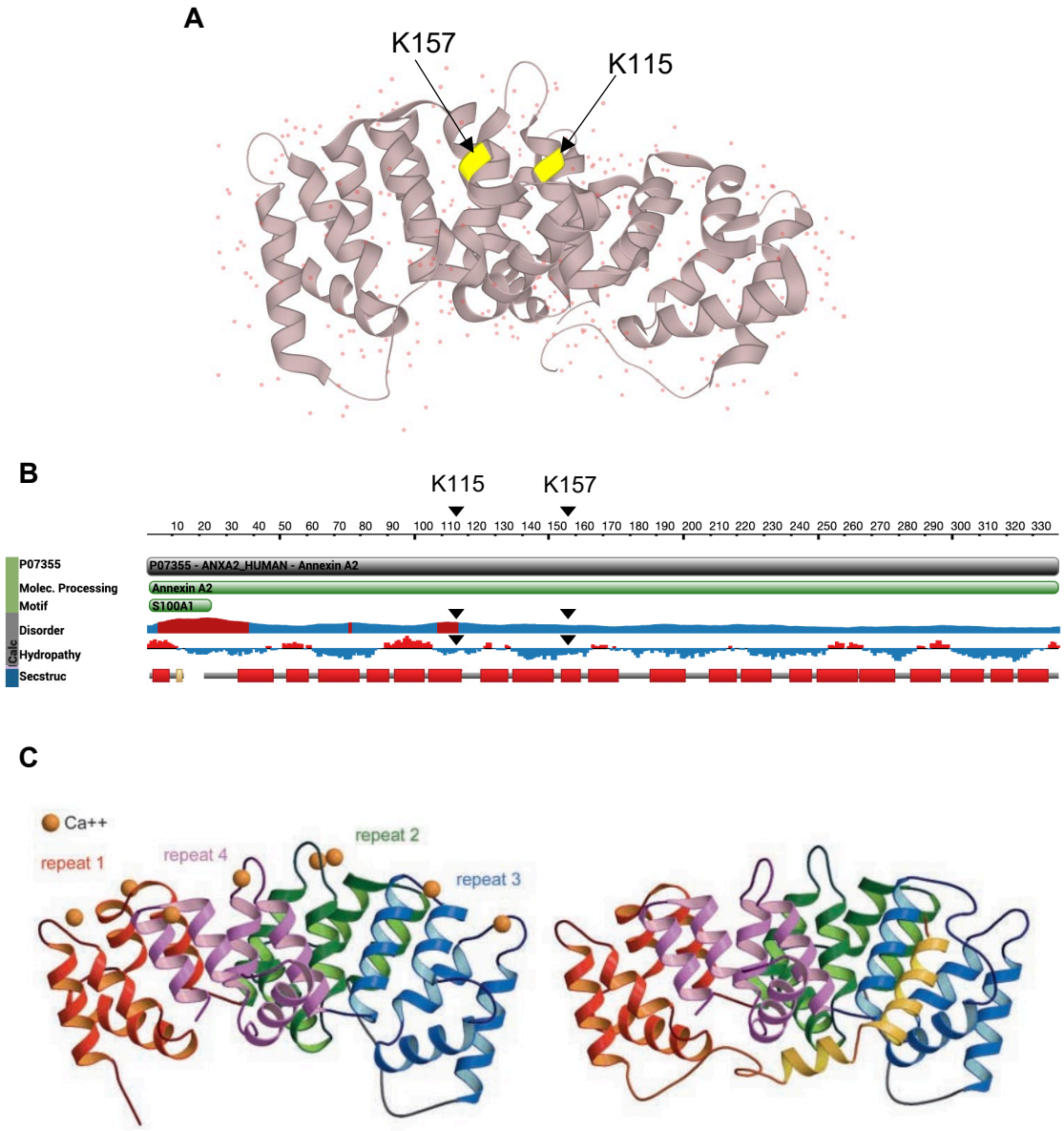


**Figure 6.20: Structure of Annexin A2**
**A)** Mapped CHIP-dependent ubiquitination sites on ANXA2 were indicated in the published crystal structure.
**B)** The extent of disorder (*red:* potentially disordered region, *blue*: probably ordered region) and hydropathy (*red*: hydrophobic, *blue*: hydrophilic) predicted from the amino acid sequence of ANXA2. The two ubiquitination sites mapped are indicated.
**C)** Globular structure of ANXA1 in the presence (*left*) and absence (*right*) of calcium. Annexins share high homology within their conserved 4 core domains, each with 5 helices. In the calcium-bound conformation, Annexins can attach to membranes through its convex (upper) side.
(**A**: Adapted from Uniprot[236], **B**: Adapted from Protein Data Bank[237], **C**: Rescher & Gerke[235])

α-Syn is considered to be an intrinsically disordered protein when in solution, lacking significant secondary structure (having 2% α-helical and nearly 70% random coil content when characterised by circular dichroism)[238]. Within such structure, K60 is likely to be exposed (Figure 6.21A)[239]. It is now largely accepted that lipid-binding induces a structural transition to α-helical (from 2 to 71%) and the interaction is believed to be mediated by 5-helices that lie within the N-terminal region[238]. The region found to adopt this helical conformation spans K60 (Figure 6.21B). Its α-helical structure is believed to be related to its physiological functions, thus it would be interesting to analyse the effect of ubiquitination of α-Syn:lipid interactions. Furthermore, K60 lies at the interface of the N-terminus with the aggregation-prone NAC region, thus how ubiquitination influences the conformational dynamics of α-Syn could be of interest in the context of disease.

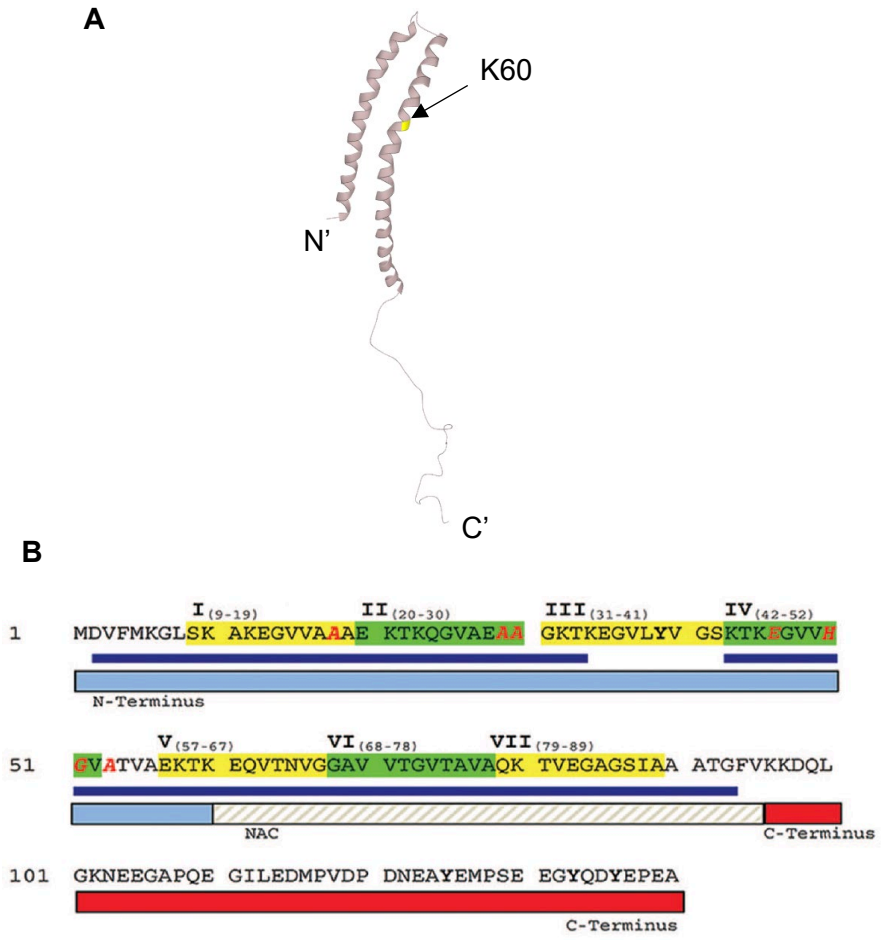


**Figure 6.21: Structure of α-synuclein**
**A)** The mapped K60 Ub site was added to the crystal structure of α-Syn.
**B**) Amino acid structure of α-Syn consisting of 7 imperfect 11-residue repeats (I-VII). Region underlined in dark blue adopts a helical conformation in the presence of micelles.
(**A**: Uniprot[239], **B**: Alderson *et al.* [238])

CHIP-dependent ubiquitination of these substrates occurred at restricted sites, rather than at multiple lysines, as observed in CHIP auto-ubiquitination. In agreement, another group has also reported a single ubiquitination site (K1047R) for CHIP-dependent monoubiquitination of the INSR[62]. This supports CHIP-dependent ubiquitination as highly specific and argues against the proposed promiscuous nature of protein ubiquitination[240]. The underlying mechanism is likely to be the previously reported docking-dependent E3 ligase activity of CHIP in the absence of Hsp70[77,80]. The ubiquitination of IRF-1 is a good example of such. One would predict ubiquitination to occur either within its Arg-Lys-Ser rich motif in the intrinsically disordered Mf2 domain of IRF-1 (a stable CHIP-binding site) or the more conformationally flexible C-terminal half of the protein. However, IRF-1 is actively ubiquitinated by CHIP in its DNA-binding domain, where CHIP binds to a lesser extent[77,80]. Potentially, E3 enzymes (including CHIP) position the charged E2 in close proximity of the target lysine residue, promoting Ub-acceptor site specificity[241].

Other studies have argued that ubiquitination is of a non-specific nature. In support, ubiquitination of α-Syn and CHIP was reported to be maintained when commonly ubiquitinated lysine residues were mutated[53,240]. Bringing into the equation cellular context, Lyumkis and colleagues[242] hypothesised that quality control substrates, such as nascent polypeptides, are highly heterogeneous with regards to the position of target lysines, whilst non-quality control (i.e. regulatory) substrates have predetermined ubiquitination sites that have been optimized through evolution. This would argue that the substrates in question (ANXA2 and α-Syn) are regulated by CHIP for non-degradative purposes.

In fact, CHIP-dependent monoubiquitination[62] and polyubiquitination via the non-canonical K63 ubiquitination-chain linkages[77] has been reported, thus it is likely that CHIP can regulate receptor turnover and cell signalling pathways, impacting on the structure, function and activity of its substrates. Its functions in ubiquitination-mediated degradative processes may be favoured in conditions of proteotoxic stress. This rational has been proposed by us[47] and others[62]. Alternatively, the limited number of conjugation sites may be a common feature across most ubiquitination events. Xu *et al.*[143] found that most peptides analysed by MS (using the diGly enrichment step)

from cell lysate contain a single diGly-modified lysine (157 proteins versus the 80 proteins identified with two or more ubiquitination sites).

### b. Known ubiquitination of identified CHIP substrates

Of the identified ubiquitination sites on ANXA2, only modification at K115 has been previously reported. This site and K80 have been found to be ubiquitinated in lung tissue collected from mice exposed to hypoxia-induced pulmonary hypertension. These results were obtained using an anti-diGly antibody capture and MS[243]. Although a few other reports have found ANXA2 to be ubiquitinated, the sites and enzymes involved are often unknown[181,182]. By sequence analysis Lauvrak and colleagues[181] have searched for Ub-binding domains with α-helical conformations that could potentially bind to the α-helical structure of ANXA2. A Ub-interacting motif (UIM) was identified (176 GRRAEDGSVID) spanning the 5$^{th}$ helix of domain II[181], which is in close proximity to the K157 residue that we have identified as a potential CHIP-mediated ubiquitination site on ANXA2. It was hypothesised that this could bind to polyubiquitin chains and promote ubiquitination in a manner that would not lead to degradation of the modified protein. Thus, given the involvement of ANXA2 in endocytosis, ubiquitination could promote internalisation of membrane proteins destined to the endolysosomal pathway, which is a reported cellular fate of monoubiquitinated species. Alternatively, ubiquitination of ANXA2 could mediate its actin-binding dynamics, since ubiquitinated ANXA2 species have been detected in the cytoskeletal fraction[181].

With regards to α-Syn, we found that CHIP-dependent ubiquitination occurs at lysine 60. This site has been previously been associated with lipid peroxidation, becoming covalently bound to by-product 4-hydroxy-2-nonenal (HNE). It was suggested that this PTM promotes α-Syn oligomerisation and cell-to-cell transmission in neuronal cell models[244]. Furthermore, although there is no published evidence to directly support K60 as a ubiquitination site, introduction of a K60R mutation in α-Syn resulted in a ~40% reduction in *in vitro* ubiquitination compared to WT (when using a Ub ligase fraction derived from rat brains)[245]. Thus, K60 may be of significance. This reduction was also observed for a K58R α-Syn mutant. Moreover, other residues have been implicated in the ubiquitination of α-Syn. Rott *et al.*[240] have suggested that SIAH-2

monoubiquitinates α-Syn *in vitro* and *in vivo* (on lysines 10, 12, 21, 23, 34, 45 and 96). While Nonaka *et al.*[245] reported that monomeric and filamentous α-Syn are ubiquitinated both *in vitro* and *in situ*, at lysines 21, 23, 32, and lysines 6, 10 and 12, respectively, although the E3 ligase(s) responsible are unknown.

The cellular consequence of α-Syn ubiquitination is also controversial and largely unknown. It was suggested that ubiquitination enhances the aggregation potential of α-Syn, possibly due to an increase in hydrophobicity, ultimately forming toxic inclusions within cells. Supporting this is the observation that ubiquitinated α-Syn is present within LBs (ubiquitinated at lysines 12, 21 and 23)[240]. Different forms of ubiquitinated α-Syn species have been found, having one, two and three Ub molecules[246] (monoubiquitinated α-Syn makes up around 10% of α-Syn purified from LBs[240]). Tofaris *et al.* suggested that rather than representing ubiquitination-dependent degradation of α-Syn, this PTM most likely reflects a disease-specific pathway. Either it represents an unsuccessful attempt at targeting α-Syn for proteasomal or lysosomal degradation, or a cytoprotective response to prevent aberrant α-Syn interactions[246].

### c. CHIP auto-ubiquitination

We have mapped the auto-ubiquitination sites of CHIP in the absence and presence of the substrates investigated (α-Syn and ANXA2). This could shed light into sites that are important for its E3 ligase activity and those that could be influenced by its substrate.

In the presence of α-Syn, K221 and K234 were detected as ubiquitination sites on CHIP (Figure 6.15). From the significant and distinctive laddering of CHIP- and Ub-positive bands on the immunoblot (Figure 6.10 & Figure 6.11), it is probable that CHIP incorporates polyubiquitin chains at these sites, yielding multiple ubiquitinated species of different molecular weights. Interestingly, the complexity and robustness of the auto-ubiquitination pattern of CHIP when in the absence of α-Syn was greater than in the presence of this substrate. The number of lysine residues involved in the auto-ubiquitination of CHIP is decreased in the presence of α-Syn (2 versus 9 sites

detected, Figure 6.15). Although this requires further validation, it seems that the bands on immunoblots representing ubiquitinated forms of CHIP are also slightly reduced in the presence of α-Syn (lane 3 compared to lane 7 in Figure 6.11D and lanes 5 versus 13 and 6 versus 14 in Figure 6.10A).

We question whether α-Syn prevents the auto-ubiquitination of CHIP, which could be of interest at both biochemical and cellular levels. In contrast, the presence of ANXA2 does not seem to impair CHIP's auto-ubiquitination. Therefore, α-Syn, specifically, could prevent the auto-ubiquitination of CHIP by sterically inhibiting its ubiquitination sites, competing with Ub or binding to an unknown non-catalytic inhibitory site on CHIP. However, this needs to be interpreted with caution, since the mapping of ubiquitination sites in the presence of ANXA2 and absence of substrates were derived from two independent experiments. Future work would investigate if this is a phenomenon of substrate inhibition[#] by introducing titration experiments, and whether it is dependent on the conformation of the substrate (i.e. folded vs. unfolded).

With regards to CHIP-dependent auto-ubiquitination in the presence of ANXA2, preliminary data identified six different potential sites of auto-ubiquitination. These included K22, K125, K221 and K255, which were also detected in the independent experiment analysing the auto-ubiquitination of CHIP in the absence of substrates. The diGly motif at K221 could be of particular interest as it was consistently detected in the absence of substrates and presence of either α-Syn or ANXA2. Future work would question the biochemical significance of these modifications.

Only two auto-ubiquitination sites on CHIP have been reported: K2[53] and K22[54]. Of these, only K22 was detected in some of the conditions that we tested. This site has been associated with K48- and K63-specific Ub chain linkages, suggesting that auto-ubiquitination of CHIP is mediated by K48- and K63-polyubiquitination and/or by mixed chains[54]. On the other hand, the K2 auto-ubiquitination has only been implicated in monoubiquitination of CHIP by Ube2w[53].

[#] Substrate inhibition: enzyme inhibition by its substrate in excess. This causes deviations from Michaelis-Menten kinetics, where the velocity curve of a reaction rises to its maximum as the substrate concentration increases and then decreases[278].

It has been proposed that auto-ubiquitination tends to occur at more highly exposed residues[139], such as K2 and K22 on the extended N-terminal region of CHIP[53,208]. Both our HDX-MS results of CHIP alone (Figure 6.16B) and those reported by Graf and colleagues[209] (Figure 6.16D) show that the N-terminal segments of the TPR domain (in particular residues 1-28 from our study and residues 2-48 from Graf *et al.*[209]) are the most exposed regions. This region contains helix-turn-helix repeats that seem largely unfolded[209]. Therefore, to some extent, our data agrees with the proposed hypothesis that auto-ubiquitination tends to occur at more exposed regions, although this is not the case for the other auto-ubiquitination sites identified.

On the contrary to some papers[53,54], we found auto-ubiquitination of CHIP to be mediated primarily by polyubiquitinated chains, rather than monoubiquitination, and highly efficient. Some discrepancies could be explained by differences in the biochemical properties of recombinant CHIP and other enzymes used, as well as the conditions used for the *in vitro* ubiquitination assay.

Different hypotheses have been proposed for the molecular significance of auto-ubiquitination. This modification has been regarded as an effective reporter of the interaction between E2 and E3, thus a read-out of the activity of the E3 ligase[247]. Others have suggested that the addition of Ub *per se* could be a driver of the ubiquitination cascade: since E3s are themselves ubiquitinated, this could represent a mechanism by which U-box E3s directly participate in the transfer of Ub from the E2 to the substrate[54]. A more generically and widely-accepted view, is that auto-ubiquitination regulates the E3 ligase activity, either by changing its intrinsic ubiquitination functions (via conformational changes) or modifying its interactome. For example, monoubiquitination of CHIP (on K2) has been suggested to enhance its activity by stabilising its interaction with the deubiquitinase ataxin-3. This allows a dynamic regulation of substrate ubiquitination by removing the Ub on CHIP once the substrate is fully modified, thus restricting the length of Ub chains added and enhancing CHIP-mediated clearance of its substrates[53].

### d. Limitations of the ubiquitination mapping strategy

Accurate mapping of the ubiquitination and auto-ubiquitination sites can be compromised by limitations of the proteomics technique and diGly strategy used. Firstly, false-positive assignments (identification of mis-localized ubiquitination sites) can occur. Typically, these span peptides that contain internal lysine residues adjacent to amino acids of a similar mass to glycine (such as Leu, Asn or Asp), where the 114.043 Da is observed as a part of the peptide sequence rather than derived from the ubiquitination of lysine. Inadequate mass accuracy (>10 ppm) and peptide coverage (<3%) contribute to this problem. Mis-cleavage events also complicate the assignment of ubiquitination. For example, Lys-Asn at the C-terminus of a peptide can be regarded as diGly-containing lysine. To prevent the assignment of false-positives, a high-mass accuracy spectrometer was used and parent ions were identified with high resolution[139]. Secondly, given the limited depth of the MS, under-sampling for low abundance or low occupancy sites is a common problem[141]. To ensure adequate levels of ubiquitinated species, mapping of ubiquitination sites on candidate substrates was performed on *in vitro* ubiquitination reactions conducted under optimal conditions.

Finally, although the use of the diGly signature allows the identification of ubiquitinated species in a direct manner, data derived must be interpreted with caution. The diGly signature is a result of ubiquitination and Ub-like modifications, such as ISG15 and NEDD8[139]. However, a study into the diGly-modified proteome by Kim and colleagues[141] concluded that >94% of the identified sites represented ubiquitination, rather than the other modifications. Another limitation of diGly-based methods is that the motif does not reveal whether a target site is mono- or polyubiquitinated[141]. For all the reasons discussed, further validation of candidate proteins and ubiquitination sites is crucial. Future work would include mutating these candidate sites and evaluating whether ubiquitination is abolished/affected.

## 6.3.3 Effect of scFv on CHIP's E3 ligase activity

A major aim of this chapter was to create tools that would manipulate CHIP activity (initially *in vitro* and later *in situ*) in order to better understand its functions. Given CHIP's intrinsic E3 ligase function, we sought to investigate the effect of scFv

antibodies on the ubiquitination activity of CHIP of ANXA2 and α-Syn. ScFv antibodies (7A and 11F) were successfully purified from bacteria (Figure 6.8) and their activity was tested using the *in vitro* ubiquitination assays.

The scFv antibody with high affinity for CHIP, 11F, inhibited α-Syn ubiquitination (Figure 6.12) and enhanced ANXA2 ubiquitination (Figure 6.13). The underlying mechanism explaining such opposing effects is unknown. Although we see scFv-induced changes in CHIP structure by HDX (Figure 6.17 & Figure 6.18), at present we cannot exclude whether these effects are a result of scFv-induced changes in the exposure of ubiquitination sites on the substrates directly, rather than CHIP-dependent effects. Moreover, the antibody with lower affinity for CHIP, 7A, only had a negative effect on the ubiquitination of α-Syn when used at a concentration that was 9.35-times higher than that of 11F (115.9 nM compared to 12.4 nM per reaction). It is unclear if the differences in binding sites or affinities for the same site explain the discrepancies in the concentration needed to have an inhibitory effect on α-Syn ubiquitination.

In attempt to investigate how the 11F scFv might modulates CHIP activity, I have analysed their interaction by HDX-MS (Figure 6.17 & Figure 6.18) and IP (Figure 6.19). The purified antibody is capable of direct-binding and capturing of endogenous CHIP from human cells. The HDX-MS data provided insights into the conformational dynamics induced by scFv on the structural and functional domains of CHIP.

ScFv binding to CHIP induced protection (HDX difference (ΔD) < 0.5) of units: TPR 2 and 3 (residues 62-105) and U-box (residues 215-233). However, more robust protection was observed in the rest of the U-box domain, where scFv induced protection of residues 238-252, 260-284 and, to a less extent, 253-259. Therefore, it is highly likely that this scFv antibody binds to residues around this region (~240-280). One would expect the high degree of flexibility in the U-box to be significantly reduced in the presence of scFv, which is likely to affect its E3 ligase activity. Changes in other regions of CHIP could be secondary to scFv binding - for example due to allosteric regulations (previously reported for CHIP[47]), compensatory structural dynamics or dimerization. The binding of scFv to CHIP induces some structural changes that are similar to the binding of E2 enzymes (UbcH5a and Ubc13) to CHIP. This includes

increased protection of the U-box residues 239-259 from HDX and the modulation of segments of the TPR domain[209].

At this point, mechanistic insight into the effect of scFv on CHIP activity is still scarce and would require further investigation. Possible mechanisms of action include scFv-induced conformational change of CHIP, modulation of CHIP's E3 ligase activity and/or interactome. These mutually non-exclusive hypotheses are entertained in the following sections and could help to explain the opposing effect of the 11F scFv antibody on CHIP-dependent ubiquitination of its substrates, α-Syn and ANXA2.

### a. Potential scFv-induced conformational change in CHIP

Binding of scFv to the U-box domain of CHIP could interfere with CHIP dimerization or higher order oligomerisation. By size exclusion chromatography (SEC) and native gel (data not shown), we have detected a scFv-dependent collapse in higher-order CHIP species. Characterisation of these species is ongoing. We hypothesise that the 11F scFv antibody promotes the transition of either dimeric to monomeric or tetrameric to dimeric isoforms of CHIP.

The binding of scFv to the U-box could affect CHIP dimerization, as it spans the E3-protomer dimer interface (residues 239-259)[47]. ScFv may sterically prevent U-box dimerization, which is key for the electrostatic repulsion between the linker and the HH, driving the bending of the extended protomer[208]. Therefore, formation of the asymmetric dimer may not form. It is unclear if a symmetric dimer would form, since it does not require U-box dimerization (the elongated-dimer model)[208]. However, if the presence of scFv induces a shift from dimeric to monomeric CHIP, major charged domain changes would be expected, becoming more exposed to deuterium as a monomer. The coiled-coil domain located within the charged region is involved in stabilisation of the dimer[40].

### b. Potential scFv-induced changes in CHIP's intrinsic activity

Protein structure is inherently associated with function[47]. Therefore, by changing the conformation of CHIP, scFv might influence its activity, including intrinsic E3 ligase

function and substrate specificity. It has been suggested that the dimer conformation of CHIP is necessary for its functioning as an E3 ligase[40,146,208]. As a monomer CHIP may be inactive. However, dimerization of the inactive monomers may activate the U-box, assembling rapidly into an active dimer[40,208]. The members of the closely related RING Ub ligase family (MDM2 and MDMX) are an example of such. By forming heterodimers, the E2-binding RING domain becomes stabilised, overcoming the lack of intrinsic E3 ligase activity of MDMX[248,249].

Although 11F scFv could induce collapse of the dimer into monomeric CHIP, both auto-ubiquitination and some substrate ubiquitination (of ANXA2, but not α-Syn) are retained. This argues against CHIP being an inactive monomer and scFv-induced modulation of auto-ubiquitination. The prevailing hypothesis that dimers are required for ubiquitination activity is also challenged by the monomeric U-box E3 ligase, E4B, which is capable of auto-ubiquitination and substrate ubiquitination[70]. Likewise, CHIP could function as both a monomer and dimer, although supporting evidence is limited. It would therefore be interesting to map the auto-ubiquitination sites on CHIP by MS in the presence and absence of 11F scFv.

Furthermore, as a monomer, the activity of CHIP may depend on its conformation. The CHIP bent promoter would be inactive due to the tight packing of the TPR-U-box interface, having the E2 binding site buried. However, in principle, the extended protomer should be active, with a single U-box exposed (according to the different dimer conformations proposed by Ye *et al.*[208]).

Alternatively, rather than inactive, CHIP may have limited activity as a monomer. Such activity may be sufficient for auto-ubiquitination, for example, but not for specific substrate ubiquitination events, which might require the fully active, dimeric form. In line with this, 11F scFv inhibits α-Syn *in vitro* ubiquitination without affecting CHIP's auto-ubiquitination. Thus, dimeric CHIP could be required for ubiquitination of this substrate. Likewise, it was hypothesised that dimeric CHIP may be required for the binding and subsequent ubiquitination of IRF-1[77].

Such dynamics have been observed by E3 ligases that follow a 1:1 stoichiometry of E2 binding to its catalytic domain where, as monomers, ubiquitination efficiency is

low[70]. The symmetric homodimer of RING finger protein 4 is an example of such[249]. Regarding CHIP, it is unlikely that stoichiometry changes between the monomer and dimer, due to its half-of-sites active asymmetric dimer conformation. Alternatively, enhanced activity may correlate with the increased binding strength of the dimer. For example, disruption of the dimeric conformation of a RING E3 ligase (by mutating C-terminal residues) completely abolished its activity, while mutating residues at the E2 interface has a weaker effect[250]. Therefore, scFv-induced collapse of the dimer may result in insufficient binding strength of the E3 ligase for the ubiquitination of α-Syn.

### c. Potential scFv-induced changes in CHIP's substrate specificity

ScFv-induced changes in CHIP's substrate specificity can be mediated inter- and intra-molecularly. This could explain the seemingly controversial effect of the scFv antibody on the ubiquitination of α-Syn and ANXA2. Dimer formation may alter the interactions and cellular functions of the E3 ligase complex. Such conformational and, in turn, functional variability has been reported for the RING family of E3 ligases, for example, which function as monomers, dimers (homodimers and heterodimers) or multi-subunit complexes[251]. More subtle intramolecular changes in the conformational dynamics of CHIP induced by scFv binding may drive a change in substrate specificity. It has been shown that changes to the TPR-domain of CHIP (e.g. via Hsp70 binding) were sufficient to modulate the docking-dependent E3 ligase activity. Hsp70 binding reduces flexibility of the TPR domain, which allosterically alters the conformation of the U-box and hence its catalytic activity[47]. Therefore, direct changes to the flexibility of the U-box (including scFv binding) are likely to have important implications in the ubiquitination cascade. Changes to the flexibility of the U-box have been predicted to influence the transfer of Ub from the CHIP-E2-Ub complex to the substrate[47].

The reduction in flexibility induced by Hsp70 binding inhibited CHIP-dependent ubiquitination of intrinsically unfolded proteins (such as IRF1 and p53), but stimulated ubiquitination of folded substrates like BAG-1s. This structural plasticity of CHIP allows it to switch its E3 ligase functions "on" and "off". Underlying this is the influence of protein motion and flexibility on substrate selection[242] and E3 ligase-mediated ubiquitination via E2:E3 interactions[47]. Like HSP binding and HSP-binding mimetic

mutations in CHIP[47], the binding of scFv to CHIP could induce structural changes that cause CHIP to favour the ubiquitination of a folded protein, like ANXA2, but not the intrinsically disordered protein, α-Syn. We believe that scFv alters the dynamics of the U-box rather than altering its accessibility to either of the U-boxes at any given time (as seen in the Hsp70-CHIP complex)[47]. A potentially significant difference between Hsp70- and scFv-binding scenarios is that under certain conditions (e.g. in the presence of IRF-1) Hsp70-bound CHIP does not undergo auto-ubiquitination[47], whilst we detect auto-ubiquitination of CHIP when scFv is present in all conditions tested. Therefore, the biochemical status of CHIP is different.

Importantly, understanding the effects of the scFv antibody on CHIP can enrich our knowledge of CHIP's conformational variability – a property that widens the scope of its substrates and, consequently, the cellular functions of CHIP[242]. The obvious next steps would be to map the ubiquitination sites on substrates and CHIP in the presence and absence of both 11F scFv and either substrate (α-Syn or ANXA2), and conduct more biophysical and biochemical analyses into scFv-induced changes of CHIP structure and function.

The main outputs from this chapter include the generation of scFv antibodies and their characterisation, including interphase mapping of the scFv:CHIP interaction and scFv-mediated regulation of CHIP activity. This foundation work and the intrabodies engineered can now be used for chemical genetics to modulate the effect of CHIP endogenously.

# Chapter 7: Final discussion & Future work

## 7.1 Final discussion: Summary

### 7.1.1 Development of CHIP models and proteomic analysis

Despite strong evidence supporting the neuroprotective effects of CHIP, the details of its intrinsic role in neuronal health and disease is largely undefined. This thesis aimed to identify the protein targets of this dual function chaperone and E3 ligase in a disease context. Given the association of CHIP with $\alpha$-Synucleinopathies, our model for target identification was derived from a patient with Lewy body Parkinsonism. However, considering that the majority of neurodegenerative diseases are proteinopathies and CHIP plays an integral role in proteostasis, understanding its effects could be relevant across different diseases. Furthermore, many E3 ligases are associated with neuronal dysfunction (about 13% of E3-encoding genes are mutated in neurological diseases – 83 genes and 70 different diseases[252]).

The project design was centred around two main criteria. Firstly, target identification was conducted prior to the manifestation of hallmarks of cell pathology (e.g. inclusion body formation and neurite degeneration) and using an unbiased approach. The underlying rational was our aim to elucidate possible early proteomic changes that could be relevant in disease initiation/progression and, in turn, for disease-modification. This contrasts with the majority of studies aimed to understand the role of CHIP in neurodegeneration, which tend to use models with proteotoxic stress.

Secondly, given the highly dynamic and tightly regulated ubiquitination processes, this project focused on studying the effect of CHIP on the proteome at endogenous levels of expression. Again, this contrasts with the norm, where overexpression systems tend to be used when studying CHIP. Here, not only are ubiquitination cascades likely to be affected, but its TPR domain may also alter the interactome of TPR-containing proteins and the dynamic nature of the chaperone network. In fact, many substrates identified using such an approach have proven difficult to validate as physiologically relevant. Our loss-of-function CHIP cell models are likely to be less disruptive to protein homeostasis.

I have engineered patient-derived iPSC so that they lack the expression of CHIP using CRISPR/Cas9 based gene-editing technology. Those cells were differentiated into mature cortical neurons (Chapter 3) and this isogenic system was used to investigate the effect of CHIP on the proteome using label-free DIA by SWATH-MS (Chapter 4). Protein targets identified were validated in these cortical neurons and iPSC, as well as another neuronal-like cell model that we have previously used to manipulate the expression of CHIP (provided by Erisa Nita[95]; Chapter 4 and 5). The use of multiple models counteracts the effects of clonal variability, differentiation variability and cell line-specific differences (that could be associated with cell cycling and/or neuronal identity).

Interestingly, a restricted number of proteins (around 35 proteins) were identified by SWATH-MS as significantly changing in the absence of CHIP function (Chapter 4). This supports its functions as a chaperone-independent, docking-dependent E3 ligase, which has been previously proposed by us[47,77] and others[62]. Moreover, it suggests that our model is likely to reflect an early state of disease, with no/low stress levels, since proteotoxic stress is associated with considerable changes in the proteome due to the activation of the molecular chaperone network.

These 35 proteins could be regarded as both an under- or over-estimation of the protein targets of CHIP. They may not all be direct targets of CHIP (i.e. ubiquitination substrates or chaperone clients). Instead, CHIP could regulate some upstream components of the pathway, which indirectly affect components downstream that could be more readily detected by SWATH-MS. Conversely, since these 35 proteins seem to belong to multiple, unrelated pathways, CHIP could regulate numerous proteins and signalling cascades. This number could also be an underestimation because only modifications that modify the trypsinisation pattern of proteins and/or protein levels can influence the candidate proteins detected. Therefore, like the majority of MS-based proteomic techniques and experimental designs, SWATH-MS analysis of a loss-of-function model can be bias towards the identification of ubiquitination substrates destined for degradation, compared to proteins that undergo K63-mediated ubiquitination, for example.

We have identified potential targets of CHIP that are involved in a vast array of cellular processes, including innate immunity (HLA-B and, previously, IRF1[77]), regulation of

metabolism (VGF) and membrane homeostasis (calcium- and phospholipid-binding proteins, such as ANXA2 and S100-A11; Chapter 4) (Figure 7.1). These may contribute to the neuroprotective effects of CHIP, independently or in a cumulative manner.

Chapter 5 focused on the effect of CHIP on ANXA2 homeostasis. ANXA2 was found to be upregulated in CHIP KO neurons and in close proximity with CHIP (interacting directly or indirectly, e.g. within 40 nm). Our SH-SY5Y CHIP model, with lower fold change in ANXA2 protein level, provided insights into CHIP-mediated changes in ANXA2 isoforms and interactome (with its binding protein S100-A11 and CHIP). I detected CHIP-dependent ubiquitination of ANXA2 *in vitro* and, possibly, *in situ*, thus CHIP could function to maintain correct homeostasis of ANXA2 (Chapter 5). The ubiquitination sites in ANXA2 were mapped to lysine residues 115 and 157, although these preliminary results need to be further validated (Chapter 6). Accordingly, dysregulation of ANXA2 could be a direct effect of the absence of CHIP.

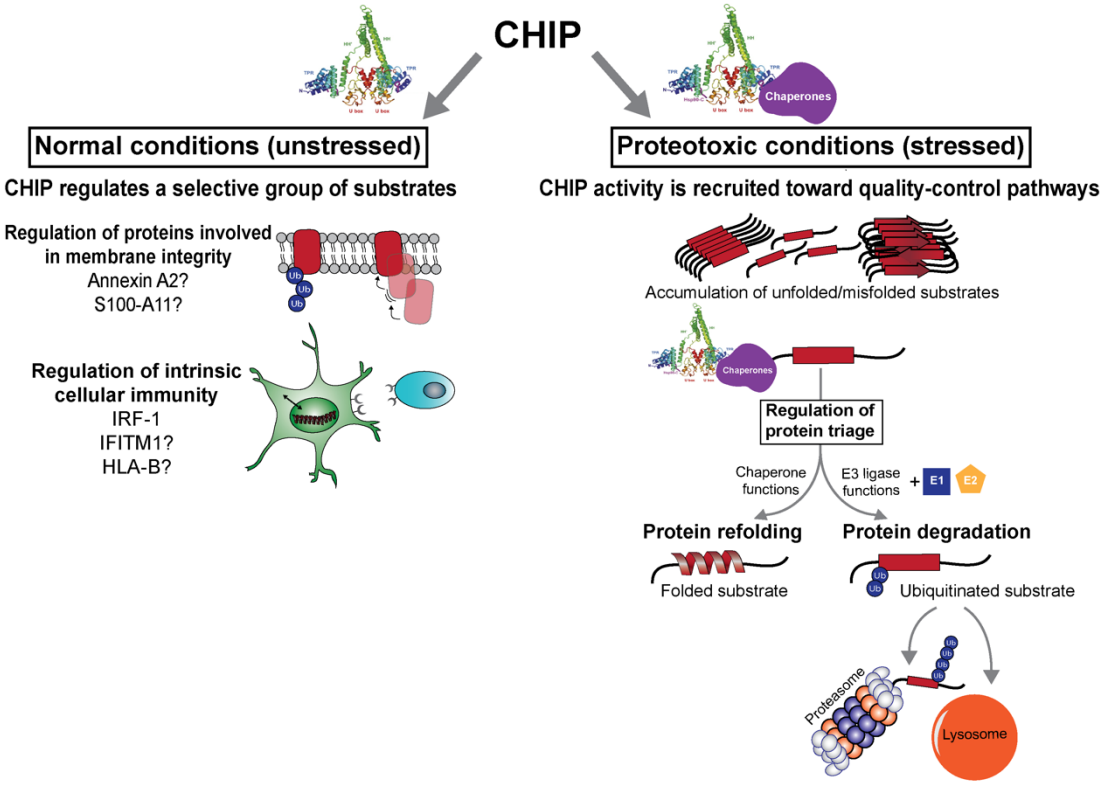


**Figure 7.1: Activity of CHIP in normal conditions and under proteotoxic stress**
In normal conditions *(left)* CHIP regulates the proteostasis of a restricted number of substrates that belong to a vast array of cellular processes, including membrane homeostasis and innate immunity. Regulation is likely to occur in a chaperone-independent, docking-dependent manner. Under proteotoxic stress *(right)* CHIP may be diverted to quality control mechanisms to counteract accumulating misfolded/unfolded proteins. Unfolded/misfolded α-Syn is illustrated in this schematic (red rectangle) as a substrate entering the protein triage, where it can become refolded into an α-helical state or targeted for proteasomal or lysosomal degradation. This may or not involve the actions of chaperone (in purple) (we have shown that CHIP is capable of ubiquitinating intrinsically unfolded α-Syn in a chaperone-independent manner, in vitro). Generally, quality control mechanisms recruit the molecular chaperone network. Oligomeric (depicted by the multiple red rectangles) and amyloid fibrils (multiple red arrows) of α-Syn induce proteotoxic stress.
(Crystal structure of CHIP derived from: Zhang *et al.,*[39])

### 7.1.2 Changes in lipid homeostasis and membrane integrity

Given the crucial role of ANXA2 in maintenance of membrane integrity and as a modulator of membrane-related cellular events (e.g. endocytosis), its dysregulation is likely to be detrimental for cells. I have presented evidence suggesting that CHIP KO cells have a compromised membrane integrity, having increased permeability and sensitivity to injury (Chapter 5). This could be a direct effect of the upregulation of ANXA2 and/or its impaired interaction dynamics with S100-A11 (the complex is important for membrane repair). Alternatively, ANXA2 upregulation could be a compensatory mechanism in attempt to restore membrane integrity (e.g. by promoting interaction with S100-A11), which could be impaired due to other CHIP-dependent or independent factors. Nonetheless, as proof-of-concept, a preliminary experiment showed that, even if the increase in ANXA2 in CHIP KO cortical neurons is a secondary protective response, it fails to restore membrane homeostasis (with regards to membrane resilience to damage and permeability at basal conditions), when compared to control cells. Finally, defects in ANXA2 homeostasis can also be an epiphenomenon that is unrelated to membrane integrity.

#### a. CHIP-dependent lipid regulation in an Annexin-independent manner

A plausible underlying mechanism for the change in membrane properties observed is CHIP-mediated regulation of lipid homeostasis, in a manner that is independent of ANXA2. CHIP plays an integral role in proteostasis, preventing activation of the UPR[65]. Recently, lipid homeostasis has been also directly associated with the UPR in the ER, at various levels[253,254]. Alterations in membrane lipid composition and fluidity (including an increase in membrane saturation and cholesterol accumulation) have been shown to induce the UPR. Such induction is independent of proteostasis, although the proteins activated (including UPR proteins, IRE-1 and PERK) are in common with those recruited during proteotoxic stress[253,254]. Such pathway convergence despite varying stimuli makes us question whether enzymes related to the UPR also have lipid-related functions. In fact, a branch of the UPR (IRE-1/XBP1) is a well-characterised positive regulator of membrane lipid synthesis[9]. Furthermore, membrane homeostasis has been correlated with the efficiency of the ER in resolving proteotoxic stress[9]. There is also evidence to suggest that abnormal lipid synthesis

itself drives ER dysfunction[26]. The relationship between the UPR and lipid metabolism has been seen in the context of neurological conditions. Dystonia is characterised by defects in membrane biology and ER homeostasis (Figure 7.2) and the underlying mechanism is the dysregulation of lipid homeostasis[255].

Therefore, we propose that CHIP-mediated changes in lipid composition could position CHIP at the interface between maintenance of lipid and protein homeostasis. Such a non-canonical, novel function of CHIP, could be important as there is increasing evidence linking proteinopathies (including neurodegenerative diseases) with lipidomic changes[254,256,257].

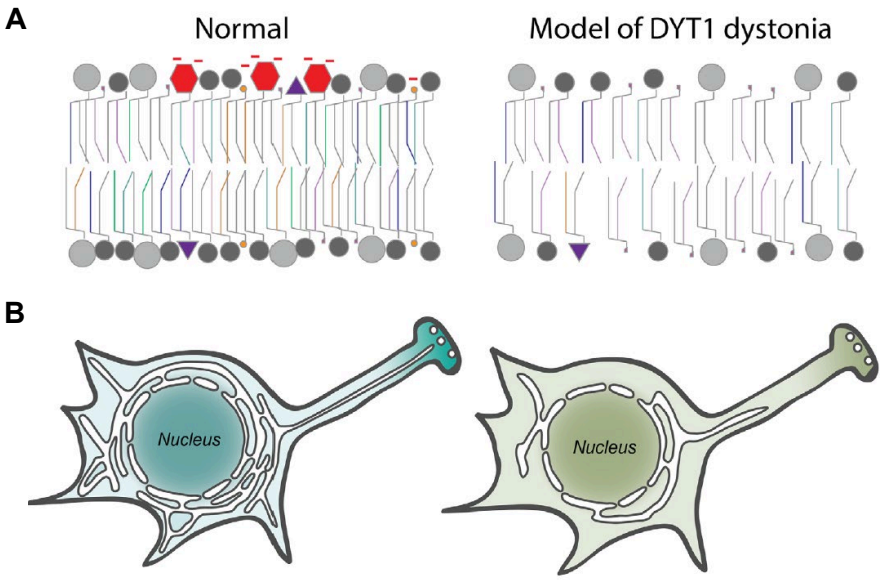


**Figure 7.2: Membrane and ER dysfunctions in neurological condition**
The neurological condition, dystonia, is caused by torsinA dysfunction. This impacts lipid composition, membrane structure and/or function, impacting organelle homeostasis. Schematics represented are based on findings from a fly model of disease.
**A)** Lipid composition of membranes in control *(left)* and dystonia pathogenesis *(right).* Diseased membrane has reduced levels of bulk membrane lipids and multiple defects, which compromises membrane properties (including fluidity, plasticity, fission and fusion).
**B)** Dystonia has reduced neuronal ER volume, which can result in defects in protein secretion and ER homeostasis.

(Adapted from Cascalho *et al.*[255])

### b. CHIP-dependent lipid regulation in an Annexin-dependent manner

CHIP-mediated lipidomic changes could be achieved through the regulation of Annexin proteins. Annexins segregate membrane lipids and are at the centre of major pathways regulating cellular cholesterol homeostasis (Figure 7.3). The later includes the incorporation of cholesterol into late endosomes and its transport along the endocytic route. Overexpression of ANXA6 has been shown to increase its association with late endosomes, promoting the redistribution of cholesterol from PM and other membranes towards endosomal membranes. Ultimately, dysregulation of Annexins impact on the intricate network of feedback mechanisms associated with cellular lipid homeostasis, including cholesterol[258]. The maintenance of adequate levels of both lipids and Annexins is critical for endosomal function and the turnover of proteins (e.g. integrins)[258,259].

Interestingly, Annexins have been shown to be upregulated in neurological conditions[188,189], which could account for the accumulation of cholesterol in late endosomes observed in neurogenerative diseases and ageing[257,258]. In parallel, cell models of AD show reduced membrane fluidity due to cholesterol depletion at the PM[260]. Our CHIP KO models show a robust increase in sensitivity to membrane damage induced by the cholesterol-sequestering agent, digitonin. Thus, varying cholesterol content, which could be directly or indirectly related to CHIP expression, could result in membrane fragility in CHIP KO cells. Although Annexins could be responsible for the lipidomic changes, we cannot exclude the possibility of CHIP interfering with lipid composition, such as cholesterol, in an Annexin-independent manner.

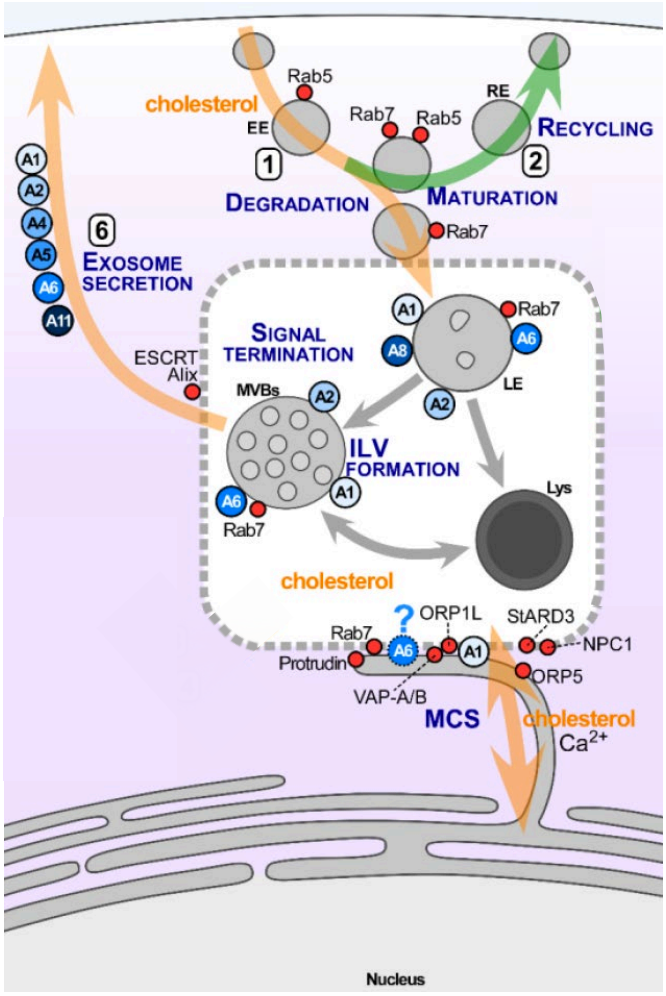


**Figure 7.3: Annexin-mediated cholesterol metabolism and trafficking within the cell**
Annexins function at multiple stages of the endocytic pathway. Routes highlighted in orange are modulated by cholesterol. Those in green are recycling pathways and indicates points of interaction with other cytosolic proteins.
Annexins are involved in the maturation of early endosomes (EE) into late endosomes (LE) (**1**). This is achieved through the recruitment of Annexins to the surface of LE through binding to acidic phospholipids and cholesterol. Also, Annexins function as ”tethers” for the formation of membrane contact sites (MCS) between the ER and late endosomes/lysosomes, which are functional platforms for the exchanges of lipids (including cholesterol) and ions. Finally, Annexins can also be involved in the secretion of exosomes from multivesicular bodies (MVBs)
(Adapted from Rentero *et al.*[258])

### 7.1.3 Modulating CHIP

We have engineered tools to manipulate the activity of CHIP in an endogenous state (Chapter 6). This contributes to our aim of comprehensively evaluating the role played by CHIP in human neuronal cell health and, specifically, its proteostasis. ScFv antibodies generated using phage display technology were purified and introduced into mammalian expression vectors for delivery as intrabodies. At present, our data indicates that the 11F scFv antibody binds to the U-box domain of CHIP and induces a shift from higher order structures to lower MW species. It is likely that the scFv interferes with the dimerization or tetramerization of CHIP. We expect its intrinsic activity and substrate specificity to be influenced by the scFv-induced conformational changes. To test this, we investigated the effect of the scFv on CHIP-dependent ubiquitination of two substrates of interest: ANXA2 and α-Syn (Chapter 6). Unlike ANXA2, the ubiquitination of α-Syn by CHIP has been previously reported[37,68] although, to our knowledge, we are the first to map the ubiquitination site involved (K60). Moreover, both the identification of ANXA2 as a ubiquitination substrate of CHIP and the ubiquitination sites involved were novel.

Accordingly, *in vitro*, we have observed a decrease and increase in CHIP-dependent ubiquitination of α-Syn and ANXA2, respectively, in the presence of scFv. Here, substrate specificity could be governed by the secondary structure of the substrate, since the lower MW isoform of CHIP (induced by the scFv and potentially monomeric) is capable of ubiquitinating the folded substrate ANXA2 but not the intrinsically unfolded α-Syn. Therefore, the scFv antibody can function as a “molecular switch” to modulate the intrinsic and dynamic E3 ligase functions of CHIP.

A couple of studies have modulated the levels of CHIP in cell models using trehalose[261] and lanosterol[262]. Both treatments protected from proteotoxic stress, oxidative stress and cell death by enhancing protein clearance mechanisms (including the UPS and autophagy)[261,262]. The authors concluded that, at the molecular level, trehalose increased the expression of Hsp70, which in turn alleviated CHIP dysfunction in patient fibroblasts with a hereditary CHIP-mutant related ataxia. The underlying hypothesis is that, since the mutation occurs at the dimer interface of CHIP, monomeric CHIP is non-functional[261]. In this thesis, we show that binding of the scFv antibody to CHIP may alter its conformation (Chapter 6), and potentially its function.

Given these observations, we believe this structure-function relationship deserved more investigation, thus we are currently working with the Hoppe Laboratory (University of Cologne, Germany) to determine the effect of monomeric CHIP on human substrates.

Lanosterol treatment induced expression of CHIP through increased stabilisation conferred by the binding of lanosterol to the TPR domain of CHIP. At a cellular level, this treatment enhanced both CHIP-mediated proteasomal and lysosomal clearance mechanisms[262]. It is unclear how binding of lanosterol influences the chaperone and E3 ligase activity of CHIP (given the reported allosteric interactions between the TPR and U-box domains[47]). Interestingly, lanosterol is an intermediate of cholesterol synthesis and induces ubiquitination and degradation of rate-limiting enzymes of cholesterol synthesis[262]. This endorses the emerging question of whether there is a relationship between cholesterol and CHIP, seeing that our CHIP models display different phenotypes towards treatment with the cholesterol-sequestering agent, digitonin (Chapter 5).

Targeting E3 ligases is known to be challenging given their involvement in multiple pathways simultaneously. CHIP, with its chaperone and E3 ligase functions, is central in various processes. Hence, merely overexpressing it is likely to result in pronounced changes to the cellular proteostasis and have detrimental side-effects[65]. The development of tools to manipulate the E3 ligase functions of CHIP in a more targeted manner, e.g. the use of scFv antibodies, is likely to minimise the problems associated with manipulating CHIP activity. Modulation of CHIP activity is likely to be beneficial when studying the homeostasis and functions of CHIP and could, potentially, contribute to the identification and development of therapeutic targets and tools. Joshi *et al.* stressed the need to investigate properties of CHIP and strategies that could increase its specificity for a substrate of interest[65].

## 7.2 Final discussion: In the context of neurodegeneration

The exercise of positioning findings in a wider context can add depth to the possible conclusions drawn. With this objective, I attempt to evaluate the underlying rational and main findings of my PhD project from the context of neurodegeneration, elucidating its potential significance within the field. The hypotheses developed within the following sections are for discussion purposes and have not necessarily been addressed in this thesis.

### 7.2.1 Relevance of CHIP loss-of-function in disease

We have focused on loss-of-function CHIP cell models. Loss-of-function of CHIP could be of relevance in a disease context, where CHIP may be recruited to the protein quality control machinery in order to counteract proteotoxic stress – a characteristic of progressive neurodegeneration (Figure 7.1). This dynamic, context-specific activity of CHIP has been previously proposed. Kanack *et al.*[49] observed that heat-stressing CHIP enhanced its chaperone activity and suppressed its E3 ligase functions. This translated to CHIP-mediated refolding of denatured/misfolded proteins rather than degradation, under conditions of cellular stress. Moreover, Tawo *et al.*[62] not only observed a shift in CHIP activity towards quality control mechanisms under proteotoxic stress, but this was accompanied by the accumulation of one of its E3 ligase target, the INSR. Likewise, ANXA2 accumulation could be due to the absence of CHIP-mediated turnover mechanisms (Figure 7.4). The same end-effect could also be achieved if CHIP becomes trapped within cytoplasmic inclusions, such as LBs (where CHIP has been detected[25]), which “diverts” it from its primary functions and reduces the effective chaperone-free concentration of CHIP in the cytoplasm. This could be an alternative mechanism, or one that arises later in the course of disease.

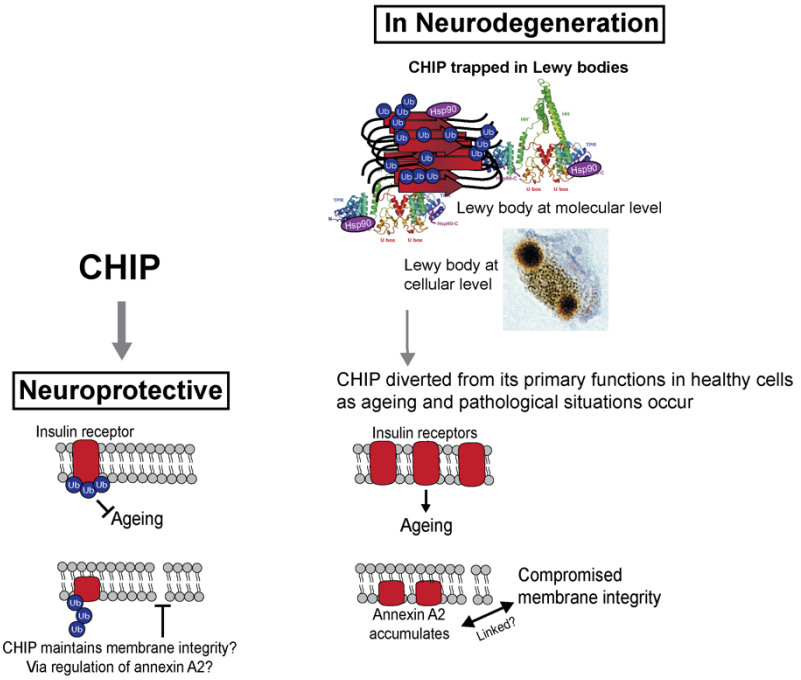


***Figure 7.4: Inhibition of the neuroprotective functions of CHIP in neurodegeneration***
CHIP may be neuroprotective by regulating the homeostasis of specific protein targets. Tawo *et al.*[5] have suggested that CHIP may regulate the turnover of the insulin receptor (INSR), preventing ageing. Possibly, CHIP-mediated regulation of ANXA2 is also part of CHIP's neuroprotective actions, and could influence membrane integrity.
In neurodegeneration, CHIP may be recruited towards quality control mechanisms and/or become trapped in Lewy bodies (represented schematically here), resulting in the accumulation of ANXA2, it was reported for the INSR[5]. This could have deleterious cellular consequences.
(LB image derived from: Spillantini *et al.*[24]; crystal structure of CHIP derived from: Zhang *et al.*[39])

## 7.2.2 Lipid-dependent α-Synuclein toxicity

### a. α-Synuclein monomers

In the context of synucleinopathy, there is growing evidence supporting lipid-dependent α-Syn toxicity. These could be influenced by changes in cellular lipid composition and membrane integrity. The "3K" α-Syn mouse and cell models shed some light on the lipid-mediated α-Syn activity and resultant toxicity[263,264]. This model amplified the effect of the PD-related E46K α-Syn mutant, by introducing two additional E-to-K mutations (E35K + E61K) on neighbouring KTKEGV motifs involved in lipid-binding[263,264]. Introduction of these mutations resulted in a stepwise increase in neurotoxicity[264]. These mutations inhibit fibril formation[264] and decrease the ratio

between aggregation-resistant α-Syn tetramers and aggregation-prone monomers[263]. Therefore, the pathomechanism of this model may be predominantly driven by the intrinsic activity of monomeric α-Syn. This supports the rational that a shift in α-Syn equilibrium from tetramer/multimer to monomer has detrimental effects. Likewise, the *SNCA* triplication line (our iPSC model) manifests this shift towards increased monomeric α-Syn, thus may result in similar defects as the E46K and 3K models[264].

Biochemically, the mutations increase the membrane avidity of α-Syn[263]. Acute/subacute consequences of expression of 3K α-Syn include defects in vesicle trafficking, vesicle clustering and, eventually, membrane rearrangements. This is due to the increased vesicle binding of the mutants (in a lipid-induced α-helical structure), and its loss of membrane curvature selectivity. The mutations trigger a change from "curvature sensor" (important for its intrinsic functions in synaptic vesicles) to a robust "curvature inducer". This leads to the formation of multiple, round cytoplasmic inclusions comprised of clusters of vesicles and tubules from diverse subcellular membranes (such as endocytic, lysosomal and Golgi), which are intimately associated with the focal accumulation of α-Syn. Here, α-Syn is diverted from its physiological functions at the synapse, which is like to have consequences for neuronal functioning. These abnormal vesicle clusters are an early pathogenic step towards Lewy-type α-Syn aggregates. Not only is such clustering likely to be detrimental for cells, the excess monomeric α-Syn eventually forms β-sheet-rich α-Syn aggregates that also contribute to the growing toxicity (Figure 7.5)[263,264].

α-Syn-induced membrane curvature, as well as expansion, can compromise membrane integrity (Figure 7.6)[265–267]. Binding of α-Syn monomers can result in uncontrolled membrane curvature, membrane remodelling (such as blebbing; Figure 7.6A)[266] and expansion via thinning and phospholipid rearrangement (Figure 7.6B). The end-effect is loss of membrane integrity, membrane remodelling and fragmentation[267,268]. Interestingly, the expansion per α-Syn is highly dependent on lipid composition[268].

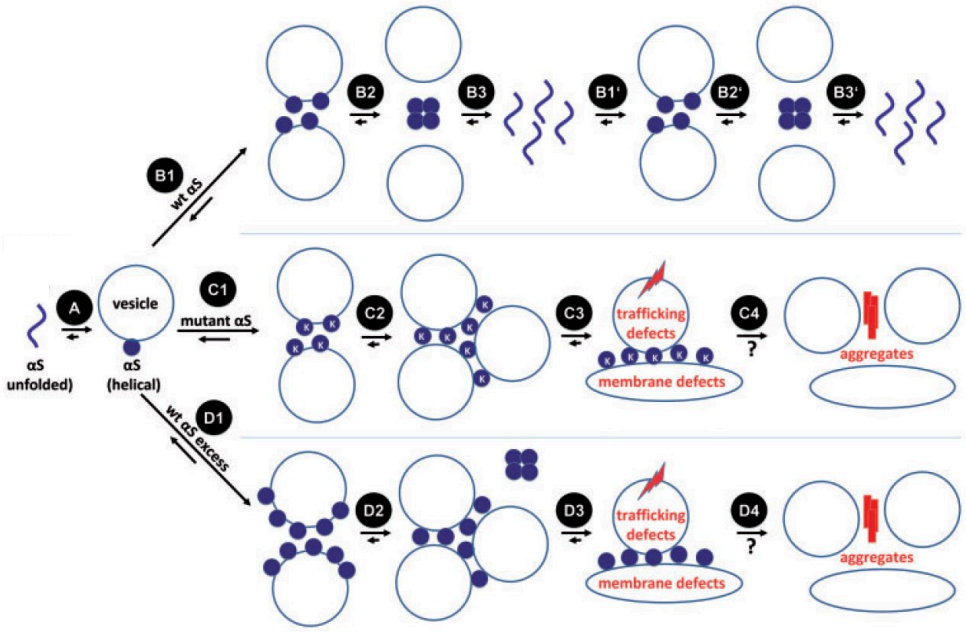


**Figure 7.5: α-Synuclein homeostasis and toxicity**
**A)** Unfolded α-Syn binds to curved membranes, adopting an a-helical conformation.
**B)** α-Syn monomers bind to vesicles (**B1**). α-Syn multimerization (**B2**) might weaken α-Syn:lipid interaction, yielding monomers (**B3**). The process repeats (B1'-B3').
**C)** KTKEGV mutant monomers (such as the 3K model) bind to vesicles (**C1**) and their inability to multimerize prolong this lipid interaction (**C2**). This can result in defects in vesicle trafficking and membrane rearrangements, such as tubulation (**C3**). A longer-term consequence is the formation of β-sheet-rich α-Syn aggregates (**C4**).
**D)** Excess monomeric α-Syn caused by *SNCA* triplication, for example, (**D1**) results in similar lipid-mediated toxicity (**D2-D4**) due to the shift towards free monomers.
(Adapted from Dettmer *et al.*[264])

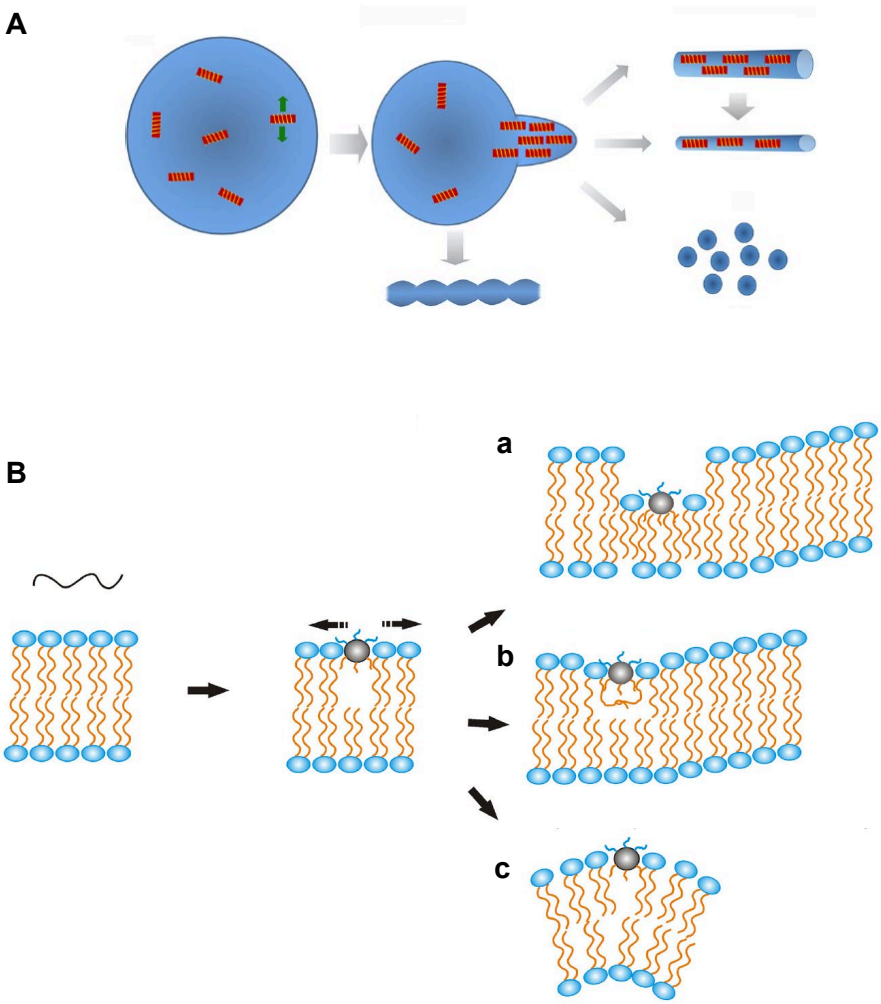


**Figure 7.6: α-Synuclein-induced defects in membrane properties**
**A)** In a concentration-dependent manner, α-helical α-Syn can bind to vesicles, causing curvature strain that induces remodelling, which initiates as membrane budding. The size and shape of the remodelling event depends on the concentration and orientation of α-Syn monomers.
**B)** α-Syn incorporation into the lipid bilayer results in lateral expansion of the lipids. This can result in:
- Thinning of the membrane due expansion of lipid molecules out of the membrane plane and interdigitation (**a**) or lipid conformational changes (**b**),
- Curvature (**c**).
Changes in bilayer thickness and curvature stress can result in loss of membrane integrity, increasing its permeability.
(**A**: Adapted from Varkey *et al.*[266]; **B**: Adapted from Ouberai *et al.*[267])

Membrane remodelling events (including blebbing) and permeability can trigger ANXA2 recruitment and upregulation, as a response mechanism[162]. Thus, it remains an open question whether CHIP KO neurons have enhanced lipid-mediated α-Syn pathology, and ANXA2 proteomic changes arise secondary to this. Alternatively, ANXA2-mediated lipidomic changes could potentially influence α-Syn toxicity. ANXA2 mediates lipid raft formation (cholesterol-rich) and lipid segregation of acidic phospholipids (including PI and PS) – to which α-Syn has preferential binding[265]. Furthermore, both ANXA2 and α-Syn bind to cholesterol and PA. Therefore, there could be some degree of cross-talk between their homeostasis and lipid-mediated interactions, which is unknown and could be relevant in our CHIP model.

### b. α-Synuclein aggregates

Another mechanism of α-Syn-induced pathology mediated by lipids relies on the action of α-Syn pathogenic aggregates. Different membrane properties (e.g. increased membrane fluidity, short hydrocarbon chains, anionic phospholipids such as PI, PUFA, rafts, and cholesterol) favour the aggregation kinetics of α-Syn[260,268,269]. Considering the changes in phospholipid composition observed in our CHIP model, membrane fluidity may be affected, which can influence α-Syn aggregation. Likewise, although not directly addressed, changes in cholesterol could also influence the interaction between α-Syn oligomers and membranes.

Monomeric α-Syn can become stabilised at membranes promoting its multimerization[264]. Different mechanisms have been proposed for lipid-induced aggregation. Firstly, lipids confer α-Syn to a small and/or two-dimensional surface (e.g. vesicle), increasing the effective concentration and driving aggregation through mass action. Mechanistically, this brings the more C-terminal unstructured regions into close proximity, which facilitates nucleation of inter-molecular β-sheet structure, forming oligomers. Secondly, lipid-induced conformational changes (i.e. an α-helical state) can favour intermolecular interactions leading to aggregation. These mechanisms are mutually non-exclusive and could have a cumulative effect[26].

As oligomers, α-Syn can disrupt membranes by forming pores in the PM (Figure 7.7)[264,269,270]. Pores result in increased permeability, allowing a detrimental calcium influx that drives cell death[269]. Pore formation is a characteristic of other amyloid proteins, such as Aβ, thus could be a pathomechanism in common across neurodegenerative diseases. Moreover, aggregate-induced permeabilization of endolysosomal membranes has been proposed as a mechanism for cell-to-cell transmission in neurodegeneration[271]. Importantly, we do not observe LB-like aggregates.

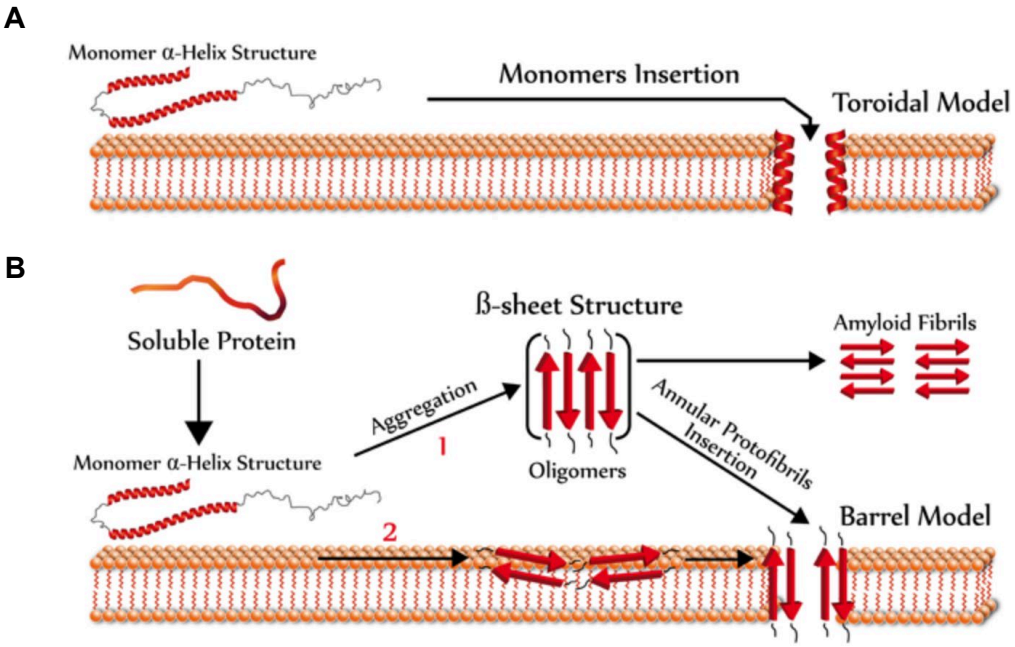


**Figure 7.7: Pore formation in the membrane by oligomeric α-synuclein**
α-Syn oligomers can induce pore formation by two mechanisms:
**A)** Toroidal model: involves the sequential binding of α-Syn monomers to the membrane, resulting in the formation of pores/channels with a α-helical conformation.
**B)** Barrel model: α-Syn oligomers with a β-sheet-rich structure form ring structures with a central pore.
These mechanisms are dose-dependent and the end-effect is increase membrane permeabilization.

(Pacheco *et al.*[270])

### c. CHIP, lipid homeostasis and α-Synuclein pathology

Taken together, lipids play a critical role in α-Syn homeostasis and pathology[269]. Therefore, dysregulation of lipid composition and alternations to the protein:lipid interactome are likely to influence pathology. We have shown preliminary evidence that CHIP, possibly through its E3 ligase functions, could influence membrane integrity and resilience to injury. Thus, CHIP could function in the regulation of membrane homeostasis by influencing lipid composition (our CHIP model shows differential lipidomics), or by regulating proteins involved in the maintenance of membrane integrity (such as the Annexin family). The exact mechanism explaining how these changes influence membrane properties, α-Syn pathology and cell functioning is unclear.

Lipidomic changes in the context of increased α-Syn expression (*SNCA* triplication), in particular, are likely to be of biological significance. Recently, it has been shown that modulation of lipid metabolism pharmacologically influenced α-Syn aggregation and pathology, possibly by preventing α-Syn:lipid interactions[272,273]. Moreover, age-related changes in lipid composition captures disease proteins (including α-Syn) in a membrane-bound state that precedes protein deposition, highlighting the important of lipid changes in disease progression[274]. The effect of lipid dysregulation in the α-Syn pathological cascade has been proposed:

1. Normal conditions: monomeric and tetrameric α-Syn are in equilibrium.
2. Mild α-Syn accumulation: α-Syn itself triggers changes in lipid homeostasis. These are counteracted by cellular compensatory mechanisms.
3. Great α-Syn accumulation accompanied by pronounced lipid dysregulation: the effects of prolonged α-Syn accumulation exceed compensatory mechanism, causing lipid accumulation, which activates the UPR and inhibits membrane trafficking. The threshold is influenced by the cell's lipid homeostasis (e.g. risk factors affecting lipid metabolism tend to promote α-Syn accumulation)[272].

Our CHIP model is in an α-Syn overexpression background. CHIP deletion may induce the unfavourable lipidomic changes that promote α-Syn toxicity, either directly or indirectly. Given the absence of LB-like aggregates, mechanisms driven by the

monomeric rather than aggregates of α-Syn may take place. Therefore, our model could mimic the lipid-mediated α-Syn toxicity seen in the 3K model. If this proves to be true (future studies are necessary), CHIP KO neurons may have poor membrane integrity due to enhanced lipid- and α-Syn-dependent deleterious effects. Thus, through lipid changes, CHIP may regulate α-Syn homeostasis and be neuroprotective against α-Syn-induced toxicity.

Other than through modulation of the lipid composition, this thesis suggests that α-Syn homeostasis could be regulated by CHIP-dependent ubiquitination (Chapter 6) (Figure 7.8). The occurrence of CHIP-dependent ubiquitination of α-Syn in cells at endogenous conditions still needs to be confirmed, and its physiological relevance addressed. α-Syn binding to lipids is achieved through electrostatic interactions between the positively charged lysine residues and negatively charged phospholipid headgroups (such as PS and PA)[275]. Therefore, ubiquitination could abolish the contact of the K60 side chain with phospholipid(s), potentially influencing its interaction with membranes and, in turn, its lipid-mediated functions in health and/or disease. Moreover, K60 lies at the interface between the lipid-binding N-terminal region and the aggregation-prone NAC region, thus ubiquitination could also modulate (and possibly inhibit) aggregation of α-Syn. If this proves to be correct, CHIP could be neuroprotective by preventing lipid-mediated toxicity and/or shifting α-Syn equilibrium from oligomers towards the monomers.

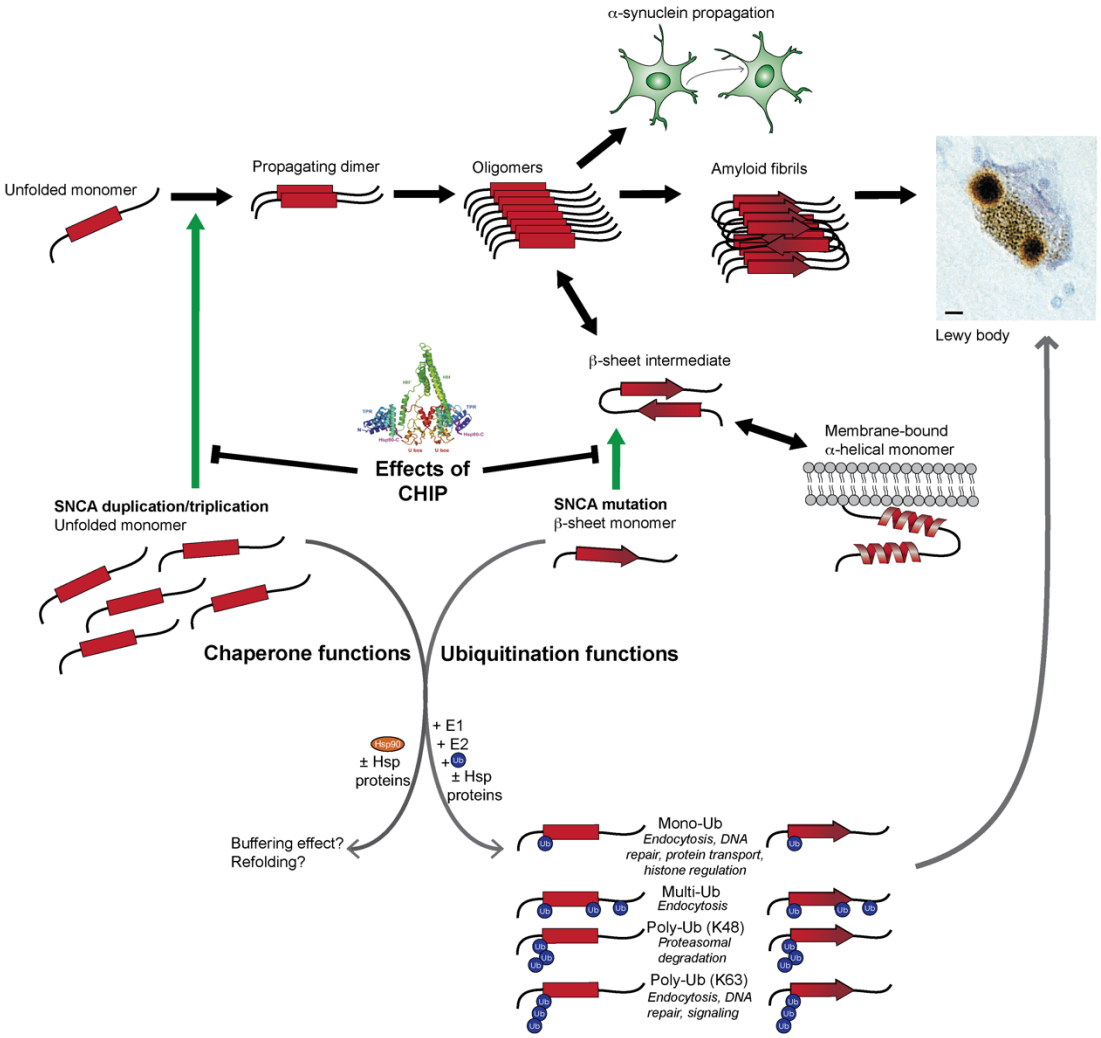


**Figure 7.8: α-Synuclein aggregation process and possible ways in which CHIP could regulate α-synuclein homeostasis**

α-Syn is prone to aggregate and this is enhanced by SNCA multiplications (through a shift in the equilibrium of α-Syn) and mutations. Through its chaperone and/or E3 ligase functions, CHIP could prevent the aggregation of α-Syn. Eventually Lewy bodies form, containing ubiquitinated α-Syn species. The dynamic conformations of α-Syn are represented: unfolded (red rectangle), β-sheet and α-helical.

(LB image derived from: Spillantini *et al.*[24]; crystal structure of CHIP derived from: Zhang *et al.*[39])

### 7.2.3 Potential neuroprotective effects of CHIP

Beyond its reported roles in α-synucleinopathies, over the years CHIP became an established neuroprotective protein[15,49,78,149], largely through its anti-ageing properties (the biggest risk factor of neurodegenerative diseases). We now question whether CHIP-mediated changes in the homeostasis of proteins and lipids could contribute to its neuroprotective functions.

In line with the established beneficial role of CHIP in cellular health, we would expect that CHIP-mediated regulation of its protein targets ensures their adequate homeostasis, preventing proteotoxicity. As a protector of ER stress, CHIP may regulate longevity by influencing the UPR[65]. Supporting evidence of the relationship between the UPR and life-span is the mdt-15 loss-of-function worm model, which has a constitutively activated UPR and reduced lifespan[253]. Interestingly, the long-lived INSR-mutant worms have altered UPR threshold[253] and CHIP has been proposed as a regulator of the INSR[62]. Furthermore, the relationship between lipid metabolism, stress response and longevity has also been proposed[253]. Mdt-15 is essential for the expression of genes involved in fatty acid metabolism and stress responses. Beyond having a reduced lifespan, Mdt-15 worms are more sensitive to stress[253]. Interestingly, both of these phenotypes were also observed in CHIP KO mice[14,15,104].

Unexpectedly, we found that the lipidomic signature of CHIP KO SH-SY5Y cells shares some similarities with the lipidomic changes observed in neurodegeneration. This opens the question whether CHIP-mediated regulation of lipid composition contributes to its neuroprotective functions. As in AD mouse models and the cortex of AD patients[256], CHIP KO cells show a decrease in PA (including 38:4) and PS. Lipid dysregulation during the course of neurodegeneration results in altered membrane properties[256], causing for example endolysosomal membrane damage and organellar dysfunction – seen in various neurodegenerative diseases, including AD and LBD[257,271]. Genes involved in lipid metabolism and cellular membrane damage have been associated with AD[256] and PD[269]. Additionally, although we have not directly quantified cholesterol content in our CHIP model, CHIP KO cells displayed enhanced sensitivity to a cholesterol-specific injury. Cholesterol levels were reported to be increased in the cortex of AD patients[256] and in exosomes of carriers of ε4 allele of apolipoprotein E[256,257].

Changes in lipid composition can contribute to neuronal vulnerability and increased risk of neurodegeneration[257]. This is not surprising, as lipid membrane integrity is crucial for the maintenance of membrane potential[269], hence neuronal function. In fact, it has been suggested that lipid dysregulation is an early pathological event in neurodegeneration[271], thus identification of early protein-lipid interactions could be of interest[274]. The modulation of lipid metabolism has been shown to have neuroprotective effects[273] and may be particularly relevant for cortical neurons, which have been shown to correlate with longevity[276]. Long-lived cortical neurons accumulate damage that progressively impairs their function[276] and is likely to compromise membrane integrity. Therefore, if lipid changes prove to be CHIP-dependent and of biological significance, they may contribute to the neuroprotective effects of CHIP, which remain largely unknown.

## 7.3 Future work

### 7.3.1 CHIP-dependent ubiquitination of substrates identified

#### a. Investigate whether the CHIP:substrate interaction is direct or indirect

We have identified a novel interaction between CHIP and ANXA2 (and, to a more preliminary degree, between CHIP and S100-A11). This was shown by co-IP and PLA assays. Given the limitations of the co-IP experiment, an additional method to confirm that CHIP and ANXA2 are in close proximity in cells should be performed. For example, proteins can be cross-linked prior to cell lysis and analysed by SEC and WB, to elucidate whether CHIP and ANXA2 are within the same fraction. If within a complex, the SEC fractions containing ANXA2 and CHIP could be analysed by MS and WB to identify binding partners.

However, none of these methods inform us whether these proteins are interacting directly or indirectly (being, for example, within the same complex). Binding site mapping, using a peptide library analysed by affinity chromatograph or ELISA and HDX-MS, would provide evidence of the kinetics of their interaction *in vitro*[77]. Regions

responsible for the interaction could be subsequently mutated to abolish CHIP:ANXA2 *in vitro* and *in situ*, for validation purposes.

### b. Validation of ubiquitination sites

Subsequent work would validate the ubiquitination sites mapped on CHIP and its substrates, α-Syn and ANXA2, using mutational experiments both *in vitro* and *in situ* – a common mechanism to confirm candidate ubiquitination sites[141,143]. This is particularly relevant seeing that these sites have not been previously reported. Accordingly, mapping of ubiquitination by MS is regarded as an effective technique for the identification of novel targets and sites (having reported 72% of substrates and 92% of sites identified as novel[143]). Importantly, previous studies have reported similarities between ubiquitination sites mapped *in vitro* and those found in human cells (e.g. CHIP-dependent ubiquitination of the INSR at K1047 was mapped *in vitro* and once mutated in human cells the turnover of the receptor was compromised)[62].

Furthermore, future experiments would assess whether these ubiquitination events happen endogenously in cells, under what conditions and with that cellular consequences. The relationship between ANXA2 ubiquitination and the ANXA2:S100-A11 interactome, lipid homeostasis and membrane integrity can also be assessed.

### c. Preliminary data to decipher the fate of ubiquitination species

Since ubiquitinated ANXA2 species were detected *in vitro* and potentially *in situ*, and may be CHIP-dependent, we performed preliminary experiments to unravel the fate of ubiquitinated ANXA2, hence elucidating its cellular significance. Cells were treated with a panel of inhibitors of ubiquitination-mediated and/or -dependent pathways to see if any definite effects on ubiquitinated ANXA2 species (evaluated by PLA; Figure 7.9). Endosomal/lysosomal inhibitors (BafA1 and chloroquine), the autophagy inhibitors (BafA1 and 3-MA), endocytosis inhibitor (V34-2) and proteasomal inhibitors (MG-132 and Lactacystin) were used. Blocking the pathway to which ubiquitinated ANXA2 is destined to would interfere with the homeostasis of ANXA2. The autophagy inhibitors (BafA1 and 3-MA) significantly decreased Ub:ANXA2 PLA signal, while the

proteasomal inhibitors (Lactacystin and MG-132) increased it. Ubiquitinated ANXA2 is likely accumulate when its degradation mechanism is impaired. This rational would suggest that ANXA2 turnover is mediated by proteasomal degradation.

It is important to note that, for practical reasons, the panel of inhibitors were tested in two groups (independent experiments), each with control conditions included (DMSO treatment). The big relative difference in the levels of Ub:ANXA2 between DMSO treated cells can be due to multiple factors, including batch-to-batch variability of the PLA kit. Since changes in the abundance of ubiquitinated ANXA2 species were detected in this preliminary experiment, this could be addressed further to better understand the mechanism underlying CHIP-dependent regulation of ANXA2 homeostasis. Future work would repeat this experiment (increasing the *n* number might overcome such batch-to-batch variability observed), inhibit these pathways with other pharmacological agents and include CHIP KO cells (potentially as negative controls, if ubiquitination of ANXA2 is CHIP-dependent). The protein levels of ANXA2 should also be measured. However, pharmacological-inhibition of such tightly regulated process, such as ubiquitination, is complicated to interpret due to the limitations of the inhibitors (including off-targets) and regulatory feedback loops. Alternatively (or in parallel), the ubiquitinated sites of ANXA2 could be mutated in cells and its homeostasis investigated.

As a preliminary approach to understand the effect of ANXA2 ubiquitination on the membrane-related functions of ANXA2, as a heterotetramer with S100-A11, the PLA assessing ANXA2:S100-A11 was also conducted following drug treatments (Figure 7.10). Only BafA1 treatment increased the ANXA2:S100-A11 PLA signal, thus it is possible that altered ANXA2 homeostasis influences its functional interactome. However, this experiment needs to be repeated to increase the *n* number, before conclusions are drawn.

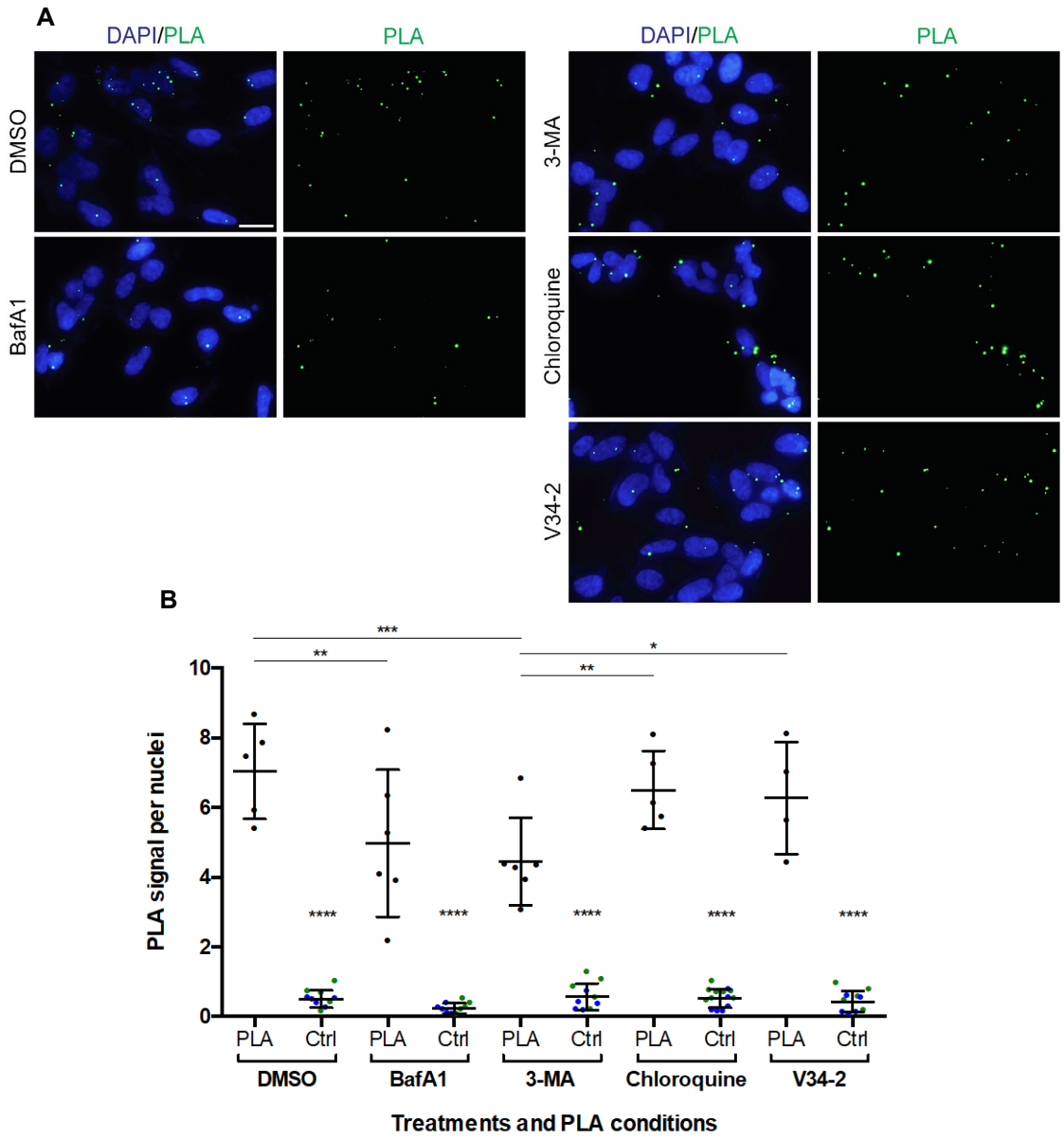


**Figure 7.9: Effect of inhibiting ubiquitin-dependent pathways on the interaction of Annexin A2 and ubiquitin, using PLA** (preliminary results)
Undifferentiated SH-SY5Y WT cells were treated with different inhibitors of ubiquitination-mediated pathways.
**A&B)** Bafilomycin A1 (BafA1): autophagy and endosomal/lysosomal inhibitor. 3-Methyladenine (3-MA): autophagy inhibitor. Chloroquine: endosomal/lysosomal inhibitor. V34-2: endosomal inhibitor.
**A)** Cells were fixed in 4% PFA and then methanol. One well per condition was stained with anti-ANXA2 pAb and anti-Ubiquitin mAb (P4D1) antibodies (referred to as "PLA" in **B**). PLA signal (puntae in green) were quantified using ImageJ in a semiautomated manner and normalised by the number of nuclei (stained with DAPI) within a field of view. In parallel, two controls were included per treatment (grouped under "Ctrl" in **B**). Wells were incubated with either antibodies alone (ANXA2 only in green and Ubiquitin only in blue). Axio Imager, Zeiss, 63x objective. Scale bars, 20 µm
**B)** Quantifications of PLA signal per nuclei of different cell lines represented in the dot plot as mean ± SD. One-way ANOVA with Holm-Sidak's multiple comparisons test (comparisons between PLA and Ctrl conditions per cell line is indicated above each Ctrl), $*P < 0.05$, $**P < 0.005$, $***P < 0.0005$, $****P < 0.0001$, n ≥ 4 images per biological duplicate and n = 5 images per control condition per treatment.

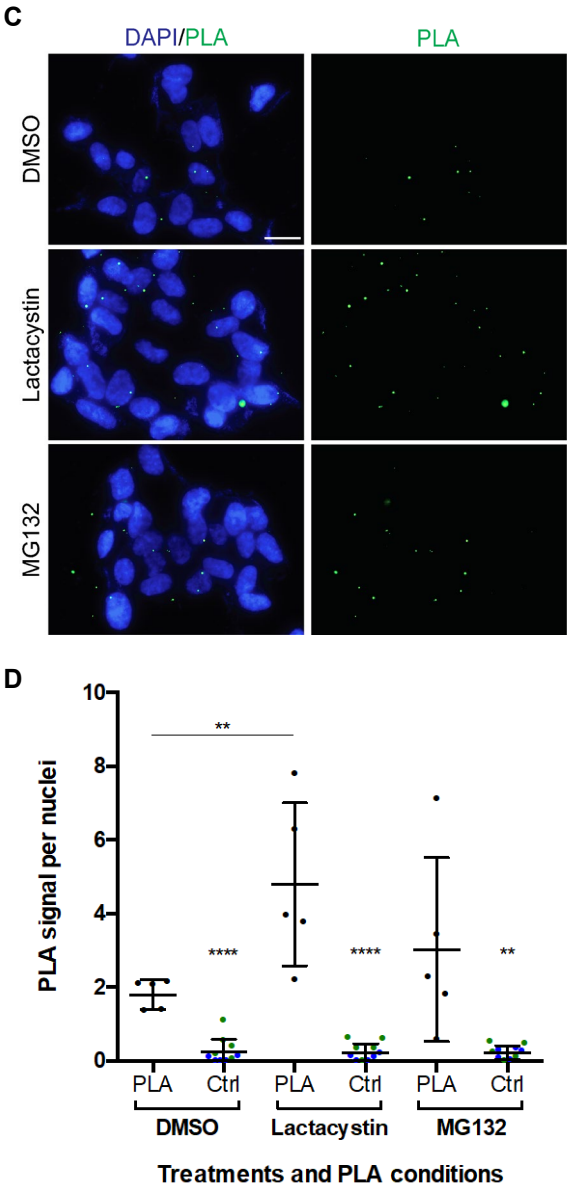


**Figure 7.9** *(continued)*
Undifferentiated SH-SY5Y WT cells were treated with different inhibitors of ubiquitination-mediated pathways.
**C&D)** Lactacystin and MG-132 are proteasomal inhibitors.
**C)** Cells were fixed in 4% PFA and then methanol. One well per condition was stained with anti-ANXA2 pAb and anti-Ubiquitin mAb (P4D1) antibodies (referred to as "PLA" in **D**). PLA signal (puntae in green) were quantified using ImageJ in a semiautomated manner and normalised by the number of nuclei (stained with DAPI) within a field of view. In parallel, two controls were included per treatment (grouped under "Ctrl" in **D**). Wells were incubated with either antibodies alone (ANXA2 only in green and Ubiquitin only in blue). Axio Imager, Zeiss, 63x objective. Scale bars, 20 µm.
**D)** Quantifications of PLA signal per nuclei of different cell lines represented in the dot plot as mean ± SD. One-way ANOVA with Holm-Sidak's multiple comparisons test (comparisons between PLA and Ctrl conditions per cell line is indicated above each Ctrl), $*P < 0.05$, $**P < 0.005$, $***P < 0.0005$, $****P < 0.0001$, n ≥ 4 images per biological duplicate and n = 5 images per control condition per treatment.

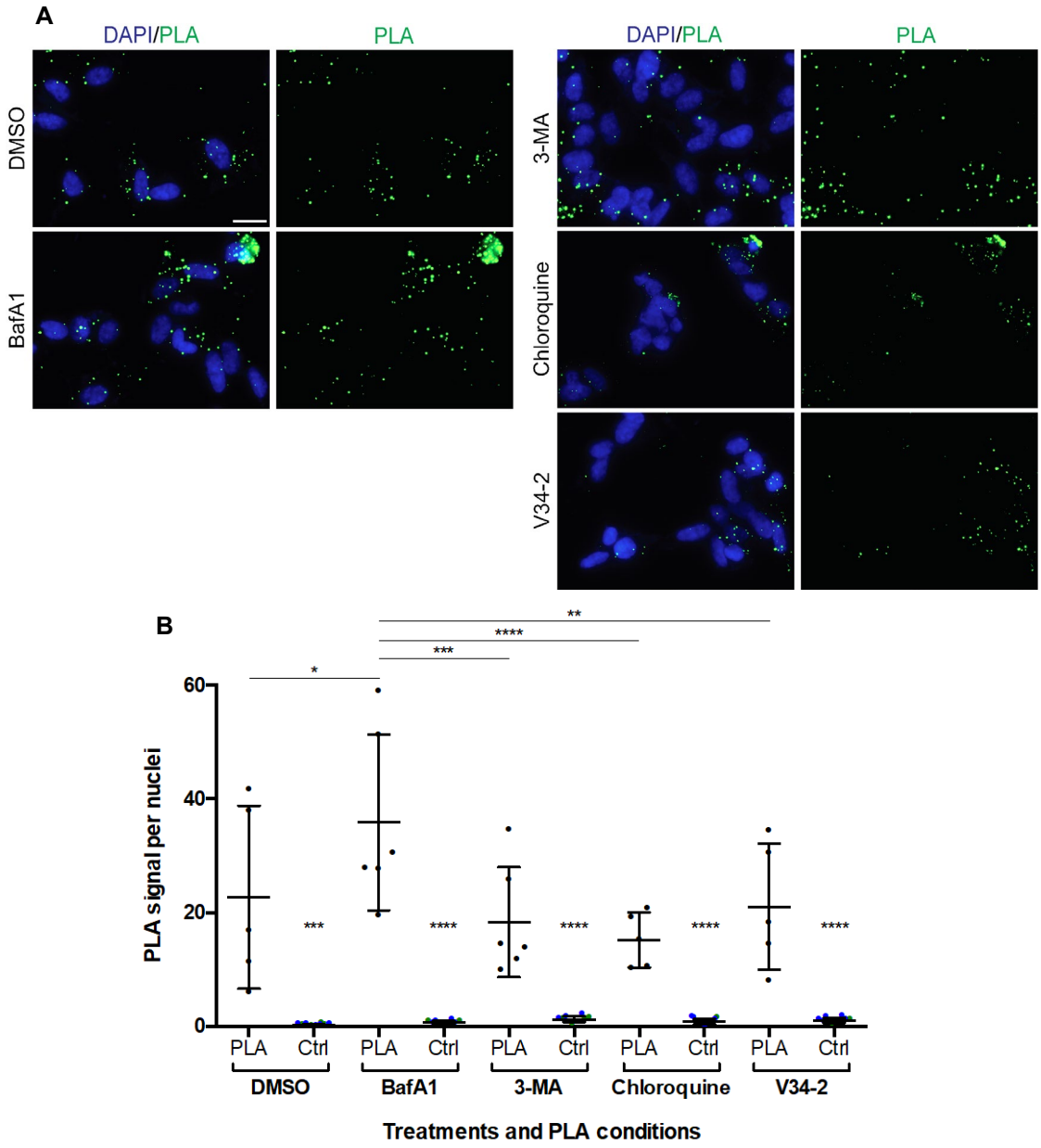


**Figure 7.10: Effect of inhibiting ubiquitin-dependent pathways on the interaction of Annexin A2 and S100-A11, using PLA** (preliminary results)
Undifferentiated SH-SY5Y WT cells were treated with different inhibitors of ubiquitination-mediated pathways. Bafilomycin A1 (BafA1): autophagy and endosomal/lysosomal inhibitor. 3-Methyladenine (3-MA): autophagy inhibitor. Choloquine: endosomal/lysosomal inhibitor. V34-2: endosomal inhibitor.
**A)** Cells were fixed in acetone & methanol. One well per condition was stained with anti-ANXA2 mAb and anti-S100-A11 pAb antibodies (referred to as "PLA" in **B**). PLA signal (puntae in green) were quantified using ImageJ in a semiautomated manner and normalised by the number of nuclei (stained with DAPI) within a field of view. In parallel, two controls were included per treatment (grouped under "Ctrl" in **B**). Wells were incubated with either antibodies alone (S100-A11 only in green and ANXA2 only in blue). Axio Imager, Zeiss, 63x objective. Scale bar, 20 µm.
**B)** Quantifications of PLA signal per nuclei of different cell lines represented in the dot plot as mean ± SD. One-way ANOVA with Holm-Sidak's multiple comparisons test (comparisons between PLA and Ctrl conditions per cell line is indicated above each Ctrl), $*P < 0.05$, $**P < 0.005$, $***P < 0.0005$, $****P < 0.0001$, $n = 5$ images per biological duplicate and $n = 5$ images per control condition per treatment.

## 7.3.2 Modulating CHIP

### a. ScFv-induced conformational changes

Despite the exciting potential of scFv in research, extra validation of the scFv antibodies both *in vitro* and *in situ* is necessary. It is important to confirm the binding site of scFv antibodies on CHIP (e.g. epitope mapping using a CHIP peptide library) and their effect on its structure by other methods (e.g. SEC in parallel to native WB), and this work is ongoing. Also, *in vitro* ubiquitination assays with scFv led us to the hypothesis that different multimerization forms of CHIP have varying substrate specificities, which could be dictated by its conformational state. Future studies will focus on testing this hypothesis with different folded and unfolded substrates and translate this to cell models. Furthermore, given the allosteric regulation between the TPR and U-box domains of CHIP, it is important to investigate the effect of scFv antibodies on the chaperone functions of CHIP (e.g. using a luciferase-based protein denaturing assay).

### b. Intrabodies

Preliminary experiments evaluated the expression and subcellular localisation of tagged scFv intrabodies by IF (Figure 7.11). It seems that in WT cells, scFv localises to the cytoplasm and nucleus. In contrast, the staining seems stronger and more restricted to the nucleus in CHIP KO cells. Therefore, it is possible that, in the presence of its target, CHIP, scFv localises to the cytoplasm potentially to interact with CHIP, whilst in its absence scFv mislocalises. Future experiments would assess this further and test whether transfected scFv and endogenous CHIP interact (e.g. by PLA and IP/pull-down assays).

Given the finding that scFv induces ANXA2 ubiquitination *in vitro*, I sought to test if Ub:ANXA2 PLA signal is enhanced in scFv-expressing cells (Figure 7.12). A preliminary data supports this hypothesis, but further experiments are needed for conclusions to be drawn. Although single-cell analysis is possible with scFv intrabodies, the transfection efficiency requires optimisation prior to whole-cell analysis. Once achieved, whole proteomic analysis by SWATH-MS of WT cells with and without scFv intrabodies could inform on substrates that are differentially

modulated by CHIP, when its activity is influenced by the scFv, compared to when CHIP is ablated.

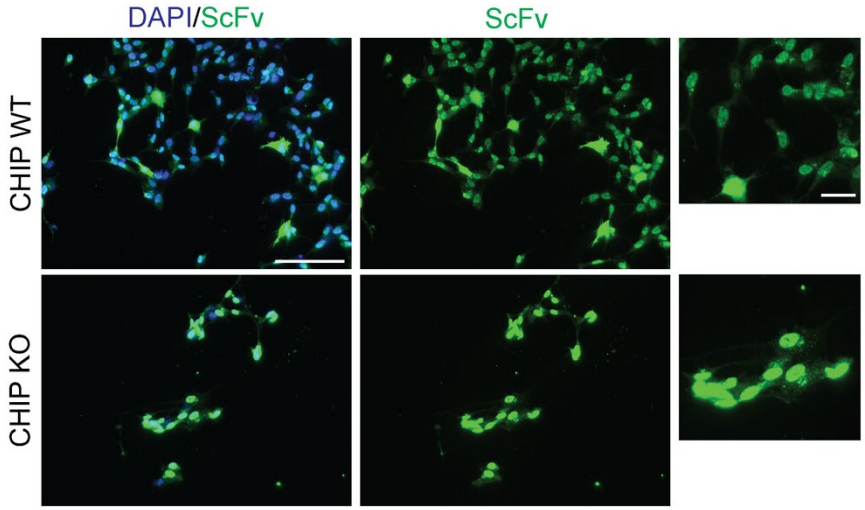


**Figure 7.11: ScFv expression in cells**
Undifferentiated CHIP KO and WT SH-SY5Y cells were transiently transfected with V5-tagged 11F scFv. Cells were fixed with 4% PFA and stained with anti-V5 mAb. Axio Imager, *Zeiss*, 20x objective. Scale bars, 100 µm and 25 µm (inlet).

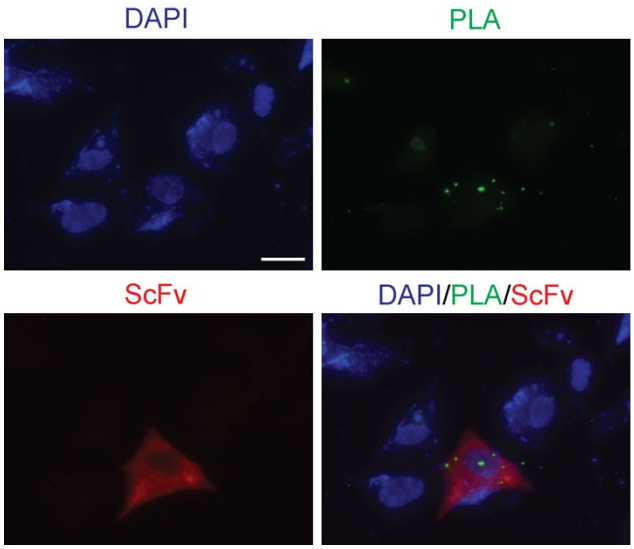


**Figure 7.12: ScFv expression enhances interaction between ubiquitin and Annexin A2 by PLA** (preliminary results)
Undifferentiated CHIP WT SH-SY5Y cells were transiently transfected with V5-tagged 11F scFv. Cells were fixed with 4% PFA and then methanol and stained with anti-V5 pAb (1:500, goat), anti-ANXA2 pAb (1:500, rabbit) and anti-Ubiquitin mAb (P4D1, mouse) (1:100) antibodies. PLA with anti-Rabbit and anti-Mouse secondary antibodies was performed to identify Ub in close proximity with ANXA2 (indicated by the green puncta). Cells were also incubated with a 630-conjugated anti-Goat secondary antibody to identify cells expressing the scFv antibody (shown in red). Axio Imager, Zeiss, 63x objective. Scale bar, 10 µm.

### 7.3.3 CHIP and lipid homeostasis

#### a. Cholesterol

As discussed, there is evidence of ANX-dependent regulation of cholesterol metabolism[258,259], proof-of-concept that CHIP may be affected by cholesterol regulation (via lanosterol administration[262]) and reports of cholesterol dysregulation in ageing and neurodegenerative diseases[257,258,260]. Together, this makes it quite interesting that our CHIP KO models are significantly more sensitive to digitonin-induced membrane damage (cholesterol-specific insult). Ongoing studies are evaluating the levels of cholesterol in our CHIP KO models and future lipidomic analysis will quantify cholesterol content.

#### b. Polyunsaturated fatty acids

We performed preliminary analysis of the polyunsaturated fatty acids (PUFAs) content in our undifferentiated SH-SY5Y CHIP model in collaboration with Dr Irena Dapic and Dr Laura Bindila[‖] (Figure 7.13). Our lipidomic analysis revealed a subtle increase in docosahexaenoic acid (DHA) in CHIP KO cells, as well as pronounced decreases in eicosapentaenoic acid (EPA) and docosapentaenoic acid (DPA). These omega-3 PUFA may have significant neuroprotective effects in acute neurological injury[201] and are decreased in neurodegenerative diseases, including AD and PD[199,277]. CHIP expression correlated with the neuroprotective EPA, which could be part of the molecular mechanisms underlying the neuroprotective functions of CHIP. Interestingly, EPA supplement showed significantly increased PE, PS and PI levels in the brain[199]. Likewise, CHIP KO cells have decreased EPA levels that correlate with PS, PI and PE total levels. Future work would repeat this experiment, assay more PUFAs, and include the SH-SY5Y lines stably expressing mutant forms of CHIP, for a more comprehensive investigation.

[‖] Institute for Physiological Chemistry, University Medical Center Mainz, Germany

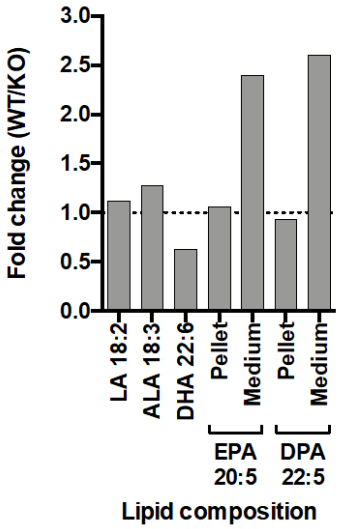


**Figure 7.13: Composition of polyunsaturated fatty acids of CHIP KO and WT undifferentiated SH-SY5Y cells** (preliminary results)
Fatty acid composition is represented as fold changes (WT/KO). For EPA and DPA both free (medium) and esterified (pellet) forms are represented. Linoleic acid (LA, omega-6), α-linoleic acid (ALA, omega-3), docosahexaenoic acid (DHA, omega-3), eicosapentaenoic acid (EPA, omega-3) and docosapentaenoic acid (DPA, omega-3).

## 7.3.4 CHIP and calcium homeostasis

Most membrane-related proteins significantly changed in the SWATH-MS analysis of patient-derived cortical neurons with and without CHIP expression are also regulated by calcium, including ANXA2. When conducting PM damage assays in the absence of calcium, in attempt to isolate sensitivity to injury from ability to repair, CHIP KO iPSC seemed to be less tolerant to calcium withdrawal. Given these two observations, it would be interesting to investigate calcium homeostasis in our CHIP models. At present, we cannot exclude the possibility that changes in phospholipid- and calcium-binding proteins and membrane sensitivity could be driven by differences in calcium handling. It has been reported that reduced calcium can result in protein misfolding and activation of the UPR, which in turn alters lipid synthesis[26].

## 7.3.5 Are the observed membrane defects and changes in Annexin homeostasis related?

Although there is supporting evidence in the literature relating Annexin dysregulation with poor membrane integrity, it is unclear whether the differences in membrane and

Annexin homeostasis observed in our models have a causal relationship and are CHIP-dependent. Supporting experiments are required to assess the following questions: is the CHIP KO + H260Q cell line (expressing the E3 ligase-dead mutant) more sensitive to injury due to diminished Ub-ANXA2 species and/or reduced ANXA2:S100-A11 interaction? Is ANXA2 ubiquitination important for the ANXA2 interactome? Are CHIP-dependent and Annexin-independent changes in lipid profile underlying the differences in integrity, which in turn influence the homeostasis of Annexins as a protective mechanism?

# References


1 Pokrzywa W, Lorenz R, Hoppe T. Chaperone-directed ubiquitylation maintains proteostasis at the expense of longevity. *Worm* 2017; **6**: e1371403.

2 Brehme M, Voisine C, Rolland T, Wachi S, Soper JH, Zhu Y *et al.* A chaperome subnetwork safeguards proteostasis in aging and neurodegenerative disease. *Cell Rep* 2014; **9**: 1135–50.

3 Kevei É, Pokrzywa W, Hoppe T. Repair or destruction-an intimate liaison between ubiquitin ligases and molecular chaperones in proteostasis. *FEBS Lett* 2017; **591**: 2616–2635.

4 Ehlers MD. Activity level controls postsynaptic composition and signaling via the ubiquitin-proteasome system. *Nat Neurosci* 2003; **6**: 231–242.

5 Upadhya SC, Ding L, Smith TK, Hegde AN. Differential regulation of proteasome activity in the nucleus and the synaptic terminals. *Neurochem Int* 2006; **48**: 296–305.

6 Segref A, Hoppe T. Think locally: control of ubiquitin-dependent protein degradation in neurons. *EMBO Rep* 2009; **10**: 44–50.

7 Cuervo AM, Wong E. Chaperone-mediated autophagy: roles in disease and aging. *Cell Res* 2014; **24**: 92–104.

8 Amm I, Sommer T, Wolf DH. Protein quality control and elimination of protein waste: The role of the ubiquitin–proteasome system. *Biochim Biophys Acta - Mol Cell Res* 2014; **1843**: 182–196.

9 Cell Signaling Technology. *CST Guide: Pathways & Protocols*. Cell Signaling Technology Inc., 2015.

10 De Vrij FM, Sluijs JA, Gregori L, Fischer DF, Hermens WT, Goldgaber D *et al.* Mutant ubiquitin expressed in Alzheimer's disease causes neuronal death. *FASEB J* 2001; **15**: 2680–8.

11 Tan Z, Sun X, Hou F-S, Oh H-W, Hilgenberg LGW, Hol EM *et al.* Mutant ubiquitin found in Alzheimer's disease causes neuritic beading of mitochondria in association with neuronal degeneration. *Cell Death Differ* 2007; **14**: 1721–1732.

12 Cummings CJ, Reinstein E, Sun Y, Antalffy B, Jiang Y, Ciechanover A *et al.* Mutation of the E6-AP ubiquitin ligase reduces nuclear inclusion frequency while accelerating polyglutamine-induced pathology in SCA1 mice. *Neuron* 1999; **24**: 879–92.

13 Hayer SN, Deconinck T, Bender B, Smets K, Züchner S, Reich S *et al.* STUB1/CHIP mutations cause Gordon Holmes syndrome as part of a widespread multisystemic neurodegeneration: evidence from four novel mutations. *Orphanet J Rare Dis* 2017; **12**: 31.

14 Min J-N, Whaley RA, Sharpless NE, Lockyer P, Portbury AL, Patterson C. CHIP Deficiency Decreases Longevity, with Accelerated Aging Phenotypes Accompanied by Altered Protein Quality Control. *Mol Cell Biol* 2008; **28**: 4018–4025.

15 Palubinsky AM, Stankowski JN, Kale AC, Codreanu SG, Singer RJ, Liebler DC *et al.* CHIP Is an Essential Determinant of Neuronal Mitochondrial Stress Signaling. *Antioxid Redox Signal* 2015; **23**: 535–549.

16 Gamerdinger M, Hajieva P, Kaya AM, Wolfrum U, Hartl FU, Behl C. Protein quality control during aging involves recruitment of the macroautophagy pathway by BAG3. *EMBO J* 2009; **28**: 889–901.

17 Vilchez D, Morantte I, Liu Z, Douglas PM, Merkwirth C, Rodrigues APC *et al.* RPN-6 determines C. elegans longevity under proteotoxic stress conditions. *Nature* 2012; **489**: 263–268.

18 Tomaru U, Takahashi S, Ishizu A, Miyatake Y, Gohda A, Suzuki S *et al.* Decreased Proteasomal Activity Causes Age-Related Phenotypes and Promotes the Development of Metabolic Abnormalities. *Am J Pathol* 2012; **180**: 963–972.

19 Walther DM, Kasturi P, Zheng M, Pinkert S, Vecchi G, Ciryam P *et al.* Widespread Proteome Remodeling and Aggregation in Aging C. elegans. *Cell* 2015; **161**: 919–932.

20 Paul I, Ghosh MK. A CHIPotle in physiology and disease. *Int J Biochem Cell Biol* 2015; **58**: 37–52.

21 Martín MJ, Tolosa E, Campdelacreu J. Clinical overview of the synucleinopathies. *Mov Disord* 2003; **18**: 21–27.
22 Brundin P, Ma J, Kordower JH. How strong is the evidence that Parkinson's disease is a prion disorder? *Curr Opin Neurol* 2016; **29**: 459–66.
23 Olanow CW, Brundin P. Parkinson's Disease and Alpha Synuclein: Is Parkinson's Disease a Prion-Like Disorder? *Mov Disord* 2013; **28**: 31–40.
24 Spillantini MG, Schmidt ML, Lee VM-Y, Trojanowski JQ, Jakes R, Goedert M. α-Synuclein in Lewy bodies. *Nature* 1997; **388**: 839–840.
25 Shin Y, Klucken J, Patterson C, Hyman BT, McLean PJ. The Co-chaperone Carboxyl Terminus of Hsp70-interacting Protein (CHIP) Mediates α-Synuclein Degradation Decisions between Proteasomal and Lysosomal Pathways. *J Biol Chem* 2005; **280**: 23727–23734.
26 Dikiy I, Eliezer D. Folding and misfolding of alpha-synuclein on membranes. *Biochim Biophys Acta - Biomembr* 2012; **1818**: 1013–1018.
27 Lashuel HA, Overk CR, Oueslati A, Masliah E. The many faces of α-synuclein: from structure and toxicity to therapeutic target. *Nat Rev Neurosci* 2013; **14**: 38–48.
28 Wirths O, Bayer TA. α-Synuclein, Aβ and Alzheimer's disease. *Prog Neuro-Psychopharmacology Biol Psychiatry* 2003; **27**: 103–108.
29 Stefanis L. α-Synuclein in Parkinson's disease. *Cold Spring Harb Perspect Med* 2012; **2**: a009399.
30 Dehay B, Bourdenx M, Gorry P, Przedborski S, Vila M, Hunot S *et al.* Targeting α-synuclein for treatment of Parkinson's disease: mechanistic and therapeutic considerations. *Lancet Neurol* 2015; **14**: 855–866.
31 Li W, West N, Colla E, Pletnikova O, Troncoso JC, Marsh L *et al.* Aggregation promoting C-terminal truncation of -synuclein is a normal cellular process and is enhanced by the familial Parkinson's disease-linked mutations. *Proc Natl Acad Sci* 2005; **102**: 2162–2167.
32 Larson ME, Sherman MA, Greimel S, Kuskowski M, Schneider JA, Bennett DA *et al.* Soluble -Synuclein Is a Novel Modulator of Alzheimer's Disease Pathophysiology. *J Neurosci* 2012; **32**: 10253–10266.
33 Fairfoul G, McGuire LI, Pal S, Ironside JW, Neumann J, Christie S *et al.* Alpha-synuclein RT-QuIC in the CSF of patients with alpha-synucleinopathies. *Ann Clin Transl Neurol* 2016; **3**: 812–818.
34 Gallegos S, Pacheco C, Peters C, Opazo CM, Aguayo LG. Features of alpha-synuclein that could explain the progression and irreversibility of Parkinson's disease. *Front Neurosci* 2015; **9**: 59.
35 Dickey CA, Kamal A, Lundgren K, Klosak N, Bailey RM, Dunmore J *et al.* The high-affinity HSP90-CHIP complex recognizes and selectively degrades phosphorylated tau client proteins. *J Clin Invest* 2007; **117**: 648–658.
36 Breydo L, Wu JW, Uversky VN. α-Synuclein misfolding and Parkinson's disease. *Biochim Biophys Acta - Mol Basis Dis* 2012; **1822**: 261–285.
37 Tetzlaff JE, Putcha P, Outeiro TF, Ivanov A, Berezovska O, Hyman BT *et al.* CHIP Targets Toxic α-Synuclein Oligomers for Degradation. *J Biol Chem* 2008; **283**: 17962–17968.
38 Pakdaman Y, Sanchez-Guixé M, Kleppe R, Erdal S, Bustad HJ, Bjørkhaug L *et al.* In vitro characterization of six STUB1 variants in spinocerebellar ataxia 16 reveals altered structural properties for the encoded CHIP proteins. *Biosci Rep* 2017; **37**. doi:10.1042/BSR20170251.
39 Zhang M, Windheim M, Roe SM, Peggie M, Cohen P, Prodromou C *et al.* Chaperoned Ubiquitylation—Crystal Structures of the CHIP U Box E3 Ubiquitin Ligase and a CHIP-Ubc13-Uev1a Complex. *Mol Cell* 2005; **20**: 525–538.
40 Nikolay R, Wiederkehr T, Rist W, Kramer G, Mayer MP, Bukau B. Dimerization of the Human E3 Ligase CHIP via a Coiled-coil Domain Is Essential for Its Activity. *J Biol Chem* 2004; **279**: 2673–2678.
41 Ballinger CA, Connell P, Wu Y, Hu Z, Thompson LJ, Yin LY *et al.* Identification of CHIP, a novel tetratricopeptide repeat-containing protein that interacts with heat shock proteins and negatively regulates chaperone functions. *Mol Cell Biol* 1999; **19**:

4535–45.
42 Aravind L, Koonin E V. The U box is a modified RING finger - a common domain in ubiquitination. *Curr Biol* 2000; **10**: R132-4.
43 Dou H, Buetow L, Sibbet GJ, Cameron K, Huang DT. BIRC7–E2 ubiquitin conjugate structure reveals the mechanism of ubiquitin transfer by a RING dimer. *Nat Struct Mol Biol* 2012; **19**: 876–883.
44 Plechanovová A, Jaffray EG, Tatham MH, Naismith JH, Hay RT. Structure of a RING E3 ligase and ubiquitin-loaded E2 primed for catalysis. *Nature* 2012; **489**: 115–120.
45 Blatch GL, Lässle M. The tetratricopeptide repeat: a structural motif mediating protein-protein interactions. *BioEssays* 1999; **21**: 932–939.
46 Zhang H, Amick J, Chakravarti R, Santarriaga S, Schlanger S, McGlone C *et al.* A Bipartite Interaction between Hsp70 and CHIP Regulates Ubiquitination of Chaperoned Client Proteins. *Structure* 2015; **23**: 472–482.
47 Narayan V, Landré V, Ning J, Hernychova L, Muller P, Verma C *et al.* Protein–Protein Interactions Modulate the Docking-Dependent E3-Ubiquitin Ligase Activity of Carboxy-Terminus of Hsc70-Interacting Protein (CHIP). *Mol Cell Proteomics* 2015; **14**: 2973–2987.
48 Swapna LS, Srikeerthana K, Srinivasan N. Extent of Structural Asymmetry in Homodimeric Proteins: Prevalence and Relevance. *PLoS One* 2012; **7**: e36688.
49 Kanack AJ, Newsom OJ, Scaglione KM. Most mutations that cause spinocerebellar ataxia autosomal recessive type 16 (SCAR16) destabilize the protein quality-control E3 ligase CHIP. *J Biol Chem* 2018; **293**: 2735–2743.
50 Kopp Y, Lang W-H, Schuster TB, Martínez-Limón A, Hofbauer HF, Ernst R *et al.* CHIP as a membrane-shuttling proteostasis sensor. *Elife* 2017; **6**. doi:10.7554/eLife.29388.
51 Kim C, Yun N, Lee J, Youdim MBH, Ju C, Kim W-K *et al.* Phosphorylation of CHIP at Ser20 by Cdk5 promotes tAIF-mediated neuronal death. *Cell Death Differ* 2016; **23**: 333–346.
52 Tatham MH, Plechanovová A, Jaffray EG, Salmen H, Hay RT. Ube2W conjugates ubiquitin to α-amino groups of protein N-termini. *Biochem J* 2013; **453**: 137–45.
53 Scaglione KM, Zavodszky E, Todi S V, Patury S, Xu P, Rodríguez-Lebró E *et al.* Molecular Cell Ube2w and Ataxin-3 Coordinately Regulate the Ubiquitin Ligase CHIP. *Mol Cell* 2011; **43**: 599–612.
54 Wang D, Xu W, McGrath SC, Patterson C, Neckers L, Cotter RJ. Direct Identification of Ubiquitination Sites on Ubiquitin-Conjugated CHIP Using MALDI Mass Spectrometry. *J Proteome Res* 2005; **4**: 1554–1560.
55 Ohtake F, Tsuchiya H, Saeki Y, Tanaka K. K63 ubiquitylation triggers proteasomal degradation by seeding branched ubiquitin chains. 2018. doi:10.1073/pnas.1716673115.
56 Marques C, Guo W, Pereira P, Taylor A, Patterson C, Evans PC *et al.* The triage of damaged proteins: degradation by the ubiquitin-proteasome pathway or repair by molecular chaperones. *FASEB J* 2006; **20**: 741–743.
57 Kampinga HH, Kanon B, Salomons FA, Kabakov AE, Patterson C. Overexpression of the cochaperone CHIP enhances Hsp70-dependent folding activity in mammalian cells. *Mol Cell Biol* 2003; **23**: 4948–58.
58 Connell P, Ballinger CA, Jiang J, Wu Y, Thompson LJ, Höhfeld J *et al.* The co-chaperone CHIP regulates protein triage decisions mediated by heat-shock proteins. *Nat Cell Biol* 2001; **3**: 93–96.
59 Demand J, Alberti S, Patterson C, Höhfeld J. Cooperation of a ubiquitin domain protein and an E3 ubiquitin ligase during chaperone/proteasome coupling. *Curr Biol* 2001; **11**: 1569–77.
60 Jiang J, Ballinger CA, Wu Y, Dai Q, Cyr DM, Höhfeld J *et al.* CHIP Is a U-box-dependent E3 Ubiquitin Ligase. *J Biol Chem* 2001; **276**: 42938–42944.
61 Murata S, Minami Y, Minami M, Chiba T, Tanaka K. CHIP is a chaperone-dependent E3 ligase that ubiquitylates unfolded protein. *EMBO Rep* 2001; **2**: 1133–1138.
62 Tawo R, Pokrzywa W, Kevei É, Akyuz ME, Balaji V, Adrian S *et al.* The Ubiquitin Ligase CHIP Integrates Proteostasis and Aging by Regulation of Insulin Receptor

Turnover. *Cell* 2017; **169**: 470–482.e13.
63 Rosser MFN, Washburn E, Muchowski PJ, Patterson C, Cyr DM. Chaperone Functions of the E3 Ubiquitin Ligase CHIP. *J Biol Chem* 2007; **282**: 22267–22277.
64 Hegde AN, Haynes KA, Bach S V, Beckelman BC. Local ubiquitin-proteasome-mediated proteolysis and long-term synaptic plasticity. *Front Mol Neurosci* 2014; **7**: 96.
65 Joshi V, Amanullah A, Upadhyay A, Mishra R, Kumar A, Mishra A. A Decade of Boon or Burden: What Has the CHIP Ever Done for Cellular Protein Quality Control Mechanism Implicated in Neurodegeneration and Aging? *Front Mol Neurosci* 2016; **9**: 93.
66 Ristic G, Tsou W-L, Todi S V. An optimal ubiquitin-proteasome pathway in the nervous system: the role of deubiquitinating enzymes. *Front Mol Neurosci* 2014; **7**: 72.
67 Wang G, Gao Y, Li L, Jin G, Cai Z, Chao J-I *et al.* K63-Linked Ubiquitination in Kinase Activation and Cancer. *Front Oncol* 2012; **2**: 5.
68 Kalia L V., Kalia SK, Chau H, Lozano AM, Hyman BT, McLean PJ. Ubiquitinylation of α-Synuclein by Carboxyl Terminus Hsp70-Interacting Protein (CHIP) Is Regulated by Bcl-2-Associated Athanogene 5 (BAG5). *PLoS One* 2011; **6**: e14695.
69 Meacham GC, Patterson C, Zhang W, Younger JM, Cyr DM. The Hsc70 co-chaperone CHIP targets immature CFTR for proteasomal degradation. *Nat Cell Biol* 2001; **3**: 100–105.
70 Nordquist KA, Dimitrova YN, Brzovic PS, Ridenour WB, Munro KA, Soss SE *et al.* Structural and Functional Characterization of the Monomeric U-Box Domain from E4B. *Biochemistry* 2010; **49**: 347–355.
71 Imai Y, Soda M, Hatakeyama S, Akagi T, Hashikawa T, Nakayama KI *et al.* CHIP is associated with Parkin, a gene responsible for familial Parkinson's disease, and enhances its ubiquitin ligase activity. *Mol Cell* 2002; **10**: 55–67.
72 Pratt WB, Gestwicki JE, Osawa Y, Lieberman AP. Targeting Proteostasis Through the Protein Quality Control Function of the Hsp90/Hsp70-based Chaperone Machinery for Treatment of Adult Onset Neurodegenerative Diseases. doi:10.1146/annurev-pharmtox-010814-124332.
73 Narayan V, Eckert M, Zylicz A, Zylicz M, Ball KL. Cooperative regulation of the interferon regulatory factor-1 tumor suppressor protein by core components of the molecular chaperone machinery. *J Biol Chem* 2009; **284**: 25889–99.
74 Morishima Y, Wang AM, Yu Z, Pratt WB, Osawa Y, Lieberman AP. CHIP deletion reveals functional redundancy of E3 ligases in promoting degradation of both signaling proteins and expanded glutamine proteins. *Hum Mol Genet* 2008; **17**: 3942–3952.
75 Zeytuni N, Zarivach R. Structural and Functional Discussion of the Tetra-Trico-Peptide Repeat, a Protein Interaction Module. *Structure* 2012; **20**: 397–405.
76 Andrade MA, Perez-Iratxeta C, Ponting CP. Protein Repeats: Structures, Functions, and Evolution. *J Struct Biol* 2001; **134**: 117–131.
77 Narayan V, Pion E, Landré V, Müller P, Ball KL. Docking-dependent Ubiquitination of the Interferon Regulatory Factor-1 Tumor Suppressor Protein by the Ubiquitin Ligase CHIP. *J Biol Chem* 2011; **286**: 607–619.
78 Dai Q, Zhang C, Wu Y, McDonough H, Whaley RA, Godfrey V *et al.* CHIP activates HSF1 and confers protection against apoptosis and cellular stress. *EMBO J* 2003; **22**: 5446–58.
79 Qian S-B, McDonough H, Boellmann F, Cyr DM, Patterson C. CHIP-mediated stress recovery by sequential ubiquitination of substrates and Hsp70. *Nature* 2006; **440**: 551–5.
80 Landré V, Pion E, Narayan V, Xirodimas DP, Ball KL. DNA-binding regulates site-specific ubiquitination of IRF-1. *Biochem J* 2013; **449**: 707–717.
81 Tripathi V, Ali A, Bhat R, Pati U. CHIP chaperones wild type p53 tumor suppressor protein. *J Biol Chem* 2007; **282**: 28441–54.
82 Wang L, Liu Y-T, Hao R, Chen L, Chang Z, Wang H-R *et al.* Molecular Mechanism of the Negative Regulation of Smad1/5 Protein by Carboxyl Terminus of Hsc70-

interacting Protein (CHIP). 2011. doi:10.1074/jbc.M110.201814.
83 McDonough H, Charles PC, Hilliard EG, Qian S-B, Min J-N, Portbury A *et al.* Stress-dependent Daxx-CHIP interaction suppresses the p53 apoptotic program. *J Biol Chem* 2009; **284**: 20649–59.
84 Wawrzynow B, Zylicz A, Wallace M, Hupp T, Zylicz M. MDM2 chaperones the p53 tumour suppressor. 2007. doi:10.1074/jbc.M702767200.
85 Jiang J, Cyr D, Babbitt RW, Sessa WC, Patterson C. Chaperone-dependent Regulation of Endothelial Nitric-oxide Synthase Intracellular Trafficking by the Co-chaperone/Ubiquitin Ligase CHIP. *J Biol Chem* 2003; **278**: 49332–49341.
86 Yang M, Wang C, Zhu X, Tang S, Shi L, Cao X *et al.* E3 ubiquitin ligase CHIP facilitates Toll-like receptor signaling by recruiting and polyubiquitinating Src and atypical PKCζ. *J Exp Med* 2011; **208**: 2099–2112.
87 Ball K, Ning J, Nita E, Dias C. The Functions of CHIP in Age Related Disease. *JSM Enzymol Protein Sci* 2016; **1**.
88 Shi Y, Wang J, Li J-D, Ren H, Guan W, He M *et al.* Identification of CHIP as a Novel Causative Gene for Autosomal Recessive Cerebellar Ataxia. *PLoS One* 2013; **8**: e81884.
89 Chen J-H, Hales CN, Ozanne SE. DNA damage, cellular senescence and organismal ageing: causal or correlative? *Nucleic Acids Res* 2007; **35**: 7417–7428.
90 Sha Y, Pandit L, Zeng S, Eissa NT. A Critical Role for CHIP in the Aggresome Pathway. *Mol Cell Biol* 2009; **29**: 116–128.
91 Sisoula C, Trachana V, Patterson C, Gonos ES. CHIP-dependent p53 regulation occurs specifically during cellular senescence. *Free Radic Biol Med* 2011; **50**: 157–165.
92 Zheng Y, Cheng X-R, Zhou W-X, Zhang Y-X. Gene expression patterns of hippocampus and cerebral cortex of senescence-accelerated mouse treated with Huang-Lian-Jie-Du decoction. *Neurosci Lett* 2008; **439**: 119–124.
93 Kalia SK, Lee S, Smith PD, Liu L, Crocker SJ, Thorarinsdottir TE *et al.* BAG5 Inhibits Parkin and Enhances Dopaminergic Neuron Degeneration. *Neuron* 2004; **44**: 931–945.
94 Dimant H, Zhu L, Kibuuka LN, Fan Z, Hyman BT, McLean PJ. Direct Visualization of CHIP-Mediated Degradation of Alpha-Synuclein In Vivo: Implications for PD Therapeutics. *PLoS One* 2014; **9**: e92098.
95 Nita E. *Role of CHIP in the proteome in a neuronal cell model*. 2016.
96 Dos Santos MCDSC. *Developing Synthetic Tools to Image and Modulate the Activity of Carboxyl terminus of Hsc70-Interacting Protein (CHIP)*. 2015.
97 Devine MJ, Ryten M, Vodicka P, Thomson AJ, Burdon T, Houlden H *et al.* Parkinson's disease induced pluripotent stem cells with triplication of the α-synuclein locus. *Nat Commun* 2011; **2**: 440.
98 Lerner R, Post J, Loch S, Lutz B, Bindila L. Targeting brain and peripheral plasticity of the lipidome in acute kainic acid-induced epileptic seizures in mice via quantitative mass spectrometry. *Biochim Biophys Acta - Mol Cell Biol Lipids* 2017; **1862**: 255–267.
99 Kavan D, Man P. MSTools—Web based application for visualization and presentation of HXMS data. *Int J Mass Spectrom* 2011; **302**: 53–58.
100 Delano WL. PyMOL: An Open-Source Molecular Graphics Tool. San Carlos, CA, 2002.
101 Schuster S, Schelling Y, Synofzik M, Höflinger P, Schöls L, Hauser S. Establishment of STUB1/ CHIP mutant induced pluripotent stem cells (iPSCs) from a patient with Gordon Holmes syndrome/SCAR16. *Stem Cell Res* 2018; **29**: 166–169.
102 Schuster S, Saravanakumar S, Schöls L, Hauser S. Generation of a homozygous CRISPR/Cas9-mediated knockout human iPSC line for the STUB1 locus. *Stem Cell Res* 2019; **34**: 101378.
103 Sahara N, Murayama M, Mizoroki T, Urushitani M, Imai Y, Takahashi R *et al. In vivo* evidence of CHIP up-regulation attenuating tau aggregation. *J Neurochem* 2005; **94**: 1254–1263.
104 McLaughlin B, Buendia MA, Saborido TP, Palubinsky AM, Stankowski JN, Stanwood

GD. Haploinsufficiency of the E3 Ubiquitin Ligase C-Terminus of Heat Shock Cognate 70 Interacting Protein (CHIP) Produces Specific Behavioral Impairments. *PLoS One* 2012; **7**: e36340.
105 Ran FA, Hsu PD, Wright J, Agarwala V, Scott DA, Zhang F. Genome engineering using the CRISPR-Cas9 system. *Nat Protoc* 2013; **8**: 2281–2308.
106 Terns MP, Terns RM. CRISPR-based adaptive immune systems. *Curr Opin Microbiol* 2011; **14**: 321–327.
107 Wiedenheft B, Sternberg SH, Doudna JA. RNA-guided genetic silencing systems in bacteria and archaea. *Nature* 2012; **482**: 331–338.
108 Jinek M, Chylinski K, Fonfara I, Hauer M, Doudna JA, Charpentier E. A Programmable Dual-RNA-Guided DNA Endonuclease in Adaptive Bacterial Immunity. *Science (80- )* 2012; **337**: 816–821.
109 Sander JD, Joung JK. CRISPR-Cas systems for editing, regulating and targeting genomes. *Nat Biotechnol* 2014; **32**: 347–355.
110 Gwinn K, Devine MJ, Jin L-W, Johnson J, Bird T, Muenter M *et al.* Clinical features, with video documentation, of the original familial lewy body parkinsonism caused by α-synuclein triplication (Iowa kindred). *Mov Disord* 2011; **26**: 2134–6.
111 Singleton AB, Farrer M, Johnson J, Singleton A, Hague S, Kachergus J *et al.* Alpha-Synuclein Locus Triplication Causes Parkinson's Disease. *Science (80- )* 2003; **302**: 841–841.
112 Hamza TH, Chen H, Hill-Burns EM, Rhodes SL, Montimurro J, Kay DM *et al.* Genome-Wide Gene-Environment Study Identifies Glutamate Receptor Gene GRIN2A as a Parkinson's Disease Modifier Gene via Interaction with Coffee. *PLoS Genet* 2011; **7**: 1002237.
113 Chambers SM, Fasano CA, Papapetrou EP, Tomishima M, Sadelain M, Studer L. Highly efficient neural conversion of human ES and iPS cells by dual inhibition of SMAD signaling. *Nat Biotechnol* 2009; **27**: 275–280.
114 Shi Y, Kirwan P, Livesey FJ. Directed differentiation of human pluripotent stem cells to cerebral cortex neurons and neural networks. *Nat Protoc* 2012; **7**: 1836–1846.
115 Shi Y, Kirwan P, Smith J, Robinson HPC, Livesey FJ. Human cerebral cortex development from pluripotent stem cells to functional excitatory synapses. *Nat Publ Gr* 2012; **15**. doi:10.1038/nn.3041.
116 Vitale AM, Matigian NA, Ravishankar S, Bellette B, Wood SA, Wolvetang EJ *et al.* Variability in the Generation of Induced Pluripotent Stem Cells: Importance for Disease Modeling. *Stem Cells Transl Med* 2012; **1**: 641–650.
117 Liang G, Zhang Y. Genetic and Epigenetic Variations in iPSCs: Potential Causes and Implications for Application. *Cell Stem Cell* 2013; **13**: 149–159.
118 Kovalevich J, Langford D. Considerations for the Use of SH-SY5Y Neuroblastoma Cells in Neurobiology. doi:10.1007/978-1-62703-640-5_2.
119 Li X-L, Li G-H, Fu J, Fu Y-W, Zhang L, Chen W *et al.* Highly efficient genome editing via CRISPR-Cas9 in human pluripotent stem cells is achieved by transient BCL-XL overexpression. *Nucleic Acids Res* 2018; **46**: 10195–10215.
120 Ihry RJ, Worringer KA, Salick MR, Frias E, Ho D, Theriault K *et al.* p53 inhibits CRISPR–Cas9 engineering in human pluripotent stem cells. *Nat Med* doi:10.1038/s41591-018-0050-6.
121 Yang L, Guell M, Byrne S, Yang JL, De Los Angeles A, Mali P *et al.* Optimization of scarless human stem cell genome editing. *Nucleic Acids Res* 2013; **41**: 9049–9061.
122 Chakrabarti AM, Henser-Brownhill T, Monserrat J, Poetsch AR, Luscombe NM, Scaffidi P. Target-Specific Precision of CRISPR-Mediated Genome Editing. *Mol Cell* 2019; **73**: 699–713.e6.
123 Xu X, Gao D, Wang P, Chen J, Ruan J, Xu J *et al.* Efficient homology-directed gene editing by CRISPR/Cas9 in human stem and primary cells using tube electroporation. *Sci Rep* 2018; **8**: 11649.
124 Park TI-H, Monzo H, Mee EW, Bergin PS, Teoh HH, Montgomery JM *et al.* Adult Human Brain Neural Progenitor Cells (NPCs) and Fibroblast-Like Cells Have Similar Properties In Vitro but Only NPCs Differentiate into Neurons. *PLoS One* 2012; **7**: e37742.

125 Vanlandewijck M, He L, Mäe MA, Andrae J, Ando K, Del Gaudio F *et al.* A molecular atlas of cell types and zonation in the brain vasculature. *Nature* 2018; **554**: 475–480.
126 You S-A, Wang QK. Proteomics With Two-Dimensional Gel Electrophoresis and Mass Spectrometry Analysis in Cardiovascular Research. In: *Cardiovascular Disease, Volume 2: Molecular Medicine*. Humana Press: New Jersey, pp 15–26.
127 Beranova-Giorgianni S. Proteome analysis by two-dimensional gel electrophoresis and mass spectrometry: strengths and limitations. *TrAC Trends Anal Chem* 2003; **22**: 273–281.
128 Penque D. Two-dimensional gel electrophoresis and mass spectrometry for biomarker discovery. *PROTEOMICS - Clin Appl* 2009; **3**: 155–172.
129 Gygi SP, Corthals GL, Zhang Y, Rochon Y, Aebersold R. Evaluation of two-dimensional gel electrophoresis-based proteome analysis technology. *Proc Natl Acad Sci* 2000; **97**: 9390–9395.
130 Huang Q, Yang L, Luo J, Guo L, Wang Z, Yang X *et al.* SWATH enables precise label-free quantification on proteome scale. *Proteomics* 2015; **15**: 1215–1223.
131 Rosenberger G, Koh CC, Guo T, Röst HL, Kouvonen P, Collins BC *et al.* A repository of assays to quantify 10,000 human proteins by SWATH-MS. *Sci data* 2014; **1**: 140031.
132 Burande CF, Heuzé ML, Lamsoul I, Monsarrat B, Uttenweiler-Joseph S, Lutz PG. A Label-free Quantitative Proteomics Strategy to Identify E3 Ubiquitin Ligase Substrates Targeted to Proteasome Degradation. *Mol Cell Proteomics* 2009; **8**: 1719–1727.
133 Ordureau A, Münch C, Harper JW. Quantifying ubiquitin signaling. *Mol Cell* 2015; **58**: 660–76.
134 Mohammed H, Taylor C, Brown GD, Papachristou EK, Carroll JS, D'Santos CS. Rapid immunoprecipitation mass spectrometry of endogenous proteins (RIME) for analysis of chromatin complexes. Nat. Protoc. 2016; **11**: 316–326.
135 Christie Hunter. SCIEX. What is SWATH™ Acquis. how does it Work what does is Provid. 2015.https://sciex.com/community/application-discussions/proteomics/swath/fundamentals/what-is-swath-acquisition-how-does-it-work-and-what-does-is-provide (accessed 10 May2019).
136 Liao H, Liu XJ, Blank JL, Bouck DC, Bernard H, Garcia K *et al.* Quantitative Proteomic Analysis of Cellular Protein Modulation upon Inhibition of the NEDD8-Activating Enzyme by MLN4924. *Mol Cell Proteomics* 2011; **10**: M111.009183.
137 Bassani-Sternberg M, Pletscher-Frankild S, Jensen LJ, Mann M. Mass Spectrometry of Human Leukocyte Antigen Class I Peptidomes Reveals Strong Effects of Protein Abundance and Turnover on Antigen Presentation. *Mol Cell Proteomics* 2015; **14**: 658–673.
138 Zhan S, Wang T, Ge W. Multiple functions of the E3 ubiquitin ligase CHIP in immunity. *Int Rev Immunol* 2017; **36**: 300–312.
139 Shi Y, Xu P, Qin J. Ubiquitinated Proteome: Ready for Global? *Mol Cell Proteomics* 2011; **10**: R110.006882.
140 Franco M, Seyfried NT, Brand AH, Peng J, Mayor U. A Novel Strategy to Isolate Ubiquitin Conjugates Reveals Wide Role for Ubiquitination during Neural Development. *Mol Cell Proteomics* 2011; **10**: M110.002188.
141 Kim W, Bennett EJ, Huttlin EL, Guo A, Li J, Possemato A *et al.* Systematic and Quantitative Assessment of the Ubiquitin-Modified Proteome. *Mol Cell* 2011; **44**: 325–340.
142 Galligan JT, Martinez-Noël G, Arndt V, Hayes S, Chittenden TW, Harper JW *et al.* Proteomic analysis and identification of cellular interactors of the giant ubiquitin ligase HERC2. *J Proteome Res* 2015; **14**: 953–66.
143 Xu G, Paige JS, Jaffrey SR. Global analysis of lysine ubiquitination by ubiquitin remnant immunoaffinity profiling. *Nat Biotechnol* 2010; **28**: 868–873.
144 Larance M, Ahmad Y, Kirkwood KJ, Ly T, Lamond AI. Global Subcellular Characterization of Protein Degradation Using Quantitative Proteomics. *Mol Cell Proteomics* 2013; **12**: 638–650.
145 Iconomou M, Saunders DN. Systematic approaches to identify E3 ligase substrates.

*Biochem J* 2016; **473**: 4083–4101.
146 Bhuripanyo K, Wang Y, Liu X, Zhou L, Liu R, Duong D *et al.* Identifying the substrate proteins of U-box E3s E4B and CHIP by orthogonal ubiquitin transfer. *Sci Adv* 2018; **4**: e1701393.
147 Taipale M, Tucker G, Peng J, Krykbaeva I, Lin Z-Y, Larsen B *et al.* A Quantitative Chaperone Interaction Network Reveals the Architecture of Cellular Protein Homeostasis Pathways. *Cell* 2014; **158**: 434–448.
148 Jaiswal JK, Lauritzen SP, Scheffer L, Sakaguchi M, Bunkenborg J, Simon SM *et al.* S100A11 is required for efficient plasma membrane repair and survival of invasive cancer cells. *Nat Commun* 2014; **5**: 3795.
149 Sisoula C, Gonos ES. CHIP E3 ligase regulates mammalian senescence by modulating the levels of oxidized proteins. *Mech Ageing Dev* 2011; **132**: 269–272.
150 Lin Y-S, Lee W-J, Wang S-J, Fuh J-L. Levels of plasma neurofilament light chain and cognitive function in patients with Alzheimer or Parkinson disease. *Sci Rep* 2018; **8**: 17368.
151 Neumann H, Schmidt H, Cavalié A, Jenne D, Wekerle H. Major Histocompatibility Complex (MHC) Class I Gene Expression in Single Neurons of the Central Nervous System: Differential Regulation by Interferon (IFN)-and Tumor Necrosis Factor (TNF). 1997.
152 Cebrián C, Loike JD, Sulzer D, Blesa J, Gonzalez-Hernandez T. Neuronal MHC-I expression and its implications in synaptic function, axonal regeneration and Parkinson's and other brain diseases. 2014. doi:10.3389/fnana.2014.00114.
153 Cifuentes RA, Murillo-Rojas J. Alzheimer's disease and HLA-A2: linking neurodegenerative to immune processes through an in silico approach. *Biomed Res Int* 2014; **2014**: 791238.
154 Lehmann DJ, Barnardo MC, Fuggle S, Quiroga I, Sutherland A, Warden DR *et al.* Replication of the association of HLA-B7 with Alzheimer's disease: a role for homozygosity? *J Neuroinflammation* 2006; **3**: 33.
155 Trujillo JA, Croft NP, Dudek NL, Channappanavar R, Theodossis A, Webb AI *et al.* The Cellular Redox Environment Alters Antigen Presentation. *J Biol Chem* 2014; **289**: 27979–27991.
156 Kettern N, Rogon C, Limmer A, Schild H, Höhfeld J. The Hsc/Hsp70 Co-Chaperone Network Controls Antigen Aggregation and Presentation during Maturation of Professional Antigen Presenting Cells. *PLoS One* 2011; **6**: e16398.
157 Lewis JE, Brameld JM, Jethwa PH. Neuroendocrine Role for VGF. *Front Endocrinol (Lausanne)* 2015; **6**: 3.
158 Schweiger S, Dorn S, Fuchs M, Köhler A, Matthes F, Müller E-C *et al.* The E3 ubiquitin ligase MID1 catalyzes ubiquitination and cleavage of Fu. *J Biol Chem* 2014; **289**: 31805–17.
159 Chen Y-C, Pristerá A, Ayub M, Swanwick RS, Karu K, Hamada Y *et al.* Identification of a receptor for neuropeptide VGF and its role in neuropathic pain. *J Biol Chem* 2013; **288**: 34638–46.
160 Cocco C, D'Amato F, Noli B, Ledda A, Brancia C, Bongioanni P *et al.* Distribution of VGF peptides in the human cortex and their selective changes in Parkinson's and Alzheimer's diseases. *J Anat* 2010; **217**: 683–693.
161 Demonbreun AR, Quattrocelli M, Barefield DY, Allen M V., Swanson KE, McNally EM. An actin-dependent annexin complex mediates plasma membrane repair in muscle. *J Cell Biol* 2016; **213**: 705–718.
162 Nylandsted J, Boye TL. Annexins in plasma membrane repair. *Biol Chem* 2016; **397**. doi:10.1515/hsz-2016-0171.
163 Lauritzen SP, Boye TL, Nylandsted J. Annexins are instrumental for efficient plasma membrane repair in cancer cells. *Semin Cell Dev Biol* 2015; **45**: 32–38.
164 McNeil AK, Rescher U, Gerke V, McNeil PL. Requirement for annexin A1 in plasma membrane repair. *J Biol Chem* 2006; **281**: 35202–7.
165 Luo M, Hajjar K. Annexin A2 System in Human Biology: Cell Surface and Beyond. *Semin Thromb Hemost* 2013; **39**: 338–346.
166 Jost M, Gerke V. Mapping of a regulatory important site for protein kinase C

phosphorylation in the N-terminal domain of annexin II. *Biochim Biophys Acta* 1996; **1313**: 283–9.
167 Hoque M, Rentero C, Cairns R, Tebar F, Enrich C, Grewal T. Annexins — Scaffolds modulating PKC localization and signaling. *Cell Signal* 2014; **26**: 1213–1225.
168 Wang C-Y, Lin C-F. Annexin A2: Its Molecular Regulation and Cellular Expression in Cancer Development. *Dis Markers* 2014; **2014**: 1–10.
169 Drücker P, Pejic M, Galla H-J, Gerke V. Lipid Segregation and Membrane Budding Induced by the Peripheral Membrane Binding Protein Annexin A2. *J Biol Chem* 2013; **288**: 24764–24776.
170 Cuervo AM, Gomes A V., Barnes JA, Dice JF. Selective Degradation of Annexins by Chaperone-mediated Autophagy. *J Biol Chem* 2000; **275**: 33329–33335.
171 Chasserot-Golaz S, Vitale N, Sagot I, Delouche B, Dirrig S, Pradel LA *et al.* Annexin II in exocytosis: catecholamine secretion requires the translocation of p36 to the subplasmalemmal region in chromaffin cells. *J Cell Biol* 1996; **133**: 1217–36.
172 Nazmi AR, Ozorowski G, Pejic M, Whitelegge JP, Gerke V, Luecke H. N-terminal acetylation of annexin A2 is required for S100A10 binding. *Biol Chem* 2012; **393**: 1141–50.
173 Aukrust I, Rosenberg LA, Ankerud MM, Bertelsen V, Hollås H, Saraste J *et al.* Post-translational modifications of Annexin A2 are linked to its association with perinuclear nonpolysomal mRNP complexes. *FEBS Open Bio* 2017; **7**: 160–173.
174 Zobiack N, Rescher U, Ludwig C, Zeuschner D, Gerke V. The Annexin 2/S100A10 Complex Controls the Distribution of Transferrin Receptor-containing Recycling Endosomes. *Mol Biol Cell* 2003; **14**: 4896–4908.
175 Madureira PA, Hill R, Lee PWK, Waisman DM. Genotoxic Agents Promote the Nuclear Accumulation of Annexin A2: Role of Annexin A2 in Mitigating DNA Damage. *PLoS One* 2012; **7**: 50591.
176 Wang C-Y, Lin Y-S, Su W-C, Chen C-L, Lin C-F. Glycogen Synthase Kinase-3 and Omi/HtrA2 Induce Annexin A2 Cleavage followed by Cell Cycle Inhibition and Apoptosis. *Mol Biol Cell* 2009; **20**: 4153–4161.
177 Regnouf F, Sagot I, Delouche B, Devilliers G, Cartaud J, Henry JP *et al.* 'In vitro' phosphorylation of annexin 2 heterotetramer by protein kinase C. Comparative properties of the unphosphorylated and phosphorylated annexin 2 on the aggregation and fusion of chromaffin granule membranes. *J Biol Chem* 1995; **270**: 27143–50.
178 Liu L. Calcium-dependent self-association of annexin II: a possible implication in exocytosis. *Cell Signal* 1999; **11**: 317–24.
179 Pradel LA, Rendon A. Annexin 1 is present in different molecular forms in rat cerebral cortex. *FEBS Lett* 1993; **327**: 41–44.
180 Deora AB, Kreitzer G, Jacovina AT, Hajjar KA. An Annexin 2 Phosphorylation Switch Mediates p11-dependent Translocation of Annexin 2 to the Cell Surface. *J Biol Chem* 2004; **279**: 43411–43418.
181 Lauvrak SU, Hollås H, Døskeland AP, Aukrust I, Flatmark T, Vedeler A. Ubiquitinated annexin A2 is enriched in the cytoskeleton fraction. *FEBS Lett* 2005; **579**: 203–206.
182 Deng S, Jing B, Xing T, Hou L, Yang Z. Overexpression of Annexin A2 Is Associated with Abnormal Ubiquitination in Breast Cancer. *Genomics Proteomics Bioinformatics* 2012; **10**: 153–157.
183 Babiychuk EB, Monastyrskaya K, Potez S, Draeger A. Blebbing confers resistance against cell lysis. *Cell Death Differ* 2011; **18**: 80–9.
184 Potez S, Luginbühl M, Monastyrskaya K, Hostettler A, Draeger A, Babiychuk EB. Tailored protection against plasmalemmal injury by annexins with different Ca2+ sensitivities. *J Biol Chem* 2011; **286**: 17982–91.
185 Boye TL, Maeda K, Pezeshkian W, Sønder SL, Haeger SC, Gerke V *et al.* Annexin A4 and A6 induce membrane curvature and constriction during cell membrane repair. *Nat Commun* 2017; **8**: 1623.
186 Xu W, Marcu M, Yuan X, Mimnaugh E, Patterson C, Neckers L. Chaperone-dependent E3 ubiquitin ligase CHIP mediates a degradative pathway for c-ErbB2/Neu. *Proc Natl Acad Sci* 2002; **99**: 12847–12852.
187 Fan HY, Heerklotz H. Digitonin does not flip across cholesterol-poor membranes. *J*

*Colloid Interface Sci* 2017; **504**: 283–293.
188 Eberhard DA, Brown MD, VandenBerg SR. Alterations of annexin expression in pathological neuronal and glial reactions. Immunohistochemical localization of annexins I, II (p36 and p11 subunits), IV, and VI in the human hippocampus. *Am J Pathol* 1994; **145**: 640–9.
189 Gauthier-Kemper A, Weissmann C, Golovyashkina N, Sebö-Lemke Z, Drewes G, Gerke V *et al.* The frontotemporal dementia mutation R406W blocks tau's interaction with the membrane in an annexin A2-dependent manner. *J Cell Biol* 2011. doi:10.1083/jcb.201007161.
190 Mishra M, Paunesku T, Woloschak GE, Siddique T, Zhu L (Julie), Lin S *et al.* Gene expression analysis of frontotemporal lobar degeneration of the motor neuron disease type with ubiquitinated inclusions. *Acta Neuropathol* 2007; **114**: 81–94.
191 Pierce NW, Kleiger G, Shan S, Deshaies RJ. Detection of sequential polyubiquitylation on a millisecond timescale. *Nature* 2009; **462**: 615–619.
192 Fieulaine S, Boularot A, Artaud I, Desmadril M, Dardel F, Meinnel T *et al.* Trapping Conformational States Along Ligand-Binding Dynamics of Peptide Deformylase: The Impact of Induced Fit on Enzyme Catalysis. *PLoS Biol* 2011; **9**: e1001066.
193 Bonvini P, Dalla Rosa H, Vignes N, Rosolen A. Ubiquitination and proteasomal degradation of nucleophosmin-anaplastic lymphoma kinase induced by 17-allylamino-demethoxygeldanamycin: role of the co-chaperone carboxyl heat shock protein 70-interacting protein. *Cancer Res* 2004; **64**: 3256–64.
194 Fang Y, Vilella-Bach M, Bachmann R, Flanigan A, Chen J. Phosphatidic Acid-Mediated Mitogenic Activation of mTOR Signaling. *Science (80- )* 2001; **294**: 1942–1945.
195 Pichler H, Emmerstorfer-Augustin A. Modification of membrane lipid compositions in single-celled organisms – From basics to applications. *Methods* 2018; **147**: 50–65.
196 Frohman MA. The phospholipase D superfamily as therapeutic targets. *Trends Pharmacol Sci* 2015; **36**: 137–144.
197 Hammond GRV, Balla T. Polyphosphoinositide binding domains: Key to inositol lipid biology. *Biochim Biophys Acta - Mol Cell Biol Lipids* 2015; **1851**: 746–758.
198 Frolov VA, Shnyrova A V., Zimmerberg J. Lipid Polymorphisms and Membrane Shape. *Cold Spring Harb Perspect Biol* 2011; **3**: a004747–a004747.
199 Dyall SC. Long-chain omega-3 fatty acids and the brain: a review of the independent and shared effects of EPA, DPA and DHA. *Front Aging Neurosci* 2015; **7**: 52.
200 Ibarguren M, López DJ. The effect of natural and synthetic fatty acids on membrane structure, microdomain organization, cellular functions and human health. *Biochim Biophys Acta - Biomembr* 2014; **1838**: 1518–1528.
201 Dyall SC, Michael-Titus AT. Neurological Benefits of Omega-3 Fatty Acids. *NeuroMolecular Med* 2008; **10**: 219–235.
202 Akbar M, Calderon F, Wen Z, Kim H-Y. Docosahexaenoic acid: A positive modulator of Akt signaling in neuronal survival. *Proc Natl Acad Sci* 2005; **102**: 10858–10863.
203 Naudí A, Jové M, Ayala V, Portero-Otín M, Barja G, Pamplona R. Membrane lipid unsaturation as physiological adaptation to animal longevity. *Front Physiol* 2013; **4**: 372.
204 Pearce PH, Johnsen RD, Wysocki SJ, Kakulas BA. Muscle lipids in Duchenne muscular dystrophy. *Aust J Exp Biol Med Sci* 1981; **59**: 77–90.
205 Pearce PH, Kakulas BA. Skeletal muscle lipids in normal and dystrophic mice. *Aust J Exp Biol Med Sci* 1980; **58**: 397–408.
206 Kunze D, Reichmann G, Egger E, Olthoff D, Döhler K. Fatty acid pattern of lipids in normal and dystrophic human muscle. *Eur J Clin Invest* 1975; **5**: 471–5.
207 Zibamanzarmofrad M. *The Role of Membrane Lipid Composition on Skeletal Muscle Damage in the Rodent Model of Duchenne Muscular Dystrophy*. 2015.
208 Ye Z, Needham PG, Estabrooks SK, Whitaker SK, Garcia BL, Misra S *et al.* Symmetry breaking during homodimeric assembly activates an E3 ubiquitin ligase. *Sci Rep* 2017; **7**: 1789.
209 Graf C, Stankiewicz M, Nikolay R, Mayer MP. Insights into the Conformational Dynamics of the E3 Ubiquitin Ligase CHIP in Complex with Chaperones and E2

Enzymes. *Biochemistry* 2010; **49**: 2121–2129.
210 Ahmad ZA, Yeap SK, Ali AM, Ho WY, Alitheen NBM, Hamid M. scFv Antibody: Principles and Clinical Application. *Clin Dev Immunol* 2012; **2012**: 1–15.
211 Holliger P, Hudson PJ. Engineered antibody fragments and the rise of single domains. *Nat Biotechnol* 2005; **23**: 1126–1136.
212 Monnier P, Vigouroux R, Tassew N, Monnier PP, Vigouroux RJ, Tassew NG. In Vivo Applications of Single Chain Fv (Variable Domain) (scFv) Fragments. *Antibodies* 2013; **2**: 193–208.
213 Bird RE, Hardman KD, Jacobson JW, Johnson S, Kaufman BM, Lee SM *et al.* Single-chain antigen-binding proteins. *Science* 1988; **242**: 423–6.
214 Inbar D, Hochman J, Givol D. Localization of antibody-combining sites within the variable portions of heavy and light chains. *Proc Natl Acad Sci U S A* 1972; **69**: 2659–62.
215 Huston JS, Levinson D, Mudgett-Hunter M, Tai MS, Novotný J, Margolies MN *et al.* Protein engineering of antibody binding sites: recovery of specific activity in an anti-digoxin single-chain Fv analogue produced in Escherichia coli. *Proc Natl Acad Sci U S A* 1988; **85**: 5879–83.
216 Skerra A, Plückthun A. Assembly of a functional immunoglobulin Fv fragment in Escherichia coli. *Science (80- )* 1988; **240**: 1038–41.
217 Smith GP, Petrenko VA. Phage Display. *Chem Rev* 1997; **97**: 391–410.
218 Schofield DJ, Pope AR, Clementel V, Buckell J, Chapple SD, Clarke KF *et al.* Application of phage display to high throughput antibody generation and characterization. *Genome Biol* 2007; **8**: R254.
219 Chames P, Van Regenmortel M, Weiss E, Baty D. Therapeutic antibodies: successes, limitations and hopes for the future. *Br J Pharmacol* 2009; **157**: 220–33.
220 Colby DW, Chu Y, Cassady JP, Duennwald M, Zazulak H, Webster JM *et al.* Potent inhibition of huntingtin aggregation and cytotoxicity by a disulfide bond-free single-domain intracellular antibody. *Proc Natl Acad Sci* 2004; **101**: 17616–17621.
221 Paganetti P, Calanca V, Galli C, Stefani M, Molinari M. beta-site specific intrabodies to decrease and prevent generation of Alzheimer's Abeta peptide. *J Cell Biol* 2005; **168**: 863–8.
222 Lynch SM, Zhou C, Messer A. An scFv Intrabody against the Nonamyloid Component of α-Synuclein Reduces Intracellular Aggregation and Toxicity. *J Mol Biol* 2008; **377**: 136–147.
223 Zhao M, Wang S, Wang Y, Zhang R, Li Y, Su Y *et al.* Pan-Amyloid Oligomer Specific scFv Antibody Attenuates Memory Deficits and Brain Amyloid Burden in Mice with Alzheimer's Disease. *Curr Alzheimer Res* 2014; **11**: 69–78.
224 Robert R, Wark KL. Engineered antibody approaches for Alzheimer's disease immunotherapy. *Arch Biochem Biophys* 2012; **526**: 132–138.
225 Ryan DA, Mastrangelo MA, Narrow WC, Sullivan MA, Federoff HJ, Bowers WJ. Aβ-directed Single-chain Antibody Delivery Via a Serotype-1 AAV Vector Improves Learning Behavior and Pathology in Alzheimer's Disease Mice. *Mol Ther* 2010; **18**: 1471.
226 Kan Z-Y, Walters BT, Mayne L, Englander SW. Protein hydrogen exchange at residue resolution by proteolytic fragmentation mass spectrometry analysis. *Proc Natl Acad Sci* 2013; **110**: 16438–16443.
227 Wei H, Mo J, Tao L, Russell RJ, Tymiak AA, Chen G *et al.* Hydrogen/deuterium exchange mass spectrometry for probing higher order structure of protein therapeutics: methodology and applications. *Drug Discov Today* 2014; **19**: 95–102.
228 Wales TE, Engen JR. Hydrogen exchange mass spectrometry for the analysis of protein dynamics. *Mass Spectrom Rev* 2006; **25**: 158–170.
229 Deng B, Lento C, Wilson DJ. Hydrogen deuterium exchange mass spectrometry in biopharmaceutical discovery and development – A review. *Anal Chim Acta* 2016; **940**: 8–20.
230 Konermann L, Pan J, Liu Y-H. Hydrogen exchange mass spectrometry for studying protein structure and dynamics. *Chem Soc Rev* 2011; **40**: 1224–1234.
231 Ye Y, Rape M. Building ubiquitin chains: E2 enzymes at work. *Nat Rev Mol Cell Biol*

2009; **10**: 755–64.
232 Bharadwaj A, Bydoun M, Holloway R, Waisman D. Annexin A2 heterotetramer: structure and function. *Int J Mol Sci* 2013; **14**: 6259–305.
233 Kawasumi M, Nghiem P. Chemical Genetics: Elucidating Biological Systems with Small-Molecule Compounds. *J Invest Dermatol* 2007; **127**: 1577–1584.
234 Shi C, Rubel C, Soss SE, Sanchez-Hodge R, Zhang S, Madrigal SC *et al.* Disrupted structure and aberrant function of CHIP mediates the loss of motor and cognitive function in preclinical models of SCAR16. *PLOS Genet* 2018; **14**: e1007664.
235 Rescher U, Gerke V. Introduction The annexins are a family of Ca 2+ /lipid-binding proteins that differ from most other Ca 2+-binding proteins in their Ca Annexins-unique membrane binding proteins with diverse functions Commentary. *J Cell Sci* 2004; **117**: 2631–2639.
236 UniProtKB - P07355 (ANXA2_HUMAN). Uniprot. https://www.uniprot.org/uniprot/P07355 (accessed 21 May2019).
237 Annexin A2 - P07355 (ANXA2_HUMAN). Protein Data Bank. https://www.rcsb.org/pdb/protein/P07355?addPDB=2HYW (accessed 21 May2019).
238 Alderson TR, Markley JL. Biophysical characterization of α-synuclein and its controversial structure. *Intrinsically Disord Proteins* 2013; **1**: e26255.
239 UniProtKB - P37840 (SYUA_HUMAN). Uniprot. https://www.uniprot.org/uniprot/P37840 (accessed 21 May2019).
240 Rott R, Szargel R, Haskin J, Shani V, Shainskaya A, Manov I *et al.* Monoubiquitylation of α-Synuclein by Seven in Absentia Homolog (SIAH) Promotes Its Aggregation in Dopaminergic Cells. *J Biol Chem* 2008; **283**: 3316–3328.
241 Passmore LA, Barford D. Getting into position: the catalytic mechanisms of protein ubiquitylation. 2004.
242 Lyumkis D, Doamekpor SK, Bengtson MH, Lee J-W, Toro TB, Petroski MD *et al.* Single-particle EM reveals extensive conformational variability of the Ltn1 E3 ligase. *Proc Natl Acad Sci* 2013; **110**: 1702–1707.
243 Wade BE, Zhao J, Ma J, Hart CM, Sutliff RL. Hypoxia-induced alterations in the lung ubiquitin proteasome system during pulmonary hypertension pathogenesis. *Pulm Circ* 2018; **8**: 204589401878826.
244 Bae E-J, Ho D-H, Park E, Jung JW, Cho K, Hong JH *et al.* Lipid peroxidation product 4-hydroxy-2-nonenal promotes seeding-capable oligomer formation and cell-to-cell transfer of α-synuclein. *Antioxid Redox Signal* 2013; **18**: 770–83.
245 Nonaka T, Takeshi Iwatsubo, Hasegawa M. Ubiquitination of α-Synuclein†. 2004. doi:10.1021/BI0485528.
246 Tofaris GK, Razzaq A, Ghetti B, Lilley KS, Spillantini MG. Ubiquitination of α-Synuclein in Lewy Bodies Is a Pathological Event Not Associated with Impairment of Proteasome Function. *J Biol Chem* 2003; **278**: 44405–44411.
247 Xu Z, Kohli E, Devlin KI, Bold M, Nix JC, Misra S. Interactions between the quality control ubiquitin ligase CHIP and ubiquitin conjugating enzymes. *BMC Struct Biol* 2008; **8**: 26.
248 Linke K, Mace PD, Smith CA, Vaux DL, Silke J, Day CL. Structure of the MDM2/MDMX RING domain heterodimer reveals dimerization is required for their ubiquitylation in trans. *Cell Death Differ* 2008; **15**: 841–848.
249 Mace PD, Linke K, Feltham R, Schumacher F-R, Smith CA, Vaux DL *et al.* Structures of the cIAP2 RING Domain Reveal Conformational Changes Associated with Ubiquitin-conjugating Enzyme (E2) Recruitment * □ S and the. 2008. doi:10.1074/jbc.M804753200.
250 Liew CW, Sun H, Hunter T, Day CL. RING DOMAIN DIMERIZATION IS ESSENTIAL FOR RNF4 FUNCTION. doi:10.1042/BJ20100957.
251 Metzger MB, Hristova VA, Weissman AM. HECT and RING finger families of E3 ubiquitin ligases at a glance. *J Cell Sci* 2012; **125**: 531–7.
252 George AJ, Hoffiz YC, Charles AJ, Zhu Y, Mabb AM. A Comprehensive Atlas of E3 Ubiquitin Ligase Mutations in Neurological Disorders. *Front Genet* 2018; **9**: 29.
253 Hou NS, Gutschmidt A, Choi DY, Pather K, Shi X, Watts JL *et al.* Activation of the endoplasmic reticulum unfolded protein response by lipid disequilibrium without

disturbed proteostasis in vivo. *Proc Natl Acad Sci U S A* 2014; **111**: E2271-80.
254 Jacquemyn J, Cascalho A, Goodchild RE. The ins and outs of endoplasmic reticulum-controlled lipid biosynthesis. *EMBO Rep* 2017; **18**: 1905–1921.
255 Cascalho A, Jacquemyn J, Goodchild RE. Membrane defects and genetic redundancy: Are we at a turning point for DYT1 dystonia? *Mov Disord* 2017; **32**: 371–381.
256 Chan RB, Oliveira TG, Cortes EP, Honig LS, Duff KE, Small SA *et al.* Comparative Lipidomic Analysis of Mouse and Human Brain with Alzheimer Disease. *J Biol Chem* 2012; **287**: 2678–2688.
257 Peng KY, Pérez-González R, Alldred MJ, Goulbourne CN, Morales-Corraliza J, Saito M *et al.* Apolipoprotein E4 genotype compromises brain exosome production. *Brain* 2019; **142**: 163–175.
258 Rentero C, Blanco-Muñoz P, Meneses-Salas E, Grewal T, Enrich C. Annexins—Coordinators of Cholesterol Homeostasis in Endocytic Pathways. *Int J Mol Sci* 2018; **19**: 1444.
259 García-Melero A, Reverter M, Hoque M, Meneses-Salas E, Koese M, Conway JRW *et al.* Annexin A6 and Late Endosomal Cholesterol Modulate Integrin Recycling and Cell Migration. *J Biol Chem* 2016; **291**: 1320–1335.
260 van Maarschalkerweerd A, Vetri V, Vestergaard B. Cholesterol facilitates interactions between α-synuclein oligomers and charge-neutral membranes. *FEBS Lett* 2015; **589**: 2661–2667.
261 Casarejos MJ, Perucho J, López-Sendón JL, García de Yébenes J, Bettencourt C, Gómez A *et al.* Trehalose Improves Human Fibroblast Deficits in a New CHIP-Mutation Related Ataxia. *PLoS One* 2014; **9**: e106931.
262 Upadhyay A, Amanullah A, Mishra R, Kumar A, Mishra A. Lanosterol Suppresses the Aggregation and Cytotoxicity of Misfolded Proteins Linked with Neurodegenerative Diseases. *Mol Neurobiol* 2018; **55**: 1169–1182.
263 Rovere M, Powers AE, Jiang H, Pitino JC, Fonseca-Ornelas L, Patel DS *et al.* E46K-like α-synuclein mutants increase lipid interactions and disrupt membrane selectivity. *J Biol Chem* 2019; : jbc.RA118.006551.
264 Dettmer U, Ramalingam N, von Saucken VE, Kim T-E, Newman AJ, Terry-Kantor E *et al.* Loss of native α-synuclein multimerization by strategically mutating its amphipathic helix causes abnormal vesicle interactions in neuronal cells. *Hum Mol Genet* 2017; **26**: 3466–3481.
265 Ugalde CL, Lawson VA, Finkelstein DI, Hill AF. The role of lipids in α-synuclein misfolding and neurotoxicity. *J Biol Chem* 2019; : jbc.REV119.007500.
266 Varkey J, Isas JM, Mizuno N, Jensen MB, Bhatia VK, Jao CC *et al.* Membrane Curvature Induction and Tubulation Are Common Features of Synucleins and Apolipoproteins. *J Biol Chem* 2010; **285**: 32486–32493.
267 Ouberai MM, Wang J, Swann MJ, Galvagnion C, Guilliams T, Dobson CM *et al.* α-Synuclein Senses Lipid Packing Defects and Induces Lateral Expansion of Lipids Leading to Membrane Remodeling. *J Biol Chem* 2013; **288**: 20883–20895.
268 Shi Z, Sachs JN, Rhoades E, Baumgart T. Biophysics of α-synuclein induced membrane remodelling. *Phys Chem Chem Phys* 2015; **17**: 15561–8.
269 Alecu I, Bennett SAL. Dysregulated Lipid Metabolism and Its Role in α-Synucleinopathy in Parkinson's Disease. *Front Neurosci* 2019; **13**: 328.
270 Pacheco C, Aguayo LG, Opazo C. An extracellular mechanism that can explain the neurotoxic effects of α-synuclein aggregates in the brain. *Front Physiol* 2012; **3**: 297.
271 Miranda AM, Lasiecka ZM, Xu Y, Neufeld J, Shahriar S, Simoes S *et al.* Neuronal lysosomal dysfunction releases exosomes harboring APP C-terminal fragments and unique lipid signatures. *Nat Commun* 2018; **9**: 291.
272 Fanning S, Haque A, Imberdis T, Baru V, Barrasa MI, Nuber S *et al.* Lipidomic Analysis of α-Synuclein Neurotoxicity Identifies Stearoyl CoA Desaturase as a Target for Parkinson Treatment. *Mol Cell* 2019; **73**: 1001–1014.e8.
273 Vincent BM, Tardiff DF, Piotrowski JS, Aron R, Lucas MC, Chung CY *et al.* Inhibiting Stearoyl-CoA Desaturase Ameliorates α-Synuclein Cytotoxicity. *Cell Rep* 2018; **25**: 2742–2754.e31.

274 Brekk OR, Moskites A, Isacson O, Hallett PJ. Lipid-dependent deposition of alpha-synuclein and Tau on neuronal Secretogranin II-positive vesicular membranes with age. *Sci Rep* 2018; **8**: 15207.
275 Wang C, Zhao C, Li D, Tian Z, Lai Y, Diao J *et al.* Versatile Structures of α-Synuclein. *Front Mol Neurosci* 2016; **9**: 48.
276 Herculano-Houzel S. Longevity and sexual maturity vary across species with number of cortical neurons, and humans are no exception. *J Comp Neurol* 2019; **527**: 1689–1705.
277 Brand A, Bauer NG, Hallott A, Goldbaum O, Ghebremeskel K, Reifen R *et al.* Membrane lipid modification by polyunsaturated fatty acids sensitizes oligodendroglial OLN-93 cells against oxidative stress and promotes up-regulation of heme oxygenase-1 (HSP32). *J Neurochem* 2010; **113**: 465–476.
278 Yoshino M, Background KM. Analysis of the substrate inhibition of complete and partial types. 2015. doi:10.1186/s40064-015-1082-8.

# Appendix I

The following figures are supplementary to Chapter 3: Engineering iPSCs to generate isogenic neuronal cell models:

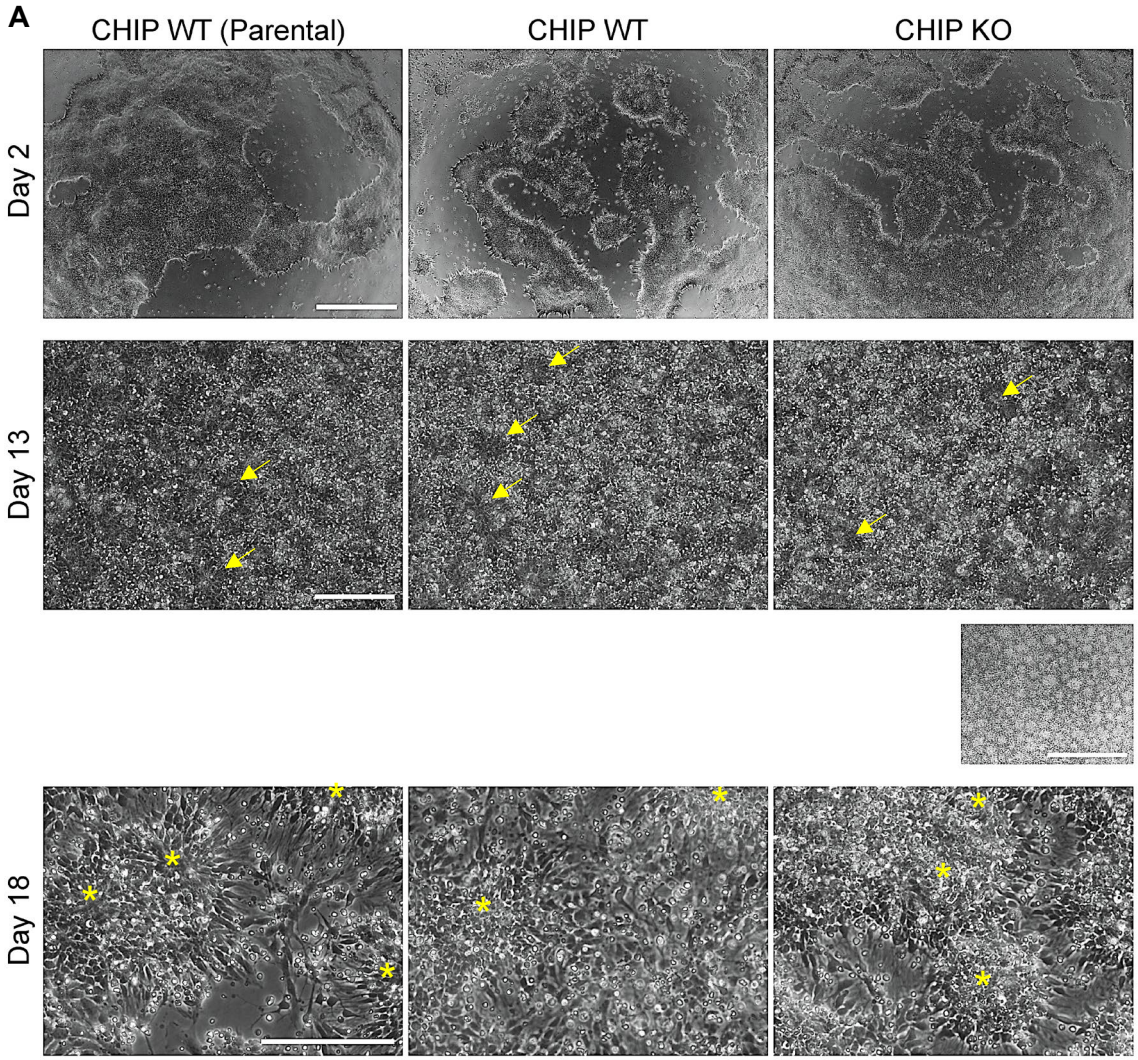


**Figure S.1: Overview of morphological changes during the course of cortical differentiation from iPSC**
Phase contrast images of the differentiating cultures over time.
**A)** Images from cultures of the second differentiation experiment. Day 62 and 80 images show maturation of neurons within the same well across the different cell lines. These wells were within the pool of cultures harvested for MS analysis at day 80. Neural rosettes are indicated by the arrows or the center of the rosette is labeled with an asterisk (*).
Scale bars (refers to images per row), 200 μm and 80 μm (in top row).

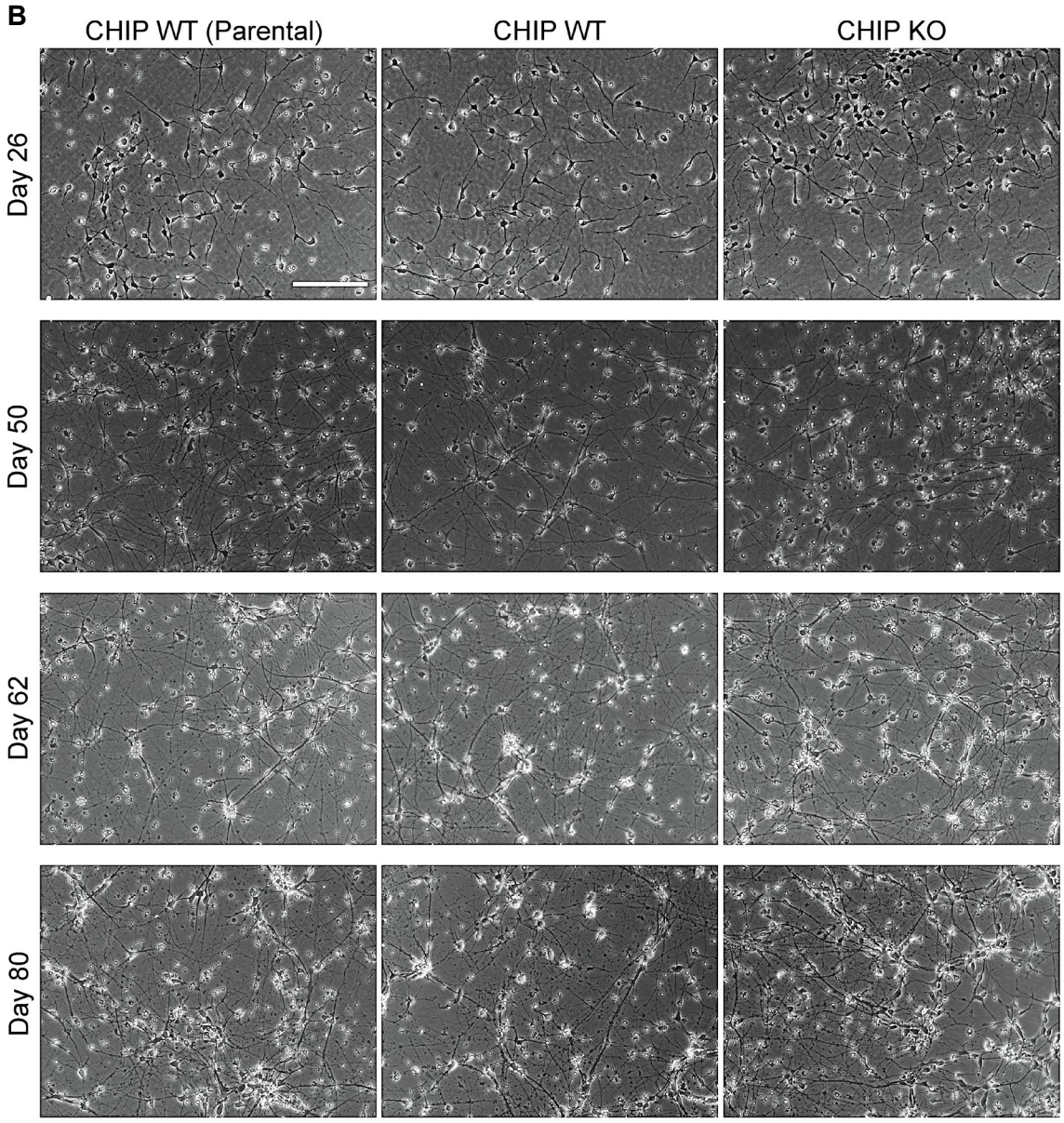


**Figure S.1** *(continued)*
Phase contrast images of the differentiating cultures over time.
**B)** Images from cultures of the first differentiation experiment.
Scale bar, 200 μm.

The following figures and tables are supplementary to Chapter 4: Effect of CHIP on the proteome.

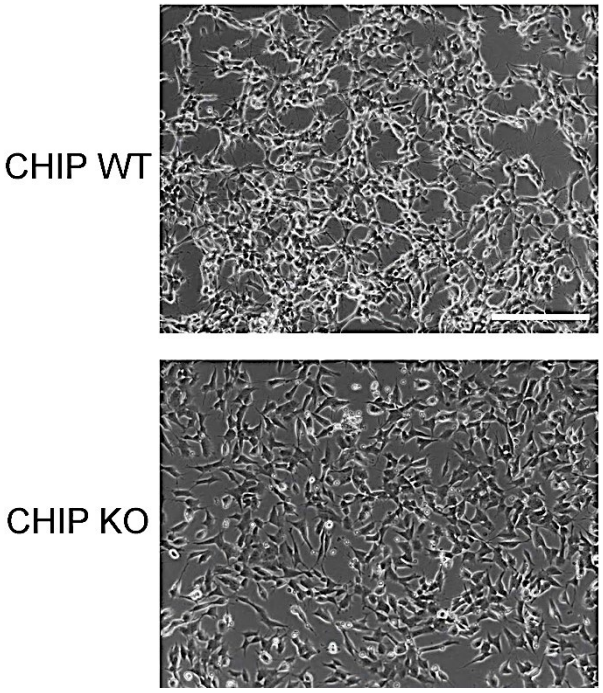


**Figure S.2: Morphology of undifferentiated CHIP SH-SY5Y model**
Phase contrast images showing the morphology of CHIP WT and KO cells. Scale bar, 200 μm.

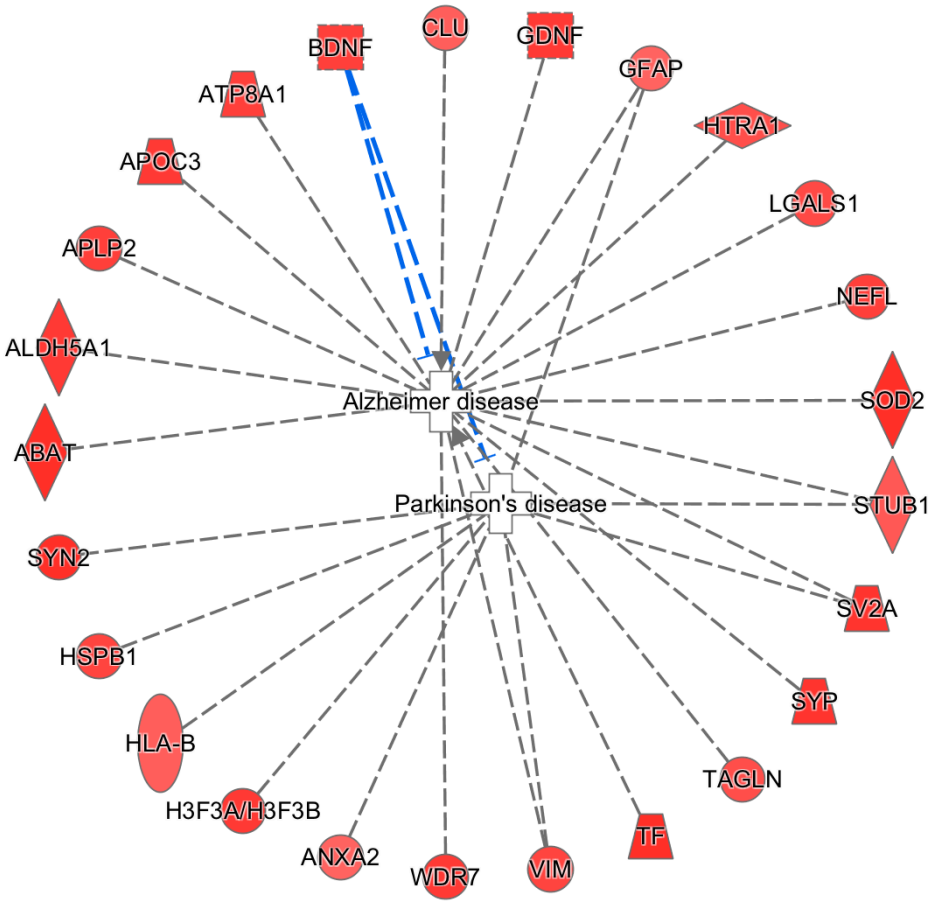


**Figure S.3: Pathway analysis derived from the proteomics of our CHIP cortical neuron model**

SWATH-MS data comparing CHIP KO with CHIP expressing lines was analysed using the Ingenuity Pathway Analysis software. Only significantly changing proteins were used for the analysis. Both Alzheimer's disease- and Parkinson's disease-related pathways were related to the proteins identified. When the relationship could be predicted between the diseases and specific proteins (represented by gene names), the dashed line is coloured (blue represents an inhibitory relationship) rather than grey.

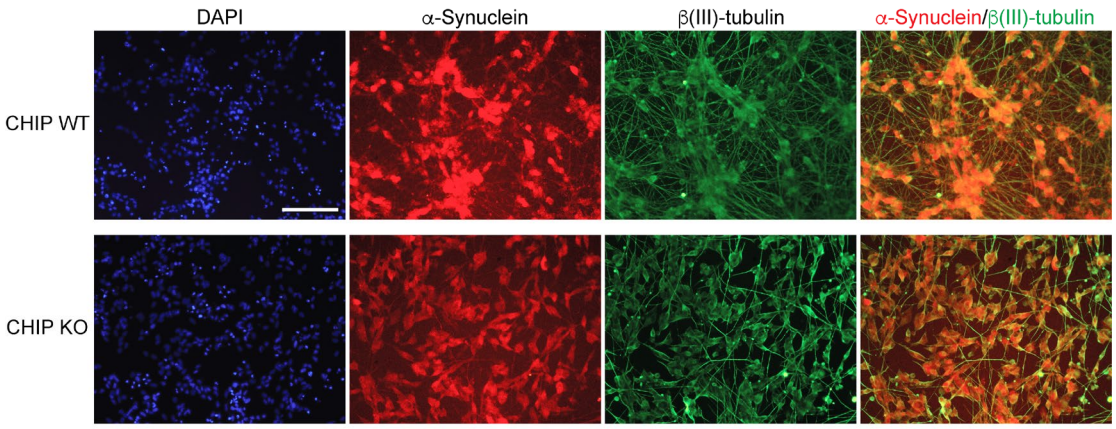


**Figure S.4: Markers of differentiated SH-SY5Y cells**
Immunofluorescence images of α-Syn and β(III)-tubulin expression in CHIP KO and WT SH-SY5Y cells. Both proteins are implicated in neurons and the latter is neuron-specific. The cell lines form complex networks of processes that resemble axons and dendrites. Cells were fixed with 4% paraformaldehyde and stained with anti-α-synuclein mAb (1:500) and anti-b(III)-tubulin mAb (1:1000). Scale bar, 100 μm.

**Table S.1: Most over-represented proteins in CHIP KO cortical neurons compared to neurons derived from the parental iPSC line.**
The top 10 most over-represented proteins that were significantly changed ($P < 0.05$) are numbered and labelled in Figure 4.7.

| Protein | p-value | Fold change | -Log (p-value) | Log (Fold change) | Label |
|---|---|---|---|---|---|
| Statherin | 7.00E-02 | 0.080 | 1.155 | -1.097 | |
| Glial fibrillary acidic protein | 2.38E-03 | 0.091 | 2.623 | -1.042 | 1 |
| Annexin A2 | 1.61E-06 | 0.100 | 5.794 | -0.999 | 2 |
| Interferon-induced transmembrane protein 2 | 6.72E-10 | 0.103 | 9.173 | -0.988 | 3 |
| Galectin-3 | 4.56E-06 | 0.108 | 5.341 | -0.968 | 4 |
| Caldesmon | 1.30E-04 | 0.168 | 3.886 | -0.775 | 5 |
| Protein S100-A11 | 6.19E-05 | 0.184 | 4.208 | -0.734 | 6 |
| Prelamin-A/C | 3.48E-06 | 0.238 | 5.459 | -0.623 | 7 |
| HLA class I histocompatibility antigen, B-78 alpha chain | 2.46E-05 | 0.264 | 4.609 | -0.579 | 8 |
| Parkinson disease 7 domain-containing protein 1 (Fragment) | 6.61E-02 | 0.271 | 1.180 | -0.567 | |
| Annexin A1 | 2.09E-07 | 0.274 | 6.680 | -0.563 | 9 |
| Guanine nucleotide-binding protein G(I)/G(S)/G(O) subunit gamma-12 | 2.23E-07 | 0.274 | 6.652 | -0.563 | 10 |

**Table S.2: Most under-represented proteins in CHIP KO cortical neurons compared to neurons derived from the parental iPSC line**

The top 10 most under-represented proteins that were significantly changed ($P < 0.05$) are numbered and labelled in Figure 4.7.

| Protein | p-value | Fold change | -Log (p-value) | Log (Fold change) | Label |
|---|---|---|---|---|---|
| Disks large homolog 4 | 0.04393 | 12.044 | 1.357 | 1.081 | 1 |
| E3 ubiquitin-protein ligase CHIP | 7.98E-03 | 11.699 | 2.098 | 1.068 | 2 |
| Corticoliberin | 6.60E-04 | 5.913 | 3.180 | 0.772 | 3 |
| STE20/SPS1-related proline-alanine-rich protein kinase | 1.38E-01 | 5.056 | 0.859 | 0.704 | |
| Propionyl-CoA carboxylase beta chain, mitochondrial | 4.09E-01 | 4.248 | 0.389 | 0.628 | |
| Sclerostin domain-containing protein 1 | 7.46E-07 | 4.213 | 6.127 | 0.625 | 4 |
| Keratin, type II cuticular Hb2 | 7.32E-02 | 3.316 | 1.135 | 0.521 | |
| Poliovirus receptor | 1.44E-01 | 2.349 | 0.843 | 0.371 | |
| Caytaxin | 8.20E-02 | 2.344 | 1.086 | 0.370 | |
| Metallophosphoesterase MPPED2 | 7.08E-09 | 2.337 | 8.150 | 0.369 | 5 |
| Amine oxidase [flavin-containing] A | 5.61E-06 | 2.250 | 5.251 | 0.352 | 6 |
| Synaptotagmin-5 | 0.0262 | 2.247 | 1.582 | 0.352 | 7 |
| Caseinolytic peptidase B protein homolog | 2.86E-03 | 2.243 | 2.544 | 0.351 | 8 |
| F-box only protein 2 | 4.62E-05 | 2.217 | 4.336 | 0.346 | 9 |
| GTP-binding protein 1 | 1.73E-01 | 2.163 | 0.761 | 0.335 | |
| U2 small nuclear ribonucleoprotein B'' | 2.50E-01 | 2.118 | 0.603 | 0.326 | |
| Serine/threonine-protein phosphatase 6 regulatory subunit 2 (Fragment) | 1.87E-01 | 2.048 | 0.728 | 0.311 | |
| WD repeat-containing protein 44 | 2.43E-16 | 2.041 | 15.614 | 0.310 | 10 |

**Table S.3: Most over-represented proteins in CHIP KO cortical neurons compared to neurons derived from the WT (CRISPR control) iPSC line**

The top 11 most over-represented proteins that were significantly changed ($P < 0.05$) are numbered and labelled in Figure 4.8.

| Protein | p-value | Fold change | -Log (p-value) | Log (Fold change) | Label |
|---|---|---|---|---|---|
| Interferon-induced transmembrane protein 2 | 5.84E-10 | 0.098 | 9.234 | -1.007 | 1 |
| Annexin A2 | 1.66E-06 | 0.107 | 5.779 | -0.969 | 2 |
| Glial fibrillary acidic protein | 2.78E-03 | 0.109 | 2.556 | -0.961 | 3 |
| Caldesmon | 5.89E-05 | 0.116 | 4.230 | -0.936 | 4 |
| Galectin-3 | 5.51E-06 | 0.120 | 5.259 | -0.920 | 5 |
| Transgelin-2 | 4.49E-06 | 0.148 | 5.348 | -0.831 | 6 |
| Annexin A1 | 3.25E-08 | 0.171 | 7.489 | -0.768 | 7 |
| HLA class I histocompatibility antigen, B-78 alpha chain | 6.51E-06 | 0.171 | 5.186 | -0.767 | 8 |
| PDZ and LIM domain protein 5 | 2.27E-07 | 0.181 | 6.643 | -0.743 | 9 |
| Clusterin | 8.83E-10 | 0.190 | 9.054 | -0.722 | 10 |
| Protein S100-A11 | 8.47E-05 | 0.206 | 4.072 | -0.686 | 11 |

**Table S.4: Most under-represented proteins in CHIP KO cortical neurons compared to neurons derived from the WT (CRISPR control) iPSC line**
The top 10 most under-represented proteins that were significantly changed ($P < 0.05$) are numbered and labelled in Figure 4.8.

| Protein | p-value | Fold change | -Log (p-value) | Log (Fold change) | Label |
|---|---|---|---|---|---|
| Corticoliberin | 2.98E-05 | 5.385 | 4.526 | 0.731 | 1 |
| E3 ubiquitin-protein ligase CHIP | 1.37E-01 | 4.444 | 0.862 | 0.648 | |
| Sclerostin domain-containing protein 1 | 1.51E-05 | 3.594 | 4.821 | 0.556 | 2 |
| F-box only protein 2 | 4.37E-06 | 2.667 | 5.360 | 0.426 | 3 |
| Glutaredoxin-related protein 5, mitochondrial | 1.94E-01 | 2.452 | 0.712 | 0.390 | |
| Semaphorin-3C | 1.87E-09 | 2.375 | 8.729 | 0.376 | 4 |
| AP-3 complex subunit mu-2 | 1.25E-01 | 2.366 | 0.905 | 0.374 | |
| Synaptosomal-associated protein 29 | 8.76E-02 | 2.254 | 1.057 | 0.353 | |
| RNA-binding protein Musashi homolog 1 | 1.36E-01 | 2.247 | 0.865 | 0.352 | |
| Testican-1 | 2.18E-10 | 2.241 | 9.661 | 0.350 | 5 |
| Metallophosphoesterase MPPED2 | 6.30E-07 | 2.203 | 6.200 | 0.343 | 6 |
| Synaptotagmin-5 | 8.34E-05 | 2.187 | 4.079 | 0.340 | 7 |
| Histone H2A type 2-A | 6.30E-04 | 2.185 | 3.201 | 0.339 | 8 |
| Caytaxin | 1.04E-01 | 2.179 | 0.982 | 0.338 | |
| Neurofilament light polypeptide | 6.54E-06 | 2.154 | 5.184 | 0.333 | 9 |
| Brain-derived neurotrophic factor | 9.55E-11 | 2.142 | 10.020 | 0.331 | 10 |

**Table S.5: Most over-represented proteins in CHIP WT (CRISPR control line) cortical neurons compared to neurons derived from the parental iPSC line**
The top 10 most over-represented proteins that were significantly changed ($P < 0.05$) are numbered and labelled in Figure 4.9.

| Protein | p-value | Fold change | -Log (p-value) | Log (Fold change) | Label |
|---|---|---|---|---|---|
| Statherin | 0.02645 | 0.086 | 1.578 | -1.067 | 1 |
| Semenogelin-1 | 5.02E-02 | 0.271 | 1.299 | -0.568 | |
| Histone H2A type 2-A | 6.77E-06 | 0.271 | 5.169 | -0.567 | 2 |
| Filaggrin-2 | 1.76E-02 | 0.320 | 1.755 | -0.495 | 3 |
| Coronin | 1.24E-01 | 0.323 | 0.906 | -0.491 | |
| NADH dehydrogenase [ubiquinone] 1 beta subcomplex subunit 6 | 9.32E-03 | 0.391 | 2.031 | -0.408 | 4 |
| Dermcidin | 2.01E-03 | 0.402 | 2.697 | -0.395 | 5 |
| Prolactin-inducible protein | 5.75E-02 | 0.426 | 1.240 | -0.371 | |
| Sarcolemmal membrane-associated protein | 3.15E-03 | 0.429 | 2.502 | -0.368 | 6 |
| Brain-derived neurotrophic factor | 4.11E-12 | 0.444 | 11.386 | -0.352 | 7 |
| RNA-binding protein Musashi homolog 1 | 1.34E-01 | 0.445 | 0.872 | -0.351 | |
| Protein BORCS7-ASMT | 1.54E-01 | 0.469 | 0.814 | -0.329 | |
| Apolipoprotein C-III | 1.91E-06 | 0.475 | 5.719 | -0.323 | 8 |
| Annexin A4 | 5.73E-09 | 0.488 | 8.242 | -0.311 | 9 |
| Junctional adhesion molecule C | 1.63E-02 | 0.494 | 1.789 | -0.307 | 10 |

**Table S.6: Most under-represented proteins in CHIP WT (CRISPR control line) cortical neurons compared to neurons derived from the parental iPSC line**
The top 10 most under-represented proteins that were significantly changed (P < 0.05) are numbered and labelled in Figure 4.9.

| Protein | p-value | Fold change | -Log (p-value) | Log (Fold change) | Label |
|---|---|---|---|---|---|
| GTP-binding protein 1 | 1.90E-02 | 8.272 | 1.721 | 0.918 | |
| STE20/SPS1-related proline-alanine-rich protein kinase | 1.27E-01 | 5.771 | 0.895 | 0.761 | |
| Pirin | 1.12E-07 | 3.553 | 6.952 | 0.551 | 1 |
| Lysosome-associated membrane glycoprotein 5 | 2.18E-01 | 3.463 | 0.662 | 0.539 | |
| Amyloid-like protein 2 | 4.30E-04 | 3.102 | 3.367 | 0.492 | 2 |
| WD repeat-containing protein 18 (Fragment) | 2.42E-02 | 2.682 | 1.617 | 0.428 | |
| E3 ubiquitin-protein ligase CHIP | 9.94E-02 | 2.636 | 1.003 | 0.421 | |
| Symplekin | 1.32E-01 | 2.541 | 0.880 | 0.405 | |
| Fermitin family homolog 2 (Fragment) | 1.64E-01 | 2.538 | 0.784 | 0.405 | |
| Serine/threonine-protein phosphatase 6 regulatory subunit 2 (Fragment) | 9.87E-02 | 2.507 | 1.006 | 0.399 | |
| U2 small nuclear ribonucleoprotein B'' | 1.95E-01 | 2.468 | 0.709 | 0.392 | |
| Peptidyl-prolyl cis-trans isomerase NIMA-interacting 4 | 1.06E-05 | 2.436 | 4.974 | 0.387 | 3 |
| FYVE, RhoGEF and PH domain-containing protein 4 | 4.27E-02 | 2.433 | 1.369 | 0.386 | 4 |
| Allograft inflammatory factor 1-like | 9.11E-02 | 2.430 | 1.040 | 0.386 | |
| Glutathione S-transferase omega-1 | 1.73E-02 | 2.373 | 1.762 | 0.375 | 5 |
| Histone H3.1 | 1.42E-03 | 2.265 | 2.848 | 0.355 | 6 |
| Transcription elongation factor SPT5 | 3.33E-01 | 2.262 | 0.478 | 0.355 | |
| mRNA export factor | 6.43E-02 | 2.254 | 1.192 | 0.353 | |
| Vesicle transport through interaction with t-SNAREs homolog 1A | 8.32E-03 | 2.253 | 2.080 | 0.353 | 7 |
| Aminopeptidase B | 3.44E-03 | 2.225 | 2.463 | 0.347 | 8 |
| RNA-binding protein 3 | 1.04E-03 | 2.199 | 2.983 | 0.342 | 9 |
| 1-acyl-sn-glycerol-3-phosphate acyltransferase alpha | 4.90E-04 | 2.167 | 3.310 | 0.336 | 10 |

**Table S.7: Most over-represented proteins in CHIP KO iPSC compared to WT iPSC**
The top 10 most over-represented proteins that were significantly changed ($P < 0.05$) are numbered and labelled in Figure 4.12.

| Protein | p-value | Fold change | -Log (p-value) | Log (Fold change) | Label |
|---|---|---|---|---|---|
| 60S ribosomal protein L36a-like | 4.52E-02 | 0.018 | 1.345 | -1.748 | |
| Small nuclear ribonucleoprotein F | 4.67E-02 | 0.072 | 1.331 | -1.141 | |
| E3 ubiquitin-protein ligase E3D | 4.21E-02 | 0.093 | 1.376 | -1.034 | |
| AP-3 complex subunit beta-2 | 1.01E-01 | 0.107 | 0.995 | -0.969 | |
| Signal recognition particle 9 kDa protein | 3.64E-02 | 0.117 | 1.439 | -0.932 | |
| Vitamin K epoxide reductase complex subunit 1 | 6.52E-02 | 0.165 | 1.186 | -0.783 | |
| Endoplasmic reticulum-Golgi intermediate compartment protein 1 | 3.55E-01 | 0.182 | 0.449 | -0.739 | |
| Guanine nucleotide-binding protein G(I)/G(S)/G(T) subunit beta-1 | 5.88E-02 | 0.210 | 1.231 | -0.679 | |
| Cellular nucleic acid-binding protein | 9.34E-02 | 0.225 | 1.030 | -0.648 | |
| Annexin A1 | 1.81E-10 | 0.229 | 9.743 | -0.641 | 1 |
| Protein FAM98B | 1.06E-01 | 0.238 | 0.977 | -0.623 | |
| DnaJ homolog subfamily C member 11 | 1.91E-01 | 0.240 | 0.720 | -0.620 | |
| Poly(rC)-binding protein 3 | 1.70E-01 | 0.263 | 0.770 | -0.581 | |
| Tubulin alpha-4A chain | 6.68E-02 | 0.263 | 1.175 | -0.580 | |
| Raftlin | 3.64E-02 | 0.264 | 1.439 | -0.578 | |
| Procollagen-lysine,2-oxoglutarate 5-dioxygenase 3 | 7.38E-02 | 0.269 | 1.132 | -0.570 | |
| Oligosaccharyltransferase complex subunit OSTC | 9.32E-02 | 0.271 | 1.031 | -0.566 | |
| Acylglycerol kinase, mitochondrial | 1.74E-01 | 0.272 | 0.759 | -0.565 | |
| Neural cell adhesion molecule L1 | 3.01E-01 | 0.282 | 0.522 | -0.549 | |
| CD81 antigen | 2.67E-02 | 0.285 | 1.574 | -0.545 | |
| Tubulin alpha-1C chain | 4.11E-02 | 0.292 | 1.387 | -0.534 | |
| Serotransferrin | 5.07E-02 | 0.292 | 1.295 | -0.534 | |
| Vimentin | 5.94E-09 | 0.293 | 8.226 | -0.532 | 2 |
| Hippocalcin-like protein 1 | 7.96E-02 | 0.307 | 1.099 | -0.512 | |

**Table S.7** *(continued)*

| Protein | p-value | Fold change | -Log (p-value) | Log (Fold change) | Label |
|---|---|---|---|---|---|
| Queuosine salvage protein | 4.05E-01 | 0.323 | 0.393 | -0.490 | |
| 40S ribosomal protein S11 | 3.79E-02 | 0.336 | 1.421 | -0.473 | |
| Tubulin polymerization-promoting protein family member 3 | 2.90E-01 | 0.347 | 0.537 | -0.460 | |
| Peptidyl-prolyl cis-trans isomerase G | 2.22E-02 | 0.347 | 1.653 | -0.460 | |
| Phosphatidylinositol transfer protein alpha isoform | 6.95E-02 | 0.358 | 1.158 | -0.446 | |
| 1-phosphatidylinositol 4,5-bisphosphate phosphodiesterase delta-1 | 2.92E-02 | 0.368 | 1.534 | -0.434 | |
| Golgin subfamily A member 2 | 5.98E-07 | 0.370 | 6.223 | -0.432 | 3 |
| Sister chromatid cohesion protein PDS5 homolog B | 4.06E-01 | 0.371 | 0.391 | -0.430 | |
| Ataxin-2 | 1.03E-01 | 0.374 | 0.988 | -0.427 | |
| 40S ribosomal protein S12 | 6.71E-02 | 0.390 | 1.173 | -0.409 | |
| Sodium/potassium-transporting ATPase subunit alpha-3 | 2.60E-01 | 0.407 | 0.584 | -0.390 | |
| Filamin-C | 4.03E-02 | 0.411 | 1.395 | -0.386 | |
| Galectin-1 | 5.01E-07 | 0.412 | 6.300 | -0.385 | 4 |
| RNA 3'-terminal phosphate cyclase | 5.80E-04 | 0.417 | 3.237 | -0.379 | 5 |
| Neuroblast differentiation-associated protein AHNAK | 7.29E-03 | 0.420 | 2.137 | -0.376 | 6 |
| cAMP-dependent protein kinase catalytic subunit alpha | 1.35E-02 | 0.437 | 1.869 | -0.360 | |
| 60S ribosomal protein L32 | 5.89E-03 | 0.439 | 2.230 | -0.358 | 7 |
| Transforming protein RhoA | 2.22E-02 | 0.444 | 1.654 | -0.353 | |
| COP9 signalosome complex subunit 7b | 1.86E-01 | 0.446 | 0.730 | -0.351 | |
| Endoplasmic reticulum resident protein 44 | 3.71E-02 | 0.448 | 1.431 | -0.349 | |
| Pro-neuropeptide Y | 3.55E-02 | 0.449 | 1.450 | -0.347 | |
| O-acetyl-ADP-ribose deacetylase MACROD1 | 2.02E-03 | 0.453 | 2.695 | -0.344 | 8 |
| Cytoplasmic FMR1-interacting protein 2 | 4.63E-02 | 0.464 | 1.335 | -0.333 | |

**Table S.7** *(continued)*

| Protein | p-value | Fold change | -Log (p-value) | Log (Fold change) | Label |
|---|---|---|---|---|---|
| Tumor protein D52 | 1.76E-01 | 0.469 | 0.755 | -0.329 | |
| CD99 antigen | 1.60E-01 | 0.469 | 0.797 | -0.329 | |
| Cell division cycle and apoptosis regulator protein 1 | 3.08E-01 | 0.472 | 0.512 | -0.326 | |
| Guanine nucleotide-binding protein subunit alpha-13 | 1.37E-01 | 0.475 | 0.864 | -0.324 | |
| 2,4-dienoyl-CoA reductase, mitochondrial | 1.55E-01 | 0.475 | 0.810 | -0.323 | |
| Acyl-coenzyme A thioesterase 9, mitochondrial | 1.49E-01 | 0.480 | 0.828 | -0.319 | |
| Chromogranin-A | 1.12E-01 | 0.480 | 0.950 | -0.319 | |
| Macrophage migration inhibitory factor | 1.12E-01 | 0.488 | 0.951 | -0.312 | |
| Guanine nucleotide-binding protein G(I)/G(S)/G(T) subunit beta-2 | 1.16E-01 | 0.493 | 0.937 | -0.307 | |
| Prostaglandin E synthase 3 | 3.79E-02 | 0.493 | 1.421 | -0.307 | |
| RNA-binding motif, single-stranded-interacting protein 3 | 1.36E-01 | 0.494 | 0.867 | -0.306 | |
| Tripeptidyl-peptidase 2 | 1.18E-01 | 0.495 | 0.928 | -0.306 | |
| Cysteine--tRNA ligase, cytoplasmic | 5.20E-03 | 0.495 | 2.284 | -0.305 | 9 |
| NADH dehydrogenase [ubiquinone] 1 alpha subcomplex subunit 5 | 1.57E-01 | 0.499 | 0.804 | -0.302 | |
| NudC domain-containing protein 1 | 7.67E-02 | 0.501 | 1.115 | -0.300 | |
| Caldesmon | 3.92E-08 | 0.502 | 7.406 | -0.299 | 10 |

**Table S.8: Most under-represented proteins in CHIP KO iPSC compared to WT iPSC**
The top 10 most under-represented proteins that were significantly changed ($P < 0.05$) are numbered and labelled in Figure 4.12.

| Protein | p-value | Fold change | -Log (p-value) | Log (Fold change) | Label |
|---|---|---|---|---|---|
| Protein SOGA3 | 3.32E-01 | 15.007 | 0.479 | 1.176 | |
| Protein PAXX | 3.44E-01 | 14.481 | 0.464 | 1.161 | |
| PRA1 family protein 2 | 4.91E-02 | 7.488 | 1.309 | 0.874 | |
| Dynactin subunit 1 | 2.45E-01 | 4.181 | 0.611 | 0.621 | |
| NADH dehydrogenase [ubiquinone] 1 alpha subcomplex subunit 13 | 1.27E-02 | 3.503 | 1.898 | 0.544 | |
| 28S ribosomal protein S28, mitochondrial | 2.10E-01 | 3.465 | 0.678 | 0.540 | |
| Poliovirus receptor | 3.09E-01 | 3.452 | 0.509 | 0.538 | |
| Non-histone chromosomal protein HMG-17 | 3.50E-04 | 3.392 | 3.456 | 0.530 | 1 |
| 5'-AMP-activated protein kinase catalytic subunit alpha-1 | 2.94E-01 | 3.141 | 0.532 | 0.497 | |
| Alkyldihydroxyacetonephosphate synthase, peroxisomal | 4.91E-02 | 3.131 | 1.309 | 0.496 | |
| ER membrane protein complex subunit 1 | 2.08E-03 | 3.009 | 2.682 | 0.478 | 2 |
| Protein C10 | 1.03E-03 | 3.008 | 2.987 | 0.478 | 3 |
| U4/U6.U5 tri-snRNP-associated protein 1 | 1.80E-03 | 2.886 | 2.745 | 0.460 | 4 |
| Ribose-phosphate pyrophosphokinase 2 | 7.55E-05 | 2.852 | 4.122 | 0.455 | 5 |
| Galectin-3 | 1.93E-01 | 2.748 | 0.714 | 0.439 | |
| Mitochondrial import inner membrane translocase subunit Tim8 B | 3.03E-03 | 2.698 | 2.519 | 0.431 | 6 |
| Gem-associated protein 5 | 2.38E-02 | 2.632 | 1.624 | 0.420 | |
| Metalloproteinase inhibitor 3 | 1.02E-01 | 2.629 | 0.993 | 0.420 | |
| Vesicle-fusing ATPase | 4.24E-01 | 2.595 | 0.373 | 0.414 | |
| E3 ubiquitin-protein ligase TRIM36 | 6.29E-02 | 2.480 | 1.201 | 0.394 | |
| Glutaminase kidney isoform, mitochondrial | 1.30E-04 | 2.475 | 3.886 | 0.394 | 7 |
| Selenocysteine-specific elongation factor | 2.24E-01 | 2.455 | 0.650 | 0.390 | |
| Putative nucleotidyltransferase MAB21L1 | 4.72E-02 | 2.414 | 1.326 | 0.383 | |
| Transmembrane emp24 domain-containing protein 5 | 2.08E-01 | 2.363 | 0.681 | 0.374 | |

**Table S.8** *(continued)*

| Protein | p-value | Fold change | -Log (p-value) | Log (Fold change) | Label |
|---|---|---|---|---|---|
| 39S ribosomal protein L24, mitochondrial | 7.43E-02 | 2.314 | 1.129 | 0.364 | |
| Microtubule-associated protein tau | 1.05E-02 | 2.296 | 1.980 | 0.361 | |
| Dopamine beta-hydroxylase | 6.03E-02 | 2.282 | 1.219 | 0.358 | |
| Kinesin-like protein KIF3B | 9.63E-02 | 2.264 | 1.016 | 0.355 | |
| Thymosin beta-4 | 1.31E-05 | 2.252 | 4.882 | 0.352 | 8 |
| 6-phosphogluconate dehydrogenase, decarboxylating | 2.71E-10 | 2.186 | 9.566 | 0.340 | 9 |
| NADH dehydrogenase [ubiquinone] 1 alpha subcomplex subunit 7 | 6.42E-03 | 2.166 | 2.192 | 0.336 | 10 |

**Table S.9: Most over-represented proteins in CHIP KO compared to WT differentiated SH-SY5Y**

The top 10 most over-represented proteins that were significantly changed ($P < 0.05$) are numbered and labelled in Figure 4.13.

| Protein | p-value | Fold change | -Log (p-value) | Log (Fold change) | Label |
|---|---|---|---|---|---|
| Protein-glutamine gamma-glutamyltransferase 2 | 8.10E-04 | 0.088 | 3.092 | -1.058 | 1 |
| Exportin-T | 2.70E-01 | 0.146 | 0.569 | -0.835 | |
| 28S ribosomal protein S28, mitochondrial | 8.50E-04 | 0.211 | 3.071 | -0.676 | 2 |
| Matrix-remodeling-associated protein 7 | 1.10E-04 | 0.270 | 3.959 | -0.568 | 3 |
| DNA (cytosine-5)-methyltransferase 3A | 1.58E-01 | 0.306 | 0.802 | -0.514 | |
| Cadherin-1 | 3.61E-01 | 0.323 | 0.443 | -0.491 | |
| Cytochrome c oxidase subunit 7C, mitochondrial | 1.24E-03 | 0.326 | 2.907 | -0.487 | 4 |
| E3 ubiquitin-protein ligase E3D | 1.39E-02 | 0.337 | 1.857 | -0.472 | |
| Cystathionine beta-synthase | 9.10E-04 | 0.340 | 3.041 | -0.468 | 5 |
| Proto-oncogene tyrosine-protein kinase receptor Ret | 3.51E-01 | 0.345 | 0.455 | -0.462 | |
| Spermatid perinuclear RNA-binding protein | 2.34E-01 | 0.347 | 0.631 | -0.460 | |
| Cell division cycle and apoptosis regulator protein 1 | 3.42E-02 | 0.349 | 1.466 | -0.458 | |
| Plastin-3 | 1.98E-01 | 0.370 | 0.702 | -0.431 | |
| Neurotrypsin | 5.97E-16 | 0.383 | 15.224 | -0.417 | 6 |
| Guanine nucleotide-binding protein G(I)/G(S)/G(T) subunit beta-1 | 1.26E-02 | 0.398 | 1.900 | -0.400 | |
| Methionine aminopeptidase 2 | 2.56E-01 | 0.404 | 0.592 | -0.393 | |
| Protein NipSnap homolog 2 | 1.32E-02 | 0.407 | 1.878 | -0.390 | |
| Transcriptional activator protein Pur-beta | 1.06E-02 | 0.411 | 1.974 | -0.387 | |
| Coactosin-like protein | 1.22E-01 | 0.420 | 0.912 | -0.377 | |
| Insulin-like growth factor 2 mRNA-binding protein 2 | 1.59E-01 | 0.422 | 0.798 | -0.375 | |
| Cathepsin B | 4.01E-07 | 0.428 | 6.397 | -0.368 | 7 |

**Table S.9** *(continued)*

| Protein | p-value | Fold change | -Log (p-value) | Log (Fold change) | Label |
|---|---|---|---|---|---|
| Glycerol-3-phosphate acyltransferase 4 | 1.86E-05 | 0.432 | 4.731 | -0.364 | 8 |
| Branched-chain-amino-acid aminotransferase, cytosolic | 1.48E-05 | 0.475 | 4.828 | -0.323 | 9 |
| Tubulin alpha-4A chain | 3.43E-02 | 0.481 | 1.464 | -0.318 | |
| Oligosaccharyltransferase complex subunit OSTC | 2.85E-02 | 0.485 | 1.545 | -0.314 | |
| Neurofilament light polypeptide | 2.92E-16 | 0.490 | 15.534 | -0.310 | 10 |

**Table S.10: Most under-represented proteins in CHIP KO compared to WT differentiated SH-SY5Y**

The top 10 most under-represented proteins that were significantly changed ($P < 0.05$) are numbered and labelled in Figure 4.13.

| Protein | p-value | Fold change | -Log (p-value) | Log (Fold change) | Label |
|---|---|---|---|---|---|
| Small nuclear ribonucleoprotein F | 6.27E-02 | 12.610 | 1.203 | 1.101 | |
| Histone H2A type 2-A | 4.07E-05 | 7.783 | 4.390 | 0.891 | 1 |
| Sodium-coupled neutral amino acid transporter 2 | 2.43E-01 | 4.243 | 0.614 | 0.628 | |
| Protein phosphatase 1 regulatory subunit 7 | 1.68E-01 | 3.683 | 0.774 | 0.566 | |
| PRKC apoptosis WT1 regulator protein | 9.37E-02 | 3.572 | 1.028 | 0.553 | |
| Metalloproteinase inhibitor 3 | 1.14E-10 | 3.460 | 9.942 | 0.539 | 2 |
| Ras-related protein R-Ras2 | 7.63E-02 | 3.323 | 1.117 | 0.521 | |
| Protein unc-45 homolog A | 3.72E-02 | 2.925 | 1.430 | 0.466 | |
| Alkyldihydroxyacetonephosphate synthase, peroxisomal | 1.01E-01 | 2.699 | 0.997 | 0.431 | |
| Metastasis-associated protein MTA2 | 5.45E-02 | 2.680 | 1.264 | 0.428 | |
| Mesoderm-specific transcript homolog protein | 1.65E-07 | 2.553 | 6.783 | 0.407 | 3 |
| Peroxidasin homolog | 9.08E-10 | 2.552 | 9.042 | 0.407 | 4 |
| ProSAAS | 1.51E-10 | 2.469 | 9.822 | 0.392 | 5 |
| UDP-glucose 4-epimerase | 3.88E-02 | 2.429 | 1.411 | 0.385 | |
| Collagen alpha-1(XXVI) chain | 5.69E-17 | 2.404 | 16.245 | 0.381 | 6 |
| OCIA domain-containing protein 2 | 8.43E-03 | 2.399 | 2.074 | 0.380 | 7 |
| Methyltransferase-like protein 7A | 3.58E-02 | 2.372 | 1.446 | 0.375 | |
| Twinfilin-1 | 2.03E-02 | 2.352 | 1.693 | 0.371 | |
| N-acetylserotonin O-methyltransferase-like protein | 4.96E-02 | 2.273 | 1.305 | 0.357 | |
| Synaptophysin-like protein 1 | 1.73E-02 | 2.246 | 1.761 | 0.351 | |
| Deaminated glutathione amidase | 5.42E-02 | 2.224 | 1.266 | 0.347 | |
| THO complex subunit 6 homolog | 1.35E-03 | 2.170 | 2.870 | 0.336 | 8 |
| Density-regulated protein | 3.02E-02 | 2.157 | 1.521 | 0.334 | |

**Table S.10** *(continued)*

| Protein | p-value | Fold change | -Log (p-value) | Log (Fold change) | Label |
|---|---|---|---|---|---|
| Nuclear cap-binding protein subunit 1 | 2.76E-02 | 2.091 | 1.559 | 0.320 | |
| YTH domain-containing family protein 2 | 2.54E-01 | 2.042 | 0.596 | 0.310 | |
| Peflin | 3.12E-01 | 2.039 | 0.507 | 0.310 | |
| Galectin-3 | 1.33E-05 | 2.019 | 4.877 | 0.305 | 9 |
| Signal transducer and activator of transcription 3 | 2.64E-03 | 1.967 | 2.578 | 0.294 | 10 |

The following figures are supplementary to Chapter 5: The possible role of CHIP in regulating the homeostasis of Annexin A2 and membrane integrity.

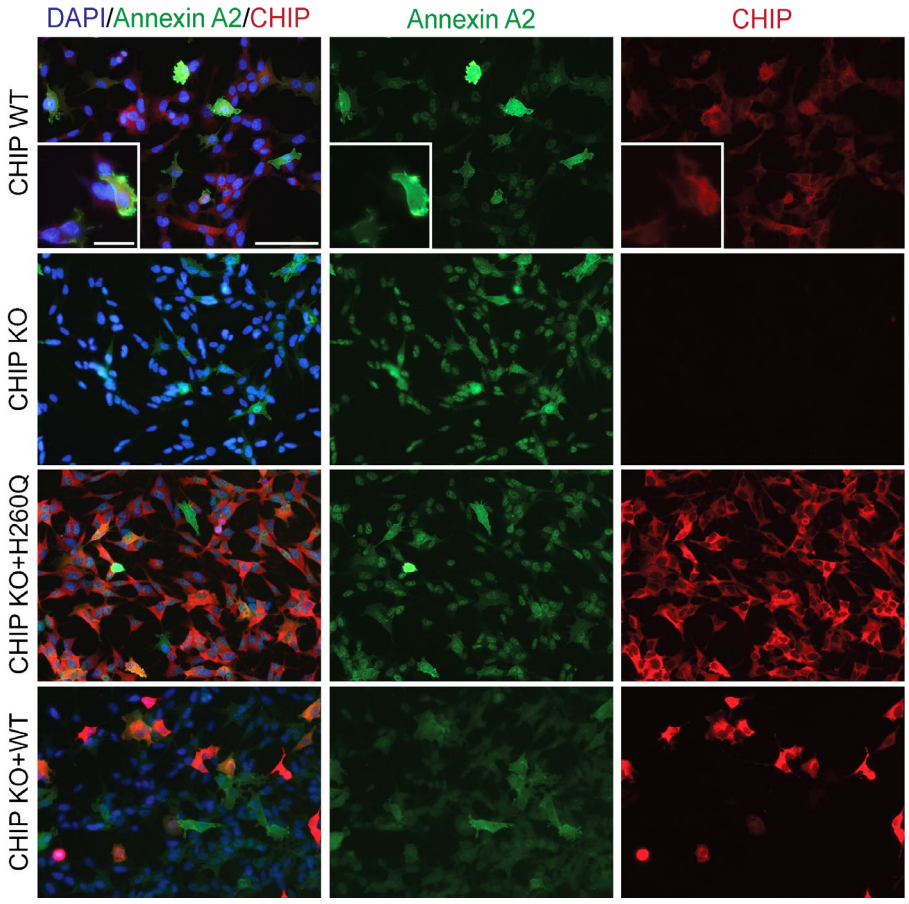


**Figure S.5: CHIP & Annexin A2 expression in undifferentiated SH-SY5Y**
Undifferentiated SH-SY5Y cells of different CHIP genotypes (WT, KO and the stable cell lines KO+H260Q and KO+WT) were fixed with 4% PFA and then methanol. Parallel wells to those used for PLA (Figure 5.13) were incubated with anti-ANXA2 pAb (1:500) and anti-CHIP mAb (1:1000) antibodies.
Axio Imager, *Zeiss*, 20x objective. Scale bar, 100 μm.

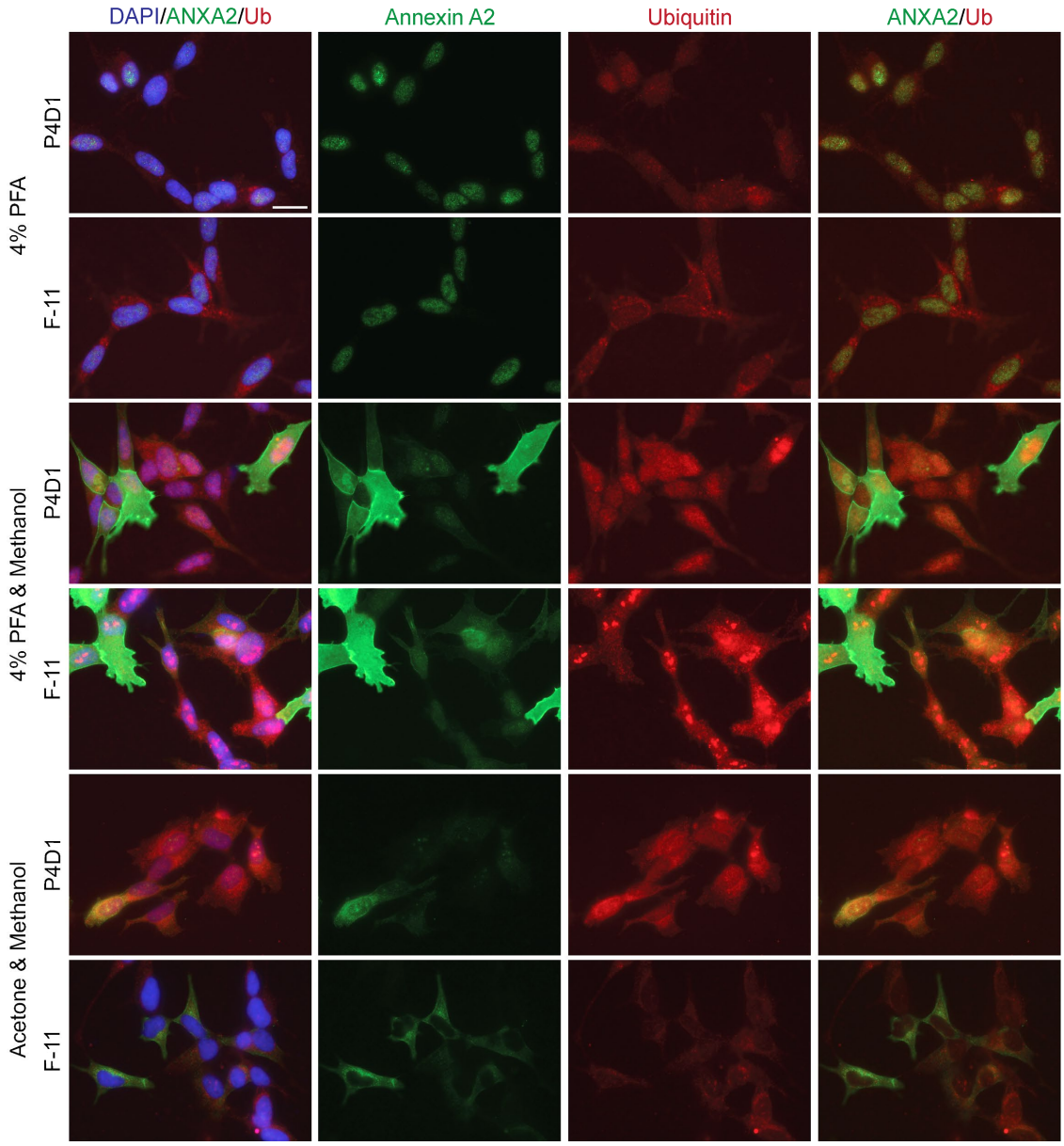


**Figure S.6: Optimisation of the detection of endogenous ubiquitin by IF**
Undifferentiated SH-SY5Y CHIP WT cells were fixed with different methods and stained using anti-ANXA2 Rb pAb (1:1000) and either anti-Ub mAbs (F-11 or P4D1) (1:100). The antibody concentration had been previously optimised (data not shown). Scale bar, 20 mm

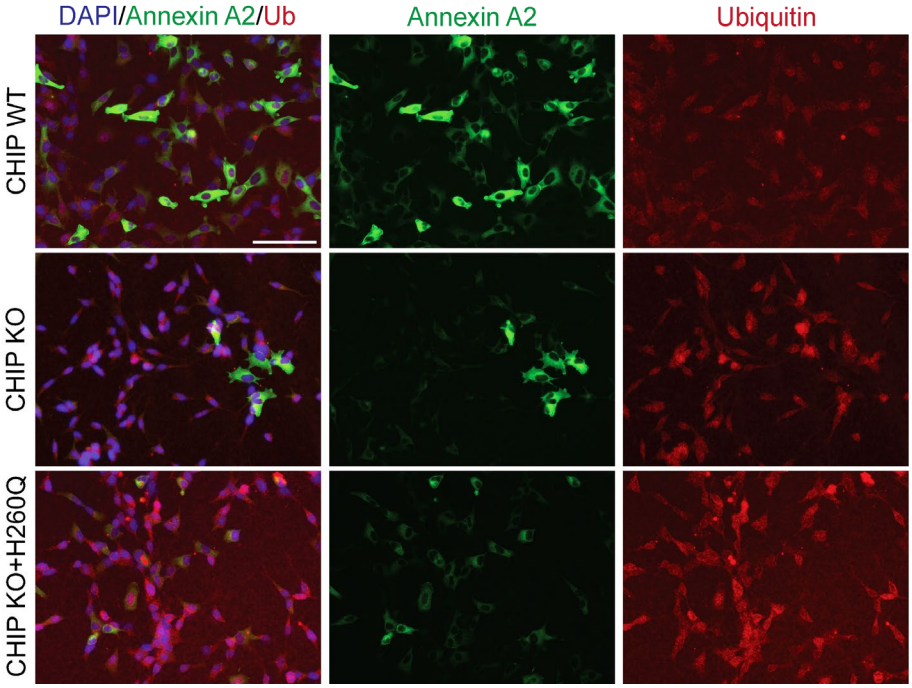


**Figure S.7: Ubiquitin and Annexin A2 expression in undifferentiated SH-SY5Y**
Undifferentiated SH-SY5Y cells of different CHIP genotypes (WT, KO and the stable cell lines KO+H260Q and KO+WT) were fixed with acetone and methanol. Parallel wells to those used for PLA (Figure 5.17) were stained with anti-ANXA2 pAb (1:500) and anti-Ubiquitin mAb (P4D1) (1:100) antibodies. Axio Imager, Zeiss, 20x objective. Scale bars, 100 μm.

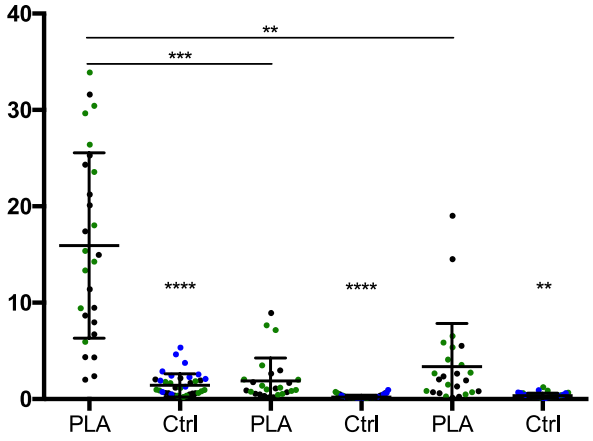


**Figure S.8: Annexin A2 & S100-A11 interaction by an independent PLA experiment in undifferentiated SH-SY5Y quantified manually**
Manual quantifications of an independent experiment to that of Figure 5.31 (performed with the same conditions). PLA signal per nuclei of different cell lines represented in the dot plot as mean ± SD. Kruskal-Wallis test and Dunn's multiple comparisons post-test (comparisons between PLA and Ctrl conditions per cell line is indicated above each Ctrl), $^{**}P < 0.005$, $^{***}P < 0.0005$, $^{****}P < 0.0001$, $n \geq 12$ images per biological duplicate and $n \geq 11$ images per control condition per cell line.

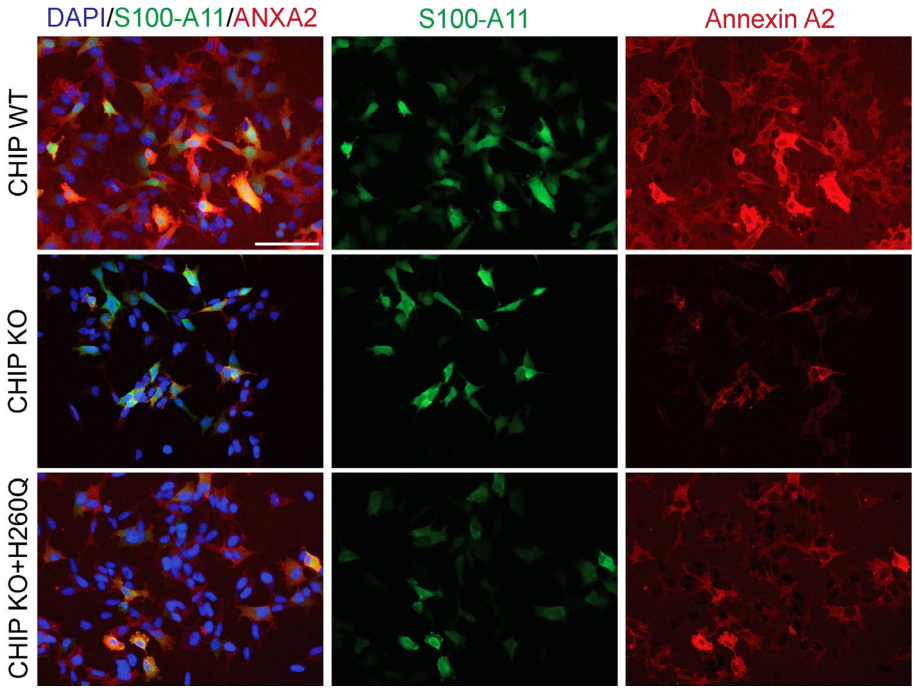


**Figure S.9: S100-A11 and Annexin A2 expression in undifferentiated SH-SY5Y**
Undifferentiated SH-SY5Y cells of different CHIP genotypes (WT, KO and the stable cell lines KO+H260Q and KO+K30A) were fixed with acetone & methanol. Parallel wells to those used for PLA (Figure 5.30) were stained with anti-ANXA2 mAb (3:500) and anti-s100-A11 pAb (1:500) antibodies. Axio Imager, *Zeiss*, 20x objective. Scale bar, 100 μm.

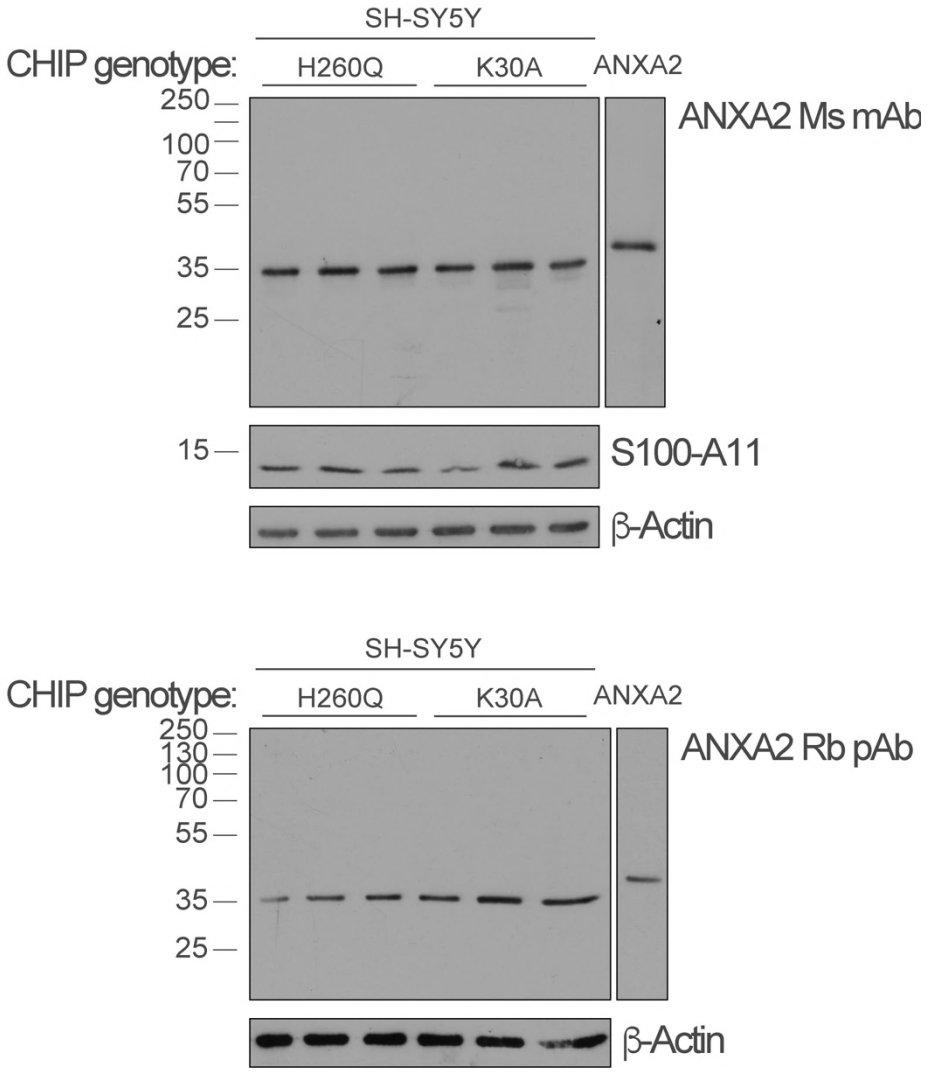


**Figure S.10: Annexin A2 expression in undifferentiated SH-SY5Y cells expressing either a U-box mutant CHIP (H260Q) or TPR-mutant CHIP (K30A)**
Undifferentiated SH-SY5Y cells stably expressing different CHIP mutants were lysed with urea-based lysis buffer (the same as that used for SWATH-MS). For each sample, 20 μg of lysate was loaded per 12% gel for SDS-PAGE/WB and two gels were ran in parallel (in the same apparatus). In parallel, 25 ng of human recombinant ANXA2 (Abcam, ab93005) was loaded as a positive control. Each immunoblot was probed firstly with either anti-ANXA2 Ms mAb (1:500) or anti-ANXA2 Rb pAb (1:1000), anti-S100-A11 pAb (1:1000) and anti-β-actin mAb (1:5000).

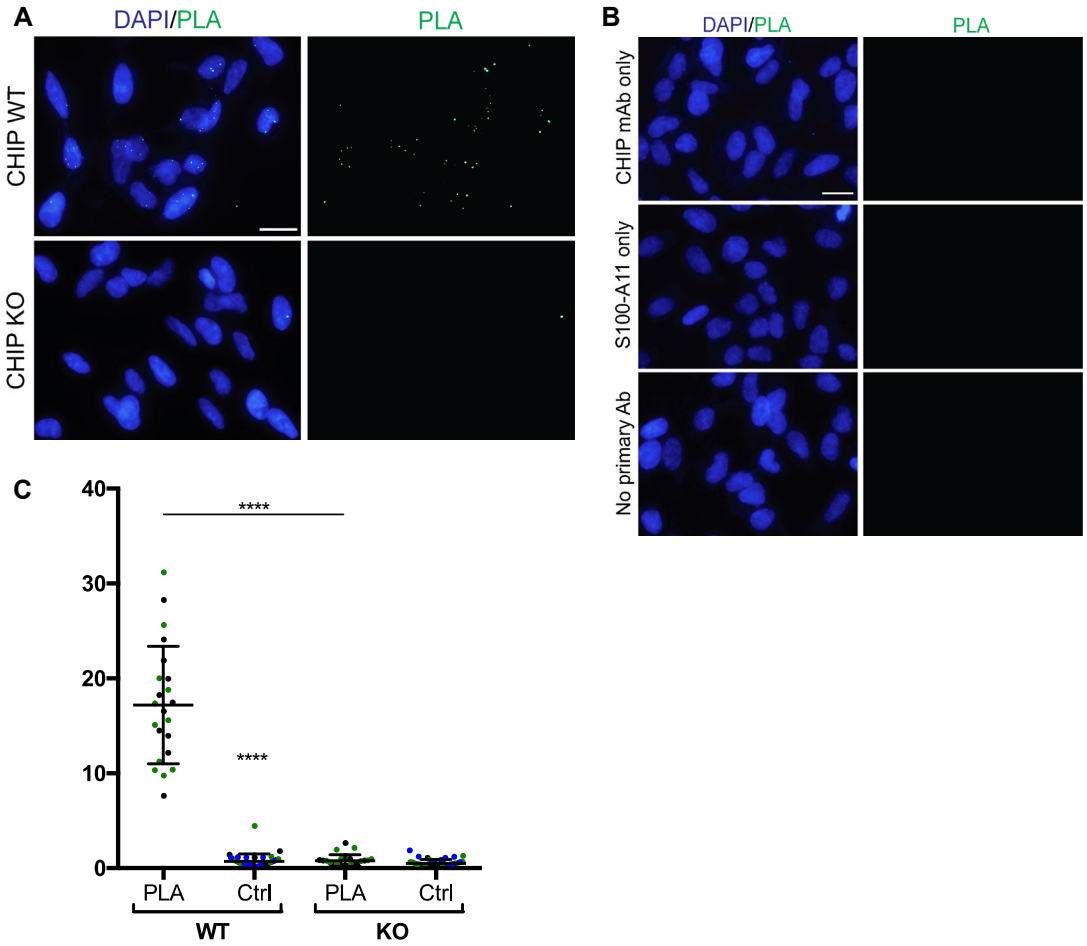


**Figure S.11: S100-A11 & CHIP interaction by PLA in undifferentiated SH-SY5Y**
**A, B, D)** Undifferentiated SH-SY5Y CHIP WT and KO cells were fixed with 4% PFA.
**A)** For each cell line, duplicate wells were stained with anti-S100-A11 pAb (1:500) and anti-CHIP mAb antibodies (1:1000) (referred to as "PLA" in **C** and biological duplicates are colour-coded with black or green dots). PLA signal (puntae in green) were quantified using ImageJ in a semi-automated manner and normalised by the number of nuclei (stained with DAPI) within a field of view.
**B)** In parallel, three controls were included (grouped under "Ctrl" in **C**): wells containing CHIP WT cells were incubated with either antibodies alone (CHIP only in green and S100-A11 only in blue) or with no primary antibodies (in black).
**C)** Quantifications of PLA signal per nuclei of different cell lines represented in the dot plot as mean ± SD. Kruskal-Wallis test and Dunn's multiple comparisons post-test (comparisons between PLA and Ctrl conditions per cell line is indicated above each Ctrl), ****$P < 0.0001$, $n \geq 11$ images per biological duplicate and $n \geq 11$ images per control condition per cell line.
Axio Imager, *Zeiss*, 63x objective (**A&B**). Scale bar, 20 μm.

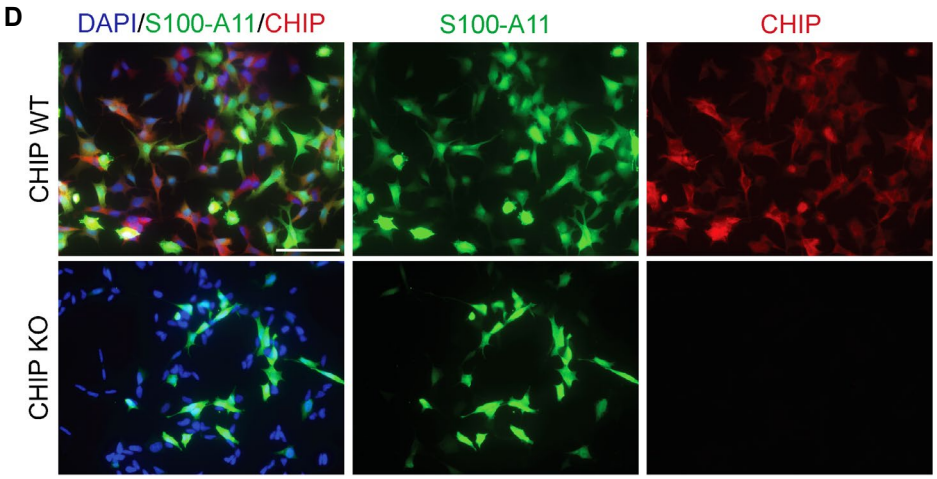


**Figure S.11** *(continued)*
**A, B, D)** Undifferentiated SH-SY5Y CHIP WT and KO cells were fixed with 4% PFA.
**D)** Parallel to wells were treated in the same way and used for IF rather than PLA, using the same antibodies.
Axio Imager, *Zeiss*, 20x objective. Scale bar, 100 μm.

# Appendix II

This appendix supports Chapter 6: Modulating the activity of CHIP using single-chain antibodies.

## Generation of ScFv intrabodies to modulate endogenous CHIP activity in cell models

### a. Cloning of tagged scFv into nanobodies for delivery

Based on the sequence of 11F scFv, I designed two DNA inserts where the scFv was C-terminally tagged with either V5 or 3xFLAG tags (Figure S.14). Host plasmids carrying the inserts were cleaved (Figure S.13A) and the inserts were introduced to a mammalian expression cassette, pSF-CMV (Figure S.13B & Figure S.14). For validation purposes, the DNA from competent cells transformed with the ligation products was digested again with the restriction enzymes to confirm the size of the insert (Figure S.13C). The sequence of the insert was confirmed by sequencing the DNA extracted from some colonies.


**Figure S.12: DNA encoding 3xFLAG- and V5-tagged 11F scFv antibodies**
A SGSG linker between the protein and tag was added to enhance flexibility and aid detection of the tag. An extra alanine was added as well to prevent methylation. Two restriction enzyme (RE) sequences were added at either end of the DNA (5' BamHI and 3' XbaI) although the REs that will be used are NcoI and XbaI, because the sequence for the former RE is created by the sequence for BamHI together with the start of the coding region of 11F, thus preventing frameshift mutations.

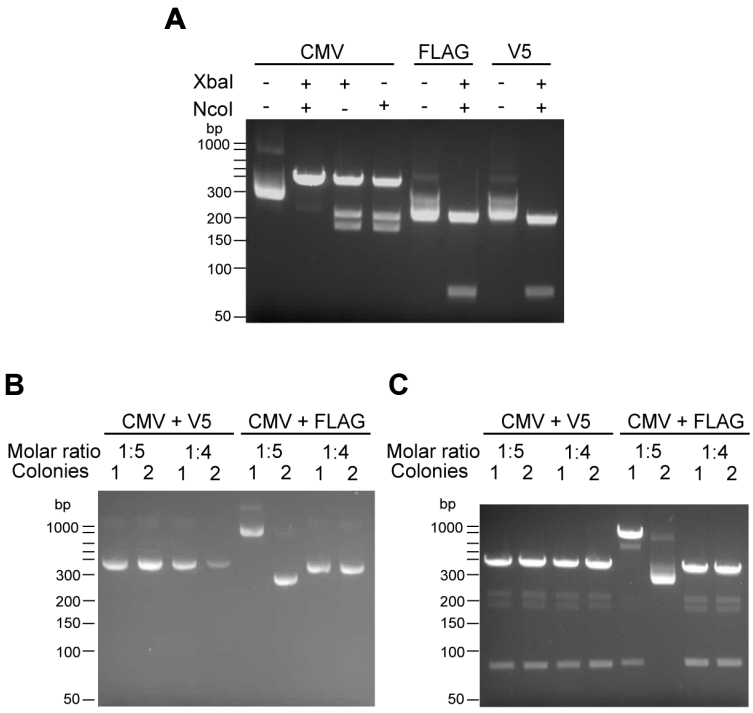


**Figure S.13: Generation of the tagged scFv 11F plasmid for mammalian expression**
**A)** The products of the double digestion of the holding plasmids (encoding 3xFLAG-tagged and V5-tagged 11F) and pSF-CMV plasmid with restriction enzymes (XbaI and NcoI) were resolved on a 1% agarose gel.
**B&C)** Ligation products were used to transform competent cells and their DNA was extracted. A fraction of the DNA was resolved on a 1% agarose gel undigested (**B**) and digested (**C**).

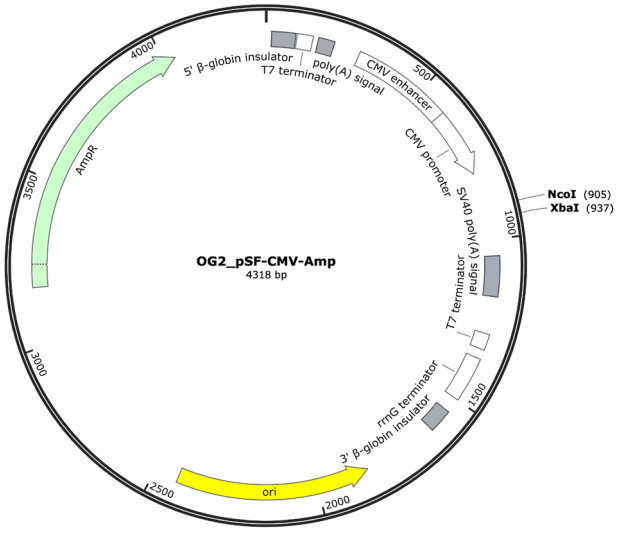


**Figure S.14: Mammalian expression vector used for the expression of nanobodies in cells**
pSF-CMV includes kozak consensus sequence to promote expression.

### b. Optimisation of scFv transfection into cells

Once generated, the scFv encoding plasmids (11F_V5 and 11F_FLAG) were used to transfect a neuroblastoma cell line, SH-SY5Y (Figure S.15). Control cells were transfected with the an empty pSF-CMV plasmid. The expression of the scFv antibodies obtained when using different transfection methods (electroporation and attractene) was evaluated by WB. Both 11F_V5 and 11F_FLAG yielded a band at around 35 kDa when transfected into cells using attractene. This suggests that the scFv antibodies are expressed intracellularly, although whether they are correctly folded and functional remains to be investigated.

### c. Effect of scFv transfection in the homeostasis of CHIP

In order to capitalise on the scFv as tools to manipulate CHIP structure and function *in situ*, cell deliverable nanobodies have been generated and expressed in mammalian cells. These induce the intracellular expression of tagged scFv (Figure S.15A), having several applications.

Since the aim of generating scFv antibodies was to manipulate the activity and interactome of CHIP in cells, rather than causing bulk changes in CHIP homeostasis (e.g. impair its turnover), the expression levels of CHIP in cells transfected with the scFv antibodies was evaluated (Figure S.15B). The immunoblot suggests that CHIP steady state levels are not affected by scFv transfection, although these are only preliminary result. If confirmed, any proteomics changes subsequently observed when scFv is expressed are likely to be due to scFv-mediated regulation of CHIP activity, rather than due to changes to its protein levels.

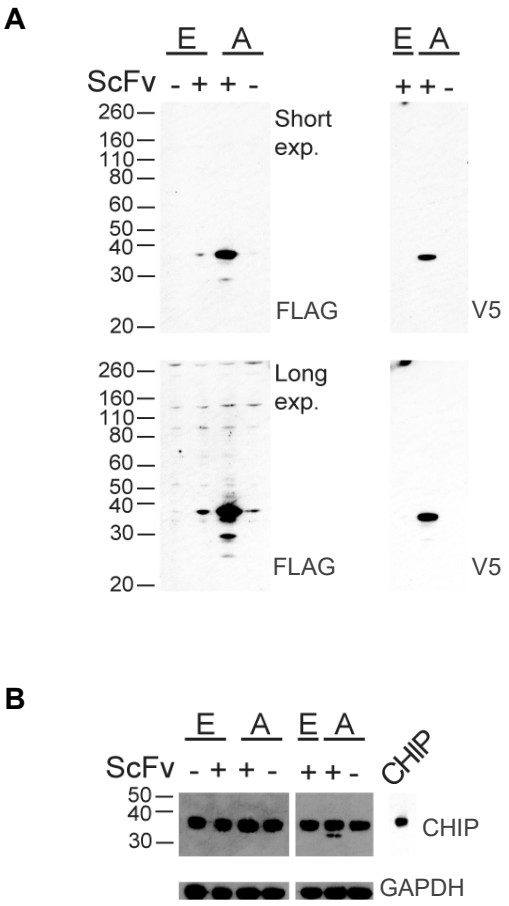


**Figure S.15: ScFv intrabodies**
Cells lysates of WT and CHIP KO SH-SY5Y cells previously transfected with 3xFLAG- and V5-tagged 11F scFv and trasnfected after 24 h were analysed using precast gradient gels (4-12 % Bis-Tris Gels, Invitrogen) SDS-PAGE/WB (40 μg per sample was loaded). As a positive control, purified CHIP dimer (3.7 ng) was loaded alongside the samples. E, electroporation used for transfection, A, attractene used for transfection.
**A)** Immunoblots was probed with either anti-FLAG mAb (1:1000) or anti-V5 mAb (1:1000).
**B)** Subsequently, immunoblots were probed with anti-CHIP mAb (1:10000) and anti-GAPDH mAb (1:5000).